

## Vol. 80 Commemorative Accounts Award Accounts

The Chemical Society of Japan Award for 2003

### Development of Conductive Organic Molecular Assemblies: Organic Metals, Superconductors, and Exotic Functional Materials

Gunzi Saito\* and Yukihiro Yoshida

Division of Chemistry, Graduate School of Science, Kyoto University, Sakyo-ku, Kyoto 606-8502

Received May 16, 2005; E-mail: saito@kuchem.kyoto-u.ac.jp

We introduce the development of conductive organic molecular assemblies including organic metals, superconductors, single component conductors, conductive films, and conductive liquids, particularly focusing on our own research achievements of molecular design within the framework of both real and energy spaces.

#### 1. Introduction: Background of Electric Conductivity

Figure 1 compares the room temperature (RT) electric conductivity ( $\sigma_{\text{RT}}$ ) of organic and inorganic materials. One may classify the materials as a metal ( $\sigma_{\text{RT}} \geq 10^2 \text{ S cm}^{-1}$ ), semiconductor ( $10^2 \geq \sigma_{\text{RT}} \geq 10^{-10} \text{ S cm}^{-1}$ ), and insulator ( $\sigma_{\text{RT}} \leq 10^{-10} \text{ S cm}^{-1}$ ). Some selected organic conductors of charge-transfer (CT) type and of single component are presented. Their chemical formulas are depicted in Fig. 2. The organic solids of CT complexes now cover almost the whole range of  $\sigma_{\text{RT}}$  up to  $10^5 \text{ S cm}^{-1}$ . Among them it is noteworthy that the organic superconductors consisting of TMTSF or ET molecules are poor metals at RT. Some of them exhibit the  $\sigma_{\text{RT}}$  as small as  $10^0 \text{ S cm}^{-1}$  with metallic or sometimes semiconductive temperature dependence. The single component organic conductors, where the transition-metal coordination compounds are not included, cover up to  $10^{-1} \text{ S cm}^{-1}$  with semiconductive behavior.

Electric conductivity is represented by Eq. 1, where  $n$ ,  $e$ , and  $\mu$  are the carrier density ( $\text{cm}^{-3}$ ), charge of electron, and carrier mobility ( $\text{cm}^2 \text{ V}^{-1} \text{ s}^{-1}$ ), respectively.

$$\sigma = ne\mu. \quad (1)$$

The  $n$  and  $\mu$  are controllable through the chemical and physical methods as described in this review. For example,  $n$  is represented by Eq. 2 based on a band model for semiconductors or insulators,

$$n \propto \exp(-\mathcal{E}_{\text{g}}/2k_{\text{B}}T), \quad (2)$$

where  $k_{\text{B}}$  is the Boltzmann constant and  $\mathcal{E}_{\text{g}}$  is the energy gap. The  $\mathcal{E}_{\text{g}}$  of a solid composed of single component molecules or CT complexes having a closed shell electronic structure (Fig. 3) is then expressed by Eq. 3,

$$\mathcal{E}_{\text{g}} = \Delta E - 2(t_1 + t_2), \quad (3)$$

where  $\Delta E$  is the HOMO–LUMO gap, and  $t_1$  and  $t_2$  are the in-

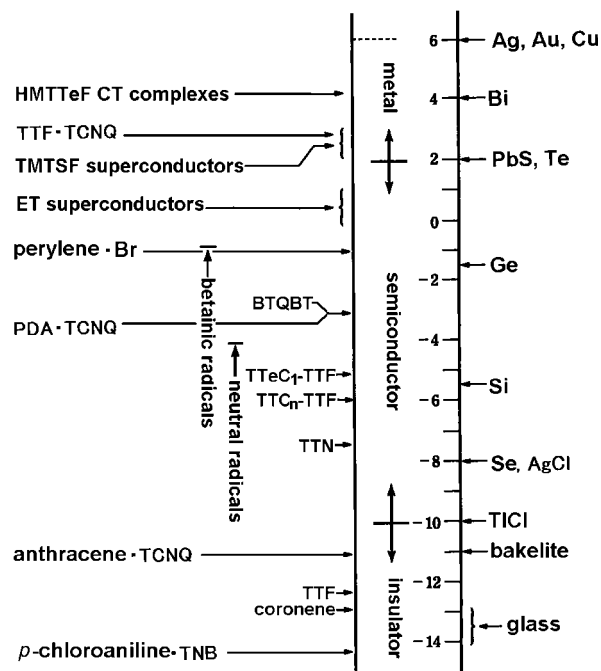


Fig. 1. The room temperature conductivity ( $\text{S cm}^{-1}$ ) is compared between inorganic solids (right) and organic (charge transfer and single component) solids (left). HMTTeF: hexamethylenetetrafulvalene, TTF: tetrathiafulvalene, TCNQ: tetracyano-*p*-quinodimethane, TMTSF: tetramethyltetraselenafulvalene, ET: bis(ethylenedithio)-TTF (BEDT-TTF), BTQBT: bis(1,2,5-thiadiazolo)-*p*-quinobis(1,3-dithiole), PDA: *p*-phenylenediamine, TTeC<sub>1</sub>-TTF: tetrakis(methyltelluro)-TTF, TTC<sub>n</sub>-TTF: tetrakis(alkylthio)-TTF, TTN: tetrathionaphthacene (naphthaceno[5,6-*c,d*:11,12-*c',d'*]bis[1,2]dithiole), TNB: *s*-trinitrobenzene.

termolecular or inter-complex (between DA pairs) transfer integrals of HOMOs and LUMOs, respectively. Therefore, the

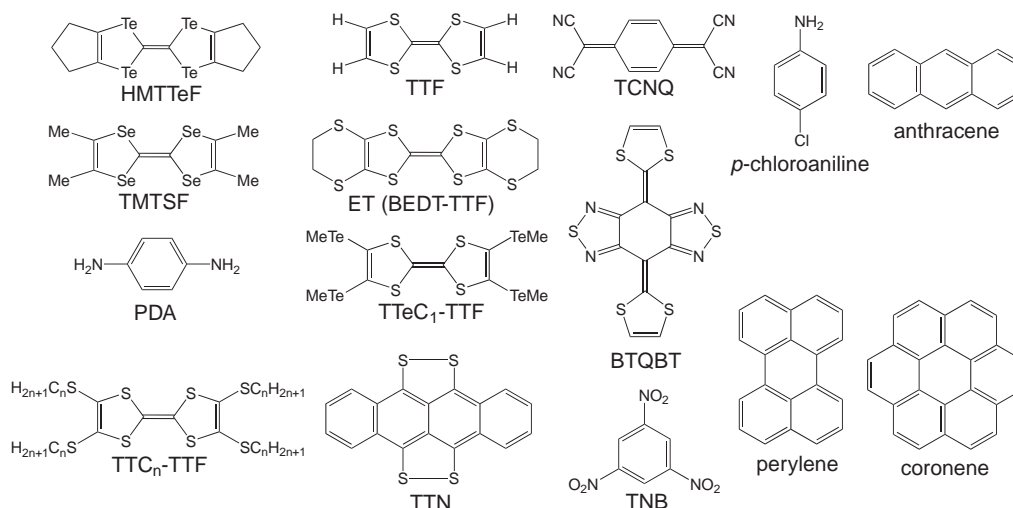


Fig. 2. Chemicals in Fig. 1.

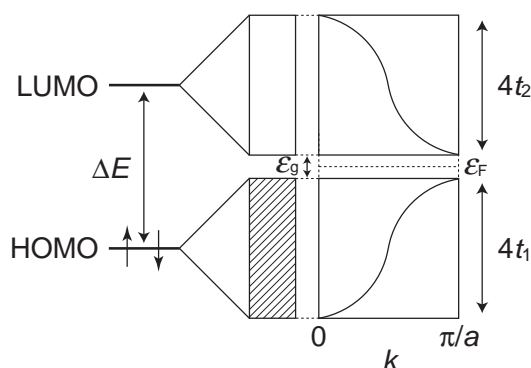


Fig. 3. Schematic energy dispersion (right) of the band structure of the crystal (middle) composed of a one-dimensional array of neutral closed shell molecules with HOMO–LUMO gap of  $\Delta E$  (left), where  $k$ ,  $\epsilon_g$ ,  $\epsilon_F$ ,  $4t_1$ , and  $4t_2$  are the wavenumber, energy gap, Fermi energy, and bandwidths of valence and conduction bands, respectively.

carrier density can be tuned by the modification of  $\Delta E$ ,  $t_1$ ,  $t_2$ , and  $T$  for semiconductors and insulators.

According to the tight binding approximation, the  $\mu$  can be represented by Eq. 4 for a one-dimensional (1D) array composed of molecules with an interplanar distance of  $a$ , indicating that the mobility is proportional to  $\tau t$ , where  $\tau$  is the relaxation time.

$$\mu = 2a^2 e \tau t \cos ka / \hbar^2 \propto \tau t. \quad (4)$$

$\tau$  depends on the scattering mechanism of the system, and is inversely proportional to the product of density of states at Fermi level  $D(\epsilon_F)$  and the square of scattering potential  $V_s$  (Eq. 5). Since  $D(\epsilon_F)$  is equal to  $N/2\pi t \sin ka$ ,  $\tau$  is represented by Eq. 5, where  $N$  is the total number of electrons in the band.

$$\tau \propto \frac{1}{D(\epsilon_F) |V_s|^2} = \frac{2\pi t \sin ka}{N |V_s|^2} \propto t. \quad (5)$$

Although there are many kinds of retarding sources such as phonon, impurity, non-periodicity in the lattice, on-site Coulomb repulsive energy, molecular vibration, etc.,  $\tau$  can be roughly proportional to a bandwidth  $W$ , which is equal to

$4t$  for 1D conductors and the  $t$  is approximately proportional to an overlap integral  $S$ .

Therefore, the conductivity of organic CT solids has been improved through the design of the structures in the real space (molecular and crystal structures) and also those in the energy space (molecular and band electronic structures). Depending on the itinerancy of electrons in the molecular assemblies, the system varies from semiconductor (insulator) to metal including exotic magnets originating from the localized spins. Under a certain condition, the system becomes a superconductor owing to the formation of Cooper pairs.

Our research interests<sup>1–10</sup> have straddled a number of conductive and magnetic organic assemblies including organic metals, superconductors, spin-ladders, spin-liquid, etc. (Fig. 4). The control of the chemical and physical parameters for electric transport, such as ionization potential ( $I_p$ ), electron affinity ( $E_A$ ), Madelung energy ( $M$ ), on-site ( $U$ ) and off-site ( $V$ ) Coulomb energies, density of state ( $D(\epsilon)$ ), Fermi level ( $\epsilon_F \approx$  chemical potential), bandwidth ( $W$ ), transfer interaction ( $t$ ), basicity ( $pK_b$ ), and acidity ( $pK_a$ ), which are controllable through the molecular and crystal designs mentioned above, is fundamental to the progress of organic (super)conductors. The control of the self-assembling ability, dimensionality, electron correlation, and geometry of the spin lattice is very important to design the ground state of the electronic structure (e.g., superconductor, metal, insulator, antiferromagnet, and spin-liquid). The anisotropic electronic structures of organic assemblies having very deformable molecular and crystal structures with strong electron–phonon coupling have afforded many fascinating electronic phase transitions caused by molecular and/or lattice deformation, charge separation (charge ordering), density wave formation, etc., which can be controlled by external stimuli: light, temperature ( $T$ ), pressure ( $P$ , hydrostatic or uni-axial), magnetic ( $H$ ), and electric ( $E$ ) fields. These features are demonstrated in Fig. 4 and will be described in detail in this review.

## 2. Conductors of Single Component

In general, single component compounds composed of organic molecules are poor conductors even if they have radical

## Development of Organic Metals, Superconductors, and Exotic Magnets (electrons in a soft, anisotropic, and nano-scale molecular world)

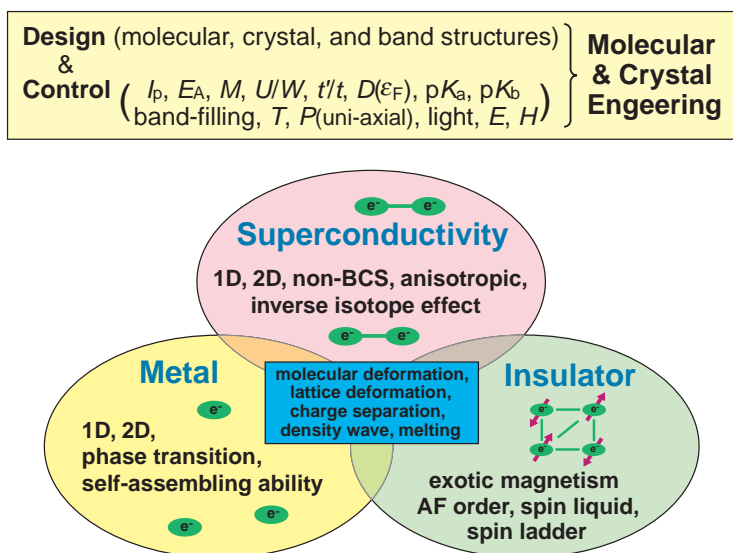
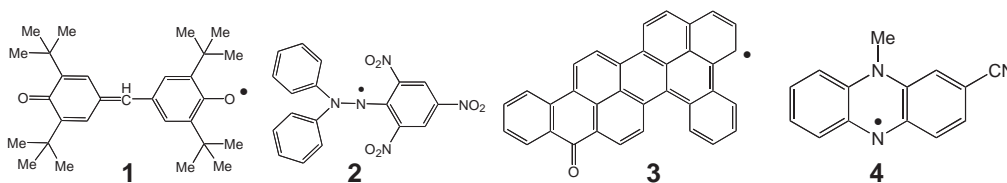


Fig. 4. Concept of the development of organic metals, superconductors, and exotic magnets is based on the dynamics of electrons in a soft, anisotropic, and nano-scaled molecular world. For inorganic electronics, charge, spin, and orbital are the three key issues. For organic materials, on the other hand, softness (lattice and molecular) and internal freedom (molecular vibration, deformation, and polarizability) should be taken into account additionally. Other keywords in Fig. 4 will be explained in the text.

Table 1. Transport Properties of Selected Single Component Compounds Composed of Neutral Radicals

Molecule	$\sigma_{RT}/\text{S cm}^{-1}$	$\epsilon_g/\text{eV}$	Ref.
<b>1</b> Galvinoxyl	$1.9 \times 10^{-11}$ (364 K)	1.36	11
<b>2</b> DPPH (radical content = 90%)	$1 \times 10^{-10}$	1.5	12
<b>3</b> Violanthrone B (radical content = 36%)	$1.4 \times 10^{-7}$	0.68	13
<b>4</b> 2-Cyano-10-methyl-5-phenazyl	$3 \times 10^{-7}$	0.72	14



electrons. Table 1 summarizes the  $\sigma_{RT}$  and  $\epsilon_g$  of selected neutral radicals. Galvinoxyl (**1**) and 1,1-diphenyl-2-picrylhydrazyl (DPPH, **2**) radicals are stabilized by the introduction of steric substituent groups, resulting in the spatial isolation of radical electrons, and hence they are insulating.<sup>11,12</sup> Violanthrone B (**3**) and 2-cyano-10-methyl-5-phenazyl (**4**) are planar molecules and the radicals are stabilized by the large  $\pi$ -moiety with a non-bonding orbital for the former<sup>13</sup> and by the capto-dative (or push-pull) effect for the latter.<sup>14</sup> The planarity of a molecule is an important factor to increase the overlap integrals  $S$  between molecules in an assembly, giving rise to the conceivable conductivity (Eq. 6). However, the poor conductivity of **3** and **4** indicates that the transfer integral  $t$  is not much improved.

$$\sigma \propto S^2 \propto t^2. \quad (6)$$

Several organic and metal coordination compounds have been reported to be highly conductive or metallic under ambi-

ent conditions or in FET (field-effect transistor) systems. Superconductivity has also been reported for some materials under pressure. The first point to be mentioned for the single component conductors is that the materials examined should be very pure. However, conventional organic materials are not highly pure compared with the inorganic ones since purification methods such as zone-melting cannot be applied except for a few compounds (benzene, naphthalene, anthracene, pyrene, perylene, etc.<sup>15</sup>). The contamination with impurity will deteriorate the intrinsic nature of the single component conductors. Apart from organic impurity, moisture and oxygen molecules affect the intrinsic transport properties. It is known that oxygen molecules act as electron acceptor forming CT complexes with many donor molecules such as polycyclic aromatic hydrocarbons, aromatic amines, phthalocyanine(Pc) (Chart 1), TTFs, etc. (vide infra).

There have been several reports on conductivity measurements under inappropriate conditions. The readers should be

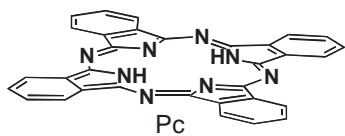


Chart 1.

careful about the reported results: 1) How was the sample purified and characterized to be a truly single component? Among several conventional methods to characterize compounds (optical, EPR, NMR, elemental analysis, EPMA, X-ray diffraction analysis, etc.), elemental analysis (should be in agreement with the calculated values within an error of 0.3%) is currently the most accurate quantitative way to check the purity of a single component bulk solid, although the purity is at most  $[100 - 0.3 \times (\text{number of elements})\%]$ . 2) In what kind of conditions was the conductivity measured? The intrinsic transport properties should be elucidated by the four-probe method using inert paste or by a contactless method, under an inert atmosphere. 3) Supporting information for the metallic nature such as magnetic susceptibility, plasma absorption, or thermoelectric power is indispensable.

**2.1 High Pressure.** Early in the 60s, the electric conductivity of several organic compounds, especially polycyclic aromatic hydrocarbons, was studied under hydrostatic pressure by Drickamer and Samara.<sup>16</sup> In most cases, a rapid decrease in resistivity was observed at the initial stage of pressuring, followed by a gradual decrease and ultimately a plateau of resistivity above ca. 30 GPa. Pentacene is the first organic metal and showed a decrease in resistivity down to ca. 200 K at 21.3 GPa.<sup>17</sup> The activation energy eventually goes to zero at 27.0 GPa for a single crystal. Besides aromatic hydrocarbons, compounds having a large  $\pi$ -moiety, such as Pc,<sup>18</sup> and compounds having heavy atoms at the peripheral positions such as tetratelluronaphthalene (tetracene) (naphthaceno[5,6-*c,d*:11,12-*c',d'*]bis[1,2]diselenole) (TSeN or TSeT, **5**),<sup>19–22</sup> *p*-iodanil (tetraiodo-*p*-benzoquinone) (**6**)<sup>23–25</sup> and BTQBT (**12**)<sup>26,27</sup> have been investigated since the 70s by Shirotani and Inokuchi et al. Under hydrostatic pressure, these compounds show a rapid decrease in resistivity and become good conductors. For example, *p*-iodanil is an insulator ( $\sigma_{\text{RT}} = 1 \times 10^{-12} \text{ S cm}^{-1}$ ) at ambient pressure and becomes conductive under pressure ( $\sigma_{\text{RT}} = 2 \times 10 \text{ S cm}^{-1}$  at 25 GPa).<sup>23–25</sup> TSeN was reported to be highly conductive ( $\sigma_{\text{RT}} = 1 \times 10^{-4} \text{ S cm}^{-1}$ ,  $\epsilon_g = 0.32 \text{ eV}$ ) at ambient conditions.<sup>19,20</sup> However, it appears that the good conductivity is due to the formation of a CT complex with oxygen as mentioned above, and the conductivity under vacuum ( $133 \times 10^{-8} \text{ Pa}$ ) is  $8 \times 10^{-7} \text{ S cm}^{-1}$  with twice the energy gap ( $\epsilon_g = 0.64 \text{ eV}$ ). By applying a pressure of 20 GPa under a nitrogen atmosphere, TSeN begins to show high conductivity ( $\sigma_{\text{RT}} = 1 \times 10 \text{ S cm}^{-1}$ ).<sup>21,22</sup> Tetratelluronaphthalene (tetracene) (naphthaceno[5,6-*c,d*:11,12-*c',d'*]bis[1,2]ditellurole) (TTeN or TTeT, **7**) also shows a fairly high conductivity ( $\sigma_{\text{RT}} = 1 \times 10^{-4} \text{ S cm}^{-1}$ ), although the measurement conditions are not clear.<sup>28</sup>

HMTTeF shows a very rapid decrease in resistivity at the initial pressure range followed by a gradual decrease above 10 GPa, but no metallic phase is expected to appear by applying further pressure (Fig. 5b).<sup>29</sup> Since HMTTeF molecules are connected to each other with two kinds of alternating intermo-

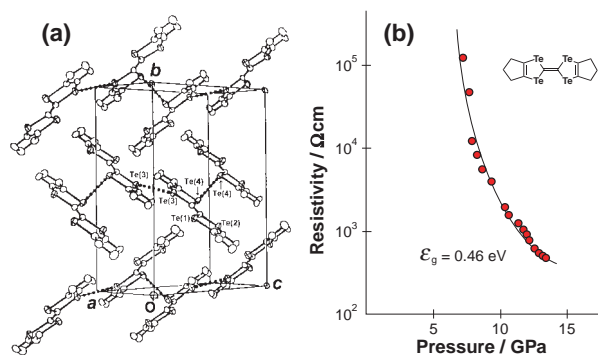


Fig. 5. (a) Crystal structure of HMTTeF by Carroll et al. indicating two kinds of short Te...Te atomic contacts (Te(3)...Te(3): 3.583 Å, Te(4)...Te(4): 3.743 Å).<sup>30</sup> Monoclinic,  $P2_1/c$ ,  $a = 6.623(2)$ ,  $b = 17.760(2)$ ,  $c = 12.859(3)$  Å,  $\beta = 99.05(3)^\circ$ ,  $Z = 4$ ,  $R = 0.035$ . (b) Pressure dependence of resistivity of HMTTeF solid.<sup>29</sup> The line is a guide to the eye. A high conductivity of  $2 \times 10^{-4} \text{ S cm}^{-1}$  ( $\epsilon_g = 0.08 \text{ eV}$ ) has also been reported on a single crystal of HMTTeF.<sup>31</sup>

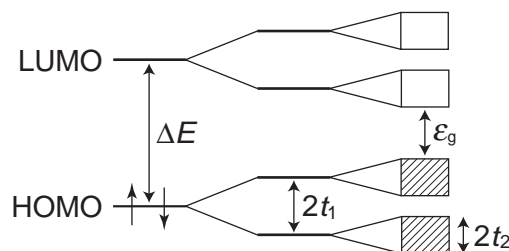


Fig. 6. Energy levels of a monomer (left), a dimer (middle), and band structure of dimerized system (right) with intra- and inter-dimer transfer interactions of  $t_1$  and  $t_2$ , respectively, and the energy gap  $\epsilon_g \approx \Delta E - 2(t_1 + t_2)$ .

lecular Te...Te atomic contacts (3.583 and 3.743 Å) in the crystal (Fig. 5a),<sup>30</sup> it is apparent that the system is composed of a dimer of HMTTeF molecules. The band structure is schematically represented by Fig. 6, where  $t_1$  and  $t_2$  are the intra- and inter-dimer transfer interactions, respectively. It is reasonable to predict that the energy gap  $\epsilon_g$  of the dimerized system is very difficult to be suppressed by applying a pressure compared to that of the uniform system since the dimerized system has additional energy associated with lattice distortion.

The development of the diamond anvil cell (DAC) method has provided a means of extremely high pressure, and the method has been applied to several organic compounds. Among them, *p*-iodanil (**6**) and hexaiodobenzene (**8**) were found to exhibit metallic (semimetallic) and superconducting nature under extremely high pressure by Shirotani, Shimizu, Amaya, et al.<sup>23–25,32</sup> *p*-Iodanil becomes metallic above 35 GPa and exhibits superconductivity with a critical temperature ( $T_c$ ) of about 2 K at around 52 GPa.<sup>24,25</sup> The  $T_c$  of hexaiodobenzene is 0.6–0.7 K at around 33 GPa and increases to about 2.3 K at around 58 GPa.<sup>32</sup> Although no details of the purity of the compounds were described in the papers<sup>23–25,32</sup> and a few % of impurities (such as bromotriiodo-*p*-benzoquinone) may be included in the *p*-iodanil examined,<sup>9</sup> it seems that such a specific impurity does not severely affect the transport property of

Table 2. Selected Examples of Organic (Super)conductors under Pressure

Molecule	$\sigma_{RT}/S\text{ cm}^{-1}$	$\varepsilon_g/\text{eV}$	Characteristics	Ref.
Pentacene	$3 \times 10^{-14}$	1.5	ambient conditions	17
	metallic		21.3 GPa	17
5 <sup>a)</sup> TSeN	$1 \times 10^{-4}$	0.32	ambient conditions	19–22
	$8 \times 10^{-7}$	0.64	$133 \times 10^{-8}$ Pa	21,22
	$1 \times 10$		20–50 GPa	21,22
6 <i>p</i> -Iodanil	$1 \times 10^{-12}$	1.37	ambient conditions	21–25
	$2 \times 10$		25 GPa	23–25
	metallic		35 GPa	23–25
	superconducting		52 GPa, $T_c \approx 2$ K	23–25
8	$10^{-14}$	1.6	ambient conditions	23
	metallic		35 GPa	32
	superconducting		33 GPa $T_c = 0.6$ – $0.7$ K	32
			58 GPa, $T_c = 2.3$ K	32

a) Compaction pellet.

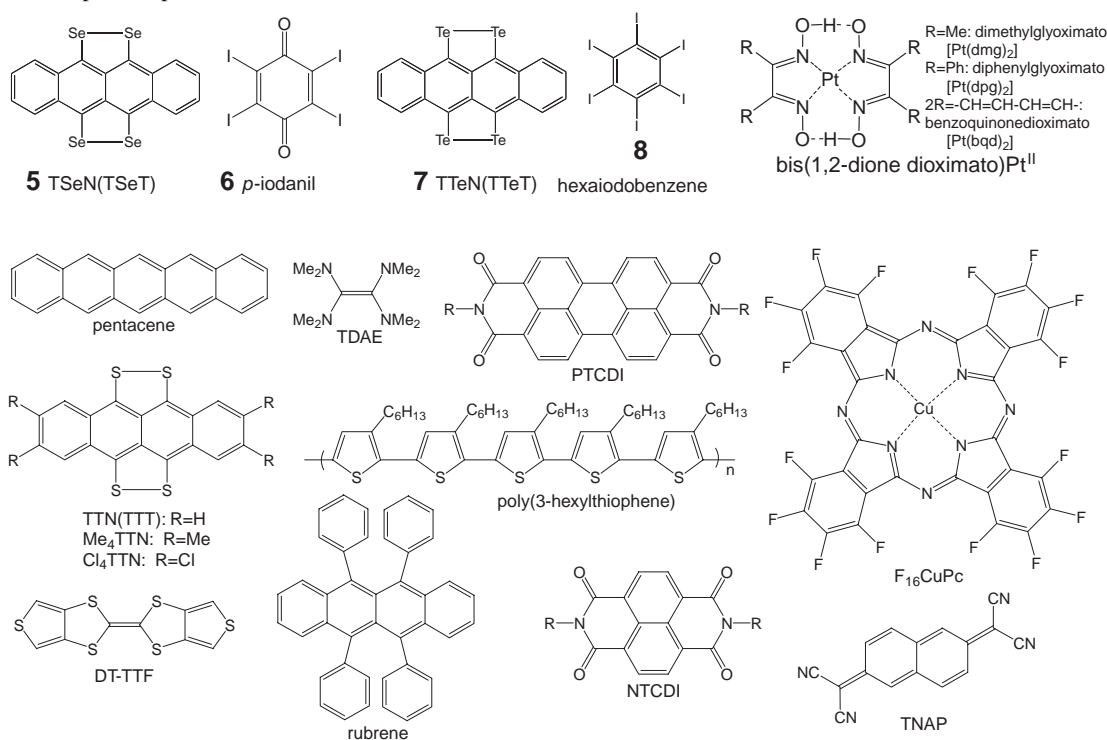


Chart 2.

*p*-iodanil since both are structurally similar electron acceptors with rather similar electron affinities.

Some metal complexes of [bis(1,2-dione dioximato)Pt<sup>II</sup>] exhibited an insulator–metal–semiconductor transition under pressure.<sup>33,34</sup> A continuous color change was observed in [bis(diphenylglyoximato)Pt<sup>II</sup>]<sup>35</sup> under pressure, and thus has been used as a pressure indicator.

## 2.2 Field Effect Transistors (FET). 2.2.1 p-Type FET:

Historically, the characteristic behaviors of FETs were observed on polythiophene in 1987.<sup>36</sup> A tutorial review article has been published.<sup>37</sup> FETs based on p-type compounds such as pentacene,<sup>38</sup> poly(3-hexylthiophene),<sup>39,40</sup> and oligothiophenes<sup>41</sup> in which holes are the major carriers, have received the most attention (Chart 2). The FET mobility of pentacene has been estimated to be  $1.5\text{ cm}^2\text{ V}^{-1}\text{ s}^{-1}$  or more, which is comparable to that of amorphous silicon. However, such high

mobility might be caused by the presence of oxygen. High FET mobilities have also been reported for naphthalene derivatives, i.e.,  $1$ – $3\text{ cm}^2\text{ V}^{-1}\text{ s}^{-1}$  for single crystals of naphthalene and 5,11-dichloronaphthalene,<sup>42</sup> and thin films of tetrachalcogenonaphthalenes (naphthaleno[5,6-*c,d*:11,12-*c',d'*]bis[1,2]dichalcogenoles) (TTN, TSeN, and TTeN) and its derivatives (Me<sub>4</sub>TTN and Cl<sub>4</sub>TTN),<sup>43</sup> and ca. 8 and ca.  $15\text{ cm}^2\text{ V}^{-1}\text{ s}^{-1}$  for a rubrene single crystal<sup>44</sup> and that on a flexible poly(dimethylsiloxane),<sup>45</sup> respectively. An FET fabricated from TMTSF, which has been comprised in many quasi 1D organic superconductors (see 3.3.1), shows a relatively high FET mobility of  $0.2\text{ cm}^2\text{ V}^{-1}\text{ s}^{-1}$ .<sup>46</sup> The value of  $1.4\text{ cm}^2\text{ V}^{-1}\text{ s}^{-1}$  has been reported for single crystals of DT-TTF by drop casting.<sup>47</sup> Also, random arrays of single-wall carbon nanotubes (SWNTs) grown on silicon wafer show an extraordinarily high mobility up to  $270\text{ cm}^2\text{ V}^{-1}\text{ s}^{-1}$ .<sup>48</sup>



However, it is uncertain whether all the reported FET mobilities of organic materials are intrinsic. For the data on films, the film morphology, grain boundaries, and roughness of the surfaces affect the mobilities apart from the purity of the materials, incorporated solvent, and physically adsorbed oxygen and water. Only the data on well-characterized single crystals measured under well characterized circumstances are reliable. Also, it should be noted that the highly conductive materials of single component (next section) or CT complexes do not exhibit FET characteristics owing to the poor on/off ratio.

**2.2.2 n-Type FET:** n-Channel compounds into which negative carriers can be injected are much rarer. The most useful compound is perfluorinated copper phthalocyanine  $F_{16}CuPc$ , which is the only n-type single component organic FET that is stable in air and also has a mobility greater than  $10^{-2} \text{ cm}^2 \text{ V}^{-1} \text{ s}^{-1}$ , although it requires vacuum deposition on substrates heated above  $100^\circ\text{C}$ .<sup>49</sup> Fullerenes  $C_{60}$ ,  $C_{70}$ , and  $C_{84}$  have shown relatively high mobilities of  $8 \times 10^{-2}$ ,<sup>50</sup>  $2 \times 10^{-3}$ ,<sup>51</sup> and  $2.1 \times 10^{-3} \text{ cm}^2 \text{ V}^{-1} \text{ s}^{-1}$ ,<sup>52</sup> respectively, but their performances degrade upon exposure to air. Under a high vacuum without exposure to air, the mobility of  $C_{60}$  increases up to  $0.56 \text{ cm}^2 \text{ V}^{-1} \text{ s}^{-1}$ .<sup>53</sup> Interestingly, treatment of the device with tetrakis(dimethylamino)ethylene (TDAE) results in an increase of the mobility by a factor of 3.<sup>50</sup> Rather high mobilities have also been reported for some FETs fabricated from aromatic hydrocarbon derivatives such as  $N,N'$ -dialkyl-1,4,5,8-naphthalenetetracarboxylic diimide (NTCDI,  $> 0.1 \text{ cm}^2 \text{ V}^{-1} \text{ s}^{-1}$ ),<sup>54</sup> and  $N,N'$ -dioctyl-3,4,9,10-perylenetetracarboxylic diimide (PTCDI,  $0.6 \text{ cm}^2 \text{ V}^{-1} \text{ s}^{-1}$ ).<sup>55</sup> However, these

devices are highly oxygen-sensitive, and thus may not be suitable for practical applications. TCNQ was found to show stable FET performance in air with a maximum mobility as low as  $3 \times 10^{-5} \text{ cm}^2 \text{ V}^{-1} \text{ s}^{-1}$ ,<sup>56</sup> but its extended  $\pi$ -system tetracyano-2,6-naphthoquinodimethane (TNAP) has an increased mobility of ca.  $3 \times 10^{-3} \text{ cm}^2 \text{ V}^{-1} \text{ s}^{-1}$ .<sup>57</sup>

Although the system does not belong to a single component, an n-type FET can be devised in terms of the combination of semiconducting and metallic CT complexes having common acceptor molecules to realize an all organic FET. For example, a device consisting of semiconductive DBTTF·TCNQ crystals ( $\sigma_{\text{RT}} = 4 \times 10^{-8} \text{ S cm}^{-1}$ ) (Chart 3) as channels and metallic TTF·TCNQ thin films as electrodes for carrier injections on top of the crystals shows high mobility (ca.  $1 \text{ cm}^2 \text{ V}^{-1} \text{ s}^{-1}$ ).<sup>58</sup> Such an all organic FET composed of CT complexes has advantages concerning its stability against oxygen, moisture and chemical impurities, and the tunability of the chemical potentials of the organic metal electrodes composed of different TTF derivatives to exhibit n-type, p-type, and bipolar FET characteristics. Superior performance would be expected regarding the on/off ratio by using insulating TCNQ CT crystals with segregated columns as channels.

**2.3 Organic Conductors at Ambient Condition.** These organic compounds are classified into three classes: 1) neutral closed shell molecule, 2) neutral  $\pi$ -radical, and 3) zwitterionic (betainic)  $\pi$ -radical.

**2.3.1 Neutral Closed Shell Molecule:** Since the HOMO of neutral closed shell molecules is occupied by two electrons, they are generally insulating with a large band gap. They have no itinerant carriers at 0 K. The band gap of the system is represented by Eq. 3, and thus the primary attempt is to use a molecule with small  $\Delta E$  (dark colored compound) to decrease  $E_g$ .

In order to increase  $t$ , the van der Waals interactions between alkyl groups have been introduced for  $\text{TXC}_n\text{-TTF}$  ( $X = \text{S}$  ( $\text{TTC}_n\text{-TTF}$ ),  $\text{Se}$  ( $\text{TSeC}_n\text{-TTF}$ ), and  $\text{Te}$  ( $\text{TTeC}_n\text{-TTF}$ ), Figs. 7a and 7b for  $X = \text{S}$ ,  $n = 9$ ) by Inokuchi, Saito,

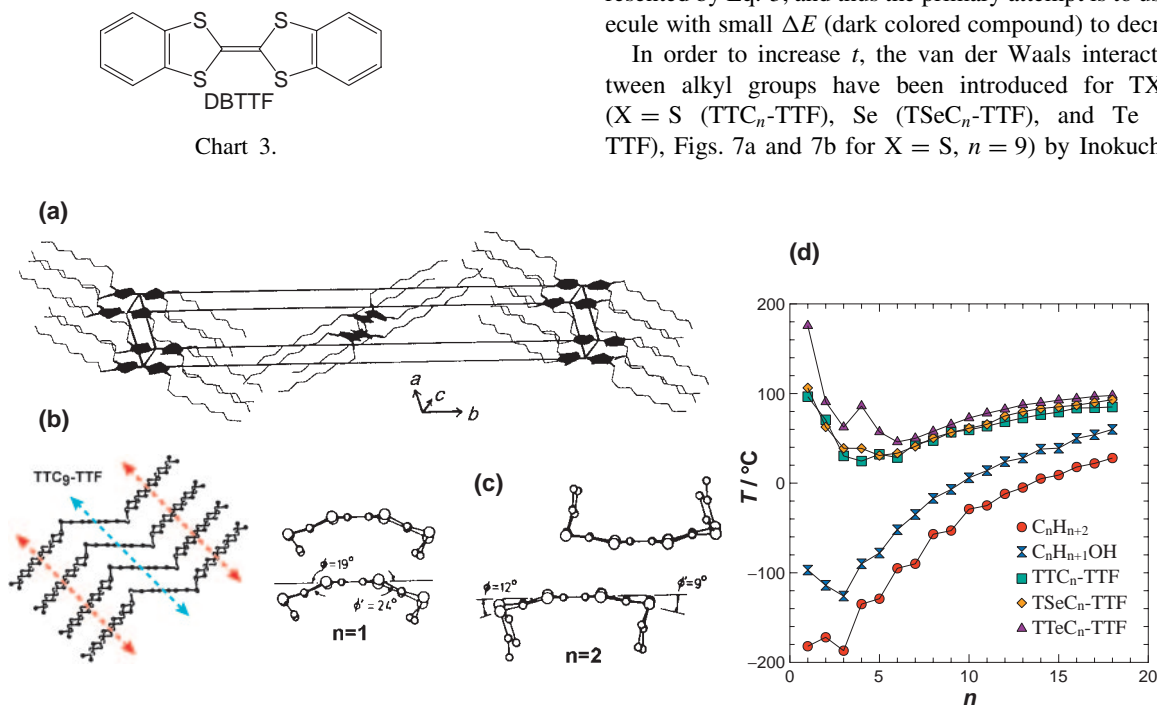


Fig. 7. (a) Crystal structure of  $\text{TTC}_9\text{-TTF}$  where the TTF skeletons are shaded.<sup>61</sup> (b) Stack of  $\text{TTC}_9\text{-TTF}$  molecules where the van der Waals interactions between the alkyl chains (red arrows) fasten the central  $\text{C}_6\text{S}_8$   $\pi$ -moieties of  $\text{TTC}_9\text{-TTF}$  tightly along the direction indicated by blue arrow to enhance the molecular overlap (labeled as fastener effect).<sup>61,62,64,66</sup> (c) Molecular stacking of  $\text{TTC}_1\text{-TTF}$ <sup>59</sup> and  $\text{TTC}_2\text{-TTF}$ <sup>61</sup> molecules in solid. (d) Melting points of  $\text{TXC}_n\text{-TTF}$ <sup>60,63,65,69</sup> are compared with those of alkanes and alkyl alcohols.

Table 3. Melting Point, Conductivity, Energy Gap, Ionization Potential, and Mobility of  $\text{TTC}_n\text{-TTF}^{60-62,64,66,68,69}$ 

$n$	$T_m$ / $^{\circ}\text{C}$	$\sigma_{\text{RT}}^{\text{a)}$ / $\text{S cm}^{-1}$	$\varepsilon_g^{\text{a)}$ /eV	$I_p$ /eV	$\mu$ / $\text{cm}^2 \text{V}^{-1} \text{s}^{-1}$
1	96.5	$3.4 \times 10^{-11}$	0.76	5.05	
2	70.6	$8.3 \times 10^{-11}$	0.58	5.15	
3	30.4	$1.0 \times 10^{-10}$	1.04		
4	24.6	$1.6 \times 10^{-7}$	0.44		
5	32.2	$1.6 \times 10^{-8}$	0.58		
6	28.6	$3.3 \times 10^{-8}$	0.56		
7	44.0	$2.6 \times 10^{-8}$	0.52		
8	47.6	$1.4 \times 10^{-8}$	0.42	4.80	6–7
9	56.8	$2.0 \times 10^{-8}$	0.42	4.65	
10	59.4	$2.7 \times 10^{-6}$	0.26	4.60	9–20
11	63.6	$1.8 \times 10^{-6}$	0.34		
12	68.5	$1.9 \times 10^{-8}$	0.50		
13	72.7	$4.3 \times 10^{-8}$	0.48		
14	76.5	$1.3 \times 10^{-8}$	0.66	4.70	
15	79.3	$3.4 \times 10^{-7}$	0.48		
16	83.6	$1.3 \times 10^{-7}$	0.56		
17	84.1	$6.3 \times 10^{-8}$	0.52		
18	85.0	$1.5 \times 10^{-10}$	0.96	4.85	

a) Single crystals for the compounds with  $n = 1$ –11 and others are compaction pellet samples.

et al.,<sup>59–69</sup> and  $\text{TTC}_n\text{-TTF}$  (**9**) and its related molecule (**10**) by Mori, Misaki, et al.<sup>70,71</sup> In the case of  $\text{TTC}_n\text{-TTF}$  (Table 3), the melting point ( $T_m$ ) decreases appreciably from  $n = 1$  to 4, since the alkyl chains prevent the  $\pi$ – $\pi$  intermolecular interactions between  $\text{C}_6\text{S}_8$  moieties with each other as shown in Fig. 7c for  $n = 1$ <sup>59</sup> and 2.<sup>61</sup> For  $n \geq 4$ , on the other hand, the melting point shows an increase with increasing the length of the alkyl chains (Fig. 7d),<sup>60,69</sup> since the van der Waals interactions between the long alkyl chains fasten the central  $\pi$ -moiety composed of a  $\text{C}_6\text{S}_8$  skeleton tightly. The resulting columnar structure of the  $\pi$ -part enhances  $t$  (Fig. 7b), giving rise to the considerably high conductivity, high mobility, and low ionization potential, even though the redox potentials of  $\text{TTC}_n\text{-TTF}$  ( $E^1_{1/2} = 0.54$ ,  $E^2_{1/2} = 0.78$  eV vs saturated calomel electrode (SCE) in  $\text{CH}_3\text{CN}$ , cf.  $E^1_{1/2} = 0.55$ ,  $E^2_{1/2} = 0.79$  eV for ET) indicates that the electronic properties of an individual molecule do not depend on the length of the alkyl chains. Similar thermal behavior was observed for  $\text{TXC}_n\text{-TTF}$  ( $X = \text{Se}$ ,<sup>65,67</sup>  $\text{Te}$ ,<sup>63,64</sup> Fig. 7d). This kind of peculiar effect observed in solids of  $\text{TXC}_n\text{-TTF}$  with long alkyl chains was labeled as the fastener effect.<sup>61</sup>

A use of heteroatomic contacts (chalcogen...chalcogen, chalcogen...nitrogen) is effective to increase conductivity as observed for  $\text{TTeN}$  by Yagubskii, Neilands, Balodis, et al.,<sup>28</sup>  $\text{TTeC}_1\text{-TTF}$  (Fig. 8) by Inokuchi, Saito, et al.,<sup>72</sup>  $\text{BTQBT}$  (Fig. 2) and  $\text{BTDA-TCNQ}$  (**11**) by Yamashita et al.,<sup>26,27,73</sup> 2,5-bis(methylthio)TCNQ (**12**) by Zambounis et al.,<sup>74</sup> and bis(ethylenethio)-TTF (**13**) by Rovira et al.<sup>75</sup> An extension of the  $\pi$ -moiety for TTF compounds is also effective to improve conductivity. Some selected examples are summarized in Table 4.

Even though such intermolecular interactions have so far been introduced into the neutral closed shell molecules in order to give conductive compounds, the  $t_1$  and  $t_2$  in Eq. 3 were

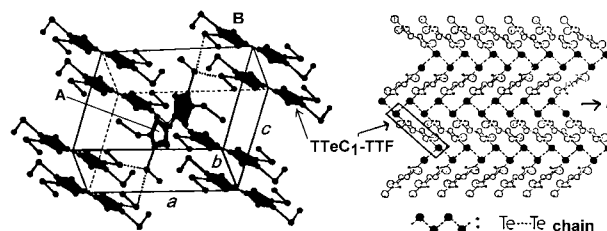


Fig. 8. Crystal structure of  $\text{TTeC}_1\text{-TTF}$ . Two crystallographically independent molecules (A and B, the TTF skeletons are shaded) form  $\text{Te}\cdots\text{Te}$  atomic contacts (dotted lines) along the  $b$ -axis to form a uniform conducting path with considerably high conductivity and mobility.<sup>72</sup>

not enough yet to afford a semimetal ( $\varepsilon_g = 0$ ). Only pressure has so far been able to extinguish the energy gap as described in section 2.1. Although they are semiconductive, the increased intermolecular interactions give rise to a high carrier mobility of 6–20  $\text{cm}^2 \text{V}^{-1} \text{s}^{-1}$  (TOF: time of flight) for  $\text{TTC}_n\text{-TTF}$  ( $n = 8$  and 10, single crystals),<sup>68,76</sup> 19–29  $\text{cm}^2 \text{V}^{-1} \text{s}^{-1}$  (TOF) for  $\text{TTeC}_1\text{-TTF}$  (single crystal),<sup>72</sup> 0.1 (TOF) and 0.2 (FET)  $\text{cm}^2 \text{V}^{-1} \text{s}^{-1}$  for  $\text{BTQBT}$  (thin film),<sup>27</sup> and 1.4  $\text{cm}^2 \text{V}^{-1} \text{s}^{-1}$  for  $\text{DT-TTF}$  (single crystal, FET).<sup>47</sup>

It appears that the unusually small band gap of 0.22 eV for **13**<sup>75</sup> arises either from increased  $t$  owing to the special intermolecular interactions or from some extrinsic cause including impurity. LB films of **14** have been reported to be highly conductive without carrier doping ( $10^{-2} \text{ S cm}^{-1}$ ).<sup>77</sup> However, since such a high conductivity has not been observed for single crystals of purified closed shell molecules based on TTF derivatives, contamination with oxygen is one of the plausible causes for the high conductivity (see section 4.4.1.3).

**2.3.2 Neutral  $\pi$ -Radical:** The conduction profile of a solid composed of radicals is markedly different from that composed of closed shell molecules. An excitation from the HOMO band to LUMO band (Eq. 3) is not necessary, but an electron correlation is the main source of excitation of electrons in the radicals. Figure 9a shows a 1D array of neutral radicals. An electron transfer from one radical to the neighboring one either by electric field or by light irradiation corresponding to the CT transition requires an extra Coulomb repulsive energy ( $U - V$ ) =  $U_{\text{eff}}$ , where  $U$  and  $V$  are the bare on-site and nearest neighboring Coulomb repulsive energies, respectively. The solid of radicals has a full-filled valence band composed of SOMOs as seen in Fig. 9b. An electron transfer between radicals makes the higher energy state of SOMO by  $U_{\text{eff}}$  with an energy gap of  $U_{\text{eff}} - 4t'$  (Eq. 8), where  $t'$  is the transfer integrals of SOMOs. In general, the bandwidth ( $W = 4t'$ ) of organic conductors lies in the range of 0.5–1 eV, while the effective on-site Coulomb repulsive energy ( $U_{\text{eff}} \approx 1$ –1.5 eV) usually exceeds  $W$  (Eq. 7). Thus, the organic conductors are strongly electron correlated systems and the Mott criterion governs the transport properties; namely, the system is a Mott insulator with an energy gap represented by Eq. 8 assuming that Eq. 7 is satisfied.<sup>78–83</sup> This is a rather common situation for organic radicals.

$$W < U_{\text{eff}}, \quad (7)$$

$$\varepsilon_g = U_{\text{eff}} - 4t'. \quad (8)$$

Table 4. Selected Organic Conductors of Closed Shell Molecules

Molecule	$\sigma_{RT}/S\text{ cm}^{-1}$	$\epsilon_g/\text{eV}$	Characteristics <sup>e)</sup>	Ref.
TSeC <sub>8</sub> -TTF	$1.3 \times 10^{-6}$	—	Fastener effect	67
<b>9</b>	$1.7 \times 10^{-4}$ ( $n = 4$ ) <sup>a)</sup>	—	Fastener effect <sup>d)</sup>	70
<b>10</b>	$2.5 \times 10^{-3}$ ( $n = 3$ ) <sup>a)</sup>	—	Fastener effect, EA: H deviates 0.36%, S deviates 0.51%	71
TTeC <sub>1</sub> -TTF	$1.4 \times 10^{-5}$ a)	0.50 <sup>a)</sup>	$\mu = 19\text{--}29\text{ cm}^2\text{ V}^{-1}\text{ s}^{-1}$ a) (TOF)	72
BTQBT	$1 \times 10^{-3}$ a)	0.84 <sup>a)</sup>	$\mu = 0.1$ (TOF), 0.2 (FET) $\text{cm}^2\text{ V}^{-1}\text{ s}^{-1}$ b)	26,27
DT-TTF	$6 \times 10^{-5}\text{--}6 \times 10^{-4}$ a)	—	$\mu = 1.4\text{ cm}^2\text{ V}^{-1}\text{ s}^{-1}$ c) (FET)	47
<b>11</b> BTDA-TCNQ	$3.7 \times 10^{-6}$ a)	—	—	73
<b>12</b>	$2 \times 10^{-5}$ (thin films)	0.48	$\mu = 6 \times 10^{-4}\text{ cm}^2\text{ V}^{-1}\text{ s}^{-1}$ (calculated)	74
<b>13</b>	$2.7 \times 10^{-4}$ a)	0.22 <sup>a)</sup>	EA: S deviates 0.3%	75
<b>14</b>	$10^{-2}$ (LB films)	—	EA: only C, H <sup>d)</sup>	77

a) Measured on single crystals. b) Thin films. c) Polycrystals by drop casting. d) The measurement conditions (under inert gas, vacuum, or not) were not reported. e) EA: elemental analysis. TOF: time of flight method under an inert atmosphere. FET: field effect transistor.

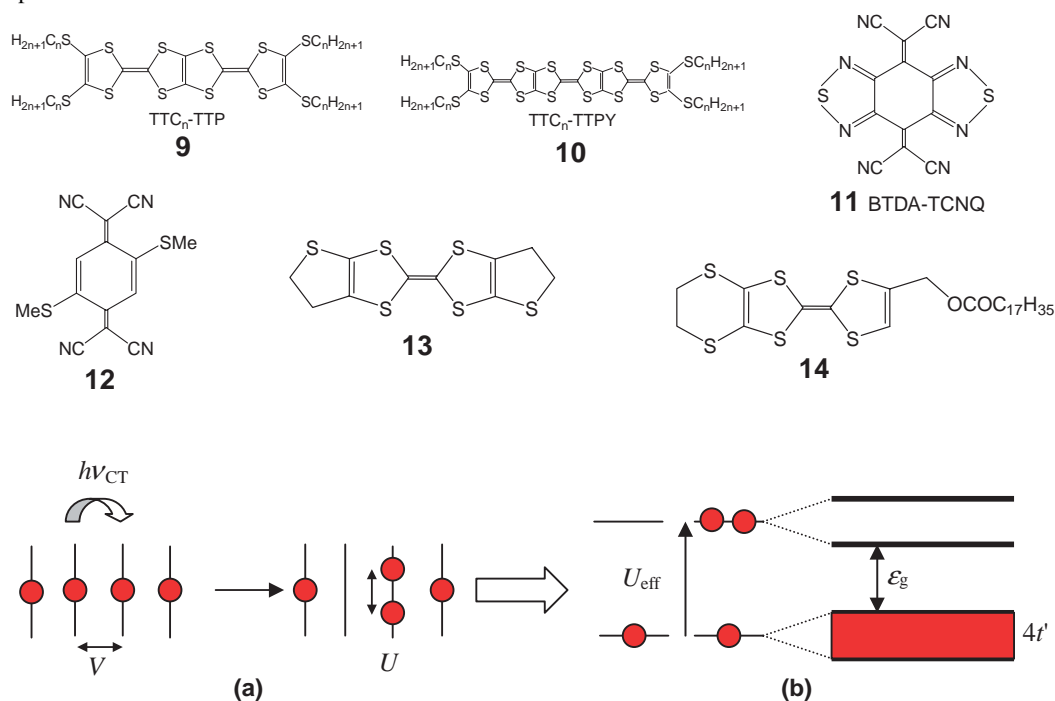


Fig. 9. (a) Electron transfer between radicals where  $V$  and  $U$  are the neighboring-site and on-site Coulomb repulsion energies, respectively. (b) The solid of radicals has a fully filled valence band composed of SOMOs, where the gap ( $\epsilon_g$ ) is  $U_{\text{eff}} - 4t'$ .

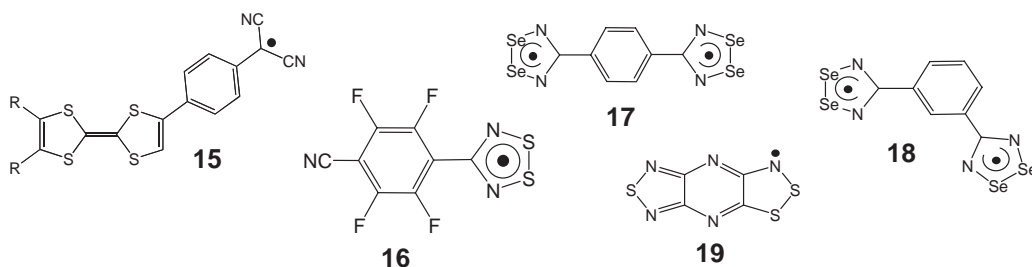


Chart 4.

The compounds **1** and **2** seem to have negligible intermolecular transfer interactions according to their insulating features and Curie-like magnetic behaviors. The radicals **4**, **15**,<sup>84</sup> and **16**<sup>85–87</sup> (Chart 4) have been developed based on the concept of the push–pull effect. Furthermore, the addition of the di-

thiadiazolyl ring is very efficient to stabilize radicals.<sup>88</sup> They have a small  $t$  since there are no special intermolecular interactions between the radical moieties for appropriate packing. Hence, **16** is a typical Mott insulator and exhibits a weak ferromagnetism with canted antiferromagnetic interactions with



Table 5. Selected Organic Conductors of Neutral Radicals and Biradicals

Molecules	$\sigma_{RT}/S\text{ cm}^{-1}$	$\varepsilon_g/\text{eV}$	Characteristics	Ref.
<b>15</b> <sup>b)</sup>	$5.7 \times 10^{-6}$	—	R = Me, black powder	84
<b>16</b> <sup>a)</sup>	no data	—	weak ferromagnet $T_c = 35.5\text{ K}$	85,86
			$T_c = 64.5\text{ K}$ at 1.6 GPa	87
<b>17</b> <sup>b)</sup>	$<10^{-2}$ (polymerize)		dimer	89
<b>18</b> <sup>a)</sup>	$2 \times 10^{-4}$	0.55	$\alpha$ : zig-zag chain	90
	$2 \times 10^{-4}$	0.77	$\beta$ : dimer	92
<b>19</b> <sup>a)</sup>	$10^{-4}$	0.44	head-to-tail dimer	91

a) Single crystal. b) Compaction pellet.

$T_c = 35.5\text{ K}$ .<sup>85,86</sup> The transition temperature is enhanced to 64.5 K by an application of pressure of 1.6 GPa.<sup>87</sup> Some selected organic conductors of neutral radicals and biradicals are presented in Table 5.

In order to increase transfer interactions, symmetrical radicals or biradicals with dithiadiazolyl or thiadiazolyl rings (or with heavy atoms such as Se) at the periphery of the  $\pi$ -moiety (**17–19**) have been developed by Cordes, Oakley, Haddon, et al.<sup>89–92</sup> instead of low-symmetric **15** and **16**. Such a modification is also effective to decrease  $U_{\text{eff}}$  owing to the extended  $\pi$ -system. Although they exhibited much improved conductivities (Table 5), the large  $U_{\text{eff}}$  and high reactivity are still crucial for the itinerancy. For example, **17** transforms to polymer through covalent bonding under weak pressure.<sup>89</sup> Therefore, the compounds **16–19** are systems in which itinerancy, localization, and reaction of the  $\pi$ -radical electrons compete with each other.

One of the most important characteristics of organic molecules for transport properties is the high polarizability. Even though the neutral molecules and radicals described above have a large polarizability, its effect on the transport properties has not been obvious. In the following, the effect of polarizability is discussed for zwitterionic radicals.

**2.3.3 Zwitterionic (Betainic)  $\pi$ -Radical:** **2.3.3.1 Atomic Wire vs Molecular Wire;** Atomic wires have received much attention in connection with the highly sophisticated electronic devices operative at high temperatures. Joachim et al. proposed a diagram (Fig. 10) for an atomic wire of length  $L$  and width  $W$  composed of noble metals at low temperatures.<sup>93</sup> The elastic mean free path  $\lambda_{\text{el}}$  of the carriers limits the dissipationless regions (ballistic and tunnel regions), which range ca.  $10\text{--}10^3\text{ \AA}$ . If the organic molecule has nearly the same ballistic and tunnel regions as those of inorganic atoms, the molecular wires can have a very wide applicability for quantum molecular electronic devices operative at RT. Application of the diagram in Fig. 10 to prepare dissipationless organic wires in the ballistic or tunnel regime is more or less feasible at low temperatures, but unfeasible at RT since the mean free path for organic materials is expected to be much shorter than those of inorganic materials, e.g.,  $\lambda_{\text{el}}$  in Cu is ca.  $300\text{ \AA}$  while that in TTF or TCNQ molecules is  $24\text{--}39\text{ \AA}$  at RT.<sup>94</sup>

Within the framework of band theory, the mean free path  $\lambda$  is represented by Eq. 9, where  $v_F$  is the Fermi velocity.

$$\lambda = v_F \tau. \quad (9)$$

Although no intramolecular  $\lambda$  has been reported for organic molecules, an intermolecular one was evaluated by Cowan.<sup>95</sup>

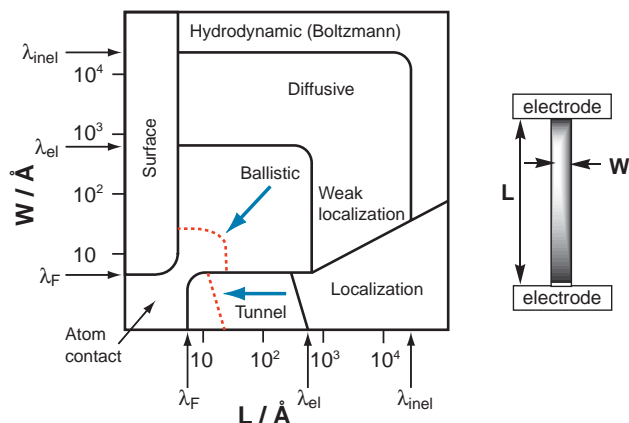


Fig. 10. Proposed transport phase diagram by Joachim et al.<sup>93</sup> for an inorganic atomic wire of length  $L$  and width  $W$  composed of noble metals at low temperature ( $\lambda_{\text{inel}}$ : the inelastic  $\lambda$ ,  $\lambda_{\text{el}}$ : the elastic  $\lambda$ ,  $\lambda_F$ : the de Broglie carrier wavelength. For other terms, see Ref. 93). The dotted lines indicate the ballistic and tunnel regions for a molecular system made of a TTF or TCNQ based molecule at RT according to the evaluated  $\lambda_{\text{intra}}$ .<sup>114</sup>

The estimated intermolecular  $\lambda$  ( $\lambda_{\text{inter}}$ ) is ca.  $3\text{ \AA}$  at RT for an organic metal TTF·TCNQ ( $\sigma_{RT} \approx 5 \times 10^2\text{ S cm}^{-1}$ ), where dissipative events are mainly originated from the interactions with defect, phonon, electron ( $U$ ), molecular vibration, and conformational change. The last three interactions are the main sources of dissipation in a single uni-molecule. The conductivity of TTF·TCNQ increases at low temperatures up to  $1.4\text{--}1.5 \times 10^4\text{ S cm}^{-1}$  and  $\lambda_{\text{inter}}$  is then estimated to be ca.  $50\text{ \AA}$  at 60 K.<sup>95</sup> Since  $v_F$  is represented by the first derivative of energy dispersion by  $k$  (Eq. 10), the mean free path is proportional to  $t^2$ .

$$v_F = \frac{1}{\hbar} \left( \frac{\partial \mathcal{E}}{\partial k} \right)_{\mathcal{E}=\mathcal{E}_F} = \frac{2ta \sin ka}{\hbar} \propto t. \quad (10)$$

Then the  $\lambda_{\text{intra}}$  is estimated as  $390\text{--}650\text{ \AA}$  ( $t_{\text{intra}}/t_{\text{inter}} \approx 0.7\text{--}0.9\text{ eV}/0.25\text{ eV}$ ) at low temperatures and  $24\text{--}39\text{ \AA}$  at RT. So, the tunneling and ballistic regimes in molecular systems might be barely realized at high temperatures (dotted lines in Fig. 10), although the band theory is not strictly applicable for the nano-scale molecular wires. Importantly, it is indispensable to weaken the interactions with charges on a molecule, which is described in terms of  $U$ , in order to improve the electronic transport via the molecule in a single uni-molecule and single component systems.

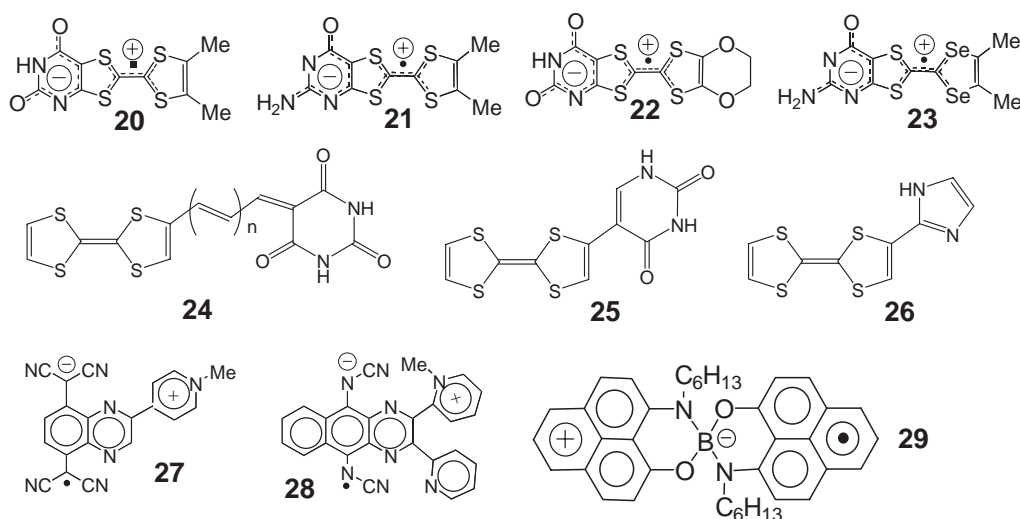


Chart 5.

Table 6. Selected Organic Conductors of Betainic Radicals

	$\sigma_{RT}$ /S cm <sup>-1</sup>	$\varepsilon_g$ /eV	$h\nu_{CT}$ /10 <sup>3</sup> cm <sup>-1</sup>	Characteristics <sup>c)</sup>	Ref.
<b>27</b>	$3.2 \times 10^{-5}$ <sup>b)</sup>	—	—	EA: <b>27</b> ·1.75H <sub>2</sub> O, N deviates ca. 0.6% Calcd: C, 63.24; H, 3.58; N, 25.81% Found: C, 63.54; H, 3.44; N, 25.18%	101
<b>29</b>	$5 \times 10^{-2}$ <sup>a)</sup>	0.26 <sup>a)</sup>	≈4.0	EA: C deviates 0.5% Calcd: C, 80.42; H, 7.10; N, 4.94; B, 1.90% Found: C, 79.92; H, 7.02; N, 5.15; B, 1.81%	103,104
<b>21</b>	$1 \times 10^{-1}$ <sup>b)</sup> $1.4 \times 10^{-1}$ <sup>b)</sup>	0.4 <sup>b)</sup> 0.23–0.46 <sup>b)</sup>	— 4.8	may be contaminated with <b>30</b> . EA: see text EA, <sup>115</sup> $U_{eff} = 0.54$ – $0.62$ eV, $U_{eff}^d = 0.28$ – $0.50$ eV, $t_d = 0.06$ – $0.13$ eV, $t_d^a) = 0.01$ – $0.03$ eV	105,106 114
<b>20</b>	$1.2 \times 10^{-3}$ <sup>b)</sup>	0.44 <sup>b)</sup>	—	EA: no data	105,106
<b>22</b>	$5 \times 10^{-4}$ <sup>b)</sup>	0.51 <sup>b)</sup>	5.0	EA, <sup>115</sup> $U_{eff} = 0.62$ eV, $U_{eff}^d = 0.52$ eV $t_d = 0.05$ eV, $t_d^a) = 0.004$ eV	113,114
<b>23</b>	$5 \times 10^{-2}$ <sup>b)</sup>	0.18–0.23 <sup>b)</sup>	4.5	EA, <sup>115</sup> $U_{eff} = 0.56$ – $0.62$ eV, $U_{eff}^d = 0.29$ – $0.38$ eV, $t_d = 0.12$ – $0.14$ eV, $t_d^a) = 0.02$ – $0.04$ eV	114

a) Single crystal. b) Compaction pellet. c) EA: elemental analysis.

**2.3.3.2 Effect of Polarizability;** To relax the Mott criterion, particular synthetic strategies such as the enlargement of molecular size, the inclusion of heavy atoms in a molecule, the increase in orbital degeneracy of SOMO, and the increment in the electronic dimensionality of the assembly have been undertaken for CT complexes.<sup>6,95</sup> Furthermore, the highly polarizable character of component molecules is predicted to decrease the  $U_{eff}$  value. For the anion radical salts of TCNQ, LeBlanc suggested that the polarizable cation will reduce the electron correlation energy on the TCNQ molecule according to Eq. 11, where  $\alpha$  is the molecular polarizability of the cation and  $r$  is the distance between TCNQ and cation molecules.<sup>96</sup>

$$U_{eff} = \left(1 - \frac{\alpha}{r^3}\right)U. \quad (11)$$

An increase in conductivity with an increase in the size of the cation dyes was reported for the TCNQ salts.<sup>97</sup> However, there have been no clear experimental evidence to certify the validity of Eq. 11. It is expected that the intramolecular CT radicals of (D- $\pi$ -A) $\cdot$  or (D- $\sigma$ -A) $\cdot$  have a largely suppressed

$U_{eff}$  value when the D or A part has significant polarizability. In addition, the suppression may be achieved by the reduced  $r$  value according to Eq. 11. Then the analogues of **19** seem to be one of the most appropriate candidates for conductors among the neutral radicals discussed in the previous section. The small  $\varepsilon_g$  value of **19** (Table 5) might be indicative of the reduced  $U_{eff}$ .

In the following we will focus on the zwitterionic (betainic) radicals since they would have a very polarized ground state. A reduction of  $U_{eff}$  can be achieved through the small molecular size of betainic radicals. The reduced  $r$  is a critical issue owing to the short  $\lambda$  of organic molecules, and distinguishes the fused betaines **20–23** ( $r = 4$ – $5$  Å) from the non-fused neutral molecules **24** ( $r > 10$  Å)<sup>98</sup> or **25** and **26** ( $r = 6$ – $7$  Å) by Morita et al.,<sup>99,100</sup> and betaines **27** and **28** ( $r > 10$  Å) by Suzuki et al.<sup>101,102</sup> (Chart 5). Selected organic conductors of betainic radicals are summarized in Table 6.

The betainic radicals based on the TCNQ- and dicyanoquinodiimine(DCNQI)-moieties (**27** and **28**) exhibit rather poor conductivities  $\sigma_{RT} = 10^{-5}$ – $10^{-9}$  S cm<sup>-1</sup>,<sup>101,102</sup> probably

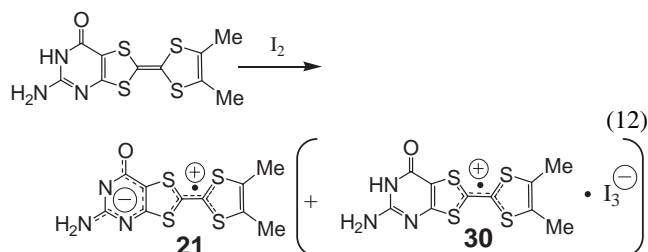
owing to the large  $r$  and poor intermolecular overlaps. A single crystal of the phenalenyl-based betainic radical (**29**) developed by Haddon et al. is one of the best conductors of purely organic materials:  $\sigma_{\text{RT}} = 5 \times 10^{-2} \text{ S cm}^{-1}$  with  $\varepsilon_{\text{g}} = 0.26 \text{ eV}$ , in spite of its non-planar molecular structure.<sup>103</sup> **29** has a characteristic feature to share one radical electron between two phenalenyl groups; that is in good accordance with the concept of the partial CT state which may give rise to high itinerancy of the radical electron even for the large  $U$  of the phenalenyl group. A bistable electronic behavior was observed between 320 and 350 K.<sup>104</sup>

The mesomeric betainic radicals **20** and **21** derived from the pyrimido fused TTFs have been reported by Neilands et al.<sup>105–107</sup> Very high  $\sigma_{\text{RT}}$  values of  $10^{-1}$ – $10^{-3} \text{ S cm}^{-1}$  on compaction pellet samples have been ascribed to strong intermolecular interactions through complementary hydrogen-bonds.

**2.3.3.3 Effect of Hydrogen Bond;** The ability to form intermolecular hydrogen bonds is of importance to attain efficient intermolecular interactions for molecular recognition of nucleobases in biochemistry<sup>108,109</sup> or for crystal engineering in supramolecular chemistry,<sup>110,111</sup> but its essential role is not clearly understood yet for electron transport in solids. The transfer interactions caused by hydrogen bonds should be uniform<sup>112</sup> for the electron transport (see section 4.2.6). Non-uniform and alternating hydrogen bonds extinguish itinerant electrons, forming spin singlet dimers. The high dimensionality generated by the network of hydrogen bonds is useful to suppress the Peierls- or Jahn–Teller-like instability relevant to low-dimensional conductors.<sup>6,95,100</sup>

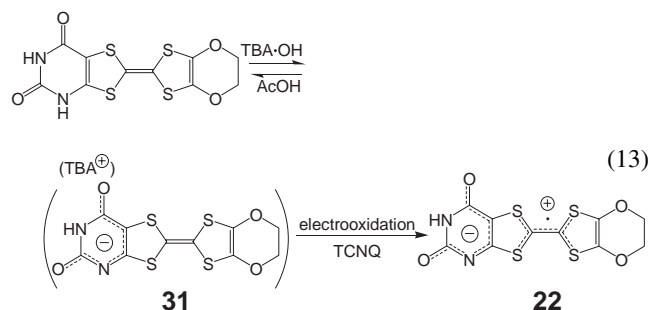
In many cases, however, non-uniform and alternating hydrogen bonds are formed. Then, the dimerized band structure generated by two kinds of  $t$  (see Fig. 6) has a rather narrow HOMO band, which is highly susceptible to the electron correlation  $U_{\text{eff}}$ . Hence, alternating hydrogen bonds may be useful to prepare radical salts composed of the dimerized unit, which have attracted current interest in the organic (super)conductors to exhibit exotic phase transitions as will be discussed in sections 3.2.2, 3.5, and 3.6.

**2.3.3.4 Betainic Radicals of Pyrimido Fused TTF;** Neilands et al. prepared the betainic solids **20** and **21** by the oxidation of the corresponding neutral species by  $\text{I}_2$  (Eq. 12).<sup>105,106</sup> However, their very insoluble nature causes difficulty in purification, and the elemental analyses showed deviation from the calculated values (**21**, Calcd for  $\text{C}_{10}\text{H}_8\text{N}_3\text{OS}_4$ : C, 38.20; H, 2.56; N, 13.36; S, 40.79%. Found: C, 37.5; H, 2.3; N, 12.9; S, 40.1%).<sup>105</sup> It may be suggested that the product in Ref. 105 includes 1–2% of the cation radical salt **30** (Eq. 12) (Calcd: C, 37.74–37.31; H, 2.54–2.51; N, 13.20–13.05; S, 40.30–39.84%).



Balodis, Saito, et al. improved the oxidation process in

Eq. 12 as shown in Eq. 13 in order to isolate the pure betainic radicals **21**, **22**,<sup>113</sup> and **23**.<sup>114</sup> For example, the crude neutral compound was converted to the tetrabutylammonium (TBA) salt **31** by  $\text{TBA}\cdot\text{OH}$ , and the betainic radical **22** was then prepared as a green powder either by the electrooxidation of **31** or by mixing **31** with equimolar TCNQ, where the unreacted TCNQ and the by-product  $\text{TBA}\cdot\text{TCNQ}$  were easily removed by washing with the solvents ( $\text{CH}_3\text{CN}$  or DMF).<sup>113,114</sup>



The obtained betainic radicals **21–23** were extremely fine powders including a small amount of solvent molecules ( $\text{CH}_3\text{CN}$ , DMF, or water). The optical, transport, and magnetic properties are not sensitive to the amount of crystal solvents. Structural refinement for **21–23** is currently unavailable even by the Rietveld method for powder X-ray diffraction patterns. On the other hand, the TBA salt **31** was obtained as single crystals of  $\text{31}\cdot\text{H}_2\text{O}$ .

As shown in Fig. 11, the anion molecules in **31** and water molecules form a layer that is sandwiched by the layers of TBA cations along the  $b$ -axis. Two non-equivalent anion molecules form a side-by-side homo-dimer connected by robust hydrogen bonds,  $\text{N}\cdots\text{O}$  (2.881(4), 2.891(4) Å vs 3.07 Å for the sum of the van der Waals radii<sup>116</sup> of N and O, Fig. 11a). Similar strong self-complementarity has been observed in uracilbetaine<sup>117</sup> and neutral species of **20**,<sup>106</sup> and it is thus likely that such a feature is realized in the related betainic radicals (**20–23**). In addition to the hydrogen bonds, short  $\text{S}\cdots\text{S}$  contacts (3.426(1) Å vs 3.60 Å) connect neighboring homo-dimers along the ( $a$ – $c$ )-axes to form infinite ribbons of homo-dimers, which are then connected with each other through hydrogen bonds by the aid of water molecules, resulting in a stable 2D sheet in the  $ac$ -plane (Fig. 11b).

**20–23** are fairly conductive even in the pellet forms. Especially, **21** and **23** are the best conductors with a small energy gap (Table 6) among the organic single component conductors at ambient pressure. The UV–vis–NIR spectra of **21–23** in KBr exhibit a characteristic low-energy band below  $5 \times 10^3 \text{ cm}^{-1}$  (Fig. 12), which is absent in solution.

It has been known that this band arises from CT between radical molecules<sup>118,119</sup> and its transition energy is, therefore, related to  $U_{\text{eff}}$ . It should be stressed that the absorption bands are located at a much lower energy than those of most 1:1 cation radical salts of TTF derivatives so far known.<sup>118–121</sup> This spectral feature emphasizes that  $U_{\text{eff}}$  of the betainic radical system is much reduced in comparison with that of the conventional cation radical system. For example, the structurally related cation radical salts,  $(\text{TMTTF}^{\bullet+})(\text{Br}^-)$  and  $(\text{EDO}^{\bullet+})(\text{IBr}_2^-)$  (curve d in Fig. 12), exhibit the optical band at  $10 \times 10^3 \text{ cm}^{-1}$  (1.24 eV). It has been known that the molecular

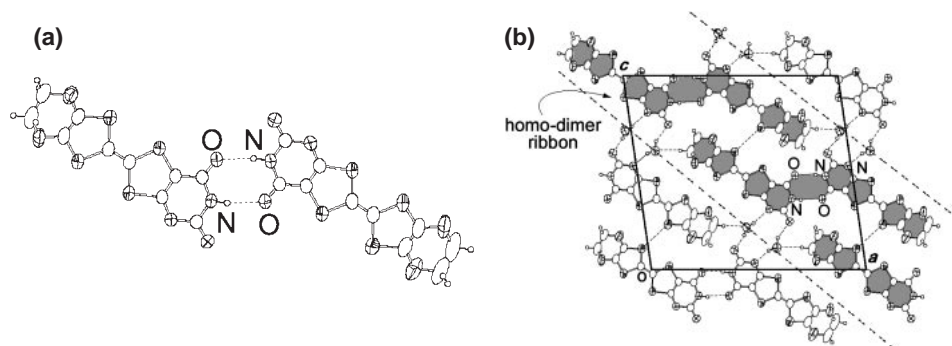


Fig. 11. (a) The homo-dimer and (b) anion layer composed of anion molecule in **31** and water molecules in **31**·H<sub>2</sub>O. Dotted lines indicate hydrogen bonds (N–H...O, O–H...O, C–H...O) and S...S atomic contacts. The anion molecules forming one infinite ribbon of homo-dimers connected by S...S contacts are shaded. Monoclinic, *Cc*, *a* = 20.251(1), *b* = 17.079(1), *c* = 18.472(1) Å,  $\beta$  = 98.339(3)°, *V* = 6321.3(5) Å<sup>3</sup>, *Z* = 4, *R* = 0.0356.<sup>114</sup>

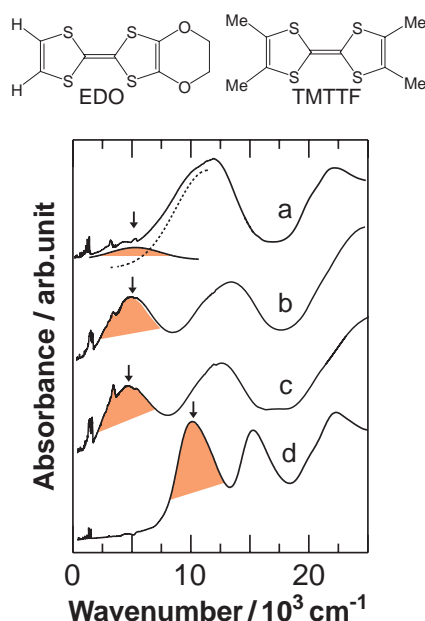


Fig. 12. Absorption spectra of betainic radicals; a) **22** (deconvoluted), b) **21**, c) **23**, and d) 1:1 salt of (EDO)IBr<sub>2</sub> dispersed in KBr. The arrows indicate the peaks of absorption bands (shaded) related to  $U_{\text{eff}}$  in solid.<sup>114</sup>

on-site Coulomb repulsion is reduced by the extension of the TTF skeleton with alkylchalcogeno groups.<sup>6,120,121</sup> For example, such a CT band appears at  $5.5\text{--}8.0 \times 10^3 \text{ cm}^{-1}$  in the cation radical salts of ET.<sup>120,121</sup> A comparison with the optical bands of (TMTTF<sup>•+</sup>)(Br<sup>−</sup>) and (EDO<sup>•+</sup>)(IBr<sub>2</sub><sup>−</sup>) implies that  $U_{\text{eff}}$  in the solids **21–23** seems to be reduced more than twice  $U_{\text{eff}} \leq 0.62 \text{ eV}$  owing to the fused betainic nature, i.e.,  $(1 - \alpha/r^3) \leq 1/2$ .

Although the conductivity of **21–23** is among the highest for pure organic single component solids, the  $\sigma_{\text{RT}}$  of the compressed pellet of **22** was as low as  $5 \times 10^{-4} \text{ S cm}^{-1}$  ( $\epsilon_g = 0.51 \text{ eV}$ ), indicating either a less than excellent mobile nature or a small number of carriers. The magnetic susceptibility ( $\chi$ ) of **22** showed a Curie behavior down to 2 K with a spin concentration of 2.8%, inferring that most of the spins are strongly coupled probably owing to the strong self-complementary dimerization. Accordingly, a weakening of the dimerization

is necessary to increase carrier density. Actually, **21** and **23**, which have no protons attached to the two pyrimido N atoms and are therefore expected to show a weaker self-complementarity than **22** in solid, exhibited a much higher conductivity,  $\sigma_{\text{RT}}(\text{pellet}) = 1.4 \times 10^{-1} \text{ S cm}^{-1}$  ( $\epsilon_g = 0.23\text{--}0.46 \text{ eV}$ ) for **21** and  $5 \times 10^{-2} \text{ S cm}^{-1}$  ( $0.18\text{--}0.23 \text{ eV}$ ) for **23**. This result confirms that **21** and **23** are some of the best single component organic conductors having no transition-metals. However, the  $\chi$  of **21** and **23** again indicate a strong coupling of radical electrons; namely, only 2–2.5% of the Curie spins were observed down to 2 K, suggesting that the dimerization of the betainic radicals is still significant.

Taking into account the dimerized feature of the compounds, the absorption energy in a solid is approximated by Eq. 14 based on a model for the isolated dimer with two electrons,<sup>118,122</sup> where  $t_d$  and  $t_d^*$  are the intra- and inter-dimer transfer integrals, respectively.

$$h\nu_{\text{CT}} = U_{\text{eff}}/2 + (U_{\text{eff}}^2/4 + 4t_d^2)^{1/2} - 4t_d^*. \quad (14)$$

For a dimerized system, the band gap  $\epsilon_g$  should take into account the effective correlation energy of the dimer,  $U_{\text{eff}}^{\text{d}}$ . This is adequately approximated as Eq. 15 for  $U_{\text{eff}} > 4t_d$ ,<sup>122</sup> based on a model of the dimer with three electrons with  $V^*$  being the inter-dimer Coulomb repulsion, and the  $\epsilon_g$  then being expressed by Eq. 16.

$$U_{\text{eff}}^{\text{d}} = (U^2 + 16t_d^2)^{1/2} - 2t_d - V^* \approx U_{\text{eff}} - 2t_d, \quad (15)$$

$$\epsilon_g = U_{\text{eff}}^{\text{d}} - 4t_d^*. \quad (16)$$

Based on all the optical and transport data and the condition  $U_{\text{eff}}/4 > t_d > t_d^*$  and  $U_{\text{eff}} \leq 0.62 \text{ eV}$ , the  $U_{\text{eff}}$ ,  $U_{\text{eff}}^{\text{d}}$ ,  $t_d$ , and  $t_d^*$  values are numerically estimated as summarized in Table 6:  $U_{\text{eff}} = 0.54\text{--}0.62 \text{ eV}$ ,  $U_{\text{eff}}^{\text{d}} = 0.28\text{--}0.52 \text{ eV}$ ,  $t_d = 0.05\text{--}0.14 \text{ eV}$ , and  $t_d^* = 0.004\text{--}0.04 \text{ eV}$  for betainic radicals **21–23**. As expected, the evaluated  $U_{\text{eff}}$  values are much smaller than those of TTF, its alkyl-substituted derivatives ( $\geq 1.0\text{--}1.3 \text{ eV}$ ),<sup>6,120,121</sup> and even ET ( $0.68\text{--}0.99 \text{ eV}$ ).<sup>120,121</sup> Furthermore, it is worth noting that these betainic radicals have a reduced  $U_{\text{eff}}^{\text{d}}$  compared to the dimerized ET superconductors  $\kappa\text{-(ET)}_2\text{X}$  ( $U_{\text{eff}}^{\text{d}} \approx 0.45\text{--}0.55 \text{ eV}$ ).<sup>6</sup> This fact demonstrates the effectiveness of self-complementarity by the hydrogen bonds both for the carrier path formation (segregated stack or layer) and for the carrier transport. However, except for the case of

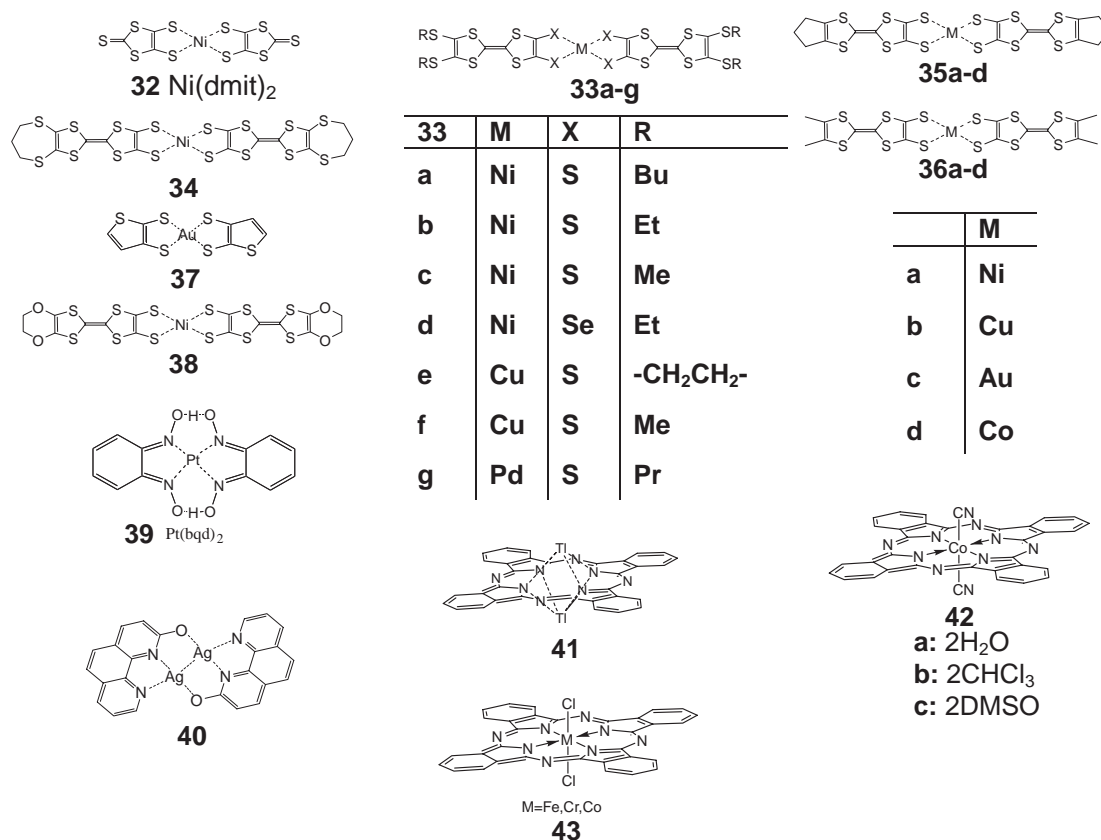


Fig. 13. Chemical structures of metal complexes.

$U_{\text{eff}}^{\text{d}} \leq W (=4t_{\text{d}}^*)$ , which corresponds to the Mott criterion for the dimerized system, a strong dimerization of the radicals normally results in both the quenching of carriers and the generation of non-uniform transfer integrals, giving rise to a band insulator. Accordingly, these results provide an advanced design to generate the carriers and lengthen the elastic  $\lambda$  for purely organic materials: namely, a weakening of the dimerization, an enhancement of inter-dimer transfer interactions or a formation of the conjugated homo-dimer bearing one electron.

The following are several important requirements for single component conducting systems composed of organic radical molecules.

1. Small electron correlation energy  $U_{\text{eff}}$ :  $U_{\text{eff}}$  is represented as  $(1 - \alpha/r^3)(U - V)$  for a solid and  $(1 - \alpha/r^3)U$  for a molecule. A betainic system is preferable to suppress  $U_{\text{eff}}$ , since it reduces the term  $(1 - \alpha/r^3)$  owing to its very polarizable nature.

2. Large  $\alpha$  and small  $r$ : Although the enlargement of the molecular size increases  $\alpha$ , a significant benefit is not expected owing to the reduced  $\alpha/r^3$ . Since the small molecular size is essential, it is important to introduce heavy atoms into the molecule. Thus, a mesomeric fused system having heavy atoms is preferable.

3. Weak or no lattice distortion: Although a dimerization provides a very diminished  $U_{\text{eff}}$ , the lattice distortion in the radical system normally results in a dimerization with a spin singlet ground state, which gives rise to a thermally activated semiconductor.

4. Large inter-dimer transfer interactions ( $2t_{\text{d}}^* > t_{\text{d}}$ ) for the

homo-dimers of radical molecules: This condition gives a semi-metallic band structure with an overlapping of the upper and lower HOMO bands of the assemblies composed of the homo-dimers. In order to form a uniform band, a uniform segregated column or layer consisting of the dimerized molecule with a radical electron is necessary.

5. The formation of a conjugated homo-dimer having one electron results in a half-filled HOMO band. This situation is essentially identical to the partial CT state as observed in many metallic and superconducting salts such as  $\kappa$ -(ET)<sub>2</sub>X, in which an ET dimer with one hole forms a half-filled upper HOMO band (see section 3.5).

Summarizing the above, a fusion of the cationic and anionic moieties in one molecule should have an effect such as that expressed by Eq. 11, and hence a zwitterionic (betainic)  $\pi$ -radical is expected to be a good candidate for a conductor composed of a single component molecule.

**2.4 Metal Complexes at Ambient Condition.** Single molecular solids composed of organometallic molecules are not well defined at present. The solids in this class (Fig. 13) satisfy the following: 1) The constituent unit of the solid is composed of transition-metals (M) coordinated by organic ligands (L):  $M + nL \rightarrow M(L)_n$ . 2) The complex  $M(L)_n$  is neutral. 3) Intramolecular chemical bonds are covalent, ionic, and/or coordination bonds. 4) Intermolecular chemical bonds are van der Waals, hydrogen bonds, and/or metallic bonds, but not covalent or coordination bonds.

Therefore, the single molecular solid system in this class includes the assemblies of molecules such as organometallic



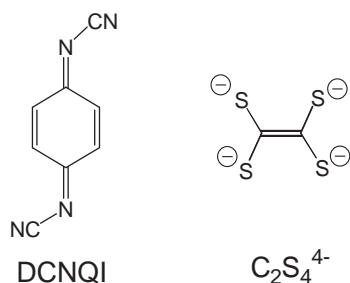


Chart 6.

molecules, metallocene, metal Pc, or many biological molecules including coordinated metals, but does not include solids composed of a transition-metal and a variety of ligands such as DCNQI, TCNE, dicyanamide  $\text{N}(\text{CN})_2^-$ , polyanion  $\text{C}_2\text{S}_4^{4-}$ , or their analogues (Chart 6), since the interaction between metal–ligand units is a covalent or coordination bond. Also, endohedral metallofullerenes are not classified into this group. These single molecular solids may be equivocal to be termed as a single component solid since the molecular unit includes more than two components.

They have some characteristic features such as 1) mixed valence of the transition-metals as deduced in cytochrome-*c*<sub>3</sub> that contains four heme moieties coordinated by a protein,<sup>123–125</sup> 2) mixing of p–d orbitals resulting in a small HOMO–LUMO gap as observed in square-planar dithiolate complexes  $\text{R}_1\text{R}_2\text{M}$  ( $\text{R}_1, \text{R}_2$ : organic ligand,  $\text{M}$ : transition-metal) **32–38**,<sup>126–139</sup> and 3) 3D crystal architectures as accomplished in Pc solids **41, 42**, etc.<sup>141–146</sup>

The metallic behavior down to low temperatures was first reported by Janczak et al. on a compaction pellet of  $\text{Ti}_2\text{Pc}$  (**41**)<sup>141</sup> with a very high conductivity of  $\sigma_{\text{RT}} \approx 10^4 \text{ S cm}^{-1}$  (four-probe method using indium lead wires). A specific 3D arrangement of  $\text{Ti}_2\text{Pc}$  is anticipated to form a 3D semimetallic band. However, the reproducibility of the transport property and even of the synthesis of the molecule is poor.<sup>142</sup> The conductivity of **41** by Suga et al.<sup>142</sup> is much less than that by Janczak et al.<sup>141</sup> by a factor of  $10^{15}$ . Although the powder X-ray diffraction patterns are identical to each other, the elemental analysis of  $\text{Ti}_2\text{Pc}$  prepared by Suga et al. indicates a small amount of deficiency of Ti. It is unclear whether the small amount of metal-free Pc contaminated in **41** breaks the conduction path composed of  $\text{Ti}_2\text{Pc}$ . Also it is not clear whether Janczak et al. measured the powder X-ray diffraction patterns on the sample that showed metallic behavior.

The  $(\text{CN})_2\text{CoPc}$  compounds (**42**)(solv)<sub>2</sub> developed by Inabe et al. are highly conductive semiconductors of  $\sigma_{\text{RT}} = 10^{-1} - 10^0 \text{ S cm}^{-1}$  with a small  $\varepsilon_{\text{g}}$  (0.12 eV for solv =  $\text{H}_2\text{O}$ ) on single crystals.<sup>143</sup> The crystals were obtained by the electrooxidation of  $\text{K}[(\text{CN})_2\text{CoPc}]$  in the appropriate solvent ( $\text{CH}_3\text{CN}$ , DMSO,  $\text{CHBr}_3$ ,  $\text{CHCl}_3$ , etc). The  $(\text{CN})_2\text{CoPc}$  molecules form a specific 3D architecture with the solvent molecules. The evacuation of the solvents deteriorates the conductivity. Therefore, the compounds are not pure single- but multi-component conductors. In fact, solvent free  $(\text{CN})_2\text{CoPc}$  obtained by the electrooxidation in  $\text{CH}_3\text{CN}$  containing  $\text{K}_2\text{CO}_3$  is a very poor conductor ( $\sigma_{\text{RT}} = 2.2 \times 10^{-4} \text{ S cm}^{-1}$ ).<sup>144</sup>

Prior to the reports by Inabe et al., a similar compound,

cyanocobalt(III)Pc [ $(\text{CN})\text{CoPc}$ ], was reported to be obtained as single crystals without any solvents by the electrooxidation of  $\text{K}[(\text{CN})_2\text{CoPc}]$  in  $\text{CH}_3\text{CN}$  in as early as 1985 by Orihashi et al., although the elemental analysis data show a deviation from the calculated values (Calcd: C, 66.34, H, 2.70; N, 21.10; Co, 9.86%; Found: C, 65.44; H, 3.47; N, 21.18; Co, 9.91%).<sup>145,146</sup> The crystal is rather conductive ( $\sigma_{\text{RT}} = 5.7 \times 10 \text{ S cm}^{-1}$ ,  $\varepsilon_{\text{g}} = 0.08 \text{ eV}$ ) without decay for several months under ambient conditions, in contrast with the case of solvated  $(\text{CN})_2\text{CoPc}$ . However, it is claimed by Inabe et al. that the crystals obtained by the electrocrystallization of  $\text{K}[(\text{CN})_2\text{CoPc}]$  in pure  $\text{CH}_3\text{CN}$  are exclusively  $\text{K}[(\text{CN})_2\text{CoPc}]_2 \cdot 5\text{CH}_3\text{CN}$ . Its calculated elemental analysis value (C, 59.35%) differs from that found in  $(\text{CN})\text{CoPc}$  prepared by Orihashi et al. So far nobody has reproduced the air stable single component conductor  $(\text{CN})\text{CoPc}$ .

$\text{Cl}_2\text{MPc}$  ( $\text{M} = \text{Fe}, \text{Cr}$ , and  $\text{Co}$ ) (**43**) has a similar molecular structure to that of  $\text{Ti}_2\text{Pc}$  or  $(\text{CN})_2\text{CoPc}$  and exhibits a good conductivity of  $1 \times 10^{-2} - 1 \times 10^{-3} \text{ S cm}^{-1}$ .<sup>147</sup>

Highly conductive metal complex solids  $\text{Pt}(\text{bqd})_2$  (**39**) ( $\sigma_{\text{RT}} = 3.3 \times 10^{-3} \text{ S cm}^{-1}$ ,  $\varepsilon_{\text{g}} = 0.50 \text{ eV}$ ) and  $\text{Ni}(\text{dmit})_2$  (**32**) ( $\sigma_{\text{RT}} = 3.5 \times 10^{-3} \text{ S cm}^{-1}$ ) were reported in as early as 1972 by Megnamisi-Belombe<sup>148</sup> and 1991 by Cassoux et al.,<sup>126</sup> respectively. The former eventually becomes a metal under pressure as described in section 2.1.<sup>34</sup> In 1996, Narvor et al. reported that a compaction pellet of **33c** ( $\text{M} = \text{Ni}$ ,  $\text{X} = \text{S}$ ,  $\text{R} = \text{Me}$ , the authors stated that the product is “analytically pure” but no elemental analysis data were presented) showed metallic behavior down to 275 K,<sup>127</sup> without any graphic data. In 1998–1999, Ueda et al. reported the highly conductive semiconductors **33b**, **33d**, **33e**, and **33f**.<sup>128,129</sup> Especially single crystals of **33d** ( $\text{M} = \text{Ni}$ ,  $\text{X} = \text{Se}$ ,  $\text{R} = \text{Et}$ ) showed a high conductivity of  $\sigma_{\text{RT}} = 2.8 \text{ S cm}^{-1}$  with a very small gap of  $\varepsilon_{\text{g}} = 0.028 \text{ eV}$ ,<sup>128</sup> and **33e** ( $\text{M} = \text{Cu}$ ,  $\text{X} = \text{S}$ ,  $2\text{R} = -\text{CH}_2\text{CH}_2-$ ) was more conductive even in the pellet sample ( $\sigma_{\text{RT}} = 3.7 \text{ S cm}^{-1}$ ).<sup>129</sup> The magnetic susceptibility of **33e** after subtracting the Curie term (Curie constant:  $1.2 \times 10^{-2} \text{ emu K mol}^{-1}$ ) is temperature independent as expected from Pauli paramagnetism ( $3.6 \times 10^{-4} \text{ emu mol}^{-1}$ ).<sup>129</sup> However, the purity is not accurately described (elemental analysis data only for C and H, or description as “analytically pure”). In 1999, Kobayashi et al. also reported the highly conductive semiconductor **34** ( $\sigma_{\text{RT}} = 7 \text{ S cm}^{-1}$ ,  $\varepsilon_{\text{g}} = 0.06 \text{ eV}$  for single crystal).<sup>130</sup> They analyzed its purity by EPMA, which gives about one order less accuracy than the elemental analysis. Although numerous reports on highly conductive single component coordination compounds have appeared since 2000,<sup>131–140</sup> the characterizations of some compounds are insufficient to claim the metallic single molecular solid, concerning the purity, measurement conditions, experimental information, etc. Note that most authors stated that their material is a “first single-component metal or good conductor,” without mentioning pentacene and *p*-iodanil under pressure (see section 2.1)<sup>17,24,25</sup> or  $\text{Ti}_2\text{Pc}$  at ambient conditions.<sup>141</sup>

**37** showed a semiconductive temperature dependence ( $\sigma_{\text{RT}} = 6 \text{ S cm}^{-1}$ ,  $\varepsilon_{\text{g}} = 0.039 \text{ eV}$ ) in the polycrystalline sample,<sup>138</sup> although the authors stated that **37** is a “metal” based on both the magnetic susceptibility at RT and the temperature dependence of susceptibility, which are indicative of the Pauli paramagnetism above 50 K. However, it seems that the material is impure according to the elemental analysis data.



Table 7. Selected Metal Complex Conductors

Sample <sup>a)</sup>	$\sigma_{RT}$ /S cm <sup>-1</sup>	Transport properties <sup>b)</sup>	Reported characteristics <sup>c)</sup>	Ref.
<b>33c</b> p, 4P	10 <sup>-1</sup>	metal (300–275 K), semi (275–90 K, $\mathcal{E}_g = 0.10$ eV)	“analytically pure,” no EA	127
<b>33d</b> s, 4P	2.8	semi ( $\mathcal{E}_g = 0.028$ eV)	crystal structure, EPR, SQUID ( $\chi_{const} = 7.2\text{--}8.1 \times 10^{-4}$ emu mol <sup>-1</sup> ), no EA	128
<b>33e</b> p, 4P	3.7	semi ( $\mathcal{E}_g = 0.10$ eV)	EA (C, H), EPR, SQUID ( $\chi_{const} = 3.6 \times 10^{-4}$ emu mol <sup>-1</sup> )	129
<b>34</b> s, 4P	7	semi ( $\mathcal{E}_g = 0.06$ eV)	EPMA (Ni/S = 1/14.6, not agreeable), crystal structure, $\sigma_{RT}(2.44$ GPa) = 20 S cm <sup>-1</sup> , band calc., no EA	130
<b>35a</b> s, 4P	$4 \times 10^2$	metal (>0.6 K)	EA (C, H, S), crystal structure, SQUID (Pauli-like $\chi = 2.6\text{--}3.1 \times 10^{-4}$ emu/mol), band calc. dHvA oscillation	132–134
<b>36a</b> p, 4P	$3\text{--}4 \times 10^2$	metal (>230 K)	EA (C, H, S), SQUID ( $\chi_{RT} = 2.9 \times 10^{-4}$ emu mol <sup>-1</sup> )	134
<b>37</b> poly, 2P	6	semi ( $\mathcal{E}_g = 0.0390$ eV at RT, 0.0070 eV at 20 K)	EA (C, H, S; C deviates ca. 0.6%), SQUID (Pauli-like down to 50 K, $\chi_{RT} = 2.5 \times 10^{-4}$ emu mol <sup>-1</sup> ), Seebeck (5.5 $\mu$ V K <sup>-1</sup> at RT)	138
<b>38</b> p, 4P	8	metal (>120 K)	EPR (Dysonian, A/B $\approx 2.1$ at 220 K), no EA	139
<b>40</b> p, 2P	14	metal?	EA (C, H, N), crystal structure, EPR ( $g = 2.00$ at RT), no SQUID signal	140
<b>41</b> p, 4P	$>10^4$	metal (>5 K)	powder X-ray, phase transition at ca. 270 K, no EA	141
<b>41</b> p, 2P	$7 \times 10^{-10}$	semi ( $\mathcal{E}_g = 0.62$ eV)	EA(C, H, N; C deviates ca. 1.3%, N deviates ca. 0.6%), powder X-ray, SEM	142
<b>42a</b> s, 2P	1	semi (RT–100 K)	crystal structure, no EA	143 144

a) s: single crystal, p: compaction pellet, poly: polycrystal, 2P: two-probe method, 4P: four-probe method. b) semi: semiconductor.

c) EA: elemental analysis (agreement is within 0.3% unless otherwise mentioned for the elements in the parenthesis), “analytically pure”: no data for the elemental analysis, MEM: maximum entropy method, dHvA: de Haas-van Alphen.

Recently, it was reported that compound **40** showed a high conductivity of  $\sigma_{RT} = 14$  S cm<sup>-1</sup> as a compressed pellet.<sup>140</sup> The authors claimed it to be the first highly conductive single-component molecular material different from the TTF (or dithiolate)-type. However, the measurement was performed by a two-probe method, which is not appropriate for highly conductive materials. Furthermore, no significant SQUID response was observed for 200 K >  $T$  > 5 K, and the color is brownish-yellow, which cannot be explained by the presence of itinerant electrons in common. Temperature dependences of resistivity and optical properties are necessary to verify the results.

In 1979, Kimura, Inokuchi, et al. reported that the thin films of cytochrome-*c*<sub>3</sub> with a mixed-valence state (Fe<sup>2+</sup>/Fe<sup>3+</sup>) exhibited a high RT conductivity, which increases as temperature decreases ( $2 \times 10^{-2}$  S cm<sup>-1</sup> at 268 K).<sup>123–125</sup> The high conductivity was interpreted in terms of the percolation theory. The temperature dependence of conductivity in the highly conductive region is opposite to that of semiconductors and may preclude the ionic conduction as a dominant contribution. However, since the high conductivity is realized under the presence of hydrogenase and hydrogen, the system is not strictly a single-but multicomponent molecular solid.

At present, **35a** prepared by Tanaka et al. is the most reliable metal in this category ( $\sigma_{RT} = 4 \times 10^2$  S cm<sup>-1</sup>, metallic down to 0.6 K) based on its purity (elemental analysis (C, H, and S), crystal structure), temperature dependence of resistivity and magnetic susceptibility, and de Haas-van Alphen (dHvA) oscillations.<sup>132–134</sup>

### 3. Conductors of Charge Transfer Type

In this section, the design of molecular and crystal structures of (super)conductors will be described. We emphasize the strategies to obtain organic metals or other functional CT complexes in connection with the ionicity in the solid. Then, we discuss the strategies to increase (or decrease) the electronic dimensionality aiming to suppress (or induce) metal–insulator transition, the structural and physical properties of the ground state, and phase diagram and multi-critical points of TMTSF and ET superconductors.

The review articles and textbooks<sup>2–10,95,149–160</sup> treat the fundamental concept, molecular design, and strategy to prepare organic metals and/or superconductors mainly from the chemical viewpoint. The readers can get information about fundamental knowledge concerning the physical properties (transport, magnetic, optical, structural, and/or superconducting) of organic conductors from many books.<sup>161–166</sup> In addition, there are many review articles and conference proceedings concerning the conductive CT complexes.<sup>167</sup> The data mainly in the period 1972–1998 were accumulated by a Japanese group<sup>168</sup> on the subjects of 1) synthesis of donor and acceptor molecules and their molecular properties, 2) ionization potentials of donor molecules and electron affinities of acceptor molecules, 3) structural and physical properties of ET, BEDT-TSF (BETS), BEDO-TTF (BO), TTP, and DCNQI complexes (molecular structures are depicted in Fig. 14), 4) transport properties of other CT complexes, 5) magnetic properties of molecules, molecular solids, and CT complexes, 6) optical

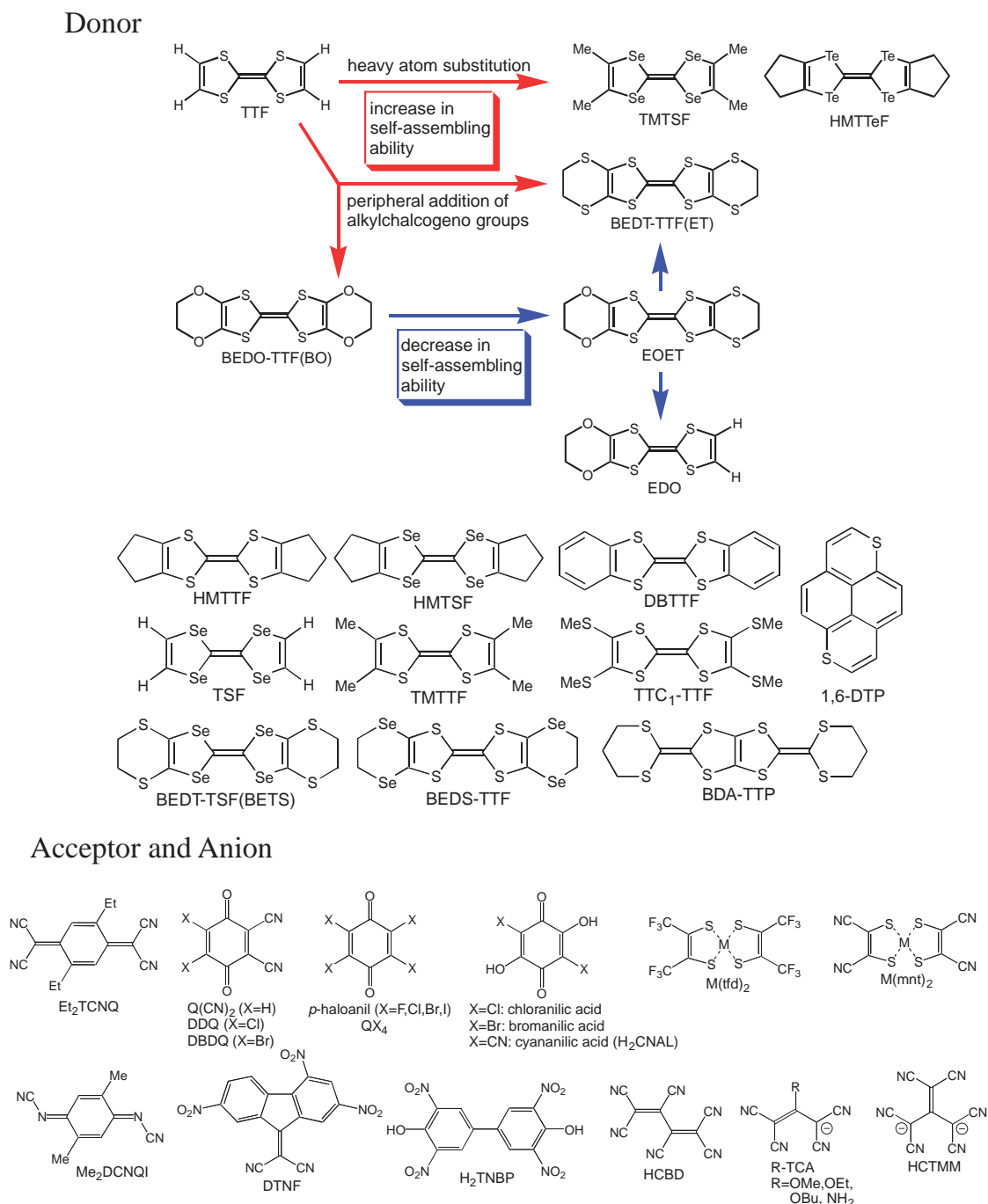


Fig. 14. Donor, acceptor, and organic anion in text. The upper figure represents the strategy for chemical modification of the TTF molecule to increase (red arrows) or decrease (blue arrows) the electronic dimensionality by the aid of an increase or suppress the self-assembling ability of the donor molecules, respectively.

properties (reflectance and absorption), 7) organic conductors under pressure, 8) neutral–ionic systems, 9) Langmuir–Blodgett films, 10) superconducting properties including C<sub>60</sub> materials, and 11) transport properties (Fermi surface, magnetoresistance, specific heat, and magnetic susceptibility) in the normal state of organic superconductors.

The first highly conducting organic CT compound, perylene•bromide was prepared by Akamatu, Inokuchi, and Matsunaga in 1954.<sup>169</sup> In as early as 1964, organic superconductors having a high critical temperature (*T<sub>c</sub>*) were predicted

by Little based on the electron–exciton interaction by the incorporation of high polarizability through a suitable molecular pendant on a conjugated 1D polymeric backbone.<sup>170</sup> Little's theory accelerated the study of organic conductors to a great extent. In 1968, Ginzburg extended Little's 1D model to a 2D model,<sup>171</sup> since the 1D system has instability inherent to low-dimensionality.<sup>172</sup> The most extensively studied acceptor molecule is TCNQ, prepared in 1960 by Acker et al.,<sup>173</sup> while the corresponding donor is TTF, prepared in 1970 by Coffen<sup>174</sup> and Wudl et al.<sup>175</sup> In 1973, the first organic metal TTF•TCNQ

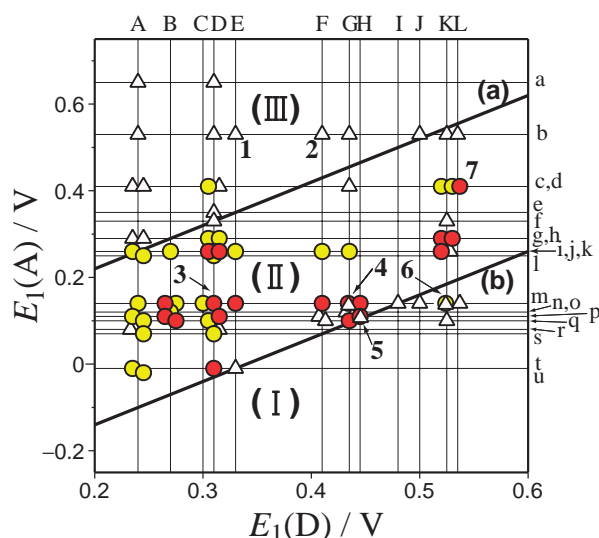


Fig. 15. Ionicity diagram for TTF·TCNQ system plotted as  $E_1(A)$  vs  $E_1(D)$  (vs SCE) after modification of the original diagram in Ref. 184.  $\Delta$ : insulators or semiconductors;  $\bullet$ : highly conducting in compaction studies;  $\bullet$ : organic metals. Some donors are A: TTN, B: TMTTF, D: TTF, E: HMTTF, F: HMTSF, G: TMTSF, H: TSF, J: TTC<sub>1</sub>-TTF, K: ET, L: DBTTF. Some TCNQs are a: 2,5-(CN)<sub>2</sub>, b: F<sub>4</sub>, c: 2,5-I<sub>2</sub>, i: F, m: TCNQ, p: 2,5-Et<sub>2</sub>. Complexes 1–7 are HMTTF·F<sub>4</sub>TCNQ, HMTSF·F<sub>4</sub>TCNQ, TTF·TCNQ, TMTSF·TCNQ, TSF·Et<sub>2</sub>TCNQ, ET·TCNQ, and DBTTF·Cl<sub>2</sub>TCNQ, respectively. ( $E_1(A)$  and  $E_1(D)$  in this figure are the peak values). Region I: neutral, II: partial CT, III: fully ionic. Line a:  $\Delta E(DA) = -0.02$  V, b:  $\Delta E(DA) = 0.34$  V.

was synthesized by Ferraris et al.<sup>176</sup> and Coleman et al.<sup>177</sup> Since then, more than two thousand metallic and highly conductive organic CT complexes have been synthesized.

**3.1 Donor–Acceptor (DA) Complexes. 3.1.1 Strategy to Obtain Organic Metals:** According to the most simplified theory by McConnell, Hoffman, and Metzger,<sup>178</sup> the boundary of the ionicity in CT complex solids is represented by the formula

$$I_D - E_A = M, \quad (17)$$

where  $I_D$ ,  $E_A$ , and  $M$  are the ionization potential of the donor (D), electron affinity of the acceptor (A), and Madelung energy in the crystal, respectively. The real system contains additional effects such as transfer interactions,<sup>179,180</sup> ionicity dependence of  $M$ ,<sup>181</sup> and size and shape effects on  $M$ .<sup>182,183</sup> As a result, there appears to be a narrow region of partial CT state, which is one of the most essential requirements for organic metals, between the fully ionic ( $I_D - E_A < M$ ) and the fully neutral ( $I_D - E_A > M$ ) regions. Consequently, conventional 1:1 CT solids  $D^{\delta+}A^{\delta-}$  are classified into three groups; namely, I) neutral insulator ( $0 \leq \delta \leq \delta_c$ ), II) partially ionic conductor when  $I_D - E_A \approx M$  ( $\delta_c \leq \delta < 1$ ), and III) fully ionic insulator ( $\delta = 1$ ) as demonstrated by Saito and Ferraris for the family of TTF·TCNQ (Fig. 15).<sup>184</sup> The threshold value  $\delta_c$  depends on the electronic dimensionality of a specific DA system and decreases with increasing the dimensionality of the system. Below the threshold value the system prefers to form alternat-

ing stacks rather than segregated ones, owing to the decrease in both the kinetic and Madelung energies with decreasing  $\delta$ , thus affording an insulator.

Figure 15 is a diagram of structurally related acceptors on the vertical line and structurally related donor molecules on the horizontal line for the conventional 1:1 TTF·TCNQ system (the donor and acceptor molecules are presented in Fig. 14).<sup>184</sup> The two lines **a** and **b** in Fig. 15 are connected with a modified Eq. 17,  $E_A = I_D - M(\delta)$ , and have been used to discriminate the three regions. The partial CT regime is represented by Eq. 18 and is located between the two lines **a** and **b** in Fig. 15, where  $\Delta E(DA) (= E_1(D) - E_1(A)$ :  $E_1$ , first redox potential vs SCE) is a redox version of ( $I_D - E_A$ ) and  $\delta_c$  is estimated as 0.5.

$$-0.02 \leq \Delta E(DA) \leq 0.34 \text{ V}. \quad (18)$$

In the partially CT regime, the complex is either highly conductive ( $\circ$ ) or metal ( $\bullet$ ) when it has uniformly spaced and charged segregated columns. Otherwise, it becomes an insulator ( $\Delta$ ) when it forms either non-uniform segregated columns, charge-ordered state, SDW (spin density wave) state, or anion-ordered state. Also, it becomes a semiconductor when it forms alternating stacks. In this case, the complex resides close to the neutral–ionic (N–I) phase transition like TTF·*p*-chloranil ( $\delta = 0.3 \leftrightarrow \delta = 0.7$ ). Some charge-ordered insulators and N–I systems exhibit photo-induced and/or electric field-induced switching phenomena (see section 4.3).

In the fully ionic region, the complex is an insulator of Mott type, Peierls type, antiferromagnet, or spin-Peierls type.

**3.1.2 Organic Metal, Mott Insulator, and Complex Isomer: Ionicity Diagram:** The 1:1 CT solids of the TTF·TCNQ system in the region of  $\Delta E(DA) < -0.02$  V (above the upper borderline **a** in Fig. 15) are fully ionic insulators including magnetic systems (Mott insulators; HMTTF·F<sub>4</sub>TCNQ<sup>185</sup> (1) and HMTSF·F<sub>4</sub>TCNQ (2)<sup>186–188</sup> in Fig. 15) and spin-Peierls ones (TTF[M(tfd)<sub>2</sub>] (M = Cu, Au)<sup>189–191</sup>). Those in the region of  $\Delta E(DA) > 0.34$  V (below the lower borderline **b** in Fig. 15) prefer an alternating stacking, and thus are insulating with small ionicity ( $\delta < 0.5$ ). Near the lower borderline, the bistability concerning the ionicity between the neutral and partial CT states is realized: namely, the monotropic complex isomers (TMTSF·TCNQ (4),<sup>192–196</sup> TSF·Et<sub>2</sub>TCNQ (5),<sup>197</sup> and ET·TCNQ (6)<sup>184,198–204</sup>). Table 8 summarizes selected examples of monotropic complex isomers. The former two (4 and 5) are within the partial CT regime in Fig. 15 and afford metallic segregated complexes preferentially. They also afford insulating alternating complexes. Even though ET·TCNQ (6) is expected to afford a neutral insulating complex based on its  $\Delta E(DA)$  value,<sup>184</sup> a highly conductive one has been prepared by Mizuno, Cava, and Garito.<sup>198</sup> Subsequent work by Saito, Enoki, et al. to explore the ionicity diagram (Fig. 15, which originally lacked the insulating ET·TCNQ) afforded the neutral and insulating complex isomers.<sup>199</sup> The conductive and insulating phases of ET·TCNQ exhibit CT bands at 3.6 and  $5.7 \times 10^3$  cm<sup>−1</sup> in KBr, respectively.<sup>199</sup> These results indicate that the ET·TCNQ system is actually located in close vicinity of the boundary of complex isomerization from the neutral side, and furthermore, suggest that the ET molecule has a significant ability to form a segregated column (see section 3.4).

Table 8. Selected Examples of Monotropic Complex Isomers

D·A <sup>a)</sup>	D:A, Ionicity( $\delta$ )	Characteristics	Ref.
TMTSF·TCNQ	1:1, 0.21	red, alternating, insulating	192–196
	1:1, 0.57	black, segregated, metal ( $\sigma_{RT} = 1.2 \times 10^3 \text{ S cm}^{-1}$ , $T_{MI} = 65 \text{ K}$ )	
TSF·Et <sub>2</sub> TCNQ	1:1, neutral	red, alternating, insulating	197
	1:1, partial	black, segregated, metal ( $\sigma_{RT} = 8 \times 10^2 \text{ S cm}^{-1}$ , $T_{MI} = 100 \text{ K}$ )	
ET·TCNQ	1:1, ca. 0.2	monoclinic, alternating, insulating ( $\sigma_{RT} = 10^{-6} \text{ S cm}^{-1}$ )	198–201
	1:1, 0.5	triclinic, segregated, metal ( $\sigma_{RT} = 10 \text{ S cm}^{-1}$ , $T_{MI} = 300 \text{ K}$ ), AF ( $T_N = 3 \text{ K}$ )	199–202
	1:1, 0.74	triclinic, segregated, metal ( $\sigma_{RT} = 30 \text{ S cm}^{-1}$ , no $T_{MI}$ , anomalies at 20 K)	203,204
TTF·QCl <sub>4</sub>	1:1, 0.3	$\sigma_{RT} = 10^{-5} \text{ S cm}^{-1}$ , neutral–ionic phase transition ( $T_{NI} = 81 \text{ K}$ )	208–213
	—, 0.71	$\sigma_{RT} = 10^{-2} \text{ S cm}^{-1}$ , black needles, stoichiometry is unknown	214
	1:1, 1	insulating, black needles, dimerized ( $D^{\bullet+}$ ) <sub>2</sub> , ( $A^{\bullet-}$ ) <sub>2</sub>	209,214
BMDTP·TCNQ	1:1, 0.31	black, $\sigma_{RT} = 3.4 \times 10^{-6} \text{ S cm}^{-1}$ , $\varepsilon_g = 0.52 \text{ eV}$	215,216
	1:1, 0.71	black, $\sigma_{RT} = 1.1 \times 10^2 \text{ S cm}^{-1}$ , $T_{MI} = 110 \text{ K}$	

a) QCl<sub>4</sub>: *p*-chloranil, BMDTP: 2,7-bis(methylthio)-1,6-dithiapyrene.

Accordingly, Saito, Enoki, et al. started to explore the CT complexes based on the ET molecules, and resulted in the discovery of the 2D ET conductors.<sup>205,206</sup> As for the ET·TCNQ system, crystal structures of both isomers (monoclinic and triclinic, Table 8) were determined by Mori and Inokuchi.<sup>200,201</sup> The triclinic phase becomes a Mott insulator with a unit of the TCNQ dimer with  $S = 1/2$  spin below the metal–insulator (MI) transition at 300 K, and then becomes an antiferromagnet with  $T_N = 3 \text{ K}$ .<sup>202</sup> Another triclinic phase with  $\delta = 0.74$  was discovered recently and is metallic down to very low temperatures.<sup>203,204</sup> TTF·TCNQ (**3**) is a typical metal with  $\delta = 0.59$  and exhibits a Peierls transition at  $T_{MI} = 59 \text{ K}$ .<sup>161,162</sup>

DBTTF·Cl<sub>2</sub>TCNQ (**7**) resides in the partial CT regime rather close to the upper border line **a**. The complex exhibits a Peierls transition at  $T_{MI} = 180 \text{ K}$ , and then the insulating phase exhibits the second phase transition at 38 K due to the spin-Peierls instability.<sup>207</sup>

**3.1.3 Neutral–Ionic System:** Torrance et al. used the CT transition energies of neutral ( $h\nu_{CT}^N$ , Eq. 19) and ionic ( $h\nu_{CT}^I$ , Eq. 20) solid complexes to discriminate between the neutral and ionic CT complexes having alternating stacks (Fig. 16).<sup>208</sup>

$$h\nu_{CT}^N = I_D - E_A - C' + X, \quad (19)$$

$$h\nu_{CT}^I = -I_D + E_A + (2\alpha - 1)C' + X', \quad (20)$$

where  $\alpha$  is the Madelung constant,  $C'$  is the averaged electrostatic attraction energy between neighboring D and A molecules, and  $X$  and  $X'$  are mainly resonance stabilization energies. So the N–I phase boundary condition ( $h\nu_{CT}^N = h\nu_{CT}^I$ ) gives

$$I_D - E_A = \alpha C' + (X' - X), \quad (21)$$

which is in principle the same criterion as Eq. 17. By the aid of Fig. 16, Torrance et al. discovered a new enantiotropic phase transition ( $T_{NI}$ ) at 81 K for TTF·QCl<sub>4</sub> (F in Fig. 16) from a neutral ( $\delta = 0.3$ ) to ionic ( $\delta = 0.7$ ) state (N–I system).<sup>208</sup>

$$D^{0.3+}A^{0.3-} \leftrightarrow D^{0.7+}A^{0.7-}. \quad (22)$$

A similar diagram to Fig. 16 for a benzidine·TCNQ system plotted as resistivity ( $\rho_{RT}$ ) or activation energy for conduction ( $\varepsilon_a$ ) vs ( $I_D - E_A$ ) revealed that 3,3',5,5'-tetramethylbenzidine·TCNQ (C in Fig. 17) is another N–I system, showing the highest  $T_{NI}$  (205 K) at ambient pressure.<sup>217,218</sup> Some selected exam-

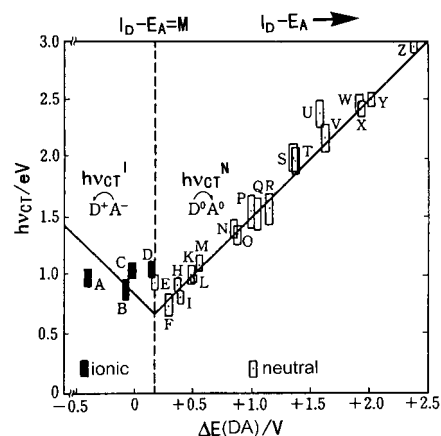


Fig. 16. Ionicity diagram by Torrance et al. for CT complexes with alternating columns plotted as  $h\nu_{CT}$  vs  $\Delta E(DA)$ .<sup>208</sup> ■: ionic and □: neutral complexes. Dashed vertical line corresponds to Eq. 21 (Eq. 17). The V-shaped line represents Eqs. 19 and 20. Some complexes are A: TMPD·F<sub>4</sub>TCNQ, B: dihydromethylphenazine·TCNQ, C: TMPD·TCNQ, E: tetramethyldiaminopyrene·TCNQ, F: TTF·QCl<sub>4</sub>, H: DBTTF·TCNQ, and L: perylene·F<sub>4</sub>TCNQ.

ples of enantiotropic N–I systems are shown in Table 9. The high conductivity of the N–I system with alternating columns has been interpreted by the soliton or domain wall model,<sup>220</sup> and they exhibit memory or switching phenomena.<sup>218,225</sup> In order to develop new molecular devices, an N–I system showing the transition near RT and ambient pressure with large ionicity change, quick response time (switching) or bistability (memory), and high durability is worth being explored.

**3.1.4 Ionicity Diagram:** Figure 18 presents the ionicity diagrams for a 1,6-dithiapyrene system by Nakasuji,<sup>233</sup> and BO,<sup>234</sup> EOET,<sup>235</sup> and HMTTeF systems<sup>236–238</sup> by Saito et al. The solid V-shaped line represents Eqs. 19 and 20 for the TTF·*p*-quinone system, where  $\Delta E(DA)$  is used instead of ( $I_D - E_A$ ). Since the  $E_1(A)$  of the TCNQ system deviates from the *p*-quinone system towards the lower side by 0.13–0.16 V, an appropriate V-shaped line for the TCNQ system was obtained by a parallel shift of the V-shaped line by such a differ-

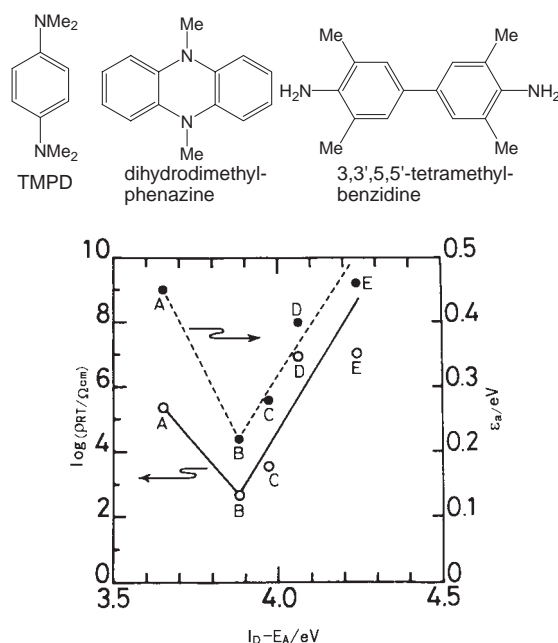


Fig. 17. Ionicity and conductivity diagram for 3,3',5,5'-tetramethylbenzidine·TCNQ system plotted as  $\log \rho_{RT}$  and activation energy for conduction  $E_a$  vs  $(I_D - E_A)$ .<sup>217</sup> A:  $\text{F}_4\text{TCNQ}$ , B:  $\text{FTCNQ}$ , C:  $\text{TCNQ}$ , D:  $\text{Me}_2\text{TCNQ}$ , E:  $(\text{MeO})_2\text{TCNQ}$ .

ence in  $E_1(\text{A})$  (Figs. 18b–18d, dotted V-shape line). The two vertical lines represent Eq. 18 and the horizontal line indicates  $h\nu_{CT} = 5 \times 10^3 \text{ cm}^{-1}$ . The following are remarks derived from Fig. 18:

1) The complexes exhibiting  $h\nu_{CT}$  values below the horizontal line have both a partial CT state and a segregated column or layer, and thus are good candidates for organic metals (Care should be taken that an insulating complex with a partial CT state having 1) a Mott insulating state with dimer as a unit, 2) a charge-separated (or charge-ordered) state, or 3) a distorted lattice, also exhibits a low  $h\nu_{CT}$ ).

2) In the metallic state, the BO, EOET, and HMTTeF complexes exhibit a wider range of  $\Delta E(\text{DA})$  than the TTF·TCNQ system. This indicates that a stable and high-dimensional metallic state is realized by the self-assembling ability of the donor molecules (see also Fig. 14),<sup>234–243</sup> which was confirmed by structural analysis. A similar wide range of  $\Delta E(\text{DA})$  was

observed for 2D CT complexes of BEDO-DBTTF.<sup>120</sup> The EDO complexes, however, exhibit nearly the same  $\Delta E(\text{DA})$  region for conductors as that for the TTF·TCNQ system (Fig. 19), indicating a substantial decrease in the self-assembling ability of EDO molecules in comparison with BO.<sup>244</sup>

3) In general, the complexes residing on the V-shaped line have an alternating column (it should be noted, however, that some fully ionic complexes having an alternating column exhibit no  $h\nu_{CT}^1$  but an absorption due to the electron transfer between radicals of the same component). All the complexes having an alternating column are insulators except those allocated near the N–I boundary (Group C). For example,  $\text{HMTTeF} \cdot \text{Et}_2\text{TCNQ} \cdot (\text{THF})_x$  (1 in Fig. 18d) and  $\text{HMTTeF} \cdot \text{BTDA} \cdot \text{TCNQ} \cdot (\text{THF})_x$  (2 in Fig. 18d) are metallic with  $\sigma_{RT}$  of 0.5–10 and 80–100  $\text{S cm}^{-1}$ , respectively. The conduction in these metallic complexes having alternating columns is explained by the soliton or domain-wall mechanism (see section 4.3.3).<sup>243</sup>

4) The complexes residing far above the V-shaped line have a molecular packing that is disadvantageous for CT interactions (such as clathrate, Group E<sup>234,235</sup>).

In summary, a metallic band structure is realized when the system has the partial CT state and molecules form uniform segregated columns or layers. The partial CT state can be predicted and controlled by  $(I_D - E_A)$  or  $\Delta E(\text{DA})$  for a specific DA system, and the complex exhibits a low lying CT band below  $5 \times 10^3 \text{ cm}^{-1}$ . The diagram of ionicity as depicted in Figs. 15–19 is a clue to explore functional conductors of CT type such as molecular metals, Mott insulators, N–I systems, complex isomers, and self-assembled 2D conductors. Similar diagrams for other systems have been proposed for *p*-phenylenediamine,<sup>182</sup> benzidine,<sup>183</sup> 1,4,6,8-tetrakis(dimethylamino)pyrene (TDAP),<sup>245</sup> and  $\text{C}_{60}$  (see section 5.2)<sup>246</sup> concerning the charge-transfer interaction, and for aniline·picric acid (see section 4.2.1),<sup>1,247</sup> 2,2'-biimidazole,<sup>248</sup> and dihydrotetracyanodiphenodimethane (4,4'-bis(dicyanomethyl)biphenyl) ( $\text{H}_2\text{TCNDQ}$ )<sup>249</sup> concerning the charge and proton-transfer interactions (Chart 7).

**3.2 Radical Salts. 3.2.1 Stoichiometry:** The Mott criterion implies that a 1:1 organic radical salt with  $W < U_{\text{eff}}$  is a Mott insulator when the salt has a uniform segregated stacking.<sup>78</sup> As a consequence, the requirement for an organic metal for the radical salt is to obtain a salt with  $m:n$  ( $m \neq n$ ) stoichiometry together with uniform segregated stacking. However,

Table 9. Selected Examples of Enantiotropic Complex Isomers (N–I System)

D <sup>a)</sup>	A <sup>b)</sup>	D:A	$T_{\text{NI}}^{\text{c)}$ /K	$P_{\text{NI}}^{\text{d)}$ /GPa	Change of $\delta$	Ref.
TTF	$\text{QCl}_4$	1:1	81	1.1	0.3 → 0.7	208–213, 219, 221–223
	$\text{QBr}_4$	2:1		2.7		
	$\text{QI}_4$	1:1		1.9		
	$\text{QI}_4$	2:1		3.1		
2,6- $\text{Me}_2\text{TTF}$	$\text{QCl}_4$	1:1	65	1.2	0.46 → 0.54	227–229
3,3',5,5'-TMB	TCNQ	1:1	205		0.59 → 0.69	230
TTF	$\text{Me}_2\text{DCNQI}$	1:1		0.9	$\Delta\delta = 0.8$	231
CMPD	$\text{Me}_2\text{DCNQI}$	1:1	200			232

a)  $\text{Me}_2\text{TTF}$ : dimethyl-TTF, TMB: tetramethylbenzidine, CMPD: 2-chloro-5-methyl-*p*-phenylenediamine.

b)  $\text{Me}_2\text{DCNQI}$ : 2,5-dimethyldicyanoquinodimethine. c) N–I transition temperature at ambient pressure.

d) N–I transition under pressure at RT.



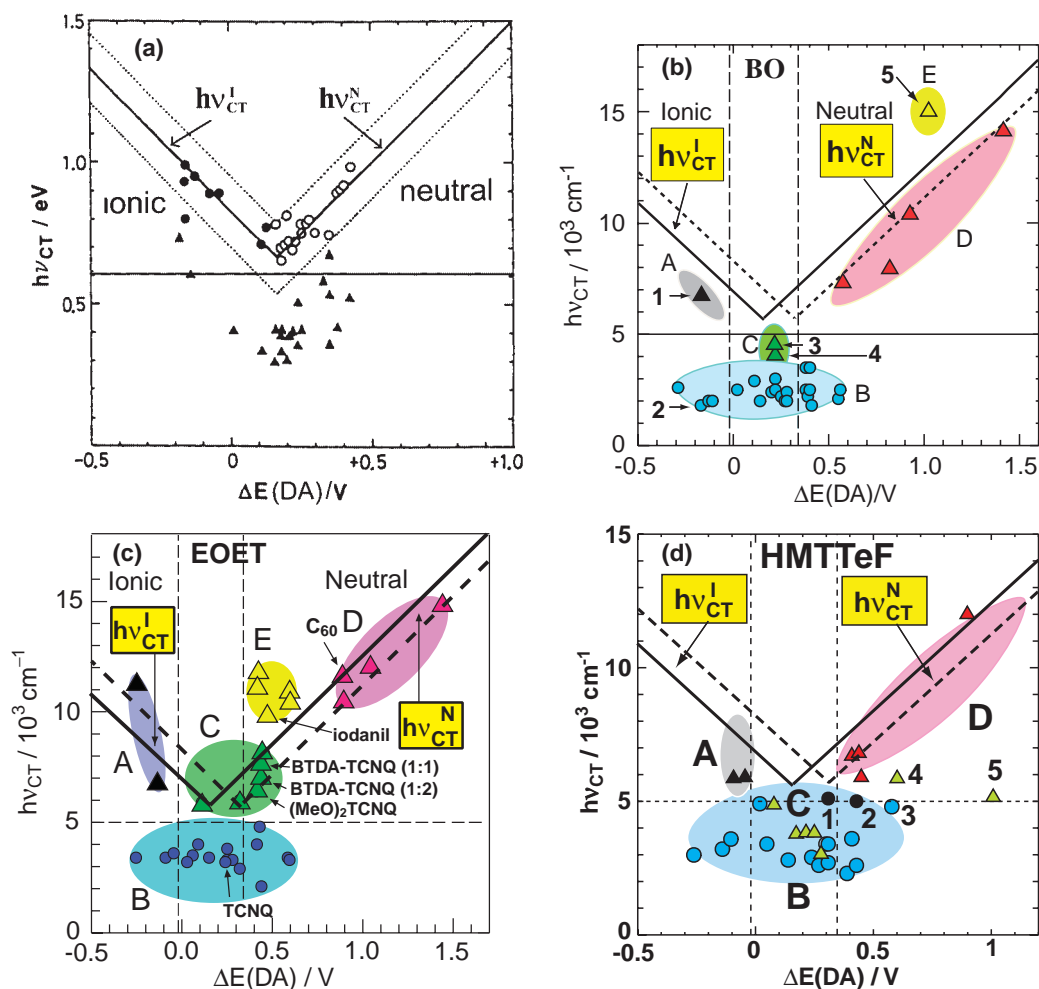


Fig. 18. Diagram of ionicity, conductivity, and stacking of DA complexes. The first transition energy in a solid ( $h\nu_{CT}$ ) is plotted against the difference in half-wave redox potential between donor ((a) 1,6-dithiapyrene,<sup>233</sup> (b) BO,<sup>234</sup> (c) EOET,<sup>235</sup> and (d) HMTTeF<sup>236–238</sup>) and acceptor molecules  $\Delta E(DA)$ . (a) by Nakasuji: See Ref. 233 as for symbols. (b)–(d) by Saito et al.: Group A: fully ionic complexes, B: partial CT one with segregated column, C: partial CT ones with alternating column, D: neutral ones with alternating column, and E: clathrate ones. Metallic or highly conductive complexes are depicted by circles (Group B) and poor conductive ones by triangles in (b)–(d) among which the complexes depicted by green triangles (mainly Group C) are considerably conductive. In general, the complexes residing on the V-shaped line have alternating columns and are insulating while those below  $5 \times 10^3 \text{ cm}^{-1}$  have segregated columns or layers and are conductive. The donor molecules having self-assembling ability afford a wider range of  $\Delta E(DA)$  for metals than that for the low-dimensional TTF•TCNQ system, which is limited within two vertical lines. (b) BO complexes with  $F_4\text{TCNQ}$  (1: 1:1, 2: 9:5:5THF), TCNQ (3),  $C_{14}\text{TCNQ}$  (4: 9:4:2H<sub>2</sub>O), and H<sub>2</sub>TNBP (5: 3,3',5,5'-tetranitrophenyl-4,4'-diol). 3 and 4 are highly conductive, while 5 is a clathrate complex. (d) HMTTeF complexes with Et<sub>2</sub>TCNQ (1) and BTDA-TCNQ (2) are metallic with alternating stacks. Complexes with bromanillic acid (3), chloranillic acid (4), and H<sub>2</sub>TNBP (5) are highly conductive probably owing to the partial proton transfer from the acceptor molecules.

several exceptions exhibiting a metallic behavior even with 1:1 stoichiometry have been reported by Shibaeva et al.,<sup>250</sup> Mori et al.,<sup>251,252</sup> and Takimiya et al.<sup>253</sup> These complexes are based on molecules having an extended  $\pi$ -moiety or self-assembling ability (Table 10).

The stoichiometry is one of the key parameters that govern the transport property of the CT complexes. Except for some special cases, however, the stoichiometry cannot be controlled or designed apriori even in the DA type complexes, where the conventional stoichiometries are 1:1, 2:1, 3:2, 2:3, and 1:2. Some have multiple and unconventional ratios (Table 11).

In several cases, the D<sub>2</sub>A or DA<sub>2</sub> complex composed of very strong acceptor or donor molecules, respectively, has

structural and physical features characteristic to radical salts; namely, the excess component molecules form a segregated column, while the counterpart molecules play the role of counter ion and stack between the columns with its molecular plane parallel to the column (i.e. (TMTTF)<sub>2</sub>HCBT,<sup>59</sup> (TMTSF)<sub>2</sub>-aza-TCNQ (Chart 8),<sup>269,270</sup> and (TMTSF)<sub>2</sub>CF<sub>3</sub>TCNQ<sup>9</sup>). Similarly, some radical salts have an unconventional ratio, i.e., (perylene)<sub>2</sub>X<sub>1.4</sub> (X = PF<sub>6</sub>, AsF<sub>6</sub>,  $\sigma_{RT} = 1.4 \times 10^3 \text{ S cm}^{-1}$ ),<sup>261</sup> (TTF)(HSO<sub>4</sub>)<sub>1.17</sub> ( $\sigma_{RT} = 29 \text{ S cm}^{-1}$ ),<sup>271,272</sup> TTN(NO<sub>3</sub>)<sub>0.74</sub> ( $\sigma_{RT} = 500 \text{ S cm}^{-1}$ ),<sup>273</sup> TTN(PF<sub>6</sub>)<sub>0.61</sub> ( $\sigma_{RT} = 762 \text{ S cm}^{-1}$ ),<sup>273,274</sup> and some of the salts listed in Table 11. Especially the unconventional stoichiometry is rather common for the transition-metal coordination compounds: (TBA)<sub>2</sub>[Ni(dmit)<sub>2</sub>]<sub>7</sub>(CH<sub>3</sub>CN)<sub>2</sub>,<sup>275</sup>



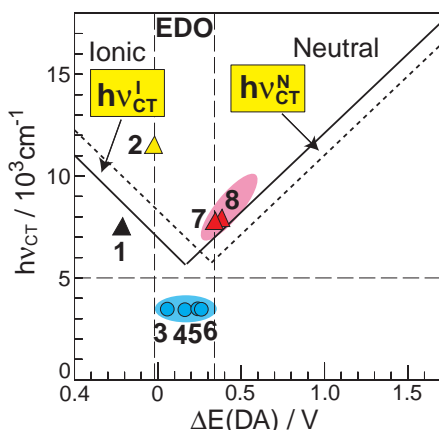


Fig. 19. EDO complexes with 1: F<sub>4</sub>TCNQ, 2: F<sub>4</sub>TCNQ (different phase from 1), 3: FTCNQ, 4: TCNQ, 5: MeTCNQ, 6: Me<sub>2</sub>TCNQ, 7: BTDA-TCNQ, 8: (EtO)<sub>2</sub>-TCNQ.<sup>244</sup>

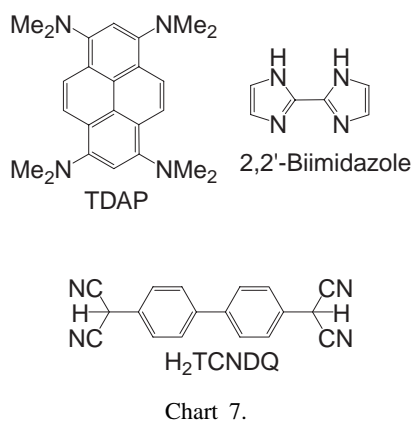
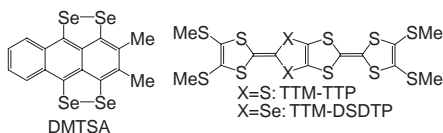


Table 10. Selected Metallic Salts with 1:1 Stoichiometry

Complex <sup>a)</sup>	$\sigma_{RT}/S\text{ cm}^{-1}$	$T_{MI}/K$	Ref.
$\delta\text{-(ET)} \cdot \text{I}_3(\text{TCE})_{1/3}$	$1\text{--}2 \times 10^2$	130	250
TTM-TTP $\cdot \text{I}_3$	$7 \times 10^2$	160	251
(TTM-DSDTP)GaCl <sub>4</sub>	$2.8 \times 10^2$	60	252
DMTSA $\cdot \text{BF}_4$	$4.5 \times 10^2$	180	253
DMTSA $\cdot \text{NO}_3$	$4.4 \times 10^2$	220	253

a) TCE: 1,1,2-trichloroethane.



$\text{K}_{1.64}[\text{Pt}(\text{ox})_2](\text{H}_2\text{O})_x$ ,<sup>276</sup>  $[\text{Ni}(\text{Pc})]\text{I}_x$  ( $x = 0.56\text{--}1.74$ , iodines are  $\text{I}_3^-$ ),<sup>277,278</sup>  $[\text{Ni}(\text{bqd})_2]\text{I}_{0.52}(\text{PhMe})_{0.32}$  (iodines are  $\text{I}_3^-$ ),<sup>279</sup> and  $[\text{Ni}(\text{dpg})_2]\text{I}$  (iodines are  $\text{I}_5^-$ ),<sup>280,281</sup> where ox and bq d are oxalato and benzoquinonedioximato, respectively. The degree of CT ( $\delta$ ) can be evaluated based on stoichiometry, where the  $\delta$  value is connected with the Fermi wavenumber ( $k_F$ ) by Eq. 23.

$$k_F = \frac{\pi}{2a} \delta. \quad (23)$$

**3.2.2 Mott Insulator with a Unit of Dimer:** The  $\text{D}_2\text{X}$  (X: monoanion) and  $\text{MA}_2$  (M: monocation) are the most common

stoichiometries for conductive radical salts including superconductors. In the framework of the weak electron correlation, the system has a three-quarter-filled band ( $k_F = (1 - \frac{\delta}{2}) \frac{\pi}{a} = \frac{3\pi}{4a}$ ) for the former or a quarter-filled band ( $k_F = \frac{\delta\pi}{2a} = \frac{\pi}{4a}$ ) for the latter. Many of the 2:1 (or 1:2) salts have a dimerized nature within the segregated stack or layer such as  $(\text{TMTSF})_2\text{X}$ ,  $\alpha'$ -,  $\beta$ -,  $\beta'$ -, or  $\kappa$ -type packing of  $(\text{ET})_2\text{X}$ , etc.,<sup>162–164</sup> and the HOMO band is split into upper and lower bands due to dimerization (Fig. 20).

The upper-HOMO band for  $\text{D}_2\text{X}$  or lower-LUMO band for  $\text{MA}_2$  is half-filled provided that  $U_{\text{eff}}$  is negligible compared to the bandwidth of the upper ( $W_U$ ) or lower band ( $W_L$ ). The energy splitting of the upper and the lower bands ( $\Delta E_d$ ) corresponds to the dimerization energy of a pair ( $\Delta E_d = 2t_d$ , where  $t_d$  is the intra-dimer transfer integral). The on-site Coulomb repulsion of a dimer ( $U_d$ ) is newly defined as<sup>122</sup>

$$U_d = \Delta E_d + \frac{(U - \sqrt{U^2 + 4\Delta E_d^2})}{2}. \quad (24)$$

Since  $U$  of a D or A molecule is much larger than the  $\Delta E_d$  values of those molecules,  $U_d$  can be approximated by  $\Delta E_d$ .<sup>282</sup> So, the Mott criterion is modified as “when the  $\Delta E_d$  value is sufficiently larger than the bandwidth of the upper or lower band ( $\Delta E_d > W_{U(\text{or } L)}$ ), the 3/4- or 1/4-filled electronic system turns into a Mott insulating state.” Therefore, the Mott criterion for dimerized  $\text{D}_2\text{X}$  or  $\text{MA}_2$  is expressed by Eq. 25.

$$\begin{aligned} \Delta E_d > W_{U(\text{or } L)} & \quad \text{Mott insulator} \\ \Delta E_d < W_{U(\text{or } L)} & \quad \text{metal} \end{aligned} \quad (25)$$

The tight-binding model based on the extended Hückel method well discriminates Mott insulators ( $W_{U(\text{or } L)}/\Delta E_d < 1$ ) and metals ( $W_{U(\text{or } L)}/\Delta E_d > 1$ ) (see section 3.6.1). Most of the 10 K class ET superconductors have the ratio of  $W_U/\Delta E_d \approx 1.1\text{--}1.2$  suggesting the significant electron correlation. Many of them are highly conductive despite their name as “Mott insulator,” and the most pronounced character is the enhanced magnetic susceptibility as expressed by Eq. 26:<sup>283</sup>

$$\chi_{\text{obs}} = \frac{\chi_0}{1 - D(\epsilon_F)U_{\text{eff}}} = \frac{\chi_0}{1 - \xi}, \quad (26)$$

where the observed  $\chi_{\text{obs}}$  is enhanced by the Stoner factor  $\xi$  ( $< 1$ ) in comparison with the noninteracting  $\chi_0$ . Usually it has been observed that the spin susceptibility of the metallic  $(\text{ET})_2\text{X}$  ranges  $3\text{--}4 \times 10^{-4} \text{ emu mol}^{-1}$ , while the typical Mott insulating  $(\text{ET})_2\text{X}$  has 2–3 times enhanced susceptibility at RT. Table 12 summarizes selected examples of  $(\text{ET})_2\text{X}$  Mott insulators, where only salts with sufficient resistivity and magnetic susceptibility data are listed.

**3.3 Strategy to Increase (or Decrease) Electronic Dimensionality Aiming to Suppress (or Induce) Metal-Insulator Transition.** Since the metallic state in the low-dimensional electronic system is unstable, an increase in the electronic dimensionality is necessary to suppress the complete nesting of Fermi surfaces by  $2k_F$  modulation. Several attempts have been made through both physical methods such as “pressure” and chemical methods such as “heavy atom substitution” (from TTF to TMTSF, HMTTeF, and their analogues) or “peripheral addition of alkylchalcogeno groups” (from TTF to BO, EOET, ET, and their analogues) (see Fig. 14).<sup>6,10</sup>

Table 11. Selected Organic Conductors Having Multiple Stoichiometries

D or cation	A or anion	Ratio <sup>a)</sup>	$\sigma_{RT}$ and characteristics <sup>b)</sup>	Ref.
DA Type				
TMTTF	HCBD	1:1	$<1 \times 10^{-15}$	59,254,255
		2:1	$3.0 \times 10^{-4}$ ( $\epsilon_g = 0.32$ eV), AF	59,254,255
TMTTF	TCNQ	1:1	$6.0 \times 10^2$ ( $T_{MI} = 65$ K)	256
		1.3:2	$1.0 \times 10$	257
		1.66:2	$5.0 \times 10$ ( $T_{MI} = 150$ K)	257
BEDO-DBTTF	Me <sub>2</sub> TCNQ	1:1	$<10^{-8}$ , alternating, neutral CT	120
		3:1:PhCl	3.3	120
	(MeO) <sub>2</sub> TCNQ	1:1	$<10^{-8}$ , alternating, neutral CT	120
		2:1	3.2	120
TTT	TCNQ	1:1	1	258
		1:2	20–160 (metal, $T_{max} = 90$ K)	155
TTC <sub>1</sub> -TTF	TCNQ	1:1	$2.6 \times 10^{-6}$ ( $\epsilon_g = 0.60$ eV), DDAA stacking	60,259
		2:1	$1.8 \times 10^{-5}$ ( $\epsilon_g = 0.34$ eV), DDADDA stacking	60,259
Ferrocene	Au(dmit) <sub>2</sub>	1:3	0.12 ( $\epsilon_g = 0.084$ eV)	260
		1:4	0.1 ( $\epsilon_g = 0.112$ eV)	261
Cation Radical Salt				
Perylene	AsF <sub>6</sub> <sup>−</sup>	2:1:0.66(THF)	50–100	262
		2:1.4	$1.4 \times 10^3$	262
		2:1.5:0.5(THF)	$1.4 \times 10^3$	262
		6:1	0.5	262
Perylene	Ni(mnt) <sub>2</sub> <sup>−</sup>	2:1 $\alpha$	300–700 (metal, $T_{MI} = 25$ K), dimerized Ni(mnt) <sub>2</sub>	263–264
		2:1 $\beta$	50 (metal, $T_{max} = 255$ K)	263–264
ET	Pd(dto) <sub>2</sub> <sup>2−</sup>	2:1 $\beta$	$6.0 \times 10^{-3}$ ( $\epsilon_g = 0.36$ eV), D <sup>•+</sup> D <sup>•+</sup> A <sup>2−</sup> alternating	121
		2:1 $\gamma$	$4.3 \times 10^{-4}$ ( $\epsilon_g = 0.44$ eV), D <sup>•+</sup> D <sup>•+</sup> A <sup>2−</sup> alternating	121
		4:1	1 (metal)	121
ET	Ni(dto) <sub>2</sub> <sup>2−</sup>	2:1	$1.5 \times 10^{-4}$ ( $\epsilon_g = 0.62$ eV)	121
		4:1	10 (metal > 60 mK)	265
ET	TNBP <sup>2−</sup>	4:1	50–80 (metal > 3 K), (ET <sup>0.5+</sup> ) <sub>4</sub> (TNBP <sup>2−</sup> )	266
		2:1	0.2 ( $\epsilon_g = 0.178$ eV), (ET <sup>0.5+</sup> ) <sub>2</sub> (HTNBP <sup>−</sup> )	266
ET	ClO <sub>4</sub> <sup>−</sup>	2:1:0.5(TCE)	25–30 (metal, see section 3.3.3)	205
		2:1:dioxane	1 (semiconductor)	267,268
		3:2	50 ( $T_{MI} = 170$ K)	267,268
		1:2	insulator	267,268
BO	I <sub>3</sub> <sup>−</sup>	2.4:1	100–280 (metal $\geq 1.2$ K)	239
		1:1	$10^{-6}$ ( $\epsilon_g = 0.86$ eV)	234
		1:2	$<10^{-9}$	241
BO	HCTMM <sup>2−</sup>	5:1:2(PhCN)	70–140 (metal $\geq 1.5$ K)	234
		4:1:2(TCE)	100–110 (metal, $T_{MI} = 170$ K)	234

a) PhCN: benzonitrile. b)  $T_{OD}$ : transition temperature of the order–disorder of anion, AF: antiferromagnet.

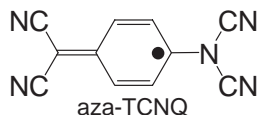


Chart 8.

**3.3.1 Heavy Atom Substitution: Self-Assembling Ability of TMTSF Molecules, Se...Se Atomic Contacts, and 1D Superconductors:** The most successful molecule by “heavy atom substitution” is the TMTSF molecule, which has provided eight organic superconductors with inorganic counter anions X; (TMTSF)<sub>2</sub>X mainly was developed by Bechgaard et al. (Table 13).<sup>162–164,319–328</sup> Among them, the superconducting NbF<sub>6</sub> salt was recently obtained by electrocrystallization

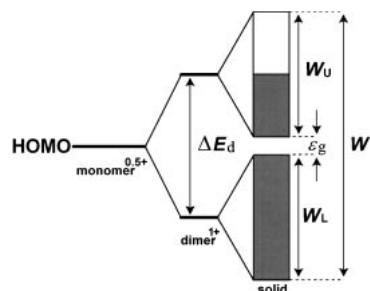


Fig. 20. Schematic band structure of the dimerized system with three electrons per dimer.  $\Delta E_d$  is the dimerization energy.  $W_U$ ,  $W_L$ , and  $W$  are the upper, lower, and total bandwidths, respectively.<sup>9</sup>

Table 12. Selected Examples of (ET)<sub>2</sub>X Mott Insulators

	X <sup>a)</sup>	$\sigma_{\text{RT}}$ /S cm <sup>-1</sup>	$\varepsilon_{\text{g}}$ /eV	$\chi_{\text{spin}}/\text{emu}$ mol <sup>-1</sup> at RT	( $ J /k_{\text{B}}$ )/K	Magnetic behavior and ground state <sup>b)</sup>	Ref. ( $\sigma, \chi$ )
$\alpha'$	IBr <sub>2</sub>	3	0.32	$\approx 1 \times 10^{-3}$	53, 26	CO(200 K)	284–286
$\alpha'$	CuCl <sub>2</sub>	$4 \times 10^{-2}$	0.4–0.6	$9.0 \times 10^{-4}$	55	Bonner–Fisher	287,288
$\alpha'$	AuBr <sub>2</sub>	$1 \times 10^{-1}$ – $5 \times 10^{-3}$	0.48	$9.0 \times 10^{-4}$	53	Bonner–Fisher	287,288
$\alpha'$	Ag(CN) <sub>2</sub>	$3 \times 10^{-2}$	0.60	$9.3 \times 10^{-4}$	59	SP( $T_{\text{SP}} = 5.8$ K)	287,288
$\alpha'$	HCl <sub>2</sub>	$6 \times 10^{-4}$	no data	$1.1 \times 10^{-3}$	no data		289
$\alpha'$	R-TCA						
	R = OMe, TCE	$1.4 \times 10^{-3}$	0.20	$1.2 \times 10^{-3}$	60	Bonner–Fisher	290,291
	OEt, THF	$2.6 \times 10^{-3}$	0.36	$1.1 \times 10^{-3}$	67	Bonner–Fisher	290,291
	OBu	$2.8 \times 10^{-3}$	0.22	$1.0 \times 10^{-3}$	80	Bonner–Fisher	290,291
	NH <sub>2</sub> , THF	$9.1 \times 10^{-4}$	0.28	$1.1 \times 10^{-3}$	65	Bonner–Fisher	290,291
$\alpha'$	HCNAL	$2.0$ – $8.3 \times 10^{-1}$	0.30	$1.0 \times 10^{-3}$	49–55	Bonner–Fisher	292
$\alpha''$	picrate, THF	$3 \times 10^{-1}$	0.11	$8.7 \times 10^{-4}$	143, 60	alternate chain model	293
$\beta'$	ICl <sub>2</sub>	$3 \times 10^{-2}$	0.24	$9.5 \times 10^{-4}$	59	AF( $T_{\text{N}} = 22$ K)	285,286
$\beta'$	IBrCl	$1.5 \times 10^{-2}$	0.22	$1.1 \times 10^{-3}$		AF( $T_{\text{N}} = 19.5$ K)	294
$\beta'$	AuCl <sub>2</sub>	$10^{-1}$ – $10^{-2}$	0.24	$9.5 \times 10^{-4}$	59	AF( $T_{\text{N}} = 28$ K)	285,286
$\eta$	Ag(CN) <sub>2</sub>	$10^{-1}$ – $10$	0.30	$8.5 \times 10^{-4}$	$\approx 156$	singlet–triplet	295
$\eta$	Au(CN) <sub>2</sub>	$10^{-1}$ – $10$	0.30	$8.5 \times 10^{-4}$	$\approx 156$	singlet–triplet	295
$\theta$	Cu <sub>2</sub> (CN)[N(CN) <sub>2</sub> ] <sub>2</sub>	2–16	$\approx 0.20$	$10^{-3}$	48.3	CO < 220 K	296,297
$\kappa$	Cu[N(CN) <sub>2</sub> ] <sub>2</sub> Cl	2	0.024	$4.6 \times 10^{-4}$	160	AF( $\leq 22$ K), AFMR	298–300
$\kappa$	Cu[N(CN) <sub>2</sub> ] <sub>2</sub> Br <sup>c)</sup>	—	—	$4.3 \times 10^{-4}$	—	AF( $\leq 15$ K), AFMR	301,302
$\kappa$	Cu <sub>2</sub> (CN) <sub>3</sub>	2–7	$\approx 0.10$	$4.7 \times 10^{-4}$	250	spin-liquid	303–305
$\delta'$	GaCl <sub>4</sub>	$1 \times 10^{-1}$	0.4	$\approx 1 \times 10^{-3}$	70	two-leg spin-ladder	286,306, 307
	Br(solv)						
	solv = EG	1.7, metal > 190 K	0.06	$1.1 \times 10^{-3}$	150		308
$\delta$	solv = PG	$2.5 \times 10^{-3}$	0.48	$1.2 \times 10^{-3}$	85	Bonner–Fisher > 180 K	308
					75	singlet–triplet < 180 K	
$\theta$	CuBr <sub>4</sub> <sup>2-</sup> 3:1	1	$\approx 0.14$	$2.8 \times 10^{-3}$		Mott insulator > 59 K, no magnetic contribution of ET below 59 K, AF(Cu <sup>2+</sup> , $T_{\text{N}} = 7.6$ K)	309

a) EG: ethylene glycol, PG: propylene glycol. b) AF: antiferromagnet, SP: spin-Peierls system, CO: charge-ordering. The ground state of the Mott insulators  $\alpha'$ -(ET)<sub>2</sub>X (X = Au(CN)<sub>2</sub>, R-TCA, HCNAL, HCTMM (4:1)) composed of twisted ET dimers has not been clarified yet. Besides the salts in the Table, the following  $\alpha'$ ,  $\beta'$ , and  $\delta'$ -salts might be Mott insulators though the magnetic data are not reported,  $\alpha'$ -(ET)<sub>2</sub>X (X = IBrCl,<sup>310,311</sup> AuBrI,<sup>312</sup> *p*-MeC<sub>6</sub>H<sub>4</sub>SO<sub>3</sub>,<sup>313</sup> Cp(CN)<sub>5</sub>(solv)<sub>x</sub> (Cp: cyclopentadienyl, solv = TCE, THF),<sup>314</sup> MeO-TCA(THF),<sup>291</sup> and 4:1 HCTMM(PhCN)<sup>315</sup>),  $\beta'$ -(ET)<sub>2</sub>InBr<sub>4</sub>,<sup>316</sup>  $\delta'$ -(ET)<sub>2</sub>AuBr<sub>2</sub>,<sup>317</sup> and  $\delta'$ -(ET)<sub>2</sub>GaI<sub>4</sub>.<sup>318</sup> c) D-salt, rapid cool; see section 3.5.4.2.

with RT ionic liquid EMI•NbF<sub>6</sub> (EMI: 1-ethyl-3-methylimidazolium) as an electrolyte by us.<sup>328</sup> It has been reported that (TMTSF)<sub>2</sub>NbF<sub>6</sub> prepared by TBA•NbF<sub>6</sub> is of low quality and does not exhibit a superconducting behavior.<sup>324</sup> The crystal structure of (TMTSF)<sub>2</sub>NbF<sub>6</sub> is depicted in Fig. 21,<sup>328</sup> where TMTSF molecules form a zig-zag dimer that forms a segregated column along the face-to-face direction (*a*-axis) with no short Se...Se atomic contacts. Along the side-by-side direction (*b*-axis), no short Se...Se contacts less than the sum of the van der Waals radii (3.80 Å) are present, although such interactions have been observed for the ClO<sub>4</sub> and FSO<sub>3</sub> salts. Therefore, it is said that the self-assembling ability of TMTSF molecules by the aid of  $\pi$ - $\pi$  and Se...Se interactions is not significant. The Fermi surface of (TMTSF)<sub>2</sub>X is not closed, but open with fair warping due to the lack of adequate side-by-side transfer interactions (Fig. 21d). The degree of warping depends on the size of X, which affects the intermolecular Se...Se atomic distances along the *b*-axis. The quasi-1D feature gives rise to a variety of phase transitions, such as the MI transition caused by the order-disorder (OD) of anion molecules and SDW formation,

and superconducting transition.

On the other hand, the isomorphous (TMTTF)<sub>2</sub>X salts developed by Fabre, Delhaes, et al.<sup>329–333</sup> have much weaker side-by-side transfer interactions and stronger dimerization along the face-to-face direction than those of (TMTSF)<sub>2</sub>X, and also undergo a wide variety of phase transitions (charge ordering, anion ordering, SDW, spin-Peierls, and superconducting, Table 14). Charge-localized feature is claimed even in the high-temperature region, where a metallic temperature dependence is experimentally observed in resistivity.<sup>334</sup> A high pressure above 2.0 GPa induced a superconducting state for X = Br,<sup>335</sup> 5.2–5.4 GPa for X = PF<sub>6</sub>,<sup>336</sup> and 3.35–3.75 GPa for X = BF<sub>4</sub>.<sup>337</sup>

For (TMTSF)<sub>2</sub>X, the anion resides at the inversion center, and thus, the OD transition of octahedral anions does not affect the lattice symmetry. On the other hand, the OD transition of tetrahedral and pseudo-tetrahedral anions modifies the lattice symmetry. When the superlattice generated by the OD transition corresponds to the nesting vector of the Fermi surface ( $2a \times 2b$ , Fig. 21d), the metallic salt becomes an insulator

Table 13. Organic Superconductors of (TMTSF)<sub>2</sub>X<sup>162–164,319–328</sup>

X	Symmetry	$\sigma_{\text{RT}}$ /S cm <sup>-1</sup>	$T_{\text{max}}^{\text{a)}$ /K	$P_{\text{c}}$ /GPa	$T_{\text{c}}$ /K	Characteristics <sup>b)</sup>
PF <sub>6</sub>	octahedral	540	12–15	0.65	1.1	SDW(12 K), FISDW
AsF <sub>6</sub>	octahedral	430	12–15	0.95	1.1	SDW(12 K, $J = 604$ K)
SbF <sub>6</sub>	octahedral	500	12–17	1.05	0.38	SDW(17 K)
NbF <sub>6</sub>	octahedral	120	12	1.2	1.12	SDW(12 K), see section 4.6.3
TaF <sub>6</sub>	octahedral	300	15	1.1	1.35	SDW(11 K)
ClO <sub>4</sub>	tetrahedral	700	—	0	1.4	OD(24 K, $a \times 2b \times 2c$ ), FISDW, $\gamma = 10.5$ , $\beta = 11.4$ , $\Theta = 213$ K SDW(5 K) by rapid cool
ReO <sub>4</sub>	tetrahedral	300	≈182	0.95	1.2	OD(177 K, $2a \times 2b \times 2c$ )
FSO <sub>3</sub>	pseudo- tetrahedral	1000	≈88	0.5	3	OD(88 K, $2a \times 2b \times 2c$ )

a)  $T_{\text{max}}$ : temperature at maximum conductivity. b) SDW: spin density wave, OD: order–disorder transition of anion and newly formed superlattice, FISDW: field induced SDW,

$$\gamma: \text{Sommerfeld coefficient, mJ mol}^{-1} \text{ K}^{-2} \quad \gamma = \pi^2 k_{\text{B}}^2 D(\varepsilon_{\text{F}})/3 \quad (27)$$

$$\beta: \text{mJ mol}^{-1} \text{ K}^{-4} \quad \beta = 48\pi n k_{\text{B}}/5\Theta^3 \quad (28)$$

$$\Theta: \text{Debye temperature, K} \quad T_{\text{c}} \propto \Theta \exp(-1/gD'(\varepsilon_{\text{F}})) \quad (29)$$

$k_{\text{B}}$ : Boltzmann constant,  $g$ : coupling constant,  $D'(\varepsilon_{\text{F}})$ : density of states at Fermi level per one spin.

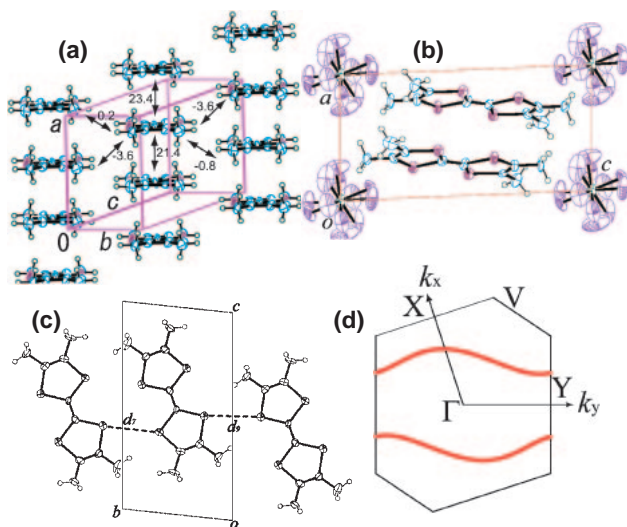


Fig. 21. Crystal structure of (TMTSF)<sub>2</sub>NbF<sub>6</sub>.<sup>328</sup> Triclinic,  $P\bar{1}$ ,  $a = 7.290(4)$ ,  $b = 7.726(2)$ ,  $c = 13.900(5)$  Å,  $\alpha = 82.86(2)$ ,  $\beta = 85.50(3)$ ,  $\gamma = 71.57(3)^\circ$ ,  $V = 735.26$  Å<sup>3</sup>.  $Z = 1$ ,  $R = 0.0682$ . (a) Segregated column of TMTSF molecules. The numbers indicate the overlap integrals in  $10^{-3}$  units. (b) View along the  $b^*$ -axis. (c) Se...Se atomic contacts ( $d_7$ ,  $d_9$ ) along the side-by-side direction. (d) Calculated Fermi surface of (TMTSF)<sub>2</sub>NbF<sub>6</sub>.

(X = ReO<sub>4</sub>, FSO<sub>3</sub>). Since the superlattice for the ClO<sub>4</sub> salt ( $a \times 2b \times 2c$ ) does not correspond to the nesting vector,<sup>338</sup> the ClO<sub>4</sub> salt remains metallic through the OD transition by slow cooling. Very rapid cooling, however, induces a disorder of the anion molecules,<sup>339</sup> and a metallic state remains until an SDW transition at 5 K.<sup>340</sup> An intermediate cooling rate produces an increase in resistivity below 5 K and then a superconducting transition near 1 K,<sup>341,342</sup> suggesting the coexistence of SDW and superconducting states. The salts with octahedral anions exhibit the SDW transition under ambient pressure. The EPR, NMR, and magnetic susceptibility measurements clearly

confirmed the antiferromagnetically ordered state.<sup>343–346</sup> The SDW wave vector was estimated as  $Q_{\text{b}} = 0.24b^*$  and  $Q_{\text{c}} = -0.06c^*$ , and its amplitude of  $0.08 \mu_{\text{B}}$  by <sup>1</sup>H NMR measurements.<sup>346</sup> An application of pressure, in general, increases the warping of the Fermi surface and suppresses the MI transition resulting in the superconductivity (see section 4.6.3 for X = NbF<sub>6</sub>). For the ReO<sub>4</sub> salt at 1.08 GPa, a metal–insulator–metal–superconductor reentrant behavior with thermal hysteresis was reported by Parkin et al. (Fig. 22).<sup>323</sup>

Williams et al. reported fairly good linear relations between the transition temperatures and unit cell volume or the average intercolumn Se...Se distance  $[(2d_7 + d_9)/3]$ .<sup>347</sup> Also, the transition temperature and critical pressure are related with the ion size of the anion as pointed out by Cowan,<sup>95</sup> Kistenmacher,<sup>348</sup> and Saito et al.<sup>6</sup> (Fig. 23).

(TMTSF)<sub>2</sub>ClO<sub>4</sub> is the only ambient pressure superconductor among the TMTSF salts. The important parameters concerning the superconductivity, i.e. upper critical magnetic field  $H_{\text{c}2}$ , critical current  $J_{\text{c}}$ , Sommerfeld coefficient  $\gamma$ , Debye temperature  $\Theta$ , etc. (the  $\gamma$  and  $\Theta$  are closely related to the  $T_{\text{c}}$  of the BCS-type superconductor as expressed by Eqs. 27–29 in the footnote of Table 13), have been extensively studied for this salt.<sup>162,164</sup> The following are remarkable observations on TMTSF superconductors.

Lee et al. reported that the upper critical magnetic field of the PF<sub>6</sub> salt ( $H_{\text{c}2} = 6(//b')$ ,  $4(//a)$  Tesla at 0.1 K) is far beyond the Pauli limit ( $H_{\text{Pauli}}$ ) for a BCS-type superconductor with weak coupling (Fig. 24).<sup>349</sup> For the 2D ET superconductors an  $H_{\text{c}2}$  value larger than  $H_{\text{Pauli}}$  has also been noticed (see 3.5.4.1). The Pauli limit is a critical magnetic field for breaking of singlet Cooper pair due to the Zeeman energy of spins. For a free-electron gas model, the Pauli limit ( $H_{\text{Pauli}}$ ) is given by Eq. 30,

$$H_{\text{Pauli}} = \frac{\Delta_0}{\sqrt{2}\mu_{\text{B}}}, \quad (30)$$

where  $\mu_{\text{B}}$  is the Bohr magneton, and  $\Delta_0$  is the gap parameter

Table 14. Selected Conductors of (TMTTF)<sub>2</sub>X<sup>329–337</sup>

X	Symmetry	$\sigma_{RT}/S\text{ cm}^{-1}$	$T_{\text{max}}/K^a)$	$P_c/\text{GPa}$	$T_c/K$ on-set	Characteristics <sup>a)</sup>
PF <sub>6</sub>	octahedral	20	245	5.2–5.4	1.4–1.8	SP(15 K), SC
AsF <sub>6</sub>	octahedral	25	105			SP(11 K)
SbF <sub>6</sub>	octahedral	10	154			SDW(7 K)
ClO <sub>4</sub>	tetrahedral	30	230			OD(71 K, $2a \times b \times c$ )
ReO <sub>4</sub>	tetrahedral	33	230			OD(162 K, $2a \times 2b \times 2c$ )
BF <sub>4</sub>	tetrahedral	50	190	3.35–3.75	1.38	OD(40 K), SDW + SC coexist
NO <sub>3</sub>	triangular	95	208			OD (40 K, $2a \times b \times c$ )
SCN	linear	60	240			OD(160 K, $a \times 2b \times 2c$ ) SDW(9 K)
Br	spherical	260	100	2.6	0.8	SDW(13 K), SC

a)  $T_{\text{max}}$ , SDW, OD: see footnote of Table 13. SP: spin-Peierls transition, SC: superconductivity.

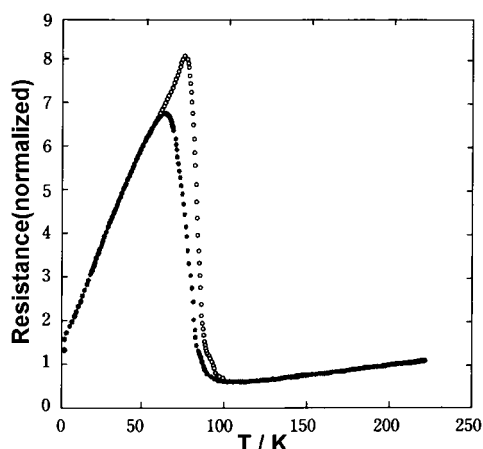


Fig. 22. Temperature dependence of resistivity of (TMTSF)<sub>2</sub>ReO<sub>4</sub> at 1.08 GPa by Parkin et al. Applying pressure partially suppresses the order–disorder transition of ReO<sub>4</sub> anion and induce metal–insulator–metal–superconductor behavior.<sup>323</sup> ●: cooling, ○: heating.

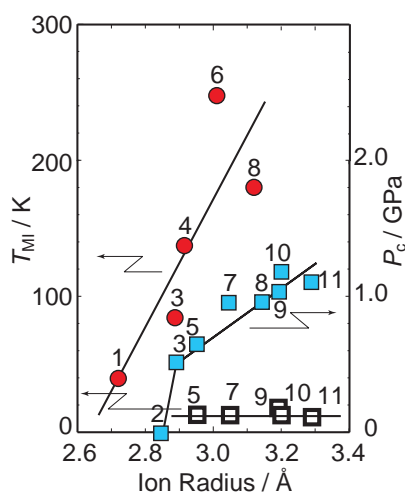


Fig. 23. Metal–insulator transition ( $T_{\text{Mi}}$ : ● OD, ■ SDW) and critical pressure ( $P_c$ : ■) of (TMTSF)<sub>2</sub>X as a function of the anion radius in parentheses (Å). 1: X = BF<sub>4</sub> (2.72), 2: ClO<sub>4</sub> (2.84), 3: FSO<sub>3</sub> (2.89), 4: F<sub>2</sub>PO<sub>2</sub> (2.92), 5: PF<sub>6</sub> (2.95), 6: BrO<sub>4</sub> (3.01), 7: AsF<sub>6</sub> (3.05), 8: ReO<sub>4</sub> (3.12), 9: SbF<sub>6</sub> (3.19), 10: NbF<sub>6</sub> (3.20), 11: TaF<sub>6</sub> (3.29).<sup>6,95,348</sup>

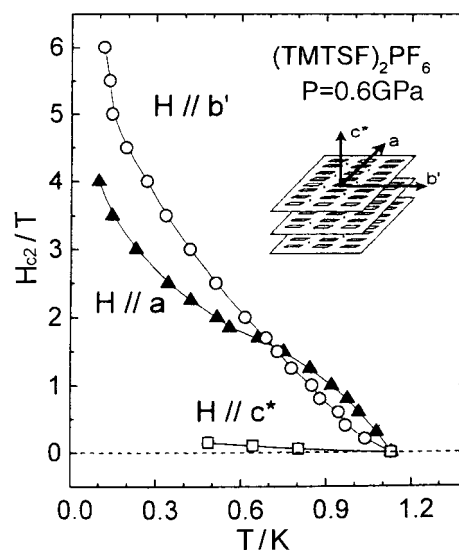


Fig. 24. Temperature dependence of  $H_{c2}$  of (TMTSF)<sub>2</sub>PF<sub>6</sub> by Lee et al. Pauli limit is 2.6 T.<sup>349</sup>

at 0 K. Since  $2\Delta_0$  is equal to  $3.53k_B T_c$  for a BCS-type superconductor with weak coupling, the  $H_{c2}$  value should be limited by  $H_{\text{Pauli}}$  expressed by Eq. 31.

$$H_{\text{Pauli}} = 1.86T_c \text{ (Tesla)} \quad (31)$$

Takigawa et al. reported for the ClO<sub>4</sub> salt that the inverse of the relaxation time of <sup>1</sup>H NMR absorption  $T_1^{-1}$  does not show the Hebel–Slichter coherence peak (Fig. 25),<sup>350</sup> which should be observed just below  $T_c$  for a normal BCS-type superconductor having an isotropic gap.<sup>351</sup> Field-induced SDW (FISDW) states were extensively studied by Chaikin et al. and others; namely, the application of magnetic field breaks the superconducting state and induces a sequence of SDW states like a cascade above 3 Tesla (Fig. 26).<sup>352,353</sup> Osada et al. observed a sliding of SDW based on the non-ohmic transport behavior in the FISDW state.<sup>354</sup>

A generalized phase diagram including (TMTTF)<sub>2</sub>X and (TMTSF)<sub>2</sub>X was proposed by Jerome (Fig. 27).<sup>355</sup> The superconducting phase neighbors the magnetic phase (SDW state) and  $T_c$  decreases with increasing the pressure owing to the decrease of  $D(\mathcal{E}_F)$ .

**3.3.2 Peripheral Addition of Alkylchalcogeno Groups: BO and ET Complexes:** The “peripheral addition of alkyl-

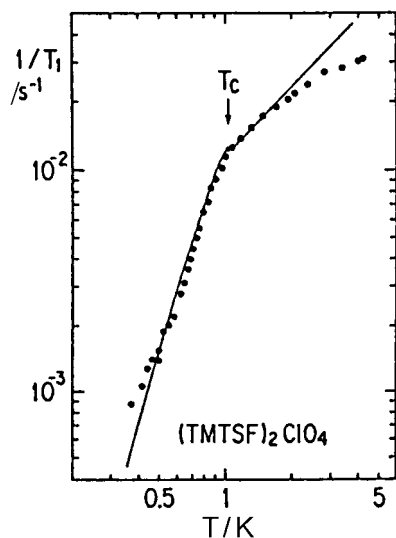


Fig. 25. Temperature dependence of  $1/T_1$  of  $^1\text{H}$ NMR of  $(\text{TMTSF})_2\text{ClO}_4$ .  $1/T_1$  below  $T_c$  shows  $T^3$  dependence.<sup>350</sup>

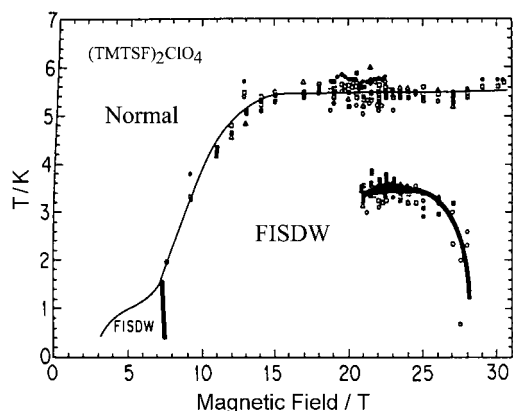


Fig. 26. Temperature-magnetic field phase diagram of  $(\text{TMTSF})_2\text{ClO}_4$  by Maesato et al. showing field-induced SDW (FISDW) states.<sup>352,353</sup>

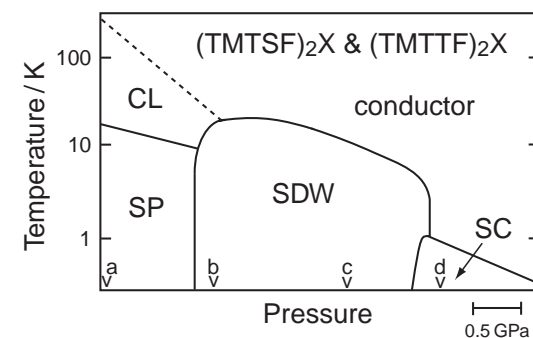
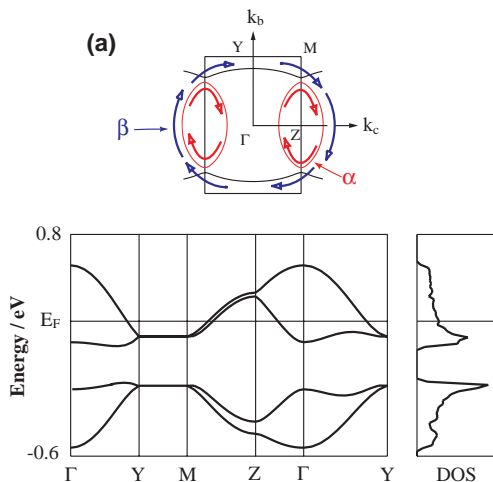


Fig. 27. Generalized phase diagram for the  $(\text{TMTSF})_2\text{X}$  and  $(\text{TMTTF})_2\text{X}$  by Jerome.<sup>355</sup> CL, SP, SDW, and SC refer to charge-localized (which corresponds to charge-ordered state), spin-Peierls, spin density wave and superconducting states, respectively. The salts **a–d** at ambient pressure locates in the generalized diagram. **a**:  $(\text{TMTTF})_2\text{PF}_6$ , **b**:  $(\text{TMTTF})_2\text{Br}$ , **c**:  $(\text{TMTSF})_2\text{PF}_6$ , **d**:  $(\text{TMTSF})_2\text{ClO}_4$ .

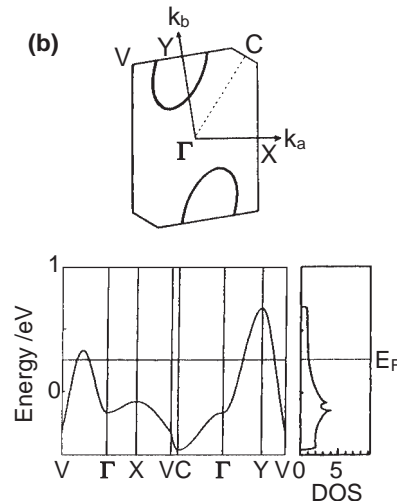


Fig. 28. Calculated Fermi surface, energy dispersion, and density of states (DOS) of (a)  $\kappa\text{-(ET)}_2\text{Cu(NCS)}_2$ <sup>356</sup> and (b)  $(\text{BO})_{2.4}\text{I}_3$ <sup>234</sup> (see also Fig. 35). Arrows in the Fermi surface (a) indicate the trajectory of electrons for the Shubnikov-de Haas effect; the  $\alpha$ -orbit (red) is that around the 2D cylindrical hole-like Fermi surface and the  $\beta$ -orbit (blue) is the magnetic breakdown orbit.

chalcogeno groups” to a parent molecule TTF has successfully produced 2D  $\text{ET}^{205,206}$  and  $\text{BO}^{234,239-241}$  conductors. The Fermi surfaces and density of states (DOS) of  $\kappa\text{-(ET)}_2\text{Cu(NCS)}_2$ <sup>356</sup> and  $(\text{BO})_{2.4}\text{I}_3$ <sup>234</sup> calculated by tight-binding approximation based on the extended Hückel calculation (Fig. 28) revealed the existence of a 2D Fermi surface, and hence, increased electronic dimensionality. The validity of the calculated Fermi surface of  $\kappa\text{-(ET)}_2\text{Cu(NCS)}_2$  has been experimentally confirmed by the magnetoresistance oscillations (Shubnikov-de Haas,<sup>356</sup> angular dependent magnetoresistance oscillations (AMRO),<sup>357</sup> and magnetic breakdown phenomenon<sup>358</sup>). General information on the quantum oscillations is available in Refs. 164–166. For  $\kappa\text{-(ET)}_2\text{Cu(NCS)}_2$ , the effective mass of electrons was evaluated to  $m_c = 3.5m_e$  from the quantum oscillations in the 2D closed ellipsoidal Fermi surface around Z-point ( $\alpha$ -orbit) and  $m_c = 6.5m_e$  in the big circular Fermi surface after magnetic breakdown ( $\beta$ -orbit), where  $m_c$  is cyclotron mass and  $m_e$  is electron mass (see section 3.5.2).

The calculation of the band structures and Fermi surfaces of



ET, BO, and their related conductors was developed by Mori et al. on the basis of the tight-binding approximation using the extended Hückel calculation.<sup>359</sup> More sophisticated methods (local density functional approximation and augmented spherical wave algorithm) do not give much different results.<sup>360</sup> The transfer integral  $t$  is readily taken to be proportional to the overlap integral  $S$ ;  $t = -\alpha S$  ( $\alpha = 10$  eV). In the cation radical salts of ET, the conduction band is solely determined by the HOMO band of ET since the LUMO and second HOMO bands of ET and the orbitals of the closed-shell anion are considerably far away in energy. Owing to the symmetry of the HOMO, the overlap integral is very sensitive to the parameter  $\phi$  in Fig. 29 and has extremes at  $\phi = 0, \approx 30, \approx 60$ , and  $90^\circ$ .

However, the calculated Fermi surface depends considerably on the  $\zeta$ -value of the Slater orbital and whether the d-orbital of the sulfur atom is included or not. The Fermi surfaces of  $\alpha$ -(ET)<sub>2</sub>KHg(SCN)<sub>4</sub> calculated based on the crystal structures at 298 and 104 K using different parameters are compared in Fig. 30.<sup>9</sup> The results in Figs. 30b–30d are inconsistent with the 2D conducting behavior, partial nesting of the Fermi surface, and reconstruction of the Fermi surface at low temperatures (see section 3.5.6). The coexistence of the 2D and 1D Fermi surfaces was confirmed by the Fermi surface topology (Fermiology)<sup>361–364</sup> and is in good agreement with Figs. 30a and 30e.

The robust intermolecular interactions in the BO complexes provide a metallic state with a wide band even in the strongly disordered systems such as LB films (see section 4.4.1), reticulate doped polymer films (see section 4.4.3), compressed pellets, etc., regardless of the sort, shape, and size of acceptor or anion molecules.<sup>234,239–241,369–372</sup> As a result, the BO complexes

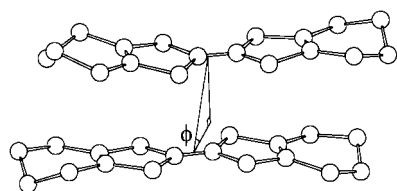


Fig. 29. Relative orientation of an ET dimer. The face-to-face and side-by-side arrangements correspond to  $\phi = 0$  and  $90^\circ$ , respectively.<sup>359</sup>

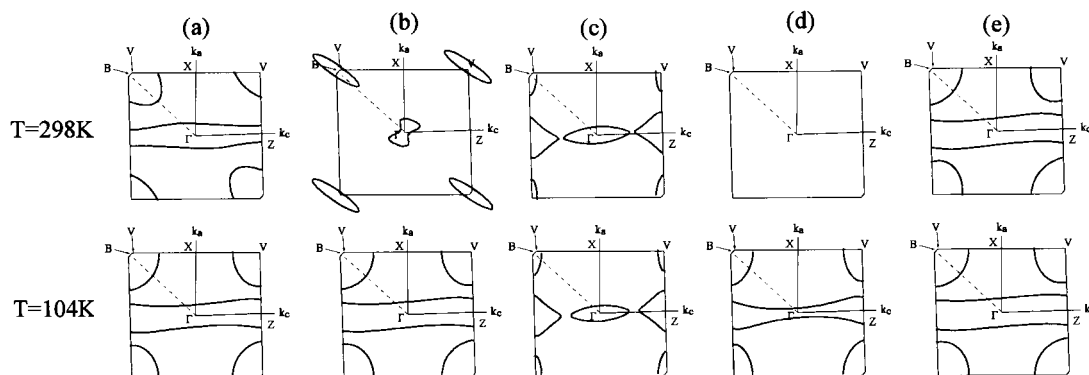


Fig. 30. Calculated Fermi surfaces of  $\alpha$ -(ET)<sub>2</sub>KHg(SCN)<sub>4</sub> by tight-binding approximation based on the extended Hückel method, (a) including d-orbital of sulfur atoms with single- $\zeta$  from Ref. 359, (b) including d-orbital of sulfur atoms with single- $\zeta$  from Ref. 365, (c) excluding d-orbital of sulfur atoms with single- $\zeta$  from Ref. 366, (d) excluding d-orbital of sulfur atoms with single- $\zeta$  from Ref. 367, and (e) excluding d-orbital of sulfur atoms with double- $\zeta$  from Ref. 368.

hardly exhibit any phase transition including the superconducting one (only two superconducting salts with  $T_c \leq 1.5$  K were found, see Table 15).<sup>373,374</sup> The structural features of 2D BO complexes are described in sections 3.4.1 and 3.4.2.

**3.3.3 Stable Organic Metal (ET)<sub>2</sub>ClO<sub>4</sub>(TCE)<sub>0.5</sub>:** The first 2D organic metal (ET)<sub>2</sub>ClO<sub>4</sub>(TCE)<sub>0.5</sub>, with  $\sigma_{\parallel}/\sigma_{\perp}$  ranging from 0.9 (RT) to 0.4 (2 K), was synthesized in 1982 by Saito et al.<sup>205,206,375–379</sup> The ET molecules form a pseudo-segregated column along the [102] direction ( $\phi = 60^\circ$ ), although there is no direct face-to-face ( $\phi = 90^\circ$ ) overlapping (Fig. 31a).<sup>379</sup> Short S...S contacts less than the sum of the van der Waals radii ( $3.60 \text{ \AA}$ )<sup>116</sup> are observed along the [100] ( $\phi = 0^\circ$ ) and [102] ( $\phi = 30^\circ$ ) directions. Therefore, the largest transfer integral is along [102], and then [100], while [102] is the smallest. The most conductive direction is along the S...S network [102] ( $\sigma_{RT} = 25\text{--}30 \text{ S cm}^{-1}$ ). The disordered TCE starts to order below 180 K and tends to be completed below about 90 K.<sup>378</sup> This disorder–order transition of TCE is associated with the conformational ordering of the ethylene groups of ET molecules.

By slow cooling of the salt in the range of 205 and 160 K, Pauli susceptibility at RT decreases sharply by 56% at 25 K, below which the value is constant. The thermopower shows an abrupt shift to the positive side below 25 K. The electrical resistivity shows  $T^2$  dependence above 80 K, a slight increase below 40–50 K, and then a constant value below about 10 K (Figs. 31c and 31d). By rapid cooling, on the other hand, the salt retains metallic behavior down to 0.8 K as confirmed both by magnetic susceptibility and resistivity (Fig. 31d).<sup>376,377</sup> The rapid cooling may cause the incomplete order–disorder transition of both terminal ethylene groups of ET molecules and the TCE molecules, and the incompleteness generates a random deformation of ET molecules, which influences the electron-hopping rate in the ET sheets. The random distribution of transfer integrals under the rapid cooling condition can suppress the phase transition at low temperatures if the randomness overcomes the gap generated by the transition. The band calculation of the salt indicates a semimetallic nature with a Fermi surface consisting of both small electron and hole parts (Fig. 31b).<sup>359</sup> Then, the semimetal–semimetal transition at 25 K seems to be associated with the disappearance of the electron Fermi surface through the nesting instability.

Table 15. Organic Superconductors of ET(1) and BO(2)

Anion, symmetry, ratio, and phase <sup>a)</sup>	$\sigma_{RT}^{b)}$ , $T_{\max}$ , $P_c^{c)}$ , and $T_c$	Characteristics <sup>d)</sup>	Ref.
<b>1</b> I <sub>3</sub> , linear, 2:1, $\beta_L$	60, no, 0, 1.5	SdH, AMRO, dHvA( $\approx 25\%$ , $\approx 0.5m_e$ ; 103%, $4.0m_e$ ), IIE	443,444
I <sub>3</sub> , linear, 2:1, $\beta$	—, no, 0, 2.0	anneal below 110 K for > 20 h	445
I <sub>3</sub> , linear, 2:1, $\beta_H$	—, no, 0, 8.1	press $\beta_L$ , SdH(51%, $4.65m_e$ ), no IIE	446–448
I <sub>3</sub> , linear, 2:1, $\alpha_t$	—, no, 0, $\approx 8$	heat $\alpha$ -, $\varepsilon$ -, or $\zeta$ -phase	449
I <sub>3</sub> , linear, 3:2.5, $\gamma$	20, no, 0, 2.5	charge of donor = +2.5/3	450
I <sub>3</sub> , linear, 2:1, $\theta$	30, no, 0, 3.6	SdH, AMRO, dHvA(19%, $1.8m_e$ ; 102%, $3.5m_e$ )	451
I <sub>3</sub> , linear, 2:1, $\kappa$	30, no, 0, 3.6	SdH, dHvA(15%, $1.9m_e$ ; 102%, $3.9m_e$ ), $\gamma = 18.9$ , $\beta = 10.3$ , $\Theta = 218$	452
IBr <sub>2</sub> , linear, 2:1, $\beta$	20, no, 0, 2.7	SdH, AMRO, dHvA( $\approx 53\%$ , $\approx 4.2m_e$ )	453
AuI <sub>2</sub> , linear, 2:1, $\beta$	60, no, 0, 4.9	SdH, dHvA( $2.0m_e$ , $0.3m_e$ )	454
ICl <sub>2</sub> , linear, 2:1, $\beta'$	—, semi, 8.2, 14.2	on-set $T_c$ , mid-point $T_c = 13.4$ K, for $\sigma_{RT}$ see Table 12	455
IBrCl, linear, 2:1, $\beta'$	—, semi, 8.0, 7.2	on-set $T_c$ , for $\sigma_{RT}$ see Table 12	294
Cu(CF <sub>3</sub> ) <sub>4</sub> •TCE, planar, 2:1, $\kappa_L$	—, —, 0, 4.0	$T_c$ is the on-set one for all M(CF <sub>3</sub> ) <sub>4</sub> salts	456,457
Cu(CF <sub>3</sub> ) <sub>4</sub> •TCE, planar, 2:1, $\kappa_H$	—, —, 0, 9.2		
Ag(CF <sub>3</sub> ) <sub>4</sub> •TCE, planar, 2:1, $\kappa_L$	—, —, 0, 2.4	$\gamma \approx 50$ , $\beta = 18$ , $\Theta = 203$	456,457
Ag(CF <sub>3</sub> ) <sub>4</sub> •TCE, planar, 2:1, $\kappa_H$	—, —, 0, 11.1		
Au(CF <sub>3</sub> ) <sub>4</sub> •TCE, planar, 2:1, $\kappa_L$	—, —, 0, 2.1		456,457
Au(CF <sub>3</sub> ) <sub>4</sub> •TCE, planar, 2:1, $\kappa_H$	—, —, 0, 10.5		
Cu(CF <sub>3</sub> ) <sub>4</sub> •TBE, planar, 2:1, $\kappa_L$	—, —, 0, 5.2		456,457
Ag(CF <sub>3</sub> ) <sub>4</sub> •TBE, planar, 2:1, $\kappa_L$	—, —, 0, 4.8		
Ag(CF <sub>3</sub> ) <sub>4</sub> •TBE, planar, 2:1, $\kappa_H$	—, —, 0, 7.2		456,457
Au(CF <sub>3</sub> ) <sub>4</sub> •TBE, planar, 2:1, $\kappa_L$	—, —, 0, 5.8		
Cu(CF <sub>3</sub> ) <sub>4</sub> •121DBC, planar, 2:1, $\kappa_L$	—, —, 0, 5.5		456,457
Ag(CF <sub>3</sub> ) <sub>4</sub> •121DBC, planar, 2:1, $\kappa_L$	—, —, 0, 4.5		
Au(CF <sub>3</sub> ) <sub>4</sub> •121DBC, planar, 2:1, $\kappa_L$	—, —, 0, 5.0		456,457
Cu(CF <sub>3</sub> ) <sub>4</sub> •121DCB, planar, 2:1, $\kappa_L$	—, —, 0, 3.5		
Ag(CF <sub>3</sub> ) <sub>4</sub> •121DCB, planar, 2:1, $\kappa_L$	—, —, 0, 3.8		456,457
Ag(CF <sub>3</sub> ) <sub>4</sub> •121DCB, planar, 2:1, $\kappa_H$	—, —, 0, 7.3		
Au(CF <sub>3</sub> ) <sub>4</sub> •121DCB, planar, 2:1, $\kappa_L$	—, —, 0, 3.2		456,457
Cu(CF <sub>3</sub> ) <sub>4</sub> •112DCB, planar, 2:1, $\kappa_L$	—, —, 0, 4.9		
Ag(CF <sub>3</sub> ) <sub>4</sub> •112DCB, planar, 2:1, $\kappa_L$	—, —, 0, 4.1		456,457
Ag(CF <sub>3</sub> ) <sub>4</sub> •112DCB, planar, 2:1, $\kappa_H$	—, —, 0, 10.2		
Au(CF <sub>3</sub> ) <sub>4</sub> •112DCB, planar, 2:1, $\kappa_L$	—, —, 0, 5.0		458,459
Cl <sub>2</sub> (H <sub>2</sub> O) <sub>2</sub> , cluster, 3:1, $\beta''$	500, 700, 1.6, 2	dianion, charge of donor = +2/3	
Pd(CN) <sub>4</sub> •H <sub>2</sub> O, cluster, 4:1, $\beta''$	100, 70, 0.7, 1.2	dianion	460
Pt(CN) <sub>4</sub> •H <sub>2</sub> O, cluster, 4:1, $\beta''$	280, 120, 0.65, 2	dianion	461
ReO <sub>4</sub> , tetrahedral, 2:1, $\beta$	200, 81, 0.04, 2		462
Fe(ox) <sub>3</sub> •H <sub>3</sub> O•PhCN, octahedral, 4:1, $\beta''$	$10^{-2}$ , no, 0, 7.0	dianion, AMRO $T_c$ (on-set) = 8.6 K	463
Cr(ox) <sub>3</sub> •H <sub>3</sub> O•PhCN, octahedral, 4:1, $\beta''$	—, —, 0, 6.0	dianion, on-set $T_c$	464
Fe(ox) <sub>3</sub> •A•PhNO <sub>2</sub> , octahedral, 4:1, $\beta''$	—, —, 0, 6.2	dianion, on-set $T_c$ , A = H <sub>3</sub> O or NH <sub>4</sub>	465
Cr(ox) <sub>3</sub> •A•PhNO <sub>2</sub> , octahedral, 4:1, $\beta''$	—, —, 0, 5.8	dianion, on-set $T_c$ , A = H <sub>3</sub> O or NH <sub>4</sub>	465
Ga(ox) <sub>3</sub> •H <sub>3</sub> O•pyridine, octahedral, 4:1, $\beta''$	10.4, 50–60, 0.2	dianion, on-set $T_c$	466
Ga(ox) <sub>3</sub> •H <sub>3</sub> O•PhNO <sub>2</sub> , octahedral, 4:1, $\beta''$	20.2, —, 0, 7.5	dianion, on-set $T_c$	466
SF <sub>5</sub> CH <sub>2</sub> CF <sub>2</sub> SO <sub>3</sub> , none, 2:1, $\beta''$	—, no, 0, 5.3	SdH(13%, $1.9m_e$ ), $\gamma = 18.7$ , $\beta = 12.2$ , $\Theta = 221$	467
	—, no, 0.2, 6.36	uniaxial strain(see section 3.5.4.3c)	566

Continued on next page.

While the neutral ET molecule is non-planar, it becomes almost flat on formation of the partial CT complex except for the terminal ethylene groups, which are thermally disordered at high temperatures (Fig. 32).<sup>379–383</sup> The main conformations of the terminal ethylene groups of the ET molecule are illustrated by **A** and **C** in Fig. 32 (**A** and **B** are equivalent with opposite conformations of the ethylene group). The relation between two terminal ethylene groups is either eclipsed (**D** in Fig. 32) or

staggered (**E** in Fig. 32) in the **A** or **B** conformation. It was pointed out by Leung et al. that the ethylene conformation is one of the key parameters determining the physical and structural properties including the superconductivity.<sup>382</sup>

**3.3.4 Packing Characteristics of ET Molecules:** ET molecules tend to pile up one after the other with sliding to each other so as to minimize the steric hindrance caused by the terminal ethylene groups. Such a molecular packing leaves

Continued.

Anion, symmetry, ratio, and phase <sup>a)</sup>	$\sigma_{RT}^{b)}$ , $T_{max}$ , $P_c^{c)}$ , and $T_c$	Characteristics <sup>d)</sup>	Ref.
KHg(SCN) <sub>4</sub> , polymer, 2:1, $\alpha$	100, no, 0, 0.3	SdH, AMRO(16%, 1.4 $m_e$ ; 13%, 2.53 $m_e$ ), $\gamma = 6.4$ , $\beta = 11.6$ , $\Theta = 223$	394,400
NH <sub>4</sub> Hg(SCN) <sub>4</sub> , polymer, 2:1, $\alpha$	—, —, 1, 1.5 380, no, 0, 1.7	uniaxial strain(see section 3.5.4.3) SdH, AMRO(13%, 2.1 $m_e$ ), $\gamma = 26$ , $\beta = 12.8$ , $\Theta = 221$	394,396
RbHg(SCN) <sub>4</sub> , polymer, 2:1, $\alpha$	—, —, 0.5, 6 6, no, 0, 0.5	uniaxial strain (see section 3.5.4.3) SdH, AMRO(16.5%, 1.5 $m_e$ ), $\gamma = 7.1$ , $\beta = 11.1$ , $\Theta = 226$	398,401
TiHg(SCN) <sub>4</sub> , polymer, 2:1, $\alpha$	—, no, 0, 0.1	SdH, AMRO(16%, 1.5 $m_e$ ; 103%, 4.0 $m_e$ )	402
Ag(CN) <sub>2</sub> ·H <sub>2</sub> O, cluster, 2:1, $\kappa$	37, 150, 0, 5.0	SdH(17%, 2.7 $m_e$ )	468
Hg <sub>2.78</sub> Cl <sub>8</sub> , polymer, 4:1, $\kappa$	30, 25, 1.2, 1.8	dianion	469
Hg <sub>2.89</sub> Br <sub>8</sub> , polymer, 4:1, $\kappa$	5, 18, 0, 4.3	dianion	470
	—, —, 0.35, 6.7		471
Cu(NCS) <sub>2</sub> , polymer, 2:1, $\kappa$	40, 90, 0, 10.4	SdH, AMRO, dHvA(15.7%, 3.5 $m_e$ ; 105%, 6.5 $m_e$ ), $\gamma = 25$ , $\beta = 11.2$ , $\Theta = 215$	472–478
Deuterated salt	—, —, 0, 11.2	IIE	300
Cu[N(CN) <sub>2</sub> ]Br, polymer, 2:1, $\kappa$	50, 50–90, 0, 11.8	SdH(106%, 6.4 $m_e$ at 0.9 GPa), AMRO, $\gamma = 22$ , $\beta = 12.8$ , $\Theta = 210$	479,480
Deuterated salt	—, —, 0, 11.2	normal isotope effect	488
Cu[N(CN) <sub>2</sub> ]Cl, polymer, 2:1, $\kappa$	2, semi, 0.03, 12.8	SdH, AMRO(15.5%, 102% at 0.77 GPa), reentrant super	481
Deuterated salt	—, —, 0.03, 13.1	IIE	298,488
Cu[N(CN) <sub>2</sub> ]Cl <sub>x</sub> Br <sub>1-x</sub> , polymer, 2:1, $\kappa$	—, —, 0, 10	$x = 0.15$	300
	—, —, 0, 11.5	$x = 0.25$	482
	—, —, 0, 11.3	$x = 0.5$	482
Cu[N(CN) <sub>2</sub> ]Br <sub>0.9</sub> I <sub>0.1</sub> , polymer, 2:1, $\kappa$	—, semi, 0.3, 5.9		483
Cu[N(CN) <sub>2</sub> ]I, polymer, 2:1, $\kappa$	1, $\approx 200$ , 0.12, 7.7		484
Cu(CN)[N(CN) <sub>2</sub> ], polymer, 2:1, $\kappa$	50, no, 0, 11.2	AMRO	304,485–
Deuterated salt	—, —, 0, 12.3	IIE	488
Cu <sub>2</sub> (CN) <sub>3</sub> , polymer, 2:1, $\kappa$	10, semi, 0.15, 2.8	SdH, AMRO(3.1% at AP; 96%, 4.5 $m_e$ at 0.8 GPa), spin-liquid	303,304, 489,490
Cu <sub>2-y</sub> (CN) <sub>3-2y</sub> [N(CN) <sub>2</sub> ] <sub>y</sub> , polymer, 2:1, $\kappa$	—, —, 0, 3–11	$\kappa'$ -(ET) <sub>2</sub> Cu <sub>2</sub> (CN) <sub>3</sub>	491–494
2 Cu <sub>2</sub> (NCS) <sub>3</sub> , polymer, 3:1	22, no, 0, 1.06	charge of donor = +1/3	373
ReO <sub>4</sub> ·H <sub>2</sub> O, tetrahedral, 2:1	200, 2.5, 0, 1.5	SdH(0.7%, 1.15 $m_e$ ; 1.5%, 0.9 $m_e$ )	374

a) TCE: 1,1,2-trichloroethane, TBE: 1,1,2-tribromoethane, 121DBC: 1,2-dibromo-1-chloroethane, 121DCB: 1,2-dichloro-1-bromoethane, 112DCBE: 1,1-dichloro-2-bromoethane, PhCN: benzonitrile, ox: oxalate dianion. b) S cm<sup>-1</sup>, semi: semiconductor. c) hydrostatic pressure until otherwise mentioned, GPa. d) IIE: inverse isotope effect, SdH: Shubnikov-de Haas oscillations, dHvA: de Haas-van Alphen oscillations, AMRO: angle dependent magnetoresistance oscillations, the numbers in parenthesis are the area of the Fermi surface relative to the first Brillouin zone and the cyclotron mass,  $m_c$ : electron mass,  $\gamma$ ,  $\beta$ ,  $\Theta$ : see footnote of Table 13.

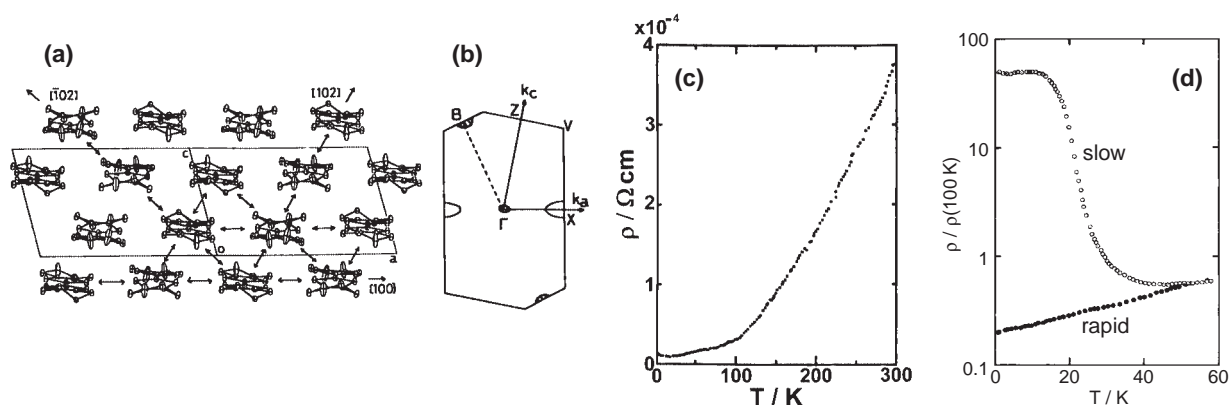


Fig. 31. (a) Packing arrangement of ET molecules in the first 2D metal (ET)<sub>2</sub>ClO<sub>4</sub>(TCE)<sub>0.5</sub> at RT.<sup>379</sup> (b) Calculated Fermi surface.<sup>359</sup> and (c, d) the temperature dependence of electrical resistivity.<sup>205,376,377</sup> The figure (d) demonstrates the difference between the slow (○) and rapid cooling conditions (●).

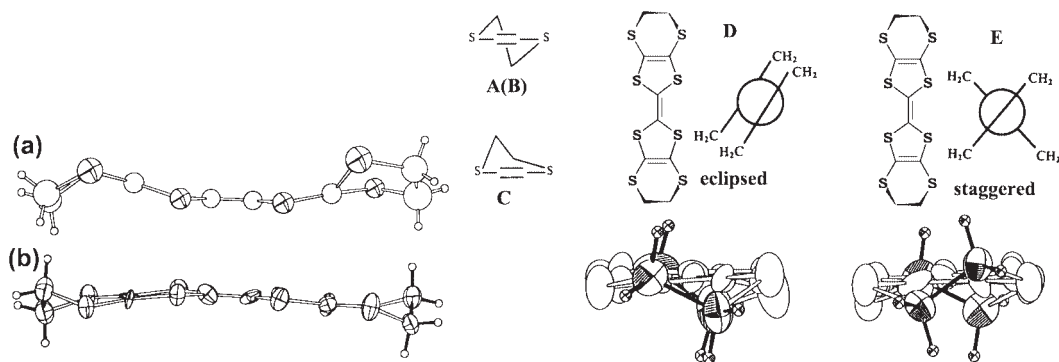


Fig. 32. Molecular shape of an ET molecule in (a) a neutral solid and (b)  $\kappa\text{-(ET)}_2\text{Cu(CN)[N(CN)}_2\text{]}$ . The main conformations of a terminal ethylene group of an ET molecule (A–C) and the relation of the two ethylene groups (D: eclipsed, E: staggered). Projection views of an ET molecule along the long molecular axis for the eclipsed and staggered ones in  $\kappa\text{-(ET)}_2\text{Cu(CN)[N(CN)}_2\text{]}$ . S=S in A(B) and C, and the big circle in D and E represent the  $\text{C}_6\text{S}_8$  plane viewed along the long molecular axis.

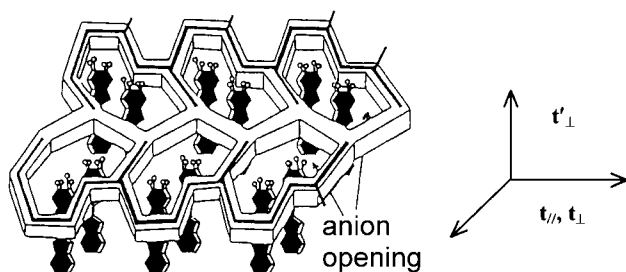


Fig. 33. Schematic view of  $\kappa\text{-(ET)}_2\text{Cu(NCS)}_2$  indicating anion openings and transfer interactions ( $t_{\parallel}$ ,  $t_{\perp}$ , and  $t'_{\perp}$ ).<sup>384</sup>

cavities along the molecular long axis, where counter anions and sometimes solvent molecules occupy. This tendency leads to a relatively small  $t_{\parallel}$ . Hence, ET salts are poorly conductive compared with BO and TMTSF salts.

ET molecules also have a strong tendency to form proximate intermolecular S...S contacts along the side-by-side direction leading to an increment of  $t_{\perp}$ . The ET conductors are composed of alternating structures of a 2D conducting layer and insulating anion layer. Significant donor–anion interactions arise from the short atomic contacts between the ethylene hydrogen atoms of ET and anion atoms around the anion openings in the anion layer as schematically shown in Fig. 33.<sup>384</sup> However, the donor–donor interactions through the anion opening are very small, since the electron densities on the terminal ethylene groups are negligible<sup>120</sup> and the distance between ET molecules along this direction is rather long. Therefore, the transfer integrals along this direction ( $t_{\perp}'$ ) is the smallest ( $t_{\parallel} \geq t_{\perp} > t_{\perp}'$ ) and the transport is governed by tunneling through the metal–insulator junction.<sup>385</sup>

These competing different kinds of donor–donor and donor–anion intermolecular interactions and the large conformational freedom of the terminal ethylene groups together with the rather flexible molecular framework give ET complexes having a variety of crystal and electronic structures. Even with a particular anion, ET molecules form a variety of CT complexes with different ET packings. They have the same composition with different crystal structures (polymorphism) or different compositions (sometimes the inclusion of solvent molecules) depending on the crystal-growth condition. Single crystals with differ-

ent crystal structures sometimes grow together and should be separated either based on the morphology under a microscope, by structural inspection, or by inspecting physical properties such as EPR signal and electrical conductivity.

In addition, the fairly narrow bandwidth and strong electron correlation of the ET complexes have afforded a variety of functional materials: namely, 2D superconductors (Table 15, more than 50 superconductors,  $T_c$  (mid-point)  $\leq 13.4$  K), Mott insulators (Table 12, including spin-Peierls systems,<sup>287,288,308</sup> antiferromagnets,<sup>285,286,294,298–302,309</sup> and spin-liquid<sup>10,305</sup>), 1D metal with CDW transition ( $\text{ReO}_4$ ,<sup>386,387</sup>  $\beta\text{-PF}_6$ ,<sup>388,389</sup>  $\beta\text{-AsF}_6$ ,<sup>390</sup>  $\beta\text{-SbF}_6$ ,<sup>390,391</sup>  $\text{C(CN)}_3$ ,<sup>392</sup> and  $\text{Pt(ox)}_2$  (4:1)<sup>387,393</sup>), 2D metal with CDW transition ( $\alpha\text{-MHg(SCN)}_4$  ( $\text{M} = \text{K}$ ,  $\text{Rb}$ ,<sup>361–364,394–401</sup> and  $\text{Tl}$ )<sup>402</sup> and  $\alpha\text{-TiHg(SeCN)}_4$ )<sup>403</sup>, 2D metal with FISDW transition ( $\beta''\text{-AuBr}_2$ )<sup>404</sup>, charge-ordered insulators<sup>296,297,405–407</sup> ( $\theta\text{-Cu}_2\text{(CN)[N(CN)}_2\text{]}_2$ ,  $\theta\text{-MM' (SCN)}_4$  ( $\text{MM}' = \text{RbCo}$ ,  $\text{RbZn}$ , and  $\text{CsZn}$ ),  $\kappa\text{-(ET)}_4\text{PtCl}_6 \cdot \text{C}_6\text{H}_5\text{CN}$ , and triclinic form of  $\kappa\text{-(ET)}_4\text{(NET)}_4\text{[M(CN)}_6\text{]} \cdot 3\text{H}_2\text{O}$  ( $\text{M} = \text{Fe}^{\text{III}}$ ,  $\text{Co}^{\text{III}}$ , and  $\text{Cr}^{\text{III}}$ )), spin-ladder systems ( $\text{Zn(SCN)}_3$  (1:1)<sup>408</sup> and  $\delta'\text{-GaCl}_4$ )<sup>286</sup>, monotropic complex isomers (Table 8),<sup>198–204</sup> and 2D metallic ones down to low temperatures ( $\text{CuCl}_4(\text{H}_2\text{O})$  (3:1),<sup>409,410</sup>  $\text{Br}$  (3:2),<sup>411</sup>  $\beta\text{-I}_2\text{Br}$ ,<sup>412,413</sup>  $\beta''\text{-ICl}_2$ ,<sup>414,415</sup>  $\beta''\text{-AuBr}_2$ ,<sup>416,417</sup>  $\beta''\text{-AuBrI}$ ,<sup>418</sup>  $\theta\text{-Ag(CN)}_2$ ,<sup>419</sup>  $\kappa\text{-Hg[(SCN)}_3\text{F]}$ ,<sup>420</sup>  $\text{Cu}_5\text{I}_6$ ,<sup>421</sup>  $\text{BF}_4(\text{TCE})_{0.5}$  (rapid cool),<sup>422,423</sup>  $\text{ClO}_4(\text{TCE})_{0.5}$  (rapid cool),<sup>376</sup>  $(\text{IBr}_2)_2(\text{TCE})_{0.5}$  (annealed),<sup>424</sup> and  $\text{Hg}_2\text{Cl}_6$  (chlorobenzene) (4:1)<sup>425</sup>).

In summary, the characteristic features of the ET molecule and complexes are the following:

1) Non-planar neutral ET molecules become almost flat except the terminal ethylene groups in the ionic and partial CT complexes. The terminal ethylene groups are orientationally disordered at high-temperature.

2) ET molecules tend to pile up one after the other with sliding into each other so as to minimize the steric hindrance caused by the terminal ethylene groups. The perpendicular transfer interactions ( $t_{\perp}$ ) originated from the side-by-side proximate S...S contacts are comparable to the parallel ones ( $t_{\parallel}$ ), giving rise to a 2D conducting layer.

3) The 2D conducting ET layer and insulating anion layer stack alternately to form a layered ET conductor. The anion layer has openings through which the neighboring ET layers have interlayer interactions ( $t_{\perp}'$ ) with each other by the tunnel-

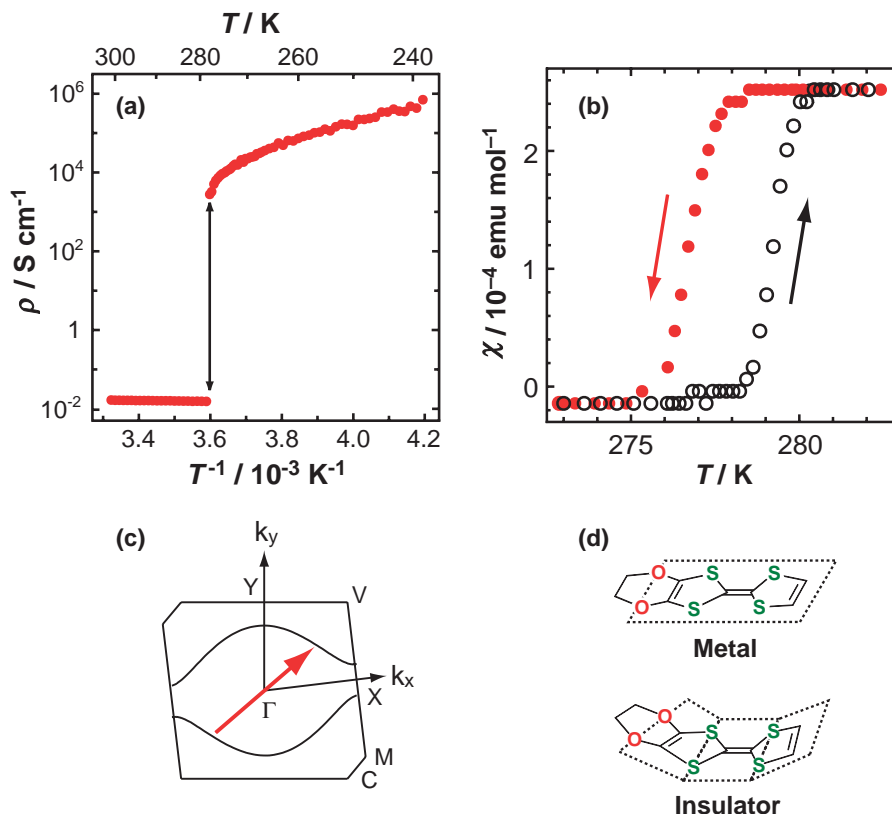


Fig. 34. Temperature dependence of (a) resistivity and (b) magnetic susceptibility of  $(\text{EDO})_2\text{PF}_6$ . Arrows indicate the MI transition. (c) Calculated Fermi surface of  $(\text{EDO})_2\text{PF}_6$ , where the arrow indicates the nesting vector. (d) Molecular structures of neutral and monocationic EDO molecules.<sup>426</sup>

ing effect, giving rise to  $t_{//} \geq t_{\perp} > t_{\perp'}$ .

4) Different kinds of ET...ET and ET...anion intermolecular interactions, large conformational freedom of ethylene groups, flexible molecular framework, fairly narrow bandwidth and strong electron correlation provide a rich variety of ET complexes with different crystal and electronic structures.

**3.3.5 New Metal–Insulator Transition:** To destabilize the metallic state of the BO complexes, the substitution of one ethylenedioxy group with an ethylenedithio group ( $\text{BO} \rightarrow \text{EOET}$ , Fig. 14)<sup>235,242</sup> or the elimination of one ethylenedioxy group ( $\text{BO} \rightarrow \text{EDO}$ , Fig. 14)<sup>244,426,427</sup> was found to be very efficient owing to the weakened self-assembling ability (Fig. 14). The  $(\text{EDO})_2\text{X}$  salts ( $\text{X} = \text{PF}_6$ ,  $\text{AsF}_6$ , and  $\text{SbF}_6$ ) have a quasi-1D Fermi surface and exhibit a peculiar first-order MI transition (Fig. 34) at rather high temperatures (240–280 K). The phase transition consists of a cooperative mechanism with charge-ordering, anion order–disorder and Peierls-like instability, which induces a doubled lattice periodicity giving rise  $2k_F$  nesting. Also, the transition has a thermal hysteresis as probed by the magnetic susceptibility and is related to the flexibility of the EDO molecules (Fig. 34d). The deformation of EDO molecules and local Coulomb interaction between EDO and anion molecules are anticipated to trigger the new cooperative MI transition. The high-temperature metallic phase is composed of flat EDO molecules with  $+0.5$  charge, while the low-temperature insulating phase is composed of both flat monocations and bent neutral EDO molecules with a charge-ordered stripe  $[+1, +1, 0, 0]$ . This stripe is different from those so far known,

$[0, +1, 0, +1]$  stripe for  $\theta$ -( $\text{ET})_2\text{MM}'(\text{SCN})_4$ ,<sup>405</sup> indicating that the neighbor-site Coulomb repulsion energy is not dominant compared to the transfer energy within the  $(\text{EDO}^{1+})_2$  dimer. Laser irradiation onto the insulating  $(\text{EDO})_2\text{PF}_6$  crystal induces a phase transition to the metallic state within a few picoseconds (see section 4.3.1.3).<sup>428</sup>

**3.4 Design of Molecular and Crystal Structures for (Super)conductors.** **3.4.1 Alternating or Segregated Packing and Donor Packing Pattern:** Many researchers still think that it is impossible to predict the packing pattern of component molecules in the solid. In some cases for CT complexes, however, it is incorrect. The key parameters are the degree of CT ( $\delta$ ) and the self-assembling ability of component molecules.

When the component molecules have no strong self-assembling ability, it is difficult to obtain neutral CT complexes ( $\delta < 0.5$ ) with segregated packing except for some special cases having a clathrate character (i.e. 4,4'-dinitrobiphenyl complexes with benzidines, biphenyls, etc.<sup>429,430</sup> and  $\text{C}_{60}$  complexes with OMTTF,<sup>246</sup> ET,<sup>431</sup> etc.).

In the TTF-*p*-benzoquinone system, both component molecules have a weak self-assembling ability. Therefore, except for several highly conductive ones, (TMTTF-2,3-dicyano-1,4-naphthoquinone, HMTTF-2,3-dicyano-*p*-benzoquinone ( $\text{Q}(\text{CN})_2$ ), DBTTF-DDQ, DBTTF-DBDQ, TTF-*p*-fluoranil (tetrafluoro-*p*-benzoquinone,  $\text{QF}_4$ ), and TMTTF- $\text{QX}_4$  ( $\text{X} = \text{F}$ ,  $\text{Cl}$ , and  $\text{Br}$ )),<sup>209,214,236,432–435</sup> most of them have the alternating stacking in the range of  $0 \leq \delta \leq 1$ . Based on a plot similar to

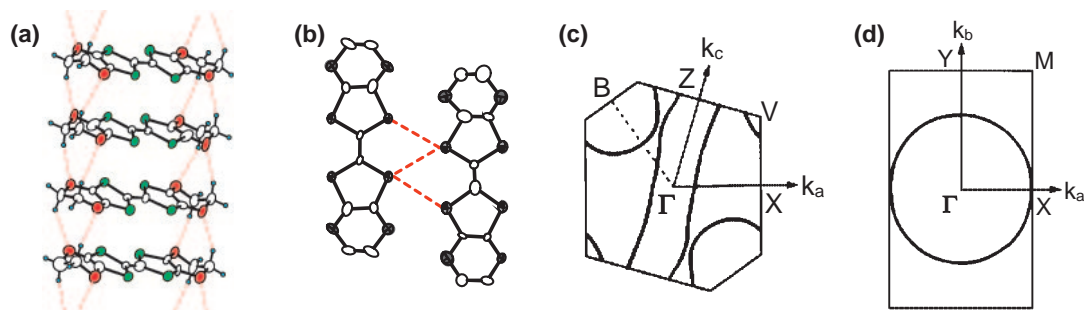


Fig. 35. Donor packing and Fermi surface for BO compounds. (a) Face-to-face packing (dotted red lines indicate the CH...O hydrogen bonds), (b) side-by-side contacts (dotted red lines indicate the short S...S atomic contacts), and calculated Fermi surfaces of (c)  $(\text{BO})_5(\text{HCTMM})(\text{PhCN})_2$  and (d)  $(\text{BO})_2\text{Cl}(\text{H}_2\text{O})_3$ .<sup>234</sup>

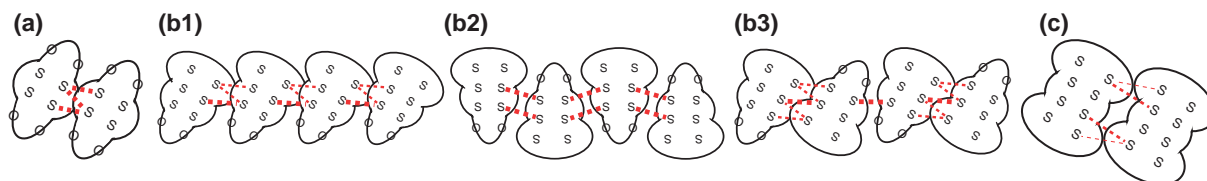


Fig. 36. Schematic figures of S...S atomic contacts in typical (a) BO, (b) EOET, and (c) ET compounds. Dotted lines indicate the comparatively short S...S atomic contacts. Thick dotted lines:  $\text{S}_{\text{in}} \cdots \text{S}_{\text{in}}$ , medium one:  $\text{S}_{\text{in}} \cdots \text{S}_{\text{out}}$  and thin one:  $\text{S}_{\text{out}} \cdots \text{S}_{\text{out}}$ . The S...S contacts in the four side-by-side EOET molecules: (b1)  $\text{EOET} \cdot \text{TCNQ}$ ,<sup>235</sup> (b2) metallic  $\beta''$ -( $\text{EOET}$ )<sub>2</sub>AuBr<sub>2</sub><sup>242</sup> and (b3) Mott insulator  $\alpha'$ -( $\text{EOET}$ )<sub>2</sub>Cu[N(CN)<sub>2</sub>]Br.<sup>242</sup>

Fig. 15 using half-wave redox potentials, all of the conductive TTF·*p*-benzoquinone complexes mentioned above belong to the range of  $-0.04$  (for  $\text{TTC}_1\text{-TTF} \cdot \text{DDQ}$ )  $\leq \Delta E(\text{DA}) \leq 0.31$  V (for  $\text{TTF} \cdot \text{QF}_4$ ), which is comparable to Eq. 18.<sup>236,435</sup>

With increasing the self-assembling ability of the component molecules (mainly donor molecules) the  $\Delta E(\text{DA})$  range for conductors expands, as shown in Fig. 18, and most of the DA complexes in this region with a low  $h\nu_{\text{CT}}$  band form segregated columns or layers. These columns and layers are stabilized by transfer interactions between the donor molecules. The typical example is the BO system. Figures 35a and 35b show one of the common packing patterns of the BO molecules. The strong self-assembling ability of the BO molecules arises from both the CH...O hydrogen bonds in the face-to-face direction (Fig. 35a) and robust transfer interactions in two different oblique directions owing to the strong S...S atomic contacts (Fig. 35b). These afford both a wide valence range of metallic state ( $0.33 \leq \delta \leq 0.63$ ) and a limited number of preferable packing patterns giving rise to a stable 2D metallic state.<sup>234,240</sup>

**3.4.2 Self-Assembling Ability of BO and EOET Molecules:** Based on the structural analysis of  $\text{EOET} \cdot \text{TCNQ}$ ,<sup>235</sup> it was observed that the EOET molecule also has a self-assembling ability, but it is much weaker than that of the BO molecule.  $\text{EOET} \cdot \text{TCNQ}$  has a sharp transition from semimetal or narrow-gap semiconductor to magnetic insulator at 120 K. Figure 36 schematically demonstrates the typical S...S atomic contacts in the side-by-side direction in (a) BO, (b) EOET, and (c) ET compounds. Since the HOMO coefficients of the inner chalcogen atoms of these molecules are generally 3–4 times greater than those of the outer chalcogens,<sup>120</sup> the transfer interactions generated by the  $\text{S}_{\text{in}} \cdots \text{S}_{\text{in}}$  contacts in the side-by-side direction are significantly important compared to those by

the  $\text{S}_{\text{in}} \cdots \text{X}_{\text{out}}$  and  $\text{X}_{\text{out}} \cdots \text{X}_{\text{out}}$  contacts (X: O or S). For the BO compounds, the size difference between the oxygen and sulfur atoms enables the formation of robust side-by-side  $\text{S}_{\text{in}} \cdots \text{S}_{\text{in}}$  contacts (Fig. 36a). On the other hand, smaller transfer interactions are expected in the EOET system owing to its molecular geometry. Furthermore, particular side-by-side S...S atomic contacts between EOET molecules can be constructed owing to the low-symmetric molecular shape of EOET (Figs. 36b1–36b3).

Figure 36b1 is of the side-by-side packing in  $\text{EOET} \cdot \text{TCNQ}$  suggesting the reduced self-assembling ability of the EOET molecule compared to that of BO. The side-by-side packing in Fig. 36b2 is the most favorable for EOET complexes with large transfer interactions, in which each EOET molecule is arranged alternately and the robust  $\text{S}_{\text{in}} \cdots \text{S}_{\text{in}}$  contacts are uniform in the side-by-side direction. This pattern affords  $\beta''$ -( $\text{EOET}$ )<sub>2</sub>-AuBr<sub>2</sub> showing a metallic behavior down to 1.6 K.<sup>242</sup> The EOET molecule is also prone to afford an  $\alpha'$ -type stacking ( $\alpha'$ -( $\text{EOET}$ )<sub>2</sub>X; X = AuBr<sub>2</sub> and Cu[N(CN)<sub>2</sub>]Br) similar to the ET molecules, where the twisted donor dimers form segregated columns and then form the side-by-side packing pattern as depicted in Fig. 36b3. Both  $\alpha'$ -salts are Mott insulators at RT and the magnetic behaviors are characteristic to an antiferromagnet for the AuBr<sub>2</sub> salt ( $T_{\text{N}} = 9$  K).<sup>242</sup>

**3.4.3 Self-Assembling Ability of ET Molecule, Packing Patterns, and Superconductors:** The steric hindrance exerted by the bulky six-membered rings of ET molecules prevents the formation of  $\text{S}_{\text{in}} \cdots \text{S}_{\text{in}}$  contacts (Fig. 36c). No particular  $\text{S}_{\text{in}} \cdots \text{S}_{\text{out}}$  patterns are favorable as well. As a consequence, various kinds of S...S contacts are produced depending on the donor packing patterns ( $\alpha$ -,  $\beta$ -,  $\theta$ -,  $\kappa$ -phases, and so forth), and are comparable to the other intermolecular interactions: i.e., face-to-face ( $\pi$ - $\pi$ ) and donor...anion (H-bonds) interactions.



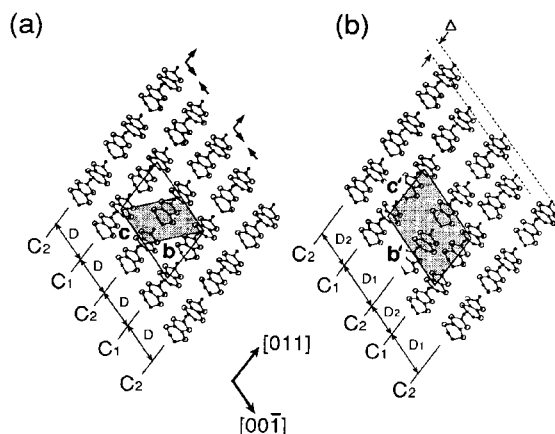


Fig. 37. The packing of ET molecules in the bulk (a) and surface (b) of  $\beta$ -(ET) $_2$ I $_3$ . Every two ET columns ( $C_2$  column) along  $[110]$  shift by  $\Delta$  in this direction in the surface structure measured by STM. The uniform separation between columns  $C_1$  and  $C_2$  in the bulk structure changes to the alternating separation  $D_1 = 8.4 \text{ \AA}$  and  $D_2 = 6.8 \text{ \AA}$  in the surface structure.<sup>438</sup>

Any interaction could not solely determine the donor packing picture. It is thus much more difficult to predict the donor packing pattern for the ET system compared to those of BO and EOET, especially for salts with small and discrete anions.

In the ET cation radical salts with discrete linear anions such as I $_3$  and I $_2$ Br, the component molecules have great freedom of motion and the donor packing pattern can be changed by thermal or pressure treatment.<sup>436,437</sup> Scanning tunneling microscope (STM) measurements revealed that the surface structure of  $\beta$ -(ET) $_2$ I $_3$  crystals contains many defects, voids, and reconstruction of donor packing (Fig. 37) attributed to the unstable structure of the anion layers,<sup>438</sup> while the surface structures of salts with polymerized anions such as  $\kappa$ -(ET) $_2$ Cu(NCS) $_2$ <sup>439</sup> and  $\alpha$ -(ET) $_2$ [MHg(SCN) $_4$ ] ( $M = \text{NH}_4$  and K)<sup>440,441</sup> are stable with no defects.

The polymerized anion molecules in  $\kappa$ -(ET) $_2$ Cu(NCS) $_2$  form an anion layer having openings, as seen in Fig. 33.<sup>384</sup> Two ET molecules form a dimer unit that fits into each opening. In more accurate detail, the hydrogen atom of one ethylene group of the ET molecule fits into the core created by anion molecules, like a key-keyhole relation. The position of such an ethylene hydrogen atom projected onto the anion cores produces unique patterns called  $\alpha$ ,  $\beta$ ,  $\theta$ , and  $\kappa$ -types (Fig. 38).<sup>442</sup> It means that the ET molecules arrange according to the anion core or opening pattern created by polymerized anions. Thereby, the intermolecular interaction within the anion layers is a dominant factor governing the donor packing pattern.

All the ET and BO superconductors so far known are summarized in Table 15. In the following sections, the  $\beta$ -type with discrete linear anions (I $_3$ , AuI $_2$ , and IBr $_2$ ) and  $\kappa$ -type with polymerized anions of ET superconductors are mainly described.

**3.5 Two-Dimensional ET Superconductors. 3.5.1  $\beta$ -(ET) $_2$ I $_3$ :**  $\beta$ -(ET) $_2$ I $_3$  ( $T_c = 1.5 \text{ K}$ ), discovered by Yagubskii et al., is the first ambient pressure superconductor in the ET family.<sup>443</sup> This salt is called “low  $T_c$   $\beta$ -(ET) $_2$ I $_3$ ” or “ $\beta_L$ -(ET) $_2$ I $_3$ .” The ET molecules are slightly dimerized in a face-

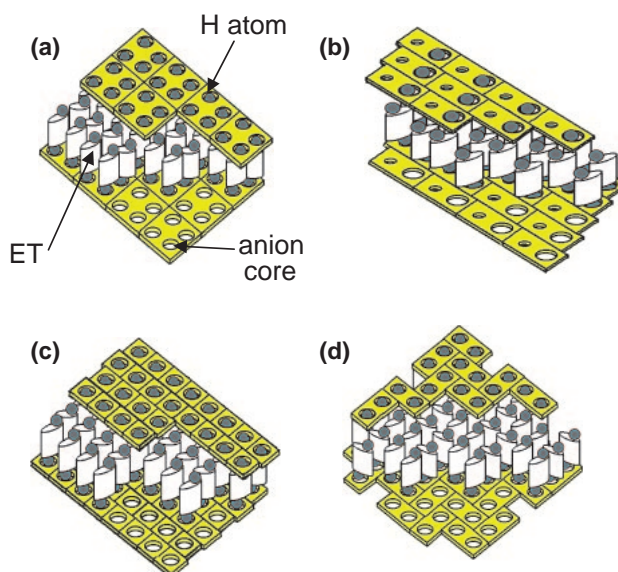


Fig. 38. The relation between anion core and donor packing patterns in ET complexes. (a)  $\alpha$ -Type (each four ET molecules are the repeating unit and fit to four uniform anion cores), (b)  $\beta$ -type (each two ET molecules are the repeating unit and fit to big and small anion cores), (c)  $\theta$ -type (each ET molecule is the repeating unit to fit to a uniform anion core), and (d)  $\kappa$ -type (each two ET molecules fit to two uniform anion cores and they are arranged orthogonally to each other. The unit of two anion cores in (d) corresponds to the anion opening in Fig. 33).<sup>442</sup>

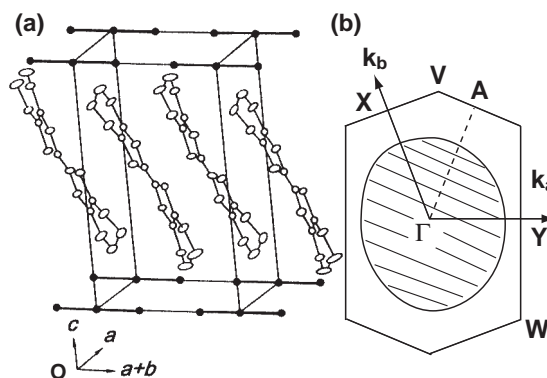


Fig. 39. (a) Crystal structure of  $\beta$ -(ET) $_2$ I $_3$  at RT. Triclinic,  $P\bar{1}$ ,  $a = 6.609(1)$ ,  $b = 9.083(1)$ ,  $c = 15.267(2) \text{ \AA}$ ,  $\alpha = 85.63(2)$ ,  $\beta = 95.62(2)$ ,  $\gamma = 70.22(2)^\circ$ ,  $V = 852.2 \text{ \AA}^3$ ,  $Z = 1$  by Shibaeva et al. The I $_3$  anions are arranged along the  $(a + b)$  axis.<sup>444</sup> (b) Calculated Fermi surface of  $\beta$ -(ET) $_2$ I $_3$  based on the donor packing in (a) and optical data.<sup>495,496</sup>

to-face manner to form a column (Fig. 39a). Short S...S atomic contacts were observed between the columns but not within a column. The linear anions are located on the inversion center. Very short C-H...I contacts were observed between orientationally disordered ethylene groups and I $_3$ .

By cooling the crystals at ambient pressure, a superlattice appears at 175 K with incommensurate modulations of ET and I $_3$  to each other.<sup>497</sup> Then, the orientationally disordered ethylene groups near I $_3$ , which have either the A or B config-

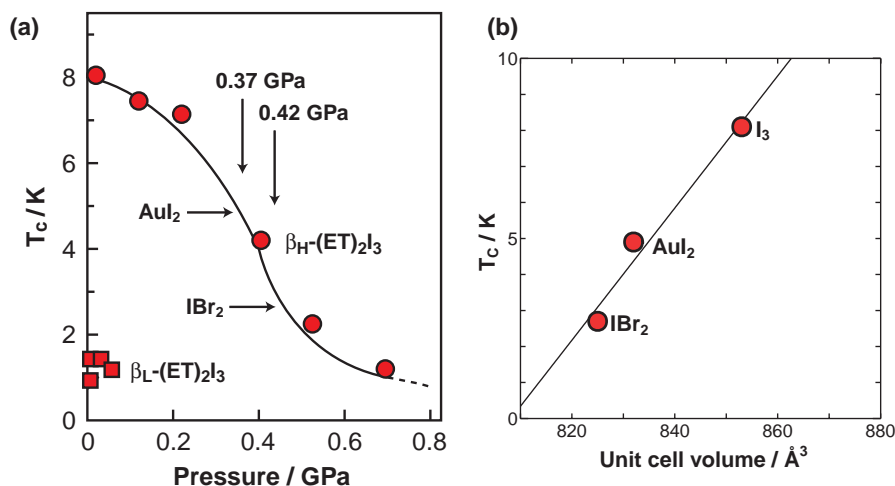


Fig. 40. Plots of  $T_c$  vs (a) pressure by Tokumoto et al.<sup>501</sup> and (b) unit cell volume (at 298 K) by Williams et al. for  $\beta-(\text{ET})_2\text{X}$  ( $\text{X} = \text{I}_3$ ,  $\text{IBr}_2$ , and  $\text{AuI}_2$ ).<sup>502</sup>

uration (Fig. 32), order so as to make a new periodicity according to the incommensurate superlattice periodicity. This is the  $\beta_L$ -phase. The formation of the superlattice at 175 K was suppressed by the pressure above 0.04 GPa. Then the two ethylene groups were fixed in the eclipsed conformation to give rise to a distinct superconductor having  $T_c$  of 8.1 K (designated as “high  $T_c$   $\beta$ -phase” or “ $\beta_H$ -phase”).<sup>446,447</sup> The high  $T_c$  phase is a metastable one and can only be isolated by depressurizing the crystal below 125 K.

The Fermi surface deduced both from the crystal structure at RT and from optical measurements exhibits a large closed hole-like surface, which shares 50% of the first Brillouin zone (Bz) (Fig. 39b).<sup>495,496</sup> The SdH measurements of the  $\beta_H$ -phase indicated that the closed Fermi surface corresponds to ca. 51% of the first Bz ( $m_c = 4.65m_e$ ), which is in good agreement with the calculated one.<sup>498</sup> From the beating of the oscillations,  $t_a/t_c \approx 30$  was evaluated. On the other hand, the SdH and dHvA results on the  $\beta_L$ -phase were not consistent with Fig. 39b; namely, a closed orbit with only 22–25% ( $m_c = 0.4\text{--}0.5m_e$ ) or 103% ( $4.0m_e$ ) of the first Bz was detected. The beating afforded  $t_{\parallel}/t_{\perp} = 23\text{--}25$ . The Fermi surface of the  $\beta_L$ -phase has not been proposed yet.

Soon after the discovery of  $\beta-(\text{ET})_2\text{I}_3$ , other superconducting phases based on  $\text{I}_3$  ( $\gamma-(\text{ET})_3\text{I}_{2.5}$ ,<sup>450</sup>  $\theta-(\text{ET})_2\text{I}_3$ ,<sup>451</sup> and  $\kappa-(\text{ET})_2\text{I}_3$ <sup>452</sup>) and the modified anions ( $\beta-(\text{ET})_2\text{IBr}_2$ ,<sup>453</sup>  $\beta-(\text{ET})_2\text{-AuI}_2$ <sup>454</sup>) have been prepared. In addition,  $\alpha-(\text{ET})_2\text{I}_3$ , which shows an MI transition at 135 K, was converted to mosaic polycrystals of  $\beta-(\text{ET})_2\text{I}_3$  with  $T_c \approx 8$  K by tempering at 70–100 °C for more than 3 days.<sup>449,450</sup> Since the  $T_c \approx 8$  K phase thus obtained was stable and can be isolated at ambient pressure, it was designated as  $\alpha_t-(\text{ET})_2\text{I}_3$ . The AMRO was first observed on  $\beta-(\text{ET})_2\text{IBr}_2$ <sup>499</sup> and  $\theta-(\text{ET})_2\text{I}_3$ ,<sup>500</sup> and subsequently has been utilized to study the precise shape of the Fermi surface topologically.<sup>164–166</sup>

The  $\beta$ -type donor stacking has been realized by use of linear counter anions  $\text{I}_3$  (anion length is 10.1–10.2 Å),  $\text{AuI}_2$  (9.4 Å),  $\text{I}_2\text{Br}$  (9.7 Å), and  $\text{IBr}_2$  (9.3–9.4 Å). Among them,  $\beta-(\text{ET})_2\text{I}_2\text{Br}$  is the only non-superconducting metal due to the disordered orientation of the unsymmetrical anion, I–I–Br. Neither the  $\text{IBr}_2$  or  $\text{AuI}_2$  salt exhibits the superlattice formation, and the

ethylene groups were in the eclipsed conformation. Therefore,  $\beta_H-(\text{ET})_2\text{I}_3$  is isostructural to those of the  $\beta$ -phase salts of  $\text{AuI}_2$  and  $\text{IBr}_2$ .

To explain the effect of the size of a linear anion on  $T_c$  of the  $\beta$ -phase salts, some interesting correlations have been proposed between  $T_c$  and structural parameters, such as lattice pressure by Tokumoto et al. (Fig. 40a),<sup>501</sup> unit cell volume by Williams et al. (Fig. 40b),<sup>502</sup> and anion length by Kistenmacher.<sup>503</sup> The lattice pressure, or sometimes termed the chemical pressure, is a hypothetical pressure to represent the lattice compression, and is used as one of the parameters to measure the effect of chemical substitution on the physical properties among isomorphous crystals. By applying the lattice-pressure model to the change in the lattice parameter along the  $(a+b)$ -axis, one finds that  $\beta-(\text{ET})_2\text{AuI}_2$  and  $\beta-(\text{ET})_2\text{IBr}_2$ , both of which have an isomorphous structure to  $\beta_H$ -salt instead of  $\beta_L$ -salt, are placed on the  $T_c$  vs pressure phase diagram of  $\beta_H-(\text{ET})_2\text{I}_3$  (Fig. 40) at ca. 0.37 and 0.42 GPa, respectively.<sup>501</sup> Figures 40a and 40b demonstrate that  $T_c$  increases with increasing the length of the symmetric linear anion or application of negative pressure, resulting in an increase in  $D(\varepsilon_F)$  mainly due to the decrease in  $t_{\parallel}$ .

Then, a longer linear anion than  $\text{I}_3$  is postulated to yield a  $\beta$ -phase salt with  $T_c$  higher than 8 K. However, triiodide is the longest one among the symmetric linear polyhalides, and thus, a variety of longer anions of metal halides and metal pseudohalides has been investigated, where the metals are Cu, Ag, Hg, Ni, Pd, etc. and the pseudohalides are CN, OCN, SCN, SeCN, etc. The first organic superconductor with  $T_c$  above 10 K was prepared by Urayama(Mori) and Saito et al. with the anion of  $\text{Cu}(\text{NCS})_2$  in 1988.<sup>472</sup> The salt was found to be  $\kappa$ -phase instead of  $\beta$ -phase, and the anion  $\text{Cu}(\text{NCS})_2$  was neither symmetric, linear, nor discrete, but formed a zig-zag polymer.

**3.5.2  $\kappa-(\text{ET})_2\text{Cu}(\text{NCS})_2$  and Other  $\kappa$ -Type 10 K Class ET Superconductors:**  $\kappa-(\text{ET})_2\text{Cu}(\text{NCS})_2$  exhibits a complicated temperature dependence of resistivity (Fig. 41). Most samples exhibited a metallic temperature dependence from RT ( $\sigma_{\text{RT}}(//c) = 10\text{--}40 \text{ S cm}^{-1}$ ,  $\sigma_a^*:\sigma_b:\sigma_c = 1/600:1:1.2$ ) to 250–270 K, followed by a semiconductor-like behavior down to ca. 90 K. Then, it showed a metallic behavior again with super-

conducting transition with  $T_c(\text{mid-point}) = 10.4 \text{ K}$ .<sup>472</sup> The deuterated salt shows an inverse isotope effect (on-set  $T_c = 11.4 \text{ K}$ , off-set  $T_c = 10.7 \text{ K}$ , and mid-point  $T_c = 11.1\text{--}11.2 \text{ K}$ <sup>474–478</sup>).

The crystal structure of  $\kappa\text{-(ET)}_2\text{Cu(NCS)}_2$  is shown in Fig. 42. Two ET molecules form a dimer with +1 charge

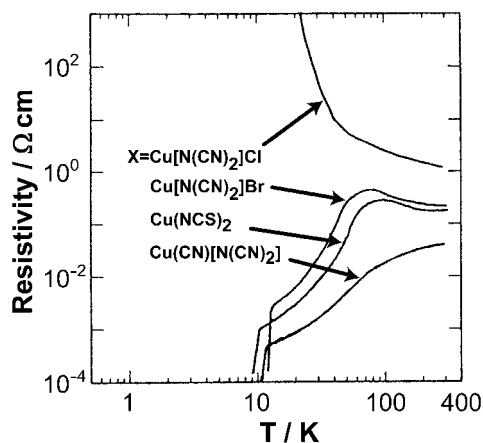


Fig. 41. Temperature dependence of the resistivity of  $\kappa\text{-(ET)}_2\text{Cu(CN)[N(CN)}_2]$ ,  $\kappa\text{-(ET)}_2\text{Cu(NCS)}_2$ ,  $\kappa\text{-(ET)}_2\text{Cu[N(CN)}_2]\text{Br}$ , and  $\kappa\text{-(ET)}_2\text{Cu[N(CN)}_2]\text{Cl}$ .<sup>384</sup>

( $S = 1/2$ ). The ET dimers are arranged orthogonally to each other to form a conducting layer of  $\kappa$ -type in the  $bc$ -plane (see also Figs. 33 and 38d), which is sandwiched by the insulating and non-magnetic anion layers along the  $a$ -axis. Based on the donor packing, the Fermi surface in Fig. 28a is calculated. The anion molecules  $\text{Cu(NCS)}_2$  are polymerized and the infinite zig-zag anion chains extend along the  $b$ -axis, where  $\text{Cu}^{1+}$  is connected with one kind of NCS to form the infinite chain and the other kind of NCS is attached to  $\text{Cu}^{1+}$  triangularly as a pendant (Fig. 43b).

The  $T_c$  of ET salts has risen by the discovery of new  $\kappa$ -type salts by Williams et al. with large and thin anions  $\text{Cu[N(CN)}_2]\text{Y}$  ( $\text{Y} = \text{Cl}$  and  $\text{Br}$ ) in 1990, where dicyanamide ( $\text{N}\equiv\text{C-N-C}\equiv\text{N}$ )<sup>-</sup> bridges  $\text{Cu}^{1+}$  to form a zig-zag polymer and  $\text{Y}$  attaches to  $\text{Cu}^{1+}$  as a pendant (Fig. 43c).<sup>298,479</sup> Figure 44a illustrates the crystal structure of  $\kappa\text{-(ET)}_2\text{Cu[N(CN)}_2]\text{Cl}$ . Another superconductor with  $T_c$  above 10 K was developed in 1991 by replacing halogen  $\text{Y}$  in the  $\text{Cu[N(CN)}_2]\text{Y}$  anion with pseudohalogen  $\text{CN}$  by Komatsu, Saito, et al.<sup>304,504</sup> In this salt, however,  $\text{Cu}^{1+}$  ions are connected by the ligand  $\text{CN}$  instead of  $\text{N(CN)}_2$ , which now plays the role of the pendant (Fig. 43a). As a consequence, the anion is represented as  $\text{Cu(CN)-[N(CN)}_2]$  instead of  $\text{Cu[N(CN)}_2]\text{(CN)}$ .

These four 10 K class superconductors,  $\kappa\text{-(ET)}_2\text{X}$  ( $\text{X} = \text{Cu(NCS)}_2$ ,  $\text{Cu(CN)[N(CN)}_2]$ ,  $\text{Cu[N(CN)}_2]\text{Cl}$ , and  $\text{Cu[N(CN)}_2]\text{Br}$ ),

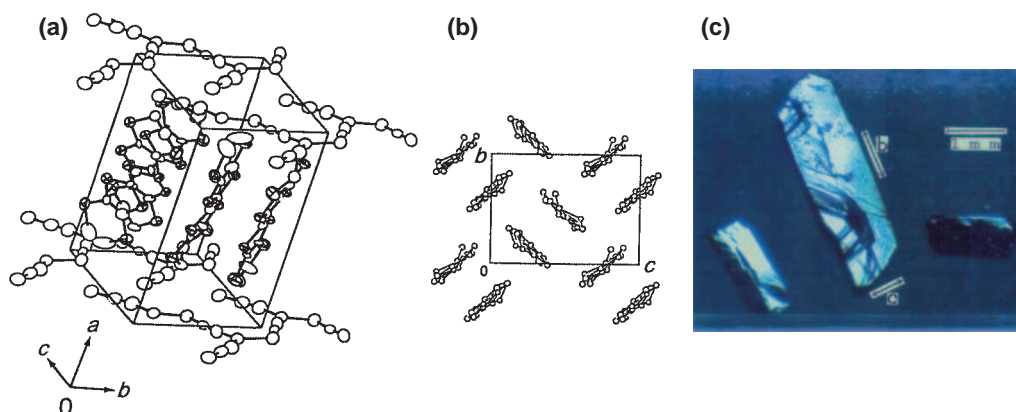


Fig. 42. (a) Crystal structure of  $\kappa\text{-(ET)}_2\text{Cu(NCS)}_2$  (dextro-rotatory form).<sup>472</sup> Monoclinic,  $P2_1$ ,  $a = 16.248(5)$ ,  $b = 8.440(2)$ ,  $c = 13.124(5) \text{ \AA}$ ,  $\beta = 110.30(3)^\circ$ ,  $V = 1688.0(9) \text{ \AA}^3$ ,  $Z = 2$ ,  $R = 0.084$ . (b) Packing of ET molecules viewed along the molecular long axis. (c) Micrograph of single crystals  $\kappa\text{-(ET)}_2\text{Cu(NCS)}_2$  (Courtesy of H. Ueoba).

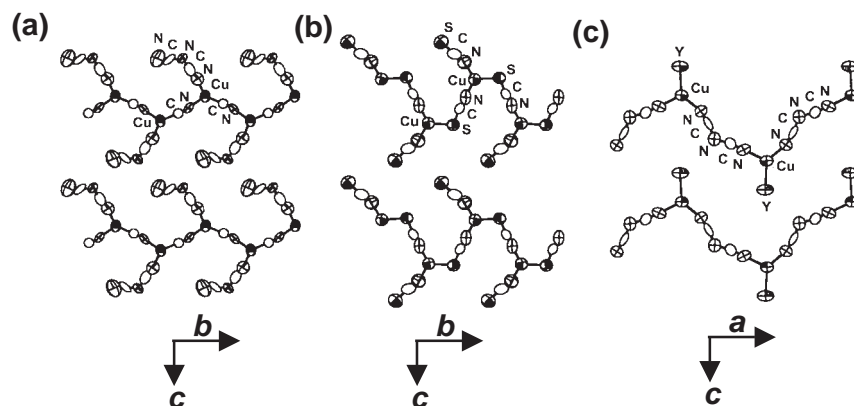


Fig. 43. Anion structures of  $\kappa\text{-(ET)}_2\text{X}$ ; (a)  $\text{X} = \text{Cu(CN)[N(CN)}_2]$ , (b)  $\text{X} = \text{Cu(NCS)}_2$ , and (c)  $\text{X} = \text{Cu[N(CN)}_2]\text{Y}$  ( $\text{Y} = \text{Cl}$  and  $\text{Br}$ ).

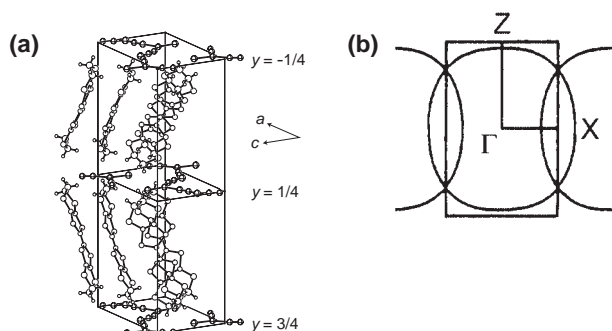


Fig. 44. (a) Crystal structure and (b) calculated Fermi surface of  $\kappa$ -(ET)<sub>2</sub>Cu[N(CN)<sub>2</sub>]Cl. Orthorhombic,  $Pnma$ ,  $a = 12.977(3)$ ,  $b = 29.977(4)$ ,  $c = 8.480(2)$  Å,  $V = 3299(1)$  Å<sup>3</sup>,  $Z = 4$ ,  $R = 0.068$ .<sup>298</sup>

share some common structural and physical properties, and hence, construct a sub-group in the study of ET superconductors. On the other hand, other 10 K class  $\kappa$ -type superconductors with the M(CF<sub>3</sub>)<sub>4</sub> anion (M = Ag and Cu) developed by Schlüter et al.<sup>456,457</sup> (Table 15) have a slight difference in the sense that the anion is not polymerized but discrete and the crystals include disordered solvent.

These four salts are classified into two groups according to the crystal symmetry: namely monoclinic  $P2_1$  for X = Cu(NCS)<sub>2</sub> and Cu(CN)[N(CN)<sub>2</sub>], and orthorhombic  $Pnma$  for X = Cu[N(CN)<sub>2</sub>]Cl and Cu[N(CN)<sub>2</sub>]Br. The donor packing patterns are similar to each other. There are two crystallographically independent ET molecules in the  $P2_1$  symmetry salts, while there is only one in the  $Pnma$  symmetry salts. Reflecting the crystal symmetry, the calculated Fermi surfaces of the  $P2_1$  salts showed the certain energy gap between a 1D electron-like Fermi surface and a 2D cylindrical hole-like one ( $\alpha$ -orbit) (Fig. 28a), while such a gap is absent in the  $Pnma$  salts (Fig. 44b).

At low temperatures,  $\kappa$ -(ET)<sub>2</sub>Cu(NCS)<sub>2</sub> has ordered ethylene groups of ET in a staggered configuration, while those of the other three salts order in an eclipsed configuration (<120 K).

Up to now only  $\kappa$ -(ET)<sub>2</sub>Cu(NCS)<sub>2</sub> shows the reliable SdH and dHvA effects at ambient pressure among these four salts (Table 15). The SdH effects (666 T, Fig. 45) corresponding to the extremal cross-sectional area of 18% of Bz were observed above 8 T by Oshima et al., which is in excellent agreement with the calculated Fermi surface in Fig. 28a.<sup>356</sup>

The estimated cyclotron mass of the  $\alpha$ -orbit  $m_{c\alpha} = 3.5$ – $3.6m_e$  which is considerably larger than the calculated band mass  $m_{b\alpha} = 0.9m_e$ . The interlayer band width  $4t_{\perp}$  was estimated to be 1.6 meV. The magnetic breakdown oscillations, which correspond just 100% of Bz or extremal  $\beta$ -orbit in Fig. 28a, were observed above 20 T ( $m_{c\beta} = 7m_e$ , cf.  $m_{b\beta} = 1.3m_e$ ).<sup>358,505</sup> The  $m_c$  and energy gap between the 1D orbit and  $\alpha$ -orbit decrease under pressure ( $m_{c\alpha} = 1.4m_e$ ,  $m_{c\beta} = 2.7m_e$ , energy gap  $\approx 1$  meV at 1.63 GPa). The cyclotron-resonance mass for the  $\alpha$ -orbit is estimated to be  $m_{cr} = 1.18m_e$ , which is close to the calculated band mass but considerably smaller than the cyclotron mass indicating the presence of strong electron–electron interaction.<sup>506</sup>  $\kappa$ -(ET)<sub>2</sub>Cu[N(CN)<sub>2</sub>]Br and  $\kappa$ -(ET)<sub>2</sub>Cu[N(CN)<sub>2</sub>]Cl exhibited quantum oscil-

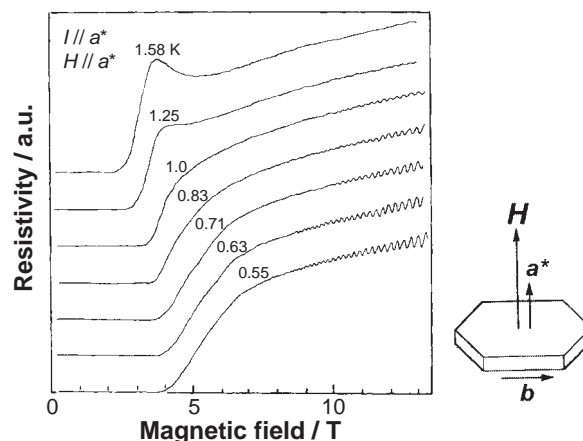


Fig. 45. Shubnikov-de Haas oscillations of  $\kappa$ -(ET)<sub>2</sub>Cu(NCS)<sub>2</sub>.<sup>356</sup> This is the first observation of quantum oscillations on an organic compound. Current and magnetic field are applied along the  $a^*$ -axis.

lations under pressure.<sup>488</sup>

Although the four 10 K class ET salts have similar structural aspects, their transport properties differ apparently (Fig. 41 for resistivity and Fig. 46 for EPR, see also section 3.6.1).  $\kappa$ -(ET)<sub>2</sub>Cu(CN)[N(CN)<sub>2</sub>] showed a monotonous decrease in resistivity (ca. 5–50 S cm<sup>-1</sup> //  $b$ ,  $\sigma_{\parallel}/\sigma_{\perp} \approx 230$  at RT) with upper curvature down to the superconducting transition (Fig. 41).  $\kappa$ -(ET)<sub>2</sub>Cu[N(CN)<sub>2</sub>]Br ( $\sigma_{RT}$  // 2D plane) = 2–50 S cm<sup>-1</sup>,  $\sigma_{\parallel}/\sigma_{\perp} = 200$ ) exhibited a similar behavior to that of  $\kappa$ -(ET)<sub>2</sub>Cu(NCS)<sub>2</sub>, usually without a metallic regime near RT (Fig. 41).  $\kappa$ -(ET)<sub>2</sub>Cu[N(CN)<sub>2</sub>]Cl ( $\sigma_{RT} \approx 2$  S cm<sup>-1</sup>,  $\sigma_{2D}/\sigma_{\perp} = 100$ –150) is semiconducting ( $E_g = 24$  meV) at ambient pressure with a semiconductor–semiconductor transition at ca. 42 K due to the occurrence of an antiferromagnetic fluctuation.<sup>298</sup> Below 42 K the resistivity increased more rapidly ( $E_g = 104$  meV). The spin canting of antiferromagnetically ordered spins gave rise to a weak ferromagnet below 22 K.<sup>299</sup> Under a weak pressure, the semiconductive behavior below 42 K was suppressed and  $\kappa$ -(ET)<sub>2</sub>Cu[N(CN)<sub>2</sub>]Cl showed a similar temperature dependence to that of  $\kappa$ -(ET)<sub>2</sub>Cu[N(CN)<sub>2</sub>]Br and  $\kappa$ -(ET)<sub>2</sub>Cu(NCS)<sub>2</sub>.

Nakamura et al. found that the temperature dependence of the EPR linewidth  $\Delta H_{pp}$  and  $g$ -values of the  $P2_1$  salts are clearly different from those of the  $Pnma$  ones (Fig. 46).<sup>507</sup> For the salt of X = Cu[N(CN)<sub>2</sub>]Br, the  $\Delta H_{pp}$  increased monotonically from RT to around 60 K, below which turned to decrease. The  $g$ -values along the principal axes were almost constant down to 50 K and then slightly decreased below it. For X = Cu[N(CN)<sub>2</sub>]Cl, the antiferromagnetic interactions caused the broadening of  $\Delta H_{pp}$  and increase in  $g$ -values below 35 K. However, the temperature dependence of  $\Delta H_{pp}$  and  $g$ -values above 60 K were essentially the same as those of the salt of X = Cu[N(CN)<sub>2</sub>]Br.

For the  $P2_1$  salts (X = Cu(NCS)<sub>2</sub> and Cu(CN)[N(CN)<sub>2</sub>]), on the other hand, the temperature dependence of  $\Delta H_{pp}$  and  $g$ -values, especially in the anisotropic behaviors along the  $b$ -axis below 40–50 K, are quite different from those of the  $Pnma$  salts. Along the  $b$ -axis,  $\Delta H_{pp}$  shows an extreme broadening (23 mT at 40 K for the Cu(NCS)<sub>2</sub> salt) and the  $g$ -values



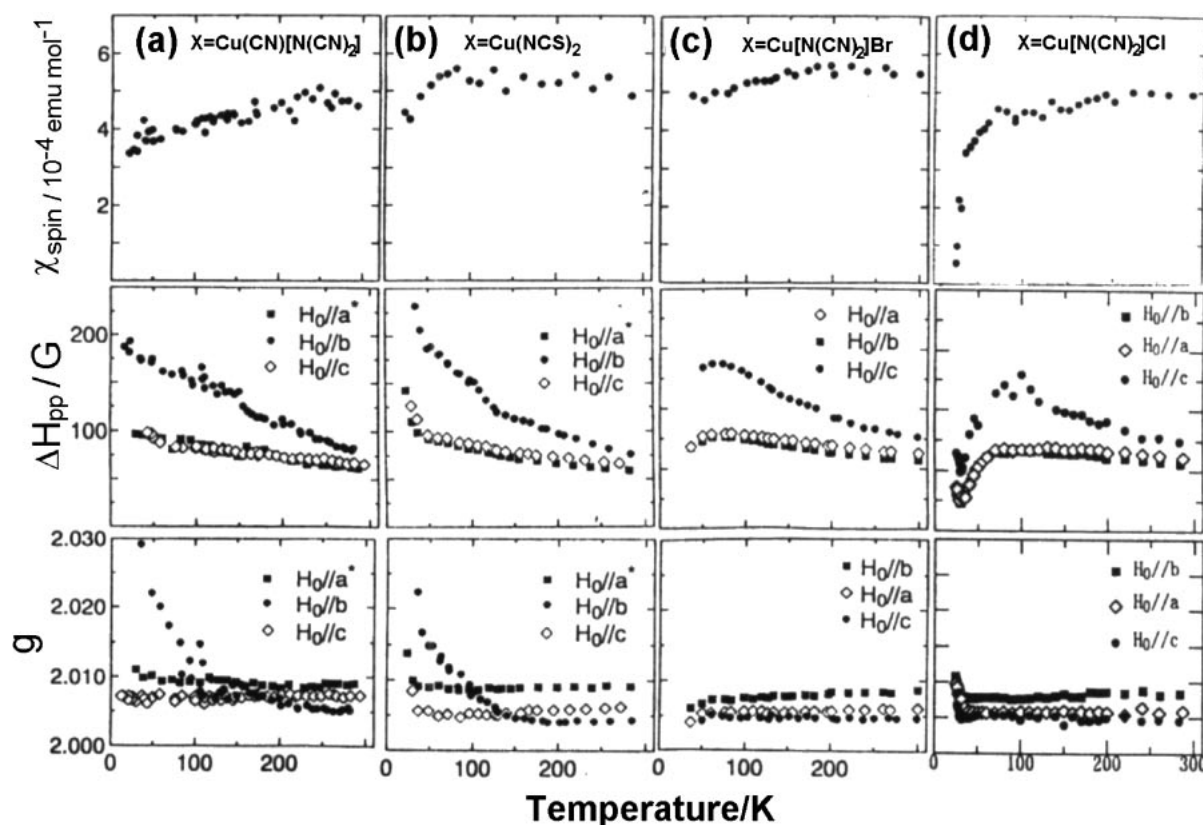


Fig. 46. Temperature dependence of EPR parameters ( $\chi_{\text{spin}}$  spin, peak-to-peak linewidth  $\Delta H_{\text{pp}}$ , and  $g$ -value) of  $\kappa$ -(ET) $_2$ X; (a)  $X = \text{Cu}(\text{CN})[\text{N}(\text{CN})_2]$  ( $P2_1$ ), (b)  $X = \text{Cu}(\text{NCS})_2$  ( $P2_1$ ), (c)  $X = \text{Cu}[\text{N}(\text{CN})_2]\text{Br}$  ( $Pnma$ ), and (d)  $X = \text{Cu}[\text{N}(\text{CN})_2]\text{Cl}$  ( $Pnma$ ).<sup>507</sup>

show a divergent increase below 50 K. The temperature dependence of  $\Delta H_{\text{pp}}$  does not follow the Elliot mechanism and that of  $g$ -values cannot be interpreted by any known theory.

The H-salt of  $\kappa$ -(ET) $_2\text{Cu}[\text{N}(\text{CN})_2]\text{Cl}$  shows a complicated  $T$ - $P$  phase diagram (Fig. 47a) as elucidated by Ishiguro, Ito, et al.<sup>488,508–511</sup> The salt exhibits a non-metallic behavior like  $\kappa$ -(ET) $_2\text{Cu}[\text{N}(\text{CN})_2]\text{Br}$  or  $\kappa$ -(ET) $_2\text{Cu}(\text{NCS})_2$  at higher temperatures (**N1**), and below 60 K the EPR linewidth and intensity start to decrease indicating the occurrence of the low-dimensional antiferromagnetic fluctuation (**N2**) down to 30–35 K.<sup>514</sup> Below it the EPR linewidth and  $g$ -value start to increase while EPR intensity still decreases sharply owing to the growth of the 3D antiferromagnetically ordered phase (**N3**). The EPR signal abruptly disappears below 22 K and the salt becomes a weak ferromagnet (**N4**). The  $^1\text{H}$  NMR and AC magnetic susceptibility indicate the coexistence of weak ferromagnetic and superconducting phases below 13 K (incomplete superconducting phase; **I-SC-2**, see section 4.7.2).<sup>515</sup> Under a pressure of ca. 20–30 MPa another incomplete superconducting phase (**I-SC-1**) appears and the complete superconducting (**C-SC**) phase neighbors this phase at higher pressures. Below these SC phases, the reentrant nonmetallic (**RN**) phase was observed. Similar  $T$ - $P$  phase diagrams were obtained for the D-salts of  $\kappa$ -(ET) $_2$ X ( $X = \text{Cu}[\text{N}(\text{CN})_2]\text{Cl}$ )<sup>511</sup> (Fig. 47b) and  $X = \text{Cu}[\text{N}(\text{CN})_2]\text{Br}$ <sup>302,481,513</sup> (Fig. 47c) with a parallel shift of pressure. They are allocated at the higher and lower pressure sides of the H-salt of  $X = \text{Cu}[\text{N}(\text{CN})_2]\text{Cl}$  for the Br and Cl salts, respectively.

Contrary to the H-salt,  $\kappa$ -(d<sub>8</sub>-ET) $_2\text{Cu}[\text{N}(\text{CN})_2]\text{Cl}$  did not ex-

hibit the coexistence of the superconducting and antiferromagnetic phases. A new signal originating from the antiferromagnetic resonance (AFMR) appeared below 15 K after the disappearance of the EPR signal originating from (ET) $_2^{•+}$  (Figs. 48a and 48b).<sup>514</sup> Subsequent investigation in the submillimeter wave region confirmed the resonance being AFMR.<sup>516</sup> The AFMR signal was also observed for the semiconductive  $\kappa$ -(d<sub>8</sub>-ET) $_2\text{Cu}[\text{N}(\text{CN})_2]\text{Br}$  obtained by rapid cooling.<sup>302,517</sup>

**3.5.3 Effective Volume and Prospect of  $T_c$  in ET Superconductors:** We have observed a linear relation between  $T_c$  and the effective volume  $V_{\text{eff}}$ , which is defined as the space that one conduction electron can occupy in a unit cell (Fig. 49).<sup>474</sup>

$$V_{\text{eff}} = (V_{\text{cell}} - V_{\text{anion}})/N, \quad (32)$$

where  $V_{\text{cell}}$ ,  $V_{\text{anion}}$ , and  $N$  are the unit-cell volume, the approximate anion volume, and the number of carriers per formula unit of the ET salt at RT, respectively.<sup>474</sup> Although the calculated  $V_{\text{eff}}$  contains an uncertainty due to the inaccurate estimation of  $V_{\text{anion}}$ , a linear relation exists between  $T_c$  and  $V_{\text{eff}}$  among ET superconductors with different phases and anions, supporting the idea that a low density of ET molecules in a crystal induces a narrow band width, and thereby, a high  $D(\epsilon_F)$ .

Large anions such as  $\text{MHg}(\text{SCN})_4^-$  ( $M = \text{K}$  and  $\text{NH}_4$ ) in  $\alpha$ -(ET) $_2\text{MHg}(\text{SCN})_4$ , developed by Oshima, Urayama (Mori), Saito, et al.,<sup>394,395</sup> increase  $V_{\text{cell}}$  considerably, and thus, are expected to increase  $V_{\text{eff}}$ . The crystal structure of  $\alpha$ -(ET) $_2$ - $\text{MHg}(\text{SCN})_4$  indicates that the 2D conducting layers are separated from each other by ca. 7 Å by a thick anion layer and the salts may have a highly 2D electronic nature (Fig. 50). These



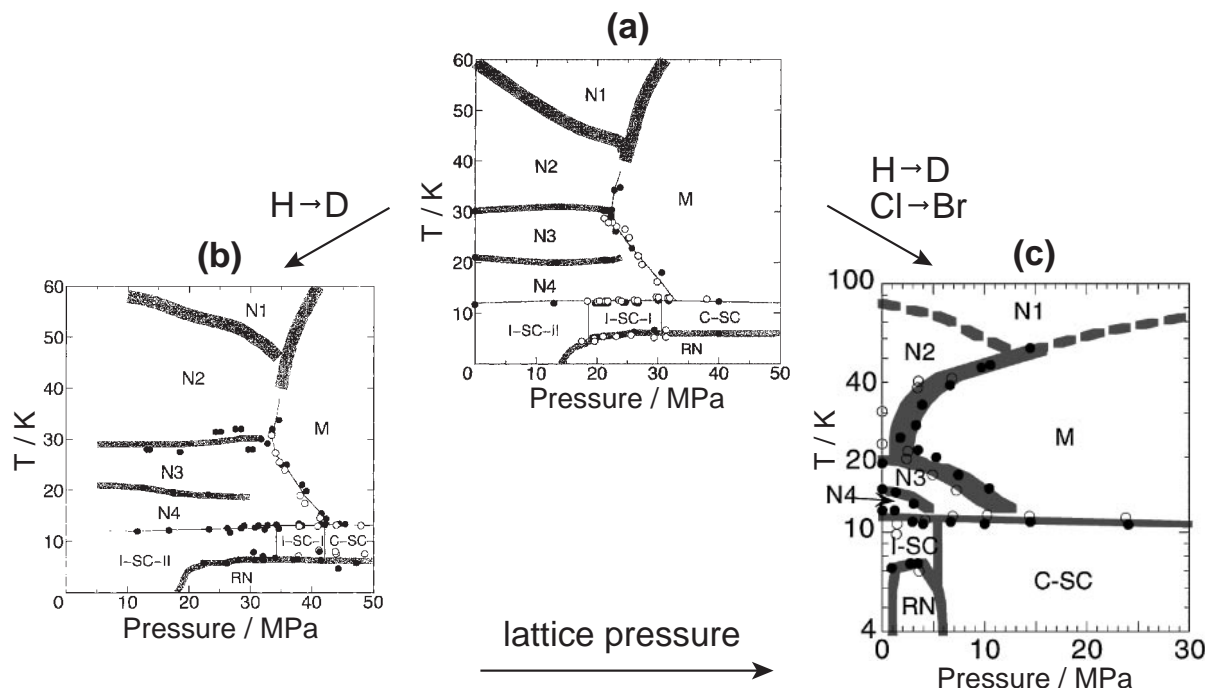


Fig. 47. Pressure-temperature phase diagram of (a) H-salt of  $\kappa$ -( $\text{ET}$ ) $_2\text{Cu}[\text{N}(\text{CN})_2]\text{Cl}$ ,<sup>488,510,511</sup> (b) D-salt of  $\kappa$ -( $\text{ET}$ ) $_2\text{Cu}[\text{N}(\text{CN})_2]\text{Cl}$ ,<sup>510,511</sup> and (c) D-salt of  $\kappa$ -( $\text{ET}$ ) $_2\text{Cu}[\text{N}(\text{CN})_2]\text{Br}$ .<sup>513</sup> (M: metallic phase, N1–N4: nonmetallic phase, RN: reentrant nonmetallic phase, C-SC: complete superconducting phase, I-SC-1, I-SC-2: incomplete superconducting phase. The nature of N1 is not clarified yet.<sup>164</sup> The triple critical points of N2, N3, and M phases indicate that the lattice pressure increases in the order of  $\kappa$ -( $\text{ET}$ ) $_2\text{Cu}[\text{N}(\text{CN})_2]\text{Cl}$  (D)  $\rightarrow$   $\kappa$ -( $\text{ET}$ ) $_2\text{Cu}[\text{N}(\text{CN})_2]\text{Cl}$  (H)  $\rightarrow$   $\kappa$ -( $\text{ET}$ ) $_2\text{Cu}[\text{N}(\text{CN})_2]\text{Br}$  (D) by ca. 10 and ca. 20 MPa, respectively.

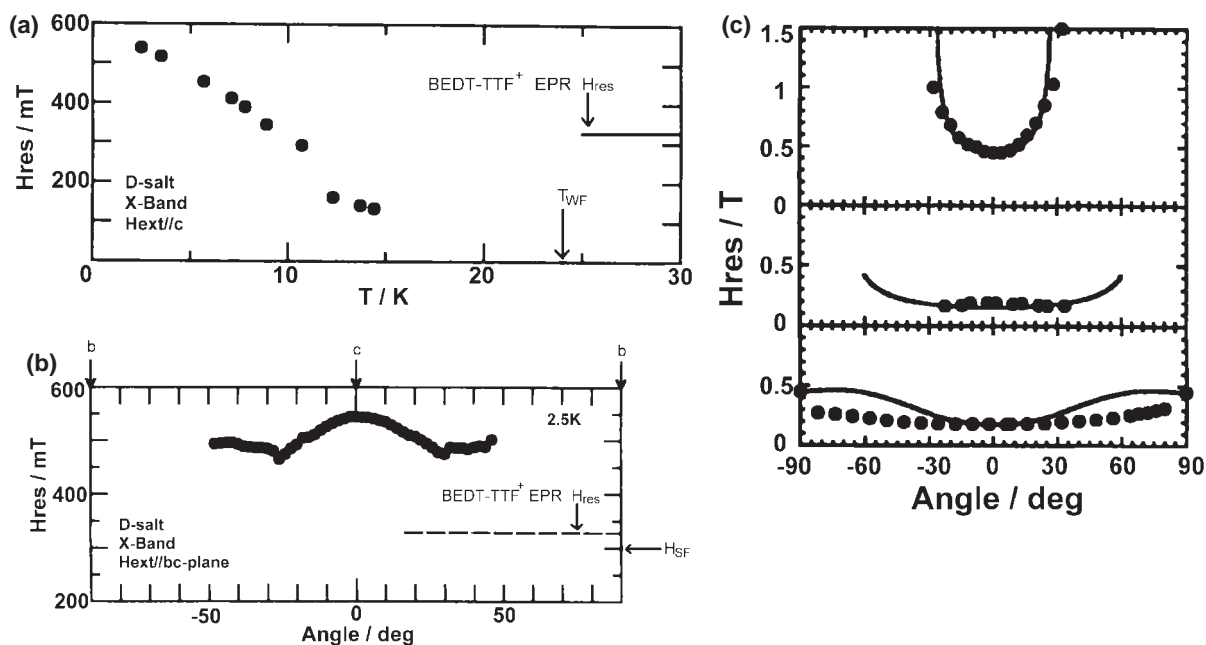


Fig. 48. Antiferromagnetic resonance (AFMR) signal of  $\kappa$ -( $\text{d}_8$ - $\text{ET}$ ) $_2\text{Cu}[\text{N}(\text{CN})_2]\text{Cl}$  (a,b)<sup>514</sup> and  $\kappa$ -( $\text{d}_8$ - $\text{ET}$ ) $_2\text{Cu}[\text{N}(\text{CN})_2]\text{Br}$  (c).<sup>517</sup> (a) AFMR appears below ca. 15 K at a different resonance field ( $H_{\text{res}}$ ) from that of ET EPR signal.  $T_{\text{WF}}$  indicates the temperature of the weak magnetic ordering ( $\approx 24$  K for the D-salt). (b) Angular dependence of the AFMR within the  $bc$ -plane at 2.5 K.  $H_{\text{SF}}$  means the spin-flop field. (c) Angular dependence of the AFMR signal within the (a)  $ab$ -, (b)  $cb$ -, and (c)  $ac$ -planes at 4.2 K. The angle  $0^\circ$  corresponds to the  $a$ -,  $c$ -, and  $c$ -directions, respectively. The solid lines fit the standard theory assuming that  $a$ -,  $b$ -, and  $c$ -axes are easy, hard, and intermediate axes, respectively.

salts were metallic down to 4 K and then superconductivity was observed below 2 K.<sup>396,400,401</sup> The results indicate that the thick and bulky anions increase  $V_{\text{anion}}$  sufficiently to suppress  $V_{\text{eff}}$  and give rise to a low  $T_c$ . As a consequence, “an expanded anion that forms a thin anion layer” has been proposed as an appropriate anion-design strategy.<sup>2,518</sup> The substantial reduction of  $T_c$  in  $\alpha\text{-(ET)}_2\text{MHg(SCN)}_4$  also suggests the importance of the interlayer interactions ( $t'_\perp$ ) through an anion opening.

The large thermal contraction of organic crystals is one of the factors reducing  $T_c$ . The unit-cell of  $\kappa\text{-(ET)}_2\text{Cu(NCS)}_2$  contracts by  $63.6 \text{ \AA}^3$  (or  $31.8 \text{ \AA}^3$  per ET dimer) from RT to 15 K.<sup>519</sup> This corresponds roughly to a 10 K reduction in  $T_c$  according to the relation in Fig. 49. In order to suppress the thermal contraction, the use of “a structurally 2D anion layer that is able to provide short anion...donor contacts” would be effective.<sup>2,518</sup>

Since the  $V_{\text{anion}}$  has a large ambiguity due to the complicated polymerized anions, a  $V_{\text{mes2}}$  value, which corresponds to the sum of the space for  $\text{C}_6\text{S}_8$  skeletons of ET and the intra-donor-

layer overlap space between them per two carriers, was proposed by Yamochi et al.<sup>442</sup> Figure 51 includes only the ambient-pressure superconductors of various phases. Except for  $\alpha\text{-(ET)}_2\text{MHg(SCN)}_4$  (M: K (a) and  $\text{NH}_4$ , (b)),  $\beta\text{-(ET)}_2\text{I}_3$  (c), and  $\kappa'\text{-(ET)}_2\text{Cu}_2(\text{CN})_3$  (g, see section 3.5.5), which have certain reasons to suppress  $T_c$ , the plot is represented by the linear relationship

$$T_c [\text{K}] = 0.131 V_{\text{mes2}} [\text{\AA}^3] - 121. \quad (33)$$

Summarizing the above, the packing density of the ET molecules and hence the  $t_{\parallel}$  and  $t_{\perp}$  in Fig. 33 decrease with increasing the basal area of the anion opening. This results in a metallic state with increased  $D(\varepsilon_F)$ , and then eventually in a Mott insulating state. With decreasing the thickness of the opening, on the other hand, the interactions between donor layers ( $t'_\perp$  in Fig. 33) and hence the 3D nature of the electronic structure will increase. This may give rise to an increase in  $T_c$  (see section 3.5.4.3). The donor...anion atomic contacts are ex-

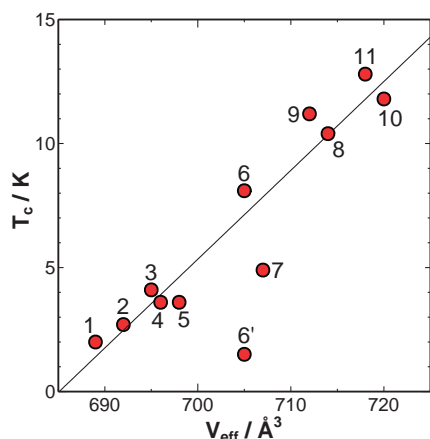


Fig. 49. A plot of  $T_c$  vs  $V_{\text{eff}}$  of 1:  $(\text{ET})_2\text{ReO}_4$ , 2:  $\beta\text{-(ET)}_2\text{IBr}_2$ , 3:  $\kappa\text{-(ET)}_2\text{Cu}_2(\text{CN})_3$ , 4:  $\kappa\text{-(ET)}_2\text{I}_3$ , 5:  $\theta\text{-(ET)}_2\text{I}_3$ , 6:  $\beta_{\text{H}}\text{-(ET)}_2\text{I}_3$ , 6':  $\beta_{\text{L}}\text{-(ET)}_2\text{I}_3$ , 7:  $\beta\text{-(ET)}_2\text{AuI}_2$ , 8:  $\kappa\text{-(ET)}_2\text{Cu(NCS)}_2$ , 9:  $\kappa\text{-(ET)}_2\text{Cu(CN)[N(CN)}_2]$ , 10:  $\kappa\text{-(ET)}_2\text{Cu[N(CN)}_2]\text{Br}$ , and 11:  $\kappa\text{-(ET)}_2\text{Cu[N(CN)}_2]\text{Cl}$ .<sup>474</sup> The line is a guide to the eye.

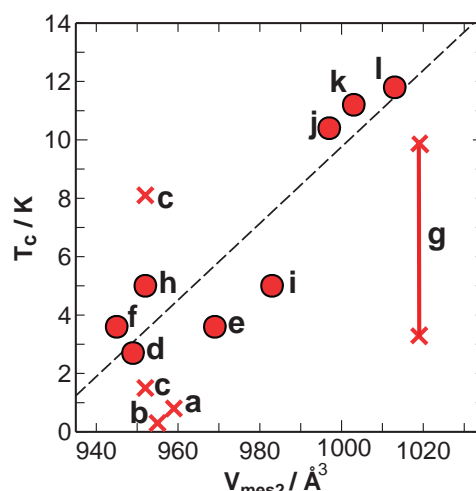


Fig. 51. A plot of  $V_{\text{mes2}}$  for  $(\text{ET})_2\text{X}$ .<sup>442</sup> (a):  $\alpha\text{-(ET)}_2\text{KHg(SCN)}_4$ , (b):  $\alpha\text{-(ET)}_2\text{NH}_4\text{Hg(SCN)}_4$ , (c)  $\beta\text{-(ET)}_2\text{I}_3$ , (d)  $\beta\text{-(ET)}_2\text{IBr}_2$ , (e)  $\kappa\text{-(ET)}_2\text{I}_3$ , (f)  $\theta\text{-(ET)}_2\text{I}_3$ , (g)  $\kappa'\text{-(ET)}_2\text{Cu}_2(\text{CN})_3$ , (h)  $\beta\text{-(ET)}_2\text{AuI}_2$ , (i)  $\kappa\text{-(ET)}_2\text{Ag(CN)}_2 \cdot \text{H}_2\text{O}$ , (j)  $\kappa\text{-(ET)}_2\text{Cu(NCS)}_2$ , (k)  $\kappa\text{-(ET)}_2\text{Cu(CN)[N(CN)}_2]$ , (l)  $\kappa\text{-(ET)}_2\text{Cu[N(CN)}_2]\text{Br}$ .

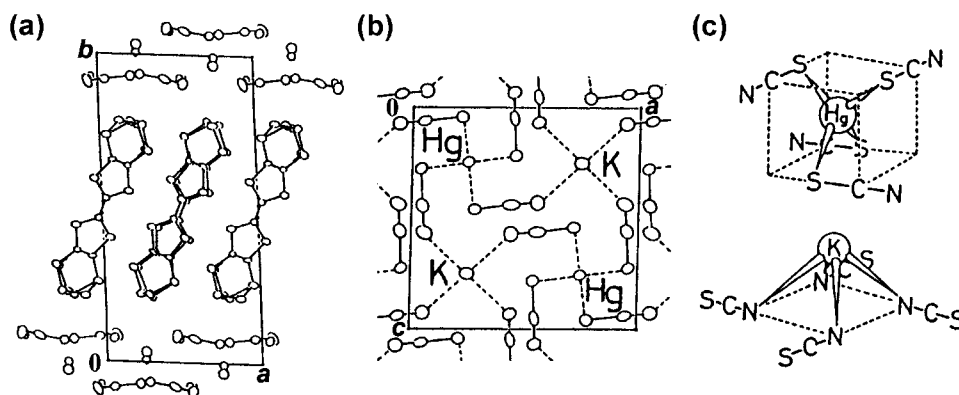


Fig. 50. (a) Crystal structure of  $\alpha\text{-(ET)}_2\text{KHg(SCN)}_4$ . The ET conducting layer is sandwiched by the anion layer. (b),(c) The schematic view of the units of anion layer,  $\text{Hg(SCN)}_4$  and  $\text{K(NCS)}_4$ .<sup>394</sup> Triclinic,  $P\bar{1}$ ,  $a = 10.082(10)$ ,  $b = 20.565(4)$ ,  $c = 9.933(2) \text{ \AA}$ ,  $\alpha = 103.70(2)$ ,  $\beta = 90.91(4)$ ,  $\gamma = 93.06(4)^\circ$ ,  $V = 1997(2) \text{ \AA}^3$ ,  $Z = 2$ ,  $R = 0.0696$ .

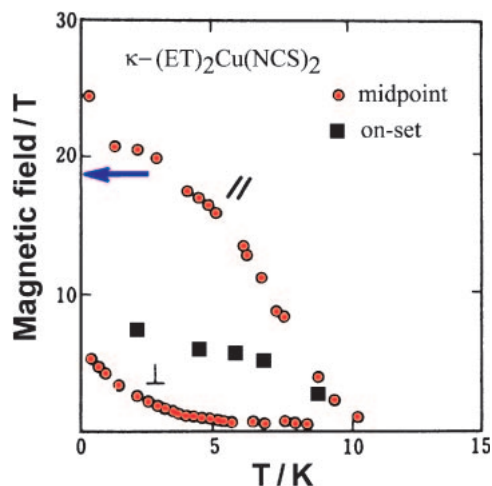


Fig. 52. Upper magnetic critical field  $H_{c2}$  of  $\kappa$ -( $\text{ET}$ ) $_2\text{Cu}(\text{NCS})_2$  determined by the resistance recovery by the magnetic field ( $\circ$ : midpoint,  $\blacksquare$ : on-set). Arrow indicates  $H_{\text{Pauli}}$ .<sup>477,478</sup> // and  $\perp$  represent the parallel and perpendicular to the 2D conducting plane.

pected to suppress the thermal contraction, which leads to the reduced  $D(\varepsilon_F)$ . Aiming to increase  $T_c$ , it is therefore proposed to “use an expanded and thin anion that forms a thin anion layer and provides both the loose donor packing to increase  $D(\varepsilon_F)$  and strong anion–donor atomic contacts to suppress thermal contraction.”<sup>2,518</sup> The superconductors having high  $T_c$  may reside close to the Mott insulating state, and it is expected that the  $T_c$  of the ET system rises to 20–25 K under optimal conditions for the crystal structure.

**3.5.4 Superconducting Characteristics of ET Superconductors: 3.5.4.1 Upper Critical Magnetic Field;** The resistance recovery curves with a magnetic field are very broad for the transition, especially at lower temperatures. Since the resistive transition under a magnetic field is dominated by the fluxoid motion or distribution of  $T_c$ , the determination of the upper critical field is rather difficult.  $\kappa$ -( $\text{ET}$ ) $_2\text{Cu}(\text{NCS})_2$  gave a higher  $H_{c2}$  value in the 2D plane than  $H_{\text{Pauli}}$ , which is indicated by the horizontal arrow in Fig. 52.<sup>477,478</sup> A recent magnetoresistance measurement at low temperature revealed that  $H_{c2}$  at 450 mK comfortably exceeded  $H_{\text{Pauli}}$  by ca. 50% without any saturation.<sup>520</sup>

The renormalization theory applied to the layered superconductors gives Ginzburg–Landau coherence lengths ( $\xi(0\text{ K}) = 29$  and  $23\text{ Å}$  for parallel to the 2D-layer, and  $3.1$  and  $5.8\text{ Å}$  for perpendicular to the 2D-layer) for  $\kappa$ -( $\text{ET}$ ) $_2\text{Cu}(\text{NCS})_2$  and  $\kappa$ -( $\text{ET}$ ) $_2\text{Cu}[\text{N}(\text{CN})_2]\text{Br}$ , respectively.<sup>481,521</sup> It is noteworthy that the  $\xi$  values perpendicular to the 2D plane are shorter than the thickness of the 2D conducting layer ( $14$ – $15\text{ Å}$ ).

**3.5.4.2 Inverse Isotope Effect;** Currently,  $\beta'$ -( $\text{ET}$ ) $_2\text{ICl}_2$  ( $T_c = 13.4\text{ K}$  at  $8.2\text{ GPa}$ , only on-set  $T_c$  of  $14.2\text{ K}$  was reported<sup>455</sup> and mid-point  $T_c$  of  $13.4\text{ K}$  is extrapolated by us) and the deuterated salt  $\kappa$ -( $\text{d}_8$ - $\text{ET}$ ) $_2\text{Cu}[\text{N}(\text{CN})_2]\text{Cl}$  ( $T_c = 13.1\text{ K}$  at  $0.03\text{ GPa}$ )<sup>300</sup> show the highest  $T_c$  under pressure, while both are Mott insulators at ambient pressure. At ambient pressure,  $\kappa$ -( $\text{d}_8$ - $\text{ET}$ ) $_2\text{Cu}(\text{CN})[\text{N}(\text{CN})_2]$  shows the highest  $T_c$  of  $12.3\text{ K}$ <sup>486</sup> followed by  $\kappa$ -( $\text{h}_8$ - $\text{ET}$ ) $_2\text{Cu}[\text{N}(\text{CN})_2]\text{Br}$  ( $T_c = 11.8\text{ K}$ ).<sup>479</sup>

The inverse isotope effect is one of the unresolved problems

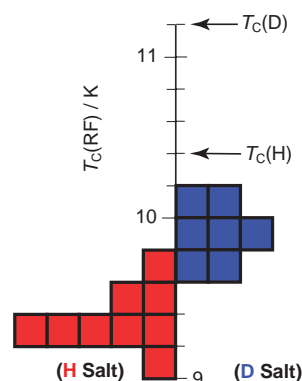


Fig. 53. Superconducting critical temperature  $T_c$  of  $\kappa$ -( $\text{ET}$ ) $_2\text{Cu}(\text{NCS})_2$  by RF penetration measurement.<sup>474</sup> The arrows indicate the highest  $T_c$  of the H- ( $T_c = 10.4\text{ K}$ ) and D- ( $T_c = 11.2\text{ K}$ ) salts determined by resistivity measurements (mid-point), where early works report the highest  $T_c$  of the D-salt as  $11.0$ – $11.1\text{ K}$ .<sup>474,477,478,486</sup>

in organic superconductors. The resistivity measurement for  $\beta_L$ -( $\text{ET}$ ) $_2\text{I}_3$  shows an inverse isotope effect: namely,  $T_c = 1.15\text{ K}$  for H-salt and  $T_c = 1.43\text{ K}$  for D-salt.<sup>444</sup> For  $\beta_H$ -( $\text{ET}$ ) $_2\text{I}_3$ , the  $T_c$  of H-salt was reported to be almost equal or a little higher than that of D-salt.<sup>448</sup> However, the inverse isotope effect for  $\beta$ -( $\text{ET}$ ) $_2\text{I}_3$  is not convincing since its  $T_c$  is so sensitive to the external and internal circumstances as described in section 3.5.1.

A clear inverse isotope effect has so far been observed for  $\kappa$ -( $\text{ET}$ ) $_2\text{Cu}(\text{NCS})_2$  (for example,  $T_c = 10.4\text{ K}$  for H-salt and  $11.2\text{ K}$  for D-salt,  $\Delta T_c = +0.8\text{ K}$ ),<sup>474,476,478,522–524</sup>  $\kappa$ -( $\text{ET}$ ) $_2$ - $\text{Cu}(\text{CN})[\text{N}(\text{CN})_2]$  (for example,  $T_c = 11.2\text{ K}$  for H-salt and  $12.3\text{ K}$  for D-salt,  $\Delta T_c = +1.1\text{ K}$ ),<sup>486</sup> and  $\kappa$ -( $\text{ET}$ ) $_2\text{Cu}[\text{N}(\text{CN})_2]\text{Cl}$  (for example,  $T_c = 12.8\text{ K}$  for H-salt and  $13.1\text{ K}$  for D-salt at  $0.03\text{ GPa}$ ,  $\Delta T_c = +0.3\text{ K}$ ),<sup>300</sup> while a normal isotope effect has been for  $\kappa$ -( $\text{ET}$ ) $_2\text{Cu}[\text{N}(\text{CN})_2]\text{Br}$  (for example,  $T_c = 12.15\text{ K}$  for H-salt and  $11.92\text{ K}$  for D-salt,  $\Delta T_c = -0.23\text{ K}$ ).<sup>480,481,522–526</sup> Since the superconductivity of  $\kappa$ -( $\text{ET}$ ) $_2$ - $\text{Cu}[\text{N}(\text{CN})_2]\text{Cl}$  appears only under pressure, no proper discussion concerning the isotope effect is possible unless the uniaxial stress method is applied on the salt (see next section). These above results were obtained by resistivity measurements.

For magnetic susceptibility measurements, where  $T_c$  is defined by the intersection of the linear extrapolations of the paramagnetic and the abrupt changing region,  $\kappa$ -( $\text{ET}$ ) $_2\text{Cu}(\text{NCS})_2$  shows the average  $T_c = 9.9\text{ K}$  for 7 samples of the D-salt and  $9.4\text{ K}$  for 9 samples of the H-salt ( $\Delta T_c = 0.5\text{ K}$ ) (Fig. 53).<sup>474</sup> Although the  $T_c$  of the salt with ET molecules containing  $^{13}\text{C}$  isotopes at the outer ethylene groups is found to lie between those of H- and D-salts determined by resistivity measurements (average  $T_c = 10.38$ ,  $10.64$ , and  $10.89\text{ K}$  for H-,  $^{13}\text{C}(\text{outer})$ -, and D-salts, respectively),<sup>478</sup> the static susceptibility measurements are indicative either of the inverse isotope effect<sup>478</sup> or of negligible change in  $T_c$ , i.e., H- ( $T_c = 8.7 \pm 0.2\text{ K}$ ), and  $^{13}\text{C}$ -salts ( $8.6 \pm 0.2\text{ K}$ );<sup>481</sup> hence the isotope effect for  $^{13}\text{C}$ -salt is not conclusive. The labeling of N atoms of the SCN ligands by  $^{15}\text{N}$  gives no significant change in  $T_c$  as determined by resistivity measurements.<sup>477</sup>

A convincing inverse isotope shift between H- and D-salts was also observed in  $\kappa$ -( $\text{ET}$ ) $_2\text{Cu}(\text{CN})[\text{N}(\text{CN})_2]$ .<sup>486</sup> Figure 54

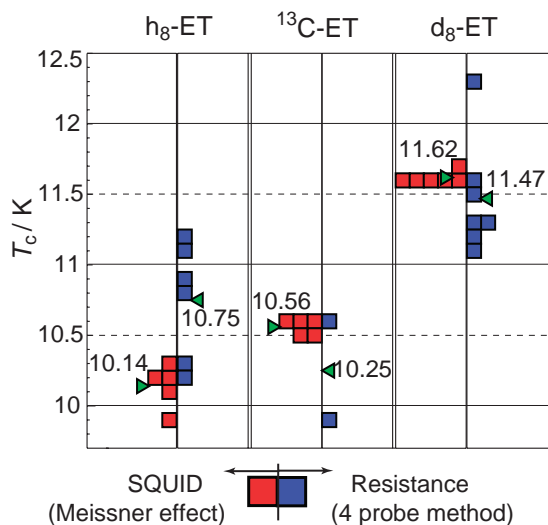


Fig. 54. Superconducting critical temperatures  $T_c$  of  $\kappa$ -(ET)<sub>2</sub>Cu(CN)[N(CN)<sub>2</sub>] determined by the magnetic susceptibility (red) and resistivity (blue, mid-point) measurements for the H-, <sup>13</sup>C-, and D-salts. Green triangles indicate the respective average values (Ref. 486 and unpublished result by N. Matsukawa and G. Saito).

demonstrates the  $T_c$  of  $\kappa$ -(ET)<sub>2</sub>Cu(CN)[N(CN)<sub>2</sub>] composed of h<sub>8</sub>-, d<sub>8</sub>-, and <sup>13</sup>C-ET determined by magnetic susceptibility and resistance measurements. The  $T_c$  determined by magnetic susceptibility (red squares) ranges 9.9–10.3 K for 5 single crystals of the H-salt (average  $T_c$  of 10.14 K), 10.5–10.6 K for 5 single crystals of the <sup>13</sup>C-salt (average  $T_c$  of 10.56 K), and 11.6–11.7 K for 6 single crystals of the D-salt (averaged  $T_c$  of 11.62 K). On the other hand,  $T_c$  determined by resistivity measurements (blue squares) are very scattered. The highest and lowest  $T_c$  are 10.2 and 11.2 K for the H-salt (average for 6 single crystals  $T_c$  = 10.75 K), 9.9 and 10.6 K for the <sup>13</sup>C-salt (only two single crystals), and 11.1 and 12.3 K for the D-salt (average for 7 single crystals  $T_c$  = 11.47 K). Although it is uncertain whether the  $T_c$  of the <sup>13</sup>C-salt is higher than that of the H-salt, it is clearly concluded that the D-salt has a much higher average  $T_c$  than the H-salt (inverse isotope effect) by 0.72 K (resistivity measurements) and 1.48 K (magnetic measurements).

The isotope effect observed in the D-salt is just the opposite to that expected from the simple BCS theory as follows:

$$T_c \propto \Theta \propto (\text{isotope mass})^{-\alpha}, \quad \alpha = 0.5. \quad (34)$$

In the above salts, the  $\alpha$  values are evaluated to be ca. −4.6 and −3.6 for X = Cu(CN)[N(CN)<sub>2</sub>] and Cu(NCS)<sub>2</sub>, respectively. Since the terminal ethylene groups of ET molecules have specific contacts of C–H...anion, it is expected that the phonon related to the C–H...anion vibration mediates the formation of Cooper pairs.<sup>475</sup>

Besides that, the following “geometrical isotope effect” was proposed by Toyota as a plausible cause.<sup>527</sup> In general, the conducting plane of the H-salt is more chemically pressurized than that of the D-salt, and the D-salt has a larger unit cell volume. The unit cell volume of  $\kappa$ -(d<sub>8</sub>-ET)<sub>2</sub>Cu[N(CN)<sub>2</sub>]Br is about 0.16% larger than that of H-salt.<sup>519</sup> A similar structural

isotope effect is seen in  $\kappa$ -(ET)<sub>2</sub>Cu[N(CN)<sub>2</sub>]Cl, where the triple-critical point of the H-salt is shifted to the higher pressure side by ca. 10 MPa in the D-salt (Fig. 47). If the geometrical isotope effect is the dominant factor and 0.16% of volume expansion is realized by deuteration for the salts X = Cu(NCS)<sub>2</sub> and Cu(CN)[N(CN)<sub>2</sub>], the increase in  $V_{\text{eff}}$  by ca. 1.3–1.4 Å<sup>3</sup> and, as a result, the increase in  $T_c$  by 0.4 K is expected from the relation in Fig. 49. Therefore, the geometrical isotope effect is not sufficient to explain the observed isotope effect ( $\Delta T_c$  = 0.72–1.48 K) for the salts X = Cu(CN)[N(CN)<sub>2</sub>] and Cu(NCS)<sub>2</sub>. Furthermore, the unit cell volume of  $\kappa$ -(d<sub>8</sub>-ET)<sub>2</sub>Cu(NCS)<sub>2</sub> is not larger, but smaller than that of the H-salt,<sup>519</sup> indicating that the inverse isotope effect cannot be rationalized by the geometrical isotope effect.

Later, Kini et al. reported a comprehensive work on the isotope effect by labeling ET molecules with D, <sup>13</sup>C, and <sup>34</sup>S isotopes and Cu(NCS)<sub>2</sub> molecules with <sup>13</sup>C and <sup>15</sup>N isotopes.<sup>522–524</sup> Static susceptibility shows an inverse isotope effect concerning hydrogen atoms with  $\Delta T_c$  = 0.30 ± 0.07 K (14 samples), which is the amount explainable by the “geometrical isotope effect” if the D-salt has a larger unit cell than the H-salt, but no discernible shift for the <sup>13</sup>C(outer)- and <sup>13</sup>C(central)-salts. The normal isotope effect with  $\alpha$  = 0.26 ± 0.11 was observed in the <sup>13</sup>C(outer)<sup>34</sup>S-salt (19 samples). No discernible isotope shift in the <sup>13</sup>C(central)- and normal shift in the <sup>13</sup>C(outer)<sup>34</sup>S-salts suggest that the intramolecular C=C (central) and C–S vibrations of the TTF skeleton, which are closely associated with electrons through the e-mv coupling,<sup>528</sup> are independent of the pairing phenomena. Furthermore, no discernible shift of  $T_c$  in the Cu(<sup>15</sup>N<sup>13</sup>CS)<sub>2</sub>-salt indicates that any intramolecular vibrations in the anion molecule are not associated with the pairing phenomena. Kini et al. summarized that the normal isotope effect is observed in the conducting layer, and the inverse isotope effect (suggesting an unconventional mechanism for electron-pairing) is seen in the non-conducting layer. They mentioned that the latter result is likely related to the interlayer coupling involving electronic tunneling, as a consequence of the quasi-2D of the system.

The isotope effect of  $\kappa$ -(ET)<sub>2</sub>Cu[N(CN)<sub>2</sub>]Br is rather complicated. Figure 55 presents the four typical temperature dependences of resistivity for a single crystal of the D-salt.<sup>525</sup> Curve 1 is similar to that of the H-salt and shows a semiconductor–metal–superconductor behavior with  $T_c$  being lower than that of the H-salt ( $T_c$ (D-salt) = 11.2 K vs  $T_c$ (H-salt) = 11.7 K, inset of Fig. 55). The magnetic susceptibility measurements indicate nearly the same shift ( $\Delta T_c$  = −0.4 K) in going from the H-salt ( $T_c$  = 11.3 K) to D-salt ( $T_c$  = 10.9 K). Tokumoto et al. reported  $\Delta T_c$  = −0.9 K by the magnetization measurements<sup>529</sup> and Wang et al. observed  $\Delta T_c$  = −0.5 K by the rf method.<sup>480</sup> Curve 2 was sometimes observed in both H- and D-salts, in the parallel and perpendicular directions to the *ac*-plane, with a resistivity maximum at around 40–50 K. A few crystals of the D-salt exhibited curve 3 with a broad superconducting transition. Curve 4 was observed only for the D-salt in one batch for the measurements along the *b*-axis, and showed no trace of superconductivity. Initially it was speculated that the gold wires (for the four probe method) for the resistivity measurements provide a subtle pressure on the sample by cooling, and the different pressure from sample

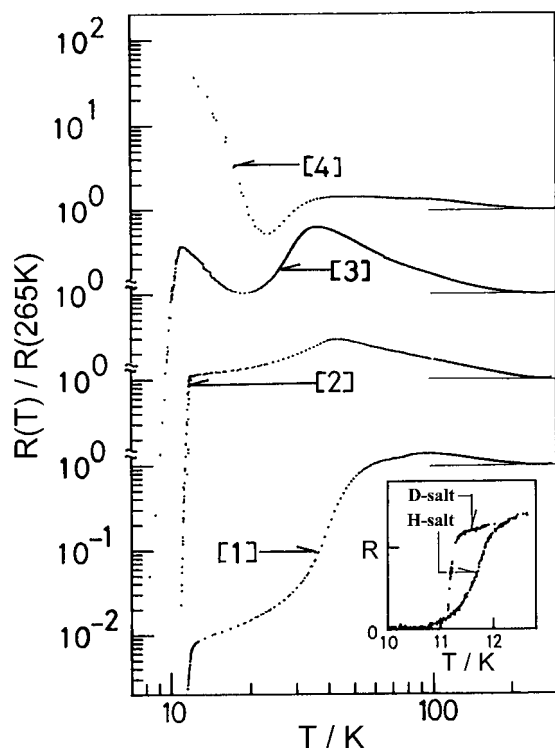


Fig. 55. Four typical temperature dependencies of resistivity ([1]–[4]) for a single crystal of  $\kappa$ -(d<sub>8</sub>-ET)<sub>2</sub>Cu[N(CN)<sub>2</sub>]Br. [1] shows a similar behavior to the H-salt and exhibits two broad maxima between 70–100 K. [2] shows a peak at around 40 K. [3] shows two peaks at 30–40 K and 11 K. [4] does not show the superconducting transition. The inset compares the superconducting transition of the H- and D-salts.<sup>525</sup>

to sample might give rise to the different behaviors as observed in Fig. 55. Later it was found that rapid cooling of the sample induces an antiferromagnetic state instead of a superconducting state in the D-salt.<sup>517</sup> Accordingly, it has been postulated that an inverse isotope effect is observed for  $\kappa$ -(ET)<sub>2</sub>Cu[N(CN)<sub>2</sub>]Br when the sample is cooled slowly through the phase transition at around 80 K associated with the abnormal lattice dilation change.<sup>530</sup> However, nobody has so far succeeded in observing the inverse isotope effect in  $\kappa$ -(ET)<sub>2</sub>Cu[N(CN)<sub>2</sub>]Br even cooling at a rate of 0.02 K min<sup>-1</sup>.<sup>526</sup> So the “geometrical isotope effect” cannot fully explain the isotope effect of  $\kappa$ -(ET)<sub>2</sub>X including the Cu[N(CN)<sub>2</sub>]Br salt.

It is very crucial to cool slowly down to near 120 and 80 K to observe the intrinsic properties of  $\kappa$ -(ET)<sub>2</sub>Cu[N(CN)<sub>2</sub>]Br. The former temperature is associated with the partial (ca. 88% in the eclipsed and 12% in the staggered) order of the ethylene conformation being connected with the ethylene dynamics, while the latter temperature is associated with lattice dilation and ethylene groups are ordered completely. This feature reflects the penetration depth measurements on  $\kappa$ -(ET)<sub>2</sub>Cu[N(CN)<sub>2</sub>]Br and  $\kappa$ -(ET)<sub>2</sub>Cu(NCS)<sub>2</sub> with cooling slowly only below 100 K as follows:<sup>531</sup> 1) The penetration depth did not change with cooling rate for the Cu(NCS)<sub>2</sub> salt since the salt does not have conformational phase transition below 100 K and gave short penetration depth ( $\lambda_{\parallel}$  = 430 nm) caused by the enhanced electron scattering by the conformational disorder

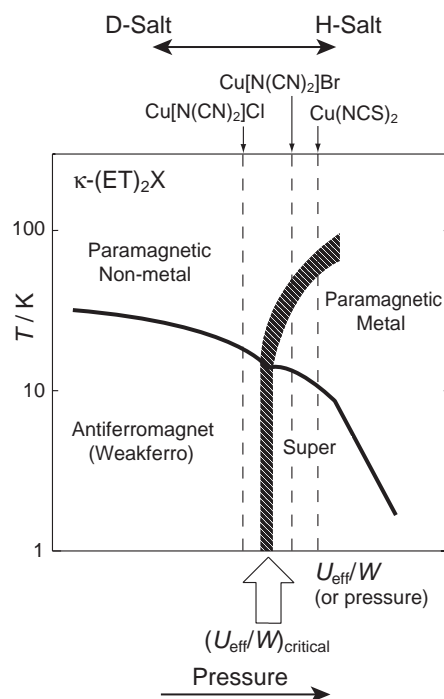


Fig. 56. Proposed phase diagram by Kanoda for  $\kappa$ -(ET)<sub>2</sub>X.<sup>532</sup> Geometrical isotope effect is represented by the arrow above the figure. The diagram can include X = Cu(NCS)<sub>2</sub>, Cu[N(CN)<sub>2</sub>]Br, and Cu[N(CN)<sub>2</sub>]Cl but cannot include both  $\kappa$ -(ET)<sub>2</sub>Cu<sub>2</sub>(CN)<sub>3</sub> (see section 3.6.3) and  $\kappa$ -(ET)<sub>2</sub>Cu(CN)[N(CN)<sub>2</sub>], which does not exhibit paramagnetic non-metallic phase although the  $T_c$  is higher than that of X = Cu(NCS)<sub>2</sub>. Also, the metallic region observed above 250–270 K in  $\kappa$ -(ET)<sub>2</sub>Cu(NCS)<sub>2</sub> is avoided in the diagram. In order to include other  $\kappa$ -type ET salts that exhibit a metal–insulator transition such as X = Hg(SCN)<sub>3–a</sub>Y<sub>a</sub> ( $a$  = 1 for Y = Cl, Br, and I;  $a$  = 2 for Y = Cl),<sup>533–535</sup> a bell-shaped region of insulating state is proposed separately far right side of the superconducting region.<sup>536</sup>

ders of ethylene groups. 2) The penetration depths for the Cu[N(CN)<sub>2</sub>]Br salt, which has a disordered ethylene conformation, were dependent on the lattice dilation at around 80 K, and were estimated to be 570 nm for slow cooling and 690 nm for rapid cooling.

Kanoda et al. prepared the deuterated ET salts substituted at different sites with different numbers of D atoms. They performed <sup>1</sup>H NMR measurement,<sup>532</sup> and found that the D-salt of  $\kappa$ -(ET)<sub>2</sub>Cu[N(CN)<sub>2</sub>]Br resides in close proximity to the boundary between metal (paramagnetic metal) and paramagnetic non-metal, which corresponds to the N1 phase in Fig. 47. They proposed a  $T$ – $P$  phase diagram for  $\kappa$ -(ET)<sub>2</sub>X (Fig. 56) and put the salts X = Cu(NCS)<sub>2</sub>, Cu[N(CN)<sub>2</sub>]Br, and Cu[N(CN)<sub>2</sub>]Cl from the right in the diagram.<sup>532</sup> This diagram is quite simplified compared with the experimentally observed complicated ones (Fig. 47), but is very convenient and useful to explain why the D-salt of  $\kappa$ -(ET)<sub>2</sub>Cu[N(CN)<sub>2</sub>]Br behaves so sensitively to pressure.

The “geometrical isotope effect” implies that the D-salt corresponds to an application of negative pressure to the H-salt along the interlayer direction. The phase diagram in Fig. 56



Table 16. Superconductivity under Hydrostatic and Uniaxial Pressure

Salt	Method <sup>a)</sup>	// <sup>b)</sup>	Max. $P$ /GPa <sup>c)</sup>	Max. $T_c$ /K <sup>d)</sup>	( $dT_c/dP$ )/K GPa <sup>-1</sup> e)	Ref.
(TMTSF) <sub>2</sub> ClO <sub>4</sub>	hydro		AP	1.4	-1.0*	539
(TMTSF) <sub>2</sub> PF <sub>6</sub>	hydro		0.65	1.4	-0.9*	546
	oil	$a$	1	0.9(on-set)	—	547
$\alpha$ -(ET) <sub>2</sub> I <sub>3</sub>	hydro 2D metal down to low $T$ (at 2 GPa), no $T_c$ at AP					548
	epoxy	$a$	0.2	7.2(on-set)	—	548
		$b$	metal down to low $T$ (0.3–0.5 GPa)			548
$\alpha$ -(ET) <sub>2</sub>			AP	0.3		399
KHg(SCN) <sub>4</sub>	epoxy	$b^*$	0.28	1.6	+6.6	549
	oil	$a$	1	no $T_c$		550
		$b^*$	1	1.2	+1.4	550
		$c$	1	1.5	+1.7	550
$\alpha$ -(ET) <sub>2</sub>			AP	1.7		396
NH <sub>4</sub> Hg(SCN) <sub>4</sub>	epoxy	$b^*$	0.38	3.4	+8.4	549
	oil	$a$	0	1.4	-1.3,	551,552
					0.4 GPa $\leq$ CDW $\leq$ 0.6 GPa	
		$b^*$	1	4.5	+2.8	551,552
		$c$	0.5	6	+9 $\rightarrow$ -6	551,552
$\beta_L$ -(ET) <sub>2</sub> I <sub>3</sub>	hydro		AP	1.5	-3*	540
$\beta_H$ -(ET) <sub>2</sub> I <sub>3</sub>	hydro		AP	8.1	-14*	541
$\beta$ -(ET) <sub>2</sub> IBr <sub>2</sub>	hydro		AP	2.7	-7*	542
$\beta$ -(ET) <sub>2</sub> AuI <sub>2</sub>	hydro		AP	4.9	-10*	543
$\kappa$ -(ET) <sub>2</sub>	hydro		AP	10.4	-(30–35)*	537
Cu(NCS) <sub>2</sub>	tensile	$b$	$\Delta b/b = 9.5 \times 10^{-3}$	$\Delta T_c = 0.6 \pm 0.5$		553
		$c$	$\Delta c/c = 2.7 \times 10^{-2}$	$\Delta T_c = 0.0 \pm 1.0$		553
	epoxy	$a$		decrease	-16	554
		$b$		decrease		554
		$c$	0.075	10.7	+16 $\rightarrow$ -18	554
	comp epoxy	$a$			-20	555
	epoxy	$b$		decrease	-1.9(0–0.2 GPa), -25(0.2–0.4 GPa)	556
		$c$	0.1	$\Delta T_c = 1.3$	+13 $\rightarrow$ -5	556
$\kappa$ -(ET) <sub>2</sub>	hydro		AP	11.8	-24*	538
Cu[N(CN) <sub>2</sub> ]Br	epoxy	$a$	0	9.0	-16.8	558
		$c$	0.2	12.2	+6.0 $\rightarrow$ -17.5	558
$\kappa$ -(ET) <sub>2</sub>	hydro		0.03	12.8	-34*	300
Cu[N(CN) <sub>2</sub> ]Cl						
$\kappa$ -(ET) <sub>2</sub>	hydro		AP	11.2	-25*	487
Cu(CN)[N(CN) <sub>2</sub> ]						
$\kappa$ -(ET) <sub>2</sub> Cu <sub>2</sub> (CN) <sub>3</sub>	hydro		0.15	2.8	-12.5	303
	epoxy	$a^*$			+10.2 $\rightarrow$ -3.0	557,559
		$b$	0.5	6.8	+13 $\rightarrow$ -2.6	557,559
		$c$	0.3	7.3	+24.7 $\rightarrow$ -3.2	557,559
					+23.3 $\rightarrow$ -4.4	

a) AP: ambient pressure, hydro: hydrostatic, epoxy: uniaxial strain by epoxy method, oil: uniaxial strain by oil method, comp: uniaxial compressive stress, tensile: uniaxial elongation stress. b) Direction of applied pressure. c) The pressure where the maximum  $T_c$  is observed. d) Maximum  $T_c$ . e) \*:  $dT_c/dP$  with hydrostatic pressure.  $\rightarrow$  indicates that  $dT_c/dP$  changes at higher pressures.

and “geometrical isotope effect” point out that  $T_c$  increases with decreasing pressure if only the parameter  $U/W$  or  $D(\mathcal{E}_F)$  is taken into account. This tendency has been observed under hydrostatic pressure. However, the geometrical isotope effect and also the  $T$ - $P$  phase diagram in Fig. 56 should be renewed taking into account the electronic and structural anisotropy since the thermal expansion coefficients of  $\kappa$ -(ET)<sub>2</sub>X salts are known to be anisotropic as discussed in the next section.

**3.5.4.3 (Super)conductivity Under Hydrostatic- and Uniaxial-Strain; a. Hydrostatic Pressure;** In general,  $T_c$  decreases rapidly with increasing hydrostatic pressure ( $dT_c/dP = -(30\text{--}35)$  K GPa<sup>-1</sup> for X = Cu(NCS)<sub>2</sub><sup>537</sup> and -24

K GPa<sup>-1</sup> for Cu[N(CN)<sub>2</sub>]Br,<sup>538</sup> in good accordance with the  $D(\mathcal{E}_F)$  consideration except for some special cases, X = Hg<sub>2.89</sub>Br<sub>8</sub> ( $dT_c/dP \approx +13$  K GPa<sup>-1</sup>)<sup>471</sup> and Cu[N(CN)<sub>2</sub>]Cl,<sup>508</sup> for which  $T_c$  increases with increasing pressure at low pressures then is suppressed at higher pressures ( $dT_c/dP = -34$  K GPa<sup>-1</sup>).<sup>300</sup> The suppression rates of  $T_c$  by pressure for the 10 K class superconductors are remarkably high compared to other superconductors ( $dT_c/dP = -1.0$  K GPa<sup>-1</sup> for (TMTSF)<sub>2</sub>ClO<sub>4</sub>,<sup>539</sup>  $-(9\text{--}10)$  K GPa<sup>-1</sup> for  $\beta_L$ -(ET)<sub>2</sub>I<sub>3</sub>,<sup>448,540</sup>  $-14$  K GPa<sup>-1</sup> for  $\beta_H$ -(ET)<sub>2</sub>I<sub>3</sub>,<sup>541</sup>  $-7$  K GPa<sup>-1</sup> for  $\beta$ -(ET)<sub>2</sub>-IBr<sub>2</sub>,<sup>542</sup>  $-10$  K GPa<sup>-1</sup> for  $\beta$ -(ET)<sub>2</sub>AuI<sub>2</sub>,<sup>543</sup>  $-7.8$  K GPa<sup>-1</sup> for K<sub>3</sub>C<sub>60</sub>,<sup>544</sup> and  $-9.7$  K GPa<sup>-1</sup> for Rb<sub>3</sub>C<sub>60</sub><sup>545</sup>). Table 16 summa-

rizes the pressure dependence of  $T_c$  for selected TMTSF and ET salts.

The hydrostatic pressure method, however, has a marked disadvantage in that it can not provide any information concerning the anisotropy of the anisotropic organic conductors. Now it becomes rather clear that physical data obtained under hydrostatic pressure do not reflect the real and even averaged electronic structures. The recent high-pressure works by the uniaxial strain method clearly indicate that the pressure dependence of  $T_c$  is very anisotropic as reflected in the anisotropic electronic structure of the organic conductors. Furthermore, for several salts the  $T_c$  increases under uniaxial strain along a certain direction as shown in Table 16. The uniaxial strain method (epoxy or oil-method in Table 16) can shrink an organic crystal in a certain direction without causing Poisson's effect when the sample embedded in epoxy resin or oil is kept in a clamp pressure cell.<sup>550</sup>

**b. Thermal Expansion Coefficient;** Kund et al. observed discontinuous changes of the thermal expansion coefficient in  $\kappa$ -(ET)<sub>2</sub>Cu[N(CN)<sub>2</sub>]Br and deduced that the uniaxial-stress dependence of  $T_c$  is highly anisotropic.<sup>560</sup> They have evaluated the uniaxial stress dependence of  $T_c$  along the  $i$ th crystallographic direction in the limit of vanishing stress:  $[dT_c/dp_i]_{\sigma_i \rightarrow 0}$  ( $i = a, b$ , and  $c$ ), based on the data for the second-order jumps of the thermal expansion coefficients  $\Delta\alpha_i$  at  $T_c$  using the Ehrenfest relation (Eq. 35), where  $\Delta C_p$  is the discontinuity in the specific heat at  $T_c$ .

$$\Delta\alpha_i = \frac{1}{V_{\text{mol}}} \frac{\Delta C_p}{T_c} \left[ \frac{dT_c}{dp_i} \right]_{\sigma_i \rightarrow 0}. \quad (35)$$

The  $dT_c/dp_i$  values of  $\kappa$ -(ET)<sub>2</sub>Cu[N(CN)<sub>2</sub>]Br obtained from the thermal expansion coefficients are  $-(22-24)$ ,  $\pm(1-2)$ , and  $-(2-4)$  K GPa<sup>-1</sup> for the  $a$ -,  $b$ -, and  $c$ -axes, respectively, indicating that the superconductivity is very sensitive to the  $a$ -axis parameter that is the direction of the 2D Fermi surface and anion chain. It is noteworthy that the negligibly small  $dT_c/dp_b$  along the interlayer direction suggests the negligible "geometrical isotope effect" in this salt. However, considerably different data were reported by Müller et al., especially along the interlayer direction, i.e.,  $dT_c/dp_i = -11.6$ ,  $-12.6$ , and  $-1.2$  K GPa<sup>-1</sup> for  $a$ -,  $b$ -, and  $c$ -axes, respectively, indicating that the "geometrical isotope effect" should be clearly detected.<sup>561</sup> So far no reliable thermal expansion coefficients have been reported on this salt.

As for  $\kappa$ -(ET)<sub>2</sub>Cu(NCS)<sub>2</sub>, the  $dT_c/dp_i$  values were reported as  $-48$  K GPa<sup>-1</sup> along the  $a$ -axis and  $-11$  K GPa<sup>-1</sup> along the  $c$ -axis by Lang et al.,<sup>562</sup> and  $-32.0$ ,  $0$ , and  $+14.6$  K GPa<sup>-1</sup> along the  $a$ -,  $b$ -, and  $c$ -axes, respectively, by Kund et al.<sup>563</sup> Again no good coincidence was observed between the values along the  $c$ -axis (direction of 2D Fermi surface). Later, Lang et al.<sup>564</sup> reported considerably different data for the D-salt of  $\kappa$ -(ET)<sub>2</sub>Cu(NCS)<sub>2</sub> from their previous data for the H-salt:  $dT_c/dp_i = -62$ ,  $-1.4$ , and  $+34.4$  K GPa<sup>-1</sup> for  $a$ -,  $b$ -, and  $c$ -axes, respectively. They claimed that the large difference between the H- and D-salts along the  $c$ -axis is due to the crystal imperfection of their H-salt. So large negative and positive values along the  $a$ - and  $c$ -axes, respectively, and a nearly negligible value along the  $b$ -axis are the experimentally expected ones.

The large negative value along the  $a$ -axis (interlayer direc-

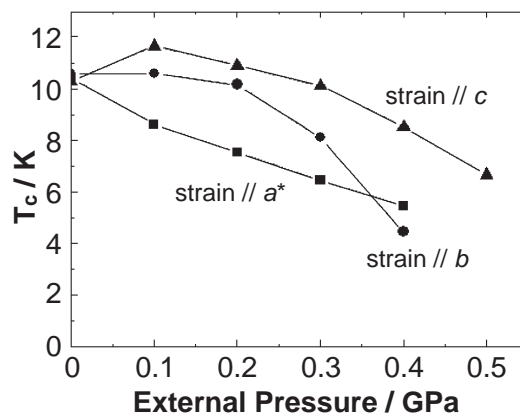


Fig. 57. Pressure dependence of  $T_c$  (on-set) of  $\kappa$ -(h<sub>8</sub>-ET)<sub>2</sub>-Cu(NCS)<sub>2</sub> under uniaxial strain.<sup>556</sup> The value of the external pressure applied at RT is adopted.

tion) suggests a large "geometrical inverse-isotope effect" in this salt, though the  $a$ -axis is invariant (ca. 0.03%) between H- and D-salts.<sup>519</sup> On the other hand, provided that the  $dT_c/dp_i$  along the  $c$ -axis is positive, an increase in  $T_c$  is readily expected by an applying pressure along this direction.

**c. Uniaxial-Strain on  $\kappa$ -(ET)<sub>2</sub>Cu(NCS)<sub>2</sub>,  $\kappa$ -(ET)<sub>2</sub>Cu[N(CN)<sub>2</sub>]Br,  $\alpha$ -(ET)<sub>2</sub>KHg(SCN)<sub>4</sub>, and Other Salts;  $\kappa$ -(ET)<sub>2</sub>-Cu(NCS)<sub>2</sub> and  $\kappa$ -(ET)<sub>2</sub>Cu[N(CN)<sub>2</sub>]Br:** The  $dT_c/dp_i$  values so far reported for  $\kappa$ -(ET)<sub>2</sub>Cu(NCS)<sub>2</sub> suggest a negligible pressure effect on  $T_c$  along the  $b$ -axis. As early as 1990, however, Kusuhashi et al. observed an increase in  $T_c$  ( $\Delta T_c = 0.6 \pm 0.5$  K) by applying elongation tensile stress along the  $b$ -axis.<sup>553</sup> On the other hand, an application of elongational stress along the  $c$ -axis, which is expected to increase  $T_c$  based on  $dT_c/dp_i$ , gave rise to a negligible effect on  $T_c$  ( $\Delta T_c = 0.0 \pm 1.0$  K).<sup>553</sup> Tokumoto et al. reported varied  $T_c$  by applying a uniaxial compressive stress.<sup>554</sup> They observed a gradual decrease in  $T_c$  along the  $b$ -axis stress, while an increase in  $T_c$  to 10.7 K at 0.07 GPa by the  $c$ -axis stress is in good agreement with the prediction of positive  $dT_c/dp_i$ . At higher pressures the  $T_c$  decreases with  $dT_c/dp_c \approx -17$  K GPa<sup>-1</sup>, which is similar to the monotonous decrease in  $T_c$  by the  $a$ -axis stress ( $dT_c/dp_a \approx -15$  K GPa<sup>-1</sup>). Campos et al. applied a uniaxial compressive stress using the epoxy-method, and found a significant decrease in  $T_c$  by  $dT_c/dp_a = -20$  K GPa<sup>-1</sup>.<sup>555</sup> Note that this method is susceptible to Poisson's effect since the epoxy resin embedding the sample is not kept in a clamp cell.

A uniaxial strain using the epoxy-method without involving Poisson's effect (Fig. 57) along the  $c$ -axis increases  $T_c$  with  $dT_c/dp_c = +13$  K GPa<sup>-1</sup> up to 0.1 GPa followed by a decrease with  $dT_c/dp_c \approx -12$  K GPa<sup>-1</sup>.<sup>556</sup> On the other hand, a uniaxial strain along the  $b$ -axis decreases  $T_c$  very gradually up to 0.2 GPa and then rather rapidly ( $dT_c/dp_b \approx -28$  K GPa<sup>-1</sup>). Along the interlayer direction ( $//a^*$ ),  $T_c$  decreases monotonically ( $dT_c/dp_a \approx -(11-17)$  K GPa<sup>-1</sup>).

Summarizing the uniaxial strain effect on  $\kappa$ -(ET)<sub>2</sub>Cu(NCS)<sub>2</sub>,  $T_c$  increases along the  $c$ -axis (direction to the 2D Fermi surface) in the initial pressure range ( $\leq 0.1$  GPa,  $\Delta T_c = 1.3$ ), while decreases by applying pressure along other directions.

As for  $\kappa$ -(ET)<sub>2</sub>Cu[N(CN)<sub>2</sub>]Br,  $T_c$  increases slightly up to

0.2 GPa ( $\Delta T_c \approx 1$  K) when the uniaxial strain is applied along the  $c$ -axis, which is parallel to the 1D Fermi surface.<sup>558</sup> The result conflicts with the prediction by the thermal expansion coefficient ( $dT_c/dp_c = -(1-4)$  K GPa<sup>-1</sup>). Along the  $a$ -axis (parallel to the 2D Fermi surface) strain,  $T_c$  decreases monotonically in agreement with the thermal expansion coefficient.

The Cu(NCS)<sub>2</sub> and Cu[N(CN)<sub>2</sub>]Br salts behave quite differently concerning the topological aspect of the Fermi surface, indicating that the  $T_c$  change can not be interpreted by the Fermi surface change under uniaxial strain.<sup>556,558,559</sup> Figure 58 demonstrates the  $T_c$  of several  $\kappa$ -(ET)<sub>2</sub>X superconductors with respect to the two parameters  $U/W$  and  $t'/t$ , where the latter represents the electronic anisotropy of the  $\kappa$ -type ET salt, and  $t$  and  $t'$  are the transfer integrals between the neighboring ET dimers (see section 3.6.3). The uniaxial strain experiments clearly revealed that  $T_c$  increases as  $U/W$  approaches unity and as  $t'/t$  departs from unity.<sup>559</sup> In order to rationalize the increased  $T_c$  under uniaxial strain along a certain axis and to investigate the relation between Fermi surface and transport properties, structural analysis under the uniaxial strain in the superconducting state is indispensable.

**$\alpha$ -(ET)<sub>2</sub>MHg(SCN)<sub>4</sub> Salts (M = K and NH<sub>4</sub>):** Campos et

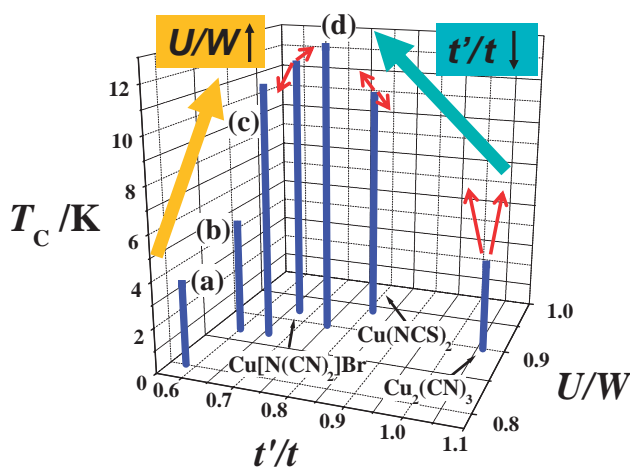


Fig. 58.  $T_c$  of  $\kappa$ -(ET)<sub>2</sub>X salts are plotted as a function of  $t'/t$  and  $U/W$ .<sup>559</sup> X = I<sub>3</sub> (a), Ag(CN)<sub>2</sub>·H<sub>2</sub>O (b), Cu(CN)[N(CN)<sub>2</sub>] (c), and Cu[N(CN)<sub>2</sub>]Cl (d). Blue and yellow arrows indicate the direction of  $t'/t$  decreases and  $U/W$  increases, respectively. Red arrows correspond to the change of  $T_c$  by applying uniaxial strain. The uniaxial strain experiments on (a)–(d) are underway.

al. observed an increase in  $T_c$  to 2 K (on-set) of  $\alpha$ -(ET)<sub>2</sub>-KHg(SCN)<sub>4</sub>, which has  $T_c$  of 0.3 K at ambient pressure, by applying uniaxial stress by the epoxy-method along the  $b^*$ -axis.<sup>549</sup> Figure 59 demonstrates the anisotropic behavior of the superconductivity of  $\alpha$ -(ET)<sub>2</sub>KHg(SCN)<sub>4</sub> under uniaxial strain using the oil-method by Maesato et al.<sup>550</sup> At ambient pressure, the resistivity hump due to the formation of density wave<sup>565</sup> (most probably CDW) is clearly seen at around 8 K in all directions. Under the  $a$ -axis (//side-by-side direction) uniaxial strain, the resistivity hump is easily suppressed but no superconductivity was detected up to 1.0 GPa down to 0.5 K. On the other hand, the hump persisted up to 0.3–0.5 GPa along the other directions and the  $T_c$  increased up to 1.2 and 1.5 K under uniaxial strain of 1.0 GPa along the  $b^*$ -(interlayer direction) and  $c$ - (//1D Fermi surface) axes, respectively.

The  $T_c$  of  $\alpha$ -(ET)<sub>2</sub>NH<sub>4</sub>Hg(SCN)<sub>4</sub> increases up to 6 and 4.5 K under uniaxial strain of 0.5 and 1.0 GPa along the  $c$ - and  $b^*$ -axes, respectively.<sup>551</sup> Along the  $a$ -axis, however,  $T_c$  decreases monotonically as an applied pressure increases up to 0.6 GPa, above which the superconductivity eventually disappears. A resistivity hump analogous to that observed in  $\alpha$ -(ET)<sub>2</sub>KHg(SCN)<sub>4</sub> appears below ca. 10 K, indicating the formation of the density wave state between 0.4 and 0.6 GPa. **Other Salts:** As for  $\kappa$ -(ET)<sub>2</sub>Cu<sub>2</sub>(CN)<sub>3</sub>, the superconductivity easily appears by uniaxial strain along all directions and the  $T_c$  increases at the initial pressure range,<sup>557</sup> in marked contrast to the monotonic decrease in  $T_c$  under hydrostatic pressure.<sup>491</sup> The details will be described in connection with the spin-liquid ground state in section 3.6.4.

At ambient pressure,  $\beta''$ -(ET)<sub>2</sub>SF<sub>5</sub>CH<sub>2</sub>CF<sub>2</sub>SO<sub>3</sub> exhibits a metallic temperature dependence in the 2D  $ab$ -plane above  $T_c$  of 5.2–5.3 K (mid-point).<sup>467</sup> The uniaxial strain along the  $b$ -axis increases the  $T_c$  at the initial compression region ( $T_c = 6.36$  K at 0.2 GPa, Fig. 60), while the  $T_c$  is nearly unchanged by the strain along the  $a'$ -axis.<sup>566</sup> Along the inter-layer direction ( $c^*$ -axis), the  $T_c$  is rapidly suppressed by the uniaxial strain. These results are qualitatively consistent with the results of the uniaxial pressure coefficients of  $T_c$  deduced from the thermal-expansion study.<sup>564</sup>

As mentioned in section 3.3.5, (EDO)<sub>2</sub>PF<sub>6</sub> exhibits a first-order metal–insulator transition consisting of cooperative mechanisms with charge-ordering with molecular deformation, partial freezing of the anion disorder, and  $2k_F$  doubling of lattice periodicity at around 280 K.<sup>426</sup> When the uniaxial strain is applied along the  $b$ - and  $a'$ -axes, which correspond to the stacking and interstack directions, respectively, the metal–in-

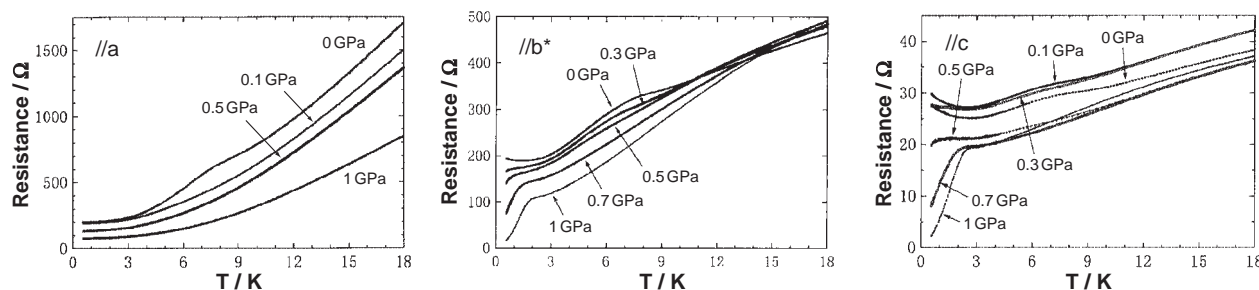


Fig. 59. Pressure dependence of  $T_c$  of  $\alpha$ -(ET)<sub>2</sub>KHg(SCN)<sub>4</sub> using uni-axial strain (oil method) along the  $a$ -,  $b^*$ -, and  $c$ -axes by Maesato et al. The  $T_c$  at ambient pressure is ca. 0.3 K. The value of the external pressure applied at RT is adopted.<sup>550,551</sup>

insulator transition temperature slightly decreases or remains unchanged and the jump of resistivity is suppressed with increasing the strain at the initial compression stage (Fig. 61a).<sup>567</sup> On the other hand, the  $T_{\text{MI}}$  increases remarkably up to above RT by the strain along the  $c^*$ -axis, which corresponds to the interlayer direction (Fig. 61a). These results indicate that the strain along the interlayer ( $//c^*$ ) direction is effective to stabilize the insulating phase in comparison with those along the intralayer directions. The low-temperature X-ray diffraction measurement at ambient pressure revealed that the intralayer direction is unexpectedly expanded just below  $T_{\text{MI}}$ , while the interlayer distance is shortened below the temperature because the anion is slightly inserted into the donor layer. Therefore, the increased  $T_{\text{MI}}$  by the uniaxial strain along the interlayer direction is consistent with the anisotropic lattice distortion.

With applying large strain along each direction, the insulator phase was suppressed and the metallic phase was stabilized. The MI transition occurred at lower than 150 K with a feature of second-order (Fig. 61b).

It should be emphasized again that the behavior under hydrostatic pressure corresponds neither to the averaged nor to

any anisotropic behaviors under uniaxial strain. Hence, the hydrostatic pressure experiments on the organic conductors having a strong anisotropic electronic structure should be replaced by a more appropriate method, a uniaxial strain (epoxy- or oil-) method; although, it should be noted that the epoxy-method is rather unreliable concerning the magnitude of pressure at low-pressure region ( $<0.1$  GPa).

**3.5.4.4 Symmetry of Superconductivity;** No Hebel–Slichter coherence peak was observed in either  $\kappa\text{-(ET)}_2\text{Cu(NCS)}_2$  (Fig. 62)<sup>568</sup> or  $\kappa\text{-(ET)}_2\text{Cu[N(CN)}_2\text{]Br}$ <sup>568</sup> in  $^1\text{H}$  NMR measurements, ruling out the possibility of the BCS  $s$ -wave state. Similar behavior has been reported for  $\beta_{\text{H}}\text{-(ET)}_2\text{I}_3$ <sup>569</sup> and  $\kappa\text{-(ET)}_2\text{Cu}_2(\text{CN})_3$  under hydrostatic pressure in  $^{13}\text{C}$  NMR measurements.<sup>570</sup> Far below  $T_{\text{c}}$  an enhancement of  $T_1^{-1}$  was observed for  $\kappa\text{-(ET)}_2\text{Cu(NCS)}_2$  just like  $\beta_{\text{H}}\text{-(ET)}_2\text{I}_3$ ,<sup>569</sup> but

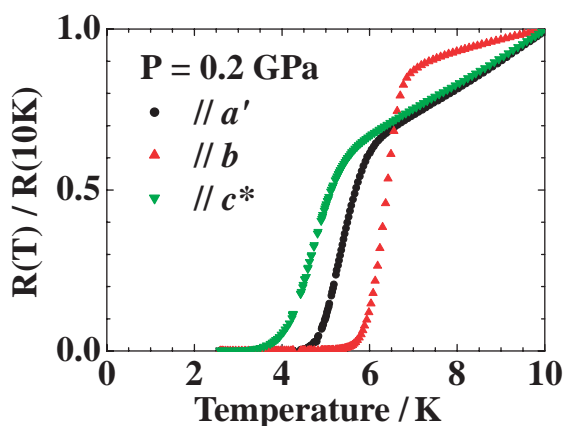


Fig. 60. Temperature dependence of resistance of  $\beta''\text{-(ET)}_2\text{SF}_5\text{CH}_2\text{CF}_2\text{SO}_3$  under the uniaxial strain at 0.2 GPa. in the low-temperature region.<sup>566</sup> The black circle, red triangle, and green triangle correspond to the strain applied parallel to the  $a'$ -,  $b$ -, and  $c^*$ -axes, respectively.

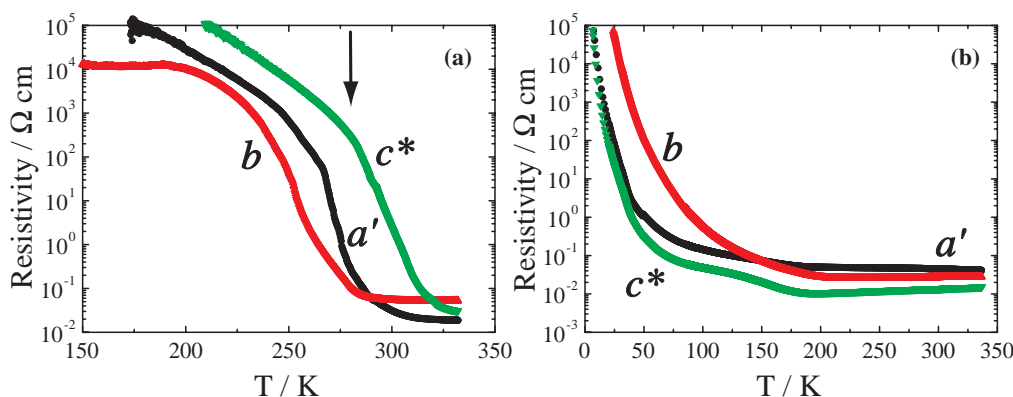


Fig. 61. Temperature dependence of resistivity of  $(\text{EDO})_2\text{PF}_6$  under the uniaxial strain (a) at 0.2 GPa, where the arrow indicates the  $T_{\text{MI}}$  at ambient pressure, and (b) at 1.6 GPa.<sup>567</sup> Black, red, and green curves correspond to the strain applied along to the  $a'$ -,  $b$ -, and  $c^*$ -axes, respectively.

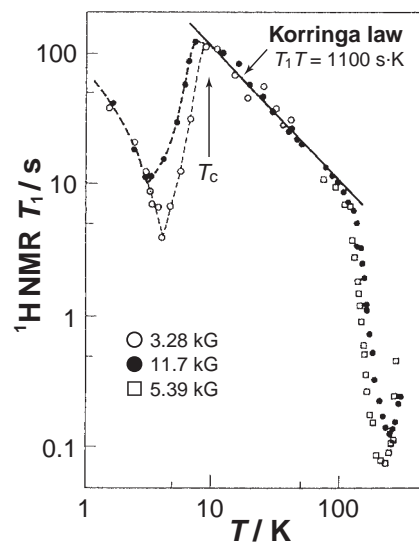


Fig. 62. Relaxation time  $T_1$  of  $^1\text{H}$  NMR of  $\kappa\text{-(ET)}_2\text{Cu(NCS)}_2$ . Korringa law ( $T_1T = 1100 \text{ s}\cdot\text{K}$ ) is seen between 100–10 K. The decrease in  $T_1$  at around 10 K is due to the superconducting transition. No Hebel–Slichter peak is observed just below  $T_{\text{c}}$  (indicated by arrow). The increase in  $T_1$  below 5 K is due to vortex motion.<sup>568</sup> The abnormal behavior above 100 K is ascribed to the dynamics of disordered ethylene protons of the ET molecules.

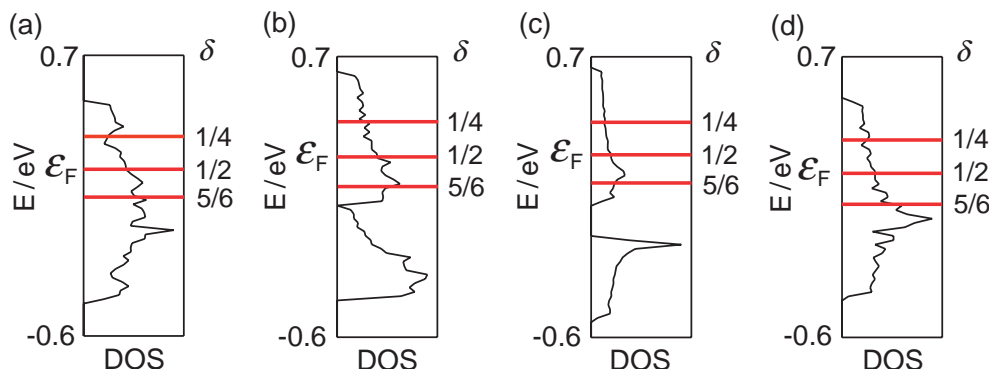


Fig. 63. Calculated density of state (DOS) of ET superconductors; (a)  $\alpha$ -(ET)<sub>2</sub>NH<sub>4</sub>Hg(SCN)<sub>4</sub>, (b)  $\beta$ -(ET)<sub>2</sub>I<sub>3</sub>, (c)  $\kappa$ -(ET)<sub>2</sub>I<sub>3</sub>, and (d)  $\theta$ -(ET)<sub>2</sub>I<sub>3</sub> based on the crystal structures at RT. The Fermi levels for the degree of CT ( $\delta$ ) of ET molecules of 1/4, 1/2, and 5/6 are depicted by solid lines.<sup>6</sup>

the enhancement was more enormous.<sup>568</sup> It seems that the  $T_1^{-1}$  enhancement in Fig. 62 is caused by vortex melting.<sup>568</sup>

The magnetic field penetration depth  $\lambda$  for  $\kappa$ -(ET)<sub>2</sub>Cu(NCS)<sub>2</sub> was estimated to be  $\lambda_{\perp} = 640\text{--}980$  nm by  $\mu$ SR<sup>571</sup> and reversible magnetization,  $\lambda_{\parallel} = 4 \times 10^4$  nm by microwave impedance,<sup>572</sup> and  $1.9\text{--}2.1 \times 10^5$  nm by complex susceptibility. Therefore, the anisotropy of the penetration depth  $\lambda_{\parallel}/\lambda_{\perp}$  is 40–310. The anisotropy of superconducting effective mass was estimated within the range of  $2 \times 10^3\text{--}10^5$ . These results imply an extreme 2D nature of the superconductivity.

The symmetry of the superconducting state of  $\kappa$ -(ET)<sub>2</sub>Cu(NCS)<sub>2</sub> has been controversially described as normal BCS-type by Harshman et al.,<sup>573</sup> Klein et al.,<sup>574</sup> Lang et al.,<sup>575</sup> and Dressel et al.,<sup>576</sup> or non-BCS type by Kanoda et al.,<sup>577</sup> Uemura et al.,<sup>578,579</sup> Achkir et al.,<sup>580</sup> and Belin et al.,<sup>581</sup> based on the penetration depth, relaxation rate, and tunnel-gap measurements. As early as 1990–1991, Kanoda et al.<sup>577</sup> and Uemura et al.<sup>578</sup> reported that  $\lambda(T)$  evaluated by the susceptibility,  $\mu$ SR, and microwave surface impedance measurements is apparently dependent on temperature ( $T^1$  or  $T^2$ ), suggesting the presence of the anisotropic superconducting gap. These results, however, contradict those of other  $\mu$ SR, surface impedance, and reversible magnetization measurements<sup>573–576</sup> that show almost temperature independent  $\lambda(T)$  as expected for BCS-type superconductors. Other types of measurements are also in disagreement with each other concerning superconducting character. DC magnetization measurements suggest that the salt is in the weak coupling limit, while the specific heat studies [ $\gamma = 34$  (or 25) mJ mol<sup>−1</sup> K<sup>−2</sup>,  $\Delta C = 7.3 \times 10^2$  (or  $5.3 \times 10^2$ ) mJ mol<sup>−1</sup> K<sup>−1</sup>,  $\Delta C/\gamma T_c > 2$ ,  $\Theta = 223$  (or 215) K] imply that the salt is a strong coupling superconductor of BCS type.<sup>582</sup>

Scanning tunneling spectroscopy showed the V-shaped gap structure in the 2D surface,<sup>583</sup> as expected for the  $d$ -wave symmetry. Perpendicular to the  $bc$ -plane, the tunneling spectrum varied its shape depending on the tip direction, strongly indicating the gap anisotropy: namely,  $d$ -wave symmetry with line nodes along the direction 45° from the  $c$ -axis.

Recently, it was found by thermal conductivity measurements that the symmetry is of  $d_{xy}$ .<sup>584</sup>

**3.5.5 Control of  $U/W$  and Band Filling: Mixed Crystals between  $\kappa$ -(ET)<sub>2</sub>Cu(CN)[N(CN)<sub>2</sub>] and  $\kappa$ -(ET)<sub>2</sub>Cu<sub>2</sub>(CN)<sub>3</sub>:  $\kappa'$ -(ET)<sub>2</sub>Cu<sub>2</sub>(CN)<sub>3</sub>:** The calculated  $D(E_F)$  of ET salts ( $\alpha$ -,

$\beta$ -,  $\theta$ -, and  $\kappa$ -types) increases with increasing  $\delta$  from 0.5 to 0.8 regardless of the packing pattern (Fig. 63).<sup>6</sup> This indicates that a highly oxidized state of ET with more than +1/2 is preferable to raise  $T_c$  with respect to  $D(E_F)$ . However, no such attempts (hole doping into (ET)<sub>2</sub>X) have so far been forwarded. Attempts to shift the Fermi level by replacing a part of Cu<sup>+</sup> with Cu<sup>2+</sup> in  $\kappa$ -(ET)<sub>2</sub>Cu(NCS)<sub>2</sub> (electron doping) during the electrocrystallization have been unsuccessful in our group. Figure 64a schematically illustrates the conversion of a Mott insulator into metal, either by applying pressure, which is in principle equal to the increase of transfer integral, or by shifting the chemical potential, which corresponds to the carrier doping. The Mott insulator  $\kappa$ -(ET)<sub>2</sub>Cu<sub>2</sub>(CN)<sub>3</sub> (see also section 3.6) is converted to metal by applying a hydrostatic pressure of 0.35 GPa (Fig. 64b), in which a Mott insulator–metal transition was observed at 13–14 K with a decrease of resistivity by a factor of 10<sup>5</sup>.<sup>491</sup> On the other hand,  $\kappa'$ -(ET)<sub>2</sub>Cu<sub>2</sub>(CN)<sub>3</sub>, which was prepared by the presence of CuCN and [N(CN)<sub>2</sub>]<sup>1−</sup> as supporting electrolytes and has nearly the same crystal structure as that of  $\kappa$ -(ET)<sub>2</sub>Cu<sub>2</sub>(CN)<sub>3</sub> containing a small amount of Cu<sup>2+</sup>, exhibited metallic behavior and superconducting transition without a Mott insulating state (Fig. 64c).<sup>491,492</sup>

Later, it was found that  $\kappa'$ -(ET)<sub>2</sub>Cu(CN)<sub>3</sub> has the chemical formula (ET)<sub>2</sub>(Cu<sup>1+</sup><sub>2− $x$ − $y$</sub> Cu<sup>2+</sup> <sub>$x$</sub> ){[N(CN)<sub>2</sub>]<sub>3− $2y$</sub> [N(CN)<sub>2</sub>] <sub>$y$</sub> } and its metallic and superconducting natures are governed by the content of Cu<sup>2+</sup> and ligand [NC–N–CN]<sup>1−</sup>, which can be replaced by the ligand [NC–Cu–CN]<sup>1−</sup> in the anion layer owing to their very similar shape, size, and equal charge (Fig. 65).<sup>493</sup> For  $x = 0$  and  $y = 0$ , the salt is the Mott insulator  $\kappa$ -(ET)<sub>2</sub>Cu<sub>2</sub>(CN)<sub>3</sub>, while the other extreme side ( $x = 0$ ,  $y = 1$ ) is  $\kappa$ -(ET)<sub>2</sub>Cu(CN)[N(CN)<sub>2</sub>] with  $T_c = 11.2$  K at ambient pressure.<sup>304,485–487</sup> By changing both  $x$  (80–1200 ppm) and  $y$  (preferential values of  $y$  are 0.05, 0.3–0.4, and 0.8), the  $T_c$  is tuned from 3 to 11 K (Fig. 66). Figure 66 shows the relation between the mixing ratio  $y$  and  $T_c$  for the  $\kappa'$ -salt (22 out of 99 batches so far prepared include superconducting crystals) and the following are the noticeable features.

1) Between Mott insulator (point **a**) and 11 K superconductor (point **e**), superconducting crystals appear with the preferential ratio  $y$  of 0.05 (point **b**), 0.3 (point **c**), and 0.8 (point **d**). It is worth mentioning that even 5% of N(CN)<sub>2</sub> induces superconductivity. The mixing of the two kinds of ligand in the anion layer was found to be uniform and homogeneous, and



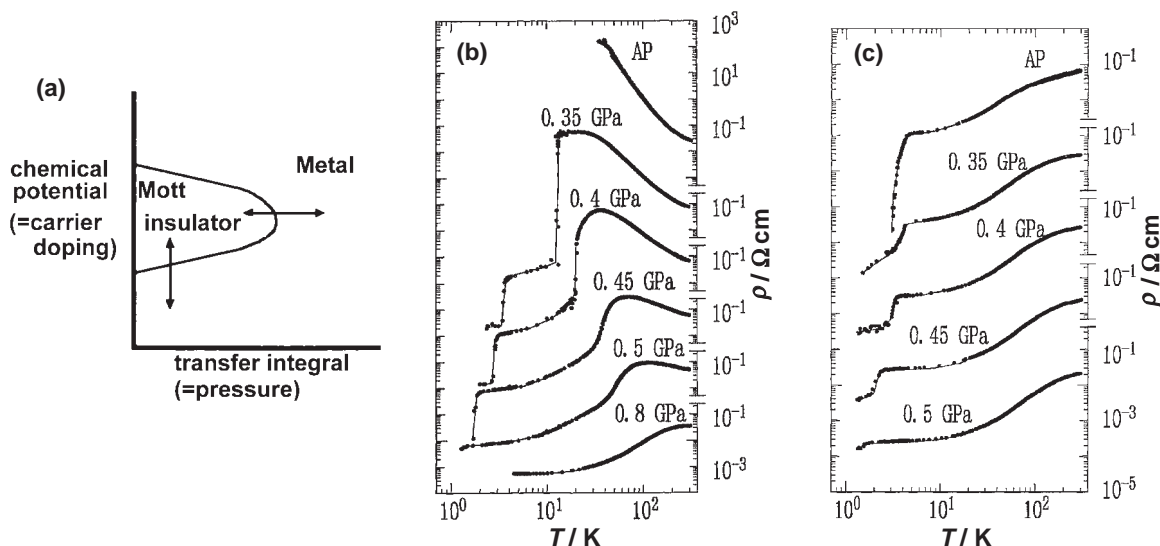


Fig. 64. (a) A schematic phase diagram of a Mott insulator. The abscissa represents intermolecular transfer interaction and the ordinate the chemical potential  $\zeta$  ( $\approx \varepsilon_F$ ). A Mott insulator can be converted into a metal either by applying pressure or carrier doping. Temperature dependence of resistivity of (b)  $\kappa\text{-(ET)}_2\text{Cu}_2(\text{CN})_3$  and (c)  $\kappa'\text{-(ET)}_2\text{Cu}_2(\text{CN})_3$  ( $\text{Cu}^{2+} = 430 \text{ ppm}$ , the content of  $[\text{N}(\text{CN})_2]^{1-}$  is unknown) under various hydrostatic pressures. The indicated pressures have been measured at RT. The solid lines are guides to the eye.<sup>6,491</sup>

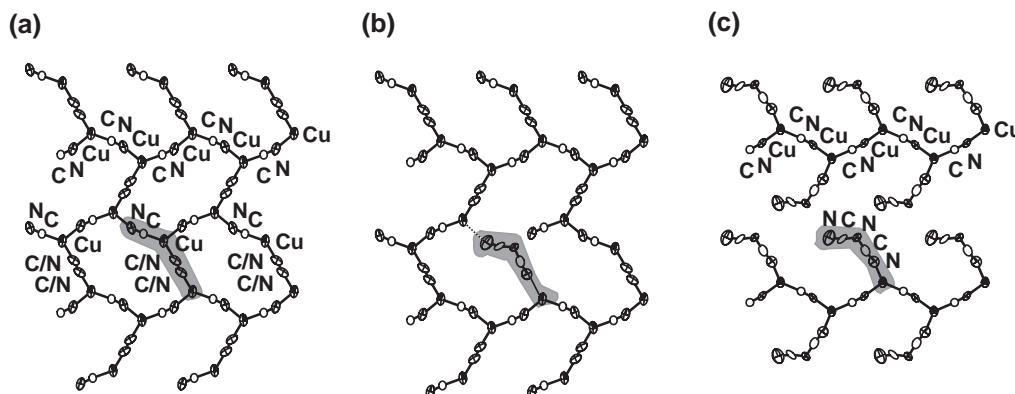


Fig. 65. The anion structures of (a)  $\kappa\text{-(ET)}_2\text{Cu}_2(\text{CN})_3$  and (c)  $\kappa'\text{-(ET)}_2\text{Cu}(\text{CN})[\text{N}(\text{CN})_2]$ . (b) A schematic figure of  $\kappa'\text{-(ET)}_2\text{-(Cu}^{+2-x-y}\text{Cu}^{2+})_x\{(\text{CN})_{3-2y}[\text{N}(\text{CN})_2]_y\}$  with  $y \approx 0.1$ .

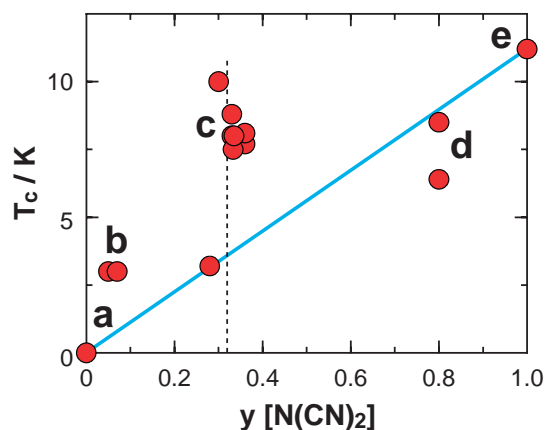


Fig. 66. Relation between the content of  $\text{N}(\text{CN})_2$ ,  $y$  and  $T_c$  in several crystals of  $\kappa'$ -salt:  $\kappa\text{-(ET)}_2(\text{Cu}^{1+})_{2-x-y}(\text{Cu}^{2+})_x(\text{CN})_{3-2y}[\text{N}(\text{CN})_2]_y$ . As for points a–e, see text. Dashed line indicates the samples of  $y \approx 0.3$ .<sup>493</sup>

it can thus be denied both the simple mixing of 95% of Mott insulator  $\kappa\text{-(ET)}_2\text{Cu}_2(\text{CN})_3$  and 5% of  $\kappa\text{-(ET)}_2\text{Cu}(\text{CN})[\text{N}(\text{CN})_2]$  domains and the random orientation of  $\text{NC-X-CN}$  ( $X = \text{Cu}$  or  $\text{N}$ ) in a single crystal. Interestingly, most of the crystals in a batch have the same  $x$  and  $y$  values (the errors in  $x$  and  $y$  are ca. 10 and 5%, respectively).

2) In general, a higher  $T_c$  is realized with larger  $y$ . This tendency is represented by line connecting points a and e in Fig. 66. Since the ratio of the bandwidth of the upper Hubbard band  $W_U$  (see Fig. 20) to  $U_d$  is evaluated to be 1.11 and 1.16 for  $\kappa\text{-(ET)}_2\text{Cu}_2(\text{CN})_3$  and  $\kappa\text{-(ET)}_2\text{Cu}(\text{CN})[\text{N}(\text{CN})_2]$ , respectively, it seems that the partial replacement of  $\text{NC-Cu-CN}$  in the Mott insulator  $\kappa\text{-(ET)}_2\text{Cu}_2(\text{CN})_3$  by  $\text{NC-N-CN}$  increases the ratio  $W_U/U_d$ . This is the direction to the horizontal right side of the Mott insulating phase in Fig. 64a. Therefore, the increase in  $y$  simply increases  $W_U/U_d$  and the  $T_c$  of the resulting salt  $\kappa\text{-(ET)}_2\text{Cu}_{2-y}\{(\text{CN})_{3-2y}[\text{N}(\text{CN})_2]_y\}$  is expected to follow the blue line in Fig. 66.

The similar size and shape as well as the same charge of

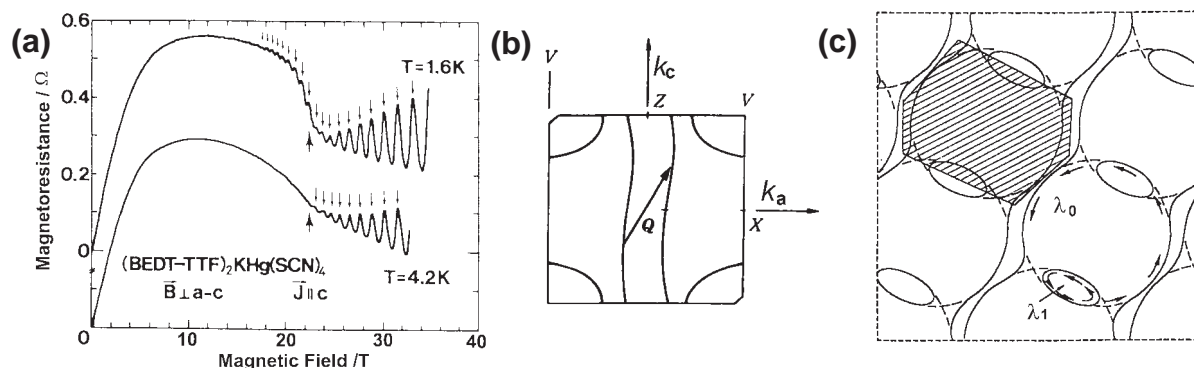


Fig. 67. (a) Magnetoresistance oscillations of  $\alpha$ -(ET)<sub>2</sub>KHg(SCN)<sub>4</sub>. The SdH oscillations are indicated by thin arrows and a kink at around 22 T is indicated by thick arrows.<sup>586</sup> (b) The arrow  $\mathbf{Q}$  in the Fermi surface of  $\alpha$ -(ET)<sub>2</sub>KHg(SCN)<sub>4</sub> indicates the  $\mathbf{Q}$  vector for the reconstruction of the Fermi surface. (c) The reconstructed Fermi surface by Kartsovnik et al.<sup>589</sup> Shaded part is the new Brillouin zone, and  $\lambda_0$  and  $\lambda_1$  are the magnetic breakdown orbital and 2D cylindrical orbit, respectively, which were experimentally confirmed by SdH and dHvA oscillations.

CN–X–CN (X = N, Cu) enable the exchange of ligand between  $\text{Cu}_2(\text{CN})_3 \{=(\text{CuCN})^0 + (\text{NC–Cu–CN})^{1-}\}$  and  $\text{Cu}(\text{CN})[\text{N}(\text{CN})_2] \{=(\text{CuCN})^0 + (\text{NC–N–CN})^{1-}\}$  resulting in the comparable lattice parameters among  $\kappa$ -(ET)<sub>2</sub>Cu<sub>2</sub>(CN)<sub>3</sub>,  $\kappa$ -(ET)<sub>2</sub>Cu(CN)[N(CN)<sub>2</sub>] and their alloy,  $\kappa'$ -salts.

There are many points far departing from the blue line in Fig. 66, which is related to the varied content of Cu<sup>2+</sup> for a fixed  $y$ . The content of Cu<sup>2+</sup> is non-zero ( $x = 80$ –1200 ppm) except for the two extreme cases of  $y = 0$  and 1 ( $x = 0$  ppm).

3) At  $y = 0.3$ , the  $T_c$  covers from 3 to 10 K and the crystals with different  $T_c$  have different  $x$  values. This corresponds to the vertical shift of the phase in Fig. 64a since the charge of ET is modified from +0.5 to +0.5(1 –  $x$ ). A tendency is observed that  $T_c$  increases with increasing the content of Cu<sup>2+</sup> up to 400 ppm and then  $T_c$  decreases.<sup>491</sup> However, the obvious relation between  $T_c$  and the content of Cu<sup>2+</sup> has still not been completely elucidated due to the lack of sufficient data.

These experimental facts indicate that this system could be an excellent model of band filling control and would be a good candidate for making a superlattice structure composed of Mott insulator/superconductor heterojunctions. It should be emphasized that their lattice parameters are kept nearly constant through such an anion modification, which is the most essential feature for achieving successful tuning of  $T_c$  in an organic superconductor.

**3.5.6 Electronic Structures of  $\alpha$ -(ET)<sub>2</sub>MHg(SCN)<sub>4</sub>:** As briefly mentioned in section 3.5.3, 2D superconductors  $\alpha$ -(ET)<sub>2</sub>MHg(SCN)<sub>4</sub> (M = K, NH<sub>4</sub>, Rb, and Tl) form a group according to their crystal and electronic structures (Fig. 50).<sup>394,395,398,399</sup> Their calculated band structures consist of 1D and 2D Fermi surfaces as depicted in Figs. 30a and 30e. The 1D Fermi surface of  $\alpha$ -(ET)<sub>2</sub>MHg(SCN)<sub>4</sub> (M = K, Rb, and Tl) tends to nest, forming a density wave state below 8 K. The diffuse X-ray study indicates the most plausible density wave to be CDW.<sup>585</sup> Since the nesting does not diminish the 2D Fermi surface, the temperature dependence of resistivity exhibits a weak hump at around 8 K without losing the metallic behavior (Fig. 59). The salt showed SdH oscillations with an abnormal kink at around 22 T, as observed by Osada et al. (Fig. 67a),<sup>586</sup> which differs from those of the NH<sub>4</sub> salt.<sup>587</sup> AMRO of the K salt showed a drastic phase change at around

8 K.<sup>588</sup> Kartsovnik et al. explained these behaviors in terms of the reconstruction of the Fermi surface through the nesting of the 1D Fermi part as seen in Figs. 67b and 67c.<sup>589</sup> However, the shape of the reconstructed Fermi surface is not completely settled for the  $\alpha$ -(ET)<sub>2</sub>MHg(SCN)<sub>4</sub> family.<sup>364,589–594</sup> For  $\alpha$ -(ET)<sub>2</sub>NH<sub>4</sub>Hg(SCN)<sub>4</sub>, the nesting of the 1D Fermi surface does not occur at ambient pressure, but occurs under an applied pressure of 0.4–0.6 GPa below 10 K. Above 0.6 GPa, the nesting disappears again and the salt shows a metallic state down to 0.5 K.<sup>553,554</sup>

**3.6 Ground State of 10 K Class ET Superconductors.** In this section, the electronic ground states of a series of  $\kappa$ -(ET)<sub>2</sub>X (10 K class superconductors with X = Cu(CN)[N(CN)<sub>2</sub>], Cu(NCS)<sub>2</sub>, Cu[N(CN)<sub>2</sub>]Br, and Cu[N(CN)<sub>2</sub>]Cl, and a Mott insulator with X = Cu<sub>2</sub>(CN)<sub>3</sub>) at both high- and low-temperatures are elucidated.

**3.6.1 Electron Correlation and Band Parameters:** The organic superconductors having  $T_c$  near 10 K exhibit intriguing transport properties originating from the strongly correlated electronic structure, similar to high  $T_c$  cuprate<sup>595</sup> and C<sub>60</sub> superconductors.<sup>596</sup> Figure 68 compares the resistivity of 10 K class superconductors ( $\kappa$ -(ET)<sub>2</sub>Cu(CN)[N(CN)<sub>2</sub>] (**2**),  $\kappa$ -(ET)<sub>2</sub>-Cu(NCS)<sub>2</sub> (**3**),  $\kappa$ -(ET)<sub>2</sub>Cu[N(CN)<sub>2</sub>]Br (**4**), and  $\kappa$ -(ET)<sub>2</sub>Cu[N(CN)<sub>2</sub>]Cl (**5**)) with those of Mott insulators  $\kappa$ -(ET)<sub>2</sub>Cu<sub>2</sub>(CN)<sub>3</sub> (**6**) and strongly electron-correlated  $\theta$ -(ET)<sub>2</sub>Cu<sub>2</sub>(CN)[N(CN)<sub>2</sub>]<sub>2</sub> (**7**),<sup>296,297</sup> and a good metal having low  $T_c$ ,  $\beta$ -(ET)<sub>2</sub>-Au<sub>2</sub> (**1**). Some characteristics of these salts together with other ET salts are summarized in Table 17.

The Mott insulator  $\kappa$ -(ET)<sub>2</sub>Cu<sub>2</sub>(CN)<sub>3</sub> (**6**) shows a comparable  $\sigma_{\text{RT}}$  value to those of **2**–**5** and **7**. The energy gap  $\varepsilon_g$  of **6** (0.10–0.12 eV) is twice that of **5** (0.024 eV) and half that of **7** (0.17–0.19 eV). The semiconductive region of **3**–**5**, which is called a paramagnetic non-metallic phase in Fig. 56, is postulated to be a Mott insulating state. In this case, the magnetic susceptibility would exhibit the enhancement due to the electron correlation (Eq. 26). However, the enhancement is not significant compared to those of typical Mott insulators of  $\alpha'$ -,  $\beta'$ -,  $\theta$ -, and  $\delta'$ -types as seen in Table 12. The magnetic susceptibility, optical, thermopower, and other measurements confirmed that the semiconductive-like region of **3** and **4** is neither a typical Mott insulator nor typical metal. The origin

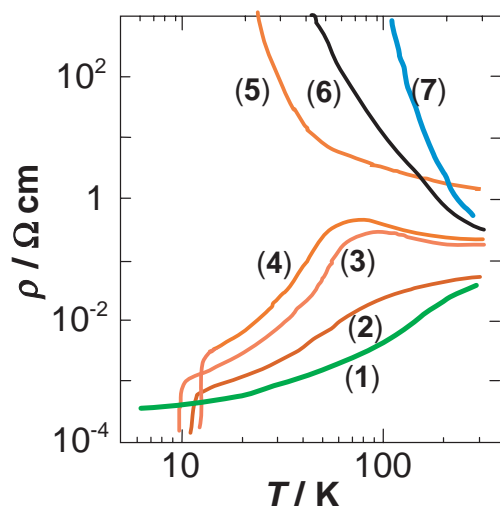


Fig. 68. Temperature dependences of resistivity for 10 K class superconductors  $\kappa$ -(ET)<sub>2</sub>X (X = Cu(CN)[N(CN)<sub>2</sub>] (2), Cu(NCS)<sub>2</sub> (3), Cu[N(CN)<sub>2</sub>]Br (4), and Cu[N(CN)<sub>2</sub>]Cl (5)) are compared with those of a good metal with low  $T_c$   $\beta$ -(ET)<sub>2</sub>AuI<sub>2</sub> (1) and Mott insulator  $\kappa$ -(ET)<sub>2</sub>Cu<sub>2</sub>(CN)<sub>3</sub> (6) and strongly electron correlated  $\theta$ -(ET)<sub>2</sub>Cu<sub>2</sub>(CN)[N(CN)<sub>2</sub>]<sub>2</sub> (7) at ambient pressure. The temperature dependences of 2–5 is the same as depicted in Fig. 41.

of the regime is still controversial.<sup>159,384,527,532,597–599</sup> namely, strong electron correlation,<sup>384,527,532,597</sup> freezing of the ethylene disorder,<sup>159</sup> the structural effect including the abnormal lattice dilation change, which was observed in **4** near 80 K<sup>530,598</sup> but not in **3**, the contribution of the thermally excited carriers from the flat portions of the occupied bands to the unoccupied bands,<sup>599</sup> mixed valency of the Cu ion, and so on, have been proposed, but the strong electron correlation is the most plausible cause.

The resistivity behavior of **2** suggests that the semiconductive region may be hidden above ca. 70 K, and hence, the electron correlation increases in the order of **1** < **2** < **3** < **4** < **5** < **6** < **7**.

Figure 69 demonstrates the temperature dependence of the  $\chi_{\text{spin}}$  of these salts. Most of the data were obtained under the same conditions by our group.  $\kappa$ -(ET)<sub>2</sub>Cu(CN)[N(CN)<sub>2</sub>], which behaves very similarly to  $\kappa$ -(ET)<sub>2</sub>Cu(NCS)<sub>2</sub>,  $\kappa$ -(ET)<sub>2</sub>Cu[N(CN)<sub>2</sub>]Br, and  $\kappa$ -(ET)<sub>2</sub>Cu[N(CN)<sub>2</sub>]Cl above 50 K, is not included in Fig. 69 to simplify the figure.

At RT, the EPR or static magnetic susceptibility ( $\chi_{\text{spin}}$ ), which is a good macroscopic probe for the electron correlation as expressed by Eq. 26,<sup>283</sup> of **2–6** lies in the range of 4.4–5.5 × 10<sup>−4</sup> emu mol<sup>−1</sup> at RT, and the values are intermediate between those of typical Mott insulators  $\beta'$ -(ET)<sub>2</sub>X (X = ICl<sub>2</sub> and AuCl<sub>2</sub>) (9.3–10 × 10<sup>−4</sup> emu mol<sup>−1</sup>) and the metal **1** (3.4 × 10<sup>−4</sup> emu mol<sup>−1</sup>) (Table 17, Fig. 69). It is noticed that the  $\chi_{\text{spin}}$  values of **2–6** are rather close to that of the good metal  $\beta$ -(ET)<sub>2</sub>I<sub>3</sub> (4.6 × 10<sup>−4</sup> emu mol<sup>−1</sup>).

Table 17. Characteristic Properties of ET Salts **1–7** and Others

I	Good metal	Conductivity	$\chi_{\text{RT}}$	$W_U$ ,	$t'/t^{(d)}$	Ethylene	Ref.
II	10 K class superconductor	$\sigma_{\text{RT}} (\epsilon_g)$	EPR, <sup>a)</sup> static <sup>b)</sup>	$W_U/\Delta E_d^{(c)}$		conformation <sup>f)</sup>	for $\chi$
III	Mott insulator	/S cm <sup>−1</sup> (eV)	/10 <sup>−4</sup> emu mol <sup>−1</sup>				
<b>I</b>							
	a) $\kappa$ -(ET) <sub>2</sub> I <sub>3</sub>	30	no data	0.61, 1.24	0.58	E at RT	—
	b) $\beta$ -(ET) <sub>2</sub> IBr <sub>2</sub>	20	— <sup>e)</sup>	0.60, 1.22	—	E at RT	—
	c) $\beta$ -(ET) <sub>2</sub> I <sub>3</sub>	60	4.6	0.59, 1.23	—	E + S < 175 K	600
	d) $\beta$ -(ET) <sub>2</sub> AuI <sub>2</sub>	<b>1</b> 20–60	3.4	0.57, 1.14	—	E at RT	601
<b>II</b>							
	e) $\kappa$ -(ET) <sub>2</sub> Ag(CN) <sub>2</sub> H <sub>2</sub> O	37	4.0	0.54, 1.15	0.60	S + E at RT	507
	f) $\kappa$ -(ET) <sub>2</sub> Cu(CN)[N(CN) <sub>2</sub> ] <b>2</b>	5–50	4.6	0.52, 1.16	0.66–0.71	S + E at RT	485,507
	g) $\kappa$ -(ET) <sub>2</sub> Cu(NCS) <sub>2</sub> <b>3</b>	5–40	4.5–4.6, 4.4–4.5	0.57, 1.24	0.82–0.86	S < 120 K	507,532
	h) $\kappa$ -(ET) <sub>2</sub> Cu[N(CN) <sub>2</sub> ]Br <b>4</b>	5–50	4.5–5.5, 4.4–4.5	0.55, 1.12	0.68	E(88%) + S(12%)	507,532
	i) $\kappa$ -(ET) <sub>2</sub> Cu[N(CN) <sub>2</sub> ]Cl <b>5</b>	2 (0.024 > 42 K)	4.5, 4.5–4.6	0.56, 1.10	0.75	at 127 K for H-salt E < 120 K	507,514
<b>III</b>							
	j) $\kappa$ -(ET) <sub>2</sub> Cu <sub>2</sub> (CN) <sub>3</sub> <b>6</b>	2–7 (0.10 > 100 K)	5.5, 4.7	0.50, 1.11	1.06	S < 120 K	490
	k) $\theta$ -(ET) <sub>2</sub> Cu <sub>2</sub> (CN)[N(CN) <sub>2</sub> ] <sub>2</sub> <b>7</b>	2–16 (0.17–0.19)	9.3, 10		—	E at RT	296
	l) ET-TCNQ	10	8.8	0.41, 0.89	—	E at RT	202
	m) $\beta'$ -(ET) <sub>2</sub> ICl <sub>2</sub>	3 × 10 <sup>−2</sup>	9.6	0.27, 0.49	—	E at RT	285,286
	n) $\beta'$ -(ET) <sub>2</sub> IBrCl	1.5 × 10 <sup>−2</sup> (0.22)	—, 11.5	0.26, 0.48	—	E > 120 K	294
	o) $\beta'$ -(ET) <sub>2</sub> AuCl <sub>2</sub>	10 <sup>−1</sup> –10 <sup>−2</sup>	9.6	0.25, 0.47	—	E at RT	285,286

a) Measured in our laboratory except a, b, d, and n. b) Measured by Kanoda for salts **5**.<sup>532</sup> c)  $W_U/\Delta E_d$  is a ratio of the upper band-width ( $W_U = 0.50$ – $0.57$  eV) to dimerization energy ( $\Delta E_d = 0.45$ – $0.51$  eV), which is a measure of  $W/U_{\text{eff}}$  (see Eq. 24 and Fig. 20). The calculated  $W$  of salt **7** (not dimerized ET system) is 0.65 eV. d) As for transfer integrals  $t$  and  $t'$ , see Fig. 72. e) E. L. Venturini et al. (*Synth. Met.* **1988**, 27, A243) reported EPR  $\chi$  below 100 K, but their  $\chi$  values are unexpectedly large ( $8.3 \times 10^{-4}$  emu mol<sup>−1</sup> for  $\beta$ -(ET)<sub>2</sub>IBr<sub>2</sub> and  $6.0 \times 10^{-4}$  emu mol<sup>−1</sup> for  $\beta$ -(ET)<sub>2</sub>I<sub>3</sub> at 100 K). f) E: eclipsed, S: staggered.

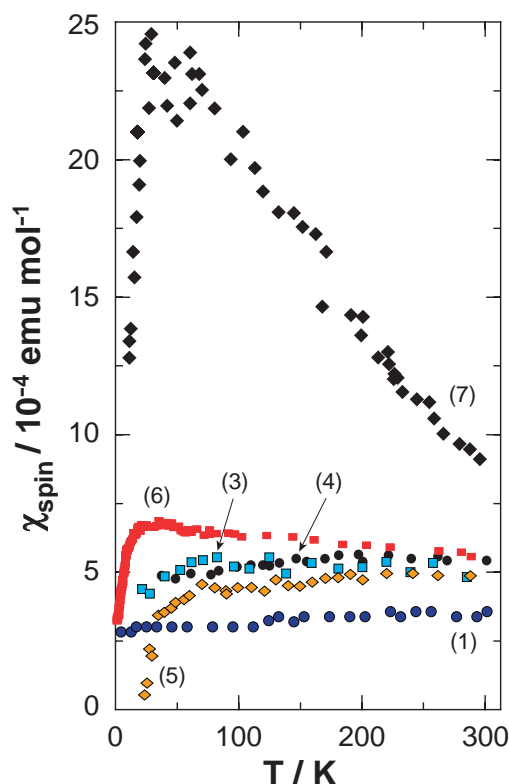


Fig. 69. Temperature dependence of EPR spin susceptibility  $\chi_{\text{spin}}$  of a single crystal of a good metal  $\beta\text{-(ET)}_2\text{AuI}_2$  (1,  $\bullet$ ), those of 10 K class superconductors  $\kappa\text{-(ET)}_2\text{X}$  ( $\text{X} = \text{Cu(NCS)}_2$  (3,  $\blacksquare$ ),  $\text{Cu[N(CN)}_2\text{]Br}$  (4,  $\bullet$ ), and  $\text{Cu[N(CN)}_2\text{]Cl}$  (5,  $\blacklozenge$ )), a Mott insulator  $\kappa\text{-(ET)}_2\text{Cu}_2(\text{CN})_3$  (6,  $\blacksquare$ ), and a strongly electron-correlated insulator  $\theta\text{-(ET)}_2\text{Cu}_2(\text{CN})\text{[N(CN)}_2\text{]}_2$  (7,  $\blacklozenge$ ).  $\kappa\text{-(ET)}_2\text{Cu(CN)[N(CN)}_2\text{]}$  (2) exhibit a very similar temperature dependence to those of 3–5 from RT ( $\approx 4.7 \times 10^{-4} \text{ emu mol}^{-1}$ ) to 30 K, and then monotonically decrease down to 20 K ( $3.3 \times 10^{-4} \text{ emu mol}^{-1}$ ) without any anomaly (not depicted in this figure).

Between RT and 100 K, the magnetic susceptibility of Mott insulators 5 and 6 indicates that both have a similar electronic state to those of the electron-correlated 10 K class superconductors 2–4 rather than the strongly electron-correlated insulator  $\theta\text{-(ET)}_2\text{Cu}_2(\text{CN})\text{[N(CN)}_2\text{]}_2$  (7) and the good metal  $\beta\text{-(ET)}_2\text{AuI}_2$  (1). The  $\chi_{\text{spin}}$  of 5 gradually decreases as temperature decreases in the range of 20–200 K as observed for 2–4 ( $\chi_{\text{spin}} \approx 7 \times 10^{-4} \text{ emu mol}^{-1}$ ). Although 6 exhibits a significant enhancement of  $\chi_{\text{spin}}$  below 200 K, the enhancement of  $\chi_{\text{spin}}$  at low temperatures is not as significant as those for 7 ( $2.2\text{--}2.4 \times 10^{-3} \text{ emu mol}^{-1}$  at  $\approx 40 \text{ K}$ ) and  $\beta'\text{-(ET)}_2\text{X}$  ( $\text{X} = \text{ICl}_2$  and  $\text{AuCl}_2$ ) ( $1.3 \times 10^{-3} \text{ emu mol}^{-1}$  at  $\approx 100 \text{ K}$ ). Since all these ET salts have nearly the same calculated bandwidth  $W$  (0.50–0.65 eV), the electron correlation in 6 is roughly analogous to those for 2–5 with slightly more enhanced electron correlation. From this aspect, the electron-correlated systems 2–6 (f–j in Table 17) form a sub-group that is distinctly different from the typical Mott insulators (l–o in Table 17) and is slightly different from the good ET metals (a–d in Table 17).

$^{13}\text{C}$ NMR measurements by Kawamoto et al.<sup>602,603</sup> on 3–5 and  $\beta_{\text{L}}\text{-(ET)}_2\text{I}_3$  clarified their electronic structures more pre-

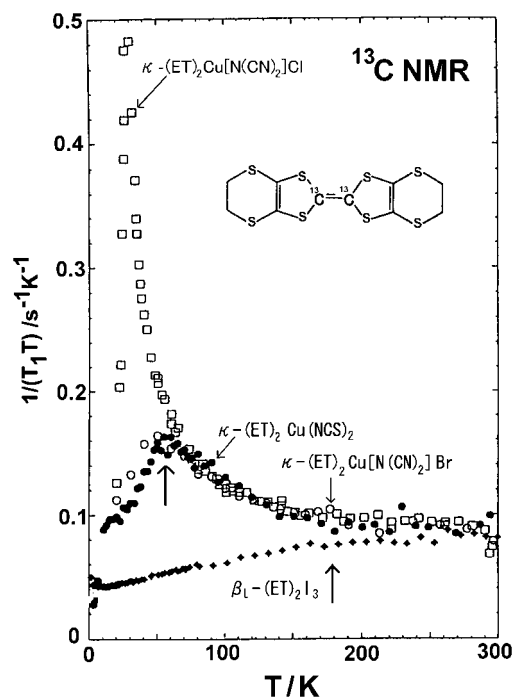


Fig. 70.  $^{13}\text{C}$ NMR measurements on  $\kappa\text{-(ET)}_2\text{Cu(NCS)}_2$  (3),  $\kappa\text{-(ET)}_2\text{Cu[N(CN)}_2\text{]Br}$  (4),  $\kappa\text{-(ET)}_2\text{Cu[N(CN)}_2\text{]Cl}$  (5), and  $\beta_{\text{L}}\text{-(ET)}_2\text{I}_3$  by Kawamoto et al.<sup>532,602,603</sup> Thick arrows indicate the points at 180 K and 50–60 K.

cisely. As seen in Fig. 70, the  $(T_1T)^{-1}$  values of 3–5 are close to that of  $\beta_{\text{L}}\text{-(ET)}_2\text{I}_3$  above 180 K, below which these values exhibited an appreciable increase down to around 50 K due to the highly correlated nature of the metallic phase. The electron correlation somehow ceased to grow in 3 and 4 below 50–60 K and they went towards the superconducting ground state. On the other hand, the electron correlation grew larger below 60 K in 5 to form an antiferromagnetic ground state at ambient pressure. This figure also indicates that the electronic states of these salts including  $\beta\text{-(ET)}_2\text{I}_3$  in the high-temperature regime are not distinctive to each other. Based on these observations, the metallic (or semiconductive) electronic states of 2–6 at high temperatures are tentatively designated by us as the “fuzzy metallic state.”<sup>384</sup>

The electronic states of these salts at high temperatures are well discriminated by the band parameters calculated by a tight-binding model based on the extended Hückel method.<sup>384,491</sup> Table 17 summarizes the ratio  $W_{\text{U}}/\Delta E_{\text{d}}$  and Fig. 71 demonstrates the relation between  $W_{\text{U}}/\Delta E_{\text{d}}$  and  $W_{\text{U}}$  for the ET compounds having dimerized ET molecules.<sup>384</sup>  $W_{\text{U}}$  and  $\Delta E_{\text{d}}$  are the calculated upper-HOMO bandwidth and the dimerization energy, respectively, and  $W_{\text{U}}/\Delta E_{\text{d}}$  corresponds to  $W/U_{\text{eff}}$  for a dimerized system since  $U_{\text{d}} \approx \Delta E_{\text{d}}$  (Eq. 24).

1) A nearly linear relation exists between the  $W_{\text{U}}/\Delta E_{\text{d}}$  and  $W_{\text{U}}$  values among the ET compounds with dimerized ET molecules. This relation suggests that  $W_{\text{U}}$  offers a measure of the ratio  $W/U_{\text{eff}}$ .

2) Typical Mott insulators reside at the lower-left side (l–o in Fig. 71), while good metals (a–d) reside at the upper-right side, though  $\beta\text{-(ET)}_2\text{AuI}_2$  (d) has a slightly small  $W_{\text{U}}/\Delta E_{\text{d}}$  owing to the rather large  $\Delta E_{\text{d}}$  value (0.50 eV).



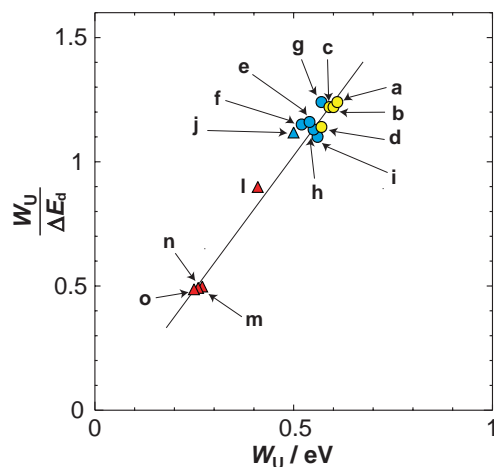


Fig. 71. A relation between dimerization energy ( $\Delta E_d$ ) and bandwidth of the upper band ( $W_U$ ) for ET compounds having dimerized ET molecules. (a)  $\kappa$ -(ET) $_2$ I $_3$ ; (b)  $\beta$ -(ET) $_2$ -IBr $_2$ ; (c)  $\beta$ -(ET) $_2$ I $_3$ ; (d)  $\beta$ -(ET) $_2$ AuI $_2$ ; (e)  $\kappa$ -(ET) $_2$ Ag-(CN) $_2$ ·H $_2$ O; (f)  $\kappa$ -(ET) $_2$ Cu(CN)[N(CN) $_2$ ]; (g)  $\kappa$ -(ET) $_2$ Cu-(NCS) $_2$ ; (h)  $\kappa$ -(ET) $_2$ Cu[N(CN) $_2$ ]Br; (i)  $\kappa$ -(ET) $_2$ Cu[N(CN) $_2$ ]Cl; (j)  $\kappa$ -(ET) $_2$ Cu $_2$ (CN) $_3$ ; (l) ET·TCNQ(triclinic); (m)  $\beta'$ -(ET) $_2$ ICl $_2$ ; (n)  $\beta'$ -(ET) $_2$ BrCl; and (o)  $\beta'$ -(ET) $_2$ Au-Cl $_2$ .<sup>384</sup> ●: good metal, ●: 10 K class superconductor, ▲: j, and ▲: typical Mott insulator.

3) The 10 K superconductors (f–i) together with  $\kappa$ -(ET) $_2$ Ag-(CN) $_2$ ·H $_2$ O (e) reside between the Mott insulators and good metals with  $W_U/\Delta E_d$  of 1.1–1.2, while  $\kappa$ -(ET) $_2$ Cu(NCS) $_2$  (g) has a slightly large  $W_U/\Delta E_d$  owing to the small  $\Delta E_d$  value (0.46 eV).

4) Figure 71 strongly suggests that compounds showing a resistivity hump (see Fig. 68) have rather a small  $W_U/\Delta E_d$  value, which displays a strong electron correlation.

5) A Mott insulator having  $W_U/\Delta E_d$  close to unity is able to be converted to a metal or a superconductor by slight band filling change [e.g.,  $\kappa$ -(ET) $_2$ Cu $_2$ (CN) $_3$  (j)  $\rightarrow$   $\kappa'$ -(ET) $_2$ Cu $_2$ (CN) $_3$ , see section 3.5.5].

6) A Mott insulator having  $W_U/\Delta E_d$  far from unity becomes a superconductor under extremely high pressure (m).<sup>455</sup>

**3.6.2 Magnetic Ordering and Superconductivity:** Figures 68–70 indicate that the ground states of the  $\kappa$ -salts 2–5 are of either superconducting or antiferromagnetic ordered state. The electronic structures of organic and cuprate superconductors have been extensively studied and it is generally observed that the superconducting state is located in close proximity to the magnetic-ordered state (SDW or antiferromagnet). This feature is also observed in the C $_{60}$  system.<sup>596</sup>

Below 20 K, the  $\chi_{\text{spin}}$  of **6** starts to decrease rapidly as if a spin-ordered state is realized such as **5** (Fig. 69) and deuterated **4**. However, the ground state of **6** differs from them distinctly; namely, the EPR, SQUID,  $^1\text{H}$ NMR, and  $\mu\text{SR}$  measurements confirmed that the  $\chi_{\text{spin}}$  approaches to zero but does not vanish down to 1.4, 1.9, 0.03, and 0.02 K, respectively, indicating that the ground state is non-spin-ordered state, i.e., spin-liquid state.<sup>305</sup> Furthermore, the spin-liquid state is found to neighbor the superconducting state in **6**, which has a strong spin frustration at ambient pressure owing to its peculiar spin-lattice geometry. These peculiar behaviors will be fully discussed in

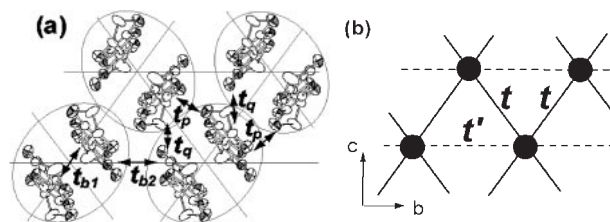


Fig. 72. (a) Donor packing pattern of  $\kappa$ -(ET) $_2$ Cu $_2$ (CN) $_3$  along the  $a$ -axis (transfer integrals;  $t_{b1} = 22$  meV,  $t_{b2} = 12$  meV,  $t_p = 8$  meV, and  $t_q = 3$  meV) and (b) triangular spin lattice ( $t'/t = 1.06$ ;  $t' = t_{b2}$ ,  $t = (|t_p| + |t_q|)/2$ ) composed of the ET dimer, which is encircled by an ellipsoid in (a) and represented by closed circles in (b).<sup>305</sup>

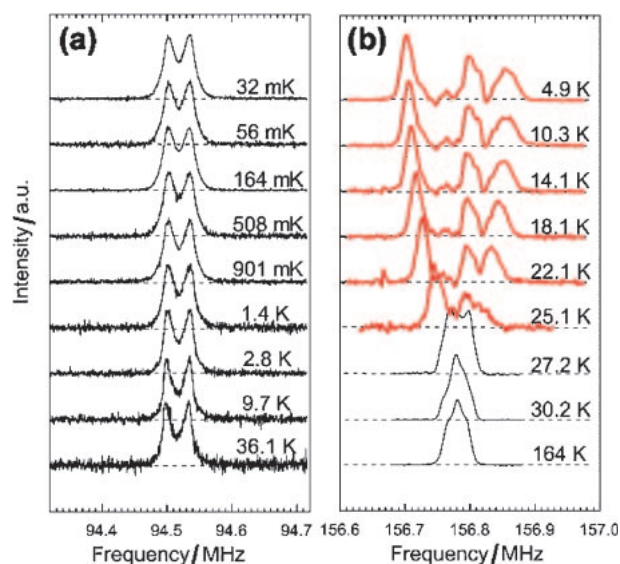


Fig. 73. Line shape of  $^1\text{H}$ NMR of (a)  $\kappa$ -(ET) $_2$ Cu $_2$ (CN) $_3$ <sup>305</sup> and (b)  $\kappa$ -(ET) $_2$ Cu[N(CN) $_2$ ]Cl.<sup>606</sup>

the next section, in connection with the significant spin frustration arising from its spin-lattice geometry.

**3.6.3 Electronic Anisotropy and Spin Ordering:**  $\kappa$ -(ET) $_2$ Cu $_2$ (CN) $_3$  (**6**) has been known to exhibit a variety of physical properties by inclusion of a very small amount of Cu $^{2+}$ , [N(CN) $_2$ ] $^{1-}$ , or other species depending on the preparation conditions as described in section 3.5.5.<sup>303–305,485–493</sup> However, the electrooxidation of ET molecules using supporting electrolytes, KCN, CuCN, and 18-crown-6 ether exclusively provides pure **6** as black plates, as confirmed by the X-ray structural analysis,<sup>491,504</sup> and EPR<sup>491</sup> and Raman spectra.<sup>493</sup> Figure 72 shows the donor packing of **6**, where an ET dimer is a unit with  $S = 1/2$  spin to form the triangular lattice with two kinds of transfer integrals,  $t = (|t_p| + |t_q|)/2$  and  $t' = t_{b2}/2$ .<sup>604,605</sup>

Figure 73 compares the line shape of the  $^1\text{H}$ NMR absorption of **6**<sup>305</sup> and  $\kappa$ -(ET) $_2$ Cu[N(CN) $_2$ ]Cl (**5**).<sup>606</sup> The latter salt exhibited a broadening of the absorption band below 30 K and a drastic change was observed below 27 K. The broadening and splitting of the band below 27 K are ascribed to the local magnetic field by the formation of 3D antiferromagnetic ordering. On the other hand, the absorption band of **6** remains almost invariant down to 32 mK.



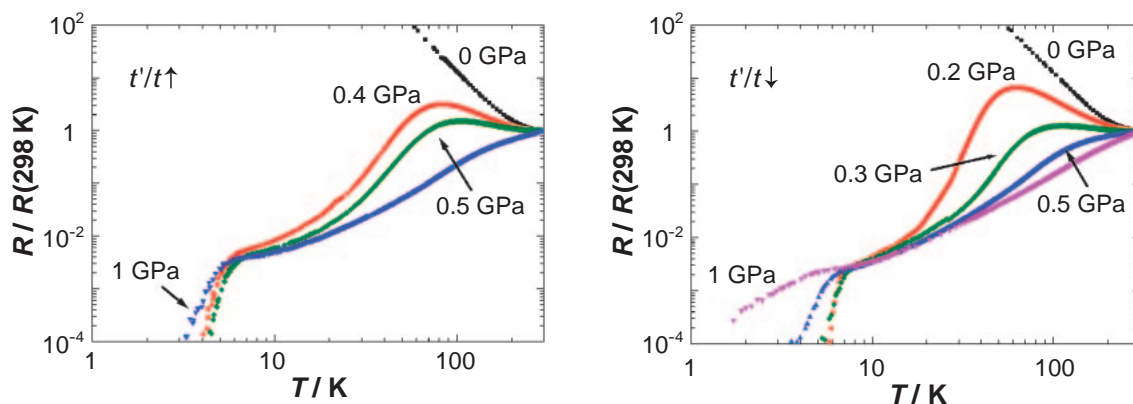


Fig. 74. Temperature dependence of resistance of  $\kappa$ -(ET) $_2$ Cu $_2$ (CN) $_3$  by uni-axial strain epoxy-method along the  $b$ - (left,  $t'/t$  increases) and  $c$ -axes (right,  $t'/t$  decreases).<sup>557</sup>

The appearance of the non-spin-ordered (spin-liquid) state in **6** can be explained in terms of the spin geometry of  $\kappa$ -(ET) $_2$ X salts, which forms an anisotropic triangular lattice with varied  $t'/t$  (Table 17). Although the Mott insulators **5** and deuterated **4** have nearly the same  $W/U_{\text{eff}}$  as that of **6**, the less frustrated spins in **5** ( $t'/t \approx 0.75$ ) and D-salt of **4** ( $t'/t = 0.68$  for the H-salt) can lead to an antiferromagnetic state. On the other hand, since the spin frustration is very significant in **6** ( $t'/t = 1.06$ ), the formation of the antiferromagnetic and superconducting states are suppressed at ambient pressure. Then the salt **6** forms the unprecedented spin-liquid state, which can be placed in Fig. 56 by adding another axis  $t'/t$  besides  $U/W$ .

In summary, the Mott insulator **6** has a similar electronic structure to those of the 10 K class superconductors (**2–5**), which are poor metals having the “fuzzy metallic state” and reside between good metals and typical Mott insulators, at high temperatures. However, owing to the nearly uniform triangular spin lattice, the salt exhibits a spin-liquid state at ambient pressure, in contrast to the spin-ordered antiferromagnetic state in **5** and D-salt of **4**.

### 3.6.4 Superconducting State Neighboring to Spin Liquid

**State:** Figure 74 shows the pressure dependence of resistance of **6** along the  $b$ - and  $c$ -axes by the uniaxial strain epoxy-method. Along the  $c$ -axis, the salt shows a characteristic semiconductor–metal–superconductor behavior in the pressure range of 0.1–0.4 GPa, and the semiconductor-like region disappears above 0.5 GPa. Along the  $b$ -axis, on the other hand, the semiconductive region remains clearly even at 0.5 GPa. The fact that **6** undergoes a transition from being a Mott insulator to metal even by a weak pressure strongly indicates a marginal  $W/U_{\text{eff}}$  value similar to **5** and deuterated **4** at higher temperatures under ambient pressure.

The uniaxial strains along the  $b$ - and  $c$ -axes result in an increase and decrease in  $t'/t$ , respectively. In both cases it is evident that a superconducting state readily appears since the  $t'/t$  deviates from unity, i.e., the spin frustration is released by the uniaxial strain. It is noteworthy that the appearance of the superconducting state and its  $T_c$ 's are fairly anisotropic.

Figure 75 compares the pressure dependence of on-set  $T_c$  using the uniaxial method with the hydrostatic one, which gives  $T_c(\text{on-set}) = 3.9$  K at  $P_c = 0.06$  GPa.<sup>491</sup> There are

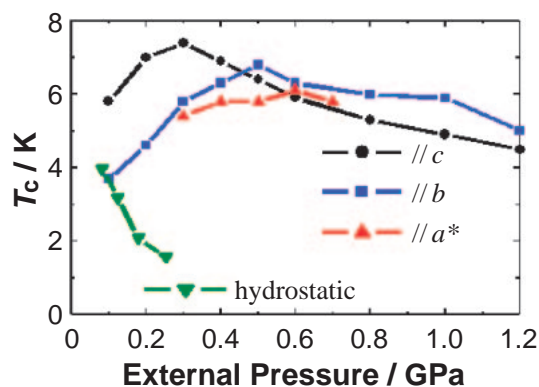


Fig. 75. Pressure dependence of on-set  $T_c$  of  $\kappa$ -(ET) $_2$ Cu $_2$ (CN) $_3$  by the uni-axial strain and hydrostatic pressure methods, where the external pressures are those applied at RT for the former and those subtracted by 0.3 GPa from the value at RT for the latter.<sup>559</sup>

marked differences between them; namely, the uniaxial method affords 1) a much higher  $T_c$  value, 2) an increase of  $T_c$  at the initial pressure region, 3) an anisotropic pressure dependence, and 4) a very slow decay of  $T_c$  by applying high pressure ( $-dT_c/dP = 2.6$  vs  $0.16$  K GPa $^{-1}$ ; however, this result is equivocal since the actual pressure applied on the crystals is not scaled between two methods with different pressure media). Under the uniaxial strain along the  $c$ -axis, the superconducting state appears at  $T_c = 5.8$  K ( $P_c = 0.1$  GPa) and  $T_c$  increases up to 7.2 K (24% increase in  $T_c$ ) at 0.3 GPa. A similar result was obtained along the  $b$ -axis. The superconducting state appears at  $P_c = 0.1$  GPa with  $T_c = 3.8$  K and  $T_c$  increases up to 6.8 K at 0.5 GPa (79% increase in  $T_c$ ). Along the  $a^*$ -axis, which is nearly perpendicular to the ET layer and is expected to be insensitive to the strain, the superconducting state appears above 0.3 GPa with  $T_c = 5.4$  K. The  $P_c$  is notably higher than those in the  $bc$ -plane and the  $T_c$  is not as sensitive to pressure as expected.

The appearance of the superconducting state is interpreted by the increase in  $W/U_{\text{eff}}$  and the deviation of  $t'/t$  from unity. The former effect promotes the delocalization of electrons and the latter reduces the spin frustration. The increase in  $T_c$  in the initial pressure regime might be ascribed to the reduction of

the spin frustration. The following decrease in  $T_c$  in whole measured directions might be explained by the decrease in  $D(\varepsilon_F)$  owing to the increase in  $W$ . It has been known that the transfer integral  $t_p$  is sensitively enhanced by applying pressure in comparison with  $t_{b2}$  for **3**,<sup>607</sup> and similar features are also expected in **6**; therefore, it is reasonable that the maximum of  $T_c$  emerges quickly in the  $c$ -axis since the strain causes greater changes in both  $W/U_{\text{eff}}$  and  $t'/t$  than in the case of  $b$ -axis strain.

A  $T$ - $P$  phase diagram for  $\kappa$ -(ET)<sub>2</sub>Cu<sub>2</sub>(CN)<sub>3</sub> in the low-temperature region is depicted in Fig. 76. An application of uniaxial strain on **6** leads to the anisotropic appearance of the superconducting state with an increase in  $T_c$  in the initial pressure region. An applying pressure can modify  $W/U_{\text{eff}}$ , electron-correlation,  $D(\varepsilon_F)$ , and  $t'/t$  simultaneously. It should be noted that all these effects are highly anisotropic in a system having anisotropic crystal and electronic structures. The appearance of the superconducting state immediately after the release of the

spin frustration in the spin liquid state is an indication of the importance of the magnetic mediation for superconductivity.

### 3.7 Other Superconductors Based on TTF and M(dmit)<sub>2</sub> Derivatives.

Table 18 contains other superconductors besides

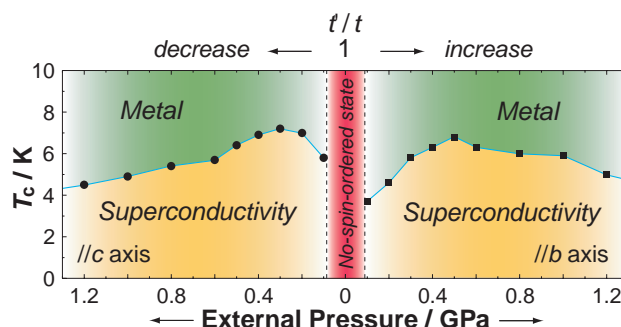


Fig. 76. Temperature-uniaxial pressure phase diagram of  $\kappa$ -(ET)<sub>2</sub>Cu<sub>2</sub>(CN)<sub>3</sub> in the low-temperature region.<sup>570</sup>

Table 18. Other Selected Superconductors Based on TTF, TTP, and M(dmit)<sub>2</sub> Derivatives

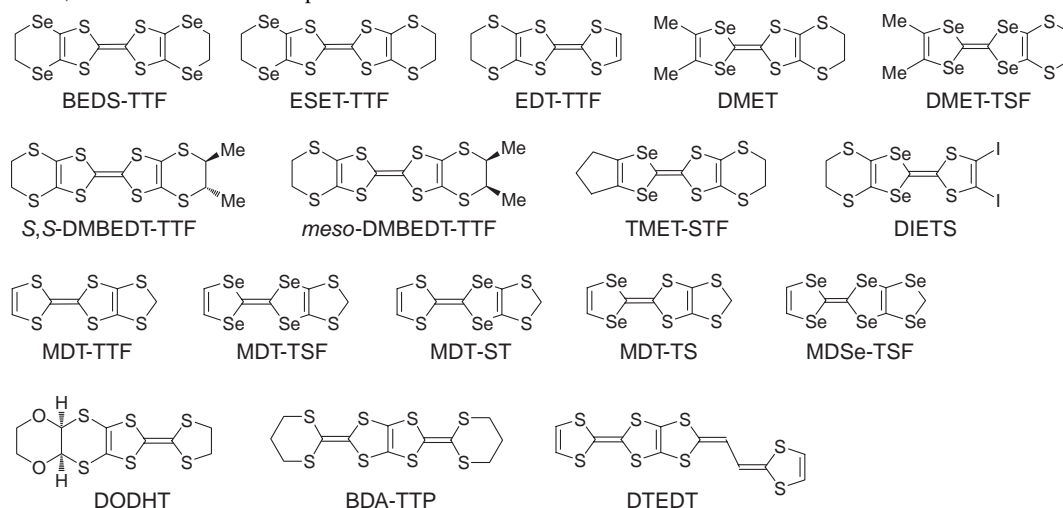
	Anion, <sup>a)</sup> symmetry, ratio, and phase	$\sigma_{RT}$ / S cm <sup>-1</sup>	$T_{\text{max}}$ / K	$P_c$ / GPa	$T_c$ / K	Characteristics <sup>b)</sup>	Ref.
BETS	GaCl <sub>4</sub> , tetrahedral, 2:1, $\lambda$	50	no	0	5.5	mid-point, SdH(100%)	609–613
	FeCl <sub>4</sub> , tetrahedral, 2:1, $\lambda$	—	no	0.3	1.8	mid-point, $T_N = T_{\text{MI}} = 8.3$ K, FISC(33 T)	
	GaBr <sub>4</sub> , tetrahedral, 2:1, $\kappa$	30–50	70	0	1	mid-point	
	FeCl <sub>4</sub> , tetrahedral, 2:1, $\kappa$	—	no	0	0.17	$T_N = 0.45$ K	
	FeBr <sub>4</sub> , tetrahedral, 2:1, $\kappa$	—	60	0	1.1	mid-point, $T_N = 2.5$ K, FISC (12.5 T)	
BEDS-TTF	TiCl <sub>4</sub> , tetrahedral, 2:1, $\kappa$	20	90	0	2.5		614
	Cl <sub>2</sub> TCNQ, planar, 2:1	—	—	0.35	1.3	mid-point	
	Cu[N(CN) <sub>2</sub> ]Br, 2:1, $\kappa$	0.1	no	0.15	7.5		
EDT-TTF	Hg <sub>3-<math>\delta</math></sub> I <sub>8</sub> ( $\delta$ : 0.1–0.2), $\beta$	15	no	0	8.1		616
DMET	I <sub>3</sub> , linear, 2:1, $\beta$	170	—	0	0.47		617,618
	AuI <sub>2</sub> , linear, 2:1, $\beta$	300	40	0.5	0.55	SDW(20 K)	
	IBr <sub>2</sub> , linear, 2:1, $\beta$	210	—	0	0.58		
	Au(CN) <sub>2</sub> , linear, 2:1, $\beta$	2500	25	0.25	1.1	SDW(25 K)	
	AuBr <sub>2</sub> , linear, 2:1, $\beta$	14	150–180	0.15	1.6	SDW(2.8 K)	
	AuBr <sub>2</sub> , linear, 2:1, $\kappa$	200	150	0	1.9	dHvA( $\approx 104\%$ , $6.0m_e$ ; $21\%$ , $3.8m_e$ )	
	AuCl <sub>2</sub> , linear, 2:1, $\beta$	230	—	0	0.83		
	CuCl <sub>2</sub> , linear, 2:1, $\beta$	1250	—	0	0.8		
	AuI <sub>2</sub> , linear, 2:1	—	—	0	0.58	on-set	
	I <sub>3</sub> , linear, 2:1	—	—	0	0.4	on-set	
S,S-DM	ClO <sub>4</sub> , tetrahedral, 2:1, $\kappa$	0.05	75	0.58	2.6	on-set	621
BEDT-TTF	PF <sub>6</sub> , octahedral, 2:1, $\beta$	15	no	0.40	4.3	on-set	622
BEDT-TTF	BF <sub>4</sub> , tetrahedral, 2:1	50	—	0	4.1	on-set	623
TMET-STF	Cu[N(CN) <sub>2</sub> ]Br, 2:1, $\kappa$	—	—	0.32	4.8	on-set	624
ESET-TTF	AuI <sub>2</sub> , linear, 2:1, $\kappa$	20	—	0	4.5	$\gamma = 35$ , $\beta = 16.50$ , Hebel–Slichter peak	625,626
MDT-TSF	AuI <sub>2</sub> , linear, 2:0.88, $\beta$	2000	no	0	4.5	on-set	627,628
	I <sub>3</sub> , linear, 2:0.85, $\beta$	1500	no	0	4.6	mid-point	
MDT-ST	I, 1:1.3, $\beta$	600–1200	no	0	3.6	mid-point	630
	I <sub>2</sub> Br, 1:1.3, $\beta$	400	no	0	3.2	mid-point	
MDT-TS	AuI <sub>2</sub> , linear, 2:0.88, $\beta$	600	no	1.14	4.7	on-set	631
MDS-STS	Br, 2:1, $\kappa$	200–1000	no	0	4	on-set	632
DIETS	Au(CN) <sub>4</sub> , planar, 2:1, $\theta$	5	no	1.0	8.6	on-set	633

Continued on next page.

Continued.

	Anion, <sup>a)</sup> symmetry, ratio, and phase	$\sigma_{RT}$ /S cm <sup>-1</sup>	$T_{max}$ /K	$P_c$ /GPa	$T_c$ /K	Characteristics <sup>b)</sup>	Ref.
DODHT	PF <sub>6</sub> , octahedral, 2:1, $\beta''$	0.92	no	1.65	3.1	on-set	634
	AsF <sub>6</sub> , octahedral, 2:1, $\beta''$	1.2	no	1.65	3.3	on-set	
	BF <sub>4</sub> ·H <sub>2</sub> O, tetrahedral, 2:1, $\beta''$	2.8	no	1.55	3.2	on-set	
DTEDT	Au(CN) <sub>2</sub> , linear, 3:1	15	4	0	4	on-set	636
BDA-TTP	PF <sub>6</sub> , octahedral, 2:1, $\beta$	3.8	—	0	5.9	on-set	637
	AsF <sub>6</sub> , octahedral, 2:1, $\beta$	2.9	160	0	5.8	on-set	
	SbF <sub>6</sub> , octahedral, 2:1, $\beta$	1.5	150	0	7.5	on-set	
	GaCl <sub>4</sub> , tetrahedral, 2:1, $\beta$	53	no	0.76	3.1	on-set, SdH	638
	FeCl <sub>4</sub> , tetrahedral, 2:1, $\beta$	9.4	no	0.63	2	on-set, SdH	639
	TTF, 1:2, $\alpha$	300	—	0.7	1.6	on-set	640
	NMe <sub>4</sub> , 1:2, $\beta$	60	100	0.7	5	on-set	641
Pd(dmit) <sub>2</sub>	EDT-TTF, 1:2, $\alpha$	100	12	0	1.3	on-set, SDW, SdH	
	TTF, 1:2, $\alpha$	800	245	2.2	1.7	on-set	
	TTF, 1:2, $\alpha'$	—	—	2.4	5.93	on-set	642
	NMe <sub>4</sub> , 1:2, $\beta$	30	semi	0.65	6.2	on-set	
	NMe <sub>2</sub> Et <sub>2</sub> , 1:2, $\alpha$	10–80	no	0.24	4	on-set	
	PMe <sub>2</sub> Et <sub>2</sub> , 1:2, $\beta$	10	no	0.70	4	on-set	644

a) NMe<sub>4</sub>: tetramethylammonium, NMe<sub>2</sub>Et<sub>2</sub>: diethyldimethylammonium, PMe<sub>2</sub>Et<sub>2</sub>: diethyldimethylphosphonium. b)  $\gamma$ ,  $\beta$ : see footnote of Table 13, FISC: Field-induced superconductor.



ET, BO, TMTSF, and TMTTF, which are composed of symmetric (BETS and BEDS-TTF) or unsymmetric donors (EDT-TTF, DMET, DMET-TSF, MDT-TTF, MDT-TS, MDT-ST, MDT-TSF, MDSe-TSF, *S,S*-DMBEDT-TTF, *meso*-DMBEDT-TTF, TMT-TSF, ESET-TTF, DIETS, DODHT, and DTEDT) as well as M(dmit)<sub>2</sub>. The  $T_c$ 's of them are less than 10 K. C<sub>60</sub> superconductors are described in section 5. The reported  $T_c$  of most superconductors recently prepared are the on-set temperatures, which are approximately 0.5–1 K higher than the mid-point values.

Compared with the ET salts, the BETS salts have large side-by-side transfer interactions and thus less weak electron correlations for the  $\kappa$ -phase.<sup>608</sup> The BETS superconductors, especially with  $\lambda$ -<sup>609,610</sup> or  $\kappa$ -type packings,<sup>611–613</sup> have been studied in terms of the competition of magnetic ordering and superconductivity, and will be briefly reviewed in section 4.7.

BEDS-TTF gave a rather high  $T_c$  (=7.5 K) under pressure with Cu[N(CN)<sub>2</sub>]Br.<sup>615</sup>

DMET is a hybrid molecule between TMTSF and ET, and

has afforded eight superconductors with linear anion molecules.<sup>617,618</sup> Except for  $\kappa$ -(DMET)<sub>2</sub>AuBr<sub>2</sub>, they have quasi-1D electronic structures like the TMTSF salts and show SDW instability in AuI<sub>2</sub>, Au(CN)<sub>2</sub>, and AuBr<sub>2</sub> salts.  $\kappa$ -(DMET)<sub>2</sub>AuBr<sub>2</sub> has a 2D electronic structure owing to the  $\kappa$ -type donor packing and exhibits dHvA oscillations. The salt exhibits a semiconductive behavior down to 120–180 K, followed by a metallic and then a superconducting transition at ambient pressure.

MDT-TTF gives a  $\kappa$ -type superconductor with the linear anion AuI<sub>2</sub>,  $\kappa$ -(MDT-TTF)<sub>2</sub>AuI<sub>2</sub><sup>625</sup> exhibiting a monotonous decrease in resistivity down to low temperatures with a superconducting transition at 4.5 K. <sup>1</sup>H NMR measurements revealed a Hebel–Slichter coherence peak just below  $T_c$ , indicating a BCS-type gap with *s*-symmetry.<sup>626</sup>

The (tetraalkylammonium)[M(dmit)<sub>2</sub>]<sub>2</sub> system is of *n*-type superconductors, while M(dmit)<sub>2</sub> superconductors with TTF derivatives have two kinds of carriers. <sup>1</sup>H NMR and diffuse X-ray measurements claimed that TTF molecules in (TTF)-[Ni(dmit)<sub>2</sub>]<sub>2</sub>, which is metallic down to 0.49 K at ambient

## Organic/Molecular Electronics (Spinics, Photonics, Ionics, etc.)

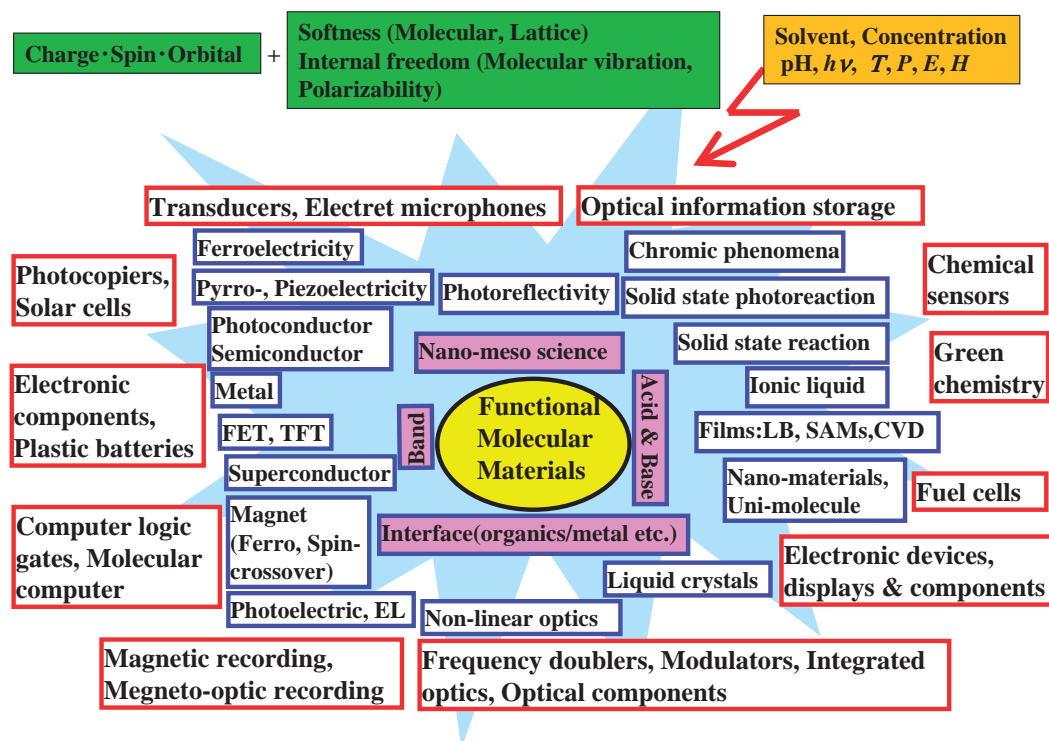


Fig. 77. Future perspectives of organic/molecular electronics. The figure was made based on the proposed one by Cowan and Wiygul<sup>645</sup> and modified by Saito taking into account the recent development of the functional molecular materials. The inorganic functional materials were rapidly developed recently by three main concepts; charge·spin·orbital, while the development of the sophisticated organic/molecular materials need further two concepts; softness and internal freedom as shown in the top of the figure. The advantage of the organic/molecular materials is the high sensitivity to the external stimuli, depicted in yellow area in the top of the figure, compared to the inorganic materials since the intermolecular transfer interactions  $t$  are commonly much smaller than those in the inorganic ones. Consequently, a gigantic and ultra-fast response can be created by small stimuli, though the small  $t$  gives rise to small band, magnetic, optical and thermal parameters. The basic materials, phenomena and concepts are represented in blue squares and the devices, applications and field of study are allocated at the very outside of the figure in red squares.

pressure and becomes superconducting below 1.62 K under 0.7 GPa, have a charge of +0.8.<sup>640</sup> There are many S...S atomic contacts between TTF and Ni(dmit)<sub>2</sub> columns. The band calculation including the HOMO and LUMO of Ni(dmit)<sub>2</sub> indicates a small 2D pocket at around the  $\Gamma$  point, which seems to suppress the Peierls instability. An application of modest pressure extinguishes the pocket, and thus the salt becomes a 1D metal exhibiting CDW instability. In this system, only (EDT-TTF)[Ni(dmit)<sub>2</sub>] is an ambient pressure superconductor,<sup>641</sup> in which the EDT-TTF and Ni(dmit)<sub>2</sub> columns extend along [110] and [010] directions, respectively. However, the degree of CT has not been determined yet.

### 4. Conductors with Other Functionalities

**4.1 Strategy.** In 1986, Cowan et al. described the future perspectives of organic materials for molecular devices.<sup>645</sup> Figure 77 depicts the modified version of organic/molecular electronics including spinics, photonics, ionics, and so on, based on the recent development of materials science.

In this chapter, we describe multi-functional solids as well as liquids that exhibit competitive or cooperative phenomena among the itinerant and/or localized electrons, protons or

molecular ions. These materials are represented by some keywords enclosed by blue squares in Fig. 77. In section 4.2,  $\pi$ -molecular solids concerning the proton-transfer (PT) and charge-transfer (CT) interactions will be described emphasizing the complex isomerization, complexes having simultaneous operation of PT and CT interactions, radical formation, band filling, nucleobase conductors, and ionic conductors based on PT interaction. Carrier doping by electric field, photon, etc. will be mentioned in section 4.3. Conducting films of Langmuir–Blodgett type, self-assembled monolayers, reticulate doped polymer films, and evaporated thin films based on CT complexes will be treated in section 4.4, followed by conducting melts of CT type and conducting CT solids with a low melting point in section 4.5. Conducting properties of ionic liquids are discussed in section 4.6, together with the magnetic behaviors of the conducting and paramagnetic ionic liquids and the preparation of superconducting radical salts using ionic liquids. Section 4.7 includes the magnetic (super)conductors. Non-linear optical properties of intramolecular betainic compounds will be discussed with respect to the intramolecular CT degree in section 4.8.

All of the organic molecules have multi-functional nature

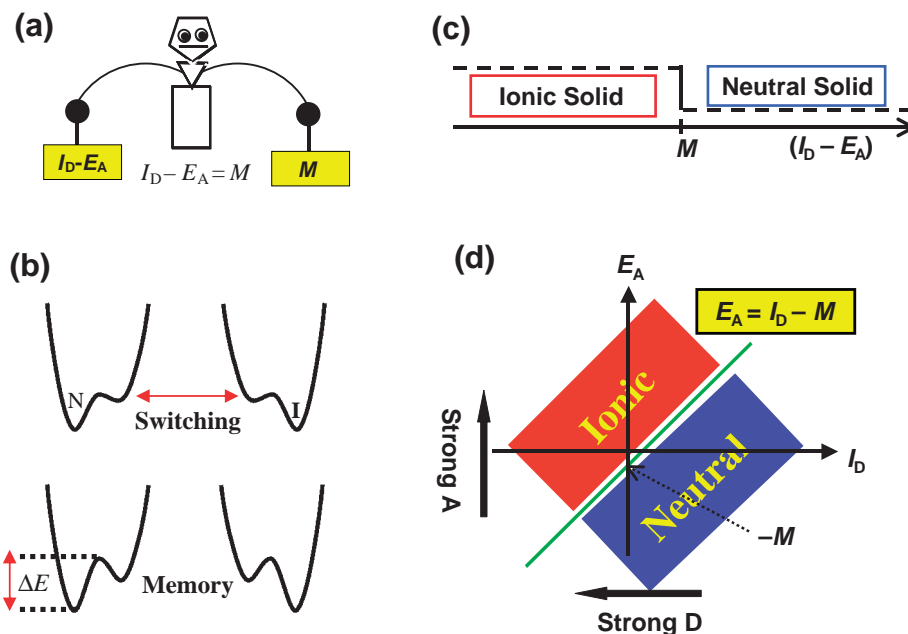


Fig. 78. (a) A schematic balance between ionization energy ( $I_D - E_A$ ) and Madelung cohesive energy  $M$ . (b) Model double minimum potential for the N–I system for switching (upper, potential barrier between stable and metastable states is small and thermally accessible) and memory (lower, potential barrier is rather high  $\Delta E \gg k_B T$ ). 1D (c) and 2D (d) diagrams for searching the boundary zone and functional materials.

and provide plural intermolecular interactions depending on the nature of counter component, morphology (solid, films, uni-molecule, etc.) and external circumstances. For example, the CT interaction between D and A molecules in a solid are broken down into two kinds of interactions; Interaction I: electron transfer from neutral D to A molecules that costs ( $I_D - E_A$ ), and Interaction II: Madelung energy  $M$ , as described in section 3.1.1. The situation is schematically illustrated in Fig. 78. Figure 78a represents the system with double-minimum potential as a balance like the Yajirobe of a Japanese toy (Fig. 78b), where the boundary condition is  $(I_D - E_A) \approx M$ . The condition is experimentally determined by a one-dimensional (Fig. 78c, i.e., Figs. 16–19) or two-dimensional plot (Fig. 78d, i.e., Fig. 15) for the combination of D and A. One can expect that the balance between the interactions I and II can be controlled easily by the external stimuli (solvent polarity, concentration, pH, temperature, pressure, electric field, magnetic field, photon irradiation, and so on). The controllability increases as the system approaches the boundary area. The system shows a variety of phase transitions (i.e., metal  $\leftrightarrow$  insulator, Mott insulator  $\leftrightarrow$  metal, spin-liquid  $\leftrightarrow$  superconductor, and neutral  $\leftrightarrow$  ionic as mentioned in Chap. 3), monotropic (see Table 8) and enantiotropic (see Table 9) complex isomerizations, and switching or memory effect depending on the potential depths and barrier height  $\Delta E$  in Fig. 78b. Also, it shows multiple stoichiometry (see Table 11), polymorphism (see Table 15), or phase transitions in solids (i.e.,  $\alpha$ -(ET) $_2$ I $_3 \rightarrow \alpha_1$ -(ET) $_2$ I $_3$ ,<sup>251</sup> see Table 15) depending on the number of potential minima.

In order to find a system that affords such intriguing phenomena (isomerization, phase transition, polymorphism, bistability, or multi-critical phenomena), one should elucidate the nature of the essential intermolecular interactions governing

the phenomena by breaking down them into the physical parameters, followed by the translation from the physical ones to chemical parameters. Then it is easy to find and develop a system close to the proximity of the boundary zone (see section 6).

**4.2 Proton-Transfer (PT) and Charge-Transfer (CT) Interactions.** Figure 79 shows a family tree of organic  $\pi$ -molecular complexes with component molecules having the ability of PT and/or CT proposed by Saito and Inokuchi.<sup>646</sup> A similar family tree has also been proposed by Herbstein.<sup>150</sup> In Chap. 3 the ionic CT complexes, radical salts and N–I transition in Fig. 79 have been described.

As shown in the next section, PT interactions contribute to the phase transition, radical formation, band filling, ionic conduction, and so on.

**4.2.1 PT, CT, and PT–CT Complex Isomerisation:** Herbstein described in his review<sup>150</sup> that Pfeiffer suggested many years ago<sup>647</sup> that the interaction between the two components in molecular compounds could be considered as an interaction between particular force fields localized in different regions of the component molecules. If more than one type of force field was present in each of the components then isomeric molecular complexes could be obtained depending on which pair of force fields predominated—termed as complex isomerization by Hertel.<sup>648,649</sup>

For example, aniline and its derivatives are bi-functional molecules concerning the charge(electron)-transfer and PT interactions (Fig. 80): anilines have an electron-donating ability as well as proton-accepting ability (Brønsted base). On the other hand, picric acid is a typical organic Brønsted acid and it also acts as an electron acceptor. For PT interaction,  $pK_a$ ,  $pK_b$ , and Coulomb energy are the important parameters, while  $I_D$ ,  $E_A$ , and  $M$  should be taken into account for CT interaction.



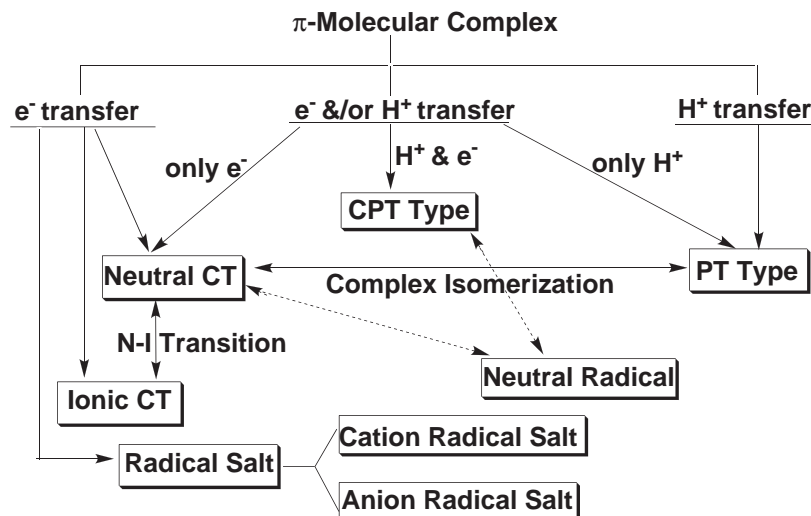


Fig. 79. Family tree of  $\pi$ -molecular complexes based on the charge-transfer and proton-transfer interactions.<sup>646</sup>

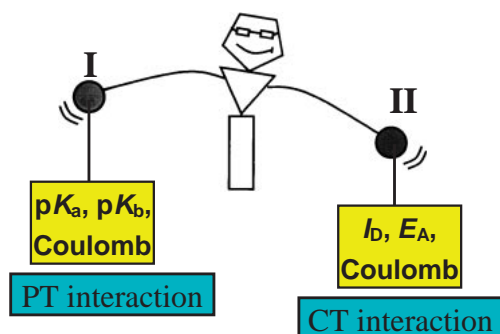
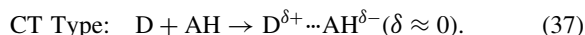
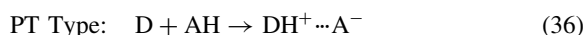


Fig. 80. Schematic figure representing a system with two competing intermolecular interactions I (PT) and II (CT). In PT interaction,  $pK_a$ ,  $pK_b$ , and Coulomb interaction are the main parameters, while in CT interaction,  $I_D$ ,  $E_A$ , and Coulomb interaction (Madelung energy,  $M$ ) are the main parameters.

As early as the 1920s and 1930s, Hertel et al.<sup>648–650</sup> noticed that “Progressive weakening of the acid–base interaction and strengthening of the donor–acceptor interaction should produce binary compounds which range in type from “true phenolates” at one end of the series to “true molecular compounds” at the other. In the intermediate situations, same partners form either phenolates or molecular compounds, depending on ambient conditions”—according to a paper by Herbstein.<sup>150</sup> As a result, the combination of a particular base (D) and acid (AH) affords either a PT complex or a CT complex in a solid (Eqs. 36 and 37).<sup>1,247,648–669</sup>



For example, aniline (D) gives an orange-yellow ionic salt with picric acid (AH), namely anilinium picrate by the PT interaction. The yellowish color is ascribed to the picrate ion ( $A^-$ ) and the salt does not exhibit a free  $NH_2$  stretching mode but rather a broad  $NH_3^+$  mode in the IR spectrum. On the other hand, diphenylamine and picric acid give a red-black solid of CT-type and the free  $NH$  stretching mode is observed in the IR

spectrum. The UV–vis and IR spectra easily distinguish the two kinds of  $\pi$ -molecular complexes, PT and CT complexes. Since picric acid is too weak an electron acceptor to withdraw an electron from the HOMO of aniline derivatives, the CT complexes based on picric acid are classified as neutral CT complexes ( $\delta \approx 0$ ) in Fig. 79.

In accordance with Hertel’s concept, we have found that in the molecular complexes between aromatic amines and picric acid ( $pK_a = 0.96$ ), both CT and PT interactions compete with each other and the complexes are clearly divided into two types in a solid<sup>1,247</sup> depending on the difference of their acidities:  $\Delta pK_a = [pK_a - (14 - pK_b)]$  as shown in Fig. 81-①.<sup>1,247,649</sup> Similarly, the complexes with 2,4-dinitrophenol ( $pK_a = 4.09$ ) and with 2,6-dinitrophenol ( $pK_a = 3.58$ ) have clearly been divided as shown in Figs. 81-②, and 81-③, respectively.<sup>1,649,661</sup> The figure demonstrates that a critical value of  $\Delta pK_a$  for the boundary between the PT and CT types lies in the range of Eq. 38:

$$-1 \leq \Delta pK_a \leq 1. \quad (38)$$

The CT complexes are afforded exclusively when  $\Delta pK_a$  is larger than the critical value, while the PT complexes are obtained when  $\Delta pK_a$  is less than the critical value. This observation indicates that the Brønsted acid–base interaction dominates over the CT interaction. A similar situation has also been observed by Johnson et al. in the combination of a variety of pyridines (pyridine, collidine, and lutidine)–benzoic acids (dimethyl, chloro, nitro, dinitro, and so on) complexes, where the critical value of  $\Delta pK_a$  is ca.  $-3.7$ .<sup>657</sup>

Several complexes near the boundary region of Eq. 38 have been known to show enantiotropic (Eq. 39) or monotropic (Eq. 40) complex isomerization as suggested by Hertel et al.<sup>648,649,651,652</sup> and Pfeiffer<sup>647</sup> prior to the birth of the Mulliken CT theory. Later, Briegleb et al. elucidated spectroscopically such an isomerization.<sup>655,656</sup> Hertel et al. studied the crystal structures of both types of 4-bromo-1-naphthylamine·2,6-dinitrophenol monotropic complexes.<sup>651</sup> Carstensen–Oeser et al. and Bernstein et al. studied structural aspects of the CT isomer of 1-bromo-2-naphthylamine·picric acid<sup>658</sup> and Kofler’s ternary complex (pyridinium·1-naphthylamine·picrate),<sup>672</sup> respectively.

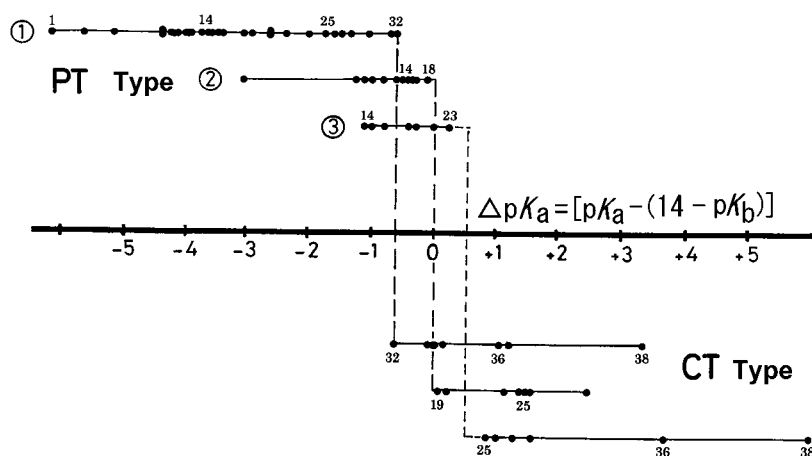
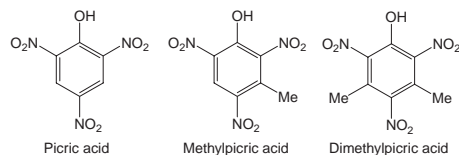


Fig. 81. Complexes between aromatic amines (1–38) and ① picric acid ( $pK_a = 0.96$ ), ② 2,4-dinitrophenol ( $pK_a = 4.09$ ), or ③ 2,6-dinitrophenol ( $pK_a = 3.58$ ). Complexes of PT type and of CT type are plotted above and below the horizontal line, respectively. Some aromatic amines are 1: *N,N*-diethyl-*m*-toluidine, 14: aniline, 18: *m*-anisidine, 19: *p*-chloroaniline, 23: *m*-chloroaniline, 25: *o*-chloroaniline, 32: 2,5-dichloroaniline, 36: skatole, 38: indole.<sup>1</sup>

Table 19. Selected Examples of Enantiotropic PT-CT Complex Isomers

Electron donor (Proton acceptor)	Electron acceptor (Proton donor)	$\Delta pK_a$	$T_{PT \leftrightarrow CT}$ /°C	$T_m$ / °C	$\Delta H$ / kcal mol <sup>-1</sup>	Ref.
<i>o</i> -Bromoaniline	picric acid	-1.59	103–110	128	6.7	648,669
<i>o</i> -Iodoaniline	picric acid	-1.64	100–107	112	6.2	649,655,669
2,5-Dichloroaniline	picric acid	-0.61	74	87	4.2	668
1-Chloro-2-naphthylamine	picric acid		128–138	174	8.0	649,669
4-Chloro-1-naphthylamine	2,6-dinitrophenol		76	80		649
<i>o</i> -Chloroaniline	1,3,5-trinitro- benzoic acid	-2.06	ca. 133		2.2	667



Saito, Matsunaga, and co-workers extended the CT–PT competing system using aromatic amines and diamines as proton acceptor molecules and polynitrophenols (picric acid, methylpicric acid, dimethylpicric acid), 3,3',5,5'-tetranitro-4,4'-biphenyldiol ( $H_2TNBP$ ) and benzoic acids (2,4,6-trinitrobenzoic acid, 3,5-dinitrobenzoic acid) as proton donor molecules.<sup>247,659–669,671</sup> For example, 2,5-dichloroaniline and picric acid afforded a yellow solid (PT type) at RT that was transformed to a red solid (CT type) by heating at 74 °C reversibly (Fig. 81-①, 32).<sup>668</sup> When chloroform was employed as the solvent and the mixture was kept in a refrigerator for a few days, the 1:1 yellow salt transformed to a 1:3 red CT solid. Table 19 summarizes selected examples of enantiotropic 1:1 PT–CT complex isomers, where  $T_{PT \leftrightarrow CT}$  and  $\Delta H$  are the transition temperature and phase-transition enthalpy, respectively. The low- and high-temperature phases are PT and CT types, respectively, and in general the transition is not sharp.

The combination of 3,3'-dimethoxybenzidine and  $H_2TNBP$  afforded both a 1:1 CT complex (black) and 1:1 PT complex (orange) simultaneously, which is monotropic complex iso-

merization.<sup>664</sup> The two kinds of complexes were separated under a microscope and Figure 82 shows their IR and UV–vis spectra. The PT complex (a) exhibited a broad  $NH_3^+$  stretching mode near 2500  $cm^{-1}$  and an absorption band at  $23 \times 10^3 cm^{-1}$  characteristic of deprotonated  $H_2TNBP$ , namely  $HTNBP^{1-}$ . On the other hand, the CT complex (b) exhibited free  $NH_2$  stretching modes at around 3500  $cm^{-1}$  and a CT band at  $15 \times 10^3 cm^{-1}$ . Selected monotropic PT–CT complex isomers are summarized in Table 20.

Summarizing the above, CT and PT interactions compete with each other in the molecular complexes composed of aromatic amines and polynitrophenols. The PT-type solid is predominantly produced for  $\Delta pK_a < -1$ , while the CT one is for  $\Delta pK_a > 1$ , indicating that the parameters in the PT interaction ( $pK_a$  and  $pK_b$ ) are very convenient to predict the type of solid. Enantiotropic or monotropic complexes are produced near the boundary region ( $-1 < \Delta pK_a < 1$ ) depending on the solvent, temperature, concentration, and so on.

**4.2.2 CPT Type and Amino Acid Complex:** In several complexes, a simultaneous operation of CT and PT interac-

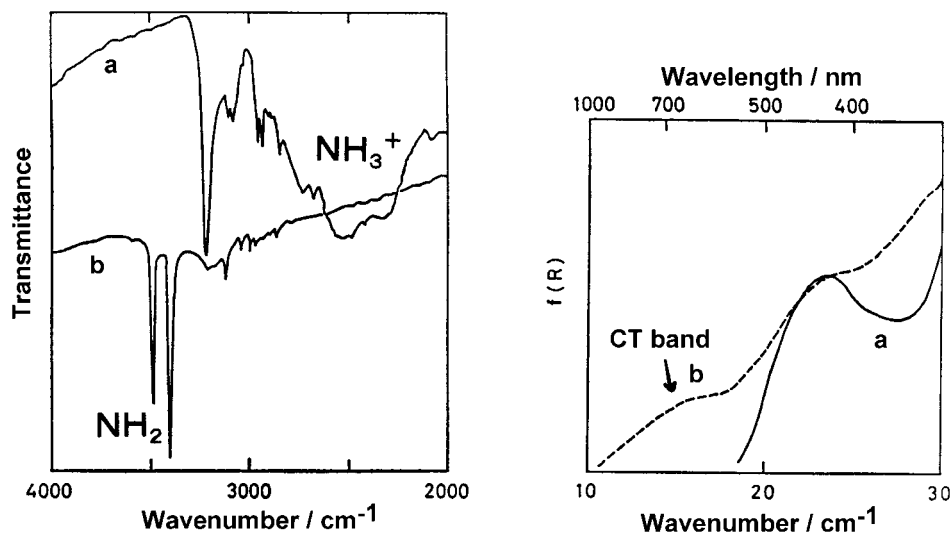


Fig. 82. IR spectra (left, hexachlorobutadiene) and UV-vis spectra (right, KBr) of the PT (a) and CT (b) type complexes of 3,3'-dimethoxybenzidine and 3,3',5,5'-tetranitro-4,4'-biphenyldiol.<sup>664</sup>

Table 20. Selected Examples of Monotropic PT-CT Complex Isomers

Electron donor (Proton acceptor)	Electron acceptor (Proton donor)	$T_m/^\circ\text{C}$	Ref.
<i>o</i> -Bromoaniline	methylpicric acid	PT type: 102–103, CT type: 74–75	665
4-Bromo-1-naphthylamine	2,6-dinitrophenol	PT type: 91.5, CT type: 84.5	651
3,3'-Dimethoxybenzidine	3,3',5,5'-tetranitro-4,4'-biphenyldiol (H <sub>2</sub> TNBP)	PT type: gradually changes to CT type above 244 °C CT type: 250 (dec.)	664

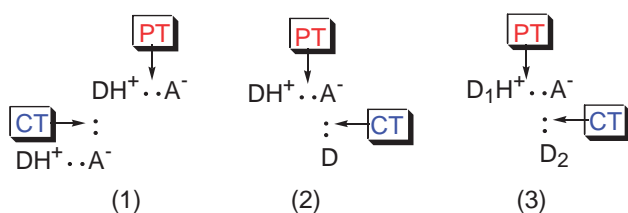


Fig. 83. Three kinds of CPT type complexes.

tions is possible as schematically illustrated in Fig. 83. These complexes are denoted as CPT type by Saito and Matsunaga<sup>662</sup> and are usually composed of the aromatic amines having a large  $\pi$ -moiety or amino acids. Figure 83 illustrates three kinds of CPT type and Table 21 summarizes selected examples for each type. It should be noted that the anion of acceptor molecule  $A^-$  acts as an electron rich species; namely, an electron donor in solution or gas, while the deprotonated Brønsted acid acts as an electron acceptor in solids. For example, the excess charge on the phenolate oxygen does not delocalize but is fixed by the nearby counter cation. Therefore, alkaline salts of picric acid have almost the same electron-accepting ability as *s*-trinitrobenzene (TNB),<sup>660</sup> contrary to the MO calculation, which predicts that the picrate molecule is an electron donor.<sup>670</sup>

(1) An electron donor (=proton acceptor) D and an electron acceptor (proton donor) AH form a complex by the PT interaction,  $DH^+ \cdots A^-$ , and in addition some part of the  $DH^+$  moiety shows CT interaction with the neighboring  $A^-$  part. This kind of CPT complex was obtained for *N,N,N',N'*-tetramethyl-

benzidine,<sup>662</sup> 3,3'-dimethylbenzidine,<sup>662</sup> tryptophan,<sup>663,670,674</sup> serotonin,<sup>670,673</sup> etc. In the case of benzidine ( $H_2N-\phi-\phi-NH_2$ ) derivatives, the donor ability of  $DH^+$  ( $H_2N-\phi-\phi-NH_3^+$ ) is considerably reduced compared with that of free benzidine. As a result, the complex is lightly colored and the CT band appears at a wavelength shorter than that expected for the benzidine·TNB complex. On the other hand, the protonated serotonin and tryptophan have nearly the same electron donor ability as those of the non-protonated molecules, and the CPT complexes exhibit CT bands similar to that of indole·picric acid. Figure 84 shows the crystal structure of serotonin·picrate·H<sub>2</sub>O by Thewald and Bugg.<sup>673</sup> The crystal structures of tryptamine·picrate and tryptophan·picrate·methanol were reported by Gartland et al.,<sup>674</sup> and the polarized reflection spectra of the picrate salts of tryptophan, serotonin, nicotinamide, and tryptamine were studied by Tanaka.<sup>670</sup>

(2) Free D molecules form CT interactions with the  $A^-$  part in the PT complex  $DH^+ \cdots A^-$  resulting in a 2:1 complex. Since the free D molecule is the electron donor, the CT band appears nearly at the same energy as that of the  $D \cdot TNB$  complex. Several examples have been found between aromatic amines and polynitrophenols (Table 21).<sup>654,659,662,664</sup>

(3) The second donor molecule ( $D_2$ ) forms a CT interaction with the  $A^-$  part in the PT complex of  $DH^+ \cdots A^-$  resulting in a 1:1:1 ternary complex. In Kofler's ternary complex of pyridine·1-naphthylamine·picric acid,<sup>654,659,672</sup> pyridine is a stronger base than 1-naphthylamine, and therefore, forms pyridinium picrate (yellowish orange). Then, the picrate ion acts as an electron acceptor to form the CT interaction with 1-naph-

Table 21. Selected Examples of CPT Complexes

	Electron donor (Proton acceptor)	Electron acceptor (Proton donor)	Ratio	Color	Ref.
(1)	<i>N,N,N',N'</i> -Tetramethylbenzidine	picric acid	1:1	yellow brown	662
	3,3'-Dimethylbenzidine	picric acid	1:1	red	662
	Tryptophan	picric acid	1:1	red	663,670,674
(2)	1-Naphthylamine	picric acid	2:1	red	654,659
	Benzidine	picric acid	2:1	black	662
	<i>o</i> -Anisidine	H <sub>2</sub> TNBP	5:1	red	664
(3)	Pyridine + 1-naphthylamine	picric acid	1:1:1	red	664,659,672

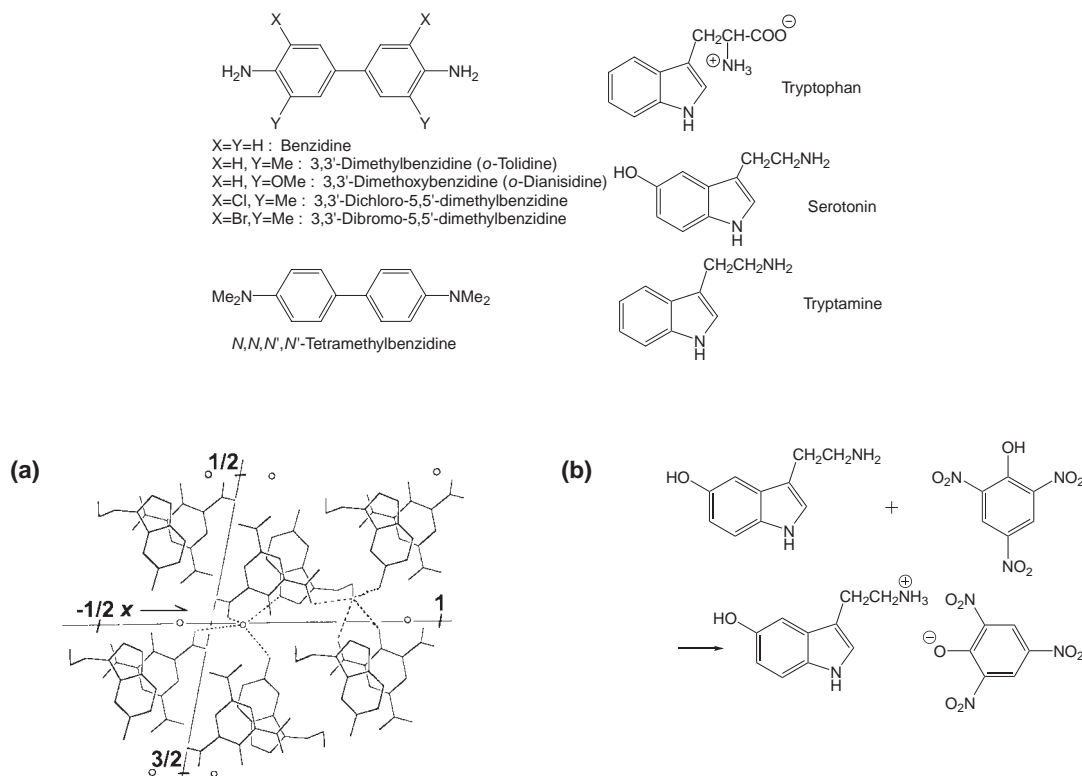


Fig. 84. (a) Crystal structure and (b) chemical reaction of CPT complex, serotonin·picrate·H<sub>2</sub>O (red) by Thewald and Bugg.<sup>673</sup> Monoclinic, *P*<sub>2</sub><sub>1</sub>/*c*, *a* = 14.172(3), *b* = 6.908(2), *c* = 18.749(3) Å, β = 101.65(2)°, *V* = 1797.7 Å<sup>3</sup>, *Z* = 4, *R* = 0.073. The red color of the crystal is due to the CT transition from the π-moiety of serotonin to the trinitrobenzene moiety of picrate.

thylamine resulting in a red CT ternary complex.

In summary, a simultaneous operation of CT and PT interactions within a molecular complex is possible and such a complex is denoted as CPT type. Three kinds of CPT type have been prepared between aromatic amines having a large π-moiety or amino acids and polynitrophenols.

**4.2.3 PT Type and Cation Radical Salt:** 3,3'-Dibromo-5,5'-dimethylbenzidine afforded an orange PT complex (1:1, a in Fig. 85) with picric acid from benzene.<sup>662</sup> The PT complex exhibited a broad absorption band at around 27–28 × 10<sup>3</sup> cm<sup>-1</sup> originating from the intramolecular transition of picrate. The IR spectrum of the PT complex exhibited both NH<sub>2</sub> and NH<sub>3</sub><sup>+</sup> stretching modes, indicating that one of the amino groups of the benzidine molecule was protonated. On the other hand, only a black 1:1 neutral CT complex (b in Fig. 85) was obtained from chloroform. The CT band is observed at

18–20 × 10<sup>3</sup> cm<sup>-1</sup>. The IR spectrum of the CT complex did not show the NH<sub>3</sub><sup>+</sup> stretching mode in the region of 2500–2800 cm<sup>-1</sup>. Therefore, this combination is another example of a monotropic complex isomer. Interestingly, the black CT complex changed to a green solid by prolonged storage in air (c in Fig. 85).<sup>675</sup> The green solid exhibited a strong absorption band in the IR region below 5 × 10<sup>3</sup> cm<sup>-1</sup> (Band A), which hid the NH<sub>2</sub> or NH<sub>3</sub><sup>+</sup> band. The Band A is ascribed to an electronic transition either in the partially charged state (intraband transition for a metal, see section 3.1.4 and Figs. 18 and 19) or in the charge-separated state, which is equal to charge-ordered or charge disproportionated state (Eq. 41).



These optical spectra indicate that the neutral CT complex

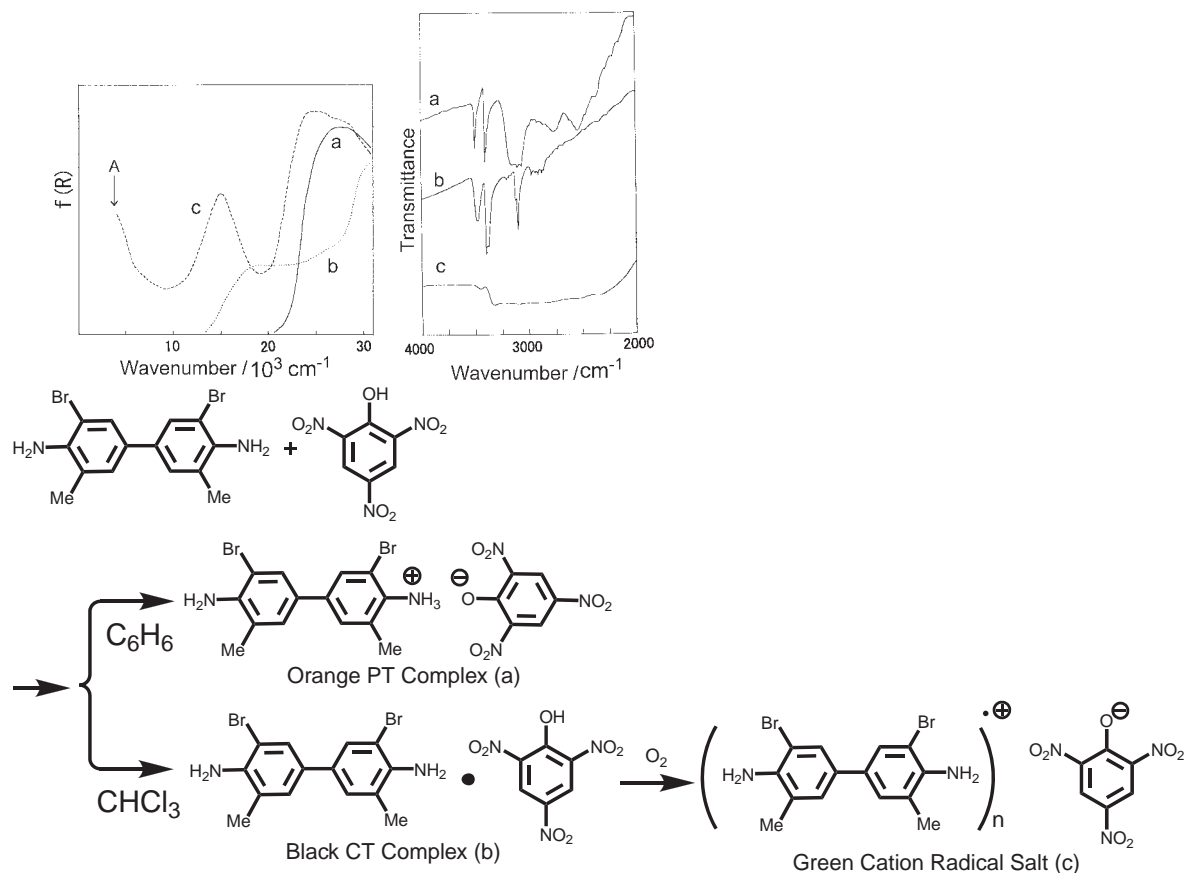
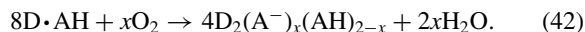


Fig. 85. UV-vis (left, KBr) and IR (right, hexachlorobutadiene) spectra of the complexes composed of 3,3'-dibromo-5,5'-dimethylbenzidine and picric acid. (a) 1:1 orange PT complex from benzene, (b) 1:1 black CT complex from chloroform, and (c) green cation radical salt obtained by air oxidation of (b).<sup>675</sup> The arrow in the UV-vis spectra indicates the Band A. The scheme below the figure illustrates the chemical reactions between 3,3'-dibromo-5,5'-dimethylbenzidine and picric acid followed by air oxidation.

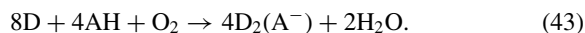
$\text{D}\cdot\text{AH}$  was changed to the cation radical salt  $\text{D}_2(\text{A}^-)_x(\text{AH})_{2-x}$  as in Eq. 42, where the cation radical of 3,3'-dibromo-5,5'-dimethylbenzidine has a partial CT state and the counter anion is the picrate as formulated in the chemical equation below Fig. 85. The content of picrate  $x$  in Eq. 42 increases with time in the month scale. Similarly, the black CT complex (b) was converted to a green cation radical salt (c) during the recrystallization from ethanol. The black CT complex is an insulator ( $\sigma_{\text{RT}} < 10^{-8} \text{ S cm}^{-1}$ ) while the green solid from ethanol is conductive ( $10^{-2}$ – $10^{-3} \text{ S cm}^{-1}$ , compressed pellet).



The complex formation of the 3,3'-dichloro-5,5'-dimethylbenzidine with picric acid in ethanol afforded a yellow 1:1 PT solid,<sup>662</sup> while prolonged boiling in ethanol in open air directly afforded the green cation radical salt of the 3,3'-dichloro-5,5'-dimethylbenzidine with the picrate anion ( $\sigma_{\text{RT}} \approx 10^{-3} \text{ S cm}^{-1}$ , compressed pellet).<sup>675</sup>

This kind of cation radical conductor  $\text{D}_2(\text{A}^-)$  produced by the mixing D and Brønsted acid AH, as in Eq. 43, has also been afforded in the combination of ET, BO, or HMTTeF with anilinic acid (2,5-dihydroxy-*p*-benzoquinone) derivatives (see Fig 14, ET·cyanilic acid,<sup>292,676,677</sup> BO·chloranilic acid,<sup>234</sup> HMTTeF·bromanilic acid,<sup>236–238</sup> and HMTTeF·chloranilic acid<sup>236–238</sup>) by losing proton(s) during the complex formation.

All of them are highly conductive even in the pellet form. It is probable that the formation of the metallic LB films based on BO and carboxylic acid (see section 4.4.1.3) is based on the same mechanism.



In summary, CT complexes of aromatic diamine and picric acid can be converted to conductive cation radical salts of picrate by air oxidation both in the solid state and in solution. Similarly, cation radical conductors  $\text{D}_2(\text{A}^-)$  based on a Brønsted acid AH (mainly anilinic acid derivatives) have been obtained by mixing D and AH in solution in open air.

**4.2.4 Band Filling Control by PT: Cation Radical Formation with 3,3',5,5'-Tetranitro-4,4'-biphenyldiol Dianion ( $\text{TNBP}^{2-}$ ):** In the preparation of cation radical salts, some deprotonated organic Brønsted acids have been incorporated as counter anion molecules by the electrochemical oxidation of donor molecules in the presence of the alkaline or tetraalkylammonium salt of each anion molecule such as oxalate, acetate, maleate, fumarate, and tosylate by Kathirgamanathan, Rosseinsky, and Muckeljohn<sup>678</sup> and cyanoforn ( $\text{CF}^-$ ) by Argonne group<sup>679</sup> and Saito's group.<sup>234,680,681</sup> Other organic anions employed in Saito's group for the preparation of conductors by electrocrystallization are depicted below in Table 22 and are 1,1,3,3-tetracyanoallyl anion derivatives ( $\text{TCA}^-$ , RO-



Table 22. Selected Metallic Cation Radical Salts Composed of Organic Counter Anion Molecules (see also Tables 11, 12, and 15 for ET•TNBP (4:1), BO•HCTMM (5:1:(PhCN)<sub>2</sub>, 4:1:(TCE)<sub>2</sub>, and ET•SF<sub>5</sub>CH<sub>2</sub>CF<sub>2</sub>SO<sub>3</sub>(2:1))

Donor	Anion	Composition D:X:(solv)	$\sigma_{RT}$ /S cm <sup>-1</sup>	$T_{MI}$ /K	Ref.
BO	CF <sup>-</sup>	10:4:3H <sub>2</sub> O	$1.1 \times 10^2$	<1.3	234
BO	PCA <sup>-</sup>	8:4:1H <sub>2</sub> O	$3.3 \times 10$	16	234
BO	MeO-TCA <sup>-</sup>	9:4:5H <sub>2</sub> O	$10^2$	—	684
BO	EtO-TCA <sup>-</sup>	2:1	10	ca. 150, metallic < 40 K	684
		2:1:0.75(H <sub>2</sub> O)	30	ca. 180	681
BO	BuO-TCA <sup>-</sup>	5:2:0.5THF	7	—	684
BO	CM-TCA <sup>-</sup>	5:2:2CH <sub>3</sub> CN	$5.0 \times 10$	—	684
BO	PiO <sup>-</sup>	6:3:1TCE	$2 \times 10^2$	<1.4	234
BO	SQA <sup>2-</sup>	4:1:6H <sub>2</sub> O	$1.7 \times 10^2$	<1.4	234
BO	DHCP <sup>2-</sup>	5:1:2THF	$10^2$	<8	684,690
BO	TNBP <sup>2-</sup>	3:1:2H <sub>2</sub> O	$3.0 \times 10$	<4.2	692
ET	CF <sup>-</sup>	2:1	5	ca. 180	679,680
ET	MeO-TCA <sup>-</sup>	2:1 ( $\beta''$ )	$1.2 \times 10^2$	<2.5	290
ET	MeS-TCA <sup>-</sup>	2:1	$1.0 \times 10^2$	<2.5	291
ET	MeNH-TCA <sup>-</sup>	2:1	$8 \times 10$	<2.5	291
ET	PiO <sup>-</sup>	3:2:xH <sub>2</sub> O	$1.6 \times 10$	ca. 100–150	693
ET	DHCP <sup>2-</sup>	4:1:xTHF( $x \approx 2$ )	$10\text{--}10^2$	180	690
ET	DHCP <sup>2-</sup>	4:1:xTHF( $x \approx 2$ )	$10\text{--}10^2$	<1.3	690
EDT-TTF	DHCP <sup>2-</sup>	unknown	$10^2$	—	690
BVDT-TTF	DHCP <sup>2-</sup>	unknown	$10^2$	—	690

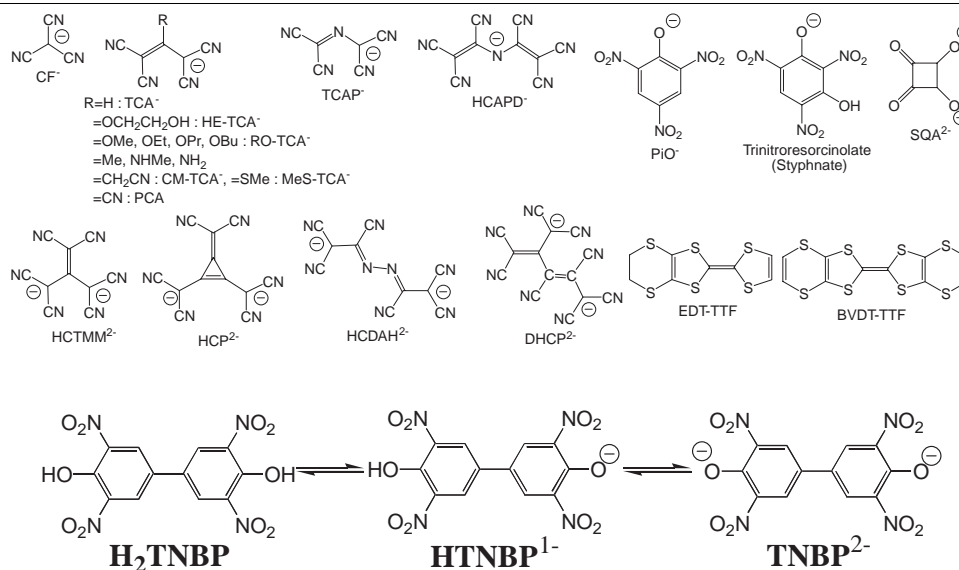


Chart 9.

TCA<sup>-</sup> (see Table 12)),<sup>290,291,681–685</sup> tetracyano-2-aza-2-propen-1-ide (TCAP<sup>-</sup>),<sup>685</sup> pentacyanoallyl anion (PCA<sup>-</sup>),<sup>234,680,685,686</sup> hexacyanotrimethylenemethanide (1,1,3,3-tetracyano-2-(dicyanomethylene)propane, HCTMM<sup>2-</sup>),<sup>234,680,685</sup> 1,1,2,5,6,6-hexacyano-3,4-diaza-2,4-hexadiene-1,6-diide (HCDAH<sup>2-</sup>),<sup>687,688</sup> 2-(dicyanomethylene)-1,1,3,4,5,5-hexacyano-3-pentene-1,5-diide (DHCP<sup>2-</sup>),<sup>234</sup> 3-(dicyanomethylene)cyclopropene-1,2-diylbis(dicyanomethanide) (HCP<sup>2-</sup>),<sup>234</sup> 1,1,2,4,5,5-hexacyano-3-aza-1,4-pentadien-3-ide (HCPAD<sup>-</sup>),<sup>293</sup> squarate (SQA<sup>2-</sup>),<sup>234</sup> picrate (PiO<sup>-</sup> (see Table 12)),<sup>234,295,691</sup> trinitroresorcinolate (styphnate<sup>-</sup>),<sup>293,691</sup> and tetranitrobiphenolate (3,3',5,5'-tetranitrobiphenyl-4,4'-diolate, TNBP<sup>2-</sup>).<sup>266,295,692</sup> Some selected metallic salts are summarized in Table 22.

In the system of the cation radical salt with a deprotonated

Brønsted acid, the precise determination of the composition and the characterization of the anion species are crucial for the understanding of the physical properties.

H<sub>2</sub>TNBP is a proton donor forming the monoanion HTNBP<sup>-</sup> and dianion TNBP<sup>2-</sup> ( $pK_{a1} = 1.92$ ,  $pK_{a2} = 4.7$  in acetone: water = 2:1) (Chart 9). Nishimura, Saito, et al. obtained two kinds of ET cation radical salts by the electrooxidation of ET molecules in the presence of (TBA)<sub>2</sub>TNBP, a 4:1 metallic complex and 2:1 semiconductive one (Table 11).<sup>266</sup> The chemical formula of the 4:1 salt was deduced to be (ET<sup>0.5+</sup>)<sub>4</sub>(TNBP<sup>2-</sup>) based on the elemental analysis, X-ray structural analysis (Fig. 86), appearance of the optical band characteristic of the partial charged state of ET molecules (Band A in Fig. 87), magnetic susceptibility, and <sup>13</sup>C CP/MAS NMR (Fig. 88).

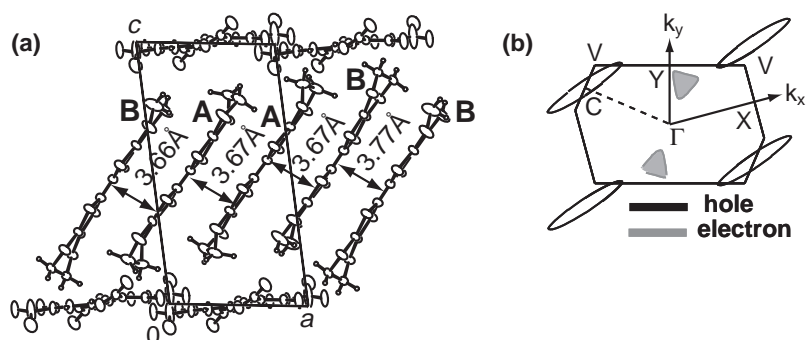


Fig. 86. (a) Crystal structure of  $(\text{ET})_4(\text{TNBP})$ . Triclinic,  $P\bar{1}$ ,  $a = 8.691(1)$ ,  $b = 12.936(1)$ ,  $c = 16.208(2)$  Å,  $\alpha = 97.376(9)$ ,  $\beta = 96.234(9)$ ,  $\gamma = 103.888(9)^\circ$ ,  $V = 1735.9(3)$  Å<sup>3</sup>,  $Z = 1$ ,  $R = 0.0656$ . A and B represent two crystallographically independent ET molecules and the numbers are interplanar distances. The 2D conducting layer of ET molecules in the  $ab$ -plane is sandwiched by the  $\text{TNBP}^{2-}$  anion molecules along the  $c$ -axis. (b) The calculated Fermi surfaces.<sup>266</sup>

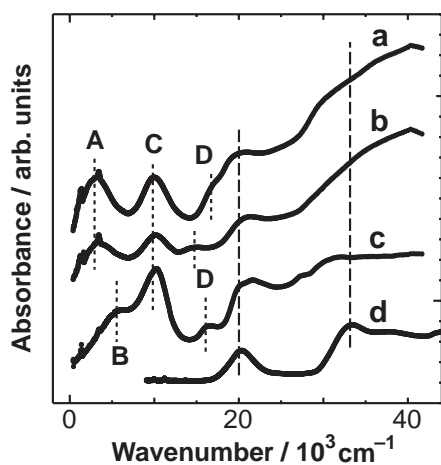


Fig. 87. Absorption spectra of (a)  $(\text{ET})_4(\text{TNBP})$ , (b)  $(\text{ET})_2$ -(HTNBP), and (c)  $\text{ET}\cdot\text{Br}$  in KBr and, (d)  $(\text{TBA})_2(\text{TNBP})$  in  $\text{CH}_3\text{CN}$ .<sup>266</sup> Band A is a transition expressed by Eq. 41. Band B is ascribed to the transition represented in Fig. 9 and Eq. 44. Band C is the intramolecular transition of an ET cation radical molecule (2nd HOMO to HOMO transition). Band D is the transition from HOMO to LUMO of the ET cation radical.

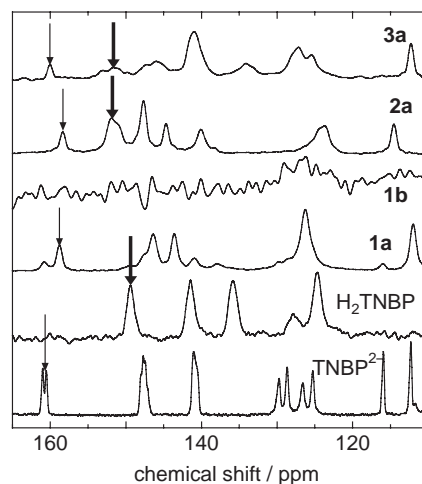


Fig. 88. <sup>13</sup>C CP/MAS NMR spectra of TNBP complexes. Peaks indicated by thin and thick arrows are derived from the neutral and ionic phenol groups, respectively. **1a**: 4:1 ET salt, **1b**: 2:1 ET salt, **2a**: 2:1 TMTSF salt (black plate), **3a**: 3:1:2( $\text{H}_2\text{O}$ ) BO salt.<sup>692</sup>

Two crystallographically independent ET molecules (A and B) form a 2D conducting layer in the  $ab$ -plane, which is sandwiched by the layers composed of one independent  $\text{TNBP}^{2-}$  (Fig. 86a). A semimetallic Fermi surface was predicted based on the crystal structure (Fig. 86b). The salt is metallic down to 3 K ( $\sigma_{3\text{K}} = 2.8 \times 10^3 \text{ S cm}^{-1}$ ) with  $T^2$  dependence of resistivity ( $\rho = 1.63 \times 10^{-7} T^2 + 7.73 \times 10^{-4}$ ). The absorption spectrum of the salt (a in Fig. 87) exhibited Band A but did not exhibit Band B, supporting the  $+0.5$  charged ET molecules. The solid-state <sup>13</sup>C CP/MAS NMR spectrum<sup>692</sup> of the 4:1 salt (1a in Fig. 88) is compared with those of  $\text{H}_2\text{TNBP}$  and  $(\text{TBA})_2(\text{TNBP}^{2-})$ . The significant distinction between the latter two species is the chemical shift of carbon atoms connected to the phenolic oxygen appeared at 150 ppm (thick arrow in Fig. 88) and 161 ppm (thin arrow), respectively. Therefore, it is concluded that the 4:1 salt is composed of  $\text{TNBP}^{2-}$  and does not contain either  $\text{HTNBP}^{1-}$  or  $\text{H}_2\text{TNBP}$  within the experimental error.

Curve b in Fig. 87 represents the absorption spectrum of the 2:1 ET salt. The spectrum clearly indicates the presence of Band A and the absence of Band B, which corresponds to the transition by Eq. 44, and all features are very similar to those of the 4:1 salt. If the anion species are  $\text{TNBP}^{2-}$  like the 4:1 salt, the 2:1 salt should be  $(\text{D}^+)_2(\text{A}^{2-})$  and exhibit Band B instead of Band A.



It is known that the intensity of Band B decreases as the ionicity ( $\delta$ ) of the ET molecule departs from  $+1$  and the band substantially extinguishes at  $+0.5$ .<sup>694</sup> The presence of Band A and the absence of Band B show that either the stoichiometry is not exactly 2:1 but the salt is anion deficient  $(\text{ET})_2(\text{TNBP}^{2-})_{1-x}$ , where  $x$  equals 0.5, or the anion species are not  $\text{TNBP}^{2-}$  but  $[(\text{TNBP}^{2-})_{1-y}(\text{HTNBP}^-)_y]^{-2+y}$  and  $y$  in  $(\text{ET})_2(\text{TNBP}^{2-})_{1-y}(\text{HTNBP}^-)_y$  nearly equals unity. The former case is completely inconsistent with the results of the elemental analysis. Hence, although the <sup>13</sup>C CP/MAS NMR

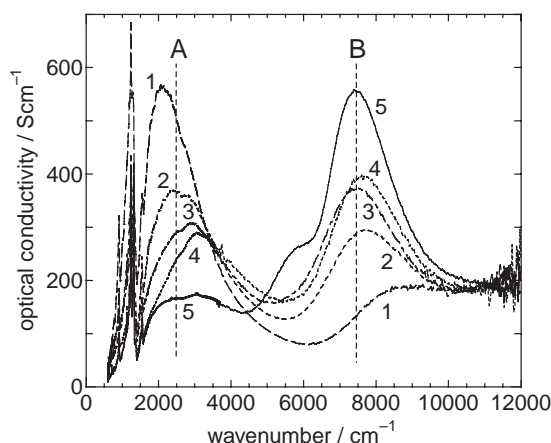
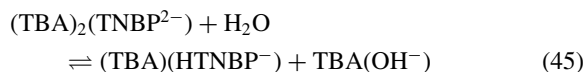


Fig. 89. Optical conductivities of five single crystals (1–5) of 2:1 TMTSF salt with  $\text{H}_2\text{TNBP}$  (plate phase).<sup>692</sup>

spectrum of the 2:1 salt is not resolved probably due to an extremely disordered structure, the optical spectrum, high conductivity ( $\sigma_{\text{RT}} = 0.2 \text{ S cm}^{-1}$ ,  $\varepsilon_{\text{g}} = 0.178 \text{ eV}$ ), nearly constant magnetic susceptibility down to 100 K ( $\chi = 8.2 \times 10^{-4} \text{ emu mol}^{-1}$ ) followed by an increase down to 20 K ( $1.5 \times 10^{-3} \text{ emu mol}^{-1}$ ), and the appearance of  $a_{\text{g}}$  mode ( $1330\text{--}1338 \text{ cm}^{-1}$ ) in the IR spectrum deduced that the 2:1 salt is  $(\text{ET})_2\text{-(HTNBP}^-)_x$  ( $x \approx 1$ ) having a distorted segregated column.

The formation of  $\text{HTNBP}^-$  during the course of electrocrystallization is ascribed to the equilibrium with water coming from moisture (Eq. 45).



The BO molecules afforded a metallic 3:1:2( $\text{H}_2\text{O}$ ) salt and the  $^{13}\text{C}$  CP/MAS NMR spectrum clearly indicates the coexistence of  $\text{TNBP}^{2-}$ ,  $\text{HTNBP}^-$ , and/or  $\text{H}_2\text{TNBP}$ . Based on the frequency of Raman active  $\text{C}=\text{C}$  stretching modes, the charge of the BO molecules was determined as  $\delta \approx 0.4$ ,<sup>240</sup> indicating that the average charge of the anion species is  $-1.2$ . Then, the anion species is regarded as the mixture of  $\text{TNBP}^{2-}$  and  $\text{HTNBP}^{1-}$ , since the fraction of  $\text{H}_2\text{TNBP}$  is negligible based on its  $\text{pK}_{\text{a}}$  value. The salt exhibited Band A at  $2.4 \times 10^3 \text{ cm}^{-1}$ . All these data pointed out that the formula of the salt is  $(\text{BO}^{0.4+})_3[(\text{TNBP}^{2-})_{0.2}(\text{HTNBP}^{1-})_{0.8}](\text{H}_2\text{O})_2$ .

The TMTSF molecules afforded three kinds of salts, i.e. elongated plates, blocks, and thin needles with the composition of 2:1, 2:1, and 6:4:1( $\text{THF}$ ), respectively.<sup>692</sup> The first one is the major product with semiconductive behavior with  $\sigma_{\text{RT}} = 2\text{--}8 \times 10^{-3} \text{ S cm}^{-1}$  ( $\varepsilon_{\text{g}} = 0.34\text{--}0.42 \text{ eV}$ ) and can be easily separated from the others by its morphology and lattice parameters. Figure 89 shows the optical conductivities of five single crystals derived from the reflection spectra along the stacking axis, where the crystals were obtained in the same batch and have the same lattice parameters. These spectra indicate that the charge of TMTSF molecules in each crystal varies between  $+0.5$  and  $+1$ , leading to the varied chemical species as  $(\text{TMTSF}^{(1-x/2)+})_2[(\text{TNBP}^{2-})_{1-x}(\text{HTNBP}^{1-})_x](0 < x < 1)$ .

Summarizing the above, the  $\text{TNBP}^{2-}$  molecules can afford  $\text{HTNBP}^{1-}$  species during the course of electrocrystallization, and thus, the variable band filling can be achieved for the cat-

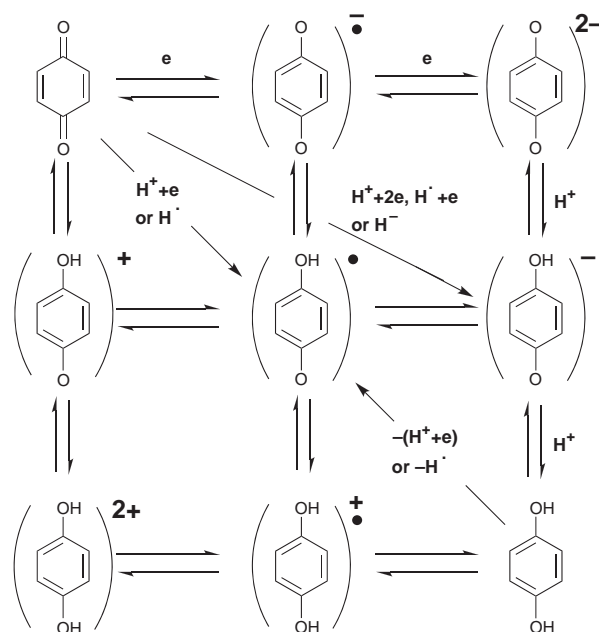


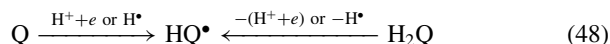
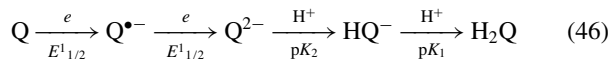
Fig. 90. The hydroquinone-*p*-benzoquinone system concerning 2 electrons  $\times$  2 protons with  $3 \times 3$  species. Important reactions are presented in Eqs. 46–48.

ion radical salts using the species  $\text{H}_n\text{TNBP}^{(2-n)-}$  by electrocrystallization in a solution with constant pH.

#### 4.2.5 Multiple PT and CT System and Neutral Radical:

The hydroquinone ( $\text{H}_2\text{Q}$ )-*p*-benzoquinone ( $\text{Q}$ ) is a well-known system of multi PT and CT (or electron transfer).<sup>695</sup> In this system, two electrons and two protons are concerned leading to  $3 \times 3$  chemical species. Some important reactions in Fig. 90 are summarized in Eqs. 46–48.

Equation 46 represents the conventional redox processes in aprotic and protic solvents. Equation 47 is the hydride-transfer process that has been used to prepare aromatic rings<sup>696</sup> and several anion radical salts<sup>697,698</sup> as shown in Fig. 91. The reaction 1 is the typical aromatization reaction by



2,3-dichloro-5,6-dicyano-*p*-benzoquinone (DDQ), while the reactions 2 and 3 have been studied from the biological aspect for the conversion from dihydronicotinamide NADH to nicotinamide having the pyridinium skeleton  $\text{NAD}^+$ .<sup>699,700</sup> By use of acridane derivatives (reaction 3 in Fig. 91), highly conductive TCNQ anion radical salts have been prepared by Saito and Colter.<sup>698</sup>

Equation 48 suggests that the hydrogen transfer from hydroquinone to *p*-benzoquinone results in a degenerate solid system composed of neutral radical species  $\text{HQ}^\bullet$ ,  $\text{Q} + \text{H}_2\text{Q} \rightarrow 2(\text{HQ}^\bullet)$ . Mitani, Saito, et al. applied pressure to the CT complex quinhydrone  $\text{H}_2\text{Q} \cdot \text{Q}$  aiming to realize the degenerate state (Fig. 92).<sup>701</sup> The neutral CT complex of quinhydrone resides at the far right side of the CT region in Fig. 81 since  $\Delta\text{pK}_{\text{a}}$  is estimated to be about  $+17$ . Consequently extremely

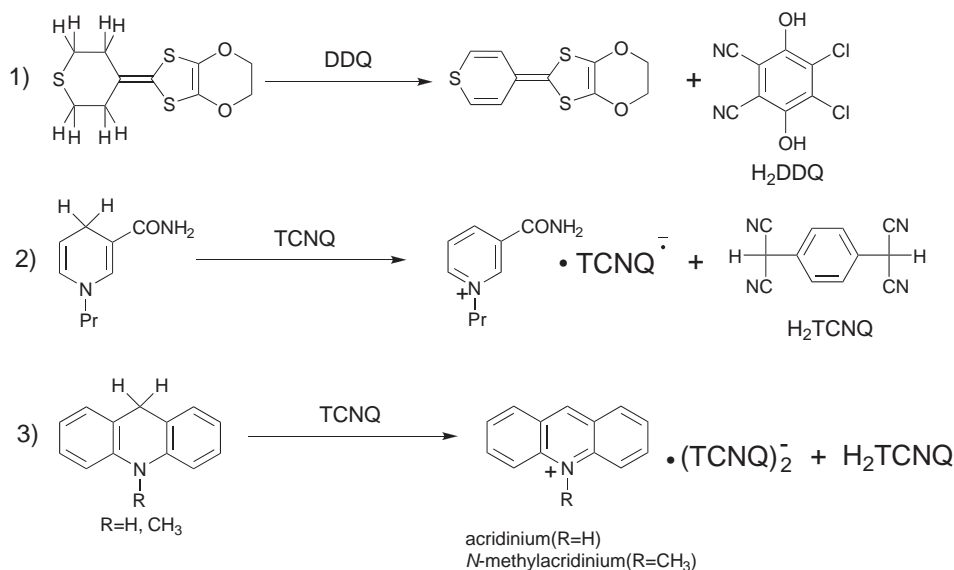
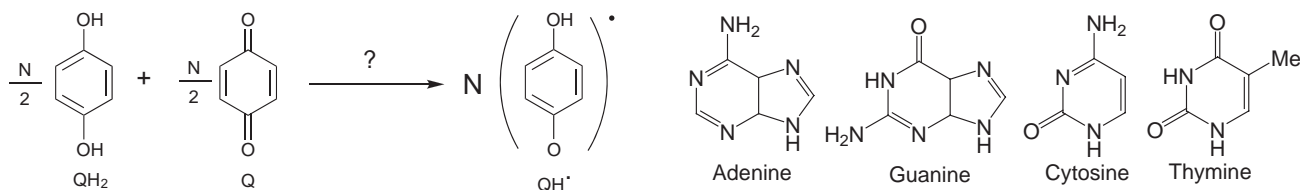
Fig. 91. Some examples of hydride (or  $\text{H}^+ + 2\text{e}$ , or  $\text{H}^\bullet + \text{e}$ ) transfer reaction.Fig. 92. Neutral radical solid based on hydroquinone•*p*-quinone system.

Chart 10.

high pressure was required to diminish the energy gap originating from the on-site Coulomb repulsion expressed by Eq. 8, and to form the metallic single component solid  $(\text{HQ}^\bullet)_n$ . However, so far no such metallic phase has been obtained under a hydrostatic pressure of up to 2.5 GPa, although the IR and UV-vis spectra indicate melting the hydrogen lattice.<sup>701</sup> A tight binding calculation on a quinhydrone type model complex, which does not include the electron correlation, predicts that the degenerate and metallic state will be achieved under extremely high pressure giving the DA distance of 2.6 Å.<sup>702</sup>

**4.2.6 Nucleobase Conductors:** Much effort has been focused into the study of electron transport in biological materials.<sup>703–705</sup> Plenty of controversial reports have forwarded concerning the metallic or highly conductive properties<sup>706</sup> of pure DNA molecules, but it seems that the DNA molecules turned out to be insulating.<sup>707</sup> A variety of transport studies have been performed on biological materials, such as hemoglobin, amino acids, proteins, polypeptides, and so on by Eley and Spivey<sup>708</sup> and others. Most of them are insulating ( $<10^{-17} \text{ S cm}^{-1}$  at RT)<sup>708</sup> except for cytochrome-*c*<sub>3</sub> (see section 2.4).<sup>123–125</sup>

Several attempts have been undertaken to investigate the CT complexes in a variety of biochemical systems, especially using nucleobases (Chart 10).<sup>703</sup> Estimation of the ionization potentials ( $I_D$ ) of the nucleobases, as potential components in CT complexes, indicate that they are reasonably effective  $\pi$ -donors, particularly in the case of guanine:  $I_D = 7.64\text{--}7.85 \text{ eV}$  vs adenine (7.80–8.26 eV), cytosine (8.45–8.74 eV), and thymine (8.74–8.87 eV).<sup>709–712</sup>

Slifkin and Kushelevsky have studied CT complex formation of nucleobases or nucleosides and *p*-chloranil.<sup>713</sup> The only CT solid they obtained was guanine•*p*-chloranil with a CT band at ca. 370 nm (in KBr), and the others afforded the unreacted components (with purine, uracil, and uridine) or the destructed *p*-chloranil (with adenine, adenosine, cytosine, thymine, and so on). The CT energy strongly suggests that the guanine•*p*-chloranil they obtained is classified as a neutral CT solid, and hence is insulating.

Sheina et al. obtained dark blue CT solids of TCNQ with nucleobases and their derivatives, and studied their spectroscopic properties in solution.<sup>714</sup> The solids can be classified as 1) 2:1 ionic CT solids composed of  $\text{TCNQ}^{\bullet-}$  (cytosine, 1-methylcytosine), 2) neutral CT solids (2:1 with *N*<sub>2</sub>,9-dimethylguanine, 4:1 with 9-methylguanine, unknown stoichiometry with 9-methyladenine). Thin films by cosublimation of nucleobases and TCNQ were also studied at 77 K and after annealing at 298–350 K.<sup>715</sup> Since they exhibit a linear relation between  $h\nu_{\text{CT}}$  and  $I_D$  as expressed by Eq. 19, all nucleobases are expected to form neutral CT complexes with DA alternating stacks in the films at 77 K. They also detected  $\text{TCNQ}^{\bullet-}$  and  $(\text{TCNQ}^{\bullet-})_2$  by heating the films up to 350 K for uracil and cytosine. No conducting property was elucidated.

Bazhina et al. have studied conductivity, EPR and the Hall effect of CT solids of TCNQ with cystein and guanine.<sup>716</sup> They reported that the conductivity of cystein•TCNQ is less than  $10^{-8} \text{ S cm}^{-1}$  with the activation energy  $\varepsilon_a = 0.5 \text{ eV}$ . The dominant carriers are electrons (Seebeck coefficient  $< 0$ ) and the mobility at 295 K are  $0.4 \times 10^{-4} \text{ cm}^2 \text{ V}^{-1} \text{ s}^{-1}$  for the guanine

Table 23. Results for Cytosine CT Complexes with TCNQ Derivatives

Acceptor	Appearance	D:A	IR $\nu_{\text{CN}}/\text{cm}^{-1}$	UV-vis/ $10^3 \text{ cm}^{-1}$				$\sigma (\epsilon_a)$ / $\text{S cm}^{-1} (\text{eV})$
				A	B	C	D	
TCNQ	black platelets	2:1	2188,2171,2157	—	7.1	11.7	16.5	$3 \times 10^{-2} (0.14)$
	black microcrystals	1:1:0.5( $\text{H}_2\text{O}$ )	2188,2169,2157	—	7.0	11.7	16.4	$1 \times 10^{-4} (0.12)$
MeTCNQ	black powder	1:1	2202,2082	3.4	—	10.5	17.1	$\approx 2 (0.042)$
						11.5		

complex and  $1.7 \times 10^{-4} \text{ cm}^2 \text{ V}^{-1} \text{ s}^{-1}$  for the cystein complex (the stoichiometry of both complexes and  $\sigma_{\text{RT}}$  of guanine•TCNQ are not described).

Although several electric conductors have been developed based on the pyrimido-fused-TTF derivatives<sup>106,114</sup> and CT complexes using TTF derivatives having a nucleobase as the pendant (see section 2.3.3),<sup>99,100</sup> no highly conductive even semiconductive CT complexes based on pure nucleobases have been prepared.

Our recent study to prepare conducting CT complexes using cytosine revealed that the protonated states and the characteristic pattern of the complementary hydrogen bonds between cytosine molecules contribute to construct effective molecular packing and to control the electronic structure of TCNQ molecules for electronic conductors.<sup>717</sup>

CT complexes based on cytosine and TCNQ were prepared by mixing a MeOH solution of cytosine and a  $\text{CH}_3\text{CN}$  solution of TCNQ derivatives (R-TCNQ) in varied mixing ratios, and the solutions were concentrated by standing in open air. The products are classified into three categories: 1) Ionic insulators of  $(\text{DHD}^+)(\text{R-TCNQ-OMe}^-)$ , 2) Fully ionic CT salts of  $(\text{DH}^+ \text{ or } \text{DHD}^+)(\text{R-TCNQ}^{\bullet-})$ , and 3) Partially ionic CT salts of  $(\text{DHD}^+)(\text{R-TCNQ}^{0.5-})_2$ , where  $\text{DH}^+$  and  $\text{DHD}^+$  are protonated cytosine and hemiprotonated cytosine pair, respectively, and R-TCNQ-OMe<sup>−</sup> is the MeO substituted R-TCNQ anion. It is amazing that even weak acceptors (2,5-Me<sub>2</sub>, 2,5-Et<sub>2</sub>TCNQ), which are hardly ionized by the ET molecule ( $I_{\text{D}} = 7.6 \text{ eV}$ ) (see Fig. 15), are ionized by cytosine to give ionic CT salts.

Table 23 summarizes the appearance, the ratio of D:A by elemental analysis, energies of UV-vis and IR absorptions in solids, and conductivity data for the TCNQ and MeTCNQ complexes.

The absorption spectra of the TCNQ complexes are presented in Fig. 93. The direct mixing of TCNQ and cytosine gave black polycrystalline 2:1 and 1:1:0.5( $\text{H}_2\text{O}$ ) complexes. IR spectra ( $2225, 2222 \text{ cm}^{-1}$  for  $\text{A}^0$  and  $2196, 2182 \text{ cm}^{-1}$  for  $\text{A}^{1-}$ )<sup>120</sup> and UV-vis spectra (no Band A) indicate that TCNQ molecules are fully ionized in both complexes. Based on the close similarity of the spectra to that of  $\text{K} \cdot \text{TCNQ}$ , it is deduced that the complexes have a segregated column of  $\text{TCNQ}^{\bullet-}$ , and thus, the optical band at ca.  $7.0 \times 10^3 \text{ cm}^{-1}$  is ascribed to Band B of the TCNQ anion instead of the CT transition from  $\text{TCNQ}^{\bullet-}$  to  $\text{cytosine}^{\bullet+}$ . The appearance of a weak Band C suggests a weak dimerization of  $\text{TCNQ}^{\bullet-}$  or isolated  $\text{TCNQ}^{\bullet-}$ . While Bands D and E are ascribed to the intramolecular transition of  $\text{TCNQ}^{\bullet-}$ . EPR spectra exhibited only a  $\text{TCNQ}^{\bullet-}$  signal ( $g = 2.0024\text{--}2.0030$ ). Therefore, the chemical formula of the 2:1 complex is deduced as  $(\text{DHD})^+(\text{TCNQ}^{\bullet-})$ .

Although the direct reaction of cytosine with TCNQ hardly afforded single crystals, slow diffusion of cytosine and TCNQ

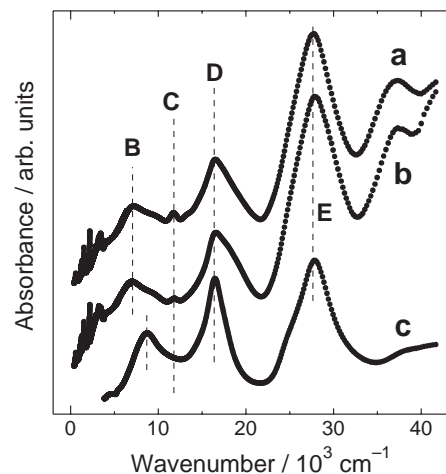


Fig. 93. Absorption spectra of cytosine•TCNQ complexes with a ratio of a) 2:1 and b) 1:1:0.5( $\text{H}_2\text{O}$ ) in comparison with c)  $\text{K} \cdot \text{TCNQ}$  complex.

or methathesis of the mixture of cytosine ( $\text{pK}_{\text{b}} = 4.55$ ) and cytosine•HCl with TCNQ provided the black platelets that gave identical elemental analysis, optical and EPR data with those of the polycrystalline sample. Figure 94 presents the crystal structure of the 2:1 complex, which has uniform segregated stacks of TCNQ. Cytosine molecules form a dimer by self-complementary three hydrogen bonds ( $\text{N-H} \cdots \text{O} = 1.86 \text{ \AA}$ ,  $\text{N-H} \cdots \text{N} = 1.94 \text{ \AA}$ ) (Figs. 94b and 95). Therefore, the cation species is the hemiprotonated pair between the cytosine molecule (D) and protonated cytosine molecule ( $\text{DH}^+$ ),  $(\text{DHD})^+$  as has been observed by Marsh and others.<sup>718</sup> Furthermore, the hydrogen-bonded cytosine dimer interacts with the neighboring dimers by self-complementary two hydrogen bonds ( $\text{N-H} \cdots \text{O} = 2.02 \text{ \AA}$ ) to form a flat 1D ribbon along the *b*-axis. The hydrogen-bonded 1D infinite ribbons of  $(\text{DHD})^+$  form a segregated 2D layer parallel to the *bc*-plane with an inter-ribbon separation of  $3.32 \text{ \AA}$  and width of  $9.10 \text{ \AA}$  (Figs. 94b and 94c), probably arising from  $\pi$ - $\pi$  interactions among the hemiprotonated dimers. This unique 2D architecture of polymerized cytosine prompts the formation of uniform 1D columns of  $\text{TCNQ}^{\bullet-}$  along the *a*-axis, and the columns arrange along the *b*-axis by the aid of short hydrogen bonds between cytosine and TCNQ ( $\text{C-H} \cdots \text{N} = 2.37 \text{ \AA}$ ,  $\text{N-H} \cdots \text{N} = 1.94 \text{ \AA}$ ) and between TCNQ molecules ( $\text{C-H} \cdots \text{N} = 2.58 \text{ \AA}$ ) to form the 2D layer. The TCNQ anions formed bond-over-ring type overlap with an interplanar distance of  $3.14 \text{ \AA}$ , which is favorable for high conductivity (Fig. 95b). Within the experimental accuracy of X-ray structural analysis, no dimerization was detected for the TCNQ anions. The overlap integral along the stacking direction ( $S = 20.4 \times 10^{-3}$ ) exceeds those of other directions



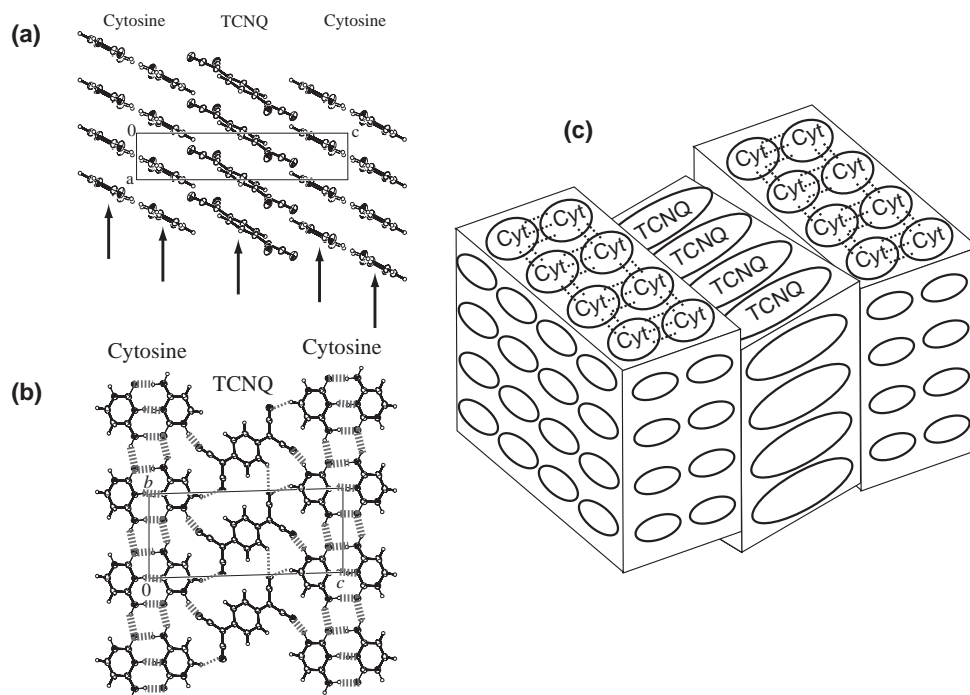


Fig. 94. (a) Crystal structure of cytosine·TCNQ 2:1 complex viewed along the *b*-axis. (b) View along the *a*-axis. Dotted lines indicate short hydrogen bonds. Triclinic,  $P\bar{1}$ ,  $a = 3.7640(9)$ ,  $b = 7.408(2)$ ,  $c = 17.010(5)$  Å,  $\alpha = 88.26(2)$ ,  $\beta = 89.74(2)$ ,  $\gamma = 84.65(2)^\circ$ ,  $V = 472.0(2)$  Å<sup>3</sup>,  $Z = 1$ ,  $R = 0.0669$ . (c) Schematic view to show the 2D layer of TCNQ and hydrogen-bonded cytosine ribbons.

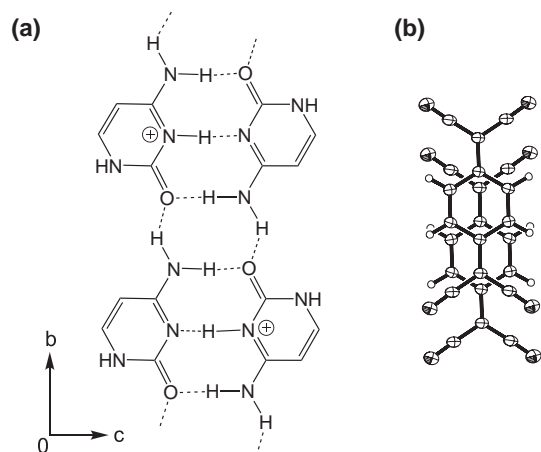


Fig. 95. (a) Cytosine dimer with self-complementary three hydrogen bonds along the *c*-axis, then the dimers are connected by two hydrogen bonds along the *b*-axis to form a thin and flat polycationic ribbon. (b) Ring over bond overlap pattern of TCNQ molecules within the conducting column.

( $S < 10^{-4}$ ), indicating 1D electronic character.

The single crystal shows a relatively high conductivity of  $\sigma_{RT} = 10^{-2}$  S cm<sup>-1</sup> ( $//b$ ,  $\epsilon_a = 0.14$  eV) in comparison with most TCNQ Mott insulators, which usually show conductivity less than  $10^{-4}$  S cm<sup>-1</sup>. It should be noted that the Band B of the 2:1 as well as 1:1 complex in Fig. 93 is allocated at lower energy ( $7.0\text{--}7.1 \times 10^3$  cm<sup>-1</sup>) than that of K·TCNQ ( $8.5 \times 10^3$  cm<sup>-1</sup>). As mentioned in section 2.3.3.4, this fact indicates that the  $U_{eff}$  in the complex is depressed by the very polarizable

nature of the cytosine cation molecules. That might be one of the most favorable features of nucleobases for highly conductive anion radical salts.

The solvated 1:1 complex is deduced as (DH<sup>+</sup>)(TCNQ<sup>•-</sup>), having nearly uniform segregated columns of TCNQ<sup>•-</sup> although no structural information was available concerning the packing mode of DH<sup>+</sup>. The IR spectrum in the hydrogen-bond region is very similar to that of the 2:1 complex. The complex is semiconductive ( $\sigma_{RT} = 10^{-4}$  S cm<sup>-1</sup>,  $\epsilon_a = 0.12$  eV) in pellet form and may be comparable to the 2:1 salt of a single crystal.

The MeTCNQ complexes show quite different features from the TCNQ complexes above mentioned. So far only the 1:1 CT complex has been produced even by changing the mixing ratio widely (products with nearly a 2:1 ratio was the salt of Me-TCNQ-OMe<sup>-</sup>). The C≡N stretching mode of the 1:1 complex ( $2202, 2082$  cm<sup>-1</sup>) is distinct from those of the neutral ( $2223$  cm<sup>-1</sup>) and monoanionic MeTCNQ ( $2190, 2171$  cm<sup>-1</sup>), and thus may indicate the partially ionized MeTCNQ molecules. The appearance of Band A at  $3.4 \times 10^3$  cm<sup>-1</sup> (Fig. 96) is in good agreement with this conjecture. The close similarity of the UV-vis-NIR spectrum to that of BMI(TCNQ)<sub>2</sub> (BMI: 1-butyl-3-methylimidazolium, see section 4.5.3 and Table 27) in Fig. 96 suggests the uniform segregated column of partially ionized MeTCNQ molecules in the solid. The characteristic optical feature is the appearance of both Band A and the slight splitting in the  $10\text{--}12 \times 10^3$  cm<sup>-1</sup> range. The former is associated with the partial CT state of the species, and the latter is ascribable to the monomerized anion molecules, as has been observed in many highly conducting 1:1 TCNQ complexes with TTF, TSF, or NMP or a 1:2 complex with acridinium.<sup>118</sup>

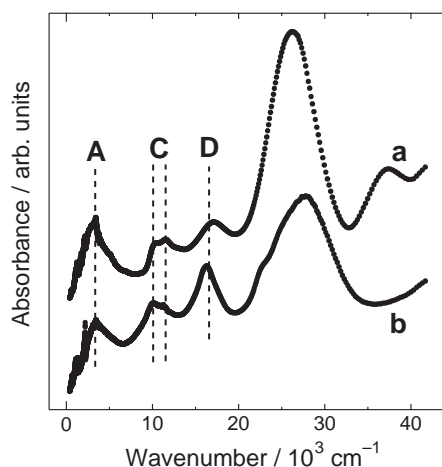


Fig. 96. Comparison of the UV-vis-NIR spectra of (a) 1:1 cytosine complexes of MeTCNQ with (b) BMI(TCNQ)<sub>2</sub>, where BMI is 1-butyl-3-methylimidazolium.

The most attractive feature of the 1:1 MeTCNQ complex is the excellent conductivity ( $\sigma_{RT} = 2 \text{ S cm}^{-1}$ ,  $\varepsilon_a = 0.042 \text{ eV}$ ) observed on the compressed pellet sample. The EPR measurements indicate a narrow absorption peak ( $\Delta H = 0.38\text{--}0.53 \text{ G}$ ) ascribable to MeTCNQ $\cdot^-$  ( $g = 2.0029\text{--}2.0032$ ). Consequently, the 1:1 complex is formulated as (DHD) $^{1+}$ (A $^{0.5-}$ )<sub>2</sub>.

Summarizing the above, a nucleobase, cytosine afforded both 2:1 and 1:1 semiconductive solids with TCNQ in the  $\sigma_{RT} = 10^{-2} \text{ S cm}^{-1}$  range. On the other hand, a 1:1 CT solid with MeTCNQ is highly conductive ( $\sigma_{RT}$  is a few  $\text{S cm}^{-1}$  for a pellet sample). The absorption spectrum and EPR measurements revealed that cytosine is not a good electron donor but a good proton acceptor and acts as a polarizable counter cation reducing on-site Coulomb energy for conduction. The characteristic pattern of the complementary hydrogen bonds of cytosine molecules contribute to construct effective molecular packing and to control the electronic structure of TCNQ molecules for electronic conductors.

**4.2.7 Band Filling Control:** The most difficult point in band filling for organic conductors is to keep the crystal structure unchanged during the control of Fermi level (chemical potential). Otherwise, the plural changes of Fermi level (carrier doping), transfer interactions, polarizability, dipole moment, and so on affect the transport properties and it is, thus, difficult to discuss solely the relation between the band filling and transport properties. Also, the induced disorder will cause some undesirable effects. Although there have been three major strategies to control the band filling in organic conductors (see also section 3.5.5), most of the reported works have failed to keep the crystal structure unchanged.

**4.2.7.1 Strategy for Band Filling Control I: Mixing of Different Charges;** This is a replacement of some fraction of the constituent molecules by analogous molecules with different charges,  $I_D$  or  $E_A$  aiming to give isostructural compounds with unchanged transfer interactions. Typical examples are as follows:

1) Anion radical salts with mixed counter cations such as (NMP)<sub>1-x</sub>(phenazine)<sub>x</sub>TCNQ,<sup>719</sup> Cu<sub>1-x</sub>M<sub>x</sub>(DCNQI)<sub>2</sub> (M = Li and Zn),<sup>720</sup> and many C<sub>60</sub> superconductors (see section 5.1).<sup>7,164</sup>

2) DA-type complexes with mixed donor molecules such as (TTF)<sub>1-x</sub>(TSF)<sub>x</sub>TCNQ,<sup>721</sup> or mixed acceptor molecules such as (ET)(TCNQ)<sub>1-x</sub>(F<sub>2</sub>TCNQ)<sub>x</sub>.<sup>722</sup>

3) Cation radical salts with mixed anions such as (ET)<sub>y</sub>[(Mn<sup>II</sup>Cl<sub>4</sub>)<sub>1-x</sub>(Fe<sup>III</sup>Cl<sub>4</sub>)<sub>x</sub>]<sup>723</sup> and (ET)<sub>y</sub>[(M<sup>II</sup>Cl<sub>4</sub>)<sub>1-x</sub>(Ga<sup>III</sup>Cl<sub>4</sub>)<sub>x</sub>] (M = Co and Zn).<sup>724</sup>

Among them, almost all systems, except for C<sub>60</sub> and the last two, used guest molecules with considerably different sizes and/or symmetry, and hence, the transfer interactions are inevitably modified from those in the parent system, although the mixed crystals have the isostructural crystal structure. Therefore, it is inappropriate to ascribe the change of transport properties of the mixed crystals to the band filling change solely.

The salt with binary counter anions or cations is an excellent way from the point of band filling control. An early work by Kumai et al. is a substitution of the tetrahedral monoanion MX<sub>4</sub> by dianion M'X<sub>4</sub> with subtle structural modification, such as (ET)<sub>y</sub>[(Mn<sup>II</sup>Cl<sub>4</sub>)<sub>x</sub>(Fe<sup>III</sup>Cl<sub>4</sub>)<sub>1-x</sub>], where the substitution of 5000 ppm of Mn<sup>II</sup>Cl<sub>4</sub> by Fe<sup>III</sup>Cl<sub>4</sub> converted the semiconducting (ET)<sub>2</sub>(MnCl<sub>4</sub>) into a metallic one.<sup>723</sup> Mori et al. have extended this idea to several ET systems with [(M<sup>II</sup>Cl<sub>4</sub>)<sub>x</sub>(Ga<sup>III</sup>Cl<sub>4</sub>)<sub>1-x</sub>] (M = Co and Zn).<sup>724</sup> They claimed that their work was the first systematic success in realizing the metallic state by band filling control. However, it is incorrect because the conversions from insulating to metallic phase in (ET)<sub>y</sub>[(Mn<sup>II</sup>Cl<sub>4</sub>)<sub>x</sub>(Fe<sup>III</sup>Cl<sub>4</sub>)<sub>1-x</sub>]<sup>723</sup> and from the Mott insulating to superconducting phase in  $\kappa$ -(ET)(Cu<sup>I</sup><sub>2-x-y</sub>Cu<sup>II</sup><sub>x</sub>){(CN)<sub>3-2y</sub>[N(CN)<sub>2</sub>]<sub>y</sub>} (see section 3.2.5)<sup>492,493</sup> have already been reported. In the latter case, the substitution of Cu<sup>I</sup> and Cu<sup>II</sup> ( $x = 0\text{--}1200$  ppm) belongs to Strategy I, while the substitution of NC-Cu-CN by NC-N-CN with analogous shape and size ( $y = 0\text{--}1$ ) belongs to Strategy II, as will be mentioned below. By keeping the anion moiety constant, for example at  $y = 0.35$ ,  $T_c$  ranges from 3.2 K to 10 K with different  $x$  indicating the modified  $T_c$  by band filling control. This is the only success in realizing an organic superconductor by band filling control. Even in these systems, of course, a subtle modification of transfer integrals caused by changing the size of the counterparts should be seriously taken into account.

Especially the smallest atomic particle, a proton, has attracted much attention in such studies. The anion radical salt [(D<sup>0</sup>)<sub>1-x</sub>(DH<sup>+</sup>)<sub>x</sub>](A<sup>x-</sup>) or cation radical salt (D) $^{x+}$ [(A<sup>-</sup>)<sub>x</sub>(AH<sup>0</sup>)<sub>1-x</sub>] is one of the target systems for band filling control when both conditions, 1) the  $x$  can be controlled continuously in a certain range and 2) the crystal structures are unchanged, are satisfied. Polynitrophenoles such as H<sub>n</sub>TNBP, described in section 4.2.4, and other kinds of compounds having a hydroxide or amino group such as diaminoglyoxime<sup>725</sup> and 2,2'-biimidazole (H<sub>2</sub>BIM)<sup>248,726,727</sup> have been used in the preparation of organic metals from the view point of band filling control, since they have a varied number of protons and charge with marginal structural modification.

**4.2.7.2 Band Filling Control by PT Interaction in 2,2'-Biimidazole System and Protonic Conductor;** Akutagawa, Saito, and co-workers have used 2,2'-biimidazole and its derivatives, which belong to a system with 4 electrons and 4 protons, i.e., 5 × 5 species with the electronic structure from 5π–5π to 7π–7π (Fig. 97).<sup>248,727</sup>

The neutral biimidazole (H<sub>2</sub>BIM) is a proton acceptor and

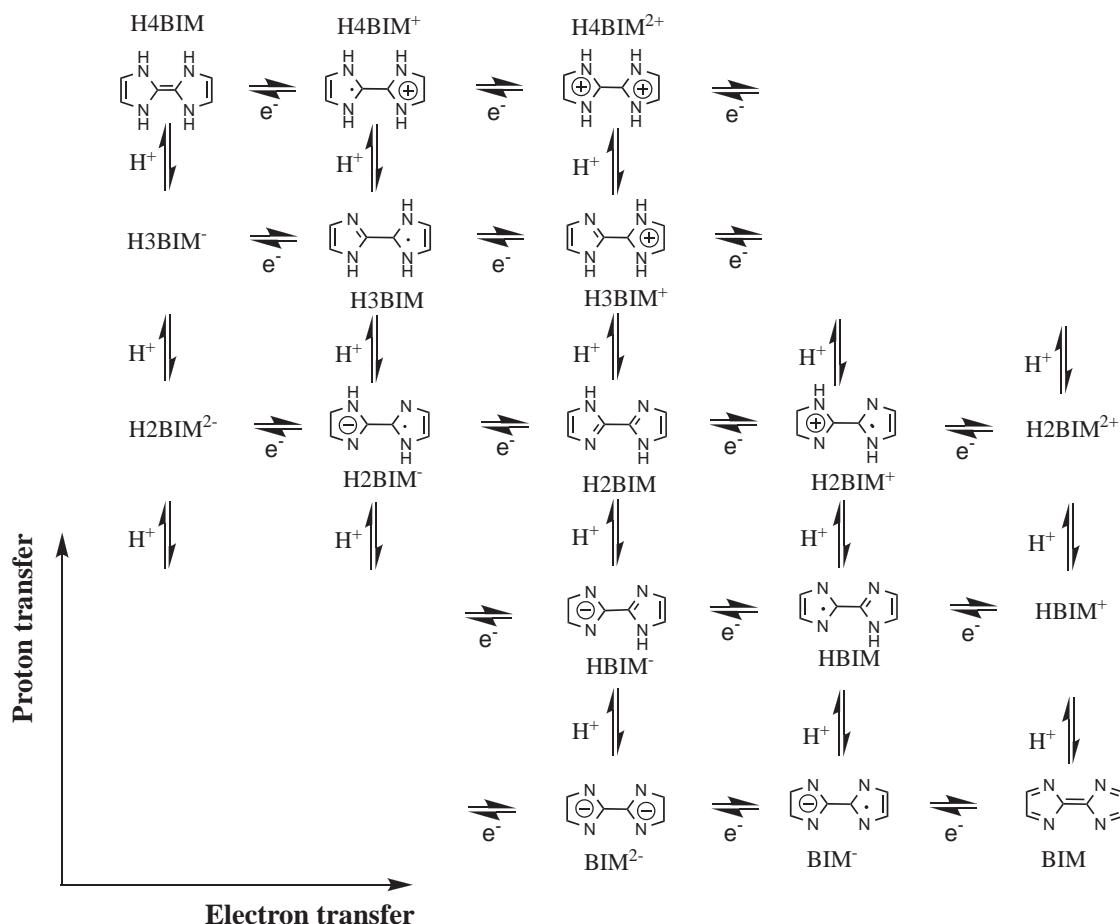
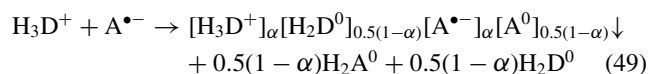
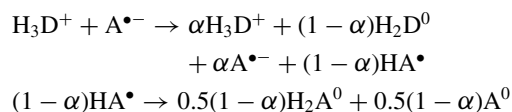


Fig. 97. Proton-transfer and electron-transfer diagram of 2,2'-biimidazole ( $\text{H}_2\text{BIM}$ ).<sup>248,727</sup> Not all species are depicted.

the  $\text{pK}_a$  values (in  $\text{DMF:H}_2\text{O} = 7:3$ ) of the monocation ( $\text{H}_3\text{BIM}^+$ , 4.60) and dication ( $\text{H}_4\text{BIM}^{2+}$ , -0.24) indicate that they are stronger proton donors than hydroquinone ( $\text{pK}_a = 10.5$ ) and  $\text{H}_2\text{DDQ}$  ( $\text{pK}_{a1} = 5.14$ ,  $\text{pK}_{a2} = 7.46$ ). Also, the  $\text{H}_2\text{BIM}$  molecule is a weak electron donor like naphthalene.<sup>82</sup>

The metathesis reaction between  $\text{H}_3\text{BIM}^+ \cdot \text{I}^-$  or  $\text{H}_4\text{BIM}^{2+} \cdot (\text{I}^-)_2$  and an anion radical salt of TCNQ affords a reaction product instead of a simple exchange product, through the CT and PT interactions.<sup>248</sup> In the metathesis reaction between  $\text{H}_3\text{BIM}^+$  and  $\text{Li} \cdot \text{TCNQ}$ , the following processes (Eq. 49) were deduced based on the spectroscopic analysis of the products, which include  $\text{H}_2\text{A}^0$  and  $\text{A}^0$ , where BIM and TCNQ are labeled as  $\text{D}^0$  and  $\text{A}^0$ , respectively.



The elemental analyses of the reaction products revealed that  $\alpha = 0.76$ ; and therefore, the complex is represented as  $[\text{H}_3\text{BIM}^+]_{0.86} [\text{H}_2\text{BIM}^0]_{0.14} [\text{TCNQ}^{\bullet-}]_{0.86} [\text{TCNQ}^0]_{0.14}$ , which is a mixed PT and CT complex. This black solid was an insulator ( $5.9 \times 10^{-8} \text{ S cm}^{-1}$ ,  $\epsilon_a = 0.37 \text{ eV}$ ) with the first CT band at  $5.1 \times 10^3 \text{ cm}^{-1}$ . Several mixed CT-PT complexes have been

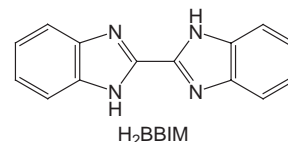


Chart 11.

prepared using  $\text{H}_n\text{BIM}$  and TCNQ derivatives.<sup>248</sup>

By using 2,2'-bi-1*H*-benzimidazole ( $\text{H}_2\text{BBIM}$ ) (Chart 11) one can obtain a metallic proton-electron mixed conductor,  $(\text{H}_3\text{BBIM}^+)(\text{TCNQ})(\text{Cl}^-)_{0.5}(\text{H}_2\text{O})$ .<sup>728</sup> By adjusting the pH of the crystallization solvent to ca. 1.2, at which  $\text{H}_3\text{BBIM}^+$  became the dominant species in the solution, single crystals of  $(\text{H}_3\text{BBIM}^+)(\text{TCNQ})(\text{Cl}^-)_{0.5}(\text{H}_2\text{O})$  were harvested. The salt is composed of individual segregated uniform stacks of  $\text{H}_3\text{BBIM}^+$  and  $\text{TCNQ}^{0.5-}$  molecules, both of which surround a channel accommodating disordered  $\text{Cl}^-$  and  $\text{H}_2\text{O}$  molecules (Fig. 98). The bond lengths of TCNQ suggest that the  $\delta$  of TCNQ is nearly 0.5 and the complex exhibits the first CT band (Band A) at  $3.2 \times 10^3 \text{ cm}^{-1}$ . The complex is metallic ( $\sigma_{\text{RT}} = 10 \text{ S cm}^{-1}$ ) down to 250 K, followed by a semiconductive behavior with  $\epsilon_a = 0.04 \text{ eV}$  down to 100 K (Fig. 99b). The complex obtained from a pH = 1.00 solution exhibits a wider metallic range (Fig. 99a), while that from a pH = 1.70 solution exhibits a semiconductive behavior in the entire temperature range (Fig. 99c).

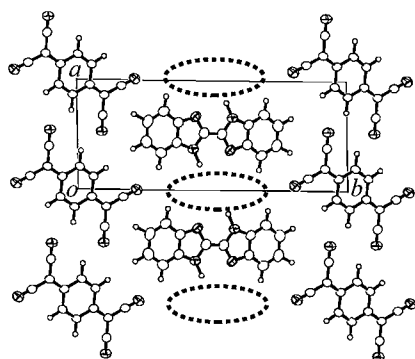


Fig. 98. Crystal structure of  $(\text{H}_3\text{BBIM}^+)(\text{TCNQ})(\text{Cl}^-)_{0.5}(\text{H}_2\text{O})$  obtained at pH = 1.20 having uniform segregated columns of TCNQ for electric conduction and channels ( $\parallel c$ , dashed circles) containing  $\text{Cl}^-$  and  $\text{H}_2\text{O}$  molecules (omitted) for protonic conduction. Triclinic,  $P\bar{1}$ ,  $a = 7.676(1)$ ,  $b = 19.050(4)$ ,  $c = 3.894(1)$  Å,  $\alpha = 91.36(2)$ ,  $\beta = 94.92(2)$ ,  $\gamma = 88.31(2)^\circ$ ,  $V = 566.9(2)$  Å<sup>3</sup>,  $Z = 1$ ,  $R = 0.065$ .<sup>728</sup>

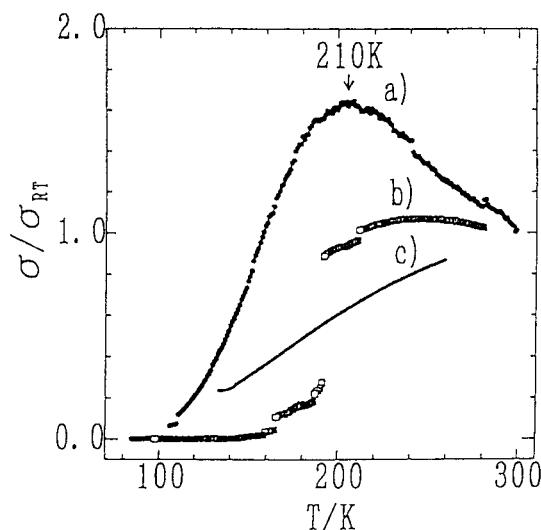


Fig. 99. Temperature dependence of conductivity of the single crystals prepared from  $\text{H}_2\text{BBIM}$  and TCNQ under constant pH. a) pH = 1.00 (crystal structure was not determined yet), b) pH = 1.20, c) pH = 1.70.<sup>726</sup>

The diffuse X-ray analysis down to 100 K and IR spectra down to 20 K indicate both the possible formation of the  $[\text{Cl}^-(\text{H}_2\text{O})_2]$  sublattice below 200 K and the dimerization of TCNQ molecules along the  $c$ -axis. The magnetic susceptibility was not extinguished by the transition, indicating that the metal-insulator transition is not due to the Peierls instability. Below 250 K, its temperature dependence is expressed by a one-dimensional linear Heisenberg antiferromagnetic chain model with a magnetic exchange energy ( $J/k_B$ ) of  $-59$  K. So, the metallic state with uniform  $\text{TCNQ}^{0.5-}$  stack becomes a Mott insulating state with dimerized TCNQ,  $(\text{TCNQ}_2)^{\bullet-}$  as a unit at low temperatures ( $<100$  K).

Since the water molecules in the channel are liquid-like before freezing into the  $[\text{Cl}^-(\text{H}_2\text{O})_2]$  sublattice above 200 K, high proton conductivity ( $\sigma_{\text{RT}} = 1 \times 10^{-3} \text{ S cm}^{-1}$ ) was realized through the 1D channel and ceased below 200 K. To our

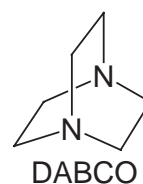
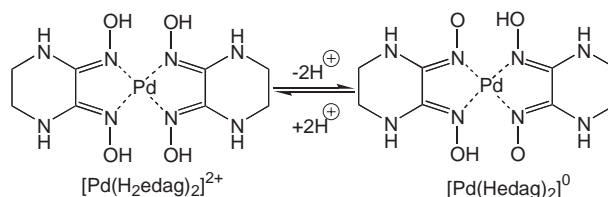


Chart 12.



Scheme 1.

knowledge, this system is the first proton-conducting metallic radical salt.

Very recently there appeared a second “first proton-conducting metallic radical salt,”<sup>729</sup>  $\beta''$ -(ET)<sub>4</sub>[(cation)M<sup>III</sup>(C<sub>2</sub>O<sub>4</sub>)<sub>3</sub>]<sub>2</sub>[(cation)<sub>2</sub>([18]crown-6 ether)]<sub>5</sub>H<sub>2</sub>O (M<sup>III</sup> = Cr and Ga; cation = H<sub>3</sub>O<sup>+</sup>/NH<sub>4</sub><sup>+</sup>), with metallic electric conductivity down to 190 K (Cr) or 240 K (Ga) ( $\sigma_{\text{RT}} = 2\text{--}3 \times 10^2 \text{ S cm}^{-1}$ ) and proton conductivity ( $\sigma_{\text{RT}} = 3 \times 10^{-3} \text{ S cm}^{-1}$ ). The latter decreases as temperature decreases and attains ca.  $10^{-6} \text{ S cm}^{-1}$  at 260 K.

The proton conduction by use of crown ether or its analogues is not unique. Akutagawa, Nakamura, et al. developed the system including a mixed counter cation [(crown ether)<sub>1-x</sub>(M<sup>+</sup>-crown ether)<sub>x</sub>] for the band filling of the TCNQ anion radical salt.<sup>730</sup> This mixed counter ion seems very appropriate for the band filling compared with biimidazole, since only the central part is modified. The system initially attracted an interest in connection with the coupled electronic and ionic conduction, but the rather strong interaction between M<sup>+</sup> and crown ether prohibited the latter conduction. A TCNQ complex of 1,4-diazabicyclo[2.2.2]octane (DABCO) (Chart 12) exhibited proton conduction.<sup>731</sup>

**4.2.7.3 Band Filling Control by PT Interaction in Diaminoglyoxime System;** Kitagawa, Mitani, et al. have developed metallic TCNQ salts using the partially deprotonated  $\text{Pd}(\text{H}_2\text{edag})_2$  molecule as the counter cation, where  $\text{H}_2\text{edag}$  is ethylenediaminoglyoxime.<sup>725</sup> The charge of the  $[\text{Pd}^{\text{II}}(\text{H}_2\text{edag})_2]^{2+}$  molecule changes from +2 to 0 depending on the pH in solution (Scheme 1). They prepared  $[\text{Pd}(\text{H}_2\text{edag})_x(\text{Hedag})_{2-x}]^{x+}\text{TCNQ}^{x-}$  complexes having partial CT and PT states (mainly  $x = 0.2, 0.7$ , and  $1.0$ ), and observed metallic temperature dependence down to typically ca. 180 K for  $x = 0.7$  ( $\sigma_{\text{RT}} \approx 90 \text{ S cm}^{-1}$ ). The crystals are insulators with  $x = 0.2$  and  $1.0$  (Mott insulator). Therefore, the partial PT from  $x = 1$  to  $x = 0.7$  corresponds to hole injection into a completely filled lower Hubbard band. The IR active  $b_{1u}$  mode of  $\text{C}\equiv\text{N}$  stretching splits into two peaks below  $T_{\text{MI}}$ , indicating the charge disproportionation. A long superstructure appears along the stacking  $c$ -axis ( $12 \times c$ ). It is currently unclear why the phase with  $x = 0.7$  (or  $3/4$  might be more plausible) is so stable.

**4.2.7.4 Strategy for Band Filling Control II: Usage of a Mixed Counterpart of Different Size but of the Same Charge;** Although this strategy is not a real band filling control, it modifies straightforwardly the transfer integrals and would affect the chemical potential depending on the band dispersion and the change of  $U_{\text{eff}}$ . In this sense this method shares a common concept with lattice or chemical pressure and has been applied to molecular superconductors such as  $(\text{TMTSF})_{2-x}(\text{TMTTF})_x\text{ClO}_4$ ,<sup>732</sup>  $\kappa\text{-(ET)}_{2-x}(\text{BEDT-STF})_x\text{Cu}[\text{N}(\text{CN})_2]\text{Br}$ ,<sup>733</sup>  $\beta\text{-(ET)}_2(\text{I}_3)_{1-x}(\text{IBr}_2)_x$ ,<sup>734</sup>  $\kappa\text{-(ET)}_2\text{Cu}[\text{N}(\text{CN})_2]\text{Cl}_{1-x}\text{Br}_x$ ,<sup>482</sup>  $\lambda\text{-(BETS)}_2\text{GaX}_{4-x}\text{X}'_x$  ( $\text{X}, \text{X}'$ : Cl, Br),<sup>735</sup> and  $\text{M}_{3-x}\text{M}'_x\text{C}_{60}$  ( $\text{M}, \text{M}'$ : K, Rb, and Cs).<sup>736</sup> In all cases, however, the band filling control has not been achieved.

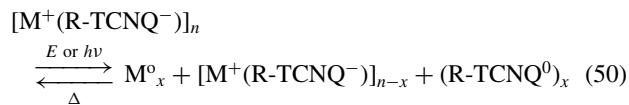
**4.2.7.5 Strategy for Band Filling Control III: External Stimulus;** For the real band filling control, an application of physical stimulus that changes the valence state of the components without any structural modification would be the ideal method. Magnetic and electric field application and photon irradiation are good candidates. Owing to the insufficient energy, an application of magnetic field has been limited to induce phase transition at low temperatures, either on the insulating phase to recover the metallic (or superconducting) phase or on the metallic phase to induce the insulating phase. The latter is rather common to organic conductors (i.e., FISDW, see section 3.3.1). In the former case, the reentrant metallic or superconducting phase has been observed on Chevrel compounds<sup>737</sup> or BETS compounds.<sup>610,613</sup>

Electric field has also been applied on a Peierls or SDW insulator to depin the density wave, giving rise to a non-linear electric conduction. However, these phenomena are not associated with the change of the valence state of the components, and hence, definitely differ from the band filling control.

FET is a typical system for carrier doping by electric field without deteriorating crystal structure (see section 2.2). Switching and memory phenomena observed in several TCNQ materials,<sup>224,738–740</sup> and photo-induced phase transition (PIPT) observed in the DA system near the N–I boundary (see section 3.1.3),<sup>218,224</sup> TCNQ,<sup>741</sup> EDO,<sup>428</sup> and DCNQI salts<sup>742,743</sup> also belong to this strategy. The PIPT is a characteristic cooperative phenomenon of a strongly coupled electron and phonon (or molecular vibration) system. In the next section, some examples in Strategy III will be described.

**4.3 Carrier Doping by Electric Field Application or Photon Irradiation.** **4.3.1 Switching and Memory Effects: Metal–Insulator System:** **4.3.1.1 Anion Radical Salts  $\text{M}^+\cdot\text{A}$  ( $\text{M} = \text{Cu}, \text{K}$ , and  $\text{Rb}$ ;  $\text{A} = \text{TCNQ}, \text{TNAP}, \text{TCNE}$ , etc.);** Potember, Cowan, and co-workers have discovered a switching and/or memory effect in the fully ionic anion radical salts of TCNQ derivatives by electric field application<sup>738</sup> or laser irradiation.<sup>739</sup> Anion radical salts of TCNQ analogues with strong electron accepting ability, such as  $\text{F}_4\text{TCNQ}$  and  $\text{TNAP}$ , exhibited both switching (from high-resistive state to high-conductive state) and memory effects (termed as memory switching; the lower double well potential in Fig. 78b), while the salts with weak acceptors such as TCNQ exhibited only the switching effect (termed as threshold switching; the upper double well potential in Fig. 78b). To our knowledge, this is the first observation of an electric field- and photo-induced insulator–metal transition (although the real metallic behavior is not

reported) at ambient conditions. They postulated that the electric field application or laser irradiation induced a back CT to give  $\text{Cu}^0\text{TCNQ}^0$ , which was confirmed by IR spectroscopy. This results in the conductive partial CT state (Eq. 50;  $\text{M} = \text{Cu}$  and  $\text{Ag}$ ), which corresponds to the hole injection to semiconductor (or Mott insulator).



Unfortunately, their works were performed on thin films of TCNQ salts and provided no detailed evidence for the changes of the electronic and crystal structures. The threshold electric field was  $8.1 \times 10^3 \text{ V cm}^{-1}$  for  $\text{Cu}^+\cdot\text{TNAP}^-$ . The switching speed is reported to be less than 10 ns. If the switching is associated only with the electronic structure, the switching time should be in the order of fs. The sensitivity (the number of molecules that are converted by one photon) was not reported.

A single crystal of  $\text{K}\cdot\text{TCNQ}$  was subjected to an electric field of more than  $10^3 \text{ V cm}^{-1}$  by Kumai, Tokura, and Okimoto, giving rise to a switch from the off- to on-state at 180 K.<sup>740</sup> Of particular interest is that the switching effect is observed when the electric field is applied along the stacking direction of TCNQ anion radicals. The authors claimed that the on-state is metallic since the resistivity is nearly temperature independent. Since  $\text{K}\cdot\text{TCNQ}$  is an insulator composed of dimerized TCNQ anions at low temperatures, the field-induced on-state might form a uniform stack of TCNQ molecules. The photo-induced conductive phase was realized for several organic salts by Koshihara et al.,<sup>741</sup> suggesting that the photo- (or electric field-) induced insulator–metal transition might be rather common for an organic Mott insulator or weakly dimerized insulator with  $\delta = 1$ .

**4.3.1.2  $\text{M}(\text{DMDCNQI})_2$  ( $\text{M} = \text{Cu}$  and  $\text{Ag}$ );** The structural MI transition observed for  $\text{Cu}(\text{d}_6\text{-DMDCNQI})_2$  at ca. 78 K, in which six methyl hydrogens of DMDCNQI are deuterated, is accompanied by the charge ordering from  $\text{Cu}^{4/3+}$  (metallic phase) to  $\text{Cu}^{2+}\text{Cu}^{1+}\text{Cu}^{1+}$  (insulating phase). The photo irradiation to the insulating state by Karutz, Wolf, et al. led to the switching to the conducting state within 20 ps.<sup>742</sup> Thus, the photo irradiation relaxed both the structural distortion and charge disproportionation.

Recently, Naito, Inabe, et al. reported that the switching mechanism of  $\text{Ag}(\text{DMDCNQI})_2$  is different from those mentioned above. The crystal is metallic at RT without light irradiation and becomes semiconductive at the place where the light was irradiated to induce the reaction in Eq. 51.<sup>743</sup> The illuminated area's color turned from black to white and persisted for several months. The authors claimed that this was a new doping method, but there have been several examples, including  $\text{Ag}\cdot\text{TCNQ}$ , in which the valence state of the components has been modified by the light irradiation to induce a switching phenomenon in the segregated CT solids (Eq. 50) and line or pattern generation has been observed for light exposure above certain threshold levels.<sup>739</sup> Moreover, the light irradiation on  $\text{Ag}(\text{DMDCNQI})_2$  generates a semiconducting phase instead of a metallic phase. Therefore, one may suspect that the irradiation afforded the decomposed segment  $(\text{Ag}^0)(\text{A}^0)$  surrounded by metallic domain  $(\text{Ag}^+)(\text{A}^{0.5-})_2$  as shown by Eq. 52, and



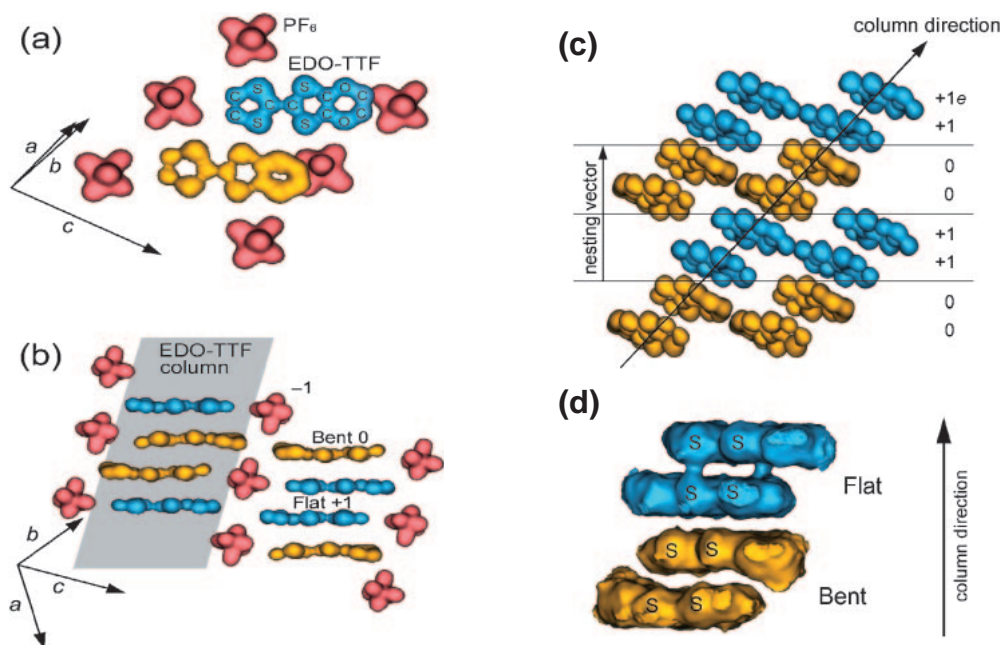
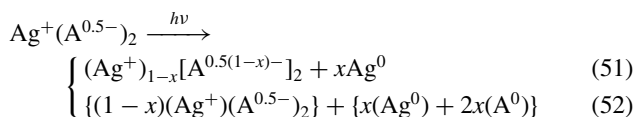


Fig. 100. Crystal structures of (EDO-TTF or EDO)<sub>2</sub>PF<sub>6</sub> in the insulating state at 260 K, where MEM equi-charge-density surfaces is at the level of  $0.7 \text{ e}\text{\AA}^{-3}$ . (a) Viewed along the EDO stacking direction. (b) Side view of the EDO column. (c) Charge-ordered pattern viewed along the *c*-axis. (d) Side view of the MEM equi-charge-density surface of the EDO column, where the level of the surface is  $0.13 \text{ e}\text{\AA}^{-3}$ . The PF<sub>6</sub> is colored in red, and the EDO molecules are colored in blue and yellow for the flat and bent shapes, respectively.<sup>745</sup>

thus, the white color may arise from the deposition of Ag<sup>0</sup> metal due to the destruction of Ag(DMDCNQI)<sub>2</sub>.



Structural information on the spot where the light was illuminated is necessary for confirming the validity of Eq. 51.

**4.3.1.3 Visualization of Charge Ordering in (EDO)<sub>2</sub>PF<sub>6</sub> and Ultrafast Photo-Induced Phase Transition (PIPT);** The 3/4-filled band conductor (EDO)<sub>2</sub>PF<sub>6</sub> shows a peculiar MI transition at  $T_{\text{MI}} = 278 \text{ K}$  (see section 3.3.5).<sup>426–428</sup> The MI transition is the cooperative actions of Peierls distortion, charge ordering, and anion ordering together with a molecular deformation of EDO molecules. The charge-ordering pattern in the insulating phase was deduced to be  $[0, 0, +1, +1, \dots]$  by Raman spectroscopy, which is associated with the weak neighbor-site Coulomb repulsion.<sup>427,744</sup> The charge density distribution of the ordered state was visualized by Aoyagi, Takata, et al., based on a combination of the MEM (maximum entropy method) and Rietveld analyses of the synchrotron X-ray powder diffraction profiles (Fig. 100).<sup>745</sup> The unit cell is doubled in the insulator phase, corresponding to a Peierls instability. The PF<sub>6</sub> anions are rotationally disordered in the metallic phase, whereas they are ordered in the insulator phase (Figs. 100a and 100b). Two types of EDO molecules are present in the insulator phase: namely, flat and bent molecules. The flat one has an excess charge close to  $+1e$ , and the positive charge is concentrated mainly on a sulfur atom nearest the PF<sub>6</sub> anion. The distance between the sulfur atom and the anion is shortened by the displacement of EDO molecules through the MI transi-

tion. Together with the varied  $T_{\text{MI}}$  for (d<sub>2</sub>-EDO)<sub>2</sub>PF<sub>6</sub> and the salts with more bulky anions (AsF<sub>6</sub>, SbF<sub>6</sub>) (vide infra), it is postulated that the local electrostatic interactions between the sulfur atom and the anion and between the hydrogen atoms attached to the five-membered ring of EDO and the anion are closely related to the hole trapping on the sulfur atom and the anion ordering. The charge rich and poor EDO dimers alternate with a periodicity of the  $2k_{\text{F}}$  nesting vector (Fig. 34c) due to the Peierls instability. As a result,  $[0, 0, +1, +1, \dots]$  type charge ordering is produced along the nesting vector as shown in Fig. 100c.

The equi-charge-density surface of the insulating EDO column at the level of  $0.13 \text{ e}\text{\AA}^{-3}$  is shown in Fig. 100d. Weak charge density overlaps between the flat molecules can be seen as two S...S bonds, whereas it is not present both between flat and bent molecules and between bent molecules, visualizing the spin-singlet dimer.

This study revealed that the molecular displacements observed in the MI transition assist both the anion ordering and the electrostatic and electronic stabilizations of the crystal structure in the insulator phase. The cooperative phenomenon in this peculiar MI transition shall be regarded as a result of the displacement and deformation of EDO molecules during the phase transition. The thermal analysis of (EDO)<sub>2</sub>PF<sub>6</sub> revealed that the MI transition is the catastrophic cooperation of multiple instabilities as mentioned above.<sup>746</sup>

Figure 101a shows the temperature dependence of reflectivity with the light polarized along the EDO stacking direction by Drozdova et al.<sup>744</sup> In the metallic phase, the reflectance ascribable to the plasma oscillations is observed below  $10 \times 10^3 \text{ cm}^{-1}$ . A weak reflectivity at around  $13.0 \times 10^3 \text{ cm}^{-1}$  is ascribed to the interband transition from the 2nd-HOMO to HOMO

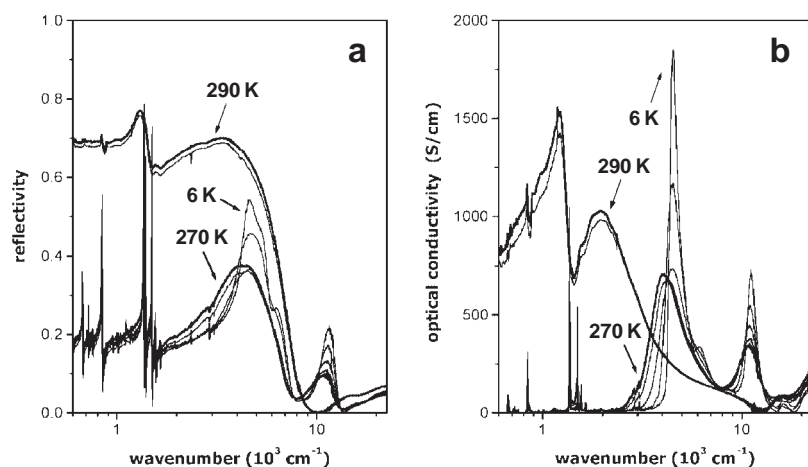


Fig. 101. Temperature dependence of (a) reflectance spectra and (b) optical conductivity of  $(\text{EDO})_2\text{PF}_6$ .<sup>744</sup> Electric field is polarized parallel to the donor stacking direction.

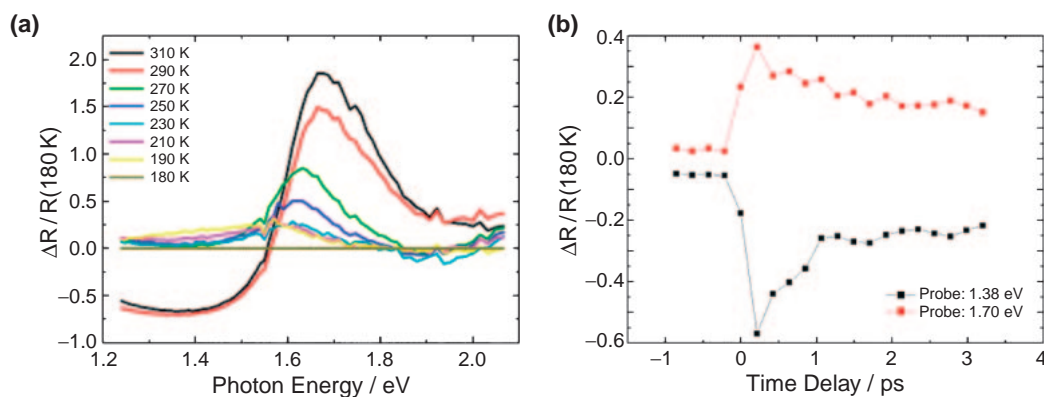


Fig. 102. (a) The temperature dependence of the reflectivity change  $\Delta R/R$  of  $(\text{EDO-TTF})$  or  $(\text{EDO})_2\text{PF}_6$ . (b) Probe photon energy dependence of the time profile for  $\Delta R/R$  observed at 180 K. The pump photon energy ( $E \parallel b$ ) was 1.55 eV and the probe photon energy ( $E \parallel b$ ) was 1.70 and 1.38 eV for the upper and lower panels, respectively. At 260 K, nearly the same result was obtained.<sup>428,747</sup>

bands in the metallic phase or that from the upper 2nd-HOMO level to upper HOMO level of an isolated dimer in the insulating phase. In the insulating phase, on the other hand, the plasma reflection disappears and new reflectances centered around  $5 \times 10^3$  and  $11.1 \times 10^3 \text{ cm}^{-1}$  appear. Figure 101b is the optical conductivity obtained by Kramers–Kronig conversion of the reflectance data. Using a Hubbard model for symmetric tetramers, the two bands in the insulating phase were mainly assigned to the transition from  $|0110\rangle$  to  $|1100\rangle$  and  $|0200\rangle$ , corresponding to  $\text{D}^+\text{D}^+\text{D}^0\text{D}^0$  and  $\text{D}^0\text{D}^2+\text{D}^0\text{D}^0$  configurations, respectively. Therefore, the bands are related to  $V$  and  $U$ .

Recently, ultrafast photo-switching from insulator to metallic phase due to the melting of the charge-ordered state was observed at around RT ( $\approx 265 \text{ K}$ ) by Koshihara et al.<sup>428,747</sup> The crystal surface was excited by laser irradiation with a pulse width of 0.12 ps. The excitation photon energy (1.55 eV) was nearly resonant to the CT band at  $11.1 \times 10^3 \text{ cm}^{-1}$  (1.37 eV), directly reflecting the excitation of the charge-ordered state. The reflectance change  $\Delta R/R$  from insulating to metallic states exhibits negative and positive maxima at 1.38 and 1.66 eV, respectively (Fig. 102a). Figure 102b clearly indicates that the positive and negative reflectance changes appear at the probe photon energies of 1.38 and 1.70 eV, respectively.

The life-time of the photo-induced metallic phase strongly depends on the excitation intensity. In the case of the  $2 \times 10^{18} \text{ cm}^{-3}$  excitation condition, the reflectance change was complete within only about 1.5 ps. Therefore, it is said that the melting of the charge-ordered state accompanied by the insulator-to-metal phase conversion occurs within the 1.5 ps after excitation with threshold-like behavior (threshold photon density is  $10^{18} \text{ cm}^{-3}$ ). The excitation intensity corresponds to a single excitation photon for 540–1500 molecules. Within the resolution time (1  $\mu\text{s}$ ), the electric conductivity was largely enhanced (more than 5 orders of magnitude) just after photo-excitation. The rate of recovery from the photo-induced metallic state to the original insulating state can be extensively controlled by changing the excitation intensity (1 ps–100  $\mu\text{s}$ ).

To realize a molecular phase-switching device controllable by light irradiation with a 1 picosecond response time (i.e., THz region), it is essential to develop a material that shows highly sensitive and ultra-fast PIPT phenomena near RT with high repeatability and durability. Such an ultra-fast transition has been observed in a purely electronic origin. Although the ultra-fast transition (within a few hundred fs) accompanied by the molecular conformational change has been observed for systems such as retinal in rhodopsin,<sup>748</sup> this is a uni-molec-

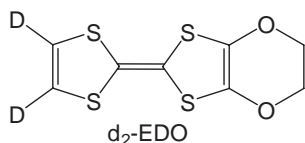


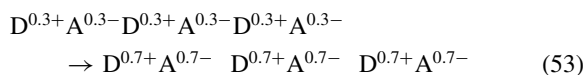
Chart 13.

ular nano-system. As for the meso-size scale switch, an electron-lattice coupled coherent system is necessary for the ultra-fast transition.

In the (EDO)<sub>2</sub>X system, the  $T_{MI}$  was tuned by the chemical modifications as mentioned above. Deuteration of EDO (d<sub>2</sub>-EDO) (Chart 13) increased  $T_{MI}$  by ca. 2.5 K, while complexation with larger counter anions decreased  $T_{MI}$  in the order of X = ClO<sub>4</sub> (>337 K) > PF<sub>6</sub> (278 K) > AsF<sub>6</sub> (ca. 268 K) > SbF<sub>6</sub> (ca. 240 K).<sup>749,750</sup> These findings indicate the important role of Coulomb attractive energy in the MI transition of the system.

The following neutral-ionic (N-I) transition system is another example for the electron-lattice coupled system in the mesoscopic region by an optical phonon mode with  $k = 0$  via an electron-lattice interacting channel; however, tuning of  $T_{NI}$  has not fully succeeded.

**4.3.2 Neutral-Ionic Phase Transition, Ferroelectricity, Soliton and Domain Wall:** The N-I phase transition described in section 3.1.3 is one of the enantiotropic complex isomerizations and some examples are summarized in Table 9. The first-order phase transition observed in TTF·*p*-chloranil at 81 K<sup>208</sup> is accompanied by the appearance of the  $a_g$  mode in the IR spectra, indicating symmetry lowering. In accordance with the spectral feature, an accurate X-ray analysis showed the dimerization of the DA pair in the ionic phase (Eq. 53, where a dimerized pair is represented by  $\underline{DA}$ ).

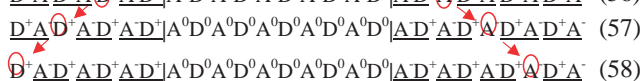


In the ionic lattice, the two sequences  $\dots \underline{D^{0.7+}A^{0.7-}} \underline{D^{0.7+}A^{0.7-}} \dots$  and  $\dots \underline{A^{0.7-}D^{0.7+}} \underline{A^{0.7-}D^{0.7+}} \dots$  are degenerate in energy. In the following, the charge of the D and A species is represented by integers for

simplicity (0 for neutral and + or – for ionic species; however, remember that the species have a fractional charge of either  $\pm\delta$  or  $\pm(1-\delta)$ ). The N-I phase transition also exhibits a rapid increase in magnetic susceptibility that follows the Curie law with very narrow EPR linewidth due to motional narrowing.<sup>219</sup> The Curie constant indicates that one molecule per about 10<sup>4</sup> molecules is ionized. The electric conductivity also increases by one order of magnitude as seen in Fig. 103a ( $\sigma \approx 5 \times 10^{-7} \text{ S cm}^{-1}$  just below 81 K). The dimerization of ionic species generally extinguishes Curie spins, but the formation of ionic solitons ( $D^{\bullet+}$  or  $A^{\bullet-}$ ) in Eq. 54 and neutral solitons in Eq. 55 can contribute to the magnetic and transport properties, respectively.<sup>751</sup>



Equation 56 shows a 1D lattice composed of three domains, A, B, and C, which are separated from each other by domain walls  $|$ . The ionic solitons can move without any energy cost as demonstrated from Eqs. 56–58.



The  $\sigma_{RT}$  of TTF·*p*-chloranil is 10<sup>−5</sup> S cm<sup>−1</sup>. The number of ionic domains increases as pressure increases up to 0.8 GPa, at which the RT conductivity attains as high as 1 S cm<sup>−1</sup>.<sup>752</sup> The transport in the low-pressure region was interpreted by the dynamics of domain wall,<sup>220,223</sup> that produce ionic solitons as shown from Eqs. 59–62. Further increases in pressure suppress the conductivity. At 1.1 GPa, the crystal is composed of only the dimerized ionic phase with no dynamic exchange of DA pairs. Figure 103a shows the temperature and pressure dependences of conductivity proposed by Mitani et al.<sup>752</sup>

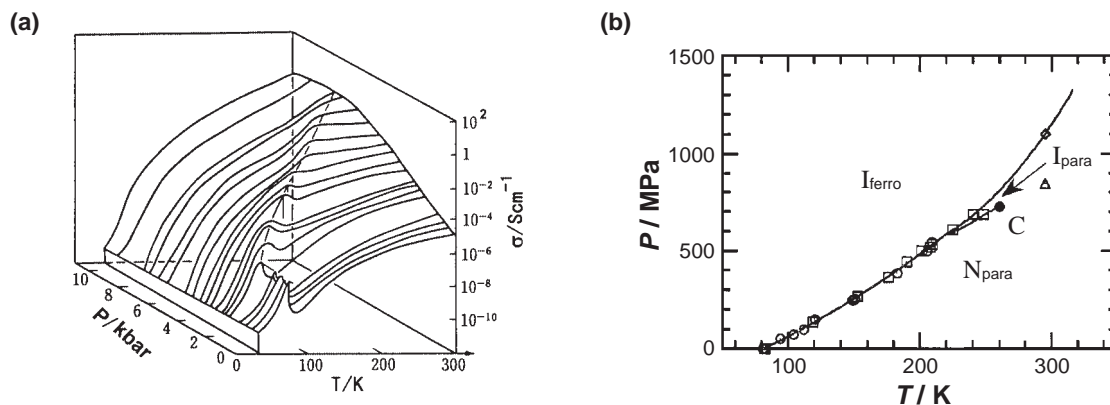


Fig. 103. (a) Temperature and pressure dependence of electric conductivity of TTF·*p*-chloranil. The first-order phase-transition temperature ( $T_{NI} = 81 \text{ K}$  at ambient pressure) shifts to higher temperatures with weakening the cusp as pressure increases.<sup>752</sup> (b)  $T$ – $P$  phase diagram by Cailleau et al. for indicating the paraelectric neutral ( $N_{para}$ ), paraelectric ionic ( $I_{para}$ ), and ferroelectric ionic ( $I_{ferro}$ ) phases. C is the estimated tricritical point.<sup>753</sup> ○: neutron scattering, □: NQR, ◇: vibrational spectroscopy, △: conductivity.

Table 24. DA Alternating CT Solids Exhibiting Switching Effect with the Threshold Electric Field ( $E_{th}$ ) at 190 K and Activation Energy for Conduction ( $\epsilon_a$ ) (Alphabet is the Symbol in Fig. 106)<sup>a)</sup>

Neutral	$E_{th}/V\text{ cm}^{-1}$	$\epsilon_a/\text{eV}$	Ionic	$E_{th}/V\text{ cm}^{-1}$	$\epsilon_a/\text{eV}$
<b>I</b> TMB•Me <sub>2</sub> TCNQ	$7.0 \times 10^4$	0.40	<b>E</b> Me <sub>2</sub> Phe•F <sub>4</sub> TCNQ	$4.7 \times 10^4$	0.38
<b>H</b> TMB•TCNQ	$2.5 \times 10^4$	0.20	<b>D</b> TMB•F <sub>4</sub> TCNQ	$1.6 \times 10^4$	0.35
<b>G</b> TTF• <i>p</i> -QCl <sub>3</sub>	$2.4 \times 10^4$	0.19	<b>C</b> TMPD•TCNQ	$1.2 \times 10^4$	0.36
<b>F</b> TTF• <i>p</i> -QCl <sub>4</sub>	$3.1 \times 10^3$	0.09	<b>B</b> TMB•FTCNQ	$6.5 \times 10^3$	0.22
			<b>A</b> TTeC <sub>1</sub> -TTF•TCNQ	$1.4 \times 10^3$	0.11

a) TMB: 3,3',5,5'-tetramethylbenzidine, *p*-QCl<sub>3</sub>: trichloro-*p*-benzoquinone, *p*-QCl<sub>4</sub>: tetrachloro-*p*-benzoquinone, Me<sub>2</sub>Phe: dihydromethylphenazine. The arrows indicate the order approaching to the N–I boundary.

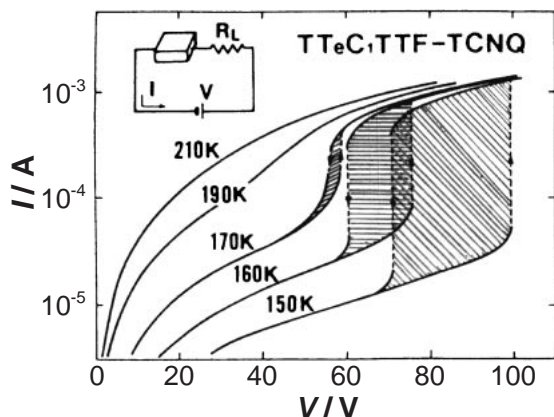


Fig. 104.  $I$ - $V$  characteristics of the TTeC<sub>1</sub>-TTF•TCNQ complex with external resistance of  $R_L = 0.1$ – $10\text{ M}\Omega$ . At 150 K, the system becomes on-state at ca. 100 V and returns back to off-state at ca. 70 V.<sup>225</sup>

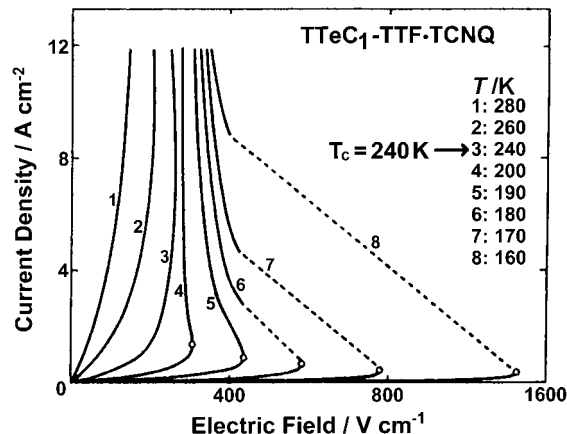


Fig. 105. Current density vs electric field of TTeC<sub>1</sub>-TTF•TCNQ complex. At 160 K, a transition to on-state occurs at around  $E = 1100\text{ V cm}^{-1}$ . The threshold electric field is indicated by open circles.<sup>225</sup>

Afterwards, Lemée-Cailleau and co-workers revealed that the transition between paraelectric N and I phases (ionicity) is distinct from the transition between paraelectric N and ferroelectric I phases (dimerization), on the basis of X-ray diffraction and NQR (nuclear quadrupole resonance) measurements (Fig. 103b).<sup>753</sup> This finding seems to be consistent with the fact that the pressure at which RT conductivity shows a maximum (ca. 0.8 GPa)<sup>752</sup> is significantly low in comparison with that of the dimerization transition (ca. 1.1 GPa).

Switching and memory effects have also been observed in the CT complexes with alternating stacks, especially when they are close to the N–I phase boundary, by Iwasa, Tokura, et al.<sup>218,221,223,224</sup> Table 24 summarizes selected examples with the threshold electric field for the switching ( $E_{th}$ ) and activation energy for conduction ( $\epsilon_a$ ).

Figure 104 shows the relation between the applied voltage and the observed current for a TTeC<sub>1</sub>-TTF•TCNQ single crystal, which is connected with the external resistance ( $R_L = 0.1$ – $10\text{ M}\Omega$ ) as depicted in the figure. At high temperatures, there are no switching or memory phenomena in the  $I$ - $V$  characteristics. At 170 K, however, the sample exhibited a switching effect at ca. 60 V from the off- to on-state with a small hysteresis. Figure 105 presents the relation between the current density and the electric field operating in the crystal. At low temperatures, the current density increased below  $T_c = 240\text{ K}$  in TTeC<sub>1</sub>-TTF•TCNQ. The  $E_{th}$  value is related with the activation energy for conduction and becomes small when the system approaches the N–I boundary as seen in Fig. 106.

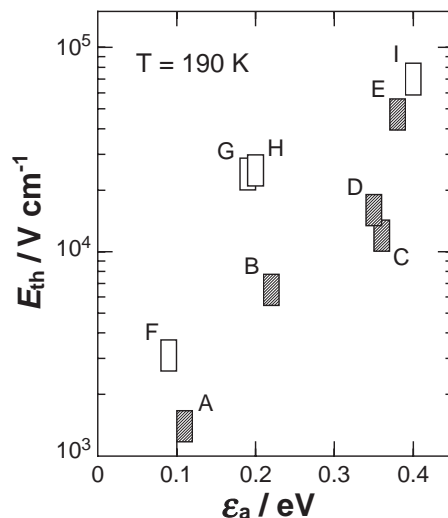


Fig. 106. Relation between threshold electric field ( $E_{th}$ ) and activation energy for conduction ( $\epsilon_a$ ) for the ionic (filled rectangle) and neutral (open rectangle) CT solids. A: TTeC<sub>1</sub>-TTF•TCNQ, B: 3,5-TMB•FTCNQ, C: TMPD•TCNQ, D: 3,5-TMB•F<sub>4</sub>TCNQ, E: Me<sub>2</sub>Phe•F<sub>4</sub>TCNQ, F: TTF•*p*-chloranil, G: TTF•trichloro-*p*-benzoquinone, H: 3,5-TMB•TCNQ, I: 3,5-TMB•Me<sub>2</sub>TCNQ.<sup>224</sup>

Laser-induced phase transition was studied on TTF•*p*-chloranil.<sup>222,741</sup> The sensitivity is 280–2800 molecules per photon and the switching rate is 100 ps. The switching requires melt-

Table 25. Selected CT Complexes with Switching, Memory, or Sliding SDW Phenomena<sup>a)</sup>

Mechanism	Complex	Electric field induced			Photo induced				Ref.
		Threshold field $E_{th}$ /V cm <sup>-1</sup>	Operating T/K	Ref.	Threshold photon density/cm <sup>-3</sup>	Sensitivity molecule /photon	Response time /s	Operating T/K	
Mott or spin-Peierls insulator ↔ Partial CT or Metal <sup>b)</sup>	Cu•TCNQ(II) <sup>d)</sup>	$4 \times 10^3$	RT	738	$1500 \text{ Wcm}^{-2}$	—	—	RT	739
	Cu•TNAP	$8 \times 10^3$	RT	738	—	—	—	—	—
	K•TCNQ	$>10^3$	$<\approx 230$	740	—	$\approx 20$ dimers	c)	$<394$	741
	Rb•TCNQ	—	—	—	—	$<10$	1.5 p	—	e)
	Ag(DMDCNQI) <sub>2</sub>	—	—	—	—	—	3–5 days	RT	743
Mott + Peierls insulator ↓ Metal	Cu(d <sub>6</sub> -DMDCNQI) <sub>2</sub>	—	—	—	$\approx 10^8 \text{ Wcm}^{-2}$	100 electrons	20 p	$<78$	742
CO insulator ↓ Metal	(EDO) <sub>2</sub> PF <sub>6</sub>	—	—	—	$2 \times 10^{18}$	500–1500	1.5–2 p	270	434,747
	$\alpha$ -(ET) <sub>2</sub> I <sub>3</sub>	—	—	—	—	—	120 n	4	f)
	$\theta$ -(ET) <sub>2</sub> CsZn(SCN) <sub>4</sub>	$3\text{--}4.5 \times 10^2$ ( <i>//b</i> )	$<20$	g)	—	—	—	—	—
Ionic ↔ Neutral	TTF• <i>p</i> -Chloranil	$3.1 \times 10^3$	190	224,225	$1.8 \times 10^{18}$	280–2800	20–100 p	77	222,754
	TTeC <sub>1</sub> -TTF•TCNQ	$1.2 \times 10^3$	$<240$	224,225	—	—	c)	$<300$	741
Sliding SDW	(TMTSF) <sub>2</sub> ClO <sub>4</sub>	$\leq 5 \times 10^{-4}$	1.5	354	—	—	—	—	—
	(TMTSF) <sub>2</sub> NO <sub>3</sub>	$4 \times 10^{-2}$	6	h)	—	—	—	—	—

a) —: no experiments. b) Partial CT or metallic behavior has not been observed by thermal variation except Ag(DMDCNQI)<sub>2</sub>. c) According to the time-dependence of photo-induced reflectivity change,<sup>741</sup> the response times for TTeC<sub>1</sub>-TTF•TCNQ and K•TCNQ are a few times and a few hundred times faster, respectively, than that for TTF•*p*-chloranil. d) R. A. Heintz, H. Zhao, X. Ouyang, G. Grandinetti, J. Cowen, K. R. Dunbar, *Inorg. Chem.* **1999**, 38, 144. e) H. Okamoto, private communication. f) N. Tajima, J. Fujisawa, N. Naka, T. Ishihara, R. Kato, Y. Nishio, K. Kajita, *J. Phys. Soc. Jpn.* **2005**, 74, 511. g) K. Inagaki, I. Terasaki, H. Mori, T. Mori, *J. Phys. Soc. Jpn.* **2004**, 73, 3364. h) S. Tomic, J. R. Cooper, D. Jerome, K. Bechgaard, *Phys. Rev. Lett.* **1989**, 62, 462.

ing of the dimerization in the ionic phase, which may reflect the rather slow switching rate in this system. Since the switching occurs at a temperature close to the N–I phase transition, it is necessary to find a N–I transition system with a transition temperature near RT with a small activation energy for conduction in order to realize excellent performance for photo-reflectivity change near RT.

The structural change from the photo-induced metastable state to the stable state was studied for TTF•*p*-chloranil by time resolved ultra-fast X-ray analysis. The switching rate from the ionic state to neutral state (probably metastable state) was found to be 20 ps (at 77 K).<sup>754</sup>

Table 25 summarizes the characteristic features of selected switching and/or memory materials in sections 4.3.1 and 4.3.2, together with sliding SDW systems.

Summarizing sections 4.3.1 and 4.3.2, the Mott insulators including weakly dimerized, charge-ordered insulators, and N–I transition systems exhibit a fast phase transition (switching or memory phenomenon) induced by electric field application or photo irradiation. For the former two systems, the phase transitions caused a pronounced change in reflectance and conductivity from insulating to metallic features. The third system also exhibited a change in conductivity and dielectric response connected with the transport of solitons and/or domain walls, dynamic dimerization, and ferroelectricity. The response is very fast in systems with weak electron–phonon interactions, but the transition efficiency is improved with increasing electron–phonon or e–mv interactions. Tuning of operating temperature up to RT and of threshold electric field or photon density is necessary work in the future.

Ferroelectric phenomena of the DA complexes have been investigated by Horiuchi et al. on the following systems: TTF•*p*-chloranil and its analogues in connection with the N–I transition phenomena,<sup>755</sup> phenazine•TCNQ and its analogues in connection with the order–disorder transition phenomena,<sup>756</sup> and phenazine•haloanilic acids (chloranilic or bromanilic acid) in connection with the displacive mechanism through intermolecular hydrogen bonds.<sup>757</sup> Although the last system is comprised of nonpolar molecules, it exhibits a large dielectric polarization ( $\epsilon_{RT}(\text{//}b) \geq 100$ ,  $\epsilon_{T_c=253\text{K}}(\text{//}b) \approx 3000$ ) with insulating nature ( $\sigma_{RT} < 10^{-8} \text{ S cm}^{-1}$ ) caused by the subtle displacement of component molecules connected by hydrogen bonds. The application of hydrostatic pressure drastically increased  $T_c$  ( $T_c \approx \text{RT}$  at 0.6 GPa).

Although the design of a system with displacive-mechanism is difficult, it should be emphasized that most  $\pi$ -molecules in this review are soft acids or soft bases in Pearson's term. Thus, they have a huge electronic polarizability and are susceptible to external stimuli when the ionicity and mutual orientation of the molecules are appropriately designed.

**4.3.3 Metallic DA Alternating Complexes with Mixed Neutral and Ionic Valence States at RT: HMTTeF Complexes of Et<sub>2</sub>TCNQ and BTDA-TCNQ:** The title complexes are the first DA alternating stack system exhibiting a metallic behavior near RT.<sup>243</sup> The transport mechanism is interpreted by the dynamics of the soliton and domain wall.

Contrary to the segregated stack CT complexes, all of the alternating stack CT complexes are semiconducting since the valence band is fully filled at any degree of CT.<sup>95</sup> Although it was predicted that the degeneration of valence and conduction



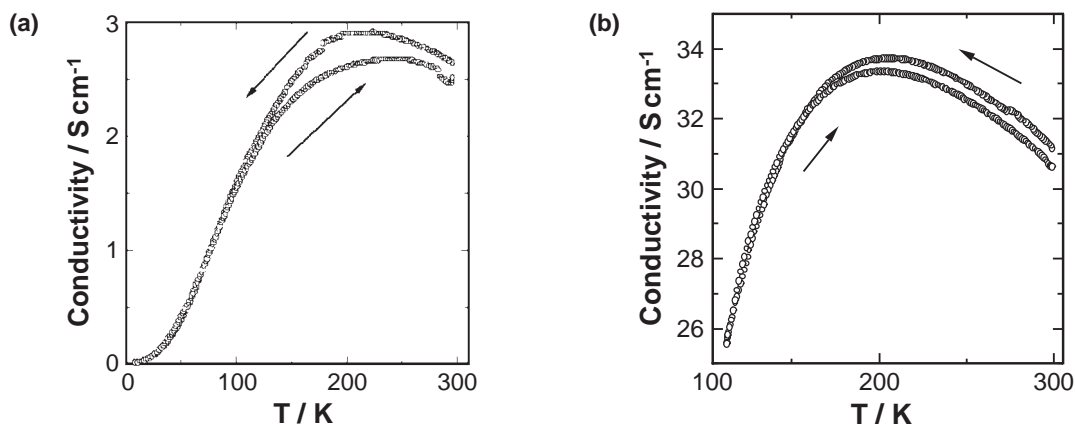


Fig. 107. Temperature dependence of conductivity of the (a) as grown and (b) tempered HMTTeF·Et<sub>2</sub>TCNQ (*//a*).

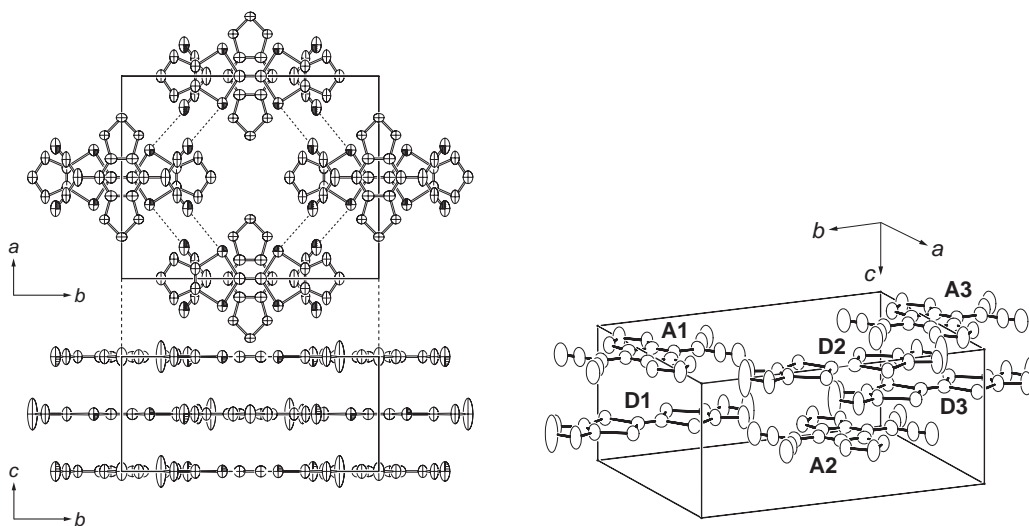


Fig. 108. Crystal structure of as-grown (HMTTeF)(Et<sub>2</sub>TCNQ)(THF)<sub>x</sub>. The ethyl groups are disordered. THF molecules are not depicted. Orthorhombic, *Immm*, *a* = 13.170(1), *b* = 16.781(2), *c* = 7.471(1) Å, *V* = 1651.1(2) Å<sup>3</sup>, *Z* = 2, *R* = 0.0524.<sup>243</sup>

bands results in a semimetallic band structure for  $\delta = 0.63$ ,<sup>758</sup> such a system has not yet been experimentally realized.

Single crystals of the HMTTeF complexes were prepared by mixing each purified component molecules in a mixed solvent of 1,2-dichloroethane/THF as dark green long plates. As-grown single crystals include the THF molecules, which can be evaporated off without deteriorating the crystal. The average amount of THF molecules (*x*) in the crystals, (HMTTeF)(A)(THF)<sub>x</sub>, changed from 1.0 to 0.5 depending on the batch. For the samples in average *x* = 0.5 batch, the  $\sigma_{RT}$  ranges 0.3–10 S cm<sup>-1</sup> for the Et<sub>2</sub>TCNQ and 80–100 S cm<sup>-1</sup> for the BTDA-TCNQ complexes. For the Et<sub>2</sub>TCNQ complex, a metallic temperature dependence was observed on 12 out of 18 crystals in a batch. The following results were obtained for the Et<sub>2</sub>TCNQ complex, and similar phenomena were also observed for the BTDA-TCNQ complex.

The complex is metallic down to 230 K and the  $\varepsilon_a$  below *T*<sub>MI</sub> is 16 meV. (Fig. 107a). The metallic behavior is improved by evaporating off the THF molecules from the crystals by heating at around 80–100 °C. Single crystals thus tempered showed well reproducible physical data. Figure 107b shows the electric conductivity of the tempered crystals along the

stacking direction. The  $\sigma_{RT}$  of the tempered crystals is 10–40 S cm<sup>-1</sup> and increases with decreasing temperature down to 200 K. Below the temperature, the conductivity decreases very gradually with an activation energy of 8–9 meV.

The HMTTeF and Et<sub>2</sub>TCNQ molecules stack alternately along the *c*-axis with an overlap integral ( $S_{D1-A1} = -4.73 \times 10^{-3}$ ), which exceeds others by more than one order of magnitude ( $S_{D1-D3} = 0.09 \times 10^{-3}$ ,  $S_{A1-A2} = 0$ ,  $S_{D1-A2} = -0.47 \times 10^{-3}$ ), where  $S_{D1-A1}$  is the overlap integral between D1 and A1 molecules in Fig. 108. The band calculation predicts that the electronic structure has no semimetallic character. The valence band would be fully filled in the range of  $0 \leq \delta \leq 1$ , and thus a metallic behavior is not expected for the HMTTeF·Et<sub>2</sub>TCNQ complex within a framework of band theory. A plot of  $h\nu_{CT}$  vs  $\Delta E$  (Fig. 18d, **1** and **2**) indicates that the Et<sub>2</sub>TCNQ ( $h\nu_{CT} = 5.1 \times 10^3$  cm<sup>-1</sup> and  $\Delta E = +0.31$  V) and BTDA-TCNQ ( $h\nu_{CT} = 5.0 \times 10^3$  cm<sup>-1</sup> and  $\Delta E = +0.43$  V) complexes are allocated in the neutral side and in close vicinity of the bottom of the V-shaped line, suggesting that the lattice energy of the ionic domain is comparable to that of the neutral domain in the crystal.

It was found that the ionicity is sensitive to and increases by

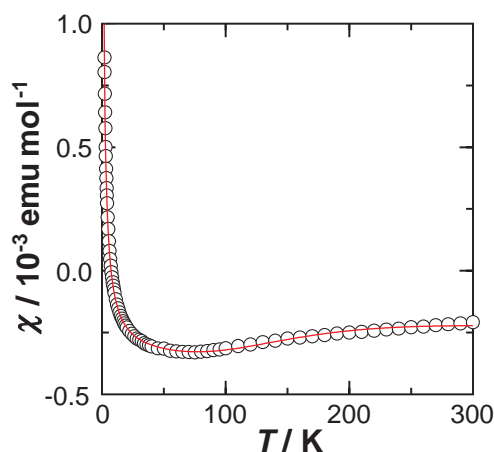


Fig. 109. Magnetic susceptibility of tempered HMTTeF·Et<sub>2</sub>TCNQ. Open circles are experimental data and the solid line is fit to Eq. 63.

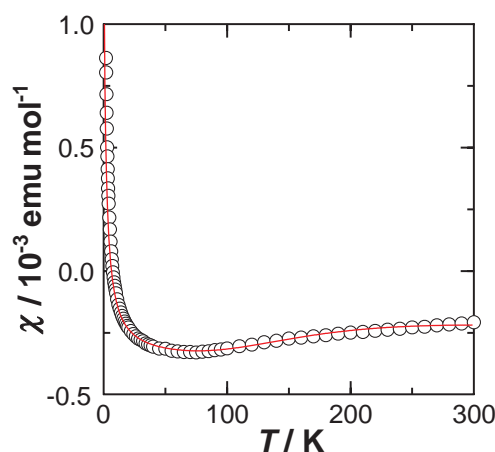


Fig. 110. Magnetic susceptibility of tempered HMTTeF·Et<sub>2</sub>TCNQ. Open circles are experimental data and the solid line is fit to Eq. 64.

mechanical stress such as pulverization of the crystals like 1,6-diaminopyrene·*p*-chloranil.<sup>759</sup> In the Raman spectrum on the single crystals, the C=C stretching modes of the quinonoid ring of Et<sub>2</sub>TCNQ and central C=C of HMTTeF support the mixing of different kinds of species with respect to the ionicity. The  $\delta$  is roughly estimated to be 0.4 and 0.6 for the neutral and ionic species, respectively. In addition, a small amount of fully neutral ( $\delta = 0$ ) and ionic ( $\delta = 1$ ) species coexist in a single crystal. The temperature dependence of the Raman spectrum reveals that the relative intensity of the peaks remained almost constant down to 5 K, indicating that the domain size is insensitive to temperature. Similarly, comparison of its C≡N modes in the IR spectrum with those of neutral and monoanionic Et<sub>2</sub>TCNQ reveals that the complex is composed of an admixture of the neutral and ionic species. In addition, the appearance of the  $a_g$  mode of C≡N stretching strongly indicates lattice dimerization in the DA alternating stack.

Temperature dependence of the magnetic susceptibility ( $\chi$ ) of HMTTeF·Et<sub>2</sub>TCNQ single crystals is shown in Fig. 109. The  $\chi$  decreases monotonically from RT to ca. 60 K and then increases rapidly below it. The  $\chi$  in the low-temperature region is represented by the Curie–Weiss law ( $\chi_{\text{Curie}} = C/(T - \theta)$ ,  $C$ : Curie constant,  $\theta$ : Weiss temperature), which is caused by solitons like TTF·*p*-chloranil.<sup>219</sup> The increase in  $\chi$  with increasing temperatures above 60 K is possibly ascribed to the formation of solitons by the migration of domain walls, and thus might be fit to the singlet–triplet excitation mechanism of DA dimers ( $D^+A^- \rightarrow D^{\bullet+} + A^{\bullet-}$ ) (Eq. 63). Then, the fitting parameters are determined as  $\chi_{\text{core}} = -3.72 \times 10^{-4}$  emu mol<sup>-1</sup>,  $A = 2.91 \times 10^{-3}$  emu K mol<sup>-1</sup>,  $\theta = -0.48$  K,  $B = 8.71 \times 10^{-2}$  emu K mol<sup>-1</sup>, and  $J/k_B = 250.0$  K. The Curie and the singlet–triplet paramagnetic species amount to 0.39 and 11.6% of the DA pairs, respectively.

$$\chi = \chi_{\text{core}} + \frac{A}{T - \theta} + \frac{B}{T} \left\{ \frac{4 \exp\left(-\frac{2J}{k_B T}\right)}{1 + 3 \exp\left(-\frac{2J}{k_B T}\right)} \right\} \quad (63)$$

The concentration of solitons depends on the speeds of migration of both solitons and domain walls. When the former is

much slower than the latter, no increase in solitons is accounted since the  $D^+$  and  $A^-$  solitons neighboring the domain wall (Eq. 60) are immediately annihilated by further migration of the domain walls toward the left hand side as shown in Eqs. 60–62, where the  $D^+$  soliton is reduced to  $D^0$  and the  $A^-$  soliton forms an  $A^-D^+$  pair. The highly conductive nature of this complex is, therefore, attributed to the pair breaking of  $D^+A^-$  by the motion of the domain wall (Eqs. 59 and 60) and more rapid migration of the  $D^+$  and  $A^-$  solitons than that of the domain walls (Eqs. 61 and 62). Therefore, the conductivity and the carrier generation are subjected to the speed of domain wall migration. Based on the conducting behavior below 200 K, the energy for the carrier generation is deduced to be 18 meV (209 K), which is much less than the energy gap between singlet and triplet in the last term of Eq. 63 ( $2J/k_B = 500$  K). Then, the spin susceptibility after subtracting the core diamagnetism ( $\chi_{\text{core}}$ ) and Curie term ( $\chi_{\text{Curie}}$ ) from Eq. 63 should include both the spins of mobile solitons ( $\chi_{\text{ms}}$ ), which are related to the conductivity with an activation energy of 8–9 meV, and the thermally activated localized spins within the ionic domains ( $\chi_{\text{ls}}$ ). Taking the exchange interactions between  $D^+$  and  $A^-$  within a dimer and between dimers as  $J$  and  $J'$ , respectively, the net spin susceptibility is represented by Eq. 64 and the total spin susceptibility  $\chi$  is shown in Fig. 110. Now the fitting parameters are  $B' = 1.19 \times 10^{-3}$  emu K mol<sup>-1</sup>,  $B'' = 8.91 \times 10^{-2}$  emu K mol<sup>-1</sup>, and  $J'/k_B = 362$  K.

$$\begin{aligned} \chi - \chi_{\text{core}} - \chi_{\text{Curie}} &= \chi_{\text{ms}} + \chi_{\text{ls}} \\ &= \frac{B'}{T} \left\{ \frac{4 \exp\left(-\frac{2(J' - J)}{k_B T}\right)}{1 + 3 \exp\left(-\frac{2(J' - J)}{k_B T}\right)} \right\} + \frac{B''}{T} \left\{ \frac{4 \exp\left(-\frac{2J}{k_B T}\right)}{1 + 3 \exp\left(-\frac{2J}{k_B T}\right)} \right\} \\ &\quad \text{with } 2(J' - J) = 0.018 \text{ eV} \end{aligned} \quad (64)$$

The metallic conduction may be explained in terms of the generation and migration of solitons and domain walls in the crystal. As temperature rises the number of solitons generated by the migration of domain walls increases according to the first term in Eq. 64. The domain wall migration is of thermally activated type with the activation energy of 8–9 meV

( $\varepsilon_g = 186\text{--}209\text{ K}$ ). The solitons thus created move rapidly in the crystal and are retarded probably due to the soliton–phonon interaction at higher temperatures.

**4.4 Conducting Films.** In this section, the conducting films of the monolayer and multilayers such as Langmuir–Blodgett (LB) films, self-assembled monolayers (SAMs), reticulate doped polymer (RDP) films, and evaporated thin films are described. Several review articles for conducting LB films,<sup>760,761</sup> SAMs,<sup>762–764</sup> and RDP films<sup>765</sup> have been published. The FET films have been summarized in section 2.2.

**4.4.1 Langmuir–Blodgett Films:** The LB films of CT type have been developed as follows.<sup>760,761</sup> 1) As for the DA type, the  $D^{\delta+}A^{\delta-}$  part acts as the hydrophilic moiety and the long alkyl chains attached to the D or A molecules act as the hydrophobic moiety. As for the radical salt type, long alkyl chains have been attached either to the radical moiety or to the counter ion. However, in order to fulfill one of the essential requirements for an organic metal, namely the aggregation of uniform segregated column, it is more appropriate to use component molecules that contribute to the conductivity, with short or no alkyl chains. 2) In general, equimolar arachic (arachidic or icosanoic) acid ( $C_{19}H_{39}COOH$ ) or behenic acid ( $C_{21}H_{43}COOH$ ) has been employed as the matrix in order to have well packed LB films. However, this process and also the use of long alkyl chains in either D or A part may depress the conductivity. 3) Therefore, the use of component molecules having self-assembling ability, such as  $M(dmit)_2$ , BO, TTP, etc. (see section 3.1), is favorable to prepare conducting LB films. 4) High conductivity is often realized after the secondary treatment by  $I_2$  or electrooxidation of the LB films. The stoichiometry of the LB films after the secondary treatment has not been confirmed. Table 26 summarizes the selective highly conductive LB films.

**4.4.1.1 TCNQ Anion Radical Salts;** The conducting LB films were first developed in 1985 based on the anion radical salt of TCNQ with pyridinium derivatives having long alkyl chains ( $C_5H_5N\text{--}C_{22}H_{45}$ ) by Ruaudel-Teixier et al.<sup>766</sup> The conductive LB films ( $\sigma_{RT} = 0.1\text{ S cm}^{-1}$ ,  $\varepsilon_g = 0.30\text{ eV}$ ) were obtained without any matrix but after the secondary treatment with  $I_2$ . It was claimed that the as-grown film consists of sheets of  $(TCNQ^{\bullet-})_2$  dimers with a molecular plane nearly parallel to the surface of the substrate, and that the secondary treatment results in the reorientation of the TCNQ molecules to arrange their molecular planes and long axes roughly perpendicular to the substrate surface.<sup>797</sup> The LB films of phosphonium and sulfonium salts [ $PMe_3(C_{18}H_{37})$ ,  $SMe_2(C_{18}H_{37})$ , and  $SMeEt(C_{18}H_{37})$ ] of TCNQ were also conductive after the secondary treatment.<sup>767–769</sup> The authors claimed high conductivity of  $\sigma_{RT} = 40\text{ S cm}^{-1}$  based on the analysis of the optical spectra of the “semiconducting” LB films. The high conductivity, however, can only be realized in the LB films consisting of a partial CT complex. Since the original TCNQ LB films before secondary treatment are insulating, the second treatment modifies not only the molecular packing but also the electronic structure from  $D^+X^-$  to  $D^+[(X^-)_{1-x}(X^0)_x + (W^-)_x]$ , where  $W^-$  is the unknown anion species. Dhindsa et al. reported that multilayer films deposited from the 1:1 salt of *N*-octadecylpyridinium•TCNQ exhibited a significant conductivity (ca.  $10^{-2}\text{ S cm}^{-1}$ ) that exceeds those of usual 1:1 TCNQ salts.<sup>798</sup> They

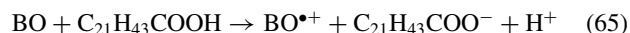
performed XPS analysis on the deposited film and found three distinct nitrogen environments: negatively, neutral, and positively charged species, while only negatively and positively charged species on the 1:1 powder sample. They deduced the composition of the complex in the LB films to be  $(N\text{-octadecylpyridinium})[(TCNQ^{\bullet-})_{1-x}(TCNQ^0)_x(OH^-)_x]$  and the generation of  $OH^-$  species from the oxygen dissolved in the water subphase.<sup>799</sup>

Since TCNQ molecules do not have excellent self-assembling ability to form segregated columns or layers by themselves, the preparation of conductive TCNQ LB films is rather difficult.

**4.4.1.2  $M(dmit)_2$  Anion Radical Salts;** The metal complex compounds  $M(dmit)_2$  have an excellent self-assembling ability in comparison with that of TCNQ, since the peripheral sulfur atoms contribute to the cohesion of the lattice. Some of the alkylammonium  $[NMe_{4-m}(C_nH_{2n+1})_m]$  salts of  $M(dmit)_2$  with a matrix of arachidic acid are highly conductive [ $(m, n, M, \sigma_{RT}/S\text{ cm}^{-1}) = (1, 10, Ni, 1.0), (2, 10, Au, 1.4), (3, 10, Ni, 1.4), (3, 14, Au, 19), \text{ and } (4, 10, Ni, 1.6)]$  after secondary treatment by  $Br_2$  or electrochemical oxidation in aqueous  $LiClO_4$  solution.<sup>770</sup> Some LB films are conductive without the matrix [(2, 10, Pd, 1.0), (4, 10, Pd, 5.1)].<sup>770,771</sup> Besides the semiconductive LB films, two metallic LB films were prepared after the secondary treatment of electrooxidation [(2, 14, Au, 40), (3, 10, Au, 40)] by Miura et al.<sup>772,773</sup> The former and the latter are metallic near RT without and with the matrix, respectively. These LB films after the secondary treatment are rather fragile and the degradation of the LB films soon destroys the conductive behaviors.

**4.4.1.3 Cation Radical Salts of TTF Derivatives;** Most of the TTF derivatives used for the conducting LB films are comprised of the basic skeleton of ET,  $TTC_n\text{-TTF}$  or  $C_n\text{TET-TTF}$ . Their self-assembling ability is inferior to that of BO, resulting in less conductive LB films ( $\sigma_{RT} \approx 1\text{--}2\text{ S cm}^{-1}$ ) than those based on BO ( $\sigma_{RT} \approx 40\text{ S cm}^{-1}$ ). In general, the LB films based on TTF derivatives have been prepared using behenic acid or arachidic acid, then the films are treated by  $I_2$  or  $FeCl_3$  to create the radical electrons to give rise to conductivity. Transport properties of the conductive LB films ( $\sigma_{RT} \geq 1\text{ S cm}^{-1}$ ) are summarized in Table 26.

Among them, the BO LB films exhibit a metallic behavior down to 14 K.<sup>777,778</sup> The films were prepared by deposition of a 2:1 and 1:1 mixture of BO and behenic acid without the secondary treatment by Ohnuki et al.<sup>777</sup> The structure was determined by X-ray diffraction measurements to be a Y-type film. Based on the IR spectra the ionization mechanism of BO in the film formation process is deduced to be the deprotonation of the carboxylic acid (Eq. 65). However, the details of the succeeding reaction of  $H^+$  thus formed is unknown.



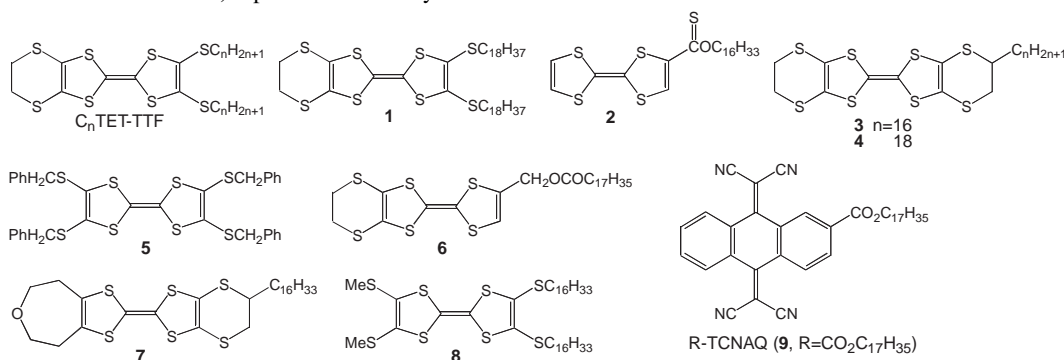
A negative magnetoresistance was observed for the LB films prepared by BO and stearic acid ( $C_{17}H_{35}COOH$ ), which showed metallic behavior down to 120 K.<sup>779</sup>

The donor molecules **2**,<sup>775</sup> **4**,<sup>776</sup> and **6**<sup>77</sup> are reported by Dhindsa et al. and Goldenberg et al. to give LB films of  $\sigma_{RT} = 4 \times 10^{-2}$ ,  $10^{-2}\text{--}10^{-3}$ , and  $10^{-2}\text{--}10^{-3}\text{ S cm}^{-1}$ , respectively, without any secondary treatment. Some LB films com-

Table 26. Selected Examples of Highly Conductive LB Films

D or A	Anion or Cation	Matrix	Treatment <sup>a)</sup>	$\sigma_{RT}/S\text{ cm}^{-1}$ ( $\epsilon_g/\text{eV}$ )	Ref.
Anion Radical Salt Type					
TCNQ	$\text{C}_5\text{H}_5\text{N}-\text{C}_{22}\text{H}_{45}$	no	$\text{I}_2$	0.1 (0.30)	766
TCNQ	$\text{PMe}_3(\text{C}_{18}\text{H}_{37})$	no	$\text{I}_2$	40 <sup>b)</sup>	767
TCNQ	$\text{SMe}_2(\text{C}_{18}\text{H}_{37})$	no	$\text{I}_2$	40 <sup>b)</sup>	768
TCNQ	$\text{SMeEt}(\text{C}_{18}\text{H}_{37})$	no	$\text{I}_2$	40 <sup>b)</sup>	769
$\text{Au(dmit)}_2$	$\text{NMe}_3(\text{C}_{10}\text{H}_{21})$	arachidic acid	$\text{Br}_2$	1.0	770
$\text{Au(dmit)}_2$	$\text{NMe}_2(\text{C}_{10}\text{H}_{21})_2$	arachidic acid	$\text{EO/LiClO}_4$	1.4	770
$\text{Ni(dmit)}_2$	$\text{NMe}(\text{C}_{10}\text{H}_{21})_3$	arachidic acid	$\text{EO/LiClO}_4$	1.4	770
$\text{Au(dmit)}_2$	$\text{NMe}(\text{C}_{14}\text{H}_{29})_3$	arachidic acid	$\text{EO/LiClO}_4$	19	770
$\text{Ni(dmit)}_2$	$\text{N}(\text{C}_{10}\text{H}_{21})_4$	arachidic acid	$\text{Br}_2$	1.6	770
$\text{Pd(dmit)}_2$	$\text{NMe}_2(\text{C}_{10}\text{H}_{21})_2$	no	$\text{EO/LiClO}_4$	1.0	770
$\text{Pd(dmit)}_2$	$\text{NMe}(\text{C}_{10}\text{H}_{21})_3$	no	$\text{EO/LiClO}_4$	5.1	771
$\text{Au(dmit)}_2$	$\text{NMe}(\text{C}_{14}\text{H}_{29})_3$	no	$\text{EO/LiClO}_4$	40 (metallic)	772
$\text{Au(dmit)}_2$	$\text{NMe}(\text{C}_{10}\text{H}_{21})_3$	arachidic acid	$\text{EO/LiClO}_4$	40 (metallic)	773
Cation Radical Salt Type					
<b>1</b>		behenic acid	$\text{I}_2$	1 (0.04)	774
<b>2</b>		no	$\text{I}_2$	1 (0.18)	775
<b>4</b>		tricosanoic acid	$\text{I}_2$	1	776
BO		behenic acid	no	40 (metallic) > 14 K	777,778
		stearic acid	no	metallic > 120 K	779
EOET		behenic acid	no	2	777
<b>6</b>	no	no	no	$10^{-2}$	77
DA Type					
TMTTF	$\text{C}_{18}\text{TCNQ}$	no	no	0.1 (0.19)	780
TMTTF	$\text{C}_{14}\text{TCNQ}$	no	no	1	781,782
BO	$\text{C}_n\text{TCNQ}(n = 10,14)$	arachidic acid	no	1–10 (metallic)	783–785
<b>3</b>	$\text{C}_{16}\text{TCNQ}$	no	no	2.5	786,787
<b>3</b>	<b>9</b>	no	$\text{I}_2$	1	788
	<b>9</b>	no	$\text{FeCl}_3$	2	789
<b>7</b>	<b>9</b>	no	no	5	790
<b>5</b>	$\text{Cu(dmit)}_2$	stearic acid	$\text{I}_2$	1.1	791
<b>5</b>	$\text{Ni(dmit)}_2$	no	no	40	792
<b>8</b>	$\text{C}_{18}\text{TCNQ}$	no	$\text{I}_2$	1 (mixed layer)	793
		no	$\text{I}_2$	150 (alternate layer)	
TTF	TCNQ	no	no	5.5	794
BO	$\text{CF}_3\text{TCNQ}$	arachidic acid	no	3.7	795
BO	$(\text{MeO})_2\text{TCNQ}$	arachidic acid	no	11.3 (metallic)	796

a) EO: electrooxidation. b) Optical conductivity.



posed of **4** showed an increase in RT conductivity ( $10^{-1} \text{ S cm}^{-1}$ ) upon storage in air for 10 days.<sup>776</sup> The conductivity is not very impressive compared with those in Table 26, but

is very remarkable considering the fact that the material is composed of a single component with a closed shell electronic structure (the highest conductivity is  $\sigma_{RT} = 1 \times 10^{-3} \text{ S cm}^{-1}$

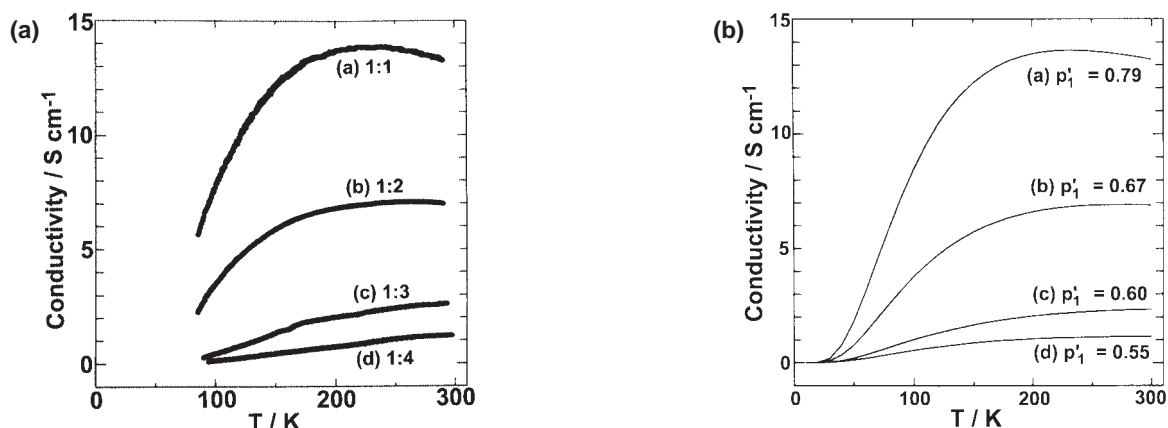
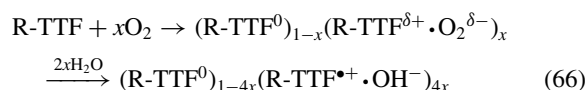


Fig. 111. (a) Temperature dependence of electrical conductivity for BO-C<sub>10</sub>TCNQ-arachidic acid LB films: (a) 1:1, (b) 1:2, (c) 1:3, and (d) 1:4 ratio of C<sub>10</sub>TCNQ to arachidic acid. (b) Simulation of the electrical conductivity based on the modified 2D metal-semiconductor-insulator percolation model with  $p_2' = 0.39$ ,  $C_{ms} = 480$ , and  $E = 120$  K.<sup>800</sup>

for BTQBT single crystals, see section 2.3.1). The formation of highly conductive LB films of **2**, **4**, and **6** suggests either that the LB method might pack  $\pi$ -moieties more tightly than that in the single crystals (compressed pellets of **2** and **4** show  $\sigma_{RT}$  values of  $10^{-15}$  and  $10^{-12}$  S cm<sup>-1</sup>, respectively),<sup>775,776</sup> or that the prepared LB films have an impurity level for transport owing to the formation of a CT complex with oxygen. The latter is more plausible based on the experimental result, which shows an increase in conductivity of the LB films upon storage in air. In the case of LB films of **4** in the matrix of 22-tricosenoic acid (9:1) ( $\sigma_{RT} = 10^{-2}$ – $10^{-3}$  S cm<sup>-1</sup>),<sup>776</sup> an ionization of **4** by a similar reaction to Eq. 65 is possible besides the formation of a CT complex with oxygen. Other explanation would be the formation of OH<sup>-</sup> from the CT complex with oxygen in the water subphase (Eq. 66) according to the proposal for the TCNQ system in section 4.4.1.1 by Ward et al.<sup>799</sup>



**4.4.1.4 DA Type;** The LB films of DA type, in general, do not need the secondary treatment but need the matrix to exhibit high conductivity as first reported on TMTTF·C<sub>18</sub>TCNQ ( $\sigma_{RT} = 0.1$  S cm<sup>-1</sup>).<sup>780</sup> The following are highly conductive ( $\geq 1$  S cm<sup>-1</sup>) LB films of DA type in which one component has a long alkyl chain: 1 S cm<sup>-1</sup> for TMTTF·C<sub>14</sub>TCNQ,<sup>781,782</sup> 1–10 S cm<sup>-1</sup> for BO·C<sub>n</sub>TCNQ ( $n = 10, 14$ ),<sup>783,784</sup> 2.5 S cm<sup>-1</sup> for **3**·C<sub>16</sub>TCNQ,<sup>786,787</sup> 5 S cm<sup>-1</sup> for **7·9**,<sup>790</sup> and 40 S cm<sup>-1</sup> for **5**·Ni(dmit)<sub>2</sub>.<sup>792</sup>

Since the C<sub>n</sub>TCNQ molecule has a similar electron affinity to that of MeTCNQ ( $E_{1/2}^1 = 0.17$ – $0.21$  V vs SCE, cf. 0.19 V for MeTCNQ), it is reasonable that **3** and **8** are not strong enough electron donors to afford a partial CT state in the complexes with C<sub>n</sub>TCNQ. Also, since TCNAQ ( $E_{1/2}^1 = -0.32$  V) is a very weak acceptor molecule, **3** and **7** can not form a partial CT state with **9**. Therefore, the high conductivity of **3**·C<sub>16</sub>TCNQ, **8**·C<sub>18</sub>TCNQ, and **3·9** was only realized by the oxidation of the donor moieties by secondary treatment with I<sub>2</sub> or FeCl<sub>3</sub>. The high conductivity of **5**·Cu(dmit)<sub>2</sub> might be explained similarly, but that of **7·9** without secondary treatment is extraordinary. The latter result suggests either that the

LB method relaxes the requirement for an organic metal concerning the ionicity owing to the densely packed aggregation or that the formation of a CT complex with oxygen. The latter is more plausible and would then explain the extremely high conductivity of the LB films by the formation of a mixed-valence state as expressed by Eq. 66.

The first metallic LB films of DA type were prepared by Nakamura et al. based on BO complexes from the water-air interface.<sup>783,784</sup> The LB films were prepared by the deposition of a 1:1 mixture of the CT complex (BO)<sub>10</sub>(C<sub>10</sub>TCNQ)<sub>4</sub>(H<sub>2</sub>O) and arachidic acid on a quartz or poly(ethylene terephthalate) substrate. The conductivity measurement exhibited metallic behavior down to ca. 250 K (Fig. 111), and both the thermoelectric power and EPR measurements proved the metallic nature within a domain ( $\approx$  a few  $\mu\text{m}^2$ ) at least down to ca. 50 K.<sup>785</sup> In relation with that, the pellet sample of the bulk CT complex exhibits a metallic behavior down to around 140 K followed by a gradual increase of resistivity.

The conducting behavior was analyzed by Ogasawara, Ishiguro, et al. utilizing a concept of the 2D percolation model. The coexistence of the metallic, semiconducting, and insulating domains in a film was assumed with the following parameters:  $p_1$ : ratio of CT complex within the film,  $p_2$ : ratio of metallic CT complex within the CT complex region,  $C_{ms}$ : ratio of conductance of the metallic one to semiconducting one, and  $E$ : activation energy between the semiconducting sites.<sup>800</sup> Since the actual dimensionality of the LB film was deduced to be 2.4, the values of site occupancy  $p_i$  ( $i = 1, 2$ ) were transformed into those for 2D ( $p_i'$ ) and the  $p_2$  was estimated from the X-ray diffraction analysis to be 0.25, which corresponds to  $p_2' = 0.39$ . The  $p_1$  values can be estimated from both the ratio of BO/C<sub>10</sub>TCNQ in the complex ( $=2.5$ ) and the mixing ratio of the C<sub>10</sub>TCNQ and arachidic acid (1: $X$ ) as  $p_1 = 2.5/(2.5 + X)$ . Then, the effective occupancy factor  $p_1'$  was evaluated as 0.78, 0.66, 0.57, and 0.52 for LB films with 1:1, 1:2, 1:3, and 1:4 ratio of C<sub>10</sub>TCNQ to arachidic acid, respectively. The temperature dependence of the conductivity (Fig. 111a) was well reproduced by the calculation based on a modified 2D percolation model with  $p_2' = 0.39$ ,  $C_{ms} = 480$ , and  $E = 120$  K with  $p_1'$  values slightly different from those calculated above; 0.79, 0.67, 0.60, and 0.55 for 1:1, 1:2, 1:3, and 1:4



LB films, respectively (Fig. 111b). The semiconducting behavior with a small activation energy of 120 K arises from the distributed disorder in the metallic CT complex.

Spin-lattice relaxation time of  $^1\text{H}$ NMR in polycrystalline  $(\text{BO})_{10}(\text{C}_{10}\text{TCNQ})_4(\text{H}_2\text{O})$  has been measured at the low-temperature range of 2–50 K by Tsukada et al.<sup>801</sup> A Korringa-like behavior was observed down to about 30 K and the Anderson localization was detected at lower temperatures. The spin-lattice relaxation time of protons in the  $\text{BO}\cdot\text{C}_{10}\text{TCNQ}$ -arachidic acid LB films also indicated the occurrence of Anderson localization in the temperature region of 2–14 K.<sup>802</sup>

Even component molecules having no long alkyl chain afford highly conductive LB films, although the films were not well organized:  $5.5\text{ S cm}^{-1}$  for  $\text{TTF}\cdot\text{TCNQ}$ ,<sup>794</sup>  $3.7\text{ S cm}^{-1}$  for  $\text{BO}\cdot\text{CF}_3\text{TCNQ}$ ,<sup>795</sup> and  $11.3\text{ S cm}^{-1}$  for  $\text{BO}\cdot(\text{MeO})_2\text{TCNQ}$ .<sup>796</sup> The 1:1 mixture of the CT complex  $\text{BO}\cdot(\text{MeO})_2\text{TCNQ}$  and arachidic acid afforded deposited films showing a metallic behavior down to ca. 180 K (Fig. 112). EPR study supports the metallic nature down to ca. 50 K.<sup>796</sup>

Accordingly, the component molecules should have a strong self-assembling ability in the  $\pi$ -moieties (see section 2.3) and short hydrophobic alkyl chains in order to have highly conductive LB films. In this case, however, the fabrication of structurally well defined LB films is difficult.

It has been reported that some LB films composed of dimethylbis(tetradecyl)ammonium $[\text{M}(\text{dmit})_2]$  ( $T_c < 3.9\text{ K}$ ),<sup>803</sup> and  $\text{C}_{60}$  doped with K ( $T_c < 8.1\text{ K}$ )<sup>804</sup> and Rb ( $T_c < 23\text{ K}$ )<sup>805</sup> exhibit superconductivity, which was detected by the AC com-

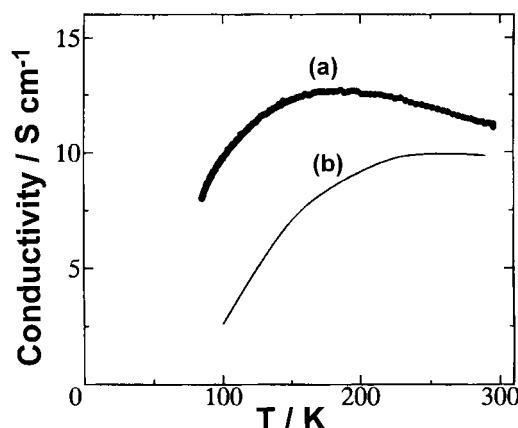


Fig. 112. Temperature dependence of electrical conductivity for (a)  $\text{BO}(\text{MeO})_2\text{TCNQ}$ -arachidic acid LB films in comparison with that of (b)  $\text{BO}\text{-C}_{10}\text{TCNQ}$ -arachidic acid LB films.<sup>796</sup>

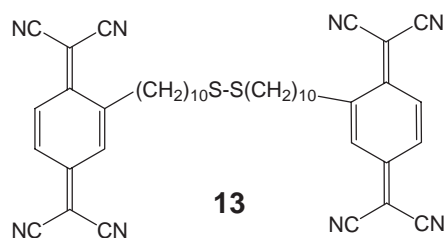
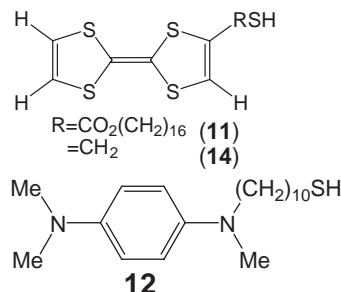


Chart 14.

plex magnetic susceptibility or low magnetic field microwave absorption measurements. However, both the structural disorder inherent to the LB films and the low-dimensional nature originating from the thin-layer structure severely prohibit the observation for the superconductivity by resistivity measurements.

**4.4.2 Self-Assembled Monolayers (SAMs):** In 1983, Nuzzo and Allara showed the formation of a covalent bond between alkanethiolates and a gold surface by adsorption of dialkyl disulfides from a dilute solution.<sup>806</sup> The films labeled as “self-assembled monolayers (SAMs)” have been an important strategy for exploiting well-ordered and stable applications such as wetting, corrosion inhibition, molecular sensors, and nanopatterning. SAMs have less voids, disorders, and defects than the LB films. Recently, alkanethiols or dialkyl disulfides have been chemically attached not only on Au, Pt, Ag, and Cu metals, but also on GaAs, CdS, and ITO (Sn-doped  $\text{In}_2\text{O}_3$ ).<sup>762,763</sup> In this section, we focus on SAMs composed both of electron-accepting and of electron-donating components.

Ward and Yip prepared SAMs with CT interactions, for which a mixed monolayer composed of 16-mercaptoalkyl-tetrathiafulvalenecarboxylate (**11**) (Chart 14) and 16-mercaptohexadecanoic acetic acid or hexadecane-1-thiol on a gold substrate was immersed in a TCNQ/chloroform solution.<sup>808</sup> The layer-by-layer method results in a sizable frequency shift of  $\text{C}\equiv\text{N}$  and  $\text{C}=\text{O}$  stretching modes, strongly indicating the presence of CT between the TTF moiety and TCNQ. Likewise, CT interactions were observed by immersing either the monolayer of TMPD thiols (**12**) into a TCNQ/acetonitrile solution or the monolayer of TCNQ disulfides (**13**) into a TMPD/benzene solution.<sup>809</sup> However, these reports have given no structural information for the resulting SAMs.

Yuge, Enoki, and co-workers prepared new-type SAMs consisting of alternating  $\text{TTF}\text{-CH}_2\text{SH}$  (**14**) and TCNQ molecules by immersing the gold substrate into a  $\text{TTF}\text{-CH}_2\text{SH}$ /TCNQ mixed solution (coadsorption method) for the purpose of getting conductive SAMs.<sup>810</sup> A downshift of the  $\text{C}\equiv\text{N}$  stretching mode by  $25\text{ cm}^{-1}$  is firm evidence for CT between  $\text{TTF}\text{-CH}_2\text{SH}$  and TCNQ. Scanning tunneling microscopy and surface plasmon resonance measurements strongly suggest that both component molecules arrange nearly normal to the gold substrate surface. The layer-by-layer method, on the other hand, gave a column structure, in which TCNQ molecules were merely placed over a  $\text{TTF}\text{-CH}_2\text{SH}$  monolayer because of the densely packed  $\text{TTF}\text{-CH}_2\text{SH}$  molecules arranged nearly normal to the gold substrate surface. Hence, CT did not appear in the resulting SAMs.

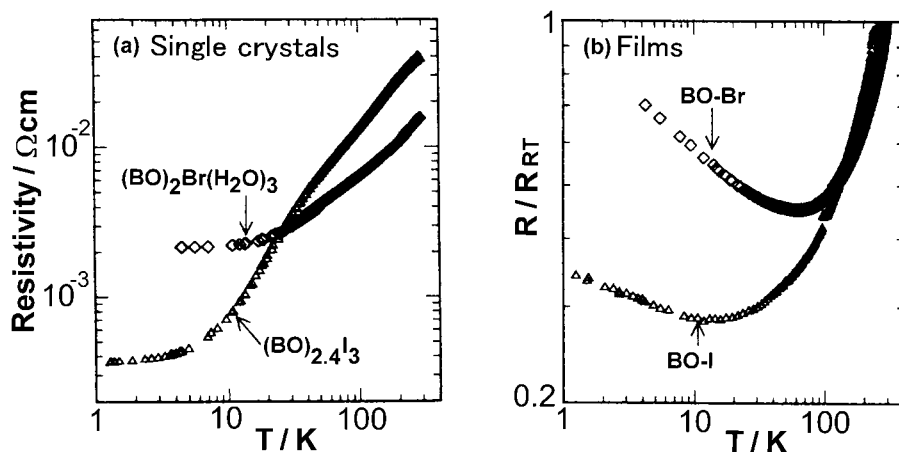


Fig. 113. Temperature dependence of resistivity of (a) single crystals of  $(\text{BO})_2\text{Br}(\text{H}_2\text{O})_3$  and  $(\text{BO})_{2.4}\text{I}_3$  and (b) halogen-doped RDP films.<sup>815</sup>

Also, they prepared SAMs containing  $\text{F}_4\text{TCNQ}$  instead of TCNQ by means of both methods.<sup>811</sup> SAMs prepared by the layer-by-layer method contain the reduced  $\text{F}_4\text{TCNQ}$  together with its neutral species despite their column structure. In the case of the co-adsorption method, complete CT was observed as expected from their redox properties.

In order to elucidate the conductive SAMs, it is necessary to replace the Au substrate with the insulating ones.

**4.4.3 Reticulate Doped Polymer (RDP) Films:** The doping of CT complexes dispersed in polymer films is one of the effective methods to prepare conducting films. The first conducting RDP films were prepared by casting a 1 wt % *o*-dichlorobenzene solution of TTN·TCNQ in polycarbonate on a glass substrate by Jeszka et al. in 1981.<sup>812</sup> The CT complex is crystallized in the polycarbonate after evaporation of the solvent and the conduction path is generated by the connection of the TTN·TCNQ microcrystals. The percolation theory satisfactorily explains the electric conductivity of the films including only 1 wt % of the CT solid. From this point of view, 2D conductors comprising molecules with self-assembling nature are good candidates for highly conducting RDP films.

Well-organized RDP films were afforded by either casting a solution of a CT solid as described above, or casting a solution of one component molecule and then generating radicals by redox reaction. However, highly conducting RDP films remain sparse because many of the highly conducting CT solids are insoluble in conventional organic solvents and the component molecules having self-assembling ability are limited ( $\text{M}(\text{dmit})_2$ , Pc, TTP, ET, BO, EOET, etc.).

Laukhina, Ulanski, et al. prepared RDP films composed of ET in polycarbonate (2 wt %) treated with  $\text{CH}_2\text{Cl}_2/\text{I}_2$  vapors and then annealed at 137 or 155 °C to convert the  $\alpha$ -form to the superconducting  $\alpha_1$ -(ET) $_2\text{I}_3$ . The film is metallic and exhibits a broad superconducting transition below 7 K.<sup>813</sup>

The RDP films of BO compounds show metallic behavior that have been prepared by Tracz, Jeszka, and our group.<sup>814</sup> The casting of a hot *o*-dichlorobenzene solution of polycarbonate containing ca. 1 wt % of BO on a glass substrate gives an insulating film. The film was subjected to the vapor of an organic solvent containing iodine or bromine to form conducting BO complexes near the film surface. The surface resistivity is

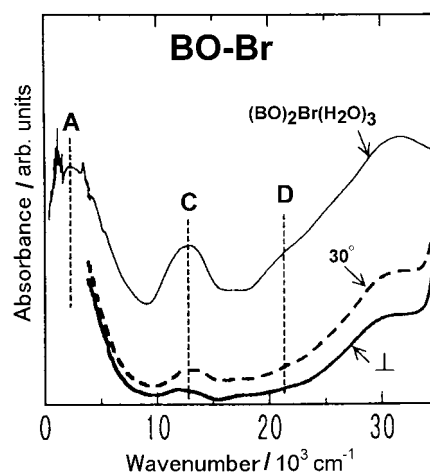


Fig. 114. Optical absorption spectra of a single crystal of  $(\text{BO})_2\text{Br}(\text{H}_2\text{O})_3$  and bromine-doped RDP films with an incident light perpendicular ( $\perp$ ) and oblique (ca.  $30^\circ$ ) to the film surface.<sup>815</sup>

$1 \times 10^{-3}\text{ S}/\square$  at RT, and the bulk conductivity concerning the thickness of the conducting layer is ca.  $10^2$  to  $10^3\text{ S cm}^{-1}$ .

Single crystals of the iodide and bromide salts are metallic down to low temperatures (1.3 and 4 K, respectively) as seen in Fig. 113a. On the other hand, the iodine- and bromine-doped RDP films are metallic down to 17 and 65 K, respectively (Fig. 113b),<sup>815</sup> with less conductivity enhancement compared to the single crystals. The resistance of the bromine-doped RDP films decreased by a factor of 2.1 down to 65 K, below which the resistance gradually increased though it was still smaller than the RT value even at 4 K.

The metallic films treated by iodine are deeply colored owing to the presence of  $\text{I}_3^-$  anions (Fig. 115a). The  $\text{I}_3^-$  anions can be replaced with  $\text{Br}^-$  by immersing the films into a KBr aqueous solution (Fig. 115b). Figure 114 shows the optical absorption spectra of the single crystal  $(\text{BO})_2\text{Br}(\text{H}_2\text{O})_3$  and the bromine-doped RDP films.<sup>815</sup> Band A is ascribed to the intra-band optical transition in metal. It has been known that the BO salts having the segregated stack of fully ionized  $\text{BO}^{\bullet+}$  or  $(\text{BO}^{\bullet+})_2$  exhibit a characteristic band around  $8\text{--}10 \times 10^3\text{ cm}^{-1}$

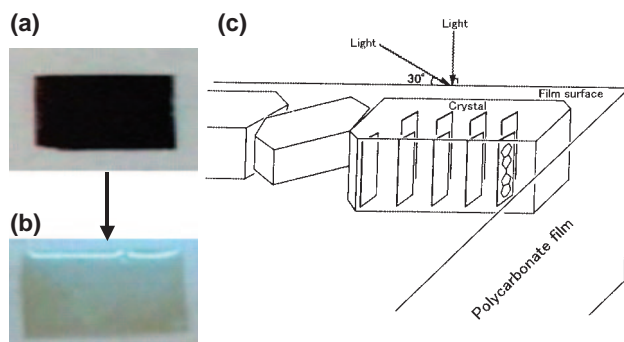


Fig. 115. The iodine-doped BO RDP film is black (a) and turned to transparent (b) after immersing into an aq. KBr solution. (c) Schematic drawing of molecular orientation in RDP films. Hexagonal thick plates represent the metallic crystallites, where only one donor layer is illustrated. In one of the rectangular plates, the molecular shape of BO is drawn.<sup>815</sup>

(Band B).<sup>234,241,815</sup> Thus, the absence of the Band B in the RDP films in Fig. 114 indicates that the segregated stack of BO molecules in the crystallites contains no aggregation of  $\text{BO}^{\bullet+}$ .

The Band C is assigned to the intramolecular excitation from the 2nd-HOMO ( $b_{3g}$ ) to HOMO ( $b_{1u}$ ) of the BO molecule and is commonly seen around  $13 \times 10^3 \text{ cm}^{-1}$ .<sup>234</sup> The weak Band D, which is also observed as the lowest electronic band of neutral BO, is attributed to the excitation from HOMO to LUMO. Compared with the spectra of the  $(\text{BO})_2\text{Br}(\text{H}_2\text{O})_3$  single crystal, the Band C is very weak in the films. The intensity of Band C is dependent on the direction of the incident light; the absorbance increases distinctly when the film surface is tilted from perpendicular to oblique to the incident light. These anisotropic optical properties strongly indicate that the ionized BO molecules are well oriented in the films. Since the intramolecular transitions C and D are polarized along the long axis of the BO molecule, it appears that this molecular axis is almost perpendicular to the film surface as schematized in Fig. 115c. The 2D donor layer in  $(\text{BO})_2\text{Br}(\text{H}_2\text{O})_3$  is nearly perpendicular to the molecular long axis of BO<sup>815</sup> and the crystal grows with the developed planes parallel to the conducting 2D layers. These observations, therefore, strongly suggest that these metallic microcrystals grow parallel to the film plane, as depicted in Fig. 115c.

Summarizing the above, the bromine-doped films are highly transparent in the visible region (Figs. 114 and 115b) since BO molecules are arranged with the molecular long axis normal to the film surface and the optical transitions in the visible region are polarized along the long axis of BO (Fig. 115c).<sup>815</sup> This orientational manner in the BO-iodide RDP films is supported by the scanning electron microscopy, X-ray diffraction, and atomic force microscopy.<sup>814,816</sup>

**4.4.4 Evaporated Thin Films:** Evaporation methods (co-sublimation, chemical vapor deposition (CVD)) are the most common to prepare thin films of CT type. Co-sublimation has also afforded single crystals  $[(\text{TTN})_2\text{I}_3, (\text{TSeN})\text{I}_x (x = 0.5, 0.71, \text{ and } 0.77), \text{TTF} \cdot \text{QCl}_4]$ <sup>219,817–819</sup> or complexes with different stoichiometry from that obtained by the solution method (TMTTF·TCNQ; 1:1 metal from solution, and 1.3:2

and 1.66:2 semiconductors by co-sublimation).<sup>256,257</sup>

**4.4.4.1 DA Type;** Immediately after the discovery of the first organic metal TTF·TCNQ, many reports on thin films processing of this complex have appeared, mainly by the sublimation of its bulk crystal in high vacuum ( $10^{-3}$ – $10^{-4}$  Pa) on single crystals such as NaCl,<sup>820</sup> KCl,<sup>821</sup> and KBr.<sup>822</sup> Thin films of TTF·TCNQ were also fabricated as electrodes for carrier injections on a semiconducting DA complex as channels for an FET device (see section 2.2.2).<sup>58</sup> Thin films grown by CVD at ambient pressure have also been reported.<sup>823</sup> Most of these films have shown semiconducting behavior even above 49–50 K, at which Peierls transition occurs in single crystals.

**4.4.4.2 Cation Radical Salt;** Yudasaka, Saito, et al. prepared thin films of  $\text{TTF} \cdot \text{I}_{0.71}$  on a mica substrate, utilizing co-sublimation of TTF and iodide.<sup>824,825</sup> By controlling the temperature of substrates ( $T_s$ ) and the iodine evaporation source temperature ( $T(I)$ ), the films were grown epitaxially as demonstrated in Fig. 116a. This is one of the first reports of epitaxially grown conducting thin films of CT type. When  $T(I)$  is kept at about 0 °C, the stacking  $c$ -axis of  $\text{TTF} \cdot \text{I}_{0.71}$  film is parallel to the mica surface and makes angles of about +30° or –30° with the  $b$ -axis of the mica substrates. While when  $T(I)$  is about 20 °C, the  $c$ -axis of  $\text{TTF} \cdot \text{I}_{0.71}$  film is perpendicular to the mica surface. The films exhibit dichroism with pale and strong purple domains (Fig. 116a), which are exchanged by rotating the polarizer or the sample with a period of 180°. The anisotropic optical absorption (Fig. 116b) indicates that the intramolecular transitions of  $\text{TTF}^{\bullet+}$  (400 and 560 nm) are polarized perpendicular to the  $c$ -axis and the intermolecular CT band (Band B, 830 nm) is parallel to the  $c$ -axis in agreement with the single crystal optical work.<sup>694</sup> The film shows semiconducting behavior, despite its RT conductivity as high as  $10^2$ – $10^3 \text{ S cm}^{-1}$  ( $//c$ ). The conductivity anisotropy (Fig. 116c) shows a clear thermal hysteresis along the  $c$ -axis reminiscent of that of a single crystal,<sup>826</sup> while no hysteresis was detected perpendicular to the  $c$ -axis with less RT conductivity than that along the  $c$ -axis by a factor of about  $10^2$ .

High vacuum evaporation ( $<1 \times 10^{-3}$  Pa) of single crystal  $\alpha$ -(ET)<sub>2</sub>I<sub>3</sub> accompanied by tempering the as-grown thin film gave the epitaxial  $\alpha_t$ -(ET)<sub>2</sub>I<sub>3</sub> phase on the glass substrate by Kawabata et al.<sup>827,828</sup> A sizeable falloff of the magnetization below ca. 5 K is indicative of the appearance of superconductivity. Afterwards it was found that the thin films of the  $\alpha_t$ -phase deposited on quartz glass showed a low-field microwave absorption below 9 K, although the semiconducting behavior was observed down to ca. 100 K ( $\sigma_{\text{RT}} = 3 \times 10^{-2} \text{ S cm}^{-1}$ ).<sup>827,828</sup> This finding suggests the occurrence of superconductivity below 9 K, which substantially exceeds that of the previous work and is comparable to that of the single crystal.<sup>449</sup>

Thin films of iodine-doped NiPc were also grown on a quartz glass substrate<sup>829</sup> in the same manner as  $\text{TTF} \cdot \text{I}_{0.71}$ . Interestingly, it shows metallic behavior, although the RT value is as low as  $0.1$ – $1 \text{ S cm}^{-1}$ .

Thin films of  $(\text{BO})_{2.4}\text{I}_3$  were grown on a single crystal NaCl under high vacuum condition of  $10^{-5}$  Pa, and showed a RT conductivity of  $1 \text{ S cm}^{-1}$  with  $\varepsilon_g = 0.04 \text{ eV}$ .<sup>830</sup>

**4.5 Conducting Melt, Conductors with Low Melting Point, and Organic Semiconductor Condensers (OS-CON).**

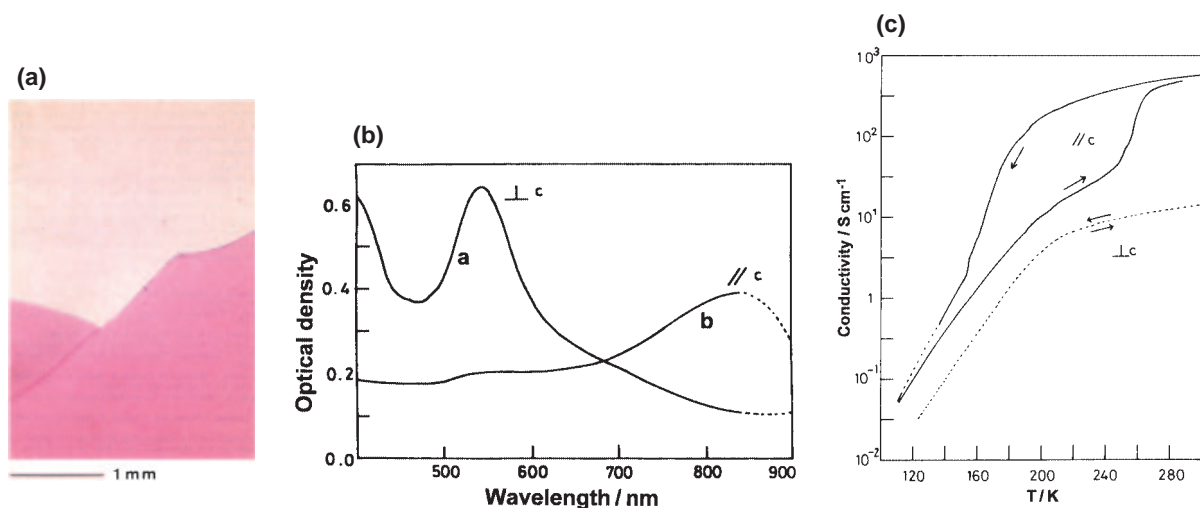


Fig. 116. (a) Polarized microscopic photograph of the  $\text{TTF} \cdot \text{I}_{0.71}$  film. (b) Optical absorption spectra of  $\text{TTF} \cdot \text{I}_{0.71}$  film. Polarization of incident light is (a) perpendicular and (b) parallel to the  $c$ -axis of the film.  $\text{TTF} \cdot \text{I}_{0.71}$  film was obtained at  $T_s = 14^\circ\text{C}$  and  $T(I) = 0^\circ\text{C}$ . (c) Temperature dependence of electrical conductivity of the  $\text{TTF} \cdot \text{I}_{0.71}$  film. Arrows indicate sweep directions of temperature.<sup>824,825</sup>

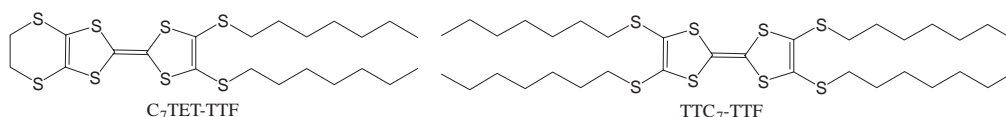


Chart 15.

In the following, the neutral DA type CT complex that exhibits a rapid increase in conductivity during melting, the cation radical salts of TTF derivatives with low melting point, and the anion radical salts of TCNQ with imidazolium cations with low melting point will be described.

#### 4.5.1 Neutral DA Complex with Low Melting Point:

Neutral CT complexes  $\text{D}^{\delta+} \cdot \text{A}^{\delta-}$  ( $\delta \approx 0$ ) normally have a lower melting temperature than those of ionic CT complexes ( $\delta \geq 0.5$ ), since the Madelung energy in the former makes a very small contribution to the lattice energy compared with that in the latter. For the neutral CT complex with alternating stack, i) the number of conduction carriers is negligible at low temperature since  $\delta \approx 0$ , and ii) there is no conduction path with a small activation energy owing to alternating stacks composed of D and A molecules having different potential energies. Consequently, neutral alternating complexes with high conductivity have rarely appeared (see sections 3.1.3 and 4.3.3). Furthermore, most studies on the transport properties of CT complexes have been made on solids, while there have been no such studies in the liquid state. Only a few studies on the optical characterization of the molten CT complexes have been reported.<sup>831</sup> In the following we describe a drastic decrease in resistivity by a factor of  $10^5$ – $10^6$  upon the melting of a neutral alternating CT complex,  $\text{C}_7\text{TET-TTF} \cdot \text{TCNQ}$  (Chart 15).

Syntheses and characterizations of  $\text{C}_n\text{TET-TTF}$  have been studied by Otsuka, Saito, et al.<sup>832</sup> The molecules with intermediate alkyl chain lengths exhibited considerably low melting points owing to the increased fusion entropy (Fig. 117, also see Fig. 7d), although  $\text{C}_n\text{TET-TTF}$  with  $n = 5, 6, 8$ , or  $9$  have not been prepared yet. Among the  $\text{C}_n\text{TET-TTF}$  molecules

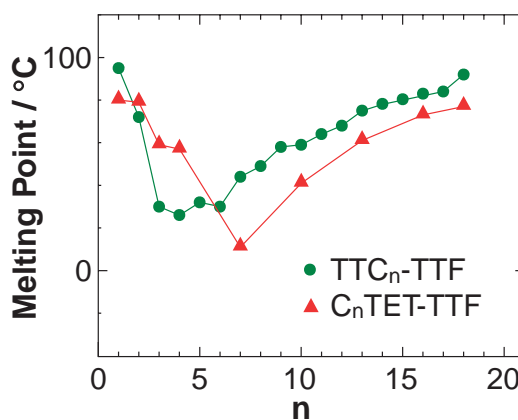


Fig. 117. Melting points of  $\text{C}_n\text{TET-TTF}$  in comparison with those of  $\text{TTC}_n\text{-TTF}$  materials. ( $n, T_m/^\circ\text{C}$ ) = (1, 80), (2, 79), (3, 59), (4, 57), (7, 11), (10, 41), (13, 61), (16, 73), and (18, 77).

in existence, the lowest melting point was observed at  $n = 7$  ( $T_m = 11^\circ\text{C}$ ). The ionization potentials of  $\text{C}_n\text{TET-TTF}$  are nearly the same as that of ET, but complex formation is considerably restricted with increasing  $n$ .

Among the CT complexes of  $\text{C}_7\text{TET-TTF}$ , the dark brown plates of  $1:1 \text{ C}_7\text{TET-TTF} \cdot \text{TCNQ}$  exhibited very peculiar structural and transport features.<sup>832,833</sup> The  $\pi$ -electron rich parts, namely the  $\text{C}_6\text{S}_8$  part of  $\text{C}_7\text{TET-TTF}$  and TCNQ, form a DA alternating stack with alternating interplanar distances of 3.44 and 3.51 Å and afford a  $\pi$ -electron layer in the  $ac$ -plane (termed  $\pi$ -electron layer in Fig. 118). The  $\pi$ -electron layer is sandwiched by the 2D hydrophobic alkyl layers

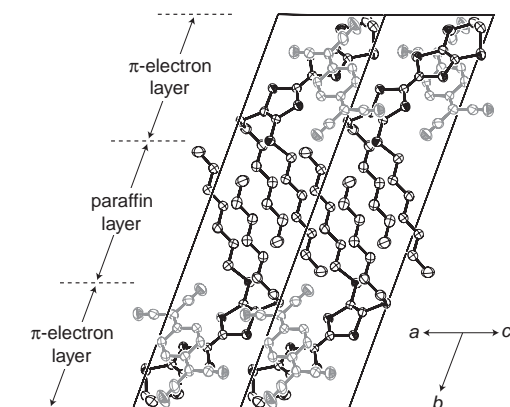


Fig. 118. Crystal structure of  $C_7TET\text{-}TTF\cdot TCNQ$ . Triclinic,  $P\bar{1}$ ,  $a = 9.732(3)$ ,  $b = 27.833(6)$ ,  $c = 7.946(2)$  Å,  $\alpha = 102.02(2)$ ,  $\beta = 108.14(3)$ ,  $\gamma = 68.27(2)^\circ$ ,  $V = 1890(1)$  Å<sup>3</sup>,  $Z = 2$ ,  $R = 0.063$ .<sup>832,833</sup>  $\pi$ -Electron layer is composed of alternating array of  $C_6S_8$  part of  $C_7TET\text{-}TTF$  and  $TCNQ$  molecules. Paraffin layer is composed of interpenetrated heptyl chains of  $C_7TET\text{-}TTF$  molecules. These two layers stack alternately along the  $b$ -axis.

(termed paraffin layer in Fig. 118) consisting of interpenetrated heptyl chains, which are alternately attached to two different adjacent DA stacks. As a result, the bilayer composed of the repeating unit of  $\pi$ -electron|paraffin| $\pi$ -electron is formed with a thickness of 8–9 Å for each segment. The very small DA overlap integrals ( $0.2\text{--}1.8 \times 10^{-3}$ ) suggest that the CT interactions of  $\pi$ -moieties do not dominate the lattice formation but the vdW ones of the alkyl chains do. Owing to these unfavorable crystal and electronic features, electron transport is considerably restricted, namely the  $\rho_{RT}$  of the compaction pellet is very high:  $10^9\text{--}10^{11}$  Ω cm with  $\varepsilon_g = 0.50$  eV up to 47–50 °C (denoted high resistive (**HR**) phase, Fig. 119a).

At around 50 °C the resistivity starts to drop by a factor of  $10^5\text{--}10^6$  and reaches  $3\text{--}8 \times 10^3$  Ω cm for the pellet sample. A single crystal also showed a drop of  $\rho$  in the range of 52–57 °C

to reach  $1.5 \times 10^4$  Ω cm at 57 °C along the nearly  $b$ -axis, while it was  $2\text{--}3 \times 10^3$  Ω cm along the  $a$ - or  $c$ -axis. The transition at 50–57 °C causes the color to change to yellow, but it is not a conventional solid–solid phase transition. A structural analysis at 47 °C indicates a significant increase in the angle (S)–C–C in one of the alkyl chains, suggesting that the thermal motion of alkyl chains triggers the transition. The intensity of each Bragg spot starts to decrease markedly above 52 °C, but they faintly remain up to 57 °C. These observations together with the anisotropic behavior in  $\rho$  in this temperature range suggest that the crystal becomes partly amorphous but includes some regular structure (denoted low resistive **I** phase (**LR-I**), Fig. 119).

Such a decrease in  $\rho$  has been observed in a liquid crystalline viologen by Tabushi et al.<sup>834</sup> A high conductivity in the liquid crystal ( $1.2 \times 10^{-3}$  S cm<sup>-1</sup> at 110 °C) is interpreted by the ionic conduction of the viologen cation, cation radical, and iodine, where the liquid-crystallite state was indispensable for yielding the conductivity. In the system of  $C_7TET\text{-}TTF\cdot TCNQ$ , however, a crystalline framework is not necessary for conduction as shown below.

The  $\rho$  increases gradually above 60 °C and no essential increases were noticed above 80 °C. This abnormal phase, where the  $\rho$  increases as temperature increases like a metal, is denoted **LR-II**. The low-resistive behavior persisted reversibly between –22 and +80 °C with  $\rho = 2.5\text{--}6.0 \times \exp(\varepsilon_g/2k_B T)$ , where  $\varepsilon_g = 0.50$  eV (denoted **LR-III**). No further thermal changes imply that the behavior of  $\rho$  in **LR-II** is intrinsic and that **LR-III** is a supercooled state: storage of **LR-III** at –75 °C for 1 year gave no appreciable change, while the storage at RT for 2 months caused it to transform back into **HR**. Without mechanical stimulus, the shape of the crystal is essentially kept up to the decomposition point at around 213 °C (Figs. 120a and 120b). Once a stimulus is added to a part of **LR (II and III)** at any temperature, however, slurry containing microcrystals and viscous oil spills from inside the crystal (Figs. 120c and 120d). The X-ray diffraction analysis and optical spectra revealed that the microcrystals are composed of

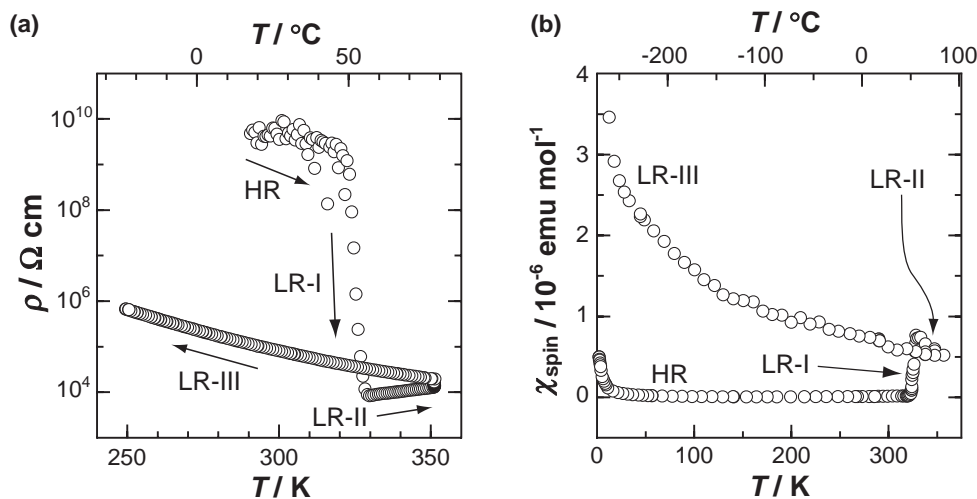


Fig. 119. Temperature dependence of (a) resistivity  $\rho$  and (b) spin susceptibility  $\chi_{\text{spin}}$  of  $C_7TET\text{-}TTF\cdot TCNQ$ .<sup>833</sup> (a) Arrows indicate the heating and cooling processes. At 80 °C the pellet sample was kept for 2 h. (b) The polycrystals were kept at 83 °C for 2 h. **HR**: high resistive state. **LR-I, II, III**: low resistive states.



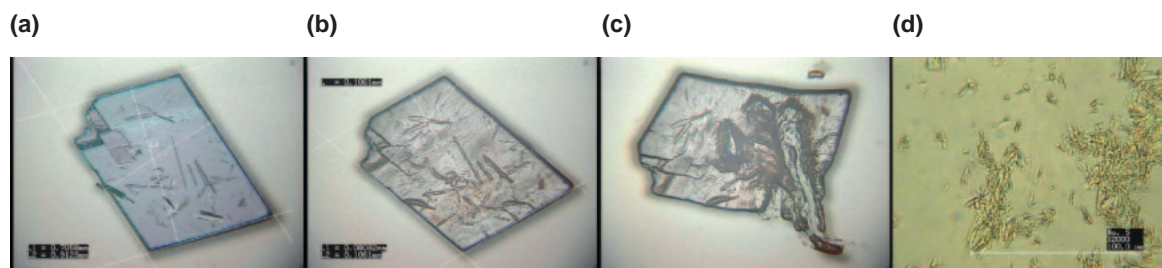


Fig. 120. Micrographs of a  $C_7TET-TTF \cdot TCNQ$  single crystal at RT before (a, **HR**) and after heating (b, **LR**, kept above  $60^\circ C$  for 10 min), then added mechanical stimulus at one edge (c), finally pulverized (d) showing a slurry composed of microcrystals ( $8-10 \times 2 \mu m^2$ ).<sup>833</sup>

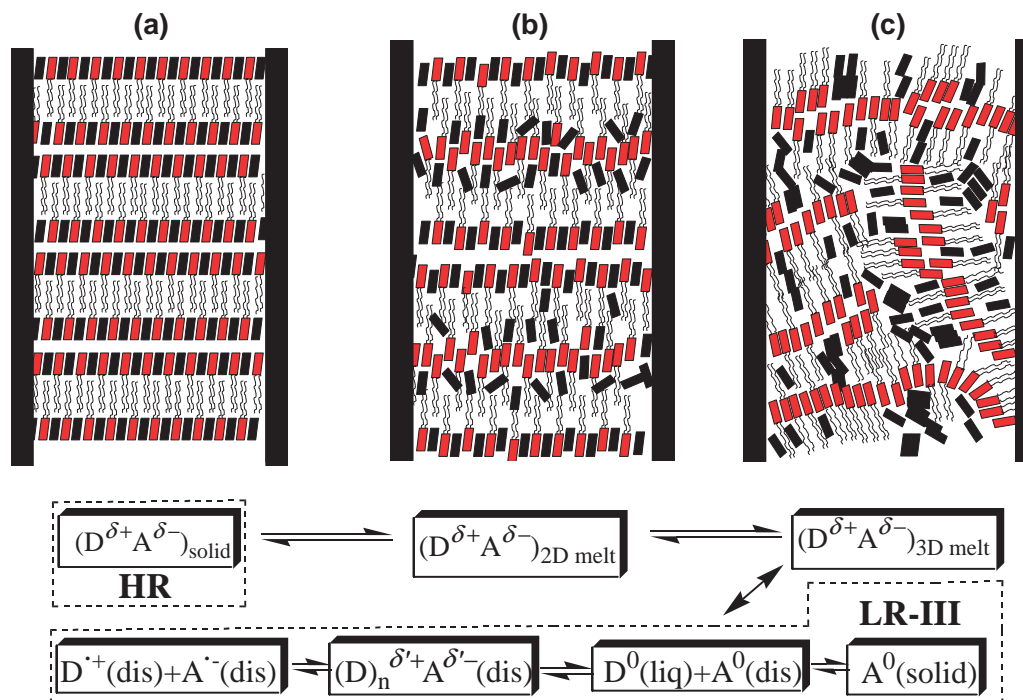


Fig. 121. Schematic illustrations of the (a) high-resistive (**HR**) phase  $(D^{\delta+}A^{\delta-})_{solid}$ , (b) one of 2D melts  $(D^{\delta+}A^{\delta-})_{2D\ melt}$ , and (c) 3D melt  $(D^{\delta+}A^{\delta-})_{3D\ melt}$  composed of  $C_7TET-TTF$  (red parallelograms with tails),  $TCNQ$  (black parallelograms without tails) molecules,  $TCNQ$  solid (closed blocks in (c)), and electrodes (thick closed bars).

$TCNQ^0$  and the oil consists of  $C_7TET-TTF^0$  and a nearly neutral CT complex  $(D)_n^{\delta'+}A^{\delta'-}$  ( $n$  is unknown,  $\delta' \approx 0$ ) dissolved in the liquid donor. The dissolved complex exhibits a broad weak CT band at  $6.7 \times 10^3\ cm^{-1}$ . Such a CT band appears at a little higher energy of  $7.5 \times 10^3\ cm^{-1}$  in the KBr pellet of **HR**. The temperature dependence of  $\rho$  of the slurry was nearly the same as that of **LR-III**.

Since the observed low  $\rho$  was not attributable to either  $C_7TET-TTF$  ( $\rho_{60^\circ C} = 10^9-10^{10}\ \Omega\ cm$ ) or  $TCNQ$  ( $2 \times 10^7\ \Omega\ cm$ ), EPR data were examined to assign the charge carriers (Fig. 119b). The EPR intensity ( $\chi_{spin}$ ) of the **HR** phase is negligible, i.e.  $10^{-4}\%$  of  $S = 1/2$  Curie spins. On heating, it starts to increase rapidly at around  $50^\circ C$  to attain  $10^{-6}\ emu\ mol^{-1}$  above  $60^\circ C$ , which corresponds to  $0.1\%$  of  $S = 1/2$  Curie spins. The  $\chi_{spin}$  follows the Curie law for **LR-III** down to 2 K with two EPR signals at  $g = 2.006-2.009$  and 2.003. The whole temperature dependence of  $\chi_{spin}$  coincides with that of  $\rho$ , confirming that the very small and constant amount of radical species,  $C_7TET-TTF^{\bullet+}$  (its  $g$  value is not known but

$\bar{g} = 2.007$  for  $ET^{\bullet+}$ ) and/or  $TCNQ^{\bullet-}$  ( $\bar{g} = 2.0027$ ), are responsible for the carrier transport.

The above results are essentially compatible with the following scenario (Fig. 121). 1) At around  $50^\circ C$ , a part of the crystalline phase **HR** (Fig. 121a) transforms gradually into a disordered bilayer phase  $(D^{\delta+}A^{\delta-})_{2D\ melt}$  (Fig. 121b), where the dynamics of carriers are restricted within the layer. 2) A part of the  $(D^{\delta+}A^{\delta-})_{2D\ melt}$  changes promptly to a 3D melt  $(D^{\delta+}A^{\delta-})_{3D\ melt}$  (Fig. 121c), which includes the neutral liquid  $C_7TET-TTF$  ( $D^0(liq)$ ), neutral  $TCNQ$  ( $A^0(dis)$ ), solid  $TCNQ$  ( $A^0(solid)$ ), and neutral CT complex  $((D)_n^{\delta'+}A^{\delta'-}(dis))$ . The complex has an equilibrium with  $A^0(dis)$  and  $D^0(liq)$ , where  $M(dis)$  represents the dissolved species in  $D^0(liq)$ . 3) The  $(D^{\delta+}A^{\delta-})_{3D\ melt}$  also includes ionic species  $(D^{\bullet+}(dis) + A^{\bullet-}(dis))$  since a simultaneous increase in conductivity and  $\chi_{spin}$  in **LR** is only possible with the presence of such species in an equilibrium with  $(D)_n^{\delta'+}A^{\delta'-}(dis)$ .

The **LR-I** state may be an inhomogeneous mixture of **HR**, and 2D and 3D melts, where the 3D melt is sandwiched by

the 2D layers of complexes and the content of the **HR** phase decreases with increasing temperature up to 60 °C. In the **LR-II** state the portion of the 2D melt decreases with increasing temperature corresponding to the increase in resistivity. In the **LR-III** state the whole 2D melt is consumed and the equilibrium described at the bottom of Fig. 121 is reasonably deduced based on the observations mentioned above.

Although a highly conductive ionic liquid (ca.  $10^{-1} \text{ S cm}^{-1}$ ) was reported for imidazolium salts (see section 4.6.1),<sup>835</sup> to our knowledge no organic melts have an electronic conductivity of  $10^{-3} \text{ S cm}^{-1}$  even at around 50 °C. It is worth noting that a rapid decrease in  $\rho$  during melting has been observed for aromatic hydrocarbons.<sup>836</sup> The decrement of  $\rho$  by a factor of  $10^2$ – $10^4$  has been interpreted by the increase in mobility of charge carriers, rather than both the increase in the number of carriers and the contribution of ionic conduction by molecular ions. For  $\text{C}_7\text{TET-TTF}\cdot\text{TCNQ}$ , the decrement of  $\rho$  in the **LR-I** is also not ascribed to the ionic conduction, but to both the generation of radical species and the dynamics of a small amount of the radicals in liquid, where the presence of  $\text{A}^0(\text{solid})$  is indispensable for the constant carrier concentration. Since the electron transport occurs in a large excess of donor liquid, a successive electron hopping between  $\text{D}^0$  and a tiny amount of  $\text{D}^{\bullet+}$  molecules, instead of between the acceptor species, is the most plausible mechanism. Two long alkyl chains attached to the melt of the  $\text{C}_7\text{TET-TTF}$  molecule might lead to the formation of a self-assembled matrix as depicted in Fig. 122. Then, the electron transfer between the donor molecules in the donor array is expected as shown by Eq. 67, which is very reminiscent of that observed in the segregated column in highly conductive CT solids.



The mobility  $\mu$  of carriers in the fluid is estimated as

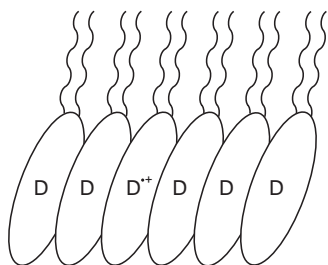


Fig. 122. Proposed schematic view of the  $\text{C}_7\text{TET-TTF}^{\bullet+}$  radical molecules ( $\text{D}^{\bullet+}$ ) in an assembly of donor molecules. Ellipsoids represent the  $\text{C}_6\text{S}_8$  moiety of  $\text{C}_7\text{TET-TTF}$  and tails represent heptyl chains.

$3.0 \times 10^{-2} \text{ cm}^2 \text{ V}^{-1} \text{ s}^{-1}$  in the range of 50–60 °C based on  $\mu = \sigma/ne$  with  $n = 2.1 \times 10^{18} \text{ cm}^{-3}$ .

**4.5.2 Cation Radical Salts with Low Melting Point:** Cation radical salts with a low melting point have been prepared in our group using  $\text{TTC}_7\text{-TTF}$  molecules ( $T_m = 44.0^\circ\text{C}$ ). Mixing of neutral  $\text{TTC}_7\text{-TTF}$  with the radical salt ( $\text{TTC}_7\text{-TTF}^{2+}\text{-(Br}_3^-)_2$ ) in a certain ratio gave mixed-valence salts ( $\text{TTC}_7\text{-TTF}^{n+}\text{-(Br}_3^-)_n$ ), and their characteristics varied depending on the dopant concentration. In the case of  $1 < n < 2$ , the resulting compounds are purple crystallites, while dark brown viscous liquids were obtained in the case of  $0 < n < 1$ . The conductivity at RT lies in the range of  $10^{-5}$ – $10^{-7} \text{ S cm}^{-1}$  for the liquid form (maximum value is  $8 \times 10^{-6} \text{ S cm}^{-1}$ ), and the ion aggregations lead to a slight increase in conductivity (maximum value is  $2 \times 10^{-5} \text{ S cm}^{-1}$ ). It is thus apparent that the conduction is entirely between  $\text{TTC}_7\text{-TTF}^{n+}$  molecules instead of the  $\text{Br}_3^-$  anions and is, therefore, attributed to electrons (holes).

When neutral  $\text{TTC}_7\text{-TTF}$  and nitrosyltetrafluoroborate ( $\text{NOBF}_4$ ) were reacted in hexane, viscous liquids ( $\text{TTC}_7\text{-TTF}^{n+}\text{(BF}_4^-)_n$ ) were obtained. As the doped concentration increased, the color changed from initially dark brown to deep green and then blue. Although the conductivity at RT increases as the mixing ratio of starting materials approaches unity ( $n = 1$ , maximum value is  $4 \times 10^{-7} \text{ S cm}^{-1}$ ), the values are much less than those of the tribromide salts.

**4.5.3 TCNQ Anion Radical Salts with Low Melting Point:** Since most of the melting (or decomposition) points of TCNQ complexes are over 200 °C, the studies of TCNQ complexes have mainly been carried out in the solid state. As for TCNQ complexes with a low melting point, a mixed crystal of propylisoquinolinium, methylisoquinolinium, TCNQ, and MeTCNQ has been reported to show a melting point as low as 80 °C.<sup>837</sup> 1:1 salts of 1-alkyl-3-methylimidazolium (alkyl = methyl, ethyl, *n*-propyl, *n*-butyl, and *n*-hexyl) also show a rather low melting point (Table 27).<sup>838</sup>  $\text{EMI}\cdot\text{TCNQ}$  forms a 1D column composed of TCNQ dimers (Chart 16).<sup>839</sup> Their RT conductivities are significantly low ( $10^{-6}$ – $10^{-9}$

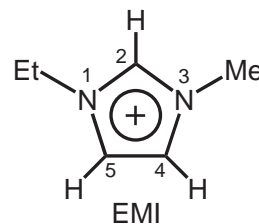


Chart 16.

Table 27. RT Conductivity ( $\sigma_{\text{RT}}/\text{S cm}^{-1}$ ) and Melting Points ( $T_m/^\circ\text{C}$ ) of TCNQ Anion Radical Salts of 1-Alkyl( $\text{R}^1$ )-3-methylimidazolium and Melting Points of 1:1 EMI Salts of R-TCNQ

$\text{R}^1$	1:1 <sup>a)</sup>		2:3 <sup>a)</sup>		1:2 <sup>b)</sup>		R-TCNQ R	1:1EMI salt <sup>b)</sup> $T_m$
	$\sigma_{\text{RT}}$	$T_m$	$\sigma_{\text{RT}}$	$\sigma_{\text{RT}}$	$T_m$ <sup>c)</sup>			
$\text{CH}_3$	$8 \times 10^{-8}$	174–177	$7 \times 10^{-5}$		no solid		H	139.9–140.2
$\text{C}_2\text{H}_5$	$4 \times 10^{-8}$	143–146	$2 \times 10^{-3}$	$5 \times 10^{-4}$	225–226		$\text{CH}_3$	128.8–129.4
<i>n</i> - $\text{C}_3\text{H}_7$	$3 \times 10^{-9}$	159–161	$2 \times 10^{-2}$		no solid		$\text{CF}_3$	144.3–144.7
<i>n</i> - $\text{C}_4\text{H}_9$	$3 \times 10^{-7}$	154–156	$2 \times 10^{-1}$	$2 \times 10^{-1}$	190–194		<i>n</i> - $\text{C}_{10}\text{H}_{21}$	ca. 40
<i>n</i> - $\text{C}_6\text{H}_{13}$	$7 \times 10^{-6}$	124–126	$4 \times 10^{-2}$		no solid			

a) Ref. 838. b) Ref. 840. c) Decomposition point.

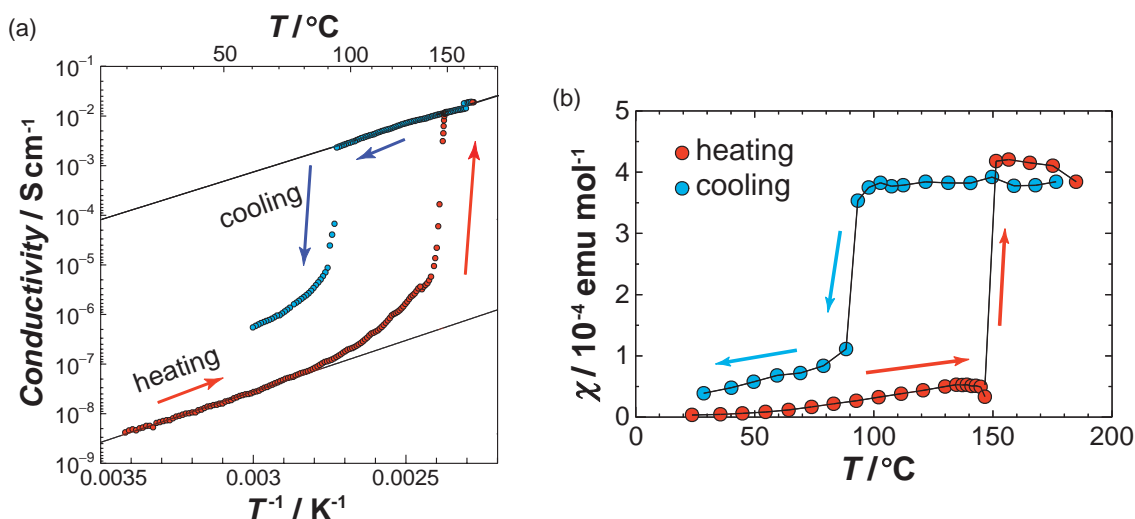


Fig. 123. (a) Temperature dependence of conductivity of 1:1 EMI·TCNQ salt. The solid state has an activation energy of 0.41 eV and shows an increase in conductivity by five orders of magnitude by melting. Supercooled liquid state has an activation energy of 0.38 eV. (b) Temperature dependence of EPR spin susceptibility.<sup>840</sup>

$\text{S cm}^{-1}$ ) in comparison with those of the 2:3 salts ( $10^{-1}$ – $10^{-5}$   $\text{S cm}^{-1}$ ), where the melting points of the 2:3 salts have not been reported.<sup>838</sup>

We prepared 1:2 salts of 1-alkyl-3-methylimidazolium (alkyl = ethyl and *n*-butyl)<sup>840</sup> and investigated their thermal and physical properties (Table 27). Both are solid at RT, and have a higher melting point than those of the 1:1 salts owing to the increased cohesive energy. The decrease in melting point was observed by utilizing TCNQ derivatives (R-TCNQ). In the 1:1 EMI salts, the melting point decreased in the order of R =  $\text{CF}_3$ , H,  $\text{CH}_3$ , and  $n\text{-C}_{10}\text{H}_{21}$ .

The conducting behavior in the liquid state has not been reported for the TCNQ salts. We found that the conductivity of 1:1 EMI·TCNQ increased by five orders of magnitude by melting and decreased by three orders of magnitude by freezing (Fig. 123a).<sup>840</sup> The salt shows the hysteresis of the temperature dependence of conductivity. The salt was semiconductive with  $\varepsilon_a = 0.41$  and 0.38 eV for the solid and liquid states, respectively. The value of conductivity in the liquid state (ca.  $10^{-2}$   $\text{S cm}^{-1}$ ) was significantly high compared with those of ordinary monovalent TCNQ salts ( $<10^{-4}$   $\text{S cm}^{-1}$ ). It seems that the high conductivity in the liquid state was realized by the increase in conducting carriers by the dissociation of dimers ( $(\text{TCNQ}^{\bullet-})_2 \rightleftharpoons 2\text{TCNQ}^{\bullet-}$ ) and the contribution of ionic conductivity in addition to electronic conductivity of  $\text{TCNQ}^{\bullet-}$ . This salt kept the supercooled liquid state down to around 100 °C, which was lower than its melting point by 40 °C.

#### 4.5.4 Organic Semiconductor Condenser (OS-CON):

Organic semiconductor condenser (OS-CON) was developed by Niwa using a highly conductive 1:2 TCNQ salt having a low melting point: *N*-*n*-butylisoquinolinium( $\text{TCNQ}$ )<sub>2</sub> ( $T_m = 210$ – $220$  °C).<sup>841</sup> The salt has a high conductivity of  $\sigma_{\text{RT}} = 0.3$   $\text{S cm}^{-1}$ , even after melting without decomposition. He used the TCNQ salt as an electrolyte of the alumina condenser, in which the static capacitance  $C$  is represented by Eq. 68:

$$C \propto \varepsilon S/d, \quad (68)$$

where  $\varepsilon$ ,  $S$ , and  $d$  are the dielectric constant ( $\varepsilon \approx 8$ – $10$ ), sur-

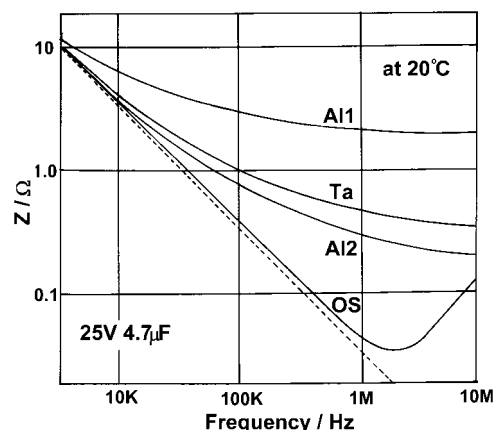


Fig. 124. Frequency dependence of impedance of several condensers taken from Ref. 843. Al1: alumina condenser (common), Ta: tantalum condenser, Al2: alumina condenser (high performance), OS: OS-CON. The dashed line represents the ideal line.<sup>843</sup>

face area and thickness of alumina, respectively. The impedance ( $Z$ ) of the alumina condenser, which is schematically represented as “lead wire | aluminium anode | dielectric substance | electrolyte | aluminium cathode | lead wire,” is formulated by Eq. 69 using the equivalent series resistance of the electrolyte ( $ESR$ ), equivalent direct inductance of the aluminium and lead wire ( $L$ ) and frequency  $f$ .

$$|Z| = \left\{ (ESR)^2 + \left( 2\pi fL - \frac{1}{2\pi fC} \right)^2 \right\}^{1/2}. \quad (69)$$

The impedance is dominated by the last term for small  $f$  ( $\leq 10$  kHz), by the middle term for large  $f$  ( $\approx$  MHz), and the first term in the intermediate region ( $10^2$ – $10^3$  kHz). The OS-CON shows better frequency characteristics compared with those of the tantalum and alumina condensers (Fig. 124).<sup>842,843</sup> Instead of the TCNQ CT solid, conductive doped polypyrrole films are also used for OS-CON.<sup>843</sup> Currently, OS-CON is com-

Table 28. Properties of Selected Conductive EMI-X Ionic Liquids

X	$T_m$ /°C	$T_d$ /°C	$d$ /g cm <sup>-3</sup>	$\eta$ /cP	$\sigma$ /S cm <sup>-1</sup>	$\chi$ /emu mol <sup>-1</sup>	Ref. for $\sigma$
F(HF) <sub>2,3</sub> <sup>a)</sup>	-90	ca. 300	1.14	4.9	$10 \times 10^{-2}$	—	835,849,850
N(CN) <sub>2</sub>	-12	ca. 240	1.08	17	2.7	—	852
AlCl <sub>4</sub>	8		1.29	18	2.3	—	853
Ga <sup>III</sup> Cl <sub>4</sub>	11	ca. 130	1.53	16	2.0	—	854
(Ga <sup>III</sup> Cl <sub>4</sub> ) <sub>0.5</sub> (Fe <sup>III</sup> Cl <sub>4</sub> ) <sub>0.5</sub>	15	ca. 190	1.46	16	2.0	$8.1 \times 10^{-3}$	854
Fe <sup>III</sup> Cl <sub>4</sub>	18	ca. 280	1.42	18	1.8	$1.6 \times 10^{-2}$	854
C(CN) <sub>3</sub>	-11	ca. 240	1.11	18	1.8	—	852
BF <sub>4</sub> <sup>b)</sup>	11	ca. 420	1.24	43	1.3–1.4	—	856–858

a)  $T_m = -65$  °C and  $d = 1.16$  g cm<sup>-3</sup> were also reported (Ref. 850). b)  $T_m = 6, 14.6$ , and  $15$  °C,  $d = 1.28$  g cm<sup>-3</sup>, and  $\eta = 32$  cP were also reported (Refs. 857, 859).

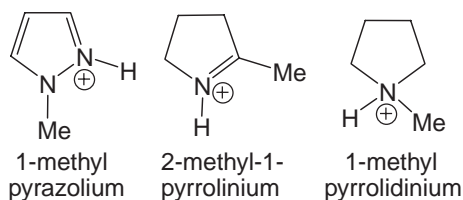


Chart 17.

mercially available and widely used in applications such as for the smoothing capacitor of the switching power supply.

**4.6 Ionic Liquids. 4.6.1 Ionic Conductivity:** The investigation of RT ionic liquids has largely focused on systems comprised of 1,3-dialkylimidazolium cations and tetrachloroaluminate (AlCl<sub>4</sub>) anions.<sup>844</sup> These systems have many fascinating properties such as negligible vapor pressure, thermal stability, wide electrochemical window, low viscosity, and high ionic conductivity, but they are unstable in air and water. Following a report on air-stable EMI-based RT ionic liquids containing tetrafluoroborate (BF<sub>4</sub>) and acetate (CH<sub>3</sub>CO<sub>2</sub>) anions in 1992 by Wilkes and Zaworotko,<sup>845</sup> a wide range of new ionic liquids have been developed incorporating many kinds of anions.<sup>846–848</sup> Among them, some EMI salts are more conductive than a 0.1 M KCl solution ( $1.3 \times 10^{-2}$  S cm<sup>-1</sup> at 25 °C), i.e.,  $1.0 \times 10^{-1}$  S cm<sup>-1</sup> for polyhydrofluoride (H<sub>2</sub>F<sub>3</sub>/H<sub>3</sub>F<sub>4</sub>),<sup>835,849,850</sup>  $2.7 \times 10^{-2}$  S cm<sup>-1</sup> for dicyanamide (N(CN)<sub>2</sub>),<sup>851,852</sup>  $2.3 \times 10^{-2}$  S cm<sup>-1</sup> for AlCl<sub>4</sub>,<sup>853</sup>  $2.0 \times 10^{-2}$  S cm<sup>-1</sup> for Ga<sup>III</sup>Cl<sub>4</sub>,<sup>854,855</sup>  $1.8 \times 10^{-2}$  S cm<sup>-1</sup> for cyanoform (C(CN)<sub>3</sub>)<sup>852</sup> and Fe<sup>III</sup>Cl<sub>4</sub>,<sup>854,855</sup> and  $1.3$ – $1.4 \times 10^{-2}$  S cm<sup>-1</sup> for BF<sub>4</sub>.<sup>856–858</sup> Table 28 summarizes the some physical properties of these ionic liquids.

Apart from the EMI cation, a few ionic liquids formed with BF<sub>4</sub> also show a relatively high ionic conductivity, i.e.,  $1.9 \times 10^{-2}$  S cm<sup>-1</sup> for 1-methylpyrazolium,  $1.6 \times 10^{-2}$  S cm<sup>-1</sup> for 2-methyl-1-pyrrolinium, and  $1.6 \times 10^{-2}$  S cm<sup>-1</sup> for 1-methylpyrrolidinium (Chart 17).<sup>860</sup> The high conductivity is closely associated with the high fluidity, and in general these liquids are prone to follow the so-called “Walden rule.”<sup>861</sup>

As early as the 1910s, Walden pointed out that the product of equivalent conductivity ( $\Lambda = \sigma M/d$ ,  $M$ : formula weight of liquid) and viscosity ( $\eta$ ) remains constant in a wide range of aqueous solution systems.<sup>861</sup> Provided that the effective hydrodynamic radius of species  $i$  ( $r_i$ ) is not much different from salt to salt, the empirical relation can be derived from the combination of the Stokes–Einstein equation (Eq. 70),<sup>862</sup> where  $D_i$

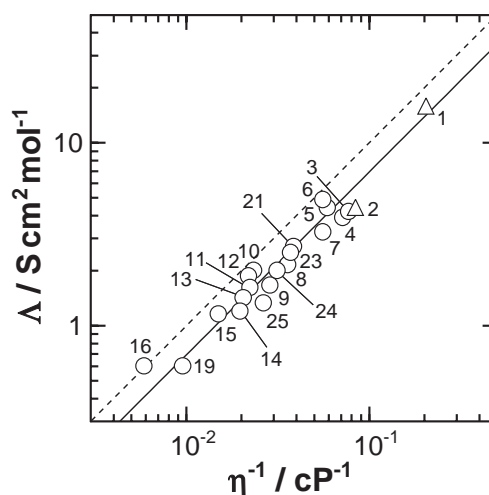


Fig. 125. A plot of the equivalent conductivity ( $\Lambda$ ) against the reciprocal of viscosity ( $\eta^{-1}$ ) for EMI-X ionic liquids with melting point below RT. Triangles represent non simple-type ionic liquids. The solid line is the least-squares fit to the data, and the dashed line is the ideal Walden line (see text). 1: X = F(HF)<sub>2,3</sub>,<sup>835,849,850</sup> 2: Fe<sub>0.5</sub>Ga<sub>0.5</sub>Cl<sub>4</sub>,<sup>854</sup> 3: GaCl<sub>4</sub>,<sup>854</sup> 4: FeCl<sub>4</sub>,<sup>854</sup> 5: N(CN)<sub>2</sub>,<sup>852</sup> 6: AlCl<sub>4</sub>,<sup>853</sup> 7: C(CN)<sub>3</sub>,<sup>852</sup> 8: (CF<sub>3</sub>SO<sub>2</sub>)<sub>2</sub>N,<sup>864</sup> 9: CF<sub>3</sub>CO<sub>2</sub>,<sup>864</sup> 10: BF<sub>4</sub>,<sup>856–858</sup> 11: CF<sub>3</sub>SO<sub>3</sub>,<sup>864</sup> 12: CuCl<sub>2</sub>,<sup>865</sup> 13: NbF<sub>6</sub>,<sup>866</sup> 14: TaF<sub>6</sub>,<sup>866</sup> 15: SbF<sub>6</sub>,<sup>867</sup> 16: WF<sub>6</sub>,<sup>867</sup> 19: C<sub>3</sub>F<sub>7</sub>CO<sub>2</sub>,<sup>864</sup> 22: CF<sub>3</sub>BF<sub>3</sub>,<sup>872</sup> 23: C<sub>2</sub>F<sub>5</sub>BF<sub>3</sub>,<sup>872</sup> 24: C<sub>3</sub>F<sub>7</sub>BF<sub>3</sub>,<sup>872</sup> 25: C<sub>4</sub>F<sub>9</sub>BF<sub>3</sub>,<sup>872</sup>

is the self-diffusivity of species  $i$  and  $N_A$  is Avogadro's number, and the Nernst–Einstein equation (Eq. 71),<sup>863</sup> where  $z_i$  is the charge of species  $i$  and  $F$  is the Faraday constant.

$$D_i = RT/6\pi\eta r_i N_A, \quad (70)$$

$$D_i = RT\Lambda_m/|z_i|^2 F^2, \quad (71)$$

$$\Lambda\eta = (|z_i|^2 F^2/6\pi N_A)(1/r_i) \approx \text{constant}. \quad (72)$$

Figure 125 demonstrates the relation between  $\Lambda$  and  $\eta^{-1}$  for EMI-based RT ionic liquids, and similar behavior was reported for the other imidazolium salts.<sup>850</sup> Of particular importance is that the ionic liquids reside below the line evaluated from the data of KCl aqueous solutions, in which the ions are completely dissociated. A departure from the ideal Walden line is strongly indicative of the formation of ion pairs and/or associations of a significant fraction of ions.



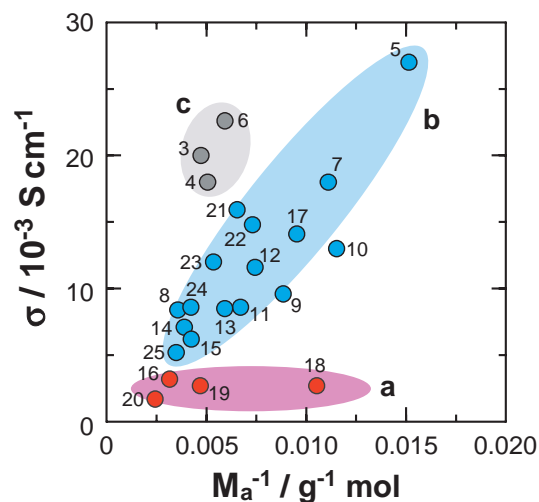


Fig. 126. A plot of the ionic conductivity ( $\sigma$ ) against the reciprocal of molecular weight of the anion ( $M_a^{-1}$ ) for EMI-X ionic liquids. Group **a** (red circles): **16**, **18** ( $\text{CH}_3\text{SO}_3$ ), **19**, **20** ( $(\text{CF}_3\text{SO}_2)_3\text{C}$ ), **b** (blue circles): **5**, **7**–**15**, **17** ( $\text{SeCN}$ ), **21** ( $\text{BCl}_4$ ), **22**–**25**, **c** (gray circles): **3**, **4**, **6**. Numbers are the same as those in Fig. 125.

For the ionic liquids, Coulomb interaction is a dominant factor in the intermolecular interaction, and depends upon the distribution of spatial charge on each component ion, Pearson's acid–base strength, coordination ability, and so on. Since  $\Delta$  can be represented by  $\sigma M/d$ , the Walden rule is equal to the relation Eq. 73, where  $C_1$  is a constant.

$$\sigma = C_1 d/r_i M \eta = (C_1/r_i)(d/\eta) M^{-1}. \quad (73)$$

Figure 126 presents a plot of the ionic conductivity ( $\sigma$ ) against the reciprocal of molecular weight of the anion ( $M_a^{-1}$ ) for simple-type EMI-based RT ionic liquids. According to Eq. 73, they can be classified into three categories (groups **a**–**c**) based on a parameter  $d/\eta$ , which roughly corresponds to a slope of the  $\sigma$  vs  $M_a^{-1}$  plot.

a)  $d/\eta < 0.02$ : X =  $\text{WF}_7$  (**16**),<sup>867</sup>  $\text{CH}_3\text{SO}_3$  (**18**),<sup>868</sup>  $\text{C}_3\text{F}_7\text{CO}_2$  (**19**),<sup>864</sup> and  $(\text{CF}_3\text{SO}_2)_3\text{C}$  (**20**).<sup>870</sup>

b)  $0.02 < d/\eta < 0.07$ : X =  $\text{N}(\text{CN})_2$  (**5**),<sup>852</sup>  $\text{C}(\text{CN})_3$  (**7**),<sup>852</sup>  $(\text{CF}_3\text{SO}_2)_2\text{N}$  (**8**),<sup>864</sup>  $\text{CF}_3\text{CO}_2$  (**9**),<sup>864</sup>  $\text{BF}_4$  (**10**),<sup>856–858</sup>  $\text{CF}_3\text{SO}_3$  (**11**),<sup>864</sup>  $\text{CuCl}_2$  (**12**),<sup>865</sup>  $\text{NbF}_6$  (**13**),<sup>866</sup>  $\text{TaF}_6$  (**14**),<sup>866</sup>  $\text{SbF}_6$  (**15**),<sup>867</sup>  $\text{SeCN}$  (**17**),<sup>870</sup>  $\text{BCl}_4$  (**21**),<sup>871</sup> and  $\text{C}_n\text{F}_{2n+1}\text{BF}_3$  ( $n = 1$ –**4**, **22**–**25**).<sup>872</sup>

c)  $d/\eta > 0.07$ : X =  $\text{GaCl}_4$  (**3**),<sup>854,855</sup>  $\text{FeCl}_4$  (**4**),<sup>854,855</sup> and  $\text{AlCl}_4$  (**6**).<sup>853</sup>

The highly viscous salts in group **a** show low ionic conductivity, which is insensitive to  $M_a$ , presumably indicating that the individual molecules are largely retarded by strong and specific intermolecular interactions to have a poor self-diffusivity. Especially for salt **18**, it appears that  $\text{CH}_3\text{SO}_3$  anion suffers severely from the significant interionic Coulomb interaction with EMI cation due to its hard basicity and the negative charge confined on the  $\text{SO}_3$  group. Since a  $\text{CH}_3$  group has a less electron-withdrawing ability in comparison with a  $\text{CF}_3$  group, it inhibits the extensive dispersion of the negative charge on each anion, and thus, gives rise to an increase in the interionic Coulomb interactions. The situation might be

the same for the acetate salt ( $M_a^{-1} = 0.0169 \text{ g}^{-1} \text{ mol}$ ; the salt is not plotted in Fig. 126 due to no density data), which shows a low conductivity of  $2.8 \times 10^{-3} \text{ S cm}^{-1}$  and high viscosity of 162 cP.<sup>845,864</sup> The long alkyl chain and hard basicity of  $\text{C}_3\text{F}_7\text{CO}_2$  in salt **19** and large molecular weight and low symmetry of  $\text{WF}_7$  ( $C_{3v}$  symmetry<sup>867</sup>) in salt **16** might cause their high viscosity and low conductivity. The poor conductivity (ca.  $4.5 \times 10^{-3} \text{ S cm}^{-1}$ ) with rather high fluidity (21 cP) of EMI·SCN ( $M_a^{-1} = 0.0172 \text{ g}^{-1} \text{ mol}$ ; the salt is also not plotted in Fig. 126 due to no density data)<sup>873</sup> might be indicative of the formation of neutral thiocyanogens, which can not contribute the ionic conductivity.

The salts in group **b** have a tendency to increase the ionic conductivity with decreasing the  $M_a$ , which is in agreement with Eq. 73. Although cyano groups included in salts **5** and **7** have a strong ability for coordination to cations (see section 3.5.2 and Ref. 874), these salts show a significantly high ionic conductivity. Especially, the planar  $\text{C}(\text{CN})_3$  anion in salt **7** shows a conformational change to a pseudo-tetrahedral shape when it coordinates to the hydrogen atoms of EMI, and such a structural change apparently inhibits the ion diffusion. Then, the observed high conductivity is associated with the extensively dispersed negative charge on each anion owing to the terminal cyano groups. Many salts in this group contain anions with  $\text{C}_n\text{F}_{2n+1}$  group (**8**, **9**, **11**, and **22**–**25**), which also promotes the dispersion of the negative charge on each anion. The tendency among group **b** predicts a high conductivity of ca.  $5 \times 10^{-2} \text{ S cm}^{-1}$  for EMI salts with light anions such as  $\text{CN}^-$  and  $\text{NH}_2^-$ , provided that these salts form a liquid state at RT.

All the salts in group **c** contain tetrachlorometalate ( $\text{M}^{\text{III}}\text{Cl}_4$ ) anions, and have less retarding sources than those in groups **a** and **b** for the ion diffusion. It appears that the chloride atoms of  $\text{GaCl}_4$  (**3**),  $\text{FeCl}_4$  (**4**), and  $\text{AlCl}_4$  (**6**) anions coordinate to the hydrogen atoms of EMI as was observed in the 2:1 salt  $(\text{EMI})_2\text{Fe}^{\text{II}}\text{Cl}_4$  ( $T_m = 86^\circ\text{C}$ ).<sup>854</sup> The crystal structure of  $(\text{EMI})_2\text{Fe}^{\text{II}}\text{Cl}_4$  was determined by synchrotron X-ray powder diffraction. In the crystal, four EMI cations surround the anion with Fe(2) in a tetrahedral fashion involving hydrogen atoms bonded to C(2) positions (Fig. 127a), suggesting the presence of hydrogen bonds. On the other hand, the anion with Fe(1) are surrounded tetrahedrally by eight EMI cations through hydrogen bonds with C(4) and C(5). Accordingly, the EMI cation is surrounded by three anions as seen in Fig. 127b. It is possible

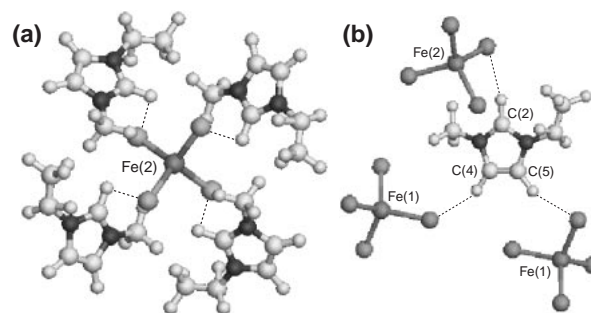


Fig. 127. Interionic contacts between EMI cation and  $\text{Fe}^{\text{II}}\text{Cl}_4$  anion in  $(\text{EMI})_2\text{Fe}^{\text{II}}\text{Cl}_4$  (a) around  $\text{Fe}^{\text{II}}\text{Cl}_4$  anion with Fe(2) and (b) around EMI cation at 300 K. Short C–H...Cl contacts are shown by dashed lines.<sup>854</sup>



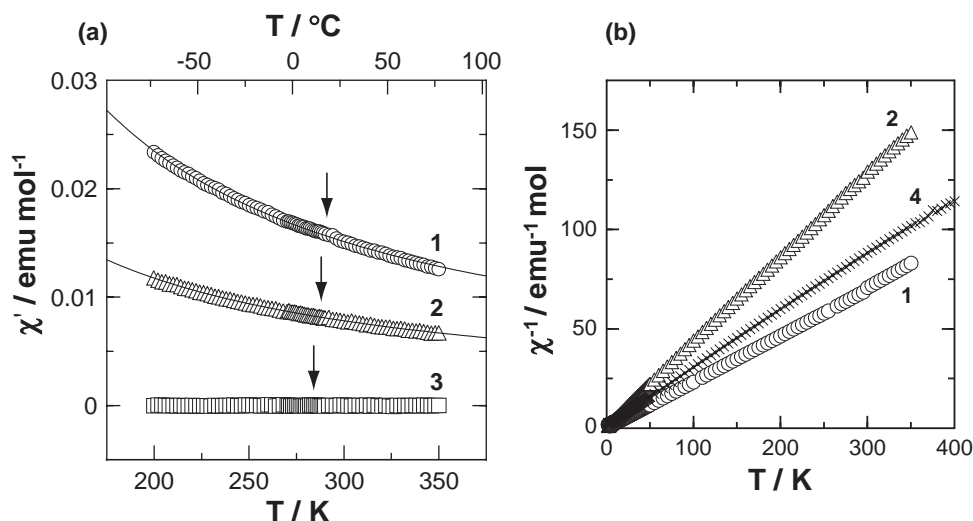


Fig. 128. Temperature dependence of (a) the real part of AC susceptibility ( $\chi'$ , 1 Oe, 20 Hz) and (b) the reciprocal of DC susceptibility ( $\chi^{-1}$ , 100 Oe) on heating process. The vertical arrows indicate the melting points. Solid curves correspond to the Curie–Weiss fit. 1:  $\text{Fe}^{\text{III}}\text{Cl}_4$ , 2:  $\text{Fe}^{\text{III}}_{0.5}\text{Ga}^{\text{III}}_{0.5}\text{Cl}_4$ , 3:  $\text{Ga}^{\text{III}}\text{Cl}_4$ , 4:  $\text{Fe}^{\text{II}}\text{Cl}_4$  salts.<sup>854,883</sup>

that such a hydrogen bond exists even in the liquid state to suppress the ion diffusion of the component ions. The highly conductive behavior might arise from the nephelauxetic (or electron cloud expanding) effect, which leads to the reduction of the negative charge on anion surface, and thus, the reduction of the interionic Coulomb interactions.

Summarizing the above, the high ionic conductivity in the simple-type ionic liquids will be realized by 1) the reduction of the molecular weight of component ions (i.e., 1,3-dimethylimidazolium salt formed with  $\text{N}(\text{CN})_2$  exhibits a higher ionic conductivity ( $3.6 \times 10^{-2} \text{ S cm}^{-1}$  at  $25^{\circ}\text{C}$ ) than that of corresponding EMI salt<sup>875</sup>), and 2) the suppression of the interionic Coulomb interactions based on the concepts of Pearson's acid–base interaction, nephelauxetic effect, and so on.

**4.6.2 Paramagnetic Ionic Liquids:** Conductive and magnetic composite liquids have been extensively studied for some inorganic systems such as alkali and transition metals and alloys,<sup>876</sup> and colloidal magnetic fluids dispersing iron nanoparticles,<sup>877</sup> in which carriers are electrons (or holes), and a copper sulfate aqueous solution showing reversed Moses effect,<sup>878</sup> in which the carriers are ions. For organic systems, however, only a few materials have been known as paramagnetic liquids. The neutral radicals, dithiazolyl or dithiadiazolyl compounds (Table 29),<sup>879–882</sup> form a liquid state at RT, but it is readily expected that the neutral radical liquids do not show an effective electric conductivity.

We found that the magnetic susceptibility of  $\text{EMI} \cdot \text{Fe}^{\text{III}}\text{Cl}_4$  containing paramagnetic  $\text{Fe}^{\text{III}}$  ions (Table 28) follows the Curie–Weiss law in both liquid and solid states (Fig. 128).<sup>854,855,883</sup> A Curie constant of  $4.33 \text{ emu K mol}^{-1}$  can be explained by uncorrelated  $S = 5/2$   $\text{Fe}^{\text{III}}$  spins (spin-only value is  $4.38 \text{ emu K mol}^{-1}$ ), suggesting a high-spin electronic state of the  $\text{Fe}^{\text{III}}\text{Cl}_4$  anions. The values substantially exceed those estimated for the paramagnetic organic liquids composed of neutral radicals with  $S = 1/2$  spins (ca.  $0.2 \text{ emu K mol}^{-1}$ ).<sup>879–882</sup> It is thus apparent that the  $\text{EMI} \cdot \text{Fe}^{\text{III}}\text{Cl}_4$  salt is a highly conductive paramagnetic RT ionic liquid and, to our knowledge, this represents the first observation

of bi-functionality on highly ionic conductivity and paramagnetic behavior among ionic liquids.

Later, Hamaguchi and Hayashi claimed<sup>884</sup> that they discovered a “magnetic” ionic liquid  $\text{BMI} \cdot \text{FeCl}_4$ , which was attracted by a magnet at RT. However, their claims are inappropriate since 1)  $\text{BMI} \cdot \text{FeCl}_4$  is a paramagnetic liquid and such liquids have been already known as mentioned above,<sup>854,855,879–882</sup> 2) it is wholly reasonable that the paramagnetic material is attracted to a magnet regardless of its form (more than 150 years ago, Faraday classified materials into either diamagnetic (repelled by magnet) or paramagnetic (attracted by magnet) ones<sup>885</sup>) and 3) the physical and chemical characterizations concerning the purity of the ionic liquid are hardly presented in their paper (Table 29), though the purities are critical for molecular magnets.

$\text{EMI} \cdot \text{Fe}^{\text{III}}\text{Cl}_4$  exhibits a slight thermal hysteresis in susceptibility at around the melting and freezing temperatures (Fig. 129). This feature might be caused by the antiferromagnetic interactions between  $\text{Fe}^{\text{III}}\text{Cl}_4$  anions within an ion association in the liquid state.

On further cooling, the magnetic susceptibility of the solidified  $\text{EMI} \cdot \text{Fe}^{\text{III}}\text{Cl}_4$  shows an antiferromagnetic transition at  $4.2 \text{ K}$  regardless of the cooling rate (Fig. 130). The data indicated by open circles in Fig. 130 were obtained after immersing the sample directly in liquid helium (quenched) and then cooling down to  $2 \text{ K}$  under zero-magnetic field (zero-field cooling, ZFC). ZFC data of the sample at the very slow cooling rate of  $-0.5 \text{ K min}^{-1}$  (relaxed) are shown by closed circles, which also indicate the occurrence of the antiferromagnetic transition at  $T_N$  with smaller magnetic susceptibility than the quenched sample below  $T_N$ . The extrapolated  $\chi_{\text{spin}}$  value to  $0 \text{ K}$  for the relaxed sample corresponds to ca.  $2/3$  of the maximum  $\chi$  value at  $T_N$  as expected from Eq. 74.

$$\begin{aligned} \chi_{\text{spin}}(T = 0 \text{ K}) &= (\chi_{\parallel} + 2\chi_{\perp})_{(T=0 \text{ K})}/3 \\ &= 2\chi_{\perp(T=0 \text{ K})}/3 = 2\chi_{\perp(T=T_N)}/3. \end{aligned} \quad (74)$$

The relaxed sample exhibits the spin-flop behavior at  $2 \text{ K}$  with a spin-flop magnetic field of  $H_{\text{SF}} \approx 8 \text{ kOe}$  (inset of Fig. 130).

Table 29. Organic Magnetic RT Liquids Other than EMI•Fe<sup>III</sup>Cl<sub>4</sub> and (EMI)[(Fe<sup>III</sup>Cl<sub>4</sub>)<sub>0.5</sub>(Ga<sup>III</sup>Cl<sub>4</sub>)<sub>0.5</sub>]<sup>a)</sup>

	$T_m$ or $T_g$ /°C	$T_d$ or $T_{bp}$ /°C	$d$ /g cm <sup>-3</sup>	$\eta$ /cP	$\sigma$ /S cm <sup>-1</sup>	$\mu_{eff}$ at RT / $\mu_B$	Ref.
<b>1) Pure organic one</b>							
Dithiazolyl (1)	12( $T_m$ )	119( $T_{bp}$ )	1.63	no	no	1.53 <sup>b)</sup>	879–881
Dithiadiazolyl (2)	0–1( $T_m$ )	no	no	no	no	1.5 <sup>b)</sup>	880
Dithiadiazolyl (3)	20–21( $T_m$ )	no	no	no	no	1.4 <sup>b)</sup>	880
<b>2) With transition metal</b>							
BMI•FeCl <sub>4</sub>	no	no	no	no	no	ca. 5.7	884
	–85( $T_g$ )	no	no	ca. 30 <sup>c)</sup>	ca. $8 \times 10^{-3c)}$	no	888
	–88( $T_g$ )	ca. 280( $T_d$ )	1.38(20 °C)	34(25 °C)	$8.9 \times 10^{-3}$ (25 °C)	5.80	889
C <sub>6</sub> MI•FeCl <sub>4</sub>	–86( $T_g$ )	ca. 320( $T_d$ )	1.33(20 °C)	45(25 °C)	$4.7 \times 10^{-3}$ (25 °C)	5.86	889
C <sub>8</sub> MI•FeCl <sub>4</sub>	–84( $T_g$ )	ca. 280( $T_d$ )	1.28(20 °C)	77(25 °C)	$2.2 \times 10^{-3}$ (25 °C)	5.86	889
BMI•FeBr <sub>4</sub>	–83( $T_g$ ), –2( $T_m$ )	ca. 290( $T_d$ )	1.98(20 °C)	62(25 °C)	$5.5 \times 10^{-3}$ (25 °C)	5.74	889
C <sub>6</sub> MI•FeBr <sub>4</sub>	–82( $T_g$ )	ca. 270( $T_d$ )	1.86(20 °C)	95(25 °C)	$2.8 \times 10^{-3}$ (25 °C)	5.76	889
C <sub>8</sub> MI•FeBr <sub>4</sub>	–81( $T_g$ )	ca. 260( $T_d$ )	1.74(20 °C)	121(25 °C)	$1.4 \times 10^{-3}$ (25 °C)	5.78	889
BDMI•FeCl <sub>4</sub>	$T_m < RT$	no	no	no	no	no	890

a) no: no data have been reported. b) Extrapolated values from solution measurements are 1.91–1.96  $\mu_B$ . c) Values were estimated from graphic data.

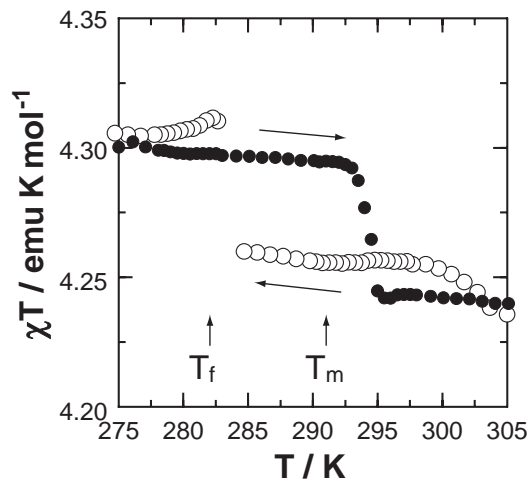
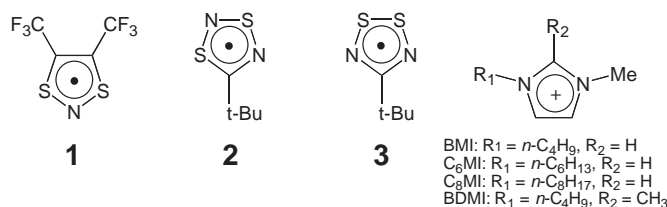


Fig. 129. Temperature dependence of  $\chi T$  of the EMI•Fe<sup>III</sup>Cl<sub>4</sub> in the temperature range of 275–305 K on heating (●) and cooling (○) processes in an applied field of 10 kOe. Melting ( $T_m$ ) and freezing ( $T_f$ ) temperatures are determined by DSC thermograms.<sup>854</sup>

Both the absence of hysteresis between ZFC and FC processes and the observation of spin-flop strongly indicate that the behavior is not due to the spin-glass forming,<sup>886,887</sup> but arises from the antiferromagnetic ordering. The fractional value of  $\chi$  by quenching suggests that the anion parts in the quenched sample consist of both the antiferromagnetic and paramagnetic domains. For (EMI)[(Fe<sup>III</sup>Cl<sub>4</sub>)<sub>0.5</sub>(Ga<sup>III</sup>Cl<sub>4</sub>)<sub>0.5</sub>], on the other hand, long-range magnetic ordering was not substantially de-

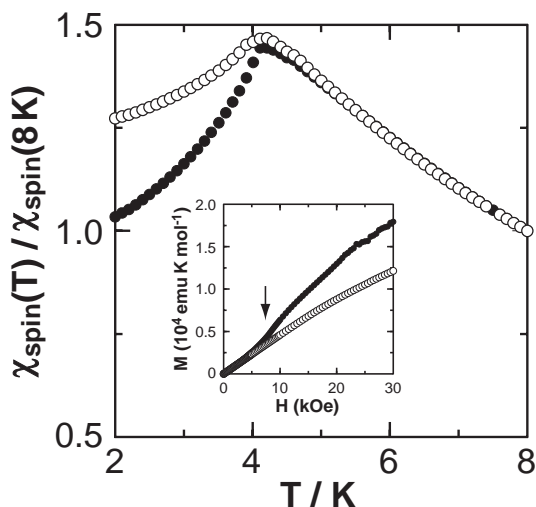


Fig. 130. Spin susceptibility of EMI•Fe<sup>III</sup>Cl<sub>4</sub> at low temperatures. Data obtained by slow cooling (–0.5 K min<sup>-1</sup>, closed circle) and by quenching (open circle). Inset shows the relaxed sample at 8 K (open circle) and 2 K (closed circle) indicating the spin-flop phenomenon at the magnetic field of ca. 8 kOe (arrow).<sup>854</sup>

veloped down to 1.9 K. This finding strongly indicates that the anion part of solidified (EMI)[(Fe<sup>III</sup>Cl<sub>4</sub>)<sub>0.5</sub>(Ga<sup>III</sup>Cl<sub>4</sub>)<sub>0.5</sub>] is a homogenous mixture instead of a mixture of segregated domains of [Fe<sup>III</sup>Cl<sub>4</sub>] and [Ga<sup>III</sup>Cl<sub>4</sub>], or that an aggregation of [Fe<sup>III</sup>Cl<sub>4</sub>], if any, has a size hardly exhibiting antiferromagnetic behavior.

**4.6.3 Preparation of Cation Radical Salts Using Ionic Liquids: Superconductor (TMTSF)<sub>2</sub>NbF<sub>6</sub> and so on:** Since ionic liquids are highly conductive and commonly composed of organic cation and inorganic anion molecules, they might be used as electrolytes for electrocrystallization of cation radical salts. No other solvents are needed when the donor species are soluble in the ionic liquids. Even a non-polar solvent such as benzene, which usually affords a less conductive solution of electrolyte and is therefore unfavorable for the electrocrystallization, can be used without any trouble.

In most cases, the obtained salts are identical with those prepared using conventional electrolytes such as TBA·X. In some cases, however, the ionic liquids have provided new or high quality salts which have not been harvested by using conventional electrolytes. In this section, the preparation of TMTSF, ET, and EDO salts using EMI·X (X = F(HF)<sub>2,3</sub>, SbF<sub>6</sub>, and NbF<sub>6</sub>) will be described briefly. Since these donor molecules are not soluble in the ionic liquids, one has to add an organic solvent such as 1,1,2-trichloroethane, THF, benzonitrile, etc.

EMI·NbF<sub>6</sub> affords needle shaped single crystals of (TMTSF)<sub>2</sub>NbF<sub>6</sub> (see section 3.3.1).<sup>328</sup> Although the salt was previously obtained by Bechgaard using TBA·NbF<sub>6</sub>,<sup>324,891</sup> no detailed data have been reported concerning the crystal structure owing to the poor quality of single crystals and no superconductivity was detected up to 1.2 GPa.<sup>324</sup>

(TMTSF)<sub>2</sub>NbF<sub>6</sub> is isostructural to the other (TMTSF)<sub>2</sub>X and includes disordered NbF<sub>6</sub> anions (Figs. 21a–21c). The transport measurements indicate a metal–insulator transition at 12 K at ambient pressure and the  $T_{MI}$  decreases with increasing pressure, ca. 5 K at 1.0 GPa (Fig. 131). A superconducting transition with an on-set temperature of 1.26 K (mid-point  $T_c = 1.12$  K) was observed at 1.2 GPa. A previous observation by Pedersen et al. that the spin susceptibility sharply drops below 14 K<sup>891</sup> strongly suggests the occurrence of the SDW transition at around 12 K in this salt.

EMI·F(HF)<sub>2,3</sub>, in which H<sub>2</sub>F<sub>3</sub><sup>−</sup> and H<sub>3</sub>F<sub>4</sub><sup>−</sup> anions are intermingled, gives single crystals of a new Mott insulator, α'-(ET)<sub>2</sub>H<sub>2</sub>F<sub>3</sub>.<sup>892</sup> The electrooxidation of EDO in the presence of TBA·SbF<sub>6</sub> provides (EDO)<sub>4</sub>(Sb<sub>2</sub>F<sub>11</sub>)<sub>0.85</sub>(H<sub>2</sub>O)<sub>4</sub>, which is not isostructural to (EDO)<sub>2</sub>X (X = PF<sub>6</sub>, AsF<sub>6</sub>) and shows no

metal–insulator transition as described in section 4.3.1.3. On the other hand, ionic liquid EMI·SbF<sub>6</sub> produces single crystals of (EDO)<sub>2</sub>SbF<sub>6</sub> having the metal–insulator transition at a lower temperature (ca. 240 K) than that for (EDO)<sub>2</sub>PF<sub>6</sub>, as expected.<sup>750</sup>

**4.7 Magnetic (Super)conductors.** For the conductive and magnetic multi-functional solids, the competitive or cooperative phenomena of the itinerant and localized electrons are currently some of the most intensively investigated subjects or systems, e.g. high  $T_c$  oxide superconductors,<sup>893</sup> organic superconductors,<sup>162,164</sup> Kondo effect,<sup>894</sup> d–π interaction,<sup>895</sup> GMR (giant magnetoresistance),<sup>896</sup> and so on, from the point of basic as well as applied researches in materials science. Most of the organic ferro- or ferrimagnets are electrically insulators composed of either pure organic compounds (single component,  $T_c \leq 1.48$  K),<sup>897</sup> fully ionic CT complexes between metallocene and acceptor molecules (i.e., decamethylferrocene·TCNE;  $T_c = 4.8$  K),<sup>898</sup> or coordination polymers between transition-metal and organic acceptor molecules (i.e. V[TCNE]<sub>x</sub>·yCH<sub>2</sub>Cl<sub>2</sub>,  $x \approx 2$ ,  $y \approx 0.5$ ,  $T_c \approx 400$  K).<sup>899</sup>

Since both the intermolecular interactions and spin degeneracy of organic species are small compared with those of transition metals, the magnetic parameters of organic magnets cannot compete with those of the inorganic magnets. Therefore, it is very common that in the organic magnetic conductors the organic part delivers the itinerant electrons and the inorganic species (transition metals) have the localized spins.

**4.7.1 Spins from Transition Metals: Organic/Inorganic Hybrid System:** CuPc(I<sub>3</sub>)<sub>1/3</sub> might have been the first compound to produce the exchange interaction between conducting π-carriers and localized d-spins reported in 1986.<sup>900</sup> An observation of negative magnetoresistance for Cu<sub>x</sub>Ni<sub>1-x</sub>Pc(I<sub>3</sub>)<sub>1/3</sub> at low temperatures supports the presence of the d–π interactions.<sup>901</sup> Recently, similar phenomena have been reported for some systems such as λ-(BETS)<sub>2</sub>FeCl<sub>4</sub> ( $T_N = 8.3$  K),<sup>902</sup> Ph<sub>4</sub>P[Fe(Pc)(CN)<sub>2</sub>]<sub>2</sub> ( $\rho_{(H=18\text{ T})}/\rho_{(H=0\text{ T})} \approx 0.07$  at 20 K),<sup>903</sup> and Eu<sub>6-x</sub>Sr<sub>x</sub>C<sub>60</sub> (ferromagnetic transition at 10–14 K,  $\rho_{(H=9\text{ T})}/\rho_{(H=0\text{ T})} = 10^{-3}$  for Eu<sub>6</sub>C<sub>60</sub> at 1 K indicating strong π–f interaction).<sup>904</sup>

The paramagnetic organic superconductor, β'-(ET)<sub>4</sub>[(H<sub>3</sub>O)-Fe<sup>III</sup>(ox)<sub>3</sub>](C<sub>6</sub>H<sub>5</sub>CN) (**1**) with  $T_c = 7.0$  K (on-set 8.6 K) was reported by Kurmoo, Day, and co-workers in 1995,<sup>463</sup> where early reports have indicated it as H<sub>2</sub>O instead of H<sub>3</sub>O<sup>+</sup>. The corresponding Cr salt is also a superconductor, but with a slightly lower  $T_c$  (6.0 K) than that of the Fe salt<sup>464</sup> (see Table 15). The crystal consists of alternating 2D layers of ET<sup>0.5+</sup> molecules and the other species that form the 2D honeycomb layer.

The bimetallic anions of [M<sup>II</sup>M'<sup>III</sup>(ox)<sub>3</sub>]<sup>1−</sup> (M = Mn, Fe, Co, Ni, and Cu; M' = Cr, Fe, and Ni) have been known to afford a 2D anion layer consisting of alternating stacks of M<sup>II</sup> and M'<sup>III</sup> ions interconnected through ox bridges for the R<sub>4</sub>N<sup>+</sup>, Ph<sub>4</sub>P<sup>+</sup>, decamethylmetallocenium, or ET salt as reported by Tamaki, Okawa, et al.<sup>905,906</sup> and others.<sup>907–910</sup> The tetraalkylammonium salts of [M<sup>II</sup>Cr<sup>III</sup>(ox)<sub>3</sub>]<sup>1−</sup> were found to be a ferromagnet with  $T_c = 6–14$  K,<sup>905</sup> while those of [M<sup>II</sup>Fe<sup>III</sup>(ox)<sub>3</sub>]<sup>1−</sup> (M = Fe and Ni) were ferrimagnets with  $T_N = 28–48$  K.<sup>906,911,912</sup> The combination of hyperpolarizable cation chromophore of *N*-heptyl-4-methoxystilbazolium with [M<sup>II</sup>M'<sup>III</sup>·

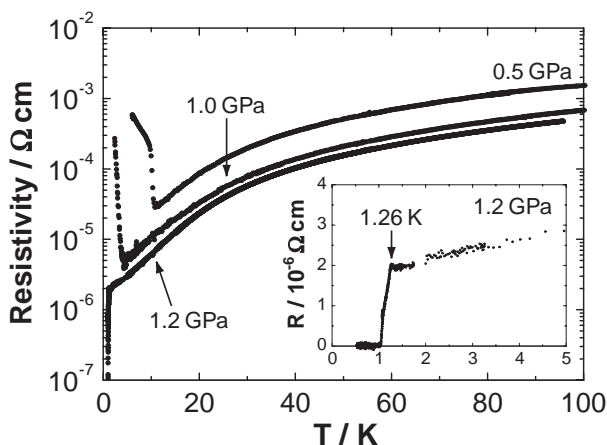


Fig. 131. Low-temperature region of resistivity of (TMTSF)<sub>2</sub>NbF<sub>6</sub> with a superconducting transition with on-set at 1.26 K at 1.2 GPa.<sup>328</sup>

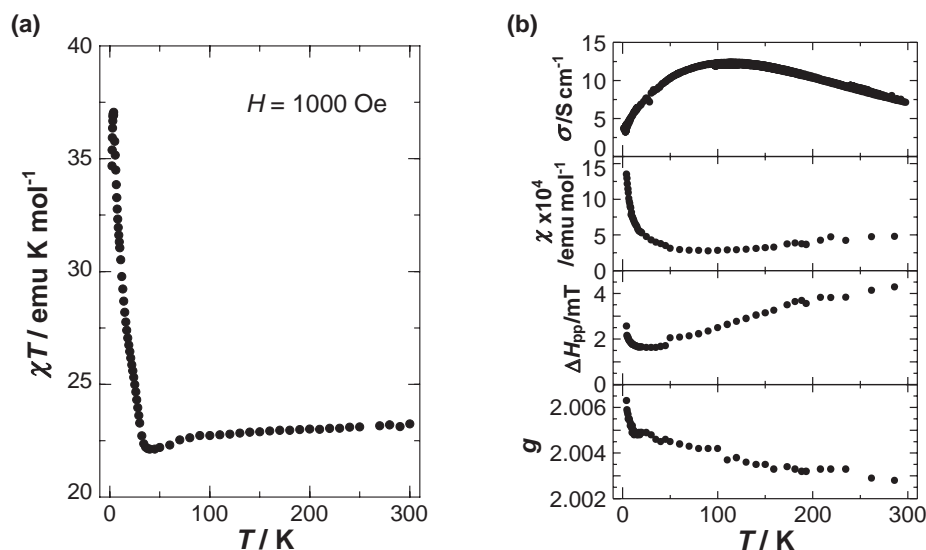


Fig. 132. Temperature dependence of magnetic and transport properties of a powder sample of  $(\text{BO})_3[\text{FeCr}(\text{ox})_3](\text{H}_2\text{O})_{3.5}$ .<sup>915</sup> (a)  $\chi T$  value after subtracting the core diamagnetism of the components and paramagnetism of the conduction electrons. (b) Conductivity ( $\sigma$ ) and EPR parameters of conduction electrons (spin susceptibility ( $\chi$ ), line width ( $\Delta H_{\text{pp}}$ ), and  $g$ -value).

$(\text{ox})_3]^{1-}$  afforded nonlinear optical ferromagnets with  $T_c = 5.7\text{--}12.5\text{ K}$ , where no significant interactions were noticed between the cation and anion parts.<sup>913</sup> Hence, in order to prepare molecular metallic ferro- or ferrimagnets, the simplest way is to combine  $[\text{M}^{\text{II}}\text{M}^{\text{III}}(\text{ox})_3]^{1-}$  with a donor molecule that has self-assembling ability such as ET or BO in the form of 2D assemblies.

In 2000, Coronado et al. prepared the conducting ET salt  $(\text{ET})_3[\text{Mn}^{\text{II}}\text{Cr}^{\text{III}}(\text{ox})_3]$  (**2**) with a ferromagnetically ordered bimetallic oxalate-based 2D honeycomb layer.<sup>914</sup> The metallic behavior remains down to 0.3 K, and is unaffected by the magnetic ordering of the bimetallic layer at 5.5 K. It seems that the small CT degree of ET molecules (+1/3) results in the difficulty in the preparation of the single crystals, and other groups have hardly succeeded in reproducing the growth of single crystals.

Similar magnetic metals have been subsequently prepared by utilizing BO:  $(\text{BO})_3[\text{Fe}^{\text{II}}\text{Cr}^{\text{III}}(\text{ox})_3](\text{H}_2\text{O})_{3.5}$  (**3**) by our group<sup>915</sup> and BETS,  $(\text{BETS})_x[\text{MnCr}(\text{ox})_3](\text{CH}_2\text{Cl}_2)$  ( $x \approx 3$ )<sup>916</sup> (**4**) by Coronado et al. Although the latter complex was claimed to be a molecular magnetic metal, it shows metallic behavior only above 150 K and the ferromagnetic ordering occurred in the non-metallic region ( $T_c \approx 5.5\text{ K}$ ). All compounds have no pronounced interactions between conducting  $\pi$ -carriers and localized d-spins.

Polycrystalline **3** was prepared by metathesis between  $(\text{BO})_2(\text{BF}_4)(\text{H}_2\text{O})_x$  ( $x \approx 2$ ) and  $\text{K}_3\text{Cr}(\text{ox})_3(\text{H}_2\text{O})_3$  in the presence of  $\text{FeSO}_4 \cdot 7\text{H}_2\text{O}$ . So far attempts to obtain single crystals have been unsuccessful. The compaction pellet sample shows a conductivity of  $\sigma_{\text{RT}} \approx 7\text{ S cm}^{-1}$  with a metallic behavior with a maximum of conductivity at around 120 K ( $\approx 15\text{ S cm}^{-1}$ ). Below it, the conductivity gradually decreases ( $3\text{--}4\text{ S cm}^{-1}$  at 2.8 K, top panel of Fig. 132b) with an energy gap for conduction being far less than  $k_B T$  ( $\varepsilon_g = 38.5$  and  $1.16\text{ K}$  for the temperature range of 70–35 and 8–4 K, respectively), suggesting that the metallic state persists down to low temperatures.

The effective magnetic moment after subtracting core diamagnetism was estimated to be  $4.82\mu_B$  at 300 K, which is considerably smaller than the spin-only value of  $6.24\mu_B$  for the magnetically dilute  $\text{Fe}^{\text{II}}(S=2)\text{--}\text{Cr}^{\text{III}}(S=3/2)$  system. The appearance of a round minimum around 40 K suggests the ferrimagnetic state of this complex. The magnetization curve measured at 1.9 K indicates that the magnetization is not saturated even at 50 kOe with  $2.71\mu_B$ , which exceeds the saturation magnetization ( $M_s$ ) for the ferrimagnetically ordered  $\text{Fe}^{\text{II}}\text{--}\text{Cr}^{\text{III}}$  network ( $M_s = 1\mu_B$ ). The coercive field and Curie temperature are ca. 50 G at 5 K and  $T_c = 10.7\text{ K}$ , respectively.

The EPR spectra (Fig. 132b) showed one Lorentzian signal down to 4 K. The  $g$ -value, linewidth ( $\Delta H_{\text{pp}}$ ), and the spin susceptibility ( $\chi$ ) at RT were 2.0028, 42.8 G, and  $4.8 \times 10^{-4}\text{ emu mol}^{-1}$ , respectively, and the signal is ascribed to the  $\text{BO}^{\bullet+}$  radical spin. No anomaly was observed for the EPR signal at around 120 K. The drastic change of the EPR parameters observed below 15 K, which is a little above  $T_c$ , definitely shows that the dynamics of itinerant electrons are influenced by the precursory fluctuation of the 3D ferromagnetic ordering on  $\text{Fe}^{\text{II}}\text{--}\text{Cr}^{\text{III}}$  layers.

Kobayashi and his co-workers have developed BETS salts formed with tetrahedral anions  $\text{MX}_4$  ( $\text{M} = \text{Fe}$  and  $\text{Ga}$ ;  $\text{X} = \text{Cl}$  and  $\text{Br}$ ).<sup>611–613,902,917</sup> The initial notable finding is the  $\lambda$ -(BETS)<sub>2</sub>GaCl<sub>4</sub> with a superconducting transition at 8 K (mid-point 5.5 K) and the  $\lambda$ -(BETS)<sub>2</sub>FeCl<sub>4</sub> (**5**) with a coupled antiferromagnetic and metal–insulator transitions at 8.3 K. For the FeCl<sub>4</sub> salt, a relaxor ferroelectric behavior in the metallic state below 70 K<sup>918</sup> and a firm nonlinear electrical transport associated with the negative resistance effect in the magnetic ordered state have been observed.<sup>919</sup> Moreover, it has been found by Uji et al. that the FeCl<sub>4</sub> salt shows the field-induced superconducting transition under a magnetic field of 18–41 T applied exactly parallel to the conducting layers.<sup>610</sup> Interestingly, the  $\lambda$ -(BETS)<sub>2</sub>Fe<sub>x</sub>Ga<sub>1–x</sub>X<sub>4</sub> passes through a superconducting to insulating transition on cooling.<sup>920</sup> The  $\kappa$ -(BETS)<sub>2</sub>FeX<sub>4</sub>

Table 30. Magnetic Conductors of Organic/Inorganic Hybrid and Organic (7) System<sup>a)</sup>

	Ferromagnet	Ferrimagnet	Antiferromagnet	Paramagnet
Metal	<b>2, 4*, 8*, 9</b>	<b>3</b>	<b>5, 11*, 12*, 13</b>	common
Superconductor	<b>10</b>		<b>6, 7</b>	<b>1, 14–16</b>

a) **1:**  $\beta''$ -(ET)<sub>4</sub>[(H<sub>3</sub>O)Fe<sup>III</sup>(ox)<sub>3</sub>](C<sub>6</sub>H<sub>5</sub>CN), **2:** (ET)<sub>3</sub>[Mn<sup>II</sup>Cr<sup>III</sup>(ox)<sub>3</sub>](CH<sub>2</sub>Cl<sub>2</sub>), **3:** (BO)<sub>3</sub>[Fe<sup>II</sup>Cr<sup>III</sup>-(ox)<sub>3</sub>](H<sub>2</sub>O)<sub>3.5</sub>, **4:** (BETS)<sub>x</sub>[MnCr(ox)<sub>3</sub>](CH<sub>2</sub>Cl<sub>2</sub>) ( $x \approx 3$ ),<sup>916</sup> which is not a metal in the ferromagnetic regime, **5:**  $\lambda$ -(BETS)<sub>2</sub>FeCl<sub>4</sub>, **6:**  $\kappa$ -(BETS)<sub>2</sub>FeX<sub>4</sub>, **7:**  $\kappa$ -(ET)<sub>2</sub>Cu[N(CN)<sub>2</sub>]Cl, **8:** (EDO-TTFI<sub>2</sub>)<sub>2</sub>-M(mnt)<sub>2</sub> (M = Ni, Pt), which has  $T_{\text{MI}}$  at around 90 K and exhibits ferromagnetic interactions between M(mnt)<sub>2</sub> molecules but no ferromagnetic order. The spins show antiferromagnetic order ( $T_{\text{N}} = 5.5$  K) for M = Pt, J. Nishijo, E. Ogura, J. Yamaura, A. Miyazaki, T. Enoki, T. Takano, Y. Kuwatani, M. Iyoda, *Solid State Commun.* **2000**, *116*, 661. **9:** polymeric C<sub>60</sub> (see next section). However, the paper was very recently retracted by a part of authors, *Nature* **2006**, *440*, 707. **10:** Ce<sub>x</sub>C<sub>60</sub>, Coexistence of superconductivity and ferromagnetism is reported by Maruyama et al. (see section 5.1),<sup>925</sup> **11:** (DMET)<sub>2</sub>FeBr<sub>4</sub>, which has  $T_{\text{MI}}$  at around 40 K and  $T_{\text{N}}$  at 3.7 K, so no real coexistence of metal and AF phases is realized, K. Enomoto, J. Yamaura, A. Miyazaki, T. Enoki, *Bull. Chem. Soc. Jpn.* **2003**, *76*, 945. **12:**  $\beta$ -(BDA-TTP)<sub>2</sub>(FeCl<sub>4</sub>), which has  $T_{\text{MI}}$  at 113 K and  $T_{\text{N}}$  at 8.5 K at ambient pressure. Under pressure it became superconducting ( $T_{\text{c}} \leq 2$  K at 0.63 GPa), E. S. Choi, D. Graf, J. S. Brooks, J. Yamada, H. Akutsu, K. Kikuchi, M. Tokumoto, *Phys. Rev. B* **2004**, *70*, 024517/1. **13:** (EDO-TTFVO)<sub>2</sub>FeCl<sub>4</sub>, H. Fujiwara, K. Wada, T. Hiraoka, T. Hayashi, T. Sugimoto, H. Nakazumi, K. Yokogawa, M. Teramura, S. Yasuzuka, K. Murata, T. Mori, *J. Am. Chem. Soc.* **2005**, *127*, 14166. **14:**  $\beta''$ -(ET)<sub>4</sub>[A·Cr(ox)<sub>3</sub>](C<sub>6</sub>H<sub>5</sub>NO<sub>2</sub>) (A = H<sub>3</sub>O or NH<sub>4</sub>)<sup>465</sup> **15:**  $\beta''$ -(ET)<sub>4</sub>[A·Fe(ox)<sub>3</sub>](C<sub>6</sub>H<sub>5</sub>NO<sub>2</sub>) (A = H<sub>3</sub>O or NH<sub>4</sub>)<sup>465</sup> **16:**  $\beta''$ -(ET)<sub>4</sub>[H<sub>3</sub>O·Fe(ox)<sub>3</sub>](C<sub>6</sub>H<sub>5</sub>Br), E. Coronado, S. Curreli, C. Gimenez-Saiz, C. J. Gómez-García, *J. Mater. Chem.* **2005**, *15*, 1429.

(X = Cl and Br) (**6**) are antiferromagnetic superconductors, where the transition temperatures were  $T_{\text{N}} = 2.5$  K and  $T_{\text{c}} = 1.1$  K for the Br salt, and  $T_{\text{N}} = 0.45$  K and  $T_{\text{c}} = 0.17$  K for the Cl salt.<sup>921</sup> These organic/inorganic hybrid systems are summarized in Table 30, where a magnetic conductor exhibiting magnetic and conducting phenomena at different temperature regimes is also included (indicated by \*), since at this moment the definition of “coexistence of multifunction” is ambiguous.

Similar phenomena, namely antiferromagnetic, ferromagnetic, or field-induced superconductivity, have been observed in several inorganic solids such as the Chevrel phase<sup>737</sup> and heavy-fermion system.<sup>922</sup>

Aiming to combine magnetic and conductive properties within a system, several donor molecules having the coordination ability for paramagnetic transition metals have been proposed.<sup>923,924</sup> Commonly such a donor consists of both  $\pi$ -donor and  $n$ -donor moieties connected by a single bond similar to **24–26** in section 2.3.3. The generation of metallic conductivity has been the key issue for such a system so far.

**4.7.2 Spins from the Same Source:** In some systems both itinerant and localized electrons arise from the same source and such systems are the real target for organic magnetic conductors. However, the experimental works remain sparse since a promising molecular design is currently not present. The Mott insulator  $\kappa$ -(ET)<sub>2</sub>Cu[N(CN)<sub>2</sub>]Cl (**7**) exhibits an antiferromagnetic transition at 27 K under ambient pressure<sup>299</sup> and a superconducting transition at 12.8 K under a subtle applied pressure (0.03 GPa, see Fig. 47).<sup>298</sup> Studies under helium gas pressure show firm evidence of the coexistence of superconducting and antiferromagnetic phases,<sup>926–929</sup> where the radical electrons of ET molecules play both roles of localized and itinerant ones (Fig. 133).

Some Mott insulators are highly conductive as mentioned in sections 2.3.2 and 3.2.2. It seems that the electrons in these sol-

ids reside near the critical region among the localization, itinerancy, and reaction.

The soft ferromagnet TDAE·C<sub>60</sub> ( $T_{\text{c}} = 16.1$  K)<sup>930</sup> was thought to belong to this group where only the spins on C<sub>60</sub> play a crucial role for magnetism. No EPR signals were detected concerning the spins on TDAE<sup>•+</sup>, suggesting strong dimerization of the spins (see section 5.5). However, the poor conductivity of single crystals ( $\sigma_{\text{RT}} = 5 \times 10^{-5}$  S cm<sup>-1</sup> and  $\varepsilon_{\text{g}} = 0.6$  eV > 150 K) reveals the localized nature.<sup>931</sup>

It was recently reported that the compressed crystals of polymeric C<sub>60</sub> exhibited a ferromagnetic ordering as high as 500 K,<sup>932</sup> although it is not a CT complex. The C<sub>60</sub> molecules were treated at 6 GPa in the range of (1025–1050) K to give a 2D [2 + 2] covalently linked and highly oriented rhombohedral phase, which exhibited a small magnetic moment of 0.4  $\mu_{\text{B}}$  per C<sub>60</sub> molecule atom. However, this paper was very recently retracted by a part of authors. As for the transport properties, the rhombohedral C<sub>60</sub> polymer is metallic down to 30 K in the (001) plane, but semiconductive for the out-of-plane conductivity.<sup>933</sup> When one applies higher pressures (<13 GPa) at higher temperatures (<2000 K) on a C<sub>60</sub> solid, a superhard (harder than diamond) polymers with semiconductive nature was realized. The density of the product (2.9–3.3 g cm<sup>-3</sup>) was between those of graphite (2.27 g cm<sup>-3</sup>) and diamond (3.51 g cm<sup>-3</sup>). The conductivity was sample dependent:  $2 \times 10^{-1}$ – $10 \times 10^{-6}$  S cm<sup>-1</sup> with  $\varepsilon_{\text{a}} = 0.01$ – $0.3$  eV.<sup>934</sup>

Some RT ferromagnets with a relatively high conductivity have been reported for 2:3 TCNQ anion radical salts, i.e., (Me<sub>4</sub>P)<sub>2</sub>(Me<sub>2</sub>TCNQ)<sub>3</sub> (37 S cm<sup>-1</sup>) and (Me<sub>4</sub>N)<sub>2</sub>(Me<sub>2</sub>TCNQ)<sub>3</sub> (15 S cm<sup>-1</sup>),<sup>935</sup> in which the valence state on anion molecules (A) is disproportionate, such as A<sup>•-</sup> A<sup>•-</sup> A<sup>0</sup>. Their saturation magnetizations are marginally small, corresponding to the unpaired spin of  $6 \times 10^{-4}$ – $2.6 \times 10^{-3}$   $\mu_{\text{B}}$  per formula unit.

A realistic model for a metallic ferromagnet has been proposed by Wudl et al.<sup>936</sup>



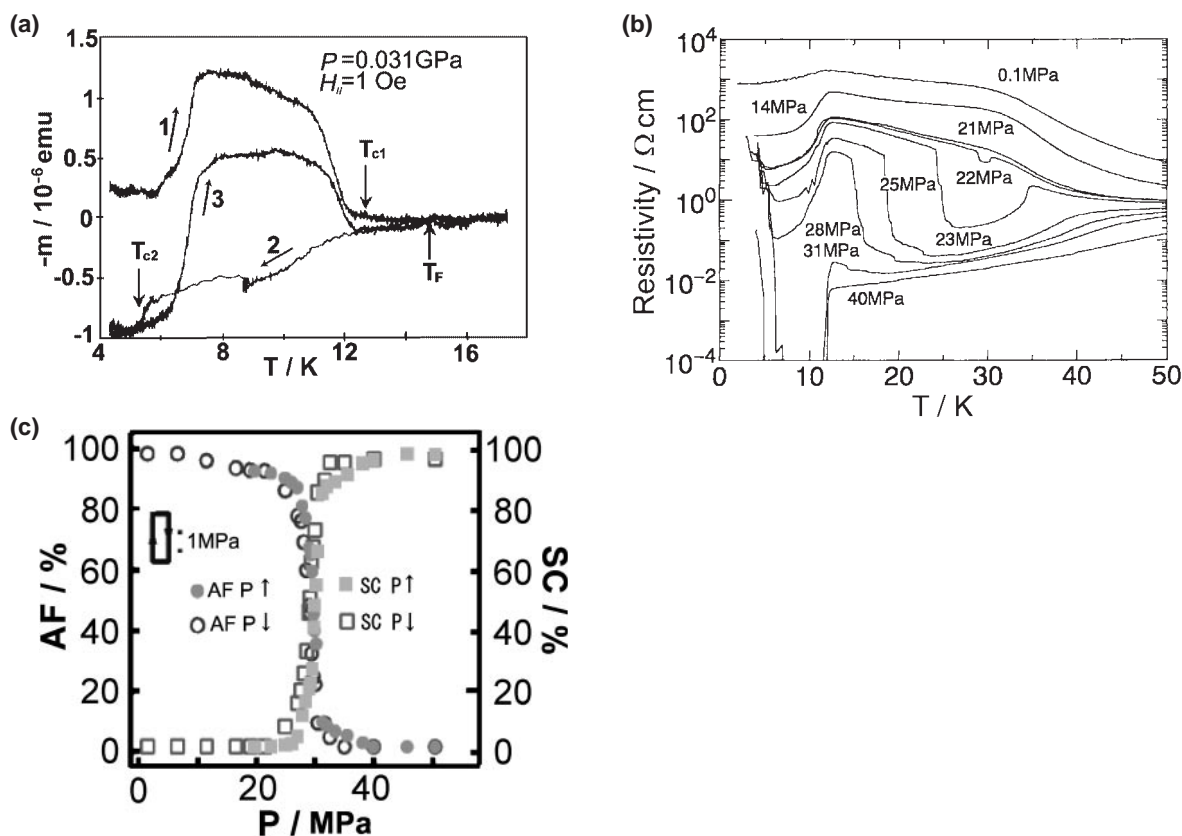


Fig. 133. Coexistence of the superconducting and antiferromagnetic phases in  $\kappa\text{-(ET)}_2\text{Cu[N(CN)}_2\text{]Cl}$ . (a) Temperature dependence of magnetization at 0.031 GPa in a magnetic field of 1 Oe in the  $ac$ -plane.  $T_F$ : weak ferromagnetic transition temperature,  $T_{c1}$  and  $T_{c2}$ : upper and lower superconducting transition temperatures. Arrows indicate the direction of the temperature sweep. In this experiment, the sample is  $\kappa\text{-(ET)}_2\text{Cu[N(CN)}_2\text{]Cl}_{0.85}\text{Br}_{0.15}$ .<sup>926</sup> (b) Temperature dependence of the intralayer resistivities.<sup>510</sup> (c) Proportion of nuclear spins in the antiferromagnetic (AF) and superconducting (SC) states evaluated by the analysis of  $^1\text{H}$  NMR spectra at 8.5 K by Lefebvre et al. Arrows indicate the direction of the pressure sweep.<sup>929</sup>

**4.8 D- $\pi$ -A Compounds: Ionicity, Structures, and Non-Linear Optical Properties.** The intramolecular CT compounds composed of donor (D) and acceptor (A) parts linked by a  $\pi$ -bond, D- $\pi$ -A, have been studied as a source of functional soft materials, such as indicators of solvent polarity,<sup>937,938</sup> molecular rectifiers,<sup>939-943</sup> non-linear optics,<sup>944-954</sup> photovoltaic<sup>954-957</sup> and photochromic materials,<sup>952,958,959</sup> molecular conductors,<sup>84,99,101,105,106,959,960</sup> and magnets.<sup>85</sup> In particular, the reaction products through a Stork enamine-type reaction between strong electron acceptors such as TCNQ,<sup>938-943,949,952,958</sup>  $\text{F}_4\text{TCNQ}$ ,<sup>938,949</sup> TCNE,<sup>945,961</sup> or  $p$ -chloranil,<sup>962</sup> and tertiary amine derivatives have been focused on. The structural information has provided valuable aspects in connection with the reaction process, molecular and solid-state properties, and ionicity ( $\delta$ ) of the D- $\pi$ -A solids.<sup>939,949,963-965</sup>

Although the ionicity of the intermolecular CT compounds has been quantitatively discussed in the description of electronic properties<sup>155,164,184</sup> and phase transitions (Peierls, Mott, charge order, neutral-ionic)<sup>178,208,966</sup> of organic (super)-conductors, not so many quantitative experiments concerning functionality vs  $\delta$  have been done for the intramolecular CT compounds except for a few cases,<sup>946-948</sup> owing to the difficulty of obtaining  $\delta$  of  $\text{D}^{\delta+}\text{-}\pi\text{-A}^{\delta-}$ . For the intramolecular CT compounds, either a complete neutral ( $\delta = 0$ ) or zwitterionic ( $\delta = 1$ ) ground state has often been antici-

pated.<sup>938,940,942,944,945,949,952,955,967-969</sup>

Here, we present an evaluation of the intramolecular CT degree  $\delta$  from the solvatochromic shift, and the crystal and molecular structures of D- $\pi$ -A compounds  $\text{I}_n\text{-3CNQ-R}$  ( $n$ : alkyl chain  $\text{C}_n\text{H}_{2n+1}$  attached to indoline (I) moiety, R: substituents attached to 3CNQ moiety, see Fig. 134) prepared by the Stork-enamine type reaction between I and TCNQ derivatives (R-TCNQ), and discuss the relation between the ionicity and the calculated molecular polarizability ( $\alpha$ ) and hyperpolarizability ( $\beta$  and  $\gamma$ ).<sup>970-972</sup> The second harmonic generation (SHG) on the hybrid LB films and clays composed of D- $\pi$ -A molecules has also been studied by Kawamata, Saito, et al.<sup>973</sup> The following compounds afforded single crystals and crystal and molecular structures were determined so far:  $(\text{I}_1\text{-3CNQ-F}_2)(\text{CH}_3\text{-CN})_{0.5}$ ,  $(\text{I}_1\text{-3CNQ-F})(\text{CH}_3\text{CN})_{0.5}$ ,  $\text{I}_1\text{-3CNQ-F}$ ,  $(\text{I}_1\text{-3CNQ-H})_2\text{-(TCNQ)}$ ,  $(\text{I}_1\text{-3CNQ-(MeO)}_2)$ ,  $(\text{I}_1\text{-3CNQ-(EtO)}_2)(\text{CH}_3\text{CN})$ ,  $(\text{I}_3\text{-3CNQ-H})(\text{CH}_3\text{CN})$ ,  $\text{I}_6\text{-3CNQ-H}$  (green plate),  $\text{I}_6\text{-3CNQ-H}$  (green rod),  $(\text{I}_6\text{-3CNQ-CF}_3)$ ,  $\text{I}_7\text{-3CNQ-H}$  (green plate),  $\text{I}_7\text{-3CNQ-H}$  (golden block),  $\text{I}_8\text{-3CNQ-H}$ ,  $\text{I}_{10}\text{-3CNQ-H}$ , and  $\text{I}_{20}\text{-3CNQ-H}$ . The  $\text{I}_n\text{-3CNQ-R}$  compounds we obtained are summarized in Table 31.

**4.8.1 Melting Points and Color:** A plot of the melting point of  $\text{I}_n\text{-3CNQ-H}$  compounds so far prepared against the alkyl chain length (Fig. 135a) is qualitatively analogous to that observed for the  $\text{TTC}_n\text{-TTF}$  compounds; namely, the melting

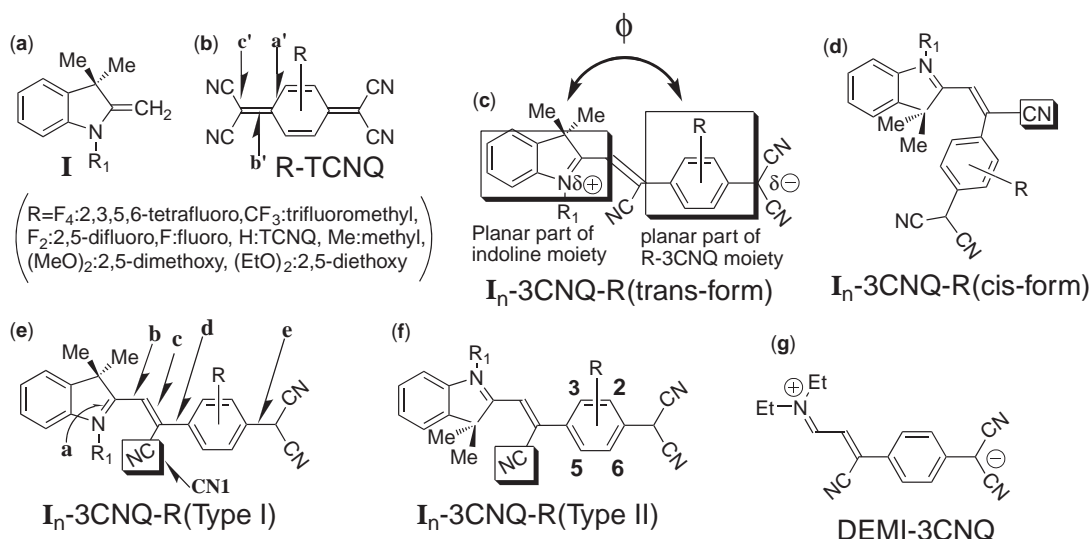


Fig. 134. Chemicals in this section.  $\phi$ : dihedral angle between the planar parts of indoline and R-3CNQ moieties (c). The schematic ionic characters of the molecules are shown in (c) and (g) with ionicity of  $\delta$  and 1, respectively. The degree of intramolecular CT ( $\delta$ ) is omitted for simplicity for (d)–(f).  $a'$ – $c'$  in (b) and  $a$ – $e$  in (e) represent the corresponding bonds or bond lengths. The C $\equiv$ N group close to the indoline moiety in  $\text{I}_n\text{-3CNQ-R}$  is labeled CN1 (e).

Table 31. Characteristics of Reaction Products  $\text{I}_n\text{-3CNQ-R}$  and R-TCNQ

No.	$R_1$ in $\text{I}$ $\text{C}_n\text{H}_{2n+1}$ $n$	$R$ in R-TCNQ $E/V^a$	$\text{I}_n\text{-3CNQ-R}^d$	Color & shape	$T_m$ or $T_d$ / $^\circ\text{C}$	$\text{IR}^b$ $\nu_{\text{CN}}/\text{cm}^{-1}$	UV-vis <sup>c</sup> /nm		
							Solution		Solid
							MeOH	PhCl	
1	1	F <sub>4</sub> +0.60	$\text{I}_1\text{-3CNQ-F}_4$	black powder	>250	2192s 2186	712 607	825	—
2	1	CF <sub>3</sub> +0.44	$\text{I}_1\text{-3CNQ-CF}_3$	green block	222	2192s	— 661	801 731	840sh 668
3	1	F <sub>2</sub> +0.41	$(\text{I}_1\text{-3CNQ-F}_2)(\text{AN})_{0.5}$	black rod	224–226	2179s 2152	— 657	803 728	810sh 674
4	1	F +0.32	$\text{I}_1\text{-3CNQ-F}$	green block	224–226	2187s 2156	798sh 720	808 734	850 694
5			$(\text{I}_1\text{-3CNQ-F})(\text{AN})_{0.5}$	black block	221–222	2178s 2147	779sh 692	795 722	830sh 690
6	1	H +0.22	$\text{I}_1\text{-3CNQ-H}$	green powder	249–251	2193s 2184sh 2167	779 720	794 726	858sh 708
7	1		$(\text{I}_1\text{-3CNQ-H})_2(\text{TCNQ})$	black block	230–232	2212 2185s 2175	780 723 656sh 394	793 726 665sh 403	1250sh 848sh 730 398
8	1	Me +0.20	$\text{I}_1\text{-3CNQ-Me}$	green powder	243–245	2214 2190s	787 726	810sh 723	838sh 754
9	1	(MeO) <sub>2</sub> +0.05	$\text{I}_1\text{-3CNQ-(MeO)}_2^e$	green plate	247–249	2214 2193s	749 694	773sh 693	820sh 702
10	1	(EtO) <sub>2</sub> +0.01	$\text{I}_1\text{-3CNQ-(EtO)}_2$	green powder	226–228	2217 2189s	750 694	771sh 691	806 716
11	1		$\text{I}_1\text{-3CNQ-(EtO)}_2 \cdot \text{AN}$	green needle	— <sup>f</sup>	— <sup>f</sup>	— <sup>f</sup>	— <sup>f</sup>	— <sup>f</sup>
12	3	H	$\text{I}_3\text{-3CNQ-H}$	green block	222–225	2189s 2181s 2148	800 732 665sh	806 733 674sh	852 744 668sh

Continued on next page.

Continued.

No.	R <sub>1</sub> in <b>I</b> C <sub>n</sub> H <sub>2n+1</sub> <i>n</i>	R in R-TCNQ <i>E/V</i> <sup>a)</sup>	<b>I</b> <sub><i>n</i></sub> -3CNQ-R <sup>d)</sup>	Color & shape	<i>T</i> <sub>m</sub> or <i>T</i> <sub>d</sub> /°C	IR <sup>b)</sup> <i>ν</i> <sub>CN</sub> /cm <sup>-1</sup>	UV-vis <sup>c)</sup> /nm		Solid
							Solution		
							MeOH	PhCl	
<b>13</b>	6	H	<b>I</b> <sub>6</sub> -3CNQ-H	green plate/ rod	190–191	2214	800	805	852
						2193s	732	734	748
						2168	664sh	675sh	674sh
<b>14</b>	6	CF <sub>3</sub>	<b>I</b> <sub>6</sub> -3CNQ-CF <sub>3</sub>	green block	190–191	2191s	756sh	814	826sh
						2127sh	716	743	738
							657sh	673sh	660sh
<b>15</b>	7	H	<b>I</b> <sub>7</sub> -3CNQ-H	green plate/ block	179–184	2215	799	805	858
						2193s	733	733	746
						2166	663sh	671sh	670sh
<b>16</b>	8	H	<b>(I</b> <sub>8</sub> -3CNQ-H) <b>(Bz)</b> <sub>0.5</sub>	green block	158–159	2211	801	804	872
						2194s	733	734	748
						2167	662sh	670sh	680sh
<b>17</b>	10	H	<b>I</b> <sub>10</sub> -3CNQ-H	green block	148	2218	800	805	842
						2182s	733	734	746
						2153	670sh	675sh	678sh
<b>18</b>	14	H	<b>I</b> <sub>14</sub> -3CNQ-H	golden powder	122	2213	800	805	846
						2196s	732	735	754
<b>19</b>	16	H	<b>I</b> <sub>16</sub> -3CNQ-H	green powder	104–105	2215	801	801	945sh
						2196s	733	733	858
							663sh	663sh	758
<b>20</b>	18	H	<b>I</b> <sub>18</sub> -3CNQ-H	green powder	93	2195s	801	806	854
						2169	733	735	750
									678sh
<b>21</b>	20	H	<b>I</b> <sub>20</sub> -3CNQ-H	golden plate	104–105	2218	800	805	852
						2192s	733	734	758
						2181	670sh	676sh	678sh
						2169			
<b>22</b>	22	H	<b>I</b> <sub>20</sub> -3CNQ-H	golden powder	105–106	2219	801	806	850
						2192s	733	734	754

a) *E*: Redox potential. 0.1 M TBA·BF<sub>4</sub>, CH<sub>3</sub>CN, Pt electrodes vs SCE. b) KBr pellet. c) Peak position. d) AN: CH<sub>3</sub>CN, Bz: benzene. e) The data for **I**-(MeO)<sub>2</sub> are those on the mixture of Phases α and β. f) Not measured owing to the poor yield.

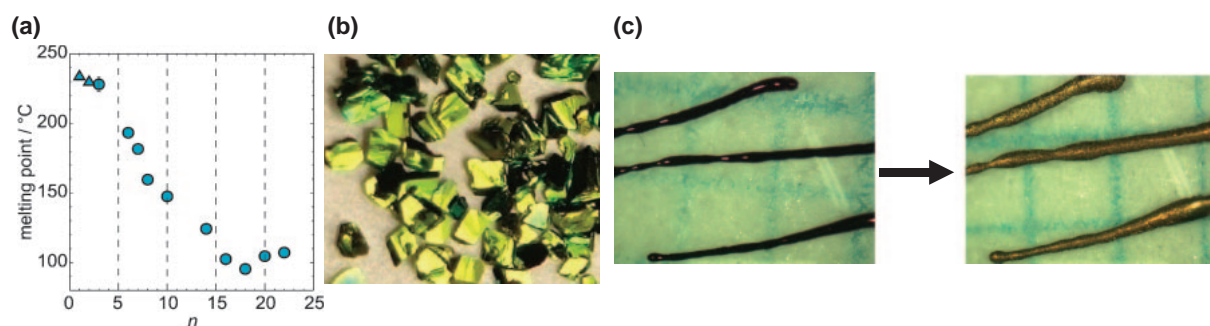


Fig. 135. (a) Melting points of **I**<sub>*n*</sub>-3CNQ-H compounds (Δ represents a decomposition point for *n* = 1 and 2). (b) Crystals of **I**<sub>6</sub>-3CNQ-CF<sub>3</sub>. (c) A supercooled melt of **I**<sub>20</sub>-3CNQ-H was stretched into strings by hand (left) then treated at around 70 °C to solidify (right).

point decreases with increasing *n* at the initial stage and then increases after having a minimum (Fig. 7d). The minimum appears at *n* = 4 for TTC<sub>*n*</sub>-TTF,<sup>60</sup> *n* = 5 for TSeC<sub>*n*</sub>-TTF,<sup>63</sup> and *n* = 6 for TTeC<sub>*n*</sub>-TTF.<sup>65</sup> For TTC<sub>*n*</sub>-TTF compounds it has been clarified that in the small *n* region (*n* ≤ 4) intermolecular interactions of the π-moieties are dominant in the crystal, while in the large *n* region (*n* > 5) intermolecular interactions associated with alkyl chains (Fastener effect) play an important

role.<sup>66</sup> Accordingly, it is most plausible that the self-assembling nature arising from the van der Waals interaction between alkyl chains emerges when *n* is around 18 for **I**<sub>*n*</sub>-3CNQ-R compounds.

**I**<sub>*n*</sub>-3CNQ-R compounds with small *n* (≤ 10) have green color and change their color to gold with further increase in *n* (Fig. 135b). A melt of **I**<sub>*n*</sub>-3CNQ-H (*n* = 20, *T*<sub>m</sub> = 104–105 °C) can be transformed into a string by elongation easily: a prelimi-

nary experiment reveals that thready strings were obtained by stretching a supercooled melt (dark brown) even by hand into 70–120  $\mu\text{m}$  in diameter. The stretched melt was solidified by treating it around 70  $^{\circ}\text{C}$ , recovering golden luster (Fig. 135c).

**4.8.2 Ionicity Determined by Solvatochromism:**  $\text{I}_n$ -3CNQ-R has four absorption bands in the visible region. However, in general, two absorption peaks (labeled A and B) between 700–850 nm and a shoulder at 550–700 nm appear (Table 31, Fig. 136) similar to those of the analogous compounds.<sup>938,940,942,949,952</sup> Peak B is used in the following analysis. When the overlap of the peaks was significant, the positions of the peaks were determined by line deconvolution into four Gaussian bands.

In polar solvents a hypsochromic band shift was observed for the molecule derived from a strong acceptor in the TCNQ system, confirming its ground state to be ionic. However, in solvents less polar than chlorobenzene, a bathochromic band shift was observed,<sup>931,967</sup> indicating a change of ground state from ionic to neutral states. Consequently, we exclude the solvents having smaller Reichardt's  $E_T$  values<sup>937</sup> than that of chlorobenzene in the evaluation of  $\delta$  so as not to mix opposite solvatochromic effects for each  $\text{I}_n$ -3CNQ-R.

The examination of the transition energy of Peak B ( $h\nu_{\text{CT}}(\text{B})$ ) in connection with the relative permittivity  $\epsilon_r$  and  $E_T$  of solvent revealed. 1)  $E_T$  has a linear relation with  $h\nu_{\text{CT}}(\text{B})$  (Eq. 75, Fig. 137) but  $\epsilon_r$  does not, and 2) the slope  $a$  of each line varies in good accordance with the redox potentials of R-TCNQ (Table 32).

$$h\nu_{\text{CT}}(\text{B}) = aE_T + b. \quad (75)$$

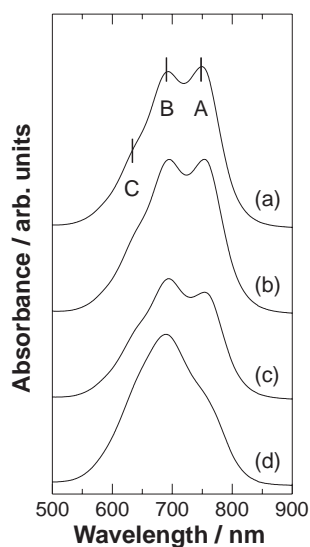


Fig. 136. Absorption spectra of the  $\text{I}_1$ -3CNQ-(EtO)<sub>2</sub> molecule in (a) methanol, (b) acetonitrile, (c) acetone, and (d) chlorobenzene.<sup>971</sup>

The CT energy for an ionic complex  $\text{D}^{\delta+}\text{A}^{\delta-}$  ( $\delta \geq 0.5$ ),  $h\nu_{\text{CT}}^{\text{I}}$  (Eq. 76), is related to  $\epsilon_r$  in terms of both the Coulomb attractive ( $\approx e^2/\epsilon_r r$ ) and solvation ( $\Delta G \approx 1 - 1/\epsilon_r$ ) energies in solution.<sup>975</sup> Here,  $r$  is the distance between  $\text{D}^{\delta+}$  and  $\text{A}^{\delta-}$ ,  $\Delta G$  is the difference between the solvation energies for  $\text{D}^0\text{A}^0$  and  $\text{D}^{1+}\text{A}^{1-}$  states, and  $X$  is the resonance stabilization energy.

$$h\nu_{\text{CT}}^{\text{I}} = -I_{\text{D}} + E_{\text{A}} + (2\delta - 1)e^2/\epsilon_r r - (2\delta - 1)\Delta G + X. \quad (76)$$

It is reasonably expected that  $h\nu_{\text{CT}}^{\text{I}} \approx h\nu_{\text{CT}}^{\text{N}}$  at  $\delta = 0.5$ , resulting in a practically  $\epsilon_r^{-1}$  independent CT energy.<sup>976</sup> We presume that Eq. 76 for  $\text{D}^{\delta+}\text{A}^{\delta-}$  complexes is valid for  $\text{D}^{\delta+}-\pi-\text{A}^{\delta-}$  molecules as well.

The  $E_T$  values are the intramolecular CT energies of the zwitterionic Reichardt's dye ( $\delta = 1$ ) (Chart 18) in various solvents,<sup>937</sup> and are formulated by Eq. 77, where  $r'$ ,  $\Delta G'$ , and  $X'$  represent the same meaning for the corresponding terms in Eq. 76.

$$E_T = -I(\text{D}-\pi-\text{A}) + E(\text{D}-\pi-\text{A}) + e^2/\epsilon_r r' - \Delta G' + X'. \quad (77)$$

Equations 76 and 77 afford an apparent linear relation between  $h\nu_{\text{CT}}$  and  $E_T$  provided that  $\delta$  is insensitive to  $E_T$ . If  $\delta$  is a function of  $E_T$ , a quadratic behavior is expected in a plot of  $h\nu_{\text{CT}}^{\text{I}}$  vs  $E_T$ , contrary to the observed linear one in Fig. 137.

To go further we need information about  $(I_{\text{D}} - E_{\text{A}})$  of  $\text{I}_n$ -3CNQ-R. Figure 138 compares the redox potentials of  $\text{I}_n$ -3CNQ-R and respective R-TCNQ with the Hammett  $\sigma$  values.<sup>977</sup> All  $\text{I}_n$ -3CNQ-R exhibit three one-electron redox

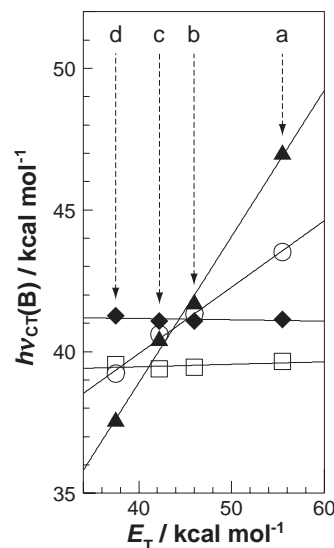


Fig. 137. A plot of  $h\nu_{\text{CT}}$  values of  $\text{I}_1$ -3CNQ-R ( $\text{R} = \text{F}_4$  ( $\blacktriangle$ ),  $\text{F}_2$  ( $\circ$ ),  $\text{H}$  ( $\square$ ), and  $(\text{MeO})_2$  ( $\blacklozenge$ )) in a variety of solvents vs Reichardt's  $E_T$  values of the solvents (a. methanol; b. acetonitrile; c. acetone; d. chlorobenzene). For  $\text{I}_1$ -3CNQ- $\text{F}_4$  the peak positions were determined by deconvolution, and for others direct peak positions were plotted.<sup>971</sup>

Table 32. Slope in Eq. 75 and Estimated CT Degree ( $\delta$ ) of Compounds  $\text{I}_1$ -3CNQ-R

	$\text{R} = \text{F}_4$	$\text{CF}_3$	$\text{F}_2$	$\text{F}$	$\text{H}$	$\text{Me}$	$(\text{MeO})_2$	$(\text{EtO})_2$
$a(\times 10^{-2})$	56.3	23.6	23.4	4.19	0.89	−0.75	−0.45	−0.85
$\delta^{\text{a)}$	1.00	0.71	0.71	0.54	0.51	0.49	0.50	0.49

a) Direct use of Peak B.

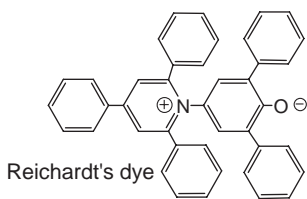


Chart 18.

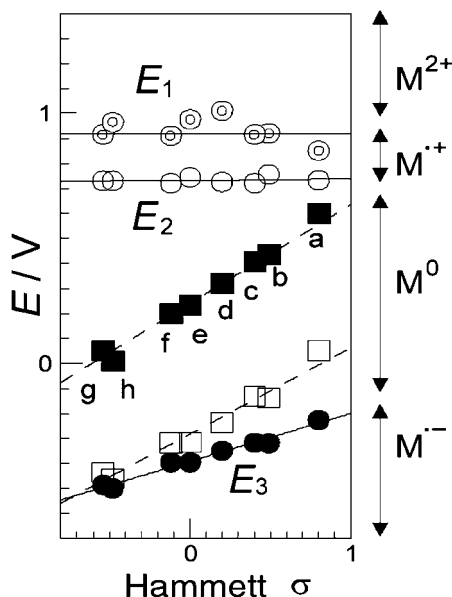
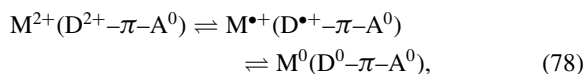
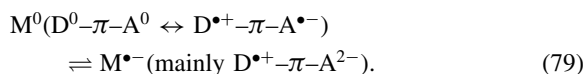


Fig. 138. Plot of redox potentials of  $I_1$ -3CNQ-R ( $\odot$ :  $E_1$ ,  $\circ$ :  $E_2$ ,  $\bullet$ :  $E_3$ ) and corresponding TCNQs ( $\blacksquare$ ,  $\square$ ) against the Hammett  $\sigma$ . The chemical species in the regions separated by solid lines are represented by  $M^{2+}$ ,  $M^{1+}$ ,  $M^0$ , and  $M^{1-}$  for  $M = I_1$ -3CNQ-R ( $R = a$ :  $F_4$ ,  $b$ :  $CF_3$ ,  $c$ :  $F_2$ ,  $d$ :  $F$ ,  $e$ :  $H$ ,  $f$ :  $Me$ ,  $g$ :  $(MeO)_2$ ,  $h$ :  $(EtO)_2$ ).<sup>971</sup>

steps. The first two, in the +0.7–+1.0 V range ( $E_1$ :  $\odot$ ,  $E_2$ :  $\circ$ ), are insensitive to the Hammett  $\sigma$  values, showing that these two are mainly associated with the D-part. Their much more positive values than those of  $E^{0/1-}_{1/2}$  of the corresponding R-TCNQ ( $\blacksquare$ ) confirm that these steps are ascribed to essentially Eq. 78,



where  $M$  represents a whole D- $\pi$ -A molecule. The third  $E_3$  at -0.25–-0.50 V ( $\bullet$ ) shows a linear dependence on the Hammett  $\sigma$  value with both a much more negative magnitude and a less steep slope compared to  $E^{1-/2-}_{1/2}$  of the corresponding R-TCNQ ( $\square$ ), indicating that this step is ascribed to



Therefore, Fig. 138 indicates that the  $(I_D - E_A)$  process of  $M^0$ , namely



which corresponds to the separation between  $E_2$  and  $E_3$  ( $\Delta E$ ), varies weakly with the Hammett  $\sigma$  value ( $\Delta E = -0.21\sigma +$

1.12), and this implies that the  $(I_D - E_A)$  term in Eq. 76 is a linear function of  $\delta$ . Hence, Eq. 76 is modified to Eq. 81.

$$h\nu_{CT}^I = (2\delta - 1)(e^2/\epsilon_r r - \Delta G + C_1) + (X - C_2). \quad (81)$$

To evaluate  $\delta$ , we need the magnitude of the slope  $a_1$  of a plot of  $h\nu_{CT}$  vs  $E_T$  for  $I_1$ -3CNQ-R having  $\delta = 1$ , where Eq. 76 is expressed as

$$h\nu_{CT}^I = (e^2/\epsilon_r r - \Delta G + C_1) + (X - C_2) = a_1 E_T + b_1, \quad (82)$$

then the ratio  $a/a_1$  ( $\approx 2\delta - 1$ ) gives the ionicity  $\delta$  on the reasonable assumption that the  $r$  and  $\Delta G$  values do not vary significantly among the  $I_1$ -3CNQ-R molecules. By taking the  $\delta$  of  $I_1$ -3CNQ- $F_4$  as unity, the relative CT degree  $\delta$  is calculated (Table 32).

The relation between the estimated  $\delta$  value in solution and the  $E^{0/1-}_{1/2}$  of R-TCNQ is utilized for the synthesis of a new  $I_1$ -3CNQ-R for desired  $\delta$ . Also, the relation of their redox properties as shown in Fig. 138 is utilized to elucidate the ionicity-functionality relation of a D- $\pi$ -A uni-molecule.

It is interesting to note that the  $\delta$  of  $I_1$ -3CNQ-H is close to 0.5, consistent with  $E_T$ -insensitive CT energy (Fig. 137,  $\square$ ), giving rise to nearly the same electronic structures between the ground  $D^{\delta+}-\pi-A^{\delta-}$  and its excited  $D^{(1-\delta)+}-\pi-A^{(1-\delta)-}$  states by intramolecular electron transfer. Thus, the  $I_1$ -3CNQ-H molecule is expected to be useful for the intermolecular electron transport but inactive for intramolecular rectification, in which a molecule with a high  $\delta$  value like  $I_1$ -3CNQ- $F_4$  is required. As for an indicator of a solvent<sup>937,938</sup> having a wide solvatochromic effect, a system not only with a large slope in Fig. 137, but also with a small  $r$  value is important according to Eq. 76. As for a photovoltaic material, which requires a stable charge-separated state, the  $I_1$ -3CNQ-R system is not adequate since it exhibits a spontaneous relaxation of the charge-separated state to the neutral one as observed in Fig. 138.

#### 4.8.3 Molecular and Crystal Structures and Ionicity:

In this section, only the typical molecular and crystal structures will be described emphasizing the molecular conformation (Types I and II, see Fig. 134), molecular planarity, and molecular packing.

**4.8.3.1 Molecular and Crystal Structures of ( $I_1$ -3CNQ- $F_2$ )( $CH_3CN$ )<sub>0.5</sub>:** Figure 139 illustrates the molecular structure of  $I_1$ -3CNQ- $F_2$  and the crystal structure of ( $I_1$ -3CNQ- $F_2$ )( $CH_3CN$ )<sub>0.5</sub> viewed along the  $c$ -axis. The  $I_1$ -3CNQ- $F_2$  molecule has a Type I conformation with a dihedral angle  $\phi$  of 31.5°. This conformation is different from the analogues of D- $\pi$ -A compounds such as DEMI-3CNQ (Type II, Fig. 134g).<sup>938,939,949,978-980</sup> The different conformation originates both from the steric repulsion between the CN1 and 3,3-dimethyl group of the indoline moiety and from the Coulomb attractive interaction between the electronegative CN1 and positively charged  $N$ -methyl group. The fluorine atoms are located at the 3,6-position of the 3CNQ moiety, and the fluorine atom closer to the indoline-moiety (F1) is located opposite to the CN1 group, probably owing to their Coulomb repulsion. In addition, an intramolecular C-H...F hydrogen bond (dashed line in Fig. 139a) with a H...F distance of 2.21 Å (cf. the sum of vdW radii of H and F is 2.67 Å) favors the 3,6-position isomer of the 3CNQ- $F_2$  moiety. Figure 139b depicts the planarity of the 3CNQ-R moiety with the angles



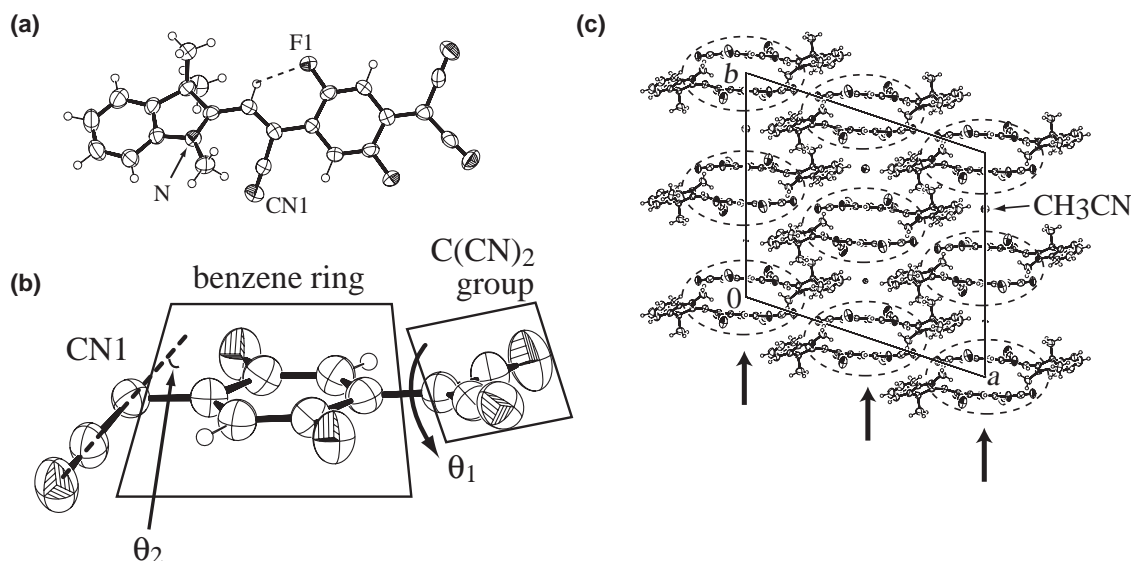


Fig. 139. Molecular (a, b) and crystal (c) structures of  $(\text{I}_1\text{-3CNQ-F}_2)(\text{CH}_3\text{CN})_{0.5}$ . Monoclinic,  $C2/c$ ,  $a = 23.588(3)$ ,  $b = 8.663(1)$ ,  $c = 20.958(3)$  Å,  $\beta = 108.549(6)^\circ$ ,  $V = 4060.1(8)$  Å<sup>3</sup>,  $Z = 8$ ,  $R = 0.051$ . The dotted line in (a) indicates an intramolecular C-H...F hydrogen bond. The dihedral and deviation angles between the benzenoid ring and the terminal dicyanomethylene group ( $\theta_1$ ) and the CN1 group ( $\theta_2$ ), respectively, are shown in (b). The dotted ellipsoid indicates dimerized 3CNQ-F<sub>2</sub> moieties of two adjacent molecules of  $\text{I}_1\text{-3CNQ-F}_2$ . The arrow indicates the segregated columns of the 3CNQ-F<sub>2</sub> moieties.

Table 33. Structural Parameters, Ionicity Derived from Bond Length Ratio (BLR) and Ground State Dipole Moment ( $\mu_g$ ) of Selected  $\text{I}_n\text{-3CNQ-R}$  Compounds and  $(\text{I}_1\text{-3CNQ-H})_2(\text{TCNQ})$

Compound	$(\text{I}_1\text{-3CNQ-F}_2)$ •(AN) <sub>0.5</sub>	$(\text{I}_1\text{-3CNQ-F})$ •(AN) <sub>0.5</sub>	$(\text{I}_3\text{-3CNQ-H})$ •(AN)	$\text{I}_6\text{-3CNQ-CF}_3$	$\text{I}_{20}\text{-3CNQ-H}$		$(\text{I}_1\text{-3CNQ-H})_2(\text{TCNQ})$	
					mol-1	mol-2	mol-1	mol-2
Type	I	I	I	II	II	II	I	II
Position of R	3,6-	3-	—	6-	—	—	—	—
Dihedral angle/ $^\circ$								
$\phi$	31.5	31.3	45.2	163.2	159.6	170.3	52.8	170.8
$\theta_1$	9.9	11.1	2.2	2.0	3.4	1.2	6.7	5.1
$\theta_2$	18.4	17.6	3.3	4.7	2.6	10.8	2.8	2.2
Interplanar distance/Å								
A-part intra	3.45	3.39	3.45	3.57	3.41		3.26	
inter	—	6.94	—	—	—		—	
D-part intra	3.49	6.52	3.49	—	—		3.50	
inter	5.31	—	5.31	—	7.41		3.83	
BLR	1.615	1.599	1.593	1.567	1.544	1.541	—	—
$\delta_{\text{BLR}}$	0.90	0.83	0.80	0.68	0.59	0.58	0.80	0.69
$\mu_g$	27.9	25.5	25.0	22.0	— <sup>a)</sup>	— <sup>a)</sup>	24.9	19.5
$\delta_{\text{dipole}}$	0.70	0.68	0.66	0.58	— <sup>a)</sup>	— <sup>a)</sup>	0.65	0.57

a) The molecule has too many atoms to calculate (MOPAC 97).

$\theta_1$  and  $\theta_2$ , which are summarized in Table 33. The 3CNQ-R moiety flattens as the  $\theta_1$  and  $\theta_2$  values decrease with decreasing the acceptor strength of R-TCNQ. This is owing to the increase in bond order of bonds *e* and *d* in Fig. 134e, respectively. The large  $\theta_1$  value of molecule  $\text{I}_1\text{-3CNQ-F}_2$  ( $9.9^\circ$ ) indicates that the bond *e* has more or less a single bond character.

In the crystal, two  $\text{I}_1\text{-3CNQ-F}_2$  molecules form a dimer of 3CNQ-F<sub>2</sub> moieties having an inversion center (dotted ellipsoids in Fig. 139c). Within the dimer, the 3CNQ-F<sub>2</sub> moieties form a face-to-face packing with an interplanar distance of 3.41 Å. Such a dimerization has been observed in many intramolecular CT compounds.<sup>931,932,942,971–973</sup> The dimers form a segregated stack along the *b*-axis (as shown by the arrows in

Fig. 139c). The long interdimer separation of 7.07 Å, which is due to the inclusion of an acetonitrile molecule between dimers, indicates that the 3CNQ-F<sub>2</sub> dimers are isolated from each other. No close contact between the indoline moieties is present due to the steric repulsion between the 3,3-dimethyl groups of adjacent dimers.

**4.8.3.2 Molecular and Crystal Structures of  $\text{I}_6\text{-3CNQ-CF}_3$** ; Molecular structure of  $\text{I}_6\text{-3CNQ-CF}_3$  in the crystal is illustrated in Fig. 140a. The molecule has a Type II conformation with a dihedral angle  $\phi$  of  $163.2^\circ$ . A trifluoromethyl group exists at the 6-position. It is noted that the 6-position is the furthest from the cyano leaving group. In contrast to  $\text{I}_1\text{-3CNQ-F}$ , which includes three positional isomers, the observation of on-

ly one 6-CF<sub>3</sub> positional isomer in **I**<sub>6</sub>-3CNQ-CF<sub>3</sub> is due to the steric hindrance of the bulky CF<sub>3</sub> group. The  $\theta_1$  and  $\theta_2$  values of each crystal are small enough to exhibit the planar structure of the 3CNQ-CF<sub>3</sub> moiety. Two adjacent 3CNQ-CF<sub>3</sub> moieties form a face-to-face dimer with an interplanar distance of 3.57 Å as shown by shaded areas in Fig. 140b, while there are no significant proximities between indoline moieties. These features are very similar to those of **I**<sub>6</sub>-3CNQ-H and **I**<sub>7</sub>-3CNQ-H (both have two polymorphs).

**4.8.3.3 Molecular and Crystal Structures of **I**<sub>20</sub>-3CNQ-H;** There are two crystallographically independent molecules, namely mol-1 and mol-2, indicated in Fig. 141a. Both molecules have a Type II conformation with  $\phi$  of 159.6 and 170.3°, respectively, and the latter has a nearly planar indoline-3CNQ moiety. In the crystal, four indoline-3CNQ moieties form a tetramer in the sequence of mol-2...mol-1...mol-1...mol-2 as shown in Fig. 141a. The inversion center lies between two mol-1s, which are parallel to each other with the interplanar distance of 3.41 Å. The dihedral angle between mol-1 and mol-2 is 14.9°. The tetramers of indoline-3CNQ-H moieties and alkyl chains (*n*-C<sub>20</sub>H<sub>41</sub>) form alternating 2D

sheets along the *c*-axis (Fig. 141b). Similar self-aggregation of  $\pi$ -moieties has been observed for TTC<sub>*n*</sub>-TTF molecules with long alkyl chains (see section 2.3.1 and Fig. 7) and the C<sub>7</sub>TET-TTF·TCNQ complex (see section 4.5.1, and Fig. 118), where tight interchain interactions assisted a proximate face-to-face contact of  $\pi$ -moieties (termed as the Fastener effect).<sup>61</sup> This layered structure between **I**<sub>20</sub>-3CNQ-H suggests that the self-assembling ability of alkyl chains is dominant in the crystal.

**4.8.3.4 Molecular and Crystal Structures of (**I**<sub>1</sub>-3CNQ-H)<sub>2</sub>(TCNQ);** Among the series of **I**<sub>*n*</sub>-3CNQ-R compounds, **I**<sub>1</sub>-3CNQ-H and **I**<sub>6</sub>-3CNQ-H molecules form 2:1 and 1:1 adducts with the starting reagent TCNQ, respectively. Here, the 2:1 adduct will be described. The crystal consists of a segregated column of the acceptor moieties (3CNQ-H and TCNQ), and the column results in an extra absorption band at 1250 nm.

Two molecules of **I**<sub>1</sub>-3CNQ-H, mol-1 (Fig. 142a) and mol-2 (Fig. 142b), and two halves of TCNQ (TCNQ-1, TCNQ-2) molecules are crystallographically independent. The 3CNQ-H moiety is almost flat in both mol-1 and mol-2 molecules ( $\theta_1 = 5.1$ – $6.7^\circ$ ,  $\theta_2 = 2.2$ – $2.8^\circ$ ). However, mol-1 is considerably deformed with  $\phi = 52.8^\circ$ , which is larger than those observed in the (**I**<sub>1</sub>-3CNQ-F<sub>2</sub>)(CH<sub>3</sub>CN)<sub>0.5</sub> and (**I**<sub>1</sub>-3CNQ-F)(CH<sub>3</sub>CN)<sub>0.5</sub>, and is similar to those in **I**<sub>1</sub>-3CNQ-(MeO)<sub>2</sub>, (**I**<sub>1</sub>-3CNQ-(EtO)<sub>2</sub>)(CH<sub>3</sub>CN) and **I**<sub>10</sub>-3CNQ-H. Mol-2 has a rather planar structure with  $\phi = 170.8^\circ$  and is similar to that in **I**<sub>20</sub>-3CNQ-H (mol-2). Mol-1 has the Type I conformation, while mol-2 has Type II. Figure 142c presents the crystal structure of (**I**<sub>1</sub>-3CNQ-H)<sub>2</sub>(TCNQ) as viewed along the *a*-axis. The most pronounced and unique feature is that the 3CNQ-H moieties of two D- $\pi$ -A molecules and a TCNQ molecule form a column composed of the triad 3CNQ-H...TCNQ...3CNQ-H along the *c*-axis as indicated by arrows in Fig. 142c. The column is comprised of two kinds of triads; triad A is (mol-1)...TCNQ-1...(mol-1) and triad B is (mol-2)...TCNQ-2...(mol-2) in a zig-zag sequence. In each triad the molecular planes of 3CNQ-H and TCNQ are nearly parallel to each other and an inversion center exists at the center of TCNQ. The interplanar separations between TCNQ and 3CNQ-H are 3.26 Å. The segregated column is distorted in a way that the neighboring triads have a slightly different stacking direction at about 21.7°.

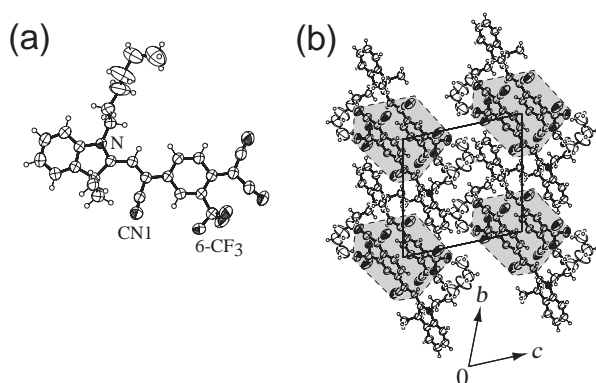


Fig. 140. (a) Molecular structure and (b) crystal structure viewed along the *a*-axis of **I**<sub>6</sub>-3CNQ-CF<sub>3</sub>. The shaded area indicates dimerized 3CNQ-CF<sub>3</sub> moieties. Triclinic,  $P\bar{1}$ ,  $a = 8.866(2)$ ,  $b = 12.388(3)$ ,  $c = 12.579(3)$  Å,  $\alpha = 76.41(1)^\circ$ ,  $\beta = 82.26(1)^\circ$ ,  $\gamma = 76.82(1)^\circ$ ,  $V = 1302.7(4)$  Å<sup>3</sup>,  $Z = 2$ ,  $R = 0.081$ .

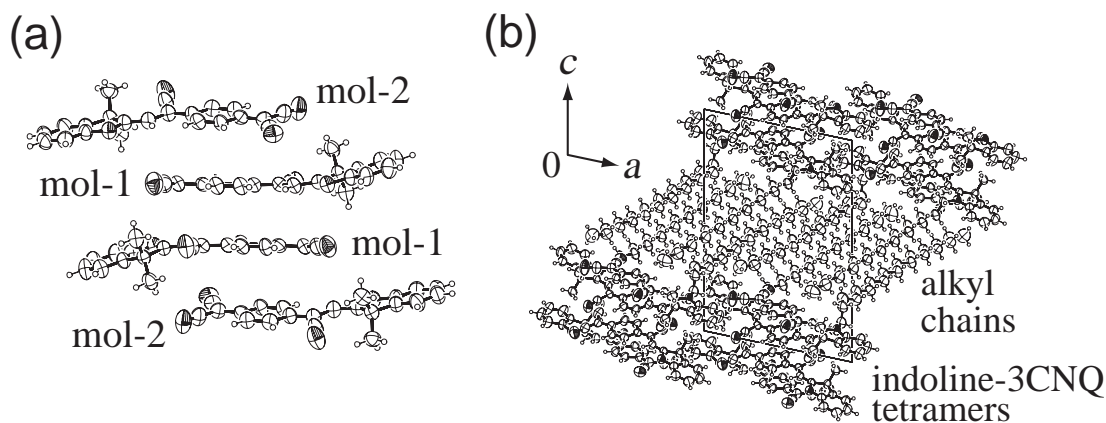


Fig. 141. (a) A tetramer of indoline-3CNQ moieties in the crystal of **I**<sub>20</sub>-3CNQ-H. (b) The *b*-axis projection of **I**<sub>20</sub>-3CNQ-H. Triclinic,  $P\bar{1}$ ,  $a = 14.240(4)$ ,  $b = 13.320(2)$ ,  $c = 21.227(5)$  Å,  $\alpha = 101.883(9)^\circ$ ,  $\beta = 100.343(9)^\circ$ ,  $\gamma = 96.11(1)^\circ$ ,  $V = 3833(1)$  Å<sup>3</sup>,  $Z = 4$ ,  $R = 0.075$ .

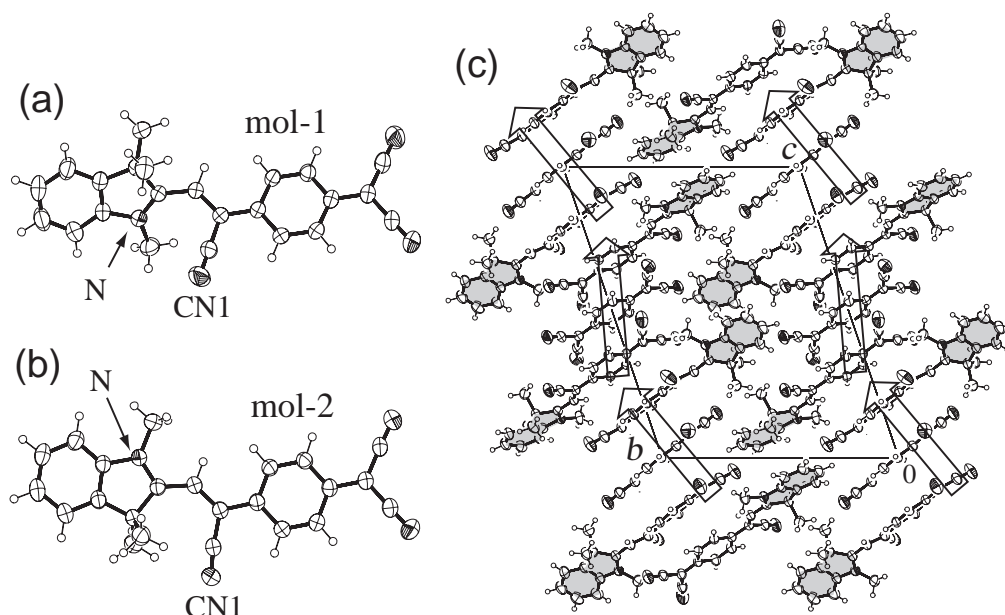


Fig. 142. Molecular structures of (a) mol-1 and (b) mol-2 of  $\mathbf{I}_1$ -3CNQ-H in  $(\mathbf{I}_1\text{-3CNQ-H})_2(\text{TCNQ})$ . (c) Crystal structure of  $(\mathbf{I}_1\text{-3CNQ-H})_2(\text{TCNQ})$  viewed along the  $a$ -axis. Zig-zag arrows indicate the segregated column of the 3CNQ-H...TCNQ...3CNQ-H moieties. The indoline moieties are hatched. Triclinic,  $P\bar{1}$ ,  $a = 8.050(1)$ ,  $b = 15.621(2)$ ,  $c = 20.489(2)$  Å,  $\alpha = 70.920(5)$ ,  $\beta = 81.897(5)$ ,  $\gamma = 87.003(6)^\circ$ ,  $V = 2410.6(4)$  Å<sup>3</sup>,  $Z = 2$ ,  $R = 0.046$ .

However, the intermolecular overlap integrals between the neighboring triads ( $3.3 \times 10^3$ ) are close to those within the triads ( $3.8 \times 10^3$ ). Thus, it is possible for the 3CNQ-H...TCNQ...3CNQ-H units to share the negative charge of  $-2\delta$  as 3CNQ-H<sup>( $\delta$ - $\zeta$ )-</sup>...TCNQ<sup>2 $\zeta$ -</sup>...3CNQ-H<sup>( $\delta$ - $\zeta$ )-</sup>, namely (D <sup>$\delta$ +</sup>- $\pi$ -A<sup>( $\delta$ - $\zeta$ )-</sup>)<sub>2</sub>(TCNQ<sup>2 $\zeta$ -</sup>). The bond lengths by structural analysis<sup>981</sup> and the C≡N stretching frequency<sup>194</sup> of the TCNQ molecule and UV-vis-NIR spectrum of the adduct deduced the ionic formula of (D<sup>0.58+</sup>- $\pi$ -A<sup>0.46-</sup>)<sub>2</sub>(TCNQ<sup>0.24-</sup>) to (D<sup>0.72+</sup>- $\pi$ -A<sup>0.60-</sup>)<sub>2</sub>(TCNQ<sup>0.24-</sup>).

The indoline moieties also align along the  $c$ -axis, where one dyad is the repeating unit with a rather large interplanar separation of 3.50 and 3.83 Å. The dihedral angle between two dyads is 26.7°. As a result, the intermolecular interactions among the indoline moieties are rarely expected in comparison with those in the segregated column of 3CNQ-H and TCNQ.

**4.8.4 Intramolecular Ionicity Based on Molecular Structures of  $\mathbf{I}_n$ -3CNQ-R:** The bond lengths  $a'$ ,  $b'$ , and  $c'$  of a TCNQ molecule (Fig. 134b) have been used to estimate the ionicity of TCNQ molecules in intermolecular CT solids.<sup>974</sup> Similarly, the bond lengths labeled  $a$ – $e$  of  $\mathbf{I}_n$ -3CNQ-R (Fig. 134e) are expected to be sensitive to the ionicity, because the bonds  $a$  and  $c$  should have a double- or single-bond character and the bonds  $b$ ,  $d$ , and  $e$  should have a single- or double-bond one in the zwitterionic ( $\delta = 1$ ) or neutral ( $\delta = 0$ ) form, respectively. It is then adequate to utilize a bond length ratio (BLR) defined as  $(b + d + e)/(a + c)$ , as a measure of the intramolecular ionicity ( $\delta$ ) of the  $\mathbf{I}_n$ -3CNQ-R compounds (Table 33). Using the experimental data for the bond lengths of single (1.451 Å) and double (1.332 Å) C–C bonds in a  $\pi$ -conjugated chain<sup>982</sup> and those of ionic (1.324 Å) and neutral (1.384 Å) C–N bonds (bond  $a$ ) in an indoline ring,<sup>983</sup> the BLR values for  $\delta = 1$  and  $\delta = 0$  are calculated to be 1.639 and 1.410, respectively. Then the ionicity ( $\delta_{\text{BLR}}$ ) is estimated

based on Eq. 83 assuming a linear relation between  $\delta_{\text{BLR}}$  and BLR values (Table 33, also  $\delta_{\text{BLR}} = 0.76$  ( $\mathbf{I}_1$ -3CNQ-F, mol-1), 0.64 ( $\mathbf{I}_1$ -3CNQ-F, mol-2), 0.53 ( $\mathbf{I}_1$ -3CNQ-(MeO)<sub>2</sub>), 0.53 ( $\mathbf{I}_1$ -3CNQ-(EtO)<sub>2</sub>), 0.58 ( $\mathbf{I}_6$ -3CNQ-H,  $\alpha$  phase), 0.56 ( $\mathbf{I}_6$ -3CNQ-H,  $\beta$  phase), 0.58 ( $\mathbf{I}_7$ -3CNQ-H,  $\beta$  phase), 0.55 ( $\mathbf{I}_8$ -3CNQ-H, mol-1), 0.54 ( $\mathbf{I}_8$ -3CNQ-H, mol-2), and 0.77 ( $\mathbf{I}_{10}$ -3CNQ-H)).

$$\delta_{\text{BLR}} = 4.36 \times (\text{BLR}) - 6.14. \quad (83)$$

As shown in Fig. 143, the BLR values are linearly related with the first redox potentials ( $E^1_{1/2}$ ) of R-TCNQ for each type of conformation. The BLR is not much affected by the alkyl chain length on the indoline moiety: namely, the compounds **13**, **15**, **16**, and **21** with different lengths of alkyl chain have nearly the same BLR values. It is worth noting that the BLR values of Type I and II conformations differ considerably. The BLR values of Type II conformation are lower than those of corresponding molecules with Type I conformation.

Ground state dipole moments ( $\mu_g$ ) evaluated by molecular orbital calculations are plotted against BLR values in Fig. 144. The  $\mu_g$  values are linearly related with the BLR values for each type of conformation. Also, the length of alkyl chain (see **13a**, **13b**, **15b**, and **16**) has no significant effect on the  $\mu_g$  value. Figure 145 compares the excited state dipole moment ( $\mu_e$ ), dipole moment difference ( $\mu_e - \mu_g$ ), and dipole moment sum ( $\mu_e + \mu_g$ ) together with  $\mu_g$  for  $\mathbf{I}_1$ -3CNQ-R compounds with Type I conformation.

The approximated dipole moments of the ground and excited states are expressed as

$$\mu_g = \delta ed, \quad (84)$$

and

$$\mu_e = (1 - \delta)ed, \quad (85)$$

respectively, where  $d$  is the distance between D and A moie-

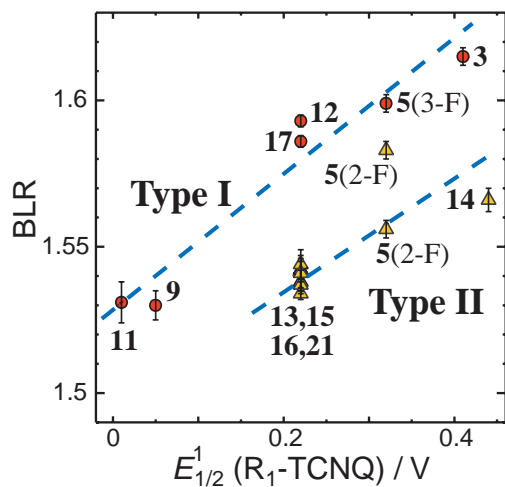


Fig. 143. A plot of bond length ratio (BLR) of  $I_n$ -3CNQ-R against the first redox potential ( $E^1_{1/2}$ ) of R-TCNQ. Red circles and yellow triangles represent the molecules with Type I and II conformations, respectively. Numbers are the same as those in Table 31. **5** has two crystallographically independent molecules (2-F, 3-F) and each molecule has two positional isomers. **9** also has two positional isomers. **13** and **15** have two polymorphs each.

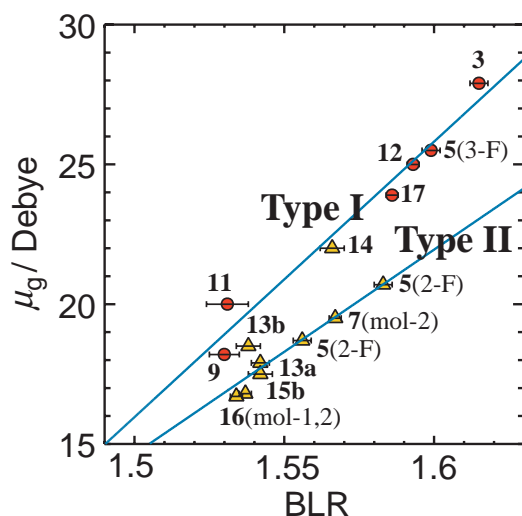


Fig. 144. Plot of ground state dipole moment ( $\mu_g$ ) evaluated by CNDO/S MO calculation against BLR. Lines are guide to eyes for Type I ( $\circ$ ) and II ( $\triangle$ ) molecules. Numbers are the same as those in Table 31.

ties. Then, the dipole difference ( $\mu_e - \mu_g$ ) is represented as

$$(\mu_e - \mu_g) = (1 - 2\delta)ed. \quad (86)$$

Although some scatter is seen in the plot of  $(\mu_e - \mu_g)$  vs BLR, the  $(\mu_e - \mu_g)$  value is equal to zero at around BLR = 1.51, which should correspond to the ionicity  $\delta = 0.5$  in the crystal as expected from Eq. 86.

Figure 145 includes a plot of  $(\mu_g + \mu_e)$  against BLR. If BLR is simply proportional to  $\delta$ , the  $(\mu_g + \mu_e)$  value is nearly constant at  $ed$ , according to Eqs. 84 and 85. However, the plot is inconsistent with the expectation, indicating that for  $I_n$ -

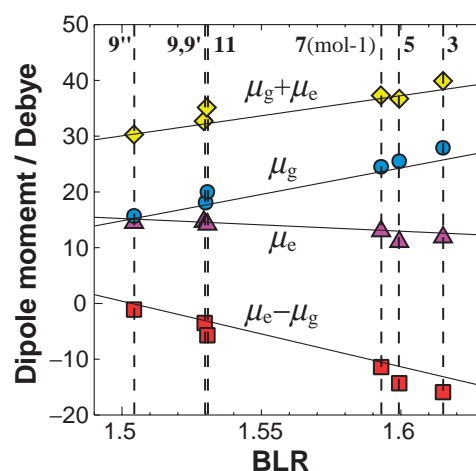


Fig. 145. Plot of CNDO/S dipole moments of the ground ( $\mu_g$ :  $\circ$ ) and excited ( $\mu_e$ :  $\triangle$ ) states, dipole difference ( $\mu_e - \mu_g$ :  $\square$ ) and dipole sum ( $\mu_g + \mu_e$ :  $\diamond$ ) evaluated by CNDO/S MO calculation against BLR for  $I_1$ -3CNQ-R with Type I conformation. Numbers are the same as those in Table 31. **9**: 2,5-(MeO) $_2$ , **9'**: 3,6-(MeO) $_2$ . **9''**: R = (MeO) $_2$ ,  $\beta$  phase. The least squares fit afford;  $\mu_g = 94.8 \times (\text{BLR}) - 127$ ,  $\mu_e = 22.8 \times (\text{BLR}) + 49.4$ ,  $\mu_e - \mu_g = -118 \times (\text{BLR}) + 177$ ,  $\mu_g + \mu_e = 72.0 \times (\text{BLR}) - 78.0$ .

3CNQ-R compounds  $d$  is variable depending on the ionicity, position of substituents, molecular conformation, etc. So, we conclude that the BLR value is not a linear function of  $\delta$  as postulated in Eq. 83. Since dipole moments (Eqs. 84 and 85) and the transition dipole moment (vide infra) are functions of  $\delta$ , we exploited a more appropriate parameter pertaining to the ionicity.

The linear BLR dependency of  $\mu_g$ ,  $\mu_e$ ,  $(\mu_e - \mu_g)$ , and  $(\mu_g + \mu_e)$  is expressed as  $a_i(\text{BLR}) + b_i$  ( $i = 1-4$ , respectively: where  $a_3 = (a_2 - a_1)$ ,  $b_3 = (b_2 - b_1)$ ,  $a_4 = (a_1 + a_2)$ , and  $b_4 = (b_1 + b_2)$ ). The relation between  $\mu_e - \mu_g = (1 - 2\delta)ed$  and  $(\mu_e + \mu_g) = ed$  in Fig. 145 provides  $a_3(\text{BLR}) + b_3 = (1 - 2\delta)[a_4(\text{BLR}) + b_4]$  and consequently affords a non-linear relation between BLR and  $\delta$ :

$$\begin{aligned} \text{BLR} &= -\frac{b_4(1 - 2\delta) - b_3}{a_4(1 - 2\delta) - a_3} \\ &= -\frac{(b_1 + b_2)(1 - 2\delta) + (b_1 - b_2)}{(a_1 + a_2)(1 - 2\delta) + (a_1 - a_2)}. \end{aligned} \quad (87)$$

Then the following relation is obtained between the calculated  $(\mu_e - \mu_g)$  ( $=\Delta$ ) and  $\delta$  for  $I_n$ -3CNQ-R as

$$\delta = (a_1\Delta + C)/[(a_1 + a_2)\Delta + 2C], \quad C = a_2b_1 - a_1b_2. \quad (88)$$

By using Eq. 88, one may obtain new  $\delta$  values ( $\delta_{\text{dipole}}$ ), which reproduce the calculated dipole moments, and hence, are more affected by BLR, molecular conformation, position of substituents, and the change of  $d$ , in comparison with  $\delta_{\text{BLR}}$ . The estimated  $\delta_{\text{dipole}}$  values are summarized in Table 33 (the following  $\delta_{\text{dipole}}$  values were also evaluated for  $I_1$ -3CNQ-R 0.55 (R = (MeO) $_2$ , 2,5-isomer and 3,6-isomer,  $\alpha$  phase), 0.52 ((MeO) $_2$ ,  $\beta$  phase), and 0.58 ((EtO) $_2$ ) for Type I conformation, and 0.60 (F, 2-isomer, mol-1), 0.59 (F, 6-isomer,



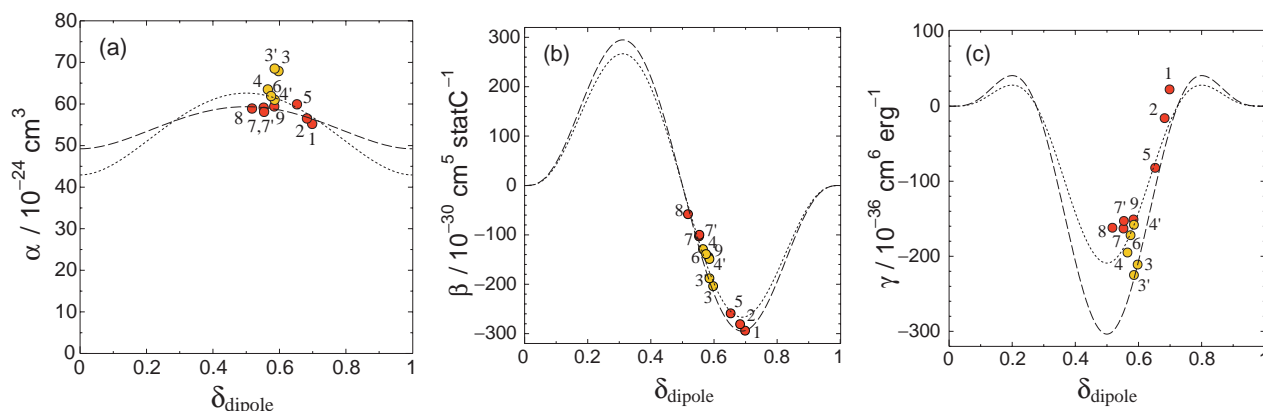


Fig. 146. Plot of CNDO/S polarizability  $\alpha$  (a),  $\beta$  (b), and  $\gamma$  (c) against  $\delta_{\text{dipole}}$  for  $\text{I}_n\text{-3CNQ-R}$  compounds. 1:  $\text{I}_1\text{-3CNQ-F}_2$  in **3**, 2:  $\text{I}_1\text{-3CNQ-F}$  in **5**, 3:  $\text{I}_1\text{-3CNQ-F}$  in **4**(mol-1) (3: 2-F isomer, 3': 6-F isomer), 4:  $\text{I}_1\text{-3CNQ-F}$  in **4**(mol-2) (4: 2-F, 4': 3-F), 5: **7**(mol-1), 6: **7**(mol-2), 7: **9**, Phase  $\alpha$  (7: 2,5-isomer, 7': 3,6-isomer), 8: **9**, Phase  $\beta$ , 9: **11**. Red and yellow circles represent Type I and Type II configurations, respectively. Dotted curves (least squares fit for all data) represent the theoretically expected ones from Eqs. 94–96:  $\alpha = 3.15 \times 10^2 \delta^2(1 - \delta)^2 + 42.9$ ,  $\beta = 7.17 \times 10^4 \delta^3(1 - \delta)^3(1 - 2\delta)$ ,  $\gamma = 2.14 \times 10^5 \delta^4(1 - \delta)^4(1 - 5\delta + 5\delta^2)$ . Dashed curves are modified ones;  $\alpha = 1.62 \times 10^2 \delta^2(1 - \delta)^2 + 49.2$  (least squares fit for only data for Type I),  $\beta = 7.93 \times 10^4 \delta^3(1 - \delta)^3(1 - 2\delta)$  (parameters are modified to fit **1**), and  $\gamma = 3.11 \times 10^5 \delta^4(1 - \delta)^4(1 - 5\delta + 5\delta^2)$  (parameters are modified to fit **3** and **3'**).

mol-1), 0.57 (F, 2-isomer, mol-2), and 0.59 (F, 3-isomer, mol-2) for Type II conformation).

Summarizing the above, the structural parameter BLR reflects well the ground and excited dipole moments, and relates the solid ionicity as expressed in Eq. 88. Among the  $\text{I}_n\text{-3CNQ-R}$  compounds, Type I conformation gives a higher  $\delta$  than Type II conformation. This feature arises from the fact that Type I is a more favorable conformation for the ionic structure, in which the positive charged *N*-alkyl group of the indoline moiety locates close to the negatively charged CN group of the 3CNQ-R moiety. In conclusion, the values of  $\delta$  and  $\mu$  of  $\text{I}_n\text{-3CNQ-R}$  compounds depend on both the electron-accepting ability of the 3CNQ-R moiety and the molecular conformation (Types I and II), but are insensitive to the alkyl chain length in the indoline moiety.

**4.8.5 Non-Linear Optical Properties:** The molecular polarization ( $p$ ) can be expanded as a power series in the electromagnetic field ( $E$ ):

$$p = \mu_g + \alpha E + \beta E^2 + \gamma E^3 + \dots \quad (89)$$

For D- $\pi$ -A molecules such as compounds  $\text{I}_n\text{-3CNQ-R}$ , the two-level model concerning the ground and CT excited states can be utilized for an adequate approximation for non-resonant  $\alpha$  and  $\beta$  as

$$\alpha \propto \mu_{\text{eg}}^2/E_{\text{eg}} \quad \beta \propto \mu_{\text{eg}}^2(\mu_e - \mu_g)/E_{\text{eg}}^2, \quad (90)$$

where  $\mu_{\text{eg}}$  is the transition dipole moment and  $E_{\text{eg}}$  is the energy difference between the ground (g) and excited (e) states. While a non-resonant  $\gamma$  is generally approximated based on the three-level model,<sup>974,984</sup>

$$\gamma \propto [\mu_{\text{eg}}^2(\mu_e - \mu_g)^2 - \mu_{\text{eg}}^4]/E_{\text{eg}}^3 + \mu_{\text{eg}}^2\mu_{\text{e'e'}}^2/E_{\text{eg}}^2E_{\text{e'g}}, \quad (91)$$

where  $\text{e'}$  means the second excited state.

However, it was reported that the two-level model, where  $\text{e'}$

is neglected, can be applied for some D- $\pi$ -A molecules, which show a lower-energy CT transition with a large transition dipole moment (large  $\mu_{\text{eg}}$  and small  $E_{\text{eg}}$ ) and a large difference in dipole moment between the ground and excited states ( $\mu_e - \mu_g$ ). In this case, Eq. 91 can be simplified to

$$\gamma \propto [\mu_{\text{eg}}^2(\mu_e - \mu_g)^2 - \mu_{\text{eg}}^4]/E_{\text{eg}}^3. \quad (92)$$

According to Mulliken's CT theory,<sup>985</sup> on the other hand, the transition dipole moment between ground and excited states can be expressed in terms of the ionicity  $\delta$  as follows:

$$\mu_{\text{eg}} = \delta^{1/2}(1 - \delta)^{1/2}ed. \quad (93)$$

Also, according to the theoretical treatment by Ducuing and Flytzanis based on the point charge model,<sup>986</sup>  $\alpha$  and  $\beta$  can be approximated using  $\delta$  by Eqs. 94 and 95, respectively.

$$\alpha \propto \delta^2(1 - \delta)^2. \quad (94)$$

$$\beta \propto \delta^3(1 - \delta)^3(1 - 2\delta). \quad (95)$$

By putting Eqs. 86, 93–95 into Eq. 92,  $\gamma$  can be expressed as a function of  $\delta$ ,

$$\begin{aligned} \gamma &\propto [\mu_{\text{eg}}^2(\mu_e - \mu_g)^2 - \mu_{\text{eg}}^4]/E_{\text{eg}}^3 \\ &= \alpha\beta\{[(\mu_e - \mu_g)^2 - \mu_{\text{eg}}^4]/[(\mu_e - \mu_g)\mu_{\text{eg}}^2]\} \\ &\propto \delta^4(1 - \delta)^4(1 - 5\delta + 5\delta^2). \end{aligned} \quad (96)$$

Based on Eqs. 94–96,  $\alpha$  has a maximum at  $\delta = 0.5$  and minima at  $\delta = 0$  and 1,  $|\beta|$  has maxima at  $\delta = 0.31$  and 0.69 and minima at  $\delta = 0$ , 0.5, and 1, and  $|\gamma|$  has maxima at  $\delta = 0.2$ , 0.5, and 0.8 and minima at  $\delta = 0$ , 0.28, 0.72 and 1. As seen in Fig. 146, the  $\alpha$ ,  $\beta$ , and  $\gamma$  values of  $\text{I}_n\text{-3CNQ-R}$  evaluated based on their molecular structures (CNDO/S polarizability) are well fit to Eqs. 94–96, respectively. The dependences of  $\alpha$ ,  $\beta$ , and  $\gamma$  on  $\delta_{\text{dipole}}$  as expressed by Eqs. 94–96 are similar to those on the bond-length alternation (BLA) by Marder et al.<sup>947</sup> and mixing between the two limiting-resonance forms (MIX) by Barzoukas et al.<sup>948</sup>



Summarizing the above, the ionicity is a fundamental parameter governing  $\alpha$ ,  $\beta$ , and  $\gamma$ . Of most importance is that these linear and non-linear optical parameters have a maximum absolute value at a certain partial degree of CT and the  $\delta$  can be tuned by chemical modification of D- and A-moieties of D- $\pi$ -A compounds, while it is difficult to control the BLA and MIX values chemically.

It has been reported that the insulating neutral CT complexes, perylene·TCNE, perylene·TCNQ, pyrene·9,10-phenanthrenequinone, and 9,10-phenanthrene·DDQ show a high third-order optical non-linearity ( $\chi^{(3)}$ ).<sup>987</sup> Their degree of CT may be close to 0.2–0.3, although no data have been reported. Also, the 2D organic metal  $\alpha$ -(ET)<sub>2</sub>I<sub>3</sub> ( $\delta = 0.5$ ) was reported to show a large  $\chi^{(3)}$  value originating from the plasma electrons based on Eq. 97,<sup>988,989</sup>

$$|\chi^{(3)}| = \frac{2\pi^3 n^4 \lambda^2}{c^4} \omega_p^2 \tau^2 \left( \frac{e}{m^*} \right)^2 \frac{n^2 + 1}{n^2 - 1}, \quad (97)$$

where  $n$  is the index of refraction,  $\lambda$  is the wavelength,  $\omega_p$  is the plasma frequency,  $\tau$  is the relaxation time, and  $m^*$  is the effective mass.

## 5. Fullerene CT Complexes

**5.1 Fullerene Superconductors.** Immediately after the isolation of macroscopic quantities of C<sub>60</sub> solid by Krätschmer and Huffman,<sup>990</sup> highly conducting<sup>991</sup> and superconducting<sup>992</sup> behaviors were verified for the K-doped compounds at Bell laboratories. The structural refinement based on the powder X-ray diffraction profile denotes that the composition of the superconducting phase is K<sub>3</sub>C<sub>60</sub> and the diffraction pattern can be indexed to be a face-centered cubic (fcc) structure.<sup>993</sup> The lattice parameter ( $a = 14.24$  Å) is apparently expanded relative to the undoped cubic C<sub>60</sub> ( $a = 14.17$  Å). In the doped compound, K<sup>+</sup> ions occupy the two types of interstitial sites, one being the larger octahedral site (*o*-site,  $r = 2.06$  Å) and the other being the two smaller tetrahedral sites (*t*-site,  $r = 1.12$  Å) per C<sub>60</sub> molecule. The space group *Fm* $\bar{3}$ *m* determined by the Rietveld method indicates that C<sub>60</sub> molecules are disordered over two orientations differing by 90° of rotation about  $\langle 100 \rangle$  (so-called “merohedral disorder”).

The superconductivity has been observed for many A<sub>3</sub>C<sub>60</sub> (A: alkali metal), e.g., K<sub>3</sub>C<sub>60</sub> ( $T_c = 19$  K by Hebard et al.<sup>992</sup>), Rb<sub>3</sub>C<sub>60</sub> ( $T_c = 29$  K by Rosseinsky et al.<sup>994</sup>), Rb<sub>2</sub>CsC<sub>60</sub> ( $T_c = 31$  K by Tanigaki et al.<sup>995</sup>) and RbCs<sub>2</sub>C<sub>60</sub> ( $T_c = 33$  K by Tanigaki et al.<sup>995</sup>), and their structures determined to be analogous to that of K<sub>3</sub>C<sub>60</sub> with varying lattice constants. The  $T_c$  varies monotonously with lattice constant, independently of the type of the alkali dopant.<sup>995,996</sup> In simple terms, this behavior arises from a narrowing of the bandwidth and an increase in  $D(\mathcal{E}_F)$  as the lattice constant increases. On the other hand, NH<sub>3</sub>K<sub>3</sub>C<sub>60</sub> and Cs<sub>3</sub>C<sub>60</sub>, both of which might be expected for higher  $T_c$  considering their sizable dopants, form a non-fcc packing at ambient pressure<sup>997–999</sup> and no longer exhibit a superconducting behavior. Under applied pressure, however, both compounds pass through a superconducting transition at 28 K<sup>1000</sup> and 40 K,<sup>998</sup> respectively. It is likely that a superconductor–nonsuperconductor boundary exists in this vicinity, and seems to be re-crossed by applying pressure. Note that the reproducibility of the pressure-induced superconduct-

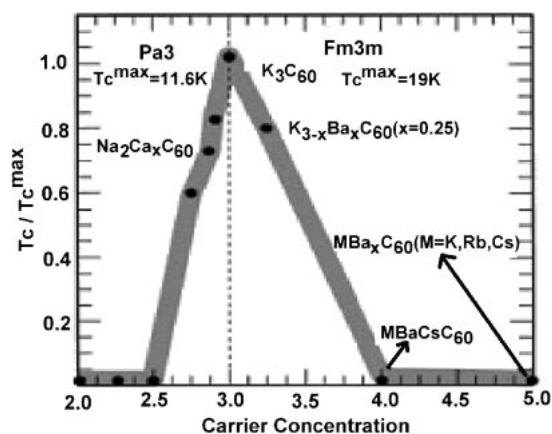


Fig. 147. A plot of  $T_c$  against carrier concentration ( $C_{60}^{n-}$ ) in C<sub>60</sub> superconductors by Yildirim et al.  $T_c$  values are scaled by those of Na<sub>2</sub>CsC<sub>60</sub> (11.6 K, left side) and K<sub>3</sub>C<sub>60</sub> (19 K, right side).<sup>1001</sup>

ing phases has not been present. Also it has been found that  $T_c$  in the Rb<sub>3-x</sub>Cs<sub>x</sub>C<sub>60</sub> system gradually increases as the mixing ratio approaches  $x = 2$ .<sup>736</sup> Further increasing the nominal ratio of Cs leads to a sizable decrease of  $T_c$ , although the lattice keeps the fcc structure for  $x < 2.65(2)$ . Band-filling control has been realized for several systems, Na<sub>2</sub>Cs<sub>x</sub>C<sub>60</sub> ( $0 \leq x \leq 1$ ),<sup>1001</sup> K<sub>3-x</sub>Ba<sub>x</sub>C<sub>60</sub> ( $0 \leq x \leq 1$ )<sup>1001</sup> and Li<sub>x</sub>CsC<sub>60</sub> ( $2 \leq x \leq 6$ ),<sup>1002</sup> and shows that the  $T_c$  decreases sharply as the valence state on C<sub>60</sub> deviates from  $-3$  (Fig. 147).

Among the alkali-doped compounds, three other well-documented systems are A<sub>3</sub>C<sub>60</sub> (A: K, Rb, and Cs; see section 5.3), A<sub>4</sub>C<sub>60</sub> (A: K and Rb),<sup>1003</sup> and A<sub>6</sub>C<sub>60</sub> (A: K, Rb, and Cs).<sup>1004</sup> A<sub>4</sub>C<sub>60</sub> has a body-centered tetragonal (bct) packing and is a nonmagnetic insulator owing to the combination of both the Jahn–Teller and electron correlation effect.<sup>1005</sup> For A<sub>6</sub>C<sub>60</sub>, on the other hand, the crystal structure is body-centered cubic (bcc) and the compounds are essentially insulators due to the full occupation of the triply degenerate LUMO ( $t_{1u}$ ) level.

Highly doped fullerides with alkali-earth or rare-earth metals afforded a variety of intriguing transport and magnetic features. Some non-cubic superconductors have been obtained for Yb<sub>2.75</sub>C<sub>60</sub> ( $T_c = 6$  K),<sup>1006</sup> Sm<sub>2.75</sub>C<sub>60</sub> ( $T_c = 8$  K),<sup>1007</sup> Ba<sub>4</sub>C<sub>60</sub> ( $T_c = 6.7$  K),<sup>1008,1009</sup> and Sr<sub>4</sub>C<sub>60</sub> ( $T_c = 4.4$  K).<sup>1009</sup> Eu<sub>6</sub>C<sub>60</sub> with bcc packing undergoes a ferromagnetic transition at 12 K, arising from Eu<sup>2+</sup> cations with  $S = 7/2$  spin,<sup>1010</sup> and shows a giant negative magnetoresistance arising from a significant  $\pi$ - $f$  coupling between the conduction electrons on C<sub>60</sub> and localized 4*f*-electrons on Eu (see section 4.7.1).<sup>904</sup> Ce<sub>x</sub>C<sub>60</sub> shows the coexistence of superconductivity and ferromagnetism below 13.5 K, although its crystal structure and composition are currently unclear.<sup>925</sup>

There have been some excellent literatures on the superconducting fullerides including the crystal structures, valence states, and superconducting properties.<sup>596,1011</sup> However, they did not mention the issue of the partial CT state, which is common for low-dimensional organic metals, being difficult to realize for C<sub>60</sub>-based CT complexes. In the following, we will focus on the fullerene-based CT complexes: their molecular and crystal structures as well as the electronic states.

## 5.2 Ionicity and Polymeric State of Fullerenes. Mono-

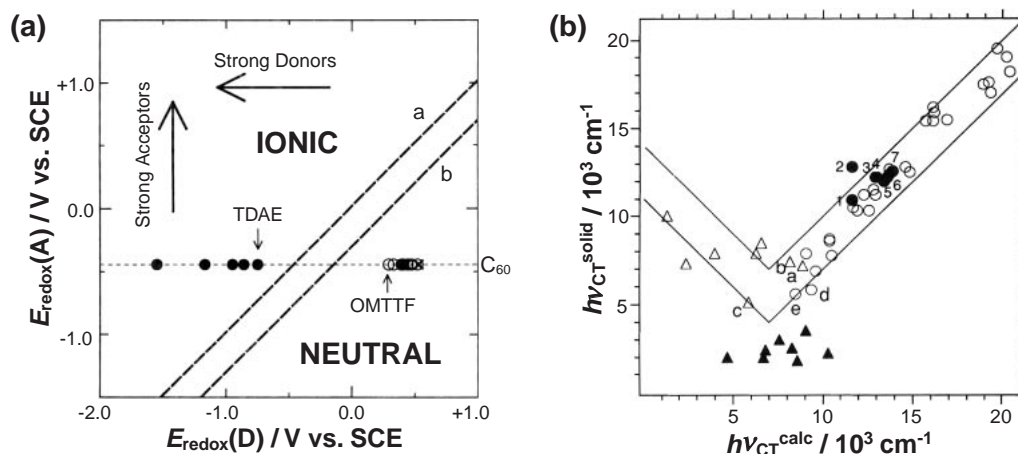


Fig. 148. (a) Phase diagram of  $C_{60}$  CT complexes plotted as  $E_1(A)$  vs  $E_1(D)$ : ●, fully ionic ground state ( $\delta \geq 1$ , complexes with TDAE and stronger electron donors); ○, ×, neutral ground state (complexes with OMTTF and weaker electron donors). Lines a and b represent the partial CT state for low-D metal.<sup>246</sup> (b) Comparison of CT bands of a number of CT complexes in the solid state ( $h\nu_{CT}^{solid}$ ) and calculated ones ( $h\nu_{CT}^{calc}$ ) for a number of CT complexes: ○, ●, complex with neutral to partially ionic ( $\delta < 0.5$ ) ground state with alternating stacking or layer; △, complex with a fully to partially ionic ( $\delta > 0.5$ ) ground state with low-to-moderate electric conductivity; ▲, complex with partially ionic ground state with high conductivity; a, 3,3',5,5'-tetramethylbenzidine(TMB)·TCNQ, b, TMB·FTCNQ, c, TTeC<sub>1</sub>-TTF·TCNQ, d, TTF·QCl<sub>4</sub>, e, perylene·HCBD; 1–7,  $C_{60}$  complexes with OMTTF, HMTTF, 1,6-DTP, BO, EDT-TTF, TSeC<sub>1</sub>-TTF, and ET, respectively.<sup>246</sup>

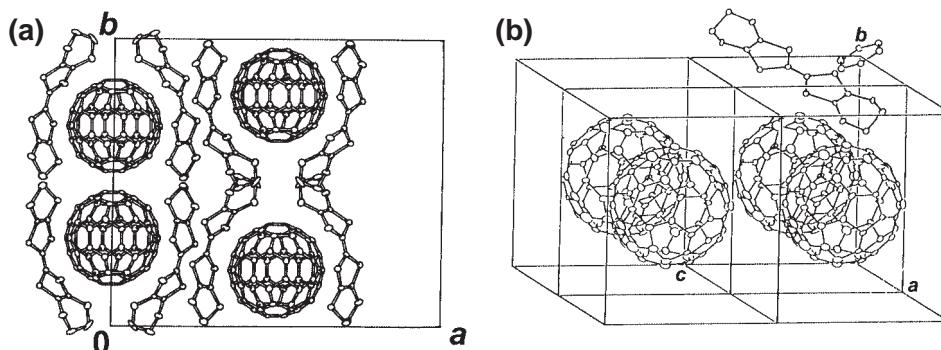


Fig. 149. (a) Crystal structure of  $(ET)_2C_{60}$  by Izuoka et al.<sup>1013</sup> Monoclinic,  $C2/c$ ,  $a = 25.956(3)$ ,  $b = 21.889(3)$ ,  $c = 9.923(2)$  Å,  $\beta = 105.08(1)^\circ$ ,  $V = 5444(1)$  Å<sup>3</sup>,  $Z = 4$ ,  $R = 0.058$ ,  $T = 150$  K. Two  $C_{60}$  molecules are surrounded by four deformed ET molecules and  $C_{60}$  molecules stack along the  $c$ -axis. (b) Crystal structure of OMTTF· $C_{60}$ ·PhH:<sup>246</sup> Triclinic,  $P\bar{1}$ ,  $a = 10.320(1)$ ,  $b = 13.676(1)$ ,  $c = 10.024(1)$  Å,  $\alpha = 95.68(1)$ ,  $\beta = 95.74(1)$ ,  $\gamma = 125.42(1)^\circ$ ,  $V = 1125.4(3)$  Å<sup>3</sup>,  $Z = 1$ ,  $R = 0.135$ . The  $C_{60}$  molecules form a 2D layer in the  $ac$ -plane, and the layers are separated from each other in the  $c$ -direction by the layer composed of OMTTF and solvent molecules.

meric neutral  $C_{60}$  and ionic  $C_{60}^{n-}$  molecules are incorporated with a variety of electron donors to afford metals, superconductors, ferromagnets, photoconductors, photovoltaic materials, etc. Since the electron-accepting ability of  $C_{60}$  is weak, ionic complexes with fullerenes are obtainable by use of strong electron donors, such as alkali metals, metallocenes, amines, or phosphines. The redox difference between two components  $\Delta E(DA)$  should satisfy Eq. 98 as discussed in section 3.1. The ionicity diagram of the  $C_{60}$  CT complex shown in Fig. 148a indicates that the redox potential of donor molecules should be less than  $-0.46$  V to afford a fully ionic  $C_{60}$  complex (Eq. 99).<sup>246</sup>

$$\Delta E \leq -0.02 \text{ V.} \quad (98)$$

$$E_1(D) \leq -0.46 \text{ V.} \quad (99)$$

Most TTF derivatives (OMTTF, HMTTF, ET, TTT, etc.)

afforded CT complexes with their CT bands allocated in the neutral regime as expected from their weak donating abilities (Fig. 148b).<sup>246</sup>

Owing to the spherical shape of fullerenes, it is commonly observed that flat donor molecules are deformed and/or solvent molecules are accommodated in CT solids, such as  $(C_2TET-TTF)(C_{60})_2$ ,<sup>1012</sup>  $(ET)_2C_{60}$  (Fig. 149a),<sup>1013</sup> and OMTTF· $C_{60}$ ·PhH (Fig. 149b).<sup>246</sup>

Besides the monomeric form, a large variety of dimeric and polymeric fullerenes have so far been prepared as summarized in Table 34. The fullerenes exhibit a reversible phase transition attributable to the dissociation from polymeric (or dimeric) to monomeric phase in a certain temperature range. Neutral fullerenes form a variety of polymeric structures under high pressure ( $>6$  GPa) and high-temperature ( $>970$  K) to afford a high  $T_c$  ferromagnet or superhard polymer as mentioned in

Table 34. Dimers and Polymers of Neutral and Ionized Fullerenes<sup>n-</sup>

<i>n</i>	Compound <sup>a)</sup>	Treatment	Characteristics	Ref.
0	C <sub>60</sub>	6 GPa, 1025–1050 K	rhombohedral 2D [2 + 2] polymer, ferromagnet ( $T_c \approx 500$ K)	932,933
	C <sub>60</sub>	<13 GPa, <2000 K	superhard polymer	934
	C <sub>60</sub>		C=C dimer (C <sub>60</sub> <sup>0</sup> ) <sub>2</sub> , dimer ↔ monomer at 435 K	1014
	C <sub>70</sub>	22 GPa, 573 K	C=C dimer (C <sub>70</sub> <sup>0</sup> ) <sub>2</sub>	1015
	C <sub>59</sub> N		C–C dimer (C <sub>59</sub> N <sup>0</sup> ) <sub>2</sub>	1016
1	KC <sub>60</sub>	slow cool <350 K	C=C linear C <sub>60</sub> <sup>-1</sup> polymer; 3D metal	1017–1020
	RbC <sub>60</sub>	slow cool <350 K	C=C linear C <sub>60</sub> <sup>-1</sup> polymer; 1D metal; $T_{MI} = 50$ K, SDW	1017–1020
	CsC <sub>60</sub>	slow cool <350 K	C=C linear C <sub>60</sub> <sup>-1</sup> polymer; 1D metal; $T_{MI} = 35$ K, SDW	1017–1020
	MC <sub>60</sub> (M = K, Rb, and Cs)	rapid cool to RT	C–C dimer (C <sub>60</sub> <sup>-</sup> ) <sub>2</sub> , dimer ↔ monomer at 270 K	1018,1021–1023
	CsC <sub>60</sub>	quenched to liq. N <sub>2</sub>	monomer, metal $\geq 4$ K, 12% of C <sub>60</sub> <sup>2-</sup>	1018,1024,1025
	Cs <sub>2</sub> (C <sub>60</sub> ) <sub>2</sub> (CTV)(DMF) <sub>6</sub>		C–C dimer (C <sub>60</sub> <sup>-</sup> ) <sub>2</sub> , dimer ↔ monomer at 140–220 K	1026
	TDAE·C <sub>60</sub>	≈1 GPa at 300 K	hydrostatic pressure: [2 + 2] 1D polymer	1027
		≈0.7 GPa at 300 K	hydrostatic pressure: polymer ↔ monomer at 520 K	1028
		no up to 0.4 GPa	uniaxial strain: $T_c = 17.5$ K ( $//b$ , 0.4 GPa)	1029
	[Bz <sub>2</sub> Cr]C <sub>60</sub> (PhCl <sub>2</sub> ) <sub>0.7</sub>		C–C dimer (C <sub>60</sub> <sup>-</sup> ) <sub>2</sub> , dimer ↔ monomer at 160–240 K	1030
	[Bz <sub>2</sub> Cr]C <sub>60</sub> (PhCN)		C–C dimer (C <sub>60</sub> <sup>-</sup> ) <sub>2</sub> , dimer ↔ monomer at $\geq 240$ K	1030
	[(Tol) <sub>2</sub> Cr]C <sub>60</sub>		C–C dimer (C <sub>60</sub> <sup>-</sup> ) <sub>2</sub> , dimer ↔ monomer at 250 K	1031,1032
	[Cp <sub>2</sub> Co]C <sub>60</sub> (PhCl <sub>2</sub> )		C–C dimer (C <sub>60</sub> <sup>-</sup> ) <sub>2</sub> , dimer ↔ monomer at 250–350 K	1030
	[Cp* <sub>2</sub> Cr]C <sub>60</sub> (PhH) <sub>2</sub>		C–C dimer (C <sub>60</sub> <sup>-</sup> ) <sub>2</sub> , dimer ↔ monomer at 160–190 K	1030
	[Cp* <sub>2</sub> Cr]C <sub>60</sub> (PhCl <sub>2</sub> ) <sub>2</sub>		C–C dimer (C <sub>60</sub> <sup>-</sup> ) <sub>2</sub> , dimer ↔ monomer at 200–230 K	1030,1033
	TDAE·C <sub>70</sub> (PhMe)		C–C dimer (C <sub>70</sub> <sup>-</sup> ) <sub>2</sub> , no monomer	1034
	CsC <sub>70</sub> (DMF) <sub>5</sub>		C–C dimer (C <sub>70</sub> <sup>-</sup> ) <sub>2</sub> , dimer ↔ monomer at $\geq 250$ K	1030
	Cs <sub>2</sub> (C <sub>70</sub> ) <sub>2</sub> (CTV)(DMF) <sub>7</sub> (PhH) <sub>0.75</sub>		C–C dimer (C <sub>70</sub> <sup>-</sup> ) <sub>2</sub> , dimer ↔ monomer at $\geq 360$ K	1035
	[Bz <sub>2</sub> Cr](C <sub>70</sub> )(PhMe)		C–C dimer (C <sub>70</sub> <sup>-</sup> ) <sub>2</sub> , dimer ↔ monomer at $\geq 300$ K	1036
	[Bz <sub>2</sub> Cr](C <sub>70</sub> )(PhCl <sub>2</sub> )		C–C dimer (C <sub>70</sub> <sup>-</sup> ) <sub>2</sub> , dimer ↔ monomer at $\geq 250$ K	1030
	[Cp <sub>2</sub> Co](C <sub>70</sub> )(PhCl <sub>2</sub> ) <sub>0.5</sub>		C–C dimer (C <sub>70</sub> <sup>-</sup> ) <sub>2</sub> , dimer ↔ monomer at $\geq 300$ K	1030
	[Cp* <sub>2</sub> Cr](C <sub>70</sub> )(PhMe)		C–C dimer (C <sub>70</sub> <sup>-</sup> ) <sub>2</sub> , dimer ↔ monomer at $\geq 300$ K	1036
	[Cp* <sub>2</sub> Ni](C <sub>70</sub> )(PhMe)		C–C dimer (C <sub>70</sub> <sup>-</sup> ) <sub>2</sub> , dimer ↔ monomer at $\geq 300$ K	1036
	[Bz <sub>2</sub> Cr][C <sub>60</sub> (CN) <sub>2</sub> ]		no monomer < 350 K	1037
2	MC <sub>70</sub> (NH <sub>3</sub> ) <sub>n</sub> (M = Ca, Sr, Ba, Eu, and Yb)		linear polymer	1038,1039
3	Na <sub>2</sub> RbC <sub>60</sub>	slow cool < RT	C–C linear polymer; metal	1040,1041
	Li <sub>3</sub> CsC <sub>60</sub>	≈1 GPa	C–C linear polymer; metal	1042
4	Na <sub>4</sub> C <sub>60</sub>	ambient condition	4 × C–C 2D polymer, polymer ↔ monomer at 500 K	1043

a) Bz or PhH: benzene, Tol or PhMe: toluene, PhCl<sub>2</sub>: *o*-dichlorobenzene, PhCN: benzonitrile, Cp: cyclopentadienyl, Cp\*: penta-methylcyclopentadienyl.

section 4.7.2.<sup>932–934</sup> Neutral C<sub>60</sub> also forms dimers having a cyclobutane ring and exhibit a dimer–monomer phase transition at 435 K.<sup>1014</sup> Also, the neutral C<sub>70</sub> dimer is bonded by two single bonds,<sup>1015</sup> while the neutral azafullerene (C<sub>59</sub>N) dimer is bonded by one single bond.<sup>1016</sup> As for the CT salts, the bonding pattern and dimer–monomer phase transition will be discussed in the following sections.

In addition to the polymeric fullerenes, the related family of  $\sigma$ -bonded [Co<sup>II</sup>TPP–fullerene]<sup>-</sup> anions was prepared in ionic multicomponent CT complexes containing tetraphenylporphyrinatocobalt(II) (CoTPP) and the fullerene radical anion as summarized in Table 35. The  $\sigma$ -bonded anions also show a transition from bonded to non-bonded form.

**5.3 AC<sub>60</sub> Phase.** At high temperatures above ca. 100 °C, AC<sub>60</sub> (A = K, Rb, and Cs) salts adopt a fcc rocksalt structure<sup>1048</sup> showing a Curie-like magnetic behavior,<sup>1017</sup> although the metallic behavior was observed for conductivity measurements.<sup>1049</sup> Upon slow cooling, the salts undergo a structural

transition from cubic to orthorhombic symmetry at ca. 350 K, leading to the air-stable polymer phase consisting of [2 + 2] cycloadduct linear chains.<sup>1020</sup> They show a metallic behavior down to 50 K for A = Rb and 35 K for A = Cs, at which the polymerized salts pass through an SDW transition.<sup>1017–1019</sup> On the other hand, rapid cooling to RT leads to a metastable insulating orthorhombic phase that consists of single-bonded (C<sub>60</sub>)<sub>2</sub><sup>2-</sup> dimers.<sup>1021–1023</sup> It has also been found that a cubic phase can be maintained in CsC<sub>60</sub> by immersing the sample into liquid nitrogen (quenching).<sup>1018</sup> In the cubic high-temperature phase the C<sub>60</sub><sup>-</sup> anions are free rotating (space group *Fm*3*m*), while in the cubic quenched phase they are orientationally ordered (space group *Pa*3̄).<sup>1050</sup> The quenched phase transforms irreversibly into the dimer phase above 130–150 K.

**5.4 C<sub>60</sub> Derivatives.** The cyclic voltammograms of halogenated C<sub>60</sub>Cl<sub>6</sub>,<sup>1051</sup> C<sub>60</sub>Br<sub>6</sub>,<sup>1052</sup> and C<sub>60</sub>Br<sub>8</sub>,<sup>1052</sup> in which sterically bulky Cl and Br place a double bond in a pentagon ring

Table 35. The  $\sigma$ -Bonded Anion  $\text{Co}^{\text{II}}\text{TPP}\text{-Fullerene}^-$ 

Compound <sup>a)</sup>	Characteristics	Ref.
(TMA)[CoTPP- $\text{C}_{60}$ ](PhCN)(PhCl <sub>2</sub> )	$\sigma$ -bonded anion $\leftrightarrow$ non-bonded units at > 300 K	1044
(TDAE)[CoTPP- $\text{C}_{60}$ ]	$\sigma$ -bonded anion $\leftrightarrow$ non-bonded units at > 190 K	1045
(MP)[CoTPP- $\text{C}_{60}$ ](PhCl <sub>2</sub> ) <sub>1.2</sub>	$\sigma$ -bonded anion $\leftrightarrow$ non-bonded units at > 300 K	1044
[Bz <sub>2</sub> Cr] <sub>1.7</sub> [CoTPP- $\text{C}_{60}$ ](PhCl <sub>2</sub> ) <sub>3.3</sub>	$\sigma$ -bonded anion $\leftrightarrow$ non-bonded units at > 300 K	1046
[Bz <sub>2</sub> Cr] <sub>2</sub> [CoTPP- $\text{C}_{60}(\text{CN})_2$ ][ $\text{C}_{60}(\text{CN})_2$ ](PhCl <sub>2</sub> ) <sub>3</sub>	$\sigma$ -bonded anion $\leftrightarrow$ non-bonded units at > 200 K	1046, 1047

a) TMA: tetramethylammonium, MP: methylpyridinium, AN: acetonitrile.

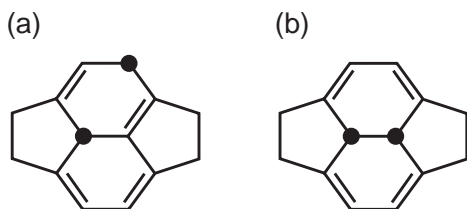
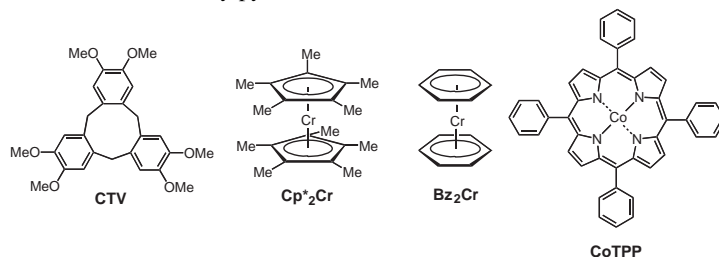


Fig. 150. Addition patterns at (a) 1,4- and (b) 1,2-positions.

(1,4-addition, Fig. 150a), actually show an anodic shift of first reduction potential from that of parent  $\text{C}_{60}$ .<sup>1053</sup> However, the reduction state of them is electrochemically unstable, and the  $\text{C}_{60}$  derivatives readily lose halogen atoms by either thermal or electrochemical perturbations. Consequently, the complex formation between these halogenated fullerenes and TTF in organic solution results in the formation of TTF·halide indicating the electrochemical instability of halogenated fullerenes.

Since the introduction of a double bond into a pentagon ring arising from 1,4-addition may cause electrochemical instability, 1,2-added  $\text{C}_{60}$  with double bonds only in the hexagon rings (Fig. 150b) seems to be favorable to prepare ionic complexes. CT complexes consisting of 1,2-dicyano  $\text{C}_{60}$ <sup>1054</sup> and TTF analogues show a distinct CN stretching mode at  $2241\text{ cm}^{-1}$ , which is invariant during cocrystallization.<sup>1055</sup> This fact indicates that these complexes still have a neutral ground state, although the considerably red-shifted CT bands compared to corresponding  $\text{C}_{60}$  complexes serve as strong evidence for an increasing of electron-accepting ability.  $\text{C}_{60}(\text{CN})_2$ -based ionic complexes have been obtained using  $\text{Cp}_2\text{Co}$ ,<sup>1056</sup>  $\text{Bz}_2\text{Cr}$ , and potassium metals<sup>1037</sup> as the case of parent  $\text{C}_{60}$ . Static susceptibility and EPR measurements strongly suggest that  $\text{C}_{60}(\text{CN})_2$  anions form diamagnetic  $[\text{C}_{60}(\text{CN})_2]^{2-}$  dimers in the solid state and the dimers are thermally stable up to 350 K.<sup>1037</sup>

**5.5  $\text{C}_{60}^-$  Monoanions in Ionic CT Complexes and Monomer-Dimer Phase Transition.** In the crystal composed of  $\text{C}_{60}$  and  $\text{Cp}^*_2\text{Cr}$ ,  $\text{C}_{60}$  molecules are reduced to  $-1$  as expected from their redox properties.<sup>1033</sup> Single crystal X-ray diffraction reveals that monovalent  $\text{C}_{60}$  forms a single-bonded dimer (Figs. 151a and 152b) at 100 K, whereas it seems to be freely rotating monomers at RT (Fig. 152a). The reversible transfor-

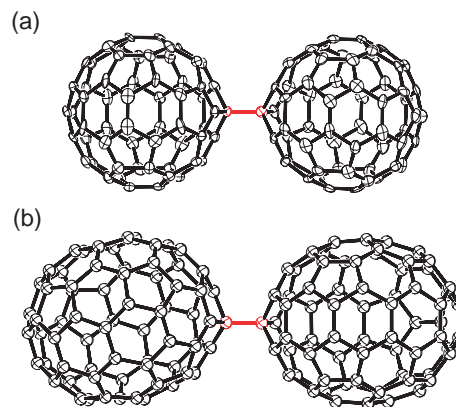


Fig. 151. Molecular structures of (a)  $(\text{C}_{60})_2^{2-}$  dimer in  $\text{Cp}^*_2\text{Cr}\cdot\text{C}_{60}\cdot(\text{PhCl}_2)_2$ <sup>1030,1033</sup> and (b)  $(\text{C}_{70})_2^{2-}$  dimer in  $(\text{Cs}^+)_2(\text{C}_{70}^-)_2(\text{CTV})(\text{DMF})_7(\text{PhH})_{0.75}$ .<sup>1035</sup>

mation between diamagnetic dimer and paramagnetic monomer phases was confirmed by an abrupt change of static susceptibility at 200–230 K as seen in Fig. 153. Structural investigation on such a transformation has so far been limited to three salts,  $\text{AC}_{60}$  ( $\text{A} = \text{K}$  and  $\text{Rb}$ )<sup>1022</sup> and  $[(\text{ToI})_2\text{Cr}]\text{C}_{60}$ ,<sup>1032</sup> and both are based on powder X-ray diffraction. Its transition temperature, below which the magnetic susceptibility of  $\text{C}_{60}$  part completely disappears, is similar to 270 K of  $\text{AC}_{60}$  and 250 K of  $[(\text{ToI})_2\text{Cr}]\text{C}_{60}$ , but is lower than 435 K of neutral  $\text{C}_{60}$  dimers.<sup>1014</sup> Similar transformation was observed for  $\text{C}_{70}^-$  anions in the multicomponent complex  $(\text{Cs}^+)_2(\text{CTV})(\text{C}_{70}^-)_2(\text{DMF})_7(\text{PhH})_{0.75}$ .<sup>1035</sup>  $\text{C}_{70}$  molecules form a dimer structure even at RT through a covalent single-bond (Fig. 151b), and show no sizable magnetic moment owing to the diamagnetic nature of  $(\text{C}_{70})_2^{2-}$  dimers. On heating, the magnetic susceptibility abruptly increases at ca. 360 K, possibly indicating cleavage of the covalent bond, and thus, the formation of paramagnetic  $\text{C}_{70}^-$  monomers. A similar magnetic behavior was observed for an ionic  $\text{C}_{70}$  salt with  $\text{Bz}_2\text{Cr}$ .<sup>1030,1036</sup> It seems likely that the transition temperature is connected with the length of the bridging intradimer bond:  $\text{C}_{60}^-$  (200–230 K) <  $\text{C}_{70}^-$  (360 K) < neutral  $\text{C}_{60}$  (435 K) vs  $\text{C}_{60}^-$  (1.597 Å) >  $\text{C}_{70}^-$  (1.584 Å) > neutral  $\text{C}_{60}$  (1.575 Å).

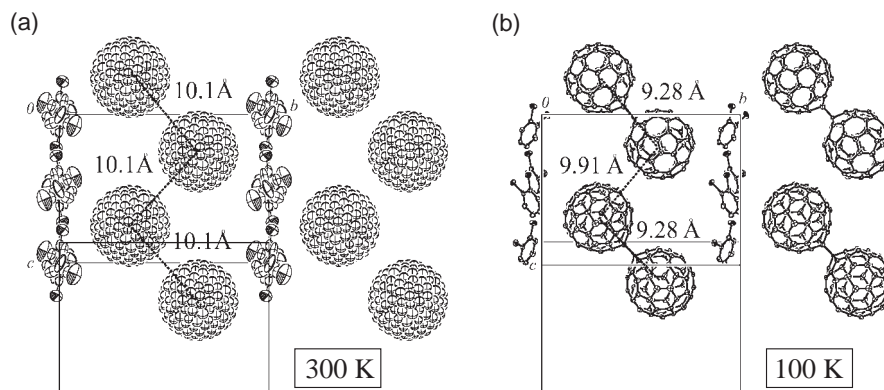


Fig. 152. Packing of  $C_{60}^-$  and  $PhCl_2$  molecules in  $Cp^*_2Cr \cdot C_{60} \cdot (PhCl_2)_2$  at (a) 300 K and (b) 100 K.  $Cp^*_2Cr$  cations are omitted for clarity. Only the major orientation of the  $(C_{60})_2^{2-}$  dimers is shown in (b).<sup>1033</sup>

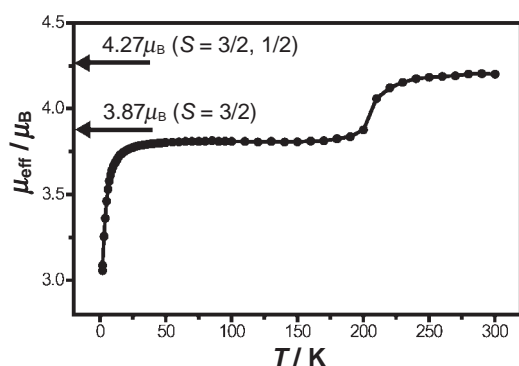


Fig. 153. Temperature dependence of magnetic moment for  $Cp^*_2Cr \cdot C_{60} \cdot (PhCl_2)_2$ .<sup>1033</sup>

The ionic complex  $TDAE \cdot C_{60}$  undergoes a ferromagnetic transition at 16.1 K,<sup>930</sup> which was the highest Curie temperature among the pure molecular materials at the time. DC conductivity for a single crystal indicates that the complex is a typical semiconductor with a sizable energy gap (see section 4.7.2).<sup>931</sup> Of particular importance is that the magnetic moment is determined to be ca.  $1 \mu_B$  through the transition, although both  $TDAE^+$  and  $C_{60}^-$  molecules have a radical spin.<sup>1057,1058</sup> The EPR,  $^{14}N$  NMR, and electron spin echo envelope modulation measurements indicate that  $C_{60}^-$  spins are mainly responsible for the magnetic moment of  $TDAE \cdot C_{60}$ ,<sup>1059</sup> which was supported by single crystal X-ray diffraction.<sup>1060</sup> In the crystal,  $TDAE^+$  molecules have a dimerized character resulting in a spin-singlet ground state.

The  $TDAE \cdot C_{60}$  prepared at around  $0^\circ C$  shows paramagnetic behavior down to 2 K (" $\alpha'$ -phase"), but transforms to the known ferromagnetic " $\alpha$ -phase" by annealing at around  $60^\circ C$ ,<sup>1061</sup> which promotes a merohedral disorder of the Jahn–Teller disordered  $C_{60}$  giving rise to the ferromagnetic coupling between  $C_{60}$  molecules.<sup>1062</sup>

Recently, it has been reported that  $C_{60}$  molecules in  $TDAE \cdot C_{60}$  are polymerized by applying pressure (" $\beta$ -phase"),<sup>1027,1028</sup> although the structural information including the polymerized pattern is currently absent. Curie temperature gradually decreases as the applied pressure increases, and the ferromagnetic ordering is completely suppressed above 1 GPa<sup>1027</sup> or 0.7 GPa.<sup>1028</sup> Below which, the monomer and polymer phases co-

exist in a single crystal with particular ratio. Of particular interest is that the  $\beta$ -phase remains stable even after releasing the pressure. The RT  $g$ -factor of the polymerized phase is determined to be 2.0025, which substantially exceeds the value of the monomer ( $\alpha$ - or  $\alpha'$ -) phase and is intermediate between those of  $C_{60}^-$  and  $TDAE^+$  spins. The EPR intensity apparently increases by polymerization, indicating that the dimerization of  $TDAE^+$  molecules is unambiguously released in the  $\beta$ -phase. The thermal transformation from polymer to monomer phases was observed on heating to 520 K.<sup>1028</sup> Unlike the hydrostatic pressure, the Curie temperature rises to 17.5 K by applying a uniaxial strain of 0.4 GPa along the  $b$ -axis.<sup>1029</sup> Although several CT complexes composed of  $C_{60}$  and  $TDAE$  analogues have been prepared, attempts to obtain new ferromagnetic CT complexes have been unsuccessful.<sup>1063,1064</sup>

Single crystals of  $TDAE \cdot C_{70} \cdot PhMe$  were grown by the diffusion method in a toluene solution.<sup>1034</sup> At RT,  $C_{70}$  anions form a dimer structure through a single bond in a similar manner of the above-mentioned  $(Cs^+)_2(CTV)(C_{70}^-)_2(DMF)_7(PhH)_{0.75}$ ,<sup>1035</sup> except for an elongated intradimer bond of 1.62 Å. The thermal stability of  $C_{70}$  dimers in  $TDAE \cdot C_{70} \cdot PhMe$  has not been reported. Temperature dependence of the EPR spectra behaves differently from the ferromagnet  $TDAE \cdot C_{60}$ ; its EPR spectra show a single Lorentzian-shaped signal down to 0.5 K with the Curie–Weiss behavior.

**5.6  $C_{60}^{2-}$  Dianions in Ionic DA-Type Complexes.** The electronic state of  $C_{60}^{2-}$  species has been a subject of interest, since the triply degenerate  $t_{1u}$  level of  $C_{60}$  leads to the expectation that Hund's rule will be obeyed; namely,  $C_{60}^{2-}$  might have a  $(t_{1u})^2$  spin-triplet ground state. However, molecular orbital calculations have predicted that the energy gap between the singlet ground state and triplet excited state is  $650^{1065}$  or  $1500 \text{ cm}^{-1}$ .<sup>1066</sup> EPR study of  $C_{60}^{2-}$  species generated electrochemically in DMSO shows a diamagnetic singlet ground state with a thermally populated excited triplet state, and the energy gap is estimated to be  $600 \pm 100 \text{ cm}^{-1}$ .<sup>1067</sup> In the solid-state, the  $\mu_{eff}$  of  $(PPN^+)_2(C_{60}^{2-})$  ( $PPN^+$ : bis(triphenylphosphine)iminium) gradually decreases as temperature is lowered, indicating the singlet ground state of  $C_{60}^{2-}$ .<sup>1068</sup> However, the value is far from zero even at low temperatures, and it is thus likely that the salt has the nearly degenerate excited triplet state and the marginal singlet-triplet energy gap of ca.  $1 \text{ cm}^{-1}$ . It might be noteworthy that grinding of the sample results in re-



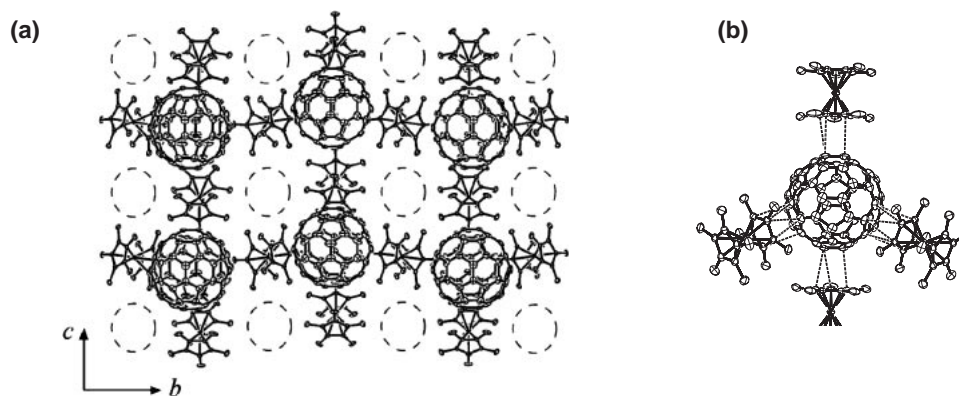


Fig. 154. (a) Crystal structure of  $(\text{Cp}^*_2\text{Co}^+)_2(\text{C}_{60}^{2-})(\text{PhCl}_2/\text{PhCN})_2$  in the  $bc$ -plane. Dashed ellipses show the channels accommodating solvent molecules. (b) van der Waals contacts ( $<3.5$  Å) between the  $\text{Cp}^*_2\text{Co}^+$  and  $\text{C}_{60}^{2-}$  ions (dashed lines). Only the major orientation of  $\text{C}_{60}^{2-}$  is shown in (a) and (b).<sup>1071</sup> Monoclinic,  $P2_1/m$ ,  $a = 12.108(2)$ ,  $b = 24.959(5)$ ,  $c = 12.418(3)$  Å,  $\beta = 96.337(5)^\circ$ ,  $V = 3729.8(13)$  Å<sup>3</sup>,  $Z = 4$ ,  $R = 0.042$ ,  $T = 120$  K.

duced susceptibility ( $1.0$ – $2.3 \mu_B$ ). The temperature dependence of  $[\text{K}(\text{[2.2.2]cryptant})^+]_2(\text{C}_{60}^{2-})(\text{DMF})_3$  shows a similar behavior to that of the PPN salt,<sup>1069</sup> and does not allow the estimation of the singlet-triplet gap. By contrast, Reed et al. reported that  $(\text{PPN}^+)_2(\text{C}_{60}^{2-})$  and  $(\text{Cp}_2\text{Co}^+)_2(\text{C}_{60}^{2-})$  prepared by highly purified  $\text{C}_{60}$  are EPR silent in solution, and thus, the signal previously assigned to  $\text{C}_{60}^{2-}$  would arise from the impurity  $\text{C}_{60}^-$ .<sup>1070</sup> Recently, we prepared a single crystal of  $(\text{Cp}^*_2\text{Co}^+)_2(\text{C}_{60}^{2-})(\text{PhCl}_2/\text{PhCN})_2$ , which forms a 3D framework built of alternating  $\text{Cp}^*_2\text{Co}^+$  and  $\text{C}_{60}^{2-}$  ions with channels accommodating solvent molecules (Fig. 154).<sup>1071</sup> Its EPR intensity and static susceptibility show a thermally activated behavior with a singlet–triplet energy gap of  $730 \pm 10 \text{ cm}^{-1}$ .

The search for alkali-doping effects on the  $\text{C}_{60}$ -based CT complexes can offer important information about superconductivity. The CT complex  $\text{OMTTF} \cdot \text{C}_{60} \cdot \text{PhH}$  has a neutral character with 2D  $\text{C}_{60}$  layers sandwiched by the other components (Fig. 149b),<sup>246</sup> and the K- and Rb-dopings give rise to the appearance of superconductivity below 17–19 and 23–26 K, respectively.<sup>1072,1073</sup> Both temperatures are less than those of corresponding  $\text{A}_3\text{C}_{60}$  superconductors (19 K for  $A = \text{K}$  and 29 K for  $A = \text{Rb}$ ), and the Raman spectrum of the Rb-doped compound shows a downshift of tangential  $A_g(2)$  mode ( $1468 \text{ cm}^{-1}$  for neutral  $\text{C}_{60}$ ) to  $1453 \text{ cm}^{-1}$ , indicating the reduction to  $\text{C}_{60}^{2-}$  instead of  $\text{C}_{60}^{3-}$ . This spectral feature is unambiguous evidence for a new type of bulk superconductor, since there is no superconductor with  $\text{C}_{60}^{2-}$  species. On the other hand, alkali-doping to the neutral CT complex  $(\text{ET})_2\text{C}_{60}$ , in which each  $\text{C}_{60}$  molecule is embedded by two bent ET molecules,<sup>1013</sup> is currently unsuccessful, possibly due to the tight molecular packing in the crystal.

**5.7  $\text{C}_{60}^{3-}$  Trianions in Ionic DA-Type Complexes.** So far some  $\text{C}_{60}^{3-}$  fullerides have been obtained with organometallic donors such as  $\text{Cp}(\text{C}_6\text{Me}_6)\text{Fe}$ <sup>1074</sup> and  $\text{Cp}^*_2\text{Co}$ ,<sup>1068</sup> or organic cations such as  $\text{PPN}^+$ <sup>1075</sup> and  $\text{Me}_4\text{N}^+$ ,<sup>1076</sup> but no information about conductivity has been given. There have been two single crystals containing  $\text{C}_{60}^{3-}$  species: one being  $\text{K}_3\text{C}_{60}(\text{THF})_{14}$ <sup>1077</sup> and the other being  $[\text{K}(\text{18-crown-6})]_3\text{C}_{60}(\text{PhMe})_2$ .<sup>1078</sup> In the former crystal, each  $\text{C}_{60}$  molecule is surrounded by two  $\text{K}(\text{THF})_4$  and two  $\text{K}(\text{THF})_5$  clusters, and the nearest neighboring interfullerene distance of  $12.905$  Å at 140 K is apparently

longer than the sum of van der Waals radii (ca.  $10$  Å). The latter compound consists of alternating layers of hexagonal-arranged  $\text{C}_{60}^{3-}$  fullerides and the others. The magnetic susceptibility follows the Curie–Weiss law with  $S = 1/2$  spin, in connection with a nearest neighboring interfullerene distance as long as  $13.89$  Å at 110 K. It is thus more likely that both salts exhibit poor conductivity owing to the localized spin system.

**5.8 Multicomponent CT Complexes.** As mentioned above, donor molecules that can reduce fullerene moieties are sparse because of the weak electron-accepting ability of the fullerene moiety. Then, the another strategy to obtain new versatile ionic complexes can be driven by the preparation of multicomponent complexes with a small-sized strong donor molecule able to ionize the fullerene ( $\text{D}_1$ ) and a structure-forming neutral molecule ( $\text{D}_2$ ), i.e.,  $(\text{D}_1^+)[(\text{D}_2^0)(\text{fullerene}^-)]$  as  $(\text{Cs}^+)_2(\text{CTV})(\text{C}_{70}^-)_2(\text{DMF})_7(\text{PhH})_{0.75}$ ,<sup>1035</sup>  $(\text{Cs}^+)(\text{CoTPP})(\text{C}_{60}^-)(\text{PhCN})_{1.64}(\text{PhCl}_2)_{0.36}(\text{AN})$ ,<sup>1044</sup>  $(\text{Bz}_2\text{Cr}^+)(\text{CoTPP})(\text{C}_{70})_2(\text{PhCl}_2)_2$ ,<sup>1046</sup>  $(\text{Bz}_2\text{Cr}^+)_{1.7}(\text{CoTPP}-\text{C}_{60})_2(\text{PhCl}_2)_{3.3}$ ,<sup>1046</sup>  $\text{TDAE} \cdot \text{CoTPP} \cdot \text{C}_{60}$ ,<sup>1045,1079</sup> and  $(\text{Bz}_2\text{Cr}^+)[\text{CoTPP}-\text{C}_{60}(\text{CN})_2][\text{C}_{60}(\text{CN})_2](\text{PhCl}_2)_3$  ( $\text{D}_1^+ = \text{Cs}^+$ ,  $\text{Bz}_2\text{Cr}^+$ , or  $\text{TDAE}^+$ ;  $\text{D}_2^0 = \text{CTV}^0$  or  $\text{CoTPP}^0$ ).<sup>1046,1047,1080</sup> The latter three complexes exhibit the  $\sigma$ -bonded  $[\text{CoTPP}-\text{fullerene}]^-$  unit confirmed by single crystal X-ray analysis. A similar bonding is conceivable for  $(\text{Bz}_2\text{Cr}^+)(\text{CoTPP})(\text{C}_{70})_2(\text{PhCl}_2)_2$ .<sup>1046</sup>

Use of a weak donor as  $\text{D}_1$  affords a neutral multicomponent complex such as  $(\text{Cp}_2\text{Fe})(\text{CoTPP} \cdot \text{Py})_2(\text{C}_{60})\text{PhMe}$  (Fig. 155).<sup>1079</sup> The cobalt atom of CoTPP in the crystal is coordinated with pyridine (Py) and TPP. The  $\text{C}_{60}$  molecules arrange near the metal atoms at the apical site opposite to the Py ligand. Slightly shortened  $\text{Co} \cdots \text{C}(\text{C}_{60})$  contacts of  $2.82$  Å involve a carbon atom of the 5–6 bond of  $\text{C}_{60}$ .

Figure 156 depicts the crystal structure of  $(\text{Cs}^+)(\text{CoTPP})(\text{C}_{60}^-)(\text{PhCN})_{1.64}(\text{PhCl}_2)_{0.36}(\text{AN})$  and the coordinations surrounding the  $\text{Cs}^+$  cation and cobalt atom of CoTPP in the crystal at 110 K.<sup>1044</sup> The  $\text{C}_{60}$  and CoTPP molecules form a zig-zag alternating chain. Each  $\text{C}_{60}$  unit forms shortened contacts with two CoTPP molecules ( $\text{Co} \cdots \text{C}(\text{C}_{60}) = 2.55$ – $3.07$  Å). These contacts are of the  $\sigma$ -type and shorter than the non-bonded van der Waals contacts ( $3.1$ – $3.3$  Å). However, they are longer than those in the  $\sigma$ -bonded diamagnetic  $[\text{CoTPP}-\text{fullerene}]^-$  anions ( $2.28$ – $2.32$  Å, see below) and close to those in the neu-

tral complexes (2.69–2.75 Å),<sup>1046</sup> indicating that CoTPP and C<sub>60</sub><sup>•−</sup> are non-bonded.

Cs cations occupy the voids in the CoTPP and C<sub>60</sub><sup>•−</sup> packing. The coordination sphere of Cs<sup>+</sup> involves three nitrogen atoms of one CH<sub>3</sub>CN and two disordered PhCN, six carbon atoms from a hexagonal facet of one C<sub>60</sub><sup>•−</sup> in one orientation and two carbon atoms of a 6–6 bond of another closest C<sub>60</sub><sup>•−</sup>, and four carbon atoms from phenyl substitutes of CoTPP. The total number of carbon and nitrogen atoms coordinated to Cs<sup>+</sup> is 15; the Cs...N distances are in the 3.05–3.21 Å range and the Cs...C distances are in the 3.43–3.86 Å range. These values are similar to those in other Cs<sup>+</sup>-containing compounds (according to the Cambridge Structural Database): the coordination number of Cs varies from 14–19, the Cs...N distances are in the range of 3.07–3.30 Å, and the Cs...C distances are in the

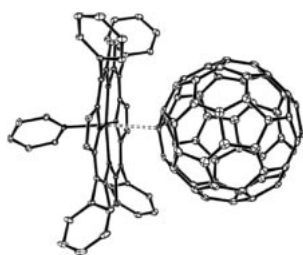


Fig. 155. Short van der Waals contact (dashed line) in (Cp<sub>2</sub>Fe)(CoTPP·Py)<sub>2</sub>(C<sub>60</sub>)PhMe.<sup>1079</sup>

range of 3.44–3.69 Å.

Single crystals consisting of Bz<sub>2</sub>Cr as D<sub>1</sub><sup>+</sup> and CoTPP as D<sub>2</sub><sup>0</sup> were prepared for C<sub>60</sub><sup>1046</sup> and C<sub>60</sub>(CN)<sub>2</sub>.<sup>1047</sup> In both crystals, the fullerene cage and cobalt centered on planar CoTPP were covalently bonded ( $\sigma$ -bonding), giving the compositions of (Bz<sub>2</sub>Cr<sup>+</sup>)<sub>1.7</sub>(CoTPP-C<sub>60</sub>)<sub>2</sub><sup>1.7−</sup>(PhCl<sub>2</sub>)<sub>3.3</sub> (Fig. 157) and (Bz<sub>2</sub>Cr<sup>+</sup>)<sub>2</sub>[CoTPP-C<sub>60</sub>(CN)<sub>2</sub>]<sub>2</sub><sup>−</sup>[C<sub>60</sub>(CN)<sub>2</sub>]<sub>2</sub>(PhCl<sub>2</sub>)<sub>3</sub> (Fig. 158), respectively. The stoichiometry requires that the  $\sigma$ -bonded unit has a charge of −0.85 and −1, respectively.

In (Bz<sub>2</sub>Cr<sup>+</sup>)<sub>1.7</sub>(CoTPP-C<sub>60</sub>)<sub>2</sub><sup>1.7−</sup>(PhCl<sub>2</sub>)<sub>3.3</sub> there are two (CoTPP-C<sub>60</sub>) units, which have different Co...C(C<sub>60</sub>) distances of 2.294 and 2.319 Å (Fig. 157a). Six fullerene cages form a honeycomb structure with large channels accommodating Bz<sub>2</sub>Cr and PhCl<sub>2</sub> molecules. No long-range magnetic ordering has been observed down to 1.9 K.

As for (Bz<sub>2</sub>Cr<sup>+</sup>)<sub>2</sub>[CoTPP-C<sub>60</sub>(CN)<sub>2</sub>]<sub>2</sub><sup>−</sup>[C<sub>60</sub>(CN)<sub>2</sub>]<sub>2</sub>(PhCl<sub>2</sub>)<sub>3</sub>, it contains the CoTPP·[C<sub>60</sub>(CN)<sub>2</sub>]<sub>2</sub> units at 120 K. One C<sub>60</sub>(CN)<sub>2</sub><sup>−</sup> coordinates the CoTPP by the  $\sigma$ -type with the shortest Co...C distance of 2.283 Å. Another C<sub>60</sub>(CN)<sub>2</sub><sup>−</sup> forms only shortened van der Waals contacts with CoTPP by the  $\eta^2$ -type with the Co...C distances of 2.790 and 2.927 Å. The complex has a unique cage structure with large channels accommodating guest molecules (Bz<sub>2</sub>Cr and PhCl<sub>2</sub>). Two types of channels with different sizes are formed (Fig. 158a). The channel I is occupied by the ordered Bz<sub>2</sub>Cr<sup>•+</sup> and negatively charged C≡N groups of four C<sub>60</sub>(CN)<sub>2</sub><sup>−</sup> directed toward the Bz<sub>2</sub>Cr<sup>•+</sup>. The channel II has a larger size than I because its walls addi-

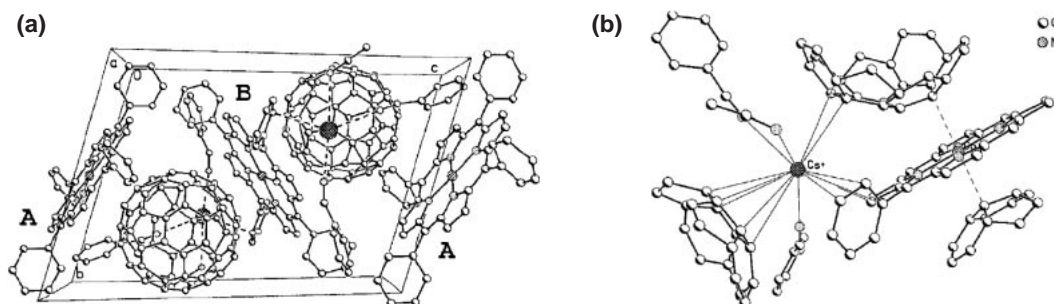


Fig. 156. (a) The crystal structure (Cs<sup>+</sup>)(CoTPP)(C<sub>60</sub><sup>−</sup>)(PhCN)<sub>1.64</sub>(PhCl<sub>2</sub>)<sub>0.36</sub>(AN). CoTPP and C<sub>60</sub> molecules are arranged in a zig-zag manner as CoTPP(A)...C<sub>60</sub>...CoTPP(B)...C<sub>60</sub>...CoTPP(A). (b) Coordination surrounding of the Cs<sup>+</sup> cation and the cobalt atom of CoTPP. The disordered PhCl<sub>2</sub> molecules are omitted and only the major orientation of C<sub>60</sub><sup>•−</sup> is shown in (a) and (b).<sup>1044</sup> Triclinic, *P*1̄, *a* = 13.553(3), *b* = 14.096(4), *c* = 20.734(5) Å,  $\alpha$  = 105.108(5),  $\beta$  = 106.148(5),  $\gamma$  = 92.160(5)°, *V* = 3642(1) Å<sup>3</sup>, *Z* = 2, *R* = 0.1215, *T* = 110 K.

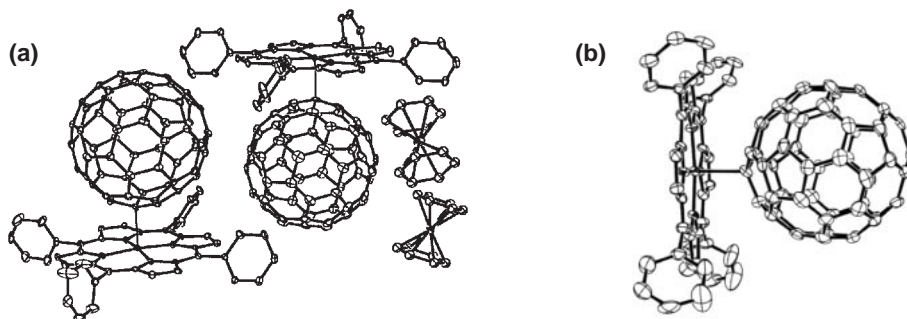


Fig. 157. (a) Fragment of crystal structure of (Bz<sub>2</sub>Cr<sup>+</sup>)<sub>1.7</sub>(CoTPP-C<sub>60</sub>)<sub>2</sub>(PhCl<sub>2</sub>)<sub>3.3</sub>. Disordered Bz<sub>2</sub>Cr<sup>•+</sup> with partial occupancy and PhCl<sub>2</sub> molecules are omitted. (b)  $\sigma$ -bonding between C<sub>60</sub><sup>−</sup> and CoTPP.<sup>1046</sup> Orthorhombic, *Pmm*2<sub>1</sub>, *a* = 15.534(1), *b* = 19.165(1), *c* = 27.038(2) Å, *V* = 8049.5(8) Å<sup>3</sup>, *Z* = 2, *R* = 0.085, *T* = 120 K.

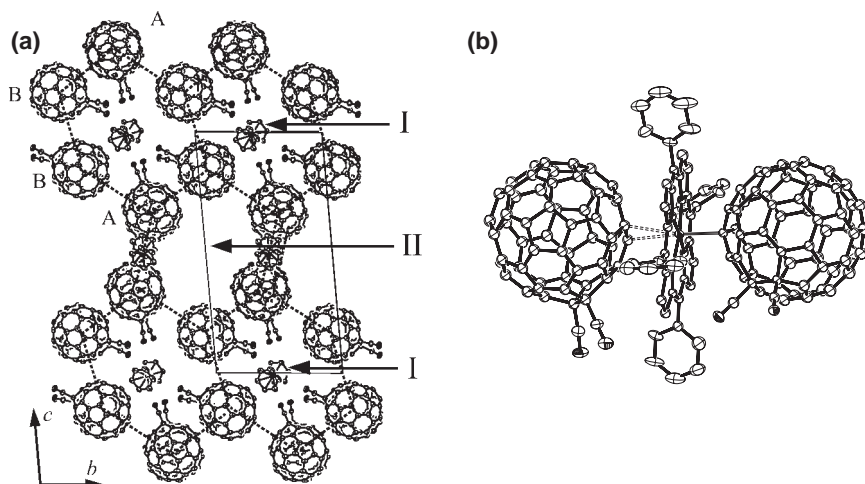


Fig. 158. (a) View of the packing of C<sub>60</sub>(CN)<sub>2</sub> and Bz<sub>2</sub>Cr<sup>•+</sup> along the *a*-axis in (Bz<sub>2</sub>Cr<sup>•+</sup>)<sub>2</sub>[CoTPP-C<sub>60</sub>(CN)<sub>2</sub>]<sup>•-</sup>[C<sub>60</sub>(CN)<sub>2</sub>]<sup>•-</sup>(PhCl<sub>2</sub>)<sub>3</sub>.<sup>1046</sup> The CoTPP, PhCl<sub>2</sub>, and disordered Bz<sub>2</sub>Cr molecules are omitted. Ordered Bz<sub>2</sub>Cr molecules are surrounded by six C<sub>60</sub>(CN)<sub>2</sub> molecules (2A + 4B) in channel I. (b) Short van der Waals contact (dashed line) and σ-bonding (solid line) between C<sub>60</sub>(CN)<sub>2</sub>•<sup>-</sup> and CoTPP. Triclinic, *P* $\bar{1}$ , *a* = 13.967(1), *b* = 15.928(1), *c* = 30.332(1) Å, α = 92.30(1), β = 100.89(1), γ = 103.46(1)°, *V* = 6419.3(6) Å<sup>3</sup>, *Z* = 2, *R* = 0.067, *T* = 120 K.

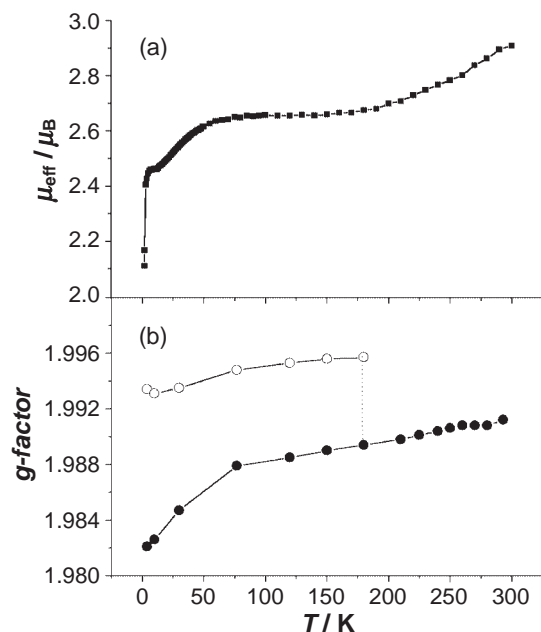


Fig. 159. (a) Temperature dependence of magnetic moment and (b) EPR *g*-factor of polycrystalline (Bz<sub>2</sub>Cr<sup>•+</sup>)<sub>2</sub>-(CoTPP)[C<sub>60</sub>(CN)<sub>2</sub>]<sup>•-</sup>2 (PhCl<sub>2</sub>)<sub>3</sub>.<sup>1026,1046</sup>

tionally contain ordered Bz<sub>2</sub>Cr<sup>•+</sup>. The channel II is occupied by the strongly disordered Bz<sub>2</sub>Cr<sup>•+</sup> and PhCl<sub>2</sub>.

The magnetic moment at RT (μ<sub>eff</sub> = 2.91 μ<sub>B</sub>) is explained by the spins from Bz<sub>2</sub>Cr<sup>•+</sup> and non-bonded C<sub>60</sub>(CN)<sub>2</sub>•<sup>-</sup>, implying that [CoTPP-C<sub>60</sub>(CN)<sub>2</sub>]<sup>•-</sup> units are diamagnetic (Fig. 159). An EPR signal at RT (*g* = 1.991) splits into two components below 180 K with *g*<sub>1</sub> = 1.996 and *g*<sub>2</sub> = 1.988. The latter is attributable to Bz<sub>2</sub>Cr<sup>•+</sup>, while the former is the resonating signal between Bz<sub>2</sub>Cr<sup>•+</sup> and C<sub>60</sub>(CN)<sub>2</sub>•<sup>-</sup> indicating a strong exchange coupling between them. Below 70 K, the magnetic moment decreases with decreasing temperature due to antiferro-

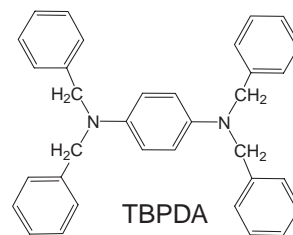


Chart 19.

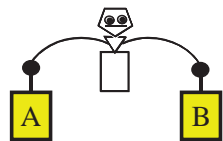
magnetic interactions. The increase in magnetic moment above 200 K with increasing temperature indicates the dissociation of non-magnetic σ-bonded [CoTPP-C<sub>60</sub>(CN)<sub>2</sub>]<sup>•-</sup> clusters into non-bonded paramagnetic CoTPP and C<sub>60</sub>(CN)<sub>2</sub>•<sup>-</sup> units analogously to (TDAE<sup>+</sup>)(CoTPP)(C<sub>60</sub>•<sup>-</sup>) as shown below.

It is of great interest to prepare multicomponent complexes formed with TDAE and C<sub>60</sub> molecules in order to develop new magnetically fascinating materials.<sup>1045</sup> The formed (TDAE<sup>+</sup>)-(CoTPP)(C<sub>60</sub>•<sup>-</sup>) complex shows a single EPR signal below 190 K, arising solely from TDAE<sup>+</sup> spins. This fact might give evidence for the formation of diamagnetic CoTPP-C<sub>60</sub>•<sup>-</sup> clusters through a covalent bond as observed for (Bz<sub>2</sub>Cr<sup>•+</sup>)<sub>1.7</sub>-(CoTPP-C<sub>60</sub>)<sub>2</sub><sup>1.7-</sup>(PhCl<sub>2</sub>)<sub>3.3</sub>,<sup>1046</sup> although crystals suitable for structural refinement have not been obtained. Then a sharp upturn of the magnetic moment at 190 K is indicative of the cleavage of the covalent bond.

On the other hand, the TBPDA and CTV complexes show paramagnetic behavior in the temperature range of 1.9–300 K without any long-range magnetic ordering. This finding is mainly associated with the isolated structure of C<sub>60</sub>•<sup>-</sup> due to the presence of neutral donor molecules, which was confirmed by structural refinement of the TBPDA complexes (Chart 19).<sup>1045</sup>

**5.9 Conductivity of Ionic DA-Type C<sub>60</sub> Complexes.** Using organic donors as counter species, no superconducting compounds have been prepared so far. Two unfavorable fea-

Table 36. Summary of the Designing Principles for Development of Functional Organic Materials

Development of Functional Organic Materials			
Balance (Yajirobe) → Designing principles			
Physical parameters → Chemical parameters			
Subject	A	B	
1 CT vs PT	$I_D - E_A, C_1$	$pK_a, pK_b, C_2$	
2 Neutral vs Ionic CT solid	$I_D - E_A$	$M$	
3 Degree of CT vs Metal	$\Delta E_{\text{redox}}$	$4t$	
4 Mott criterion: general	$U - V$	$W (4t)$	
dimer	$\Delta E_d$	$W_{U(\text{or } L)}$	
5 1D vs 2D	face-to-face	side-by-side	
6 Dimensionality vs	1D	metallic state is unstable	
(Super)conductivity	2D with large $t$	metallic state is stable	
	2D with small $t$	superconductor vs Mott insulator	
7 Uniform charge vs Charge ordering	$U - V$	$t$	
8 Charge-ordered stripe	$U$	$V$	
9 Antiferromagnet vs Spin-liquid	$t'$	$t$	

tures that  $C_{60}$  has a fairly weak electron-accepting ability<sup>246</sup> and the molecular symmetry of the organic donors is low, turn down the electronic structure similar to that of  $A_3C_{60}$ . However, some CT complexes with donors containing transition-metals have shown a semiconductive behavior with relatively high RT conductivities;  $10^{-2} \text{ S cm}^{-1}$  for  $[\text{Ru}(\text{bpy})_3](\text{C}_{60})_2$  (bpy: 2,2'-bipyridine,  $\varepsilon_g = 0.30 \text{ eV}$ ),<sup>1080</sup>  $\approx 10^{-2} \text{ S cm}^{-1}$  for  $\text{Cp}^*\text{Ni} \cdot \text{C}_{60} \cdot \text{CS}_2$ ,<sup>1081</sup>  $2.4 \times 10^{-2} \text{ S cm}^{-1}$  for  $\text{Bz}_2\text{Cr} \cdot \text{C}_{60}$  ( $\varepsilon_g = 0.38 \text{ eV}$ ),<sup>1082</sup> and  $2 \times 10^{-2} \text{ S cm}^{-1}$  for  $\text{Cp}_2\text{Co} \cdot \text{C}_{60} \cdot \text{PhCl}_2$ .<sup>1030</sup> Also, it has been reported that the  $C_{60}$ -based salt with organic dye cations shows an increase in conductivity as temperature decreases in the temperature range of 100–150 K.<sup>1083</sup>

## 6. Concluding Remarks

Molecular functional materials, which are composed of organic, inorganic, or molecular compounds, or their hybrids in the form of conventional bulk, assemblies, or mono-molecule have been a rapidly developing multidisciplinary field of research. These modern materials involve everything from fundamental science to applied science and technology, as shown in Figs. 4 and 77. An important feature of these materials is the almost unlimited possibility to tune their electronic and macroscopic structures, and thus, functionality in their assemblies. This field is the science of the design, synthesis, and fabrication from the combined aspects between the “molecular, crystal, and nano-hybrid structures” in direct-space and the “electronic and band structures and periodicity” in  $k$ -space. These materials are also important from the viewpoint of nano-fabrication, the science and technology of the future, because nano-fabrication needs very high density, small size integrated, and multifunctional properties that can be fabricated under mild conditions. In this review, we focused on the exploration of a system with peculiar transport behaviors including superconductivity and the development of functional materials in our group. In addition to the solid conductors, we have investigated conductive composite polymer films, LB films, melts, and ionic liquids. We have also developed novel functional materials, showing CPT, N–I, electric field- or photo-induced phase transition, nonlinear optics, and so on.

The key features underlying functional organic materials are the basic concepts: charge, spin, orbital, softness, and internal freedom. For a molecule, ionization potential, electron affinity, polarizability, fractional charge, soft acidity and basicity, molecular vibration, softness in molecular conformation, self-assembling ability, molecular size, and symmetry are of importance to develop functionality. For an assembly, on the other hand, the anisotropy in the hierarchical crystal structure, high anisotropy of the electronic system, small intermolecular transfer and Coulomb interactions, softness in the lattice, and a variety of phonon modes are the essential aspects in the organic functional solid. Furthermore, band filling control is of particular importance, though it is very difficult to achieve.

Table 36 summarizes a part of the guiding principles we have elucidated, to find a system that affords an intriguing function (isomerization, phase transition, polymorphism, bistability, or multi-critical phenomena), where only two interactions, A and B, are schematically illustrated for simplicity.

For CT and PT systems, two competing interactions are ( $I_D - E_A$  and  $C_1$ ) vs ( $pK_a$ ,  $pK_b$ , and  $C_2$ ), where  $C_1$  and  $C_2$  are the Coulomb interactions.

For the N–I system, ( $I_D - E_A$ ) and  $M$  are the basic competing parameters. However, not all compounds near the boundary condition, ( $I_D - E_A$ )  $\approx M$ , exhibit the enantiotropic (N–I phase-transition system) or monotropic isomerization. Dimensionality of the crystal structure or self-assembling ability of the component molecules is the other factor to develop the enantiotropic isomer; complexes composed of a constituent with strong self-assembling ability such as  $\text{BO}$ ,<sup>234</sup> BEDO-DBTTF,<sup>120</sup> or HMTTF<sup>238</sup> tend to exhibit monotropic isomers, while constituents with weak self-assembling ability such as perylene afford simply a 1D alternating CT complex without the complex isomerization even if the combination is close to the NI boundary, such as perylene·HCBT.<sup>1084,1085</sup> The N–I system so far prepared has a little higher dimensionality than pure 1D.

The requirement for DA type organic metals is common to that for the N–I phase transition system,  $\Delta E_{\text{redox}} (\approx I_D - E_A)$  vs  $M$  ( $0.5 \leq \delta < 1$ ), with segregated stacks arising from the



strong self-assembling ability of the constituent molecules. The degree of CT ( $\delta$ ) extends to a wider range with increasing dimensionality of the system. For organic materials, Mott criterion is essential due to the large on-site Coulomb repulsion energy:  $(U - V)$  vs  $4t$ . For an organic metal comprising dimers, Mott criterion is modified as  $\Delta E_d$  vs  $W_{U(\text{or } L)}$ .

The electronic dimensionality of organic metal can be controlled by the self-assembling ability of the constituent molecules by face-to-face vs side-by-side intermolecular interactions through  $\pi$ - $\pi$ , van der Waals (including heteroatomic contacts), or hydrogen-bond interactions. The electronic dimensionality is strongly connected with the hierarchical and anisotropic 3D architecture, which can be controlled chemically. The topology of the Fermi surface depends on the electronic dimensionality and band filling.

While organic metals with a 1D Fermi surface exhibit a metal-insulator instability (Peierls or SDW), 2D organic metals with enhanced transfer interactions owing to the strong self-assembling ability like BO materials exhibit a stable metallic state, and thus, the phase transitions are rarely observed. 2D organic metals with medium transfer interactions, such as ET compounds, exhibit a variety of electronic structures, including superconductor, Mott transition, MI transition, charge-ordered state, polymorphism, etc. Especially, ET complexes cover a wide range of functionalities: 1D-2D metals, Mott insulators, 10 K class superconductors, spin-ladder, spin liquid, complex isomerization, and so on.<sup>164</sup>

In general, uniform charge distribution is required for metallic materials, while charge disproportionation (charge-ordered state) causes the non-metallic state except in some rare cases.<sup>1086</sup> In the charge-ordered state, the competing parameters are the on-site Coulomb repulsion and transfer interaction,  $U$  vs  $t$ , e.g., for the transformation from [0.5, 0.5] uniform charged metallic state to [0, 1] charge-ordered insulating state. The charge order stripe of [0, 1, 0, 1] is common for a system with strong  $V$ , and that of [0, 1, 1, 0] appears in the EDO salts owing to the decreased  $V$ . In the EDO salts, the Coulomb interactions between EDO and anion molecules also play an important role.<sup>1087</sup>

In order to describe the electronic structure of  $\kappa$ -type superconductors, the anisotropy (or geometry) of the transfer interactions  $t'/t$  is critical besides  $U/W$ . For the case where  $t'/t$  is nearly equal to unity, neither the magnetic ordered (antiferromagnetic) state nor superconducting state appears but a spin-liquid state is realized.<sup>305</sup> Application of uni-axial strain in the direction departing from  $t'/t = 1$  induces superconductivity and  $T_c$  increases with deviating  $t'/t$  from unity.

To obtain stable ionic CT complexes of fullerenes, the multicomponent system is proposed utilizing a small-sized strong donor molecule able to ionize fullerene ( $D_1$ ) and a structure-forming neutral molecule ( $D_2$ ), i.e.,  $(D_1^+)[(D_2^0)(\text{fullerene}^-)]$ , which has an enhanced stability owing to the protection of the ionized fullerene by bulky  $D_2^0$  molecules.<sup>1026</sup>  $\sigma$ -Bonded dimers formed by two negatively charged fullerenes and  $\sigma$ -bonded anions between fullerene and CoTPP ( $D_2^0$ ) are characterized.

Besides the CT solids, composite polymer film conductors, LB film conductors, evaporated thin film conductors, and conducting melts have been developed essentially based on the

same designing concepts for the crystals. For the first two conductors, the self-assembling ability and partial CT state are the key issues, and for the last one, the formation of a radical species in the melt is essential. A bifunctional CT material with a coexistence of metallic conductivity and other functions such as magnetism, optical features, etc. is not much more difficult to develop when one uses a component with strong self-assembling ability for conductivity and the other component for the other function. In general, however, these functions are independent of each other. It is an urgent task to develop a cooperative system with multifunctions displayed at moderately high temperatures.

For ionic liquids, the nephelauxetic effect, Pearson's acid-base interaction, molecular weight, size, and symmetry are the key parameters for ionic conductivity, although material design based on the first term is difficult.

Apart from the intermolecular CT compounds, single component conductors based on betainic radicals have been described, where the decreased on-site Coulomb repulsion by enhanced polarizability and decreased distance between D and A moieties are the important parameters to increase the mean free path:  $\lambda_{\text{intra}}$  vs  $(1 - \alpha/r^3)(U - V)$ .

The ionicity ( $\delta$ ) of intramolecular CT molecules,  $D^{\delta+}-\pi-A^{\delta-}$  system, is closely related to the non-linear optical hyperpolarizability and depends not only on the site energy difference ( $I_D - E_A$ ), but also on the molecular conformation; a rotational isomer with a larger ground state dipole moment has a higher ionicity.

We are very grateful to Professors Y. Matsunaga, H. Inokuchi, F. M. Menger, A. K. Colter, J. P. Ferraris, D. O. Cowan, R. M. Metzger, F. Wudl, E. B. Yagubskii, R. N. Lyubovskaya, R. P. Shibaeva, J. Ulanski, A. Tracz, K. Andres, L. Ouahab, G. J. Ashwell, O. Neilands, J. A. Schlueter, J. Tanaka, M. Kinoshita, Y. Maruyama, I. Shirotni, T. Enoki, K. Seki, N. Sato, K. Imaeda, M. Kobayashi, T. Inabe, K. Nakasuji, K. Yakushi, H. Kobayashi, T. Ishiguro, S. Kagoshima, M. Tokumoto, T. Takahashi, K. Kanoda, T. Osada, T. Koda, T. Mitani, Y. Tokura, Y. Iwasa, S. Koshihara, T. Hasegawa, K. Oshima, J. Kawamata, S. Kashino, Y. Kubozono, N. Kojima, H. Yamochi, A. Otsuka, M. Maesato, T. Mori, H. Mori(Urayama), T. Nakamura, many postdoctoral fellows (Drs. P. Wu, L. A. Kushch, O. Drozdova, K. Balodis, D. V. Konarev, S. S. Khasanov, M. A. Tanatar, K. Nishimura, M. Sakata, and T. Murata) and many students (Drs. N. Iwasawa(Okada), H. Kitagawa, T. Nakamura, T. Akutagawa, T. Komatsu, S. Horiuchi, N. Matsukawa, S. Sekizaki, S. S. Pac, A. Ota, Y. Shimizu, and others) whose names are in the references for the illuminating experiments and discussions. Finally, one of the authors (GS) wishes to thank his wife, Atsuko.

We also acknowledge the financial support from a Grant-in-Aid (21st Century COE program on Kyoto University Alliance for Chemistry), a COE Research on Elements Science (No. 12CE2005), and Grants-in-Aid for Scientific Research (Nos. 60470004, 05403013, 09304065, 10894023, 15205019, and 17750126) from the Ministry of Education, Culture, Sports, Science and Technology, Japan, a Grant for CREST of JST, and a fund for "Research for Future" from JSPS.



## References

- G. Saito, T. Inukai, *Cryst. Growth* **1989**, *16*, 2.
- G. Saito, in *Lower-Dimensional Systems and Molecular Electronics*, ed. by R. M. Metzger, P. Day, G. Papavassiliou, Plenum Press, New York, **1991**, pp. 67–84.
- G. Saito, in *New Materials*, ed. by S. K. Joshi, T. Tsuruta, C. N. R. Rao, S. Nagakura, Narosa Pub. House, New Delhi, **1992**, pp. 127–148.
- G. Saito, in *Metal-Insulator Transition Revisited*, ed. by P. P. Edwards, C. N. R. Rao, Taylor & Francis, London, **1995**, pp. 231–267.
- G. Saito, in *Organic Molecular Solids, Properties and Applications*, ed. by W. Jones, CRC Press, New York, **1997**, pp. 309–340.
- T. Ishiguro, K. Yamaji, G. Saito, *Organic Superconductors*, 2nd ed., Springer-Verlag, Berlin, **1998**, Chap. 11.
- G. Saito, Y. Yoshida, in *Studies of High Temperature Superconductors*, ed. by A. Narlikar, Nova Science Publishers, New York, **2000**, Vol. 34, pp. 133–173.
- G. Saito, in *Handbook of Superconducting Materials*, ed. by D. A. Cardwell, D. S. Ginley, Institute of Physics Pub., Bristol, **2003**, pp. 1947–1976.
- G. Saito, *Chemistry of Organic Conductors (Semiconductor, Metal and Superconductor)*, Maruzen, Tokyo, **2003**.
- G. Saito, H. Yamochi, M. Maesato, Y. Yoshida, A. Ota, Y. Shimizu, *NATO Sci. Ser., II* **2004**, *139*, 19.
- D. D. Eley, K. W. Jones, J. G. F. Littler, M. R. Willis, *Trans. Faraday Soc.* **1966**, *62*, 3192.
- H. Inokuchi, Y. Harada, Y. Maruyama, *Bull. Chem. Soc. Jpn.* **1962**, *35*, 1559.
- H. Akamatu, T. Maekawa, Y. Iida, M. Kinoshita, *Bull. Chem. Soc. Jpn.* **1964**, *37*, 849.
- K. Awaga, T. Sugano, M. Kinoshita, *Bull. Chem. Soc. Jpn.* **1985**, *58*, 1886.
- N. Karl, *Crystals: Growth, Properties, and Applications*, Springer-Verlag, **1980**.
- G. A. Samara, H. G. Drickamer, *J. Chem. Phys.* **1962**, *37*, 474.
- R. B. Aust, W. H. Bentley, H. G. Drickamer, *J. Chem. Phys.* **1964**, *41*, 1856.
- A. Onodera, N. Kawai, T. Kobayashi, *Solid State Commun.* **1975**, *17*, 775.
- Y. Matsunaga, *J. Chem. Phys.* **1965**, *42*, 2248.
- I. Shirotni, K. Kawada, H. Inokuchi, *Bull. Chem. Soc. Jpn.* **1970**, *43*, 2381.
- I. Shirotni, Y. Kamura, H. Inokuchi, T. Hirooka, *Chem. Phys. Lett.* **1976**, *40*, 257.
- A. Onodera, I. Shirotni, H. Inokuchi, N. Kawai, *Chem. Phys. Lett.* **1974**, *25*, 296.
- I. Shirotni, A. Onodera, Y. Kamura, H. Inokuchi, N. Kawai, *J. Solid State Chem.* **1976**, *18*, 235.
- T. Yokota, N. Takeshita, K. Shimizu, K. Amaya, A. Onodera, I. Shirotni, S. Endo, *Czech. J. Phys.* **1996**, *46*, Suppl. S2, 817.
- K. Amaya, K. Shimizu, N. Takeshita, M. I. Eremets, T. C. Kobayashi, S. Endo, *J. Phys.: Condens. Matter* **1998**, *10*, 11179.
- Y. Yamashita, S. Tanaka, K. Imaeda, H. Inokuchi, M. Sano, *J. Org. Chem.* **1992**, *57*, 5517.
- K. Imaeda, Y. Yamashita, Y. Li, T. Mori, H. Inokuchi, M. Sano, *J. Mater. Chem.* **1992**, *2*, 115.
- E. B. Yagubskii, N. D. Kushch, A. V. Zvarykina, O. Neilands, R. Mende, K. Balodis, *Izv. Akad. Nauk, Ser. Khim.* **1981**, *6*, 1432.
- I. Shirotni, G. Saito, unpublished results.
- P. J. Carroll, M. V. Lakshmikantham, M. P. Cava, F. Wudl, E. C. Aharon-Shalom, D. Sherman, *J. Chem. Soc., Chem. Commun.* **1982**, 1316.
- S. Matsuzaki, H. Okumura, H. Takenouchi, T. Kyouda, M. Sano, *Synth. Met.* **1991**, *39*, 385.
- E. Iwasaki, K. Shimizu, K. Amaya, A. Nakayama, K. Aoki, R. P. Carlon, *Synth. Met.* **2001**, *120*, 1003.
- I. Shirotni, M. Konno, Y. Taniguchi, *Synth. Met.* **1989**, *29*, 123.
- I. Shirotni, A. Kawamura, K. Suzuki, W. Utsumi, T. Yagi, *Bull. Chem. Soc. Jpn.* **1991**, *64*, 1607.
- I. Shirotni, Y. Inagaki, W. Utsumi, T. Yagi, *J. Mater. Chem.* **1991**, *1*, 1041.
- H. Koezuka, A. Tsumura, T. Ando, *Synth. Met.* **1987**, *18*, 699.
- C. P. Newman, C. D. Frisbie, D. A. da Silva Filho, J.-L. Bredas, P. C. Ewbank, K. R. Mann, *Chem. Mater.* **2004**, *16*, 4436.
- Y. Lin, D. J. Gundlach, S. Nelson, T. N. Jackson, *IEEE Electron Device Lett.* **1997**, *18*, 606.
- Z. Bao, A. Dodabalapur, A. J. Lovinger, *Appl. Phys. Lett.* **1996**, *69*, 4108.
- H. Sirringhaus, P. J. Brown, R. H. Friend, M. M. Nielsen, K. Bechgaard, B. M. W. Langeveld-Voss, A. J. H. Spiering, R. A. J. Janssen, E. W. Meijer, P. Herwiq, D. M. de Leeuw, *Nature* **1999**, *401*, 685.
- F. Garnier, R. Hajlaoui, A. Yasser, P. Srivastava, *Science* **1994**, *265*, 1864.
- H. Moon, R. Zeis, E.-J. Borkent, C. Besnard, A. J. lovinger, T. Siegrist, C. Kloc, Z. Bao, *J. Am. Chem. Soc.* **2004**, *126*, 15322.
- M. Wakaki, S. Ishihara, A. Aratani, M. Ando, Jpn. Kokai Tokkyo Koho 2000-66233, **2000**.
- V. Podzorov, S. E. Sysoev, E. Loginova, V. M. Pudalov, M. E. Gershenson, *Appl. Phys. Lett.* **2003**, *83*, 3504.
- V. C. Sundar, J. Zaumseil, V. Podzorov, E. Menard, R. L. Willett, T. Someya, M. E. Gershenson, J. A. Rogers, *Science* **2004**, *303*, 1644.
- M.-S. Nam, A. Ardavan, R. J. Cava, P. M. Chaikin, *Appl. Phys. Lett.* **2003**, *83*, 4782.
- M. Mas-Torrent, M. Durkut, P. Hadley, X. Ribas, C. Rovira, *J. Am. Chem. Soc.* **2004**, *126*, 984.
- E. S. Snow, J. P. Novak, P. M. Campbell, D. Park, *Appl. Phys. Lett.* **2003**, *82*, 2145.
- Z. Bao, A. J. Lovinger, J. Brown, *J. Am. Chem. Soc.* **1998**, *120*, 207.
- R. C. Haddon, A. S. Perel, R. C. Morris, T. T. M. Palstra, A. F. Hebard, R. M. Fleming, *Appl. Phys. Lett.* **1995**, *67*, 121.
- R. C. Haddon, *J. Am. Chem. Soc.* **1996**, *118*, 3041.
- K. Shibata, Y. Kubozono, T. Kanbara, T. Hosokawa, A. Fujiwara, Y. Ito, H. Shinohara, *Appl. Phys. Lett.* **2004**, *84*, 2572.
- S. Kobayashi, T. Takenobu, S. Mori, A. Fujiwara, Y. Iwasa, *Appl. Phys. Lett.* **2003**, *82*, 4581.
- H. E. Katz, J. Johnson, A. J. Lovinger, W. Li, *J. Am. Chem. Soc.* **2000**, *122*, 7787.
- P. R. L. Malenfant, C. D. Dimitrakopoulos, J. D. Gelorme, L. L. Kosbar, T. O. Graham, A. Curioni, W. Andreoni, *Appl. Phys. Lett.* **2002**, *80*, 2517.
- A. R. Brown, D. M. de Leeuw, E. J. Lous, E. E. Havinga, *Synth. Met.* **1994**, *66*, 257.

- 57 J. G. Laquindanum, H. E. Katz, A. Dodabalapur, A. J. Lovinger, *J. Am. Chem. Soc.* **1996**, *118*, 11331.
- 58 Y. Takahashi, T. Hasegawa, Y. Abe, Y. Tokura, K. Nishimura, G. Saito, *Appl. Phys. Lett.* **2005**, *86*, 063504.
- 59 C. Katayama, M. Honda, H. Kumagai, J. Tanaka, G. Saito, H. Inokuchi, *Bull. Chem. Soc. Jpn.* **1985**, *58*, 2272.
- 60 P. Wu, G. Saito, K. Imaeda, Z. Shi, T. Mori, T. Enoki, H. Inokuchi, *Chem. Lett.* **1986**, 441.
- 61 H. Inokuchi, G. Saito, K. Seki, P. Wu, T. B. Tang, T. Mori, K. Imaeda, T. Enoki, Y. Higuchi, K. Inaka, N. Yasuoka, *Chem. Lett.* **1986**, 1263.
- 62 K. Seki, T. B. Tang, T. Mori, W. P. Ji, G. Saito, H. Inokuchi, *J. Chem. Soc., Faraday Trans. 2* **1986**, *82*, 1067.
- 63 N. Okada, H. Yamochi, F. Shinozaki, K. Oshima, G. Saito, *Chem. Lett.* **1986**, 1861.
- 64 K. Imaeda, T. Enoki, Z. Shi, P. Wu, N. Okada, H. Yamochi, G. Saito, H. Inokuchi, *Bull. Chem. Soc. Jpn.* **1987**, *60*, 3163.
- 65 H. Yamochi, N. Iwasawa, H. Urayama, G. Saito, *Chem. Lett.* **1987**, 2265.
- 66 Z. Shi, T. Enoki, K. Imaeda, K. Seki, H. Inokuchi, G. Saito, *J. Phys. Chem.* **1988**, *92*, 5044.
- 67 P. Wang, T. Enoki, K. Imaeda, N. Iwasawa, H. Yamochi, H. Urayama, G. Saito, H. Inokuchi, *J. Phys. Chem.* **1989**, *93*, 5947.
- 68 Y. Li, C. Nakano, K. Imaeda, H. Inokuchi, Y. Maruyama, N. Iwasawa, G. Saito, *Bull. Chem. Soc. Jpn.* **1990**, *63*, 1857.
- 69 G. Saito, H. Yamochi, N. Iwasawa, H. Murofushi, T. Tachikawa, *Phosphorus, Sulfur Silicon* **1992**, *67*, 367.
- 70 S. Kimura, H. Kurai, T. Mori, *Tetrahedron* **2002**, *58*, 1119.
- 71 M. Ashizawa, S. Kimura, T. Mori, Y. Misaki, K. Tanaka, *Synth. Met.* **2004**, *141*, 307.
- 72 H. Inokuchi, K. Imaeda, T. Enoki, T. Mori, Y. Maruyama, G. Saito, N. Okada, H. Yamochi, K. Seki, Y. Higuchi, N. Yasuoka, *Nature* **1987**, *329*, 39.
- 73 Y. Yamashita, private communication.
- 74 J. S. Zambounis, J. Mizuguchi, G. Rihs, O. Chauvet, L. Zuppiroli, *J. Appl. Phys.* **1994**, *76*, 1824.
- 75 M. C. Rovira, J. J. Novoa, J. Tarres, C. Rovira, J. Veciana, S. Yang, D. O. Cowan, E. Canadell, *Adv. Mater.* **1995**, *7*, 1023.
- 76 Y. Maruyama, private communication.
- 77 L. M. Goldenberg, R. Andreu, M. Saviron, A. J. Moore, J. Garin, M. R. Bryce, M. C. Petty, *J. Mater. Chem.* **1995**, *5*, 1593.
- 78 N. F. Mott, *Metal-Insulator Transitions*, 2nd ed., Taylor and Francis, London, **1990**.
- 79 A. J. Epstein, S. Etemad, A. F. Garito, A. J. Heeger, *Phys. Rev. B* **1972**, *5*, 952.
- 80 A. F. Garito, A. J. Heeger, *Acc. Chem. Res.* **1974**, *7*, 232.
- 81 J. Singleton, F. L. Pratt, M. D'Amore, T. J. M. Janssen, M. Kurmoo, J. A. A. Perenboom, W. Hayes, P. Day, *Phys. Rev. Lett.* **1992**, *68*, 2500.
- 82 T. Akutagawa, G. Saito, *Bull. Chem. Soc. Jpn.* **1995**, *68*, 1753.
- 83 A. Fortunelli, A. Painelli, *Phys. Rev. B* **1997**, *55*, 16088.
- 84 T. Suzuki, M. Yamada, M. Ohkita, T. Tsuji, *Heterocycles* **2001**, *54*, 387.
- 85 A. J. Banister, N. Bricklebank, I. Lavender, J. M. Rawson, C. I. Gregory, B. K. Tanner, W. Clegg, M. R. J. Elsegood, F. Palacio, *Angew. Chem., Int. Ed. Engl.* **1996**, *35*, 2533.
- 86 F. Palacio, G. Antorrena, M. Castro, R. Burriel, J. Rawson, J. N. B. Smith, N. Bricklebank, J. Novoa, C. Ritter, *Phys. Rev. Lett.* **1997**, *79*, 2336.
- 87 M. Mito, T. Kawae, K. Takeda, S. Takagi, Y. Matsushita, H. Deguchi, J. M. Rawson, F. Palacio, *Polyhedron* **2001**, *20*, 1509.
- 88 J. M. Rawson, G. D. McManus, *Coord. Chem. Rev.* **1999**, *189*, 135.
- 89 A. W. Cordes, R. C. Haddon, R. T. Oakley, L. F. Schneemeyer, J. V. Waszczak, K. M. Young, N. M. Zimmerman, *J. Am. Chem. Soc.* **1991**, *113*, 582.
- 90 M. P. Andrews, A. W. Cordes, D. C. Douglass, R. M. Fleming, S. H. Glarum, R. C. Haddon, P. Marsh, R. T. Oakley, T. T. M. Palstra, L. F. Schneemeyer, G. W. Trucks, R. Tycko, J. V. Waszczak, K. M. Young, N. M. Zimmerman, *J. Am. Chem. Soc.* **1991**, *113*, 3559.
- 91 T. M. Barclay, A. W. Cordes, R. C. Haddon, M. E. Itkis, R. T. Oakley, R. W. Reed, H. Zhang, *J. Am. Chem. Soc.* **1999**, *121*, 969.
- 92 A. W. Cordes, R. C. Haddon, R. G. Hicks, R. T. Oakley, T. T. M. Palstra, L. F. Schneemeyer, J. V. Waszczak, *J. Am. Chem. Soc.* **1992**, *114*, 1729.
- 93 C. Joachim, J. K. Gimzewski, A. Aviram, *Nature* **2000**, *408*, 541.
- 94 C. Kittel, *Introduction to Solid State Physics*, 5th ed., John Wiley & Sons, Inc., New York, **1976**, p. 169.
- 95 D. O. Cowan, in *Proceedings of the 4th International Kyoto Conference on New Aspects of Organic Chemistry*, ed. by Z. Yoshida, T. Shiba, Y. Ohshiro, Kodansha Ltd., Tokyo, **1989**.
- 96 O. H. LeBlanc, Jr., *J. Chem. Phys.* **1965**, *42*, 4307.
- 97 B. H. Klanderman, D. C. Hoesterey, *J. Chem. Phys.* **1969**, *51*, 377.
- 98 J. Garin, J. Orduna, J. I. Ruperez, R. Alcalá, B. Villacampa, C. Sanchez, N. Martin, J. L. Segura, M. Gonzalez, *Tetrahedron Lett.* **1998**, *39*, 3577.
- 99 S. Maki, Y. Morita, H. Kitagawa, T. Mitani, K. Nakasuji, *Synth. Met.* **2001**, *120*, 741.
- 100 M. Murata, Y. Morita, K. Fukui, K. Sato, D. Shiomi, T. Takui, M. Maesato, H. Yamochi, G. Saito, K. Nakasuji, *Angew. Chem., Int. Ed.* **2004**, *43*, 6343.
- 101 Y. Tsubata, T. Suzuki, T. Miyashi, Y. Yamashita, *J. Org. Chem.* **1992**, *57*, 6749.
- 102 T. Suzuki, S. Miyanari, Y. Tsubata, T. Fukushima, T. Miyashi, Y. Yamashita, K. Imaeda, T. Ishida, T. Nogami, *J. Org. Chem.* **2001**, *66*, 216.
- 103 X. Chi, M. E. Itkis, B. O. Patrick, T. M. Barclay, R. W. Reed, R. T. Oakley, A. W. Cordes, R. C. Haddon, *J. Am. Chem. Soc.* **1999**, *121*, 10395.
- 104 M. E. Itkis, X. Chi, A. W. Cordes, R. C. Haddon, *Science* **2002**, *296*, 1443.
- 105 O. Neiland, V. Tilika, I. Sudmale, I. Grigorjeva, A. Edzina, E. Fonavs, I. Muzikante, *Adv. Mater. Opt. Electron.* **1997**, *7*, 39.
- 106 O. Neilands, *Mol. Cryst. Liq. Cryst.* **2001**, *355*, 331.
- 107 O. Neilands, S. Belyakov, V. Tilika, A. Edzina, *J. Chem. Soc., Chem. Commun.* **1995**, 325.
- 108 W. Saenger, *Principles of Nucleic Acid Structure*, Springer, New York, **1984**, p. 117.
- 109 L. Chen, L. Cai, X. Zhang, A. Rich, *Biochemistry* **1994**, *33*, 13540.
- 110 *Chem. Mater.* **1994**, *6*, No. 8.
- 111 *Organic Molecular Solids, Properties and Applications*, ed. by W. Jones, CRC Press, New York, **1997**, Chap. 6.
- 112 T. Inoue, H. Yamochi, G. Saito, K. Matsumoto, *Synth. Met.* **1995**, *70*, 1139.
- 113 K. Balodis, S. Khasanov, C. Chong, M. Maesato, H. Yamochi, G. Saito, O. Neilands, *Synth. Met.* **2003**, *133–134*, 353.

- 114 G. Saito, A. Ota, Y. Yoshida, M. Maesato, H. Yamochi, K. Balodis, O. Neilands, S. Khasanov, M. A. Tanatar, *Mol. Cryst. Liq. Cryst.* **2004**, 423, 99.
- 115 Elemental analysis for **21** (electrooxidation in DMF), calcd for  $(C_{10}H_8N_3OS_4)(C_3H_7NO)_{0.1}(H_2O)_{0.2}$ : C, 38.02; H, 2.82; N, 13.35; O, 6.39; S, 39.42%. Found: C, 38.28; H, 3.01; N, 13.09; O, 6.29; S, 39.45%. For **22** (oxidized with TCNQ in  $CH_3CN$ ), calcd for  $(C_{10}H_5N_2O_4S_4)(CH_3CN)_{0.1}(H_2O)_{0.3}$ : C, 34.52; H, 1.68; N, 8.29; O, 19.38; S, 36.14%. Found: C, 34.80; H, 1.50; N, 8.14; O, 19.34; S, 36.05%. For **23** (oxidized with TCNQ in  $CH_3CN$ ), calcd for  $(C_{10}H_8N_3OS_2Se_2)(CH_3CN)_{0.3}$ : C, 30.27; H, 2.13; N, 10.99%. Found: C, 30.00; H, 2.00; N, 11.16%.
- 116 A. Bondi, *J. Phys. Chem.* **1964**, 86, 441.
- 117 A. Schmidt, M. K. Kindermann, P. Vainiotalo, M. Nieger, *J. Org. Chem.* **1999**, 64, 9499.
- 118 C. S. Jacobsen, in *Semiconductors and Semimetals*, ed. by E. Conwell, Academic Press, New York, **1988**, Vol. 27, Chap. 5.
- 119 J. B. Torrance, B. A. Scott, B. Welber, F. B. Kaufman, P. E. Seiden, *Phys. Rev. B* **1979**, 19, 730.
- 120 T. Senga, K. Kamoshida, L. A. Kushch, G. Saito, T. Inamoto, I. Ono, *Mol. Cryst. Liq. Cryst.* **1997**, 296, 97.
- 121 G. Saito, H. Izukashi, M. Shibata, K. Yoshida, L. A. Kushch, T. Kondo, H. Yamochi, O. O. Drozdova, K. Matsumoto, M. Kusunoki, K. Sakaguchi, N. Kojima, E. B. Yagubskii, *J. Mater. Chem.* **2000**, 10, 893.
- 122 A. B. Harris, R. V. Lange, *Phys. Rev.* **1967**, 157, 295.
- 123 Y. Nakahara, K. Kimura, H. Inokuchi, T. Yagi, *Chem. Lett.* **1979**, 877.
- 124 K. Kimura, Y. Nakahara, T. Yagi, H. Inokuchi, *J. Chem. Phys.* **1979**, 70, 3317.
- 125 K. Kimura, S. Nakajima, K. Niki, H. Inokuchi, *Bull. Chem. Soc. Jpn.* **1985**, 58, 1010.
- 126 P. Cassoux, L. Valade, H. Kobayashi, A. Kobayashi, R. A. Clark, A. E. Underhill, *Coord. Chem. Rev.* **1991**, 110, 115.
- 127 N. Le Narvor, N. Robertson, T. Weyland, J. D. Kilburn, A. E. Underhill, M. Webster, N. Svenstrup, J. Becher, *Chem. Commun.* **1996**, 1363.
- 128 K. Ueda, Y. Kamata, M. Iwamatsu, T. Sugimoto, H. Fujita, *J. Mater. Chem.* **1999**, 9, 2979.
- 129 K. Ueda, M. Goto, M. Iwamatsu, T. Sugimoto, S. Endo, N. Toyota, K. Yamamoto, H. Fujita, *J. Mater. Chem.* **1998**, 8, 2195.
- 130 H. Kobayashi, H. Tanaka, M. Kumasaki, H. Torii, B. Narymbetov, T. Adachi, *J. Am. Chem. Soc.* **1999**, 121, 10763.
- 131 W. Suzuki, E. Fujiwara, A. Kobayashi, A. Hasegawa, T. Miyamoto, H. Kobayashi, *Chem. Lett.* **2002**, 936.
- 132 H. Tanaka, Y. Okano, H. Kobayashi, W. Suzuki, A. Kobayashi, *Science* **2001**, 291, 285.
- 133 H. Tanaka, M. Tokumoto, S. Ishibashi, D. Graf, E. S. Choi, J. M. Brooks, S. Yasuzuka, Y. Okano, H. Kobayashi, A. Kobayashi, *J. Am. Chem. Soc.* **2004**, 126, 10518.
- 134 A. Kobayashi, H. Tanaka, H. Kobayashi, *J. Mater. Chem.* **2001**, 11, 2078.
- 135 H. Tanaka, H. Kobayashi, A. Kobayashi, *Synth. Met.* **2003**, 135–136, 549.
- 136 W. Suzuki, E. Fujiwara, A. Kobayashi, Y. Fujishiro, E. Nishibori, M. Tanaka, M. Sakata, H. Fujiwara, H. Kobayashi, *J. Am. Chem. Soc.* **2003**, 125, 1486.
- 137 H. Tanaka, H. Kobayashi, A. Kobayashi, *J. Am. Chem. Soc.* **2002**, 124, 10002.
- 138 D. Belo, H. Alves, E. B. Lopes, M. T. Duarte, V. Gama, R. T. Henriques, M. Almeida, A. Pérez-Benítez, C. Rovira, J. Veciana, *Chem. Eur. J.* **2001**, 7, 511.
- 139 E. Fujiwara, A. Kobayashi, H. Kobayashi, *Synth. Met.* **2003**, 135–136, 535.
- 140 S.-L. Zheng, J.-P. Zhang, W.-T. Wong, X.-M. Chen, *J. Am. Chem. Soc.* **2003**, 125, 6882.
- 141 J. Janczak, R. Kubiak, A. Zaleski, J. Olejniczak, *Chem. Phys. Lett.* **1994**, 225, 72.
- 142 T. Suga, S. Isoda, T. Kobayashi, *J. Porph. Phthal.* **1999**, 3, 397.
- 143 K. Morimoto, T. Inabe, *J. Mater. Chem.* **1995**, 5, 1749.
- 144 A. Fujita, H. Hasegawa, T. Naito, T. Inabe, *J. Porph. Phthal.* **1999**, 3, 720.
- 145 Y. Orihashi, N. Kobayashi, E. Tsuchida, H. Matsuda, H. Nakanishi, M. Kato, *Chem. Lett.* **1985**, 1617.
- 146 Y. Orihashi, N. Kobayashi, H. Ohno, E. Tsuchida, H. Matsuda, H. Nakanishi, M. Kato, *Synth. Met.* **1987**, 19, 751.
- 147 B. Moubaraki, M. Ley, D. Benlian, *Acta Crystallogr., Sect. C* **1990**, 46, 379.
- 148 M. Megnamisi-Belombe, *J. Solid State Chem.* **1977**, 22, 151.
- 149 R. Foster, *Organic Charge-Transfer Complexes*, Academic Press, New York, **1969**.
- 150 F. H. Herstein, in *Perspectives in Structural Chemistry*, ed. by J. D. Dunitz, J. A. Ibers, Wiley, New York, **1971**, Vol. IV, pp. 165–395.
- 151 I. F. Shchegolev, *Phys. Status Solidi A* **1972**, 12, 9.
- 152 A. N. Bloch, in *Energy and Charge Transfer in Organic Semiconductors*, ed. by K. Masuda, M. Silver, Plenum Press, New York, **1974**, pp. 159–166.
- 153 F. Wudl, in *Chemistry and Physics of One-Dimensional Metals*, ed. by H. J. Keller, Plenum Press, New York, **1976**, pp. 233–256.
- 154 R. C. Wheland, *J. Am. Chem. Soc.* **1976**, 98, 3926.
- 155 J. B. Torrance, *Acc. Chem. Res.* **1979**, 12, 79.
- 156 F. Wudl, *Pure Appl. Chem.* **1982**, 54, 1051.
- 157 D. J. Sandman, G. P. Ceasar, *Isr. J. Chem.* **1986**, 27, 293.
- 158 P. Delhaes, in *Low-dimensional Systems and Molecular Electronics*, ed. by R. M. Metzger, P. Day, G. C. Papavassiliou, Plenum Press, New York, **1990**, pp. 43–65.
- 159 J. P. Pouget, *Mol. Cryst. Liq. Cryst.* **1993**, 230, 101.
- 160 *TTF Chemistry, Fundamentals and Application of Tetrathiafulvalene*, ed. by J. Yamada, T. Sugimoto, Kodansha, Springer, **2004**.
- 161 *Semiconductors and Semimetals*, ed. by E. Conwell, Academic Press, New York, **1988**, Vol. 27.
- 162 D. Jérôme, H. J. Schulz, *Adv. Phys.* **1982**, 31, 299.
- 163 J. M. Williams, J. R. Ferraro, R. J. Thorn, K. D. Carlson, U. Geiser, H. H. Wang, A. M. Kini, M.-H. Whangbo, *Organic Superconductors (Including Fullerenes)*, Prentice Hall, Englewood Cliffs, NJ, **1992**.
- 164 T. Ishiguro, K. Yamaji, G. Saito, *Organic Superconductors*, 2nd ed., Springer-Verlag, Berlin, **1998**.
- 165 J. Wosnitza, *Fermi Surfaces of Low-Dimensional Organic Metals and Superconductors*, Springer-Verlag, Berlin, **1996**.
- 166 J. Singleton, *Rep. Prog. Phys.* **2000**, 63, 1111.
- 167 *Mol. Cryst. Liq. Cryst.* **1982**, 78; P. D. Pathak, N. G. Vasavada, *J. Phys.* **1983**, C3, L44; *Mol. Cryst. Liq. Cryst.* **1985**, 117–121; *Physica B* **1986**, 143; *Synth. Met.* **1987**, 17–18; *Synth. Met.* **1989**, 27; *Synth. Met.* **1991**, 41–43; *Synth. Met.* **1993**, 55–57; *Synth. Met.* **1995**, 69–71; *Synth. Met.* **1997**, 84–86; *Synth. Met.* **1999**, 103; *Synth. Met.* **2001**, 120; *Synth. Met.* **2003**, 133–134; *Synth. Met.* **2003**, 135–136; *Chem. Rev.* **2004**, 104, No. 11.
- 168 <http://www.ossckuchem.kyoto-u.ac.jp/database/file-link>.

html.

- 169 H. Akamatu, H. Inokuchi, Y. Matsunaga, *Nature* **1954**, 173, 168.
- 170 W. A. Little, *Phys. Rev. A* **1964**, 134, 1416.
- 171 V. L. Ginzburg, *Contemp. Phys.* **1968**, 9, 355.
- 172 R. E. Peierls, *Quantum Theory of Solids*, Oxford Univ. Press, London, **1955**.
- 173 D. S. Acker, R. J. Harder, W. R. Hertler, W. Mahler, L. R. Melby, R. E. Benson, W. E. Mochel, *J. Am. Chem. Soc.* **1960**, 82, 6408.
- 174 D. L. Coffen, *Tetrahedron Lett.* **1970**, 11, 2633.
- 175 F. Wudl, G. M. Smith, E. J. Hufnagel, *J. Chem. Soc., Chem. Commun.* **1970**, 1453.
- 176 J. P. Ferraris, D. O. Cowan, V. Walatka, Jr., J. H. Perlstein, *J. Am. Chem. Soc.* **1973**, 95, 948.
- 177 L. B. Coleman, M. J. Cohen, D. J. Sandman, F. G. Yamagishi, A. F. Garito, A. J. Heeger, *Solid State Commun.* **1973**, 12, 1125.
- 178 H. M. McConnell, B. M. Hoffman, R. M. Metzger, *Proc. Natl. Acad. Sci. U.S.A.* **1965**, 53, 46.
- 179 H. Shiba, *Phys. Rev. B* **1972**, 6, 930.
- 180 Z. G. Soos, S. Kuwajima, R. H. Harding, *J. Chem. Phys.* **1986**, 85, 601.
- 181 J. B. Torrance, B. D. Silverman, *Phys. Rev. B* **1977**, 15, 788.
- 182 Y. Matsunaga, *Bull. Chem. Soc. Jpn.* **1969**, 42, 2490.
- 183 Y. Matsunaga, G. Saito, *Bull. Chem. Soc. Jpn.* **1971**, 44, 958.
- 184 G. Saito, J. P. Ferraris, *Bull. Chem. Soc. Jpn.* **1980**, 53, 2141.
- 185 J. B. Torrance, Y. Tomkiewicz, R. Bozio, C. Pecile, C. R. Wolfe, K. Bechgaard, *Phys. Rev. B* **1982**, 26, 2267.
- 186 E. M. Hawley, T. O. Poehler, T. F. Carruthers, A. N. Bloch, D. O. Cowan, T. J. Kistenmacher, *Bull. Am. Phys. Soc.* **1978**, 23, 424.
- 187 J. B. Torrance, J. J. Mayerle, K. Bechgaard, B. D. Silverman, Y. Tomkiewicz, *Phys. Rev. B* **1980**, 22, 4960.
- 188 T. J. Emge, D. O. Cowan, A. N. Bloch, T. J. Kistenmacher, *Mol. Cryst. Liq. Cryst.* **1983**, 95, 191.
- 189 J. W. Bray, H. R. Hart, Jr., L. V. Interrante, I. S. Jacobs, J. S. Kasper, G. D. Watkins, S. H. Wei, J. C. Bonner, *Phys. Rev. Lett.* **1975**, 35, 744.
- 190 D. Bloch, J. Voiron, J. C. Bonner, J. W. Bray, I. S. Jacobs, L. V. Interrante, *Phys. Rev. Lett.* **1980**, 44, 294.
- 191 J. W. Bray, L. V. Interrante, I. S. Jacobs, J. C. Bonner, in *Extended Linear Chain Compounds*, ed. by J. S. Miller, Plenum Press, New York, **1983**, Vol. 3, pp. 353–415.
- 192 K. Bechgaard, D. O. Cowan, A. N. Bloch, *J. Chem. Soc., Chem. Commun.* **1974**, 937.
- 193 K. Bechgaard, D. O. Cowan, A. N. Bloch, *Mol. Cryst. Liq. Cryst.* **1976**, 32, 227.
- 194 J. S. Chappell, A. N. Bloch, W. A. Bryden, M. Maxfield, T. O. Poehler, D. O. Cowan, *J. Am. Chem. Soc.* **1981**, 103, 2442. It should be noted, however, that the authors of this paper used both  $b_{1u}$  and  $a_g$  modes of  $C\equiv N$  stretching in their analysis. If one uses only  $b_{1u}$  modes of IR spectra, the linear relation between  $\nu_{C\equiv N}$  and the degree of CT ( $\delta$ ) is held only below  $\delta = 0.5$ .
- 195 T. J. Emge, F. M. Wiygul, J. S. Chappell, A. N. Bloch, J. P. Ferraris, D. O. Cowan, T. J. Kistenmacher, *Mol. Cryst. Liq. Cryst.* **1982**, 87, 137.
- 196 T. J. Kistenmacher, T. J. Emge, A. N. Bloch, D. O. Cowan, *Acta Crystallogr., Sect. B* **1982**, 38, 1193.
- 197 J. R. Andersen, R. A. Craven, J. E. Weidenborner, E. M. Engler, *J. Chem. Soc., Chem. Commun.* **1977**, 526.
- 198 M. Mizuno, A. F. Garito, M. P. Cava, *J. Chem. Soc., Chem. Commun.* **1978**, 18.
- 199 G. Saito, H. Hayashi, T. Enoki, H. Inokuchi, *Mol. Cryst. Liq. Cryst.* **1985**, 120, 341.
- 200 T. Mori, H. Inokuchi, *Solid State Commun.* **1986**, 59, 355.
- 201 T. Mori, H. Inokuchi, *Bull. Chem. Soc. Jpn.* **1987**, 60, 402.
- 202 Y. Iwasa, K. Mizuhashi, T. Koda, Y. Tokura, G. Saito, *Phys. Rev. B* **1994**, 49, 3580.
- 203 H. M. Yamamoto, M. Hagiwara, R. Kato, *Synth. Met.* **2003**, 133–134, 449.
- 204 H. M. Yamamoto, N. Tajima, M. Hagiwara, R. Kato, J.-I. Yamaura, *Synth. Met.* **2003**, 135–136, 623.
- 205 G. Saito, T. Enoki, K. Toriumi, H. Inokuchi, *Solid State Commun.* **1982**, 42, 557.
- 206 G. Saito, T. Enoki, H. Inokuchi, H. Kobayashi, *J. Phys.* **1983**, C44, 1215.
- 207 C. S. Jacobsen, H. J. Pedersen, K. Mortensen, K. Bechgaard, *J. Phys. C: Solid State Phys.* **1980**, 13, 3411.
- 208 J. B. Torrance, J. E. Vazquez, J. J. Mayerle, V. Y. Lee, *Phys. Rev. Lett.* **1981**, 46, 253.
- 209 J. B. Torrance, J. J. Mayerle, V. Y. Lee, K. Bechgaard, *J. Am. Chem. Soc.* **1979**, 101, 4747.
- 210 P. Batail, S. J. LaPlaca, J. J. Mayerle, J. B. Torrance, *J. Am. Chem. Soc.* **1981**, 103, 951.
- 211 J. B. Torrance, A. Girlando, J. J. Mayerle, J. L. Crowley, V. Y. Lee, P. Batail, S. J. LaPlaca, *Phys. Rev. Lett.* **1981**, 47, 1747.
- 212 J. Hubbard, J. B. Torrance, *Phys. Rev. Lett.* **1981**, 47, 1750.
- 213 R. M. Metzger, J. B. Torrance, *J. Am. Chem. Soc.* **1985**, 107, 117.
- 214 S. Matsuzaki, T. Moriyama, M. Onomichi, K. Toyoda, *Bull. Chem. Soc. Jpn.* **1983**, 56, 369.
- 215 K. Nakasuji, M. Sasaki, T. Kotani, I. Murata, T. Enoki, K. Imaeda, H. Inokuchi, A. Kawamoto, J. Tanaka, *J. Am. Chem. Soc.* **1987**, 109, 6970.
- 216 K. Imaeda, T. Enoki, H. Inokuchi, M. Sasaki, K. Nakasuji, I. Murata, *Bull. Chem. Soc. Jpn.* **1989**, 62, 372.
- 217 K. Imaeda, T. Enoki, H. Inokuchi, G. Saito, *Mol. Cryst. Liq. Cryst.* **1986**, 141, 131.
- 218 Y. Iwasa, T. Koda, Y. Tokura, A. Kobayashi, N. Iwasawa, G. Saito, *Phys. Rev. B* **1990**, 42, 2374.
- 219 T. Mitani, G. Saito, Y. Tokura, T. Koda, *Phys. Rev. Lett.* **1984**, 53, 842.
- 220 N. Nagaosa, J. Takimoto, *J. Phys. Soc. Jpn.* **1986**, 55, 2735; **1986**, 55, 3488.
- 221 Y. Tokura, H. Okamoto, T. Koda, T. Mitani, G. Saito, *Phys. Rev. B* **1988**, 38, 2215.
- 222 S. Koshihara, Y. Tokura, T. Mitani, G. Saito, T. Koda, *Phys. Rev. B* **1990**, 42, 6853.
- 223 Y. Tokura, S. Koshihara, Y. Iwasa, H. Okamoto, T. Komatsu, T. Koda, N. Iwasawa, G. Saito, *Phys. Rev. Lett.* **1989**, 21, 2405.
- 224 Y. Iwasa, T. Koda, S. Koshihara, Y. Tokura, N. Iwasawa, G. Saito, *Phys. Rev. B* **1989**, 39, 10441.
- 225 Y. Iwasa, T. Koda, Y. Tokura, S. Koshihara, N. Iwasawa, G. Saito, *Appl. Phys. Lett.* **1989**, 55, 2111.
- 226 R. Sadohara, S. Matsuzaki, *Mol. Cryst. Liq. Cryst.* **1997**, 296, 269.
- 227 S. Matsuzaki, T. Hiejima, M. Sano, *Bull. Chem. Soc. Jpn.* **1991**, 64, 2052.
- 228 S. Matsuzaki, T. Hiejima, M. Sano, *Solid State Commun.*

1992, 82, 301.

229 K. Tasaki, S. Matsuzaki, V. M. Yartsev, *Solid State Commun.* **1997**, 103, 365.

230 S. Aoki, T. Nakayama, A. Miura, *Phys. Rev. B* **1993**, 48, 626.

231 S. Basaki, S. Matsuzaki, *Solid State Commun.* **1994**, 91, 865.

232 S. Aoki, T. Nakayama, *Phys. Rev. B* **1997**, 56, R2893.

233 K. Nakasuji, *Pure Appl. Chem.* **1990**, 62, 477.

234 S. Horiuchi, H. Yamochi, G. Saito, K. Sakaguchi, M. Kusunoki, *J. Am. Chem. Soc.* **1996**, 118, 8604.

235 G. Saito, H. Sasaki, T. Aoki, Y. Yoshida, A. Otsuka, H. Yamochi, O. O. Drozdova, K. Yakushi, H. Kitagawa, T. Mitani, *J. Mater. Chem.* **2002**, 12, 1640.

236 G. Saito, T. Enoki, H. Inokuchi, H. Kumagai, J. Tanaka, *Chem. Lett.* **1983**, 503.

237 G. Saito, H. Kumagai, J. Tanaka, T. Enoki, H. Inokuchi, *Mol. Cryst. Liq. Cryst.* **1985**, 120, 337.

238 S. S. Pac, G. Saito, *J. Solid State Chem.* **2002**, 168, 486.

239 F. Wudl, H. Yamochi, T. Suzuki, H. Isotalo, C. Fite, H. Kasmai, K. Liou, G. Srdanov, P. Coppens, K. Maly, K. Frost-Jensen, *J. Am. Chem. Soc.* **1990**, 112, 2461.

240 O. Drozdova, H. Yamochi, K. Yakushi, M. Uruichi, S. Horiuchi, G. Saito, *J. Am. Chem. Soc.* **2000**, 122, 4436.

241 S. Horiuchi, H. Yamochi, G. Saito, K. Matsumoto, *Mol. Cryst. Liq. Cryst.* **1996**, 284, 357.

242 Y. Yoshida, T. Aoki, H. Sasaki, M. Shiinoki, H. Yamochi, G. Saito, *Mol. Cryst. Liq. Cryst.* **2003**, 394, 105.

243 G. Saito, S. S. Pac, O. O. Drozdova, *Synth. Met.* **2001**, 120, 667.

244 A. Ota, H. Yamochi, G. Saito, *Mol. Cryst. Liq. Cryst.* **2002**, 376, 177.

245 G. Saito, S. Hirate, K. Nishimura, H. Yamochi, *J. Mater. Chem.* **2001**, 11, 723.

246 G. Saito, T. Teramoto, A. Otsuka, Y. Sugita, T. Ban, M. Kusunoki, K. Sakaguchi, *Synth. Met.* **1994**, 64, 359.

247 G. Saito, Y. Matsunaga, *Bull. Chem. Soc. Jpn.* **1971**, 44, 3328.

248 T. Akutagawa, G. Saito, M. Kusunoki, K. Sakaguchi, *Bull. Chem. Soc. Jpn.* **1996**, 69, 2487.

249 K. Nishimura, S. S. Khasanov, G. Saito, *J. Mater. Chem.* **2002**, 12, 1693.

250 R. P. Shibaeva, V. F. Kaminskii, E. B. Yagubskii, *Mol. Cryst. Liq. Cryst.* **1985**, 119, 361.

251 T. Mori, H. Inokuchi, Y. Misaki, T. Yamabe, H. Mori, S. Tanaka, *Bull. Chem. Soc. Jpn.* **1994**, 67, 661.

252 M. Ashizawa, A. Akutsu, B. Noda, H. Nii, T. Kawamoto, T. Mori, T. Nakayashiki, Y. Misaki, K. Tanaka, K. Takimiya, T. Otsubo, *Bull. Chem. Soc. Jpn.* **2004**, 77, 1449.

253 K. Takimiya, A. Ohnishi, Y. Aso, T. Otsubo, F. Ogura, K. Kawabata, K. Tanaka, M. Mizutani, *Bull. Chem. Soc. Jpn.* **1994**, 67, 766.

254 G. Saito, T. Enoki, H. Inokuchi, H. Kumagai, C. Katayama, J. Tanaka, *Mol. Cryst. Liq. Cryst.* **1985**, 120, 345.

255 J. Tanaka, C. Katayama, H. Kumagai, G. Saito, T. Enoki, H. Inokuchi, *Mol. Cryst. Liq. Cryst.* **1985**, 125, 223.

256 J. P. Ferraris, T. O. Poehler, A. N. Bloch, D. O. Cowan, *Tetrahedron Lett.* **1973**, 27, 2253.

257 E. Ehrenfreund, S. K. Khanna, A. F. Garito, A. J. Heeger, *Solid State Commun.* **1977**, 22, 139.

258 L. I. Buravov, O. N. Eremenko, R. B. Lyubovskii, L. P. Rozenberg, M. L. Khidekel, R. P. Shibaeva, I. F. Shchegolev,

E. B. Yagubskii, *Pis'ma Zh. Eksp. Teor. Fiz.* **1974**, 20, 457.

259 T. Mori, P. Wu, K. Imaeda, T. Enoki, H. Inokuchi, *Synth. Met.* **1987**, 19, 545.

260 G. Matsubayashi, A. Yokozawa, *Inorg. Chim. Acta* **1992**, 193, 137.

261 G. Matsubayashi, A. Yokozawa, *J. Chem. Soc., Dalton Trans.* **1990**, 3535.

262 D. Meenenga, K. P. Dinse, D. Schweitzer, H. J. Keller, *Mol. Cryst. Liq. Cryst.* **1985**, 120, 243.

263 L. Alcacer, A. H. Maki, *J. Phys. Chem.* **1974**, 78, 215.

264 V. Gama, M. Almeida, R. T. Henriques, I. C. Santos, A. Domingos, S. Ravy, J. P. Pouget, *J. Phys. Chem.* **1991**, 95, 4263.

265 M. Schiller, W. Schmidt, E. Balthes, D. Schweitzer, H.-J. Koo, M.-H. Whangbo, I. Heinen, T. Klaus, P. Kircher, W. Strunz, *Europhys. Lett.* **2000**, 51, 82.

266 K. Nishimura, T. Kondo, O. O. Drozdova, H. Yamochi, G. Saito, *J. Mater. Chem.* **2000**, 10, 911.

267 H. Kobayashi, R. Kato, T. Mori, A. Kobayashi, Y. Sasaki, G. Saito, T. Enoki, H. Inokuchi, *Chem. Lett.* **1984**, 179.

268 L.-K. Chou, M. A. Quijada, M. B. Clevenger, G. F. de Oliveira, K. A. Abboud, D. B. Tanner, D. R. Talham, *Chem. Mater.* **1995**, 7, 530.

269 H. Urayama, G. Saito, T. Inabe, T. Mori, Y. Maruyama, *Synth. Met.* **1987**, 19, 469.

270 H. Urayama, T. Inabe, T. Mori, Y. Maruyama, G. Saito, *Bull. Chem. Soc. Jpn.* **1988**, 61, 1831.

271 D. R. Rosseinsky, P. Kathirgamanathan, *Mol. Cryst. Liq. Cryst.* **1982**, 86, 1783.

272 P. Kathirgamanathan, D. R. Rosseinsky, *J. Chem. Soc., Chem. Commun.* **1980**, 356.

273 T. Otsubo, Y. Nobuhara, K. Kanefuji, Y. Aso, F. Ogura, *J. Phys. Org. Chem.* **1988**, 1, 275.

274 T. Nogami, H. Tanaka, S. Ohnishi, Y. Tasaka, H. Mikawa, *Bull. Chem. Soc. Jpn.* **1984**, 57, 22.

275 L. Valade, J. P. Legros, M. Bousseau, P. Cassoux, M. Garbaskas, L. V. Interrante, *J. Chem. Soc., Dalton Trans.* **1985**, 783.

276 A. E. Underhill, D. W. Watkins, J. M. Williams, K. Carneiro, in *Extended Linear Chain Compounds*, ed. by J. S. Miller, Plenum Press, New York, **1981**, Vol. 1, pp. 119–156.

277 J. L. Petersen, C. S. Schramm, D. R. Stojakovic, B. M. Hoffman, T. J. Marks, *J. Am. Chem. Soc.* **1977**, 99, 286.

278 C. S. Schramm, R. P. Djordje, D. R. Stojakovic, B. M. Hoffman, J. A. Ibers, T. J. Marks, *J. Am. Chem. Soc.* **1980**, 102, 6702.

279 L. D. Brown, D. W. Kalina, M. S. McClure, S. Schulz, S. L. Ruby, J. A. Ibers, C. R. Kannewurf, T. J. Marks, *J. Am. Chem. Soc.* **1979**, 101, 2937.

280 J. S. Miller, C. H. Griffiths, *J. Am. Chem. Soc.* **1977**, 99, 749.

281 M. Cowie, A. Gleizes, G. W. Grynkeiwich, D. W. Kalina, M. S. McClure, R. P. Scaringe, R. C. Teitelbaum, S. L. Ruby, J. A. Ibers, C. R. Kannewurf, T. J. Marks, *J. Am. Chem. Soc.* **1977**, 99, 2921.

282 M. Tamura, R. Kato, *J. Phys. Soc. Jpn.* **2004**, 73, 3108.

283 J. C. Scott, in Ref. 161, Chap. 6.

284 M. Tokumoto, H. Anzai, T. Ishiguro, G. Saito, H. Kobayashi, R. Kato, A. Kobayashi, *Synth. Met.* **1987**, 19, 215.

285 N. Yoneyama, A. Miyazaki, T. Enoki, G. Saito, *Synth. Met.* **1997**, 86, 2029.

286 N. Yoneyama, A. Miyazaki, T. Enoki, G. Saito, *Bull. Chem. Soc. Jpn.* **1999**, 72, 639.



- 287 S. D. Obertelli, R. H. Friend, D. R. Talham, M. Kurmoo, P. Day, *J. Phys.: Condens. Matter* **1989**, *1*, 5671.
- 288 I. D. Parker, R. H. Friend, M. Kurmoo, P. Day, *J. Phys.: Condens. Matter* **1989**, *1*, 5681.
- 289 B. H. Ward, C. E. Granroth, K. A. Abboud, M. W. Meisel, D. R. Talham, *Chem. Mater.* **1998**, *10*, 1102.
- 290 S. Sekizaki, H. Yamochi, G. Saito, *Synth. Met.* **2001**, *120*, 961.
- 291 S. Sekizaki, N. Matsukawa, H. Yamochi, G. Saito, *Synth. Met.* **2003**, *133–134*, 455.
- 292 Md. B. Zaman, J. Toyoda, Y. Morita, S. Nakamura, H. Yamochi, G. Saito, K. Nishimura, N. Yoneyama, T. Enoki, K. Nakasuji, *J. Mater. Chem.* **2001**, *11*, 2211.
- 293 K. Nishimura, G. Saito, G. G. Abashev, A. G. Tenishev, *Synth. Met.* **2001**, *120*, 911.
- 294 K. Uchiyama, M. Miyashita, H. Taniguchi, K. Satoh, N. Mori, K. Miyagawa, K. Kanoda, M. Hedo, Y. Uwatoko, *J. Phys. IV* **2004**, *114*, 387.
- 295 M. Kurmoo, P. Day, T. Mitani, H. Kitagawa, H. Shimoda, D. Yoshida, P. Guionneau, Y. Barrans, D. Chasseau, L. Ducasse, *Bull. Chem. Soc. Jpn.* **1996**, *69*, 1233.
- 296 T. Komatsu, H. Sato, T. Nakamura, N. Matsukawa, H. Yamochi, G. Saito, M. Kusunoki, K. Sakaguchi, S. Kagoshima, *Bull. Chem. Soc. Jpn.* **1995**, *68*, 2223.
- 297 T. Yamamoto, K. Yakushi, Y. Shimizu, G. Saito, *J. Phys. Soc. Jpn.* **2004**, *73*, 2326.
- 298 J. M. Williams, A. M. Kini, H. H. Wang, K. D. Carlson, U. Geiser, L. K. Montgomery, G. J. Pyrk, D. M. Watkins, J. M. Kommers, S. J. Boryschuk, A. V. Crouch, W. K. Kwok, J. E. Schirber, D. L. Overmyer, D. Jung, M.-H. Whangbo, *Inorg. Chem.* **1990**, *29*, 3272.
- 299 U. Welp, S. Fleshler, W. K. Kwok, G. W. Crabtree, K. D. Carlson, H. H. Wang, U. Geiser, J. M. Williams, V. M. Hitsman, *Phys. Rev. Lett.* **1992**, *69*, 840.
- 300 J. E. Schirber, D. L. Overmyer, K. D. Carlson, J. M. Williams, A. M. Kini, H. H. Wang, H. A. Charlier, B. J. Love, D. M. Watkins, G. A. Yaconi, *Phys. Rev. B* **1991**, *44*, 4666.
- 301 A. Kawamoto, K. Miyagawa, K. Kanoda, *Phys. Rev. B* **1997**, *55*, 14140.
- 302 H. Ito, T. Kondo, H. Sasaki, G. Saito, T. Ishiguro, *Synth. Met.* **1999**, *103*, 1818.
- 303 U. Geiser, H. H. Wang, K. D. Carlson, J. M. Williams, H. A. Charlier, Jr., J. E. Heindl, G. A. Yaconi, B. H. Love, M. W. Lathrop, J. E. Schirber, D. L. Overmyer, J. Ren, M.-H. Whangbo, *Inorg. Chem.* **1991**, *30*, 2586.
- 304 T. Komatsu, T. Nakamura, N. Matsukawa, H. Yamochi, G. Saito, *Solid State Commun.* **1991**, *80*, 843.
- 305 Y. Shimizu, K. Miyagawa, K. Kanoda, M. Maesato, G. Saito, *Phys. Rev. Lett.* **2003**, *91*, 107001.
- 306 M. Kurmoo, M. Allan, R. H. Friend, D. Chasseau, G. Bravic, P. Day, *Synth. Met.* **1991**, *42*, 2127.
- 307 M. Kurmoo, P. Day, P. Guionneau, G. Bravic, D. Chasseau, L. Ducasse, M. L. Allan, I. D. Marsden, R. H. Friend, *Inorg. Chem.* **1996**, *35*, 4719.
- 308 A. Miyazaki, K. Yamaguchi, T. Enoki, G. Saito, *Synth. Met.* **1997**, *86*, 2033.
- 309 J.-I. Yamaura, K. Suzuki, Y. Kaizu, T. Enoki, K. Murata, G. Saito, *J. Phys. Soc. Jpn.* **1996**, *65*, 2645.
- 310 H. Kobayashi, R. Kato, A. Kobayashi, G. Saito, M. Tokumoto, H. Anzai, T. Ishiguro, *Chem. Lett.* **1986**, 93.
- 311 T. J. Emge, H. H. Wang, P. C. W. Leung, P. R. Rust, J. D. Cook, P. L. Jackson, K. D. Carlson, J. M. Williams, M.-H. Whangbo, E. L. Venturini, J. E. Schirber, L. J. Azevedo, J. R. Ferraro, *J. Am. Chem. Soc.* **1986**, *108*, 695.
- 312 A. Ugawa, K. Yakushi, H. Kuroda, A. Kawamoto, J. Tanaka, *Synth. Met.* **1988**, *22*, 305.
- 313 D. Chasseau, D. Watkin, M. J. Rosseinsky, M. Kurmoo, D. R. Talham, P. Day, *Synth. Met.* **1988**, *24*, 117.
- 314 W. H. Watson, A. M. Kini, M. A. Beno, L. K. Montgomery, H. H. Wang, K. D. Carlson, B. D. Gates, S. F. Tytko, J. Derose, C. Carris, C. A. Rohl, J. M. Williams, *Synth. Met.* **1989**, *33*, 1.
- 315 H. Yamochi, T. Tsuji, G. Saito, T. Suzuki, T. Miyashi, C. Kabuto, *Synth. Met.* **1988**, *27*, A479.
- 316 M. A. Beno, D. D. Cox, J. M. Williams, J. F. Kwak, *Acta Crystallogr., Sect. C* **1984**, *40*, 1334.
- 317 T. Mori, F. Sakai, G. Saito, H. Inokuchi, *Chem. Lett.* **1986**, 1589.
- 318 U. Geiser, H. H. Wang, J. A. Schlueter, S. L. Hallenbeck, T. J. Allen, M. Y. Chen, H.-C. I. Kao, K. D. Carlson, L. E. Gerdorn, J. M. Williams, *Acta Crystallogr., Sect. C* **1988**, *44*, 1544.
- 319 K. Bechgaard, C. S. Jacobsen, K. Mortensen, J. H. Pedersen, N. Thorup, *Solid State Commun.* **1980**, *33*, 1119.
- 320 D. Jerome, A. Mazaud, M. Ribault, K. Bechgaard, *J. Phys., Lett.* **1980**, *41*, L95.
- 321 K. Bechgaard, K. Carneiro, F. B. Rasmussen, M. Olsen, G. Rindorf, C. S. Jacobsen, H. J. Pedersen, J. C. Scott, *J. Am. Chem. Soc.* **1981**, *103*, 2440.
- 322 C. S. Jacobsen, K. Mortensen, M. Weger, K. Bechgaard, *Solid State Commun.* **1981**, *38*, 423.
- 323 S. S. P. Parkin, D. Jerome, K. Bechgaard, *Mol. Cryst. Liq. Cryst.* **1982**, *79*, 213.
- 324 K. Bechgaard, *Mol. Cryst. Liq. Cryst.* **1982**, *79*, 1.
- 325 F. Wudl, E. Aharon-Shalom, D. Nalewajek, J. V. Waszczak, W. M. Walsh, Jr., L. W. Rupp, Jr., P. M. Chaikin, R. Lacoe, M. Burns, T. O. Poehler, J. M. Williams, M. A. Beno, *J. Chem. Phys.* **1982**, *76*, 5497.
- 326 P. M. Grant, *J. Phys. C: Solid State Phys.* **1983**, *3*, 847.
- 327 D. Jerome, *Chem. Rev.* **2004**, *104*, 5565.
- 328 M. Sakata, Y. Yoshida, M. Maesato, G. Saito, K. Matsumoto, R. Hagiwara, *Mol. Cryst. Liq. Cryst.* **2006**, *452*, 103.
- 329 R. Laversanne, C. Coulon, B. Gallois, J. P. Pouget, R. Moret, *J. Phys., Lett.* **1984**, *45*, L393.
- 330 G. Brun, B. Liautard, S. Peytavin, M. Maurin, E. Toreilles, J. M. Fabre, L. Giral, J. L. Galigne, *J. Phys.* **1977**, *38*, 266.
- 331 P. Delhaes, C. Coulon, J. Amiel, S. Flandrois, E. Toreilles, J. M. Fabre, L. Giral, *Mol. Cryst. Liq. Cryst.* **1979**, *50*, 43.
- 332 C. Coulon, S. S. P. Parkin, R. Laversanne, *Mol. Cryst. Liq. Cryst.* **1985**, *119*, 325.
- 333 S. Flandrois, A. Maaroufi, *Nouv. J. Chim.* **1985**, *9*, 369.
- 334 F. Nad', P. Monceau, J. M. Fabre, *Eur. Phys. J. B* **1998**, *3*, 301.
- 335 L. Balicas, K. Behnia, W. Kang, E. Canadell, P. Auban-Senzier, D. Jerome, M. Ribault, J. M. Fabre, *J. Phys. I* **1994**, *4*, 1539.
- 336 T. Adachi, E. Ojima, K. Kato, H. Kobayashi, T. Miyazaki, M. Tokumoto, A. Kobayashi, *J. Am. Chem. Soc.* **2000**, *122*, 3238.
- 337 P. Auban-Senzier, C. Pasquier, D. Jerome, C. Carcel, J. M. Fabre, *Synth. Met.* **2003**, *133–134*, 11.
- 338 J. P. Pouget, G. Shirane, K. Bechgaard, J. M. Fabre, *Phys. Rev. B* **1983**, *27*, 5203.
- 339 S. Kagoshima, T. Yasunaga, T. Ishiguro, H. Anzai, G. Saito, *Solid State Commun.* **1983**, *46*, 867.

- 340 T. Takahashi, D. Jerome, K. Bechgaard, *J. Phys., Lett.* **1982**, 43, L565.
- 341 H. Schwenk, K. Andres, F. Wudl, *Phys. Rev. B* **1984**, 29, 500.
- 342 T. Ishiguro, K. Murata, K. Kajimura, N. Kinoshita, H. Tokumoto, M. Tokumoto, T. Ukachi, H. Anzai, G. Saito, *J. Phys. C: Solid State Phys.* **1983**, 3, 831.
- 343 K. Mortensen, Y. Tomkiewicz, K. Bechgaard, *Phys. Rev. B* **1982**, 25, 3319.
- 344 J. B. Torrance, H. J. Pedersen, K. Bechgaard, *Phys. Rev. Lett.* **1982**, 49, 881.
- 345 S. S. P. Parkin, J. C. Scott, J. B. Torrance, E. M. Engler, *Phys. Rev. B* **1982**, 26, 6319.
- 346 T. Takahashi, Y. Maniwa, H. Kawamura, G. Saito, *Physica B* **1986**, 143, 417.
- 347 J. M. Williams, M. A. Beno, J. C. Sullivan, L. M. Banovetz, J. M. Braam, G. S. Blackman, K. D. Carlson, D. L. Greer, D. M. Loesing, K. Carneiro, *Phys. Rev. B* **1983**, 28, 2873.
- 348 T. J. Kistenmacher, *Mol. Cryst. Liq. Cryst.* **1986**, 136, 361.
- 349 I. J. Lee, M. J. Naughton, G. M. Tanner, P. M. Chaikin, *Phys. Rev. Lett.* **1997**, 78, 3555.
- 350 M. Takigawa, H. Yasuoka, G. Saito, *J. Phys. Soc. Jpn.* **1987**, 56, 873.
- 351 Y. Hasegawa, H. Fukuyama, *J. Phys. Soc. Jpn.* **1987**, 56, 877.
- 352 J. F. Kwak, J. E. Schirber, R. L. Greene, E. M. Engler, *Phys. Rev. Lett.* **1981**, 46, 1296.
- 353 S. K. McKernan, S. T. Hannahs, U. M. Scheven, G. M. Danner, P. M. Chaikin, *Phys. Rev. Lett.* **1995**, 75, 1630.
- 354 T. Osada, N. Miura, I. Ogura, G. Saito, *Phys. Rev. Lett.* **1987**, 58, 1563.
- 355 D. Jerome, *Science* **1991**, 252, 1509.
- 356 K. Oshima, T. Mori, H. Inokuchi, H. Urayama, H. Yamochi, G. Saito, *Phys. Rev. B* **1988**, 38, 938.
- 357 M. V. Kartsovnik, A. E. Kovalev, V. N. Laukhin, H. Ito, T. Ishiguro, N. D. Kushch, H. Anzai, G. Saito, *Synth. Met.* **1995**, 70, 819.
- 358 T. Sasaki, H. Sato, N. Toyota, *Solid State Commun.* **1990**, 76, 507.
- 359 T. Mori, A. Kobayashi, Y. Sasaki, H. Kobayashi, G. Saito, H. Inokuchi, *Bull. Chem. Soc. Jpn.* **1984**, 57, 627.
- 360 J. Kübler, C. B. Sommers, in *The Physics and Chemistry of Organic Superconductors*, ed. by G. Saito, S. Kagoshima, Springer-Verlag, Berlin, **1990**, pp. 208–211.
- 361 T. Osada, A. Kawasumi, R. Yagi, S. Kagoshima, N. Miura, M. Oshima, H. Mori, T. Nakamura, G. Saito, *Solid State Commun.* **1990**, 75, 901.
- 362 T. Osada, R. Yagi, A. Kawasumi, S. Kagoshima, N. Miura, M. Oshima, G. Saito, *Phys. Rev. B* **1990**, 41, 5428.
- 363 T. Sasaki, H. Sato, N. Toyota, *Synth. Met.* **1991**, 42, 2211.
- 364 Y. Iye, R. Yagi, N. Hanasaki, S. Kagoshima, H. Mori, H. Fujimoto, G. Saito, *J. Phys. Soc. Jpn.* **1994**, 63, 674.
- 365 A. J. Berlinsky, J. F. Carolan, L. Weiler, *Solid State Commun.* **1974**, 15, 795.
- 366 R. Kato, Y.-L. Liu, H. Sawa, S. Aonuma, A. Ichikawa, H. Takahashi, N. Mori, *Solid State Commun.* **1995**, 94, 973.
- 367 R. Ramakumar, Y. Tanaka, K. Yamaji, *Phys. Rev. B* **1997**, 56, 795.
- 368 M.-H. Whangbo, J. M. Williams, P. C. W. Leung, M. A. Beno, T. J. Emge, H. H. Wang, *Inorg. Chem.* **1985**, 24, 3500.
- 369 J. K. Jeszka, A. Tracz, A. Sroczynska, M. Kryszewski, H. Yamochi, S. Horiuchi, G. Saito, J. Ulanski, *Synth. Met.* **1999**, 106, 75.
- 370 T. Nakamura, G. Yunome, R. Azumi, M. Tanaka, H. Tachibana, M. Matsumoto, S. Horiuchi, H. Yamochi, G. Saito, *J. Phys. Chem.* **1994**, 98, 1882.
- 371 K. Ogasawara, K. Ishiguro, S. Horiuchi, H. Yamochi, G. Saito, *Jpn. J. Appl. Phys.* **1996**, 35, L571.
- 372 M. Izumi, V. M. Yartsev, H. Ohnuki, L. Vignau, P. Delhaes, *Recent Res. Dev. Phys. Chem.* **2001**, 5, 37.
- 373 M. A. Beno, H. H. Wang, A. M. Kini, K. D. Carlson, U. Geiser, W. K. Kwok, J. E. Thompson, J. M. Williams, J. Ren, M.-H. Whangbo, *Inorg. Chem.* **1990**, 29, 1599.
- 374 S. Kahlich, D. Schweitzer, I. Heinen, S. E. Lan, B. Nuber, H. J. Keller, K. Winzer, H. W. Helberg, *Solid State Commun.* **1991**, 80, 191.
- 375 G. Saito, T. Enoki, H. Inokuchi, *Chem. Lett.* **1982**, 1345.
- 376 T. Enoki, K. Imaeda, M. Kobayashi, H. Inokuchi, G. Saito, *Phys. Rev. B* **1986**, 33, 1553.
- 377 M. Kobayashi, T. Enoki, K. Imaeda, H. Inokuchi, G. Saito, *Phys. Rev. B* **1987**, 36, 1457.
- 378 S. Kagoshima, J. P. Pouget, G. Saito, H. Inokuchi, *Solid State Commun.* **1983**, 45, 1001.
- 379 H. Kobayashi, A. Kobayashi, Y. Sasaki, G. Saito, T. Enoki, H. Inokuchi, *J. Am. Chem. Soc.* **1983**, 105, 297.
- 380 H. Kobayashi, A. Kobayashi, Y. Sasaki, G. Saito, H. Inokuchi, *Bull. Chem. Soc. Jpn.* **1986**, 59, 301.
- 381 P. Guionneau, C. J. Kepert, D. Chasseau, M. R. Truter, P. Day, *Synth. Met.* **1997**, 86, 1973.
- 382 P. C. W. Leung, T. J. Emge, M. A. Beno, H. H. Wang, J. M. Williams, V. Patrick, P. Coppens, *J. Am. Chem. Soc.* **1985**, 107, 6184.
- 383 G. Saito, H. Kumagai, C. Katayama, C. Tanaka, J. Tanaka, P. Wu, T. Mori, K. Imaeda, T. Enoki, H. Inokuchi, Y. Higuchi, N. Yasuoka, *Isr. J. Chem.* **1986**, 27, 319.
- 384 G. Saito, A. Otsuka, A. A. Zakhidov, *Mol. Cryst. Liq. Cryst.* **1996**, 284, 3.
- 385 P. Muller, *Physica C* **1994**, 235–240, 289.
- 386 S. Ravy, R. Moret, J. P. Pouget, R. Comes, S. S. P. Parkin, *Phys. Rev. B* **1986**, 33, 2049.
- 387 M.-H. Whangbo, J. Ren, W. Liang, J.-P. Pouget, S. Ravy, J. M. Williams, M. A. Beno, *Inorg. Chem.* **1992**, 31, 4169.
- 388 H. Kobayashi, T. Mori, R. Kato, A. Kobayashi, Y. Sasaki, G. Saito, H. Inokuchi, *Chem. Lett.* **1983**, 581.
- 389 T. Mori, A. Kobayashi, Y. Sasaki, R. Kato, H. Kobayashi, *Solid State Commun.* **1985**, 53, 627.
- 390 R. Laversanne, J. Amiel, P. Delhaes, D. Chasseau, C. Hauw, *Solid State Commun.* **1984**, 52, 177.
- 391 P. C. W. Leung, M. A. Beno, G. S. Blackman, B. R. Coughlin, C. A. Miderski, W. Joss, G. W. Crabtree, J. M. Williams, *Acta Crystallogr., Sect. C* **1984**, 40, 1331.
- 392 M. A. Beno, H. H. Wang, L. Soderholm, K. D. Carlson, L. N. Hall, L. Nunez, H. Rummens, B. Anderson, J. A. Schlueter, J. M. Williams, M.-H. Whangbo, M. Evain, *Inorg. Chem.* **1989**, 28, 150.
- 393 S. Görtner, I. Heinen, D. Schweitzer, B. Nuber, H. J. Keller, *Synth. Met.* **1989**, 31, 199.
- 394 M. Oshima, H. Mori, G. Saito, K. Oshima, *Chem. Lett.* **1989**, 1159.
- 395 M. Oshima, H. Mori, G. Saito, K. Oshima, in *The Physics and Chemistry of Organic Superconductors*, ed. by G. Saito, S. Kagoshima, Springer-Verlag, Berlin, **1990**, pp. 257–261.
- 396 H. H. Wang, K. D. Carlson, U. Geiser, W. K. Kwok, M. D. Vashon, J. E. Thompson, N. F. Larsen, G. D. McCabe,

- R. S. Hulscher, J. M. Williams, *Physica C* **1990**, 166, 57.
- 397 T. Sasaki, N. Toyota, M. Tokumoto, N. Kinoshita, H. Anzai, *Solid State Commun.* **1990**, 75, 93.
- 398 H. Mori, S. Tanaka, K. Oshima, M. Oshima, G. Saito, T. Mori, Y. Maruyama, H. Inokuchi, *Solid State Commun.* **1990**, 74, 1261.
- 399 H. Mori, S. Tanaka, M. Oshima, G. Saito, T. Mori, Y. Maruyama, H. Inokuchi, *Bull. Chem. Soc. Jpn.* **1990**, 63, 2183.
- 400 H. Ito, H. Kaneko, T. Ishiguro, H. Ishimoto, K. Kono, S. Horiuchi, T. Komatsu, G. Saito, *Solid State Commun.* **1993**, 85, 1005.
- 401 H. Ito, M. V. Kartsovnik, H. Ishimoto, K. Kono, H. Mori, N. D. Kushch, G. Saito, T. Ishiguro, S. Tanaka, *Synth. Met.* **1995**, 70, 899.
- 402 N. D. Kushch, L. I. Buravov, M. V. Kartsovnik, V. N. Laukhin, S. I. Pesotskii, R. P. Shibaeva, R. P. Rozenberg, E. B. Yagubskii, A. V. Zvarikina, *Synth. Met.* **1992**, 46, 271.
- 403 L. I. Buravov, N. D. Kushch, V. N. Laukhin, A. G. Khomenko, E. B. Yagubskii, M. V. Kartsovnik, A. E. Kovalev, L. P. Rozenberg, R. P. Shibaeva, M. A. Tanatar, V. S. Yefanov, V. V. Dyakin, V. A. Bondarenko, *J. Phys. I* **1994**, 4, 441.
- 404 A. House, N. Harrison, S. J. Blundell, J. Deckers, J. Singleton, F. Herlach, W. Hayes, J. A. A. J. Perenboom, M. Kurmoo, P. Day, *Phys. Rev. B* **1996**, 53, 9127.
- 405 H. Mori, S. Tanaka, T. Mori, Y. Maruyama, *Bull. Chem. Soc. Jpn.* **1995**, 68, 1136.
- 406 A. A. Galimzyanov, A. A. Ignatev, N. D. Kushch, V. N. Laukhin, M. K. Makova, V. A. Merzhanov, L. P. Rozenberg, R. P. Shibaeva, E. B. Yagubskii, *Synth. Met.* **1989**, 33, 81.
- 407 P. Le Magueré, L. Ouahab, N. Conan, C. J. Gómez-García, P. Delhaës, J. Even, M. Bertault, *Solid State Commun.* **1996**, 97, 27.
- 408 T. Komatsu, N. Kojima, G. Saito, *Solid State Commun.* **1997**, 103, 519.
- 409 M. Kurmoo, T. Mallah, P. Day, I. Marsden, M. Allan, R. H. Friend, F. L. Pratt, W. Hayes, D. Chasseau, J. Gaultier, G. Bravic, in *The Physics and Chemistry of Organic Superconductors*, ed. by G. Saito, S. Kagoshima, Springer-Verlag, Berlin, **1990**, pp. 290–293.
- 410 A. V. Gudenko, V. B. Ginodman, V. E. Korotkov, A. V. Koshelap, N. D. Kushch, V. H. Laukhin, L. P. Rozenberg, A. G. Khomenko, R. P. Shibaeva, E. B. Yagubskii, in *The Physics and Chemistry of Organic Superconductors*, ed. by G. Saito, S. Kagoshima, Springer-Verlag, Berlin, **1990**, pp. 364–368.
- 411 T. Nogami, T. Ishida, H. Yoshikawa, M. Tanaka, T. Naito, H. Kobayashi, A. Kobayashi, *Synth. Met.* **1993**, 56, 2039. One of the samples exhibited a semiconductive behavior down to 100 K like  $\kappa$ -(ET)<sub>2</sub>Cu(NCS)<sub>2</sub>. No data for the lattice constants.
- 412 T. J. Emge, H. H. Wang, M. A. Beno, P. C. W. Leung, M. A. Firestone, H. C. Jenkins, J. D. Cook, K. D. Carlson, J. M. Williams, E. L. Venturini, L. J. Azevedo, J. E. Schirber, *Inorg. Chem.* **1985**, 24, 1736.
- 413 H. Kobayashi, R. Kato, A. Kobayashi, G. Saito, M. Tokumoto, H. Anzai, T. Ishiguro, *Chem. Lett.* **1985**, 1293.
- 414 A. Ugawa, Y. Okawa, K. Yakushi, H. Kuroda, A. Kawamoto, J. Tanaka, M. Tanaka, Y. Nogami, S. Kagoshima, K. Murata, T. Ishiguro, *Synth. Met.* **1988**, 27, A407.
- 415 L. I. Buravov, A. V. Zvarykina, A. A. Ignat'ev, A. I. Kotov, V. N. Laukhin, M. K. Makova, V. A. Merzhanov, L. P. Rozenberg, R. P. Shibaeva, E. B. Yagubskii, *Izv. Akad. Nauk, Ser. Khim.* **1988**, 2027.
- 416 T. Mori, F. Sakai, G. Saito, H. Inokuchi, *Chem. Lett.* **1986**, 1037.
- 417 E. Amberger, H. Fuchs, K. Polborn, *Synth. Met.* **1987**, 19, 605.
- 418 A. Ugawa, K. Yakushi, H. Kuroda, A. Kawamoto, J. Tanaka, *Chem. Lett.* **1986**, 1875.
- 419 M. Kurmoo, D. R. Talham, K. L. Pritchard, P. Day, A. M. Stringer, J. A. K. Howard, *Synth. Met.* **1988**, 27, A177.
- 420 M. Z. Aldoshina, R. N. Lyubovskaya, S. V. Konovalikhin, O. A. Dyachenko, G. V. Shilov, M. K. Makova, R. B. Lyubovskii, *Synth. Met.* **1993**, 56, 1905.
- 421 R. P. Shibaeva, R. M. Lobkovskaya, *Kristallografiya* **1988**, 33, 408.
- 422 K. Armbruster, P. Bele, H. Brunner, C. Benming, S. Dahm, R. Geiger, I. Heinen, H. J. Keller, D. Schweitzer, *Synth. Met.* **1991**, 42, 2025.
- 423 A. Miyazaki, I. Ichikawa, T. Enoki, G. Saito, *Bull. Chem. Soc. Jpn.* **1997**, 70, 2647.
- 424 H. Yamochi, H. Urayama, G. Saito, K. Oshima, A. Kawamoto, J. Tanaka, *Synth. Met.* **1988**, 27, A485.
- 425 R. N. Lyubovskaya, O. A. Dyachenko, V. V. Gritsenko, Sh. G. Mkoyan, L. O. Atovmyan, R. B. Lyubovskii, V. N. Laukhin, A. V. Zvarykina, A. G. Khomenko, *Synth. Met.* **1991**, 42, 1907.
- 426 A. Ota, H. Yamochi, G. Saito, *J. Mater. Chem.* **2002**, 12, 2600.
- 427 O. Drozdova, K. Yakushi, A. Ota, H. Yamochi, G. Saito, *Synth. Met.* **2003**, 133–134, 277.
- 428 M. Chollet, L. Guerin, N. Uchida, S. Fukaya, H. Shimoda, T. Ishikawa, K. Matsuda, T. Hasegawa, A. Ota, H. Yamochi, G. Saito, R. Tazaki, S. Adachi, S. Koshihara, *Science* **2005**, 307, 86.
- 429 W. S. Rapson, D. H. Saunderson, E. T. Stewart, *J. Chem. Soc.* **1946**, 1110.
- 430 K. Abe, Y. Matsunaga, G. Saito, *Bull. Chem. Soc. Jpn.* **1968**, 41, 2852.
- 431 A. Izuoka, T. Tachikawa, T. Sugawara, Y. Suzuki, M. Konno, Y. Saito, H. Shinohara, *J. Chem. Soc., Chem. Commun.* **1992**, 1472.
- 432 J. J. Mayerle, in *Mixed-Valence Compounds*, ed. by D. R. Brown, D. Reidel, Dordrecht, **1980**, pp. 451–473.
- 433 H. Kobayashi, J. Nakayama, *Bull. Chem. Soc. Jpn.* **1981**, 54, 2408.
- 434 J. J. Mayerle, J. B. Torrance, *Bull. Chem. Soc. Jpn.* **1981**, 54, 3170.
- 435 G. Saito, *Physica B* **1986**, 143, 296.
- 436 O. Baram, L. I. Buravov, L. S. Degtyarev, M. E. Kozlov, V. N. Laukhin, E. E. Laukhina, V. G. Onishchenko, K. I. Pokhodnya, M. K. Sheinkman, R. P. Shibaeva, E. B. Yagubskii, *JETP Lett.* **1986**, 44, 376.
- 437 D. Schweitzer, P. Bele, H. Brunner, E. Gogu, U. Haeberlen, I. Hennig, I. Klutz, R. Świetlik, H. J. Keller, *Z. Phys. B* **1987**, 67, 489.
- 438 M. Yoshimura, H. Shigekawa, H. Yamochi, G. Saito, A. Kawazu, *Phys. Rev. B* **1991**, 44, 1970.
- 439 M. Yoshimura, H. Shigekawa, H. Nejoh, G. Saito, Y. Saito, A. Kawazu, *Phys. Rev. B* **1991**, 43, 13590.
- 440 A. Kawazu, M. Yoshimura, H. Shigekawa, H. Mori, G. Saito, *J. Vac. Sci. Technol., B* **1991**, 9, 1006.
- 441 M. Yoshimura, N. Ara, M. Kageshima, R. Shiota, A. Kawazu, H. Shigekawa, Y. Saito, M. Oshima, H. Mori, H. Yamochi, G. Saito, *Surf. Sci.* **1991**, 242, 18.
- 442 H. Yamochi, T. Komatsu, N. Matsukawa, G. Saito, T. Mori, K. Kusunoki, K. Sakaguchi, *J. Am. Chem. Soc.* **1993**, 115,

11319.

- 443 E. B. Yagubskii, I. F. Shchegolev, V. N. Laukhin, P. A. Kononovich, M. V. Karstovnik, A. V. Zvarykina, L. I. Buravov, *JETP Lett.* **1984**, 39, 12.
- 444 R. P. Shibaeva, V. F. Kaminskii, E. B. Yagubskii, *Mol. Cryst. Liq. Cryst.* **1985**, 119, 361.
- 445 S. Kagoshima, M. Hasumi, Y. Nogami, N. Kinoshita, H. Anzai, M. Tokumoto, G. Saito, in *The Physics and Chemistry of Organic Superconductors*, ed. by G. Saito, S. Kagoshima, Springer-Verlag, Berlin, **1990**, pp. 126–129.
- 446 V. N. Laukhin, E. E. Kostyuchenko, Yu. V. Sushko, I. F. Shchegolev, E. B. Yagubskii, *Pis'ma Zh. Eksp. Teor. Fiz.* **1985**, 41, 68.
- 447 K. Murata, M. Tokumoto, H. Anzai, H. Bando, G. Saito, K. Kajimura, T. Ishiguro, *J. Phys. Soc. Jpn.* **1985**, 54, 1236.
- 448 J. E. Schirber, L. J. Azevedo, J. F. Kwak, E. L. Venturini, P. C. W. Leung, M. A. Beno, H. H. Wang, J. M. Williams, *Phys. Rev. B* **1986**, 33, 1987.
- 449 D. Schweitzer, P. Bele, H. Brunner, E. Gogu, U. Haebleren, I. Hennig, I. Klutz, R. Swietlik, H. J. Keller, *Z. Phys. B* **1987**, 67, 489.
- 450 R. P. Shibaeva, V. F. Kaminskii, E. B. Yagubskii, *Mol. Cryst. Liq. Cryst.* **1985**, 119, 361.
- 451 H. Kobayashi, R. Kato, A. Kobayashi, Y. Nishio, K. Kajita, W. Sasaki, *Chem. Lett.* **1986**, 789.
- 452 A. Kobayashi, R. Kato, H. Kobayashi, S. Moriyama, Y. Nishio, K. Kajita, W. Sasaki, *Chem. Lett.* **1987**, 459.
- 453 J. M. Williams, H. H. Wang, M. A. Beno, T. J. Emge, L. M. Sowa, P. T. Copps, F. Behrooz, L. N. Hall, K. D. Carlson, G. W. Vrabtree, *Inorg. Chem.* **1984**, 23, 3839.
- 454 H. H. Wang, L. Nunez, G. W. Carlson, J. M. Williams, J. L. Azevedo, J. F. Kwak, J. E. Schirber, *Inorg. Chem.* **1985**, 24, 2465.
- 455 H. Taniguchi, M. Miyashita, K. Uchiyama, K. Satoh, N. Mori, H. Okamoto, K. Miyagawa, K. Kanoda, M. Hedo, Y. Uwatoko, *J. Phys. Soc. Jpn.* **2003**, 72, 468. They reported on-set  $T_c = 14.2$  K at 8.2 GPa, and mid-point  $T_c = 13.4$  K can be estimated from graphic data.
- 456 J. A. Schlueter, U. Geiser, H. H. Wang, M. E. Kelly, J. D. Dudek, J. M. Williams, D. Naumann, T. Roy, *Mol. Cryst. Liq. Cryst.* **1996**, 284, 195.
- 457 J. A. Schlueter, K. D. Carlson, J. M. Williams, U. Geiser, H. H. Wang, U. Welp, W.-K. Kwok, J. A. Fendrich, J. D. Dudek, C. A. Achenbach, P. M. Keane, A. S. Komosa, D. Naumann, T. Roy, J. E. Schirver, W. R. Bayless, *Physica C* **1994**, 230, 378.
- 458 T. Mori, H. Inokuchi, *Chem. Lett.* **1987**, 1657.
- 459 T. Mori, H. Inokuchi, *Solid State Commun.* **1987**, 64, 335.
- 460 T. Mori, K. Kato, Y. Maruyama, H. Inokuchi, H. Mori, I. Hirabayashi, S. Tanaka, *Solid State Commun.* **1992**, 82, 177.
- 461 H. Mori, I. Hirabayashi, S. Tanaka, T. Mori, Y. Maruyama, H. Inokuchi, *Solid State Commun.* **1991**, 80, 411.
- 462 S. S. P. Parkin, E. M. Engler, R. R. Schumaker, R. Lagier, V. Y. Lee, J. C. Scott, R. L. Greene, *Phys. Rev. Lett.* **1983**, 50, 270.
- 463 M. Kurmoo, A. W. Graham, P. Day, S. L. Coles, M. B. Hursthouse, J. L. Caufield, J. Singleton, F. L. Pratt, W. Hayes, L. Ducasse, P. Guionneau, *J. Am. Chem. Soc.* **1995**, 117, 12209.
- 464 L. Martin, S. S. Turner, P. Day, F. E. Mabbs, E. J. L. McInnes, *Chem. Commun.* **1997**, 1367.
- 465 S. Rashid, S. S. Turner, P. Day, J. A. K. Howard, P. Guionneau, E. J. L. McInnes, F. E. Mabbs, R. J. H. Clark, S. Firth, T. Biggs, *J. Mater. Chem.* **2001**, 11, 2095.
- 466 H. Akutsu, A. Akutsu-Sato, S. S. Turner, D. Le Pevelen, P. Day, V. Laukhin, A.-K. Klehe, J. Singleton, D. A. Tocher, M. R. Probert, J. A. K. Howard, *J. Am. Chem. Soc.* **2002**, 124, 12430.
- 467 U. Geiser, J. A. Schlueter, H. H. Wang, A. M. Kini, J. M. Williams, P. P. Sche, H. I. Zakowicz, M. L. VanZile, J. D. Dudek, *J. Am. Chem. Soc.* **1996**, 118, 9996.
- 468 H. Mori, I. Hirabayashi, S. Tanaka, T. Mori, H. Inokuchi, *Solid State Commun.* **1990**, 76, 35.
- 469 R. N. Lyubovskaya, R. B. Lyubovskii, R. P. Shibaeva, M. Z. Aldoshina, L. M. Gol'denberg, L. P. Rosenberg, M. L. Khidekel, Yu. F. Shul'pyakov, *JETP Lett.* **1985**, 42, 468.
- 470 R. N. Lyubovskaya, E. I. Zhilyaeva, A. V. Zvarykina, V. N. Laukhin, R. B. Lyubovskii, S. I. Pesotskii, *Pis'ma Zh. Eksp. Teor. Fiz.* **1987**, 45, 416.
- 471 J. E. Schirber, D. L. Overmyer, E. L. Venturini, H. H. Wang, K. D. Carlson, W. K. Kwok, S. Kleinjan, J. M. Williams, *Physica C* **1989**, 161, 412.
- 472 H. Urayama, H. Yamochi, G. Saito, K. Nozawa, T. Sugano, M. Kinoshita, S. Sato, K. Oshima, A. Kawamoto, J. Tanaka, *Chem. Lett.* **1988**, 55.
- 473 T. Sugano, K. Terui, S. Mino, K. Nozawa, H. Urayama, H. Yamochi, G. Saito, M. Kinoshita, *Chem. Lett.* **1988**, 1171.
- 474 G. Saito, H. Urayama, H. Yamochi, K. Oshima, *Synth. Met.* **1988**, 27, A331.
- 475 K. Oshima, H. Urayama, H. Yamochi, G. Saito, *J. Phys. Soc. Jpn.* **1988**, 57, 730.
- 476 G. Saito, *Physica C* **1989**, 162–164, 577.
- 477 G. Saito, *Mol. Cryst. Liq. Cryst.* **1990**, 181, 65.
- 478 G. Saito, H. Yamochi, T. Nakamura, T. Komatsu, T. Ishiguro, Y. Nogami, Y. Ito, H. Mori, K. Oshima, M. Nakashima, S. Uchida, H. Takagi, S. Kagoshima, T. Osada, *Synth. Met.* **1991**, 42, 1993.
- 479 M. Kini, U. Geiser, H. H. Wang, K. D. Carlson, J. M. Williams, W. K. Kwok, K. G. Vandervoort, J. E. Thompson, D. L. Stupka, D. Jung, M.-H. Whangbo, *Inorg. Chem.* **1990**, 29, 2555.
- 480 H. H. Wang, K. D. Carlson, U. Geiser, A. M. Kini, A. J. Schultz, J. M. Williams, L. K. Montgomery, W. K. Kwok, U. Welp, K. G. Vandervoort, S. J. Boryschuk, A. V. Striby Crouch, J. M. Kommers, D. M. Watkins, J. E. Schirber, D. L. Overmyer, D. Jung, J. J. Novoa, M.-H. Wangbo, *Synth. Met.* **1991**, 42, 1983.
- 481 H. Ito, M. Watanabe, Y. Nogami, T. Ishiguro, T. Komatsu, G. Saito, N. Hosoi, *J. Phys. Soc. Jpn.* **1991**, 60, 3230.
- 482 N. C. Kushch, S. I. Pesotskii, V. N. Topnikov, *JETP Lett.* **1992**, 56, 506.
- 483 R. P. Shibaeva, S. S. Khasanov, N. D. Kushch, E. B. Yagubskii, K. Boubekeur, P. Batail, E. Canadell, *NATO ASI Ser., Ser. C* **1999**, 518, 409.
- 484 N. D. Kushch, M. A. Tanatar, E. B. Yagubskii, T. Ishiguro, *JETP Lett.* **2001**, 73, 429.
- 485 T. Nakamura, T. Komatsu, G. Saito, T. Osada, S. Kagoshima, N. Miura, K. Kato, Y. Maruyama, K. Oshima, *J. Phys. Soc. Jpn.* **1993**, 62, 4373.
- 486 G. Saito, H. Yamochi, T. Nakamura, T. Komatsu, N. Matsukawa, T. Inoue, H. Ito, T. Ishiguro, M. Kusunoki, K. Sakaguchi, T. Mori, *Synth. Met.* **1993**, 56, 2883.
- 487 G. Saito, T. Komatsu, T. Nakamura, H. Yamochi, *Mater. Res. Soc. Symp. Proc.* **1992**, 247, 483.
- 488 T. Ishiguro, H. Ito, Y. Yamochi, E. Ohmichi, M. Kubota, H. Yamochi, G. Saito, M. V. Kartsovnik, M. A. Tanatar, Yu. V. Sushko, G. Yu. Logvenov, *Synth. Met.* **1997**, 85, 1471.

- 489 X. Bu, A. Frost-Jensen, R. Allendoerfer, P. Coppens, B. Lederle, M. Naughton, *Solid State Commun.* **1991**, 79, 1053.
- 490 G. C. D. Papavassiliou, J. Lagouvardos, V. C. Kakoussis, A. Terzis, A. Hountas, B. Hilti, C. Mayer, J. S. Zambounis, J. Pfeiffer, M.-H. Whangbo, J. Ren, D. B. Kang, *Mater. Res. Soc. Symp. Proc.* **1992**, 247, 535.
- 491 T. Komatsu, N. Matsukawa, T. Inoue, G. Saito, *J. Phys. Soc. Jpn.* **1996**, 65, 1340.
- 492 T. Komatsu, G. Saito, *Mol. Cryst. Liq. Cryst.* **1996**, 285, 51.
- 493 O. Drozdova, G. Saito, H. Yamochi, K. Okubo, K. Yakushi, M. Uruichi, L. Ouahab, *Inorg. Chem.* **2001**, 40, 3265.
- 494 G. Saito, K. Okubo, O. Drozdova, K. Yakushi, *Mol. Cryst. Liq. Cryst.* **2002**, 380, 23.
- 495 T. Mori, A. Kobayashi, Y. Sasaki, R. Kato, H. Kobayashi, G. Saito, H. Inokuchi, *Chem. Lett.* **1984**, 957.
- 496 H. Tajima, K. Yakushi, H. Kuroda, G. Saito, *Solid State Commun.* **1985**, 56, 159.
- 497 T. J. Emge, P. C. W. Leung, M. A. Beno, A. J. Schultz, H. H. Wang, L. M. Sowa, J. M. Williams, *Phys. Rev. B* **1984**, 30, 6780.
- 498 W. Kang, G. Montambaux, J. R. Cooper, D. Jerome, P. Batail, C. Lenoir, *Phys. Rev. Lett.* **1989**, 62, 2559.
- 499 M. V. Kartsovnik, P. A. Kononovich, V. N. Laukhin, I. F. Schegolev, *Pis'ma Zh. Eksp. Teor. Fiz.* **1988**, 48, 498.
- 500 K. Kajita, Y. Nishio, T. Takahashi, R. Kato, H. Kobayashi, W. Sasaki, A. Kobayashi, Y. Iye, *Solid State Commun.* **1989**, 70, 1189.
- 501 M. Tokumoto, H. Bando, K. Murata, H. Anzai, N. Kinoshita, K. Kajimura, T. Ishiguro, G. Saito, *Synth. Met.* **1986**, 13, 9.
- 502 J. M. Williams, M. A. Beno, H. H. Wang, U. W. Geiser, T. J. Emge, P. C. W. Leung, G. W. Crabtree, K. D. Carlson, L. J. Azevedo, E. L. Venturini, J. E. Schirber, J. F. Kwak, M.-H. Whangbo, *Physica B* **1986**, 136, 371.
- 503 T. J. Kistenmacher, *Solid State Commun.* **1987**, 63, 977.
- 504 H. Yamochi, T. Nakamura, T. Komatsu, N. Matsukawa, T. Inoue, G. Saito, *Solid State Commun.* **1992**, 82, 101.
- 505 H. Müller, C.-P. Heidmann, A. Lerf, W. Biberacher, R. Sieburger, K. Andres, in *The Physics and Chemistry of Organic Superconductors*, ed by G. Saito, S. Kagoshima, Springer-Verlag, Berlin, **1990**, pp. 195–199.
- 506 S. Hill, J. Singleton, F. L. Pratt, M. Doporto, W. Hayes, T. J. B. M. Janssen, J. A. A. J. Perenboom, M. Kurmoo, P. Day, *Synth. Met.* **1993**, 56, 2566.
- 507 T. Nakamura, T. Nobutoki, T. Takahashi, G. Saito, H. Mori, T. Mori, *J. Phys. Soc. Jpn.* **1994**, 63, 4110.
- 508 Y. V. Sushko, H. Ito, T. Ishiguro, S. Horiuchi, G. Saito, *J. Phys. Soc. Jpn.* **1993**, 62, 3372.
- 509 Y. V. Sushko, H. Ito, T. Ishiguro, S. Horiuchi, G. Saito, *Solid State Commun.* **1993**, 87, 997.
- 510 H. Ito, T. Ishiguro, M. Kubota, G. Saito, *J. Phys. Soc. Jpn.* **1996**, 65, 2987.
- 511 H. Ito, M. Kubota, T. Ishiguro, G. Saito, *Synth. Met.* **1997**, 85, 1517.
- 512 H. Ito, T. Kondo, H. Sasaki, G. Saito, T. Ishiguro, *Synth. Met.* **1999**, 103, 1818.
- 513 H. Ito, T. Ishiguro, T. Kondo, G. Saito, *J. Phys. Soc. Jpn.* **2000**, 69, 290.
- 514 M. Kubota, G. Saito, H. Ito, T. Ishiguro, N. Kojima, *Mol. Cryst. Liq. Cryst.* **1996**, 284, 367.
- 515 T. Ishiguro, H. Ito, Y. Yamochi, E. Ohshima, M. Kubota, H. Yamochi, G. Saito, M. V. Kartsovnik, M. A. Tanatar, Yu. V. Sushko, G. Yu. Logvenov, *Synth. Met.* **1997**, 85, 1471.
- 516 H. Ohta, S. Kimura, Y. Yamamoto, J. Azuma, K. Akioka, M. Motokawa, K. Kanoda, *Synth. Met.* **1997**, 86, 2079.
- 517 H. Ito, T. Ishiguro, T. Kondo, G. Saito, *Phys. Rev. B* **2000**, 61, 3243.
- 518 G. Saito, *Phosphorus, Sulfur Silicon Relat. Elem.* **1992**, 67, 345.
- 519 Y. Watanabe, T. Shimazu, N. Toyota, T. Sasaki, *Synth. Met.* **1997**, 86, 1917.
- 520 M.-S. Nam, J. A. Symington, J. Singleton, S. J. Blundell, A. Ardavan, J. A. A. J. Perenboom, M. Kurmoo, P. Day, *J. Phys.: Condens. Matter* **1999**, 11, L477.
- 521 H. Ito, Y. Nogami, T. Ishiguro, T. Komatsu, G. Saito, N. Hosoi, *Jpn. J. Appl. Phys.* **1992**, Series 7, 419.
- 522 A. M. Kini, J. D. Dudek, K. D. Carlson, U. Geiser, R. A. Klemm, J. M. Williams, K. R. Lykke, J. A. Schlueter, H. H. Wang, P. Wurz, J. R. Ferraro, G. A. Yaconi, P. Stout, *Physica C* **1993**, 204, 399.
- 523 A. M. Kini, K. D. Carlson, H. H. Wang, J. A. Schlueter, J. D. Dudek, S. A. Sirchio, U. Geiser, K. R. Lykke, J. M. Williams, *Physica C* **1996**, 264, 81.
- 524 A. M. Kini, K. D. Carlson, J. D. Dudek, U. Geiser, H. H. Wang, J. M. Williams, *Synth. Met.* **1997**, 85, 1617.
- 525 T. Komatsu, N. Matsukawa, T. Nakamura, H. Yamochi, G. Saito, *Phosphorus, Sulfur Silicon Relat. Elem.* **1992**, 67, 295.
- 526 M. Tokumoto, N. Kinoshita, Y. Tanaka, H. Anzai, *Mater. Res. Soc. Symp. Proc.* **1998**, 488, 903.
- 527 N. Toyota, in *Physical Phenomena at High Magnetic Fields-II*, World Scientific, Singapore, **1996**, pp. 282–294.
- 528 K. Yamaji, *Solid State Commun.* **1987**, 61, 413.
- 529 M. Tokumoto, N. Kinoshita, Y. Tanaka, H. Anzai, *J. Phys. Soc. Jpn.* **1991**, 60, 1426.
- 530 M. Kund, H. Müller, W. Biberacher, K. Andres, G. Saito, *Physica B* **1993**, 191, 274.
- 531 N. Yoneyama, A. Higashihara, T. Sasaki, T. Nojima, N. Kobayashi, *J. Phys. Soc. Jpn.* **2004**, 73, 1290.
- 532 K. Kanoda, *Hyperfine Interact.* **1997**, 104, 235.
- 533 M. Z. Aldoshina, R. N. Lyubovskaya, S. V. Konovalikhin, O. A. Dyachenko, G. V. Shilov, M. K. Makova, R. B. Lyubovskii, *Synth. Met.* **1993**, 56, 1905.
- 534 E. I. Yudanov, S. K. Hoffmann, A. Graja, S. V. Konovalikhin, O. A. Dyachenko, R. B. Lyubovskii, R. N. Lyubovskaya, *Synth. Met.* **1995**, 73, 227.
- 535 E. I. Yudanov, L. M. Makarova, S. V. Konovalikhin, O. A. Dyachenko, R. B. Lyubovskii, R. N. Lyubovskaya, *Synth. Met.* **1996**, 79, 201.
- 536 T. Mori, H. Mori, S. Tanaka, *Bull. Chem. Soc. Jpn.* **1999**, 72, 179.
- 537 J. E. Schirber, E. L. Venturini, A. M. Kini, H. H. Wang, J. R. Whitworth, J. M. Williams, *Physica C* **1988**, 152, 157.
- 538 J. E. Schirber, D. L. Overmyer, J. M. Williams, A. M. Kini, H. H. Wang, *Physica C* **1990**, 170, 231.
- 539 S. S. P. Parkin, M. Ribault, D. Jerome, K. Bechgaard, *J. Phys. C: Solid State Phys.* **1981**, 14, 5305.
- 540 L. J. Azevedo, E. L. Venturini, J. E. Schirber, J. M. Williams, H. H. Wang, T. J. Emge, *Mol. Cryst. Liq. Cryst.* **1985**, 119, 389.
- 541 K. Murata, M. Tokumoto, H. Anzai, H. Bando, G. Saito, K. Kajimura, T. Ishiguro, *J. Phys. Soc. Jpn.* **1985**, 54, 2084.
- 542 M. Tokumoto, H. Anzai, H. Bando, G. Saito, N. Kinoshita, K. Kajimura, T. Ishiguro, *J. Phys. Soc. Jpn.* **1985**, 54, 1669.



- 543 K. D. Carlson, G. W. Crabtree, L. Nunez, H. H. Wang, M. A. Beno, U. Geiser, M. A. Firestone, K. S. Webb, J. M. Williams, *Solid State Commun.* **1986**, 57, 89.
- 544 G. Sparn, J. D. Thompson, S.-M. Huang, R. B. Kaner, F. Diederich, R. L. Whetten, G. Grüner, K. Holczer, *Science* **1991**, 252, 1829.
- 545 G. Sparn, J. D. Thompson, R. L. Whetten, S.-M. Huang, R. B. Kaner, F. Diederich, G. Grüner, K. Holczer, *Phys. Rev. Lett.* **1992**, 68, 1228.
- 546 R. L. Greene, E. M. Engler, *Phys. Rev. Lett.* **1980**, 45, 1587.
- 547 K. Murata, K. Iwashita, Y. Mizuno, F. Z. Guo, S. Shodai, H. Yoshino, J. S. Brooks, L. Balicas, D. Graf, K. Storr, I. Rutel, S. Uji, C. Terakura, Y. Imanaka, *J. Phys. Chem. Solids* **2002**, 63, 1263.
- 548 N. Tajima, A. Ebina-Tajima, M. Tamura, Y. Nishio, K. Kajita, *J. Phys. Soc. Jpn.* **2002**, 71, 1832.
- 549 C. E. Campos, J. S. Brooks, P. J. M. van Bentum, J. A. A. J. Perenboom, S. J. Klepper, P. S. Sandhu, S. Valfells, Y. Tanaka, T. Kinoshita, N. Kinoshita, M. Tokumoto, H. Anzai, *Phys. Rev. B* **1995**, 52, R7014.
- 550 M. Maesato, Y. Kaga, R. Kondo, S. Kagoshima, *Rev. Sci. Instrum.* **2000**, 71, 176.
- 551 M. Maesato, Y. Kaga, R. Kondo, S. Kagoshima, *Phys. Rev. B* **2001**, 64, 155104.
- 552 R. Kondo, S. Kagoshima, M. Maesato, *Phys. Rev. B* **2003**, 67, 134519.
- 553 H. Kusunohara, Y. Sakata, Y. Ueba, K. Tada, M. Kaji, T. Ishiguro, *Solid State Commun.* **1990**, 74, 251.
- 554 T. Mizutani, M. Tokumoto, T. Kinoshita, J. S. Brooks, Y. Uwatoko, O. Drozdova, K. Yakushi, I. Tamura, H. Kobayashi, T. Mangetsu, J. Yamada, K. Ishida, *Synth. Met.* **2003**, 133–134, 229.
- 555 C. E. Campos, J. S. Brooks, P. J. M. van Bentum, J. A. A. Perenboom, J. Rooks, S. J. Klepper, M. Tokumoto, *Rev. Sci. Instrum.* **1995**, 66, 1061.
- 556 T. Ishikawa, M. Maesato, G. Saito, *Synth. Met.* **2003**, 133–134, 227.
- 557 Y. Shimizu, M. Maesato, G. Saito, O. Drozdova, L. Ouahab, *Synth. Met.* **2003**, 133–134, 225.
- 558 M. Maesato, Y. Shimizu, T. Ishikawa, G. Saito, *Synth. Met.* **2003**, 137, 1243.
- 559 M. Maesato, Y. Shimizu, T. Ishikawa, G. Saito, K. Miyagawa, K. Kanoda, *J. Phys. IV* **2004**, 114, 227.
- 560 M. Kund, H. Veith, H. Müller, K. Andres, G. Saito, *Physica C* **1994**, 221, 119.
- 561 J. Müller, M. Lang, F. Steglich, J. A. Schlueter, A. M. Kini, *Phys. Rev. B* **2002**, 65, 144521.
- 562 M. Lang, R. Modler, F. Steglich, N. Toyota, T. Sasaki, *Physica B* **1994**, 194–196, 2005.
- 563 M. Kund, J. Lehrke, W. Biberacher, A. Lerf, K. Andres, *Synth. Met.* **1995**, 70, 949.
- 564 J. Müller, M. Lang, F. Steglich, J. A. Schlueter, A. M. Kini, U. Geiser, J. Mohtasham, R. W. Winter, G. L. Gard, T. Sasaki, N. Toyota, *Phys. Rev. B* **2000**, 61, 11739.
- 565 T. Sasaki, N. Toyota, M. Tokumoto, N. Kinoshita, H. Anzai, *Solid State Commun.* **1990**, 75, 93.
- 566 M. Maesato, G. Saito, J. A. Schlueter, J. Mohtasham, G. L. Gard, R. Kondo, S. Kagoshima, to be published.
- 567 M. Sakata, M. Maesato, A. Ota, H. Yamochi, G. Saito, *Synth. Met.* **2005**, 153, 393.
- 568 T. Takahashi, K. Kanoda, G. Saito, *Jpn. J. Appl. Phys.* **1992**, 7, 414.
- 569 F. Creuzet, C. Bourbonnais, G. Creuzet, D. Jerome, D. Schweitzer, H. J. Keller, *Physica B* **1986**, 143, 363.
- 570 Y. Shimizu, Ph.D. Thesis, Kyoto University, **2005**.
- 571 D. R. Harshman, R. N. Kleiman, R. C. Haddon, S. V. Chichester-Hicks, M. L. Kaplan, L. W. Rupp, Jr., T. Pfiz, D. L. Williams, D. B. Mitzi, *Phys. Rev. Lett.* **1990**, 64, 1293.
- 572 M. Dressel, O. Klein, G. Grüner, K. D. Carlson, H. H. Wang, J. M. Williams, *Phys. Rev. B* **1994**, 50, 13603.
- 573 D. R. Harshman, R. N. Kleiman, R. C. Haddon, S. V. Chichester-Hicks, M. L. Kaplan, L. W. Rupp, Jr., T. Pfiz, D. L. Williams, D. B. Mitzi, *Phys. Rev. Lett.* **1990**, 64, 1293.
- 574 O. Klein, K. Holczer, G. Grüner, J. J. Chang, F. Wudl, *Phys. Rev. Lett.* **1991**, 66, 655.
- 575 M. Lang, N. Toyota, T. Sasaki, H. Sato, *Phys. Rev. B* **1992**, 46, 5822.
- 576 M. Dressel, S. Bruder, G. Grüner, K. D. Carlson, H. H. Wang, J. M. Williams, *Phys. Rev. B* **1993**, 48, 9906.
- 577 K. Kanoda, K. Akiba, K. Suzuki, T. Takahashi, G. Saito, *Phys. Rev. Lett.* **1990**, 65, 1271.
- 578 Y. J. Uemura, L. P. Le, G. M. Luke, B. J. Sternlieb, W. D. Wu, J. H. Brewer, T. M. Riseman, C. L. Seaman, M. B. Maple, M. Ishikawa, D. G. Hinks, J. D. Jorgensen, G. Saito, H. Yamochi, *Phys. Rev. Lett.* **1991**, 66, 2665.
- 579 L. P. Le, G. M. Luke, B. J. Sternlieb, W. D. Wu, Y. J. Uemura, J. H. Brewer, T. M. Riseman, C. E. Stronach, G. Saito, H. Yamochi, H. H. Wang, A. M. Kini, K. D. Carlson, J. M. Williams, *Phys. Rev. Lett.* **1992**, 68, 1923.
- 580 D. Achkir, M. Poirier, C. Bourbonnais, G. Quirion, C. Lenoir, P. Batail, D. Jerome, *Phys. Rev. B* **1993**, 47, 11595.
- 581 S. Belin, K. Behnia, A. Deluzet, *Phys. Rev. Lett.* **1998**, 81, 4728.
- 582 J. E. Graebner, R. C. Haddon, S. V. Chichester, S. H. Glarum, *Phys. Rev. B* **1990**, 41, 4808.
- 583 K. Ichimura, T. Arai, K. Nomura, S. Takasaki, J. Yamada, S. Nakatsuji, H. Anzai, *Physica C* **1997**, 282–287, 1895.
- 584 K. Izawa, H. Yamaguchi, T. Sasaki, Y. Matsuda, *Phys. Rev. Lett.* **2002**, 88, 27002.
- 585 P. Foury-Leylekian, S. Ravy, J.-P. Pouget, H. Müller, *Synth. Met.* **2003**, 137, 1271.
- 586 T. Osada, R. Yagi, A. Kawasumi, S. Kagoshima, N. Miura, M. Oshima, G. Saito, *Phys. Rev. B* **1990**, 41, 5428.
- 587 T. Osada, A. Kawasumi, R. Yagi, S. Kagoshima, N. Miura, M. Oshima, H. Mori, T. Nakamura, G. Saito, *Solid State Commun.* **1990**, 75, 901.
- 588 T. Kouno, T. Osada, M. Hasumi, S. Kagoshima, N. Miura, M. Oshima, H. Mori, T. Nakamura, G. Saito, *Synth. Met.* **1993**, 56, 2425.
- 589 M. V. Kartsovnik, A. E. Kovalev, N. D. Kushch, *J. Phys. I* **1993**, 3, 1187.
- 590 J. S. Brooks, X. Chen, S. J. Klepper, S. Valfells, G. J. Athas, Y. Tanaka, T. Kinoshita, N. Kinoshita, M. Tokumoto, H. Anzai, C. C. Agosta, *Phys. Rev. B* **1995**, 52, 14457.
- 591 T. Sasaki, N. Toyota, *Phys. Rev. B* **1994**, 49, 10120.
- 592 J. Caulfield, J. Singleton, P. T. J. Hendriks, J. A. A. J. Perenboom, F. L. Pratt, M. D'operto, W. Hayes, M. Kurmoo, P. Day, *J. Phys.: Condens. Matter* **1994**, 6, L155.
- 593 S. Uji, T. Terashima, H. Aoki, J. S. Brooks, M. Tokumoto, N. Kinoshita, T. Kinoshita, Y. Tanaka, H. Anzai, *Phys. Rev. B* **1996**, 54, 9332.
- 594 M. V. Kartsovnik, H. Ito, T. Ishiguro, H. Mori, T. Mori, G. Saito, S. Tanaka, *J. Phys.: Condens. Matter* **1994**, 6, L479.
- 595 P. W. Anderson, *Science* **1987**, 235, 1196.

- 596 Y. Iwasa, T. Takenobu, *J. Phys.: Condens. Matter* **2003**, *15*, R495.
- 597 N. Toyota, T. Sasaki, *Solid State Commun.* **1990**, *74*, 361.
- 598 M. Kund, K. Andres, H. Müller, G. Saito, *Physica B* **1994**, *203*, 129.
- 599 R. C. Yu, J. M. Williams, H. H. Wang, J. E. Thompson, A. M. Kini, K. D. Carlson, J. Ren, M.-H. Whangbo, P. M. Chaikin, *Phys. Rev. B* **1991**, *44*, 6932.
- 600 S. Klotz, J. S. Schilling, S. Gärtner, D. Schweitzer, *Solid State Commun.* **1988**, *67*, 981.
- 601 D. R. Talham, M. Kurmoo, P. Day, D. S. Obertelli, I. D. Parker, R. H. Friend, *J. Phys. C: Solid State Phys.* **1986**, *19*, 383.
- 602 A. Kawamoto, K. Miyagawa, Y. Nakazawa, K. Kanoda, *Phys. Rev. Lett.* **1995**, *74*, 3455.
- 603 A. Kawamoto, K. Miyagawa, Y. Nakazawa, K. Kanoda, *Phys. Rev. B* **1995**, *52*, 15522.
- 604 R. H. McKenzie, *Comments Condens. Matter Phys.* **1998**, *18*, 309.
- 605 H. Kino, H. Fukuyama, *J. Phys. Soc. Jpn.* **1995**, *64*, 2726.
- 606 K. Miyagawa, A. Kawamoto, Y. Nakazawa, K. Kanoda, *Phys. Rev. Lett.* **1995**, *75*, 1174.
- 607 M. Rahal, D. Chasseau, J. Gaultier, L. Ducasse, M. Kurmoo, P. Day, *Acta Crystallogr., Sect. B* **1997**, *53*, 159.
- 608 H. Kobayashi, H. Cui, A. Kobayashi, *Chem. Rev.* **2004**, *104*, 5265.
- 609 H. Kobayashi, T. Udagawa, H. Tomita, K. Bun, T. Naito, A. Kobayashi, *Chem. Lett.* **1993**, 1559.
- 610 S. Uji, H. Shinagawa, T. Terashima, T. Yakabe, Y. Terai, M. Tokumoto, A. Kobayashi, H. Tanaka, H. Kobayashi, *Nature* **2001**, *410*, 908.
- 611 H. Tanaka, E. Ojima, H. Fujiwara, Y. Nakazawa, H. Kobayashi, A. Kobayashi, *J. Mater. Chem.* **2000**, *10*, 245.
- 612 V. Gritsenko, H. Tanaka, H. Kobayashi, A. Kobayashi, *J. Mater. Chem.* **2001**, *11*, 2410.
- 613 T. Konoike, S. Uji, T. Terashima, M. Nishimura, S. Yasuzuka, K. Enomoto, H. Fujiwara, B. Zhang, H. Kobayashi, *Phys. Rev. B* **2004**, *70*, 094514.
- 614 R. Kondo, T. Hasegawa, S. Kagoshima, T. Mochida, Y. Iwasa, *Chem. Lett.* **1999**, 333.
- 615 J. Sakata, H. Sato, A. Miyazaki, T. Enoki, Y. Okano, R. Kato, *Solid State Commun.* **1998**, *108*, 377.
- 616 R. N. Lyubovskaya, E. I. Zhilyaeva, S. A. Torunova, G. A. Mousdis, G. C. Papavassiliou, J. A. A. J. Perenboom, S. I. Pesotskii, R. B. Lyubovskii, *J. Phys. IV* **2004**, *114*, 463.
- 617 K. Kikuchi, K. Murata, Y. Honda, T. Namiki, K. Saito, T. Ishiguro, K. Kobayashi, I. Ikemoto, *J. Phys. Soc. Jpn.* **1987**, *56*, 3436.
- 618 K. Kikuchi, K. Murata, Y. Honda, T. Namiki, K. Saito, H. Anzai, K. Kobayashi, T. Ishiguro, I. Ikemoto, *J. Phys. Soc. Jpn.* **1987**, *56*, 4241.
- 619 H. Ito, D. Suzuki, Y. Yokochi, S. Kuroda, M. Umemiya, H. Miyasaka, K.-I. Sugiura, M. Yamashita, H. Tajima, *Phys. Rev. B* **2005**, *71*, 212503.
- 620 R. Kato, S. Aonuma, Y. Okano, H. Sawa, M. Tamura, M. Kinoshita, K. Oshima, A. Kobayashi, K. Bun, H. Kobayashi, *Synth. Met.* **1993**, *61*, 199.
- 621 J. S. Zambounis, C. W. Mayer, K. Hauenstein, B. Hilti, W. Hofherr, J. Pfeiffer, M. Buerkle, G. Rihs, *Adv. Mater.* **1992**, *4*, 33.
- 622 S. Kimura, T. Maejima, H. Suzuki, R. Chiba, H. Mori, T. Kawamoto, T. Mori, H. Moriyama, Y. Nishio, K. Kajita, *Chem. Commun.* **2004**, 2454.
- 623 R. Kato, K. Yamamoto, Y. Okano, H. Tajima, H. Sawa, *Chem. Commun.* **1997**, 947.
- 624 Y. Okano, M. Iso, Y. Kashimura, J. Yamaura, R. Kato, *Synth. Met.* **1999**, *102*, 1703.
- 625 G. C. Papavassiliou, G. A. Mousdis, J. S. Zambounis, A. Terzis, A. Hountas, B. Hilti, C. W. Mayer, J. Pfeiffer, *Synth. Met.* **1988**, *B27*, 379.
- 626 T. Takahashi, Y. Kobayashi, T. Nakamura, K. Kanoda, B. Hilti, J. S. Zambounis, *Physica C* **1994**, *235–240*, 2461.
- 627 K. Takimiya, Y. Kataoka, Y. Aso, T. Otsubo, H. Fukuoka, S. Yamanaka, *Angew. Chem., Int. Ed.* **2001**, *40*, 1122.
- 628 T. Kawamoto, T. Mori, K. Takimiya, Y. Kataoka, Y. Aso, T. Otsubo, *Phys. Rev. B* **2002**, *65*, 140508.
- 629 K. Takimiya, M. Kodani, Y. Kataoka, Y. Aso, T. Otsubo, T. Kawamoto, T. Mori, *Chem. Mater.* **2003**, *15*, 3250.
- 630 K. Takimiya, A. Takamori, Y. Aso, T. Otsubo, T. Kawamoto, T. Mori, *Chem. Mater.* **2003**, *15*, 1225.
- 631 K. Takimiya, M. Kodani, N. Niihara, Y. Aso, T. Otsubo, Y. Bando, T. Kawamoto, T. Mori, *Chem. Mater.* **2004**, *16*, 5120.
- 632 M. Kodani, A. Takamori, K. Takimiya, Y. Aso, T. Otsubo, *J. Solid State Chem.* **2002**, *168*, 582.
- 633 T. Imakubo, N. Tajima, M. Tamura, R. Kato, Y. Nishio, K. Kajita, *J. Mater. Chem.* **2002**, *12*, 159.
- 634 H. Nishikawa, T. Morimoto, T. Kodama, I. Ikemoto, K. Kikuchi, J. Yamada, H. Yoshino, K. Murata, *J. Am. Chem. Soc.* **2002**, *124*, 730.
- 635 H. Nishikawa, A. Machida, T. Morimoto, K. Kikuchi, T. Kodama, I. Ikemoto, J. Yamada, H. Yoshino, K. Murata, *Chem. Commun.* **2003**, 494.
- 636 Y. Misaki, N. Higuchi, H. Fujiwara, T. Yamabe, T. Mori, H. Mori, S. Tanaka, *Angew. Chem., Int. Ed. Engl.* **1995**, *34*, 1222.
- 637 J. Yamada, M. Watanabe, H. Akutsu, S. Nakatsuji, H. Nishikawa, I. Ikemoto, K. Kikuchi, *J. Am. Chem. Soc.* **2001**, *123*, 4174.
- 638 J. Yamada, T. Toita, H. Akutsu, S. Nakatsuji, H. Nishikawa, I. Ikemoto, K. Kikuchi, E. S. Choi, D. Graf, J. S. Brooks, *Chem. Commun.* **2003**, 2230.
- 639 E. S. Choi, D. Graf, J. S. Brooks, J. Yamada, H. Akutsu, K. Kikuchi, M. Tokumoto, *Phys. Rev. B* **2004**, *70*, 024517.
- 640 M. Bousseau, L. Valade, J. P. Legros, P. Cassoux, M. Garbauskas, L. V. Interrante, *J. Am. Chem. Soc.* **1986**, *108*, 1908.
- 641 H. Tajima, M. Inokuchi, A. Kobayashi, T. Ohta, R. Kato, H. Kobayashi, H. Kuroda, *Chem. Lett.* **1993**, 1235.
- 642 L. Brossard, H. Hurdequint, M. Ribault, L. Valade, J. P. Legros, P. Cassoux, *Synth. Met.* **1988**, *27*, B157.
- 643 H. Kobayashi, K. Bun, T. Naito, R. Kato, A. Kobayashi, *Chem. Lett.* **1992**, 1909.
- 644 R. Kato, Y. Kashimura, S. Aonuma, N. Hanasaki, H. Tajima, *Solid State Commun.* **1998**, *105*, 561.
- 645 D. O. Cowan, F. M. Wiygul, *Chem. Eng. News* **1986**, July 21, 28; **1986**, July 21, 34.
- 646 G. Saito, H. Inokuchi, in *Kagaku, Zokan: Electroorganic Chemistry*, ed. by T. Osa, T. Shono, K. Honda, Kagaku Dojin, **1980**, Vol. 6, pp. 45–64.
- 647 P. Pfeiffer, *Organische Molekülverbindungen*, 2nd ed., Ferdinand Enke Pub., Stuttgart, **1928**.
- 648 E. Hertel, *Ber.* **1924**, *57*, 1559.
- 649 E. Hertel, *Ann.* **1926**, *451*, 179.
- 650 E. Hertel, J. van Cleef, *Ber.* **1928**, *61B*, 1545.
- 651 E. Hertel, K. Schneider, *Z. Phys. Chem.* **1931**, *B13*, 387.
- 652 E. Hertel, H. Frank, *Z. Phys. Chem.* **1934**, *27*, 460.
- 653 C. Shinomiya, *Bull. Chem. Soc. Jpn.* **1940**, *15*, 137.
- 654 A. Kofler, *Z. Elektrochem.* **1944**, *50*, 200.

- 655 G. Briegleb, H. Delle, *Z. Phys. Chem.* **1960**, 24, 359.
- 656 G. Briegleb, H. Delle, *Z. Elektrochem.* **1960**, 64, 347.
- 657 S. L. Johnson, K. A. Rumon, *J. Phys. Chem.* **1965**, 69, 74.
- 658 E. Carstensen-Oeser, S. Göttlicher, G. Habermehl, *Chem. Ber.* **1968**, 101, 1648.
- 659 Y. Matsunaga, G. Saito, *Bull. Chem. Soc. Jpn.* **1972**, 45, 963.
- 660 G. Saito, Y. Matsunaga, *Bull. Chem. Soc. Jpn.* **1972**, 45, 2214.
- 661 N. Inoue, Y. Matsunaga, *Bull. Chem. Soc. Jpn.* **1972**, 45, 3478.
- 662 G. Saito, Y. Matsunaga, *Bull. Chem. Soc. Jpn.* **1973**, 46, 714.
- 663 Y. Matsunaga, *Bull. Chem. Soc. Jpn.* **1973**, 46, 998.
- 664 G. Saito, Y. Matsunaga, *Bull. Chem. Soc. Jpn.* **1973**, 46, 1609.
- 665 N. Inoue, Y. Matsunaga, *Bull. Chem. Soc. Jpn.* **1973**, 46, 3345.
- 666 G. Saito, Y. Matsunaga, *Bull. Chem. Soc. Jpn.* **1974**, 47, 1020.
- 667 Y. Matsunaga, R. Osawa, *Bull. Chem. Soc. Jpn.* **1974**, 47, 1589.
- 668 Y. Matsunaga, G. Saito, N. Sasaki, *Bull. Chem. Soc. Jpn.* **1974**, 47, 2873.
- 669 Y. Matsunaga, E. Osawa, R. Osawa, *Bull. Chem. Soc. Jpn.* **1975**, 48, 37.
- 670 M. Tanaka, *Bull. Chem. Soc. Jpn.* **1977**, 50, 3194.
- 671 Y. Matsunaga, R. Usui, *Bull. Chem. Soc. Jpn.* **1980**, 53, 3985.
- 672 J. Bernstein, H. Regev, F. H. Herstein, *Acta Crystallogr., Sect. B* **1980**, 36, 1170.
- 673 U. Thewalt, C. E. Bugg, *Acta Crystallogr., Sect. B* **1972**, 28, 82.
- 674 G. L. Gartland, G. R. Freeman, C. E. Bugg, *Acta Crystallogr., Sect. B* **1974**, 30, 1841.
- 675 G. Saito, Ph.D. thesis, Hokkaido University, **1972**.
- 676 Md. B. Zaman, Y. Morita, J. Toyoda, H. Yamochi, G. Saito, N. Yoneyama, T. Enoki, K. Nakasuji, *Chem. Lett.* **1997**, 729.
- 677 B. Zaman, Y. Morita, J. Toyoda, H. Yamochi, S. Sekizaki, K. Nakasuji, *Mol. Cryst. Liq. Cryst.* **1996**, 287, 249.
- 678 P. Kathirgamanathan, S. A. Mucklejohn, D. R. Rosseinsky, *J. Chem. Soc., Chem. Commun.* **1979**, 86.
- 679 M. A. Beno, H. H. Wang, L. Soderholm, K. D. Carlson, L. N. Hall, L. Lunez, H. Rummens, B. Andersen, J. A. Schluter, J. M. Williams, M.-H. Whangbo, M. Evain, *Inorg. Chem.* **1989**, 28, 150.
- 680 H. Yamochi, T. Tsuji, G. Saito, T. Suzuki, T. Miyashi, C. Kabuto, *Synth. Met.* **1988**, 27, A479.
- 681 H. Yamochi, C. Tada, S. Sekizaki, G. Saito, M. Kusunoki, K. Sakaguchi, *Mol. Cryst. Liq. Cryst.* **1996**, 284, 379.
- 682 S. Sekizaki, H. Yamochi, G. Saito, *Synth. Met.* **1999**, 102, 1711.
- 683 S. Sekizaki, C. Tada, H. Yamochi, G. Saito, *J. Mater. Chem.* **2001**, 11, 2293.
- 684 S. Sekizaki, A. Konsha, H. Yamochi, G. Saito, *Mol. Cryst. Liq. Cryst.* **2002**, 376, 207.
- 685 S. Sekizaki, H. Yamochi, G. Saito, *Synth. Met.* **2003**, 135–136, 631.
- 686 Y. Morita, E. Miyazaki, H. Yamochi, G. Saito, K. Nakasuji, *Synth. Met.* **2003**, 135–136, 581.
- 687 H. Yamochi, K. Tsutsumi, T. Kawasaki, G. Saito, *Mater. Res. Soc. Symp. Proc.* **1998**, 488, 641.
- 688 H. Yamochi, K. Tsutsumi, T. Kawasaki, G. Saito, *Synth. Met.* **1999**, 103, 2004.
- 689 H. Yamochi, A. Konsha, G. Saito, K. Matsumoto, M. Kusunoki, K. Sakaguchi, *Mol. Cryst. Liq. Cryst.* **2000**, 350, 265.
- 690 G. Saito, S. Sekizaki, A. Konsha, H. Yamochi, K. Matsumoto, M. Kusunoki, K. Sakaguchi, *J. Mater. Chem.* **2001**, 11, 364.
- 691 G. G. Abashev, O. N. Kazheva, O. A. Dyachenko, V. V. Gritsenko, A. G. Tenishev, K. Nishimura, G. Saito, *Mendeleev Commun.* **2001**, 125.
- 692 K. Nishimura, G. Saito, S. Takeda, O. O. Drozdova, *Synth. Met.* **2003**, 133–134, 437.
- 693 C. Rodrigues, E. B. Lopes, M. Almeida, R. T. Henriques, Proceedings of ISCOM-99, Oxford, p. 108.
- 694 T. Sugano, K. Yakushi, H. Kuroda, *Bull. Chem. Soc. Jpn.* **1978**, 51, 1041.
- 695 S. Warren, *The Chemistry of the Carbonyl Group*, Wiley, London, **1974**.
- 696 D. J. Sandman, A. P. Fisher, III, T. J. Holmes, A. J. Epstein, *J. Chem. Soc., Chem. Commun.* **1977**, 687.
- 697 L. R. Melby, R. J. Harder, W. R. Hertler, W. Mahler, R. E. Benson, W. E. Mochel, *J. Am. Chem. Soc.* **1962**, 84, 3374.
- 698 G. Saito, A. K. Colter, *Tetrahedron Lett.* **1977**, 18, 3325.
- 699 A. K. Colter, G. Saito, F. J. Sharom, A. P. Hong, *J. Am. Chem. Soc.* **1976**, 98, 7833.
- 700 A. K. Colter, G. Saito, F. J. Sharom, *Can. J. Chem.* **1977**, 55, 2741.
- 701 T. Mitani, G. Saito, H. Urayama, *Phys. Rev. Lett.* **1988**, 60, 2299.
- 702 M. C. Böhm, H. Vogler, *Solid State Commun.* **1983**, 46, 201.
- 703 Ref. 149, Chap. 12.
- 704 M. A. Slifkin, *Charge Transfer Interactions of Biomolecules*, Academic Press, New York, **1971**.
- 705 A. Szent-Györgyi, *Bioelectronics*, Academic Press, New York, **1968**.
- 706 H.-W. Fink, C. Schönenberger, *Nature* **1999**, 398, 407.
- 707 Y. Zhang, R. H. Austin, J. Kraeft, E. C. Cox, N. P. Ong, *Phys. Rev. Lett.* **2002**, 89, 198102.
- 708 D. D. Eley, D. I. Spivey, *Discuss. Faraday Soc.* **1960**, 56, 1432.
- 709 Y. M. Orlov, A. N. Smirnov, Y. M. Varshavsky, *Tetrahedron Lett.* **1976**, 18, 4377.
- 710 D. Dougherty, E. S. Yountan, R. Voll, S. Abdunur, S. P. McGlynn, *J. Electron Spectrosc. Relat. Phenom.* **1978**, 13, 379.
- 711 S. G. Lias, J. E. Bartmess, J. F. Liebman, L. J. Holmes, R. D. Levin, W. G. Mallard, *J. Phys. Chem. Ref. Data* **1988**, 17, 861.
- 712 S. D. Wetmore, R. J. Boyd, L. A. Eriksson, *Chem. Phys. Lett.* **2000**, 322, 129, and references therein.
- 713 M. A. Slifkin, A. P. Kushelevsky, *Spectrochim. Acta, Part A* **1971**, 27, 1999.
- 714 G. G. Sheina, E. D. Radchenko, Yu. P. Blagoi, B. I. Verkin, *Dokl. Akad. Nauk SSSR* **1978**, 240, 463.
- 715 G. G. Sheina, E. D. Radchenko, S. A. Egupov, Yu. P. Blagoi, V. M. Orlov, *Int. J. Quantum Chem.* **1979**, 16, 387.
- 716 I. N. Bazhina, V. S. Verzilov, V. S. Grechishkin, R. V. Grechishkina, V. M. Gusarov, *Zh. Strukt. Khim.* **1973**, 14, 930.
- 717 K. Nishimura, T. Murata, Y. Enomoto, G. Honda, Y. Shimizu, M. Sakata, G. Saito, in *Multifunctional Conducting Molecular Materials*, ed. by G. Saito, F. Wudl, R. C. Haddon,

- K. Tanigaki, T. Enoki, H. E. Katz, M. Maesato, RSC Publishing, Cambridge, **2007**, pp. 49–54.
- 718 R. E. Marsh, R. Bierstedt, E. L. Eichhorn, *Acta Crystallogr.* **1962**, *15*, 310.
- 719 A. J. Epstein, J. S. Miller, in *The Physics and Chemistry of Low Dimensional Solids*, ed. by L. Alcacer, D. Reidel, Dordrecht, **1980**, pp. 339–351.
- 720 R. Kato, *Bull. Chem. Soc. Jpn.* **2000**, *73*, 515.
- 721 J. C. Scott, S. Etemad, E. M. Engler, *Phys. Rev. B* **1978**, *17*, 2269.
- 722 T. Hasegawa, S. Kagoshima, T. Mochida, S. Sugiura, Y. Iwasa, *Solid State Commun.* **1997**, *103*, 489.
- 723 R. Kumai, A. Asamitsu, Y. Tokura, *J. Am. Chem. Soc.* **1998**, *120*, 8263.
- 724 H. Mori, M. Kamiya, M. Haemori, H. Suzuki, S. Tanaka, Y. Nishio, K. Kajita, H. Moriyama, *J. Am. Chem. Soc.* **2002**, *124*, 1251.
- 725 D. Yoshida, H. Kitagawa, T. Mitani, T. Ito, K. Nakasuji, *Mol. Cryst. Liq. Cryst.* **1996**, *285*, 257.
- 726 T. Akutagawa, G. Saito, H. Yamochi, M. Kusunoki, K. Sakaguchi, *Synth. Met.* **1995**, *69*, 591.
- 727 T. Akutagawa, G. Saito, T. Nakamura, K. Sakaguchi, M. Kusunoki, *Mol. Cryst. Liq. Cryst.* **1996**, *278*, 257.
- 728 T. Akutagawa, T. Hasegawa, T. Nakamura, T. Inabe, G. Saito, *Chem. Eur. J.* **2002**, *8*, 4402.
- 729 A. Akutsu-Sato, H. Akutsu, S. S. Turner, P. Day, M. R. Probert, J. A. K. Howard, T. Akutagawa, S. Tkeda, T. Nakamura, T. Mori, *Angew. Chem., Int. Ed.* **2005**, *44*, 292.
- 730 T. Nakamura, T. Akutagawa, K. Honda, A. E. Underhill, A. T. Coomber, R. H. Friend, *Nature* **1998**, *394*, 159.
- 731 T. Akutagawa, S. Takeda, T. Hasegawa, T. Nakamura, *J. Am. Chem. Soc.* **2004**, *126*, 291.
- 732 C. Coulon, P. Delhaes, J. Amiel, J. P. Manceau, J. M. Fabre, L. Giral, *J. Phys.* **1982**, *43*, 1721.
- 733 T. Naito, A. Miyamoto, H. Kobayashi, R. Kato, A. Kobayashi, *Chem. Lett.* **1992**, 119.
- 734 M. Tokumoto, H. Anzai, K. Murata, K. Kajimura, T. Ishiguro, *Jpn. J. Appl. Phys.* **1987**, *26*, Suppl. 26-3, 1977.
- 735 H. Tanaka, A. Kobayashi, T. Saito, K. Kawamoto, T. Naito, H. Kobayashi, *Adv. Mater.* **1996**, *8*, 812.
- 736 P. Dahlke, M. S. Denning, P. F. Henry, M. J. Rosseinsky, *J. Am. Chem. Soc.* **2000**, *122*, 12352.
- 737 H. W. Meul, C. Rossel, M. Decroux, Ø. Fischer, G. Remenyi, A. Briggs, *Phys. Rev. Lett.* **1984**, *53*, 497.
- 738 R. S. Potember, T. O. Poehler, D. O. Cowan, A. N. Bloch, in *The Physics and Chemistry of Low Dimensional Solids*, ed. by L. Alcacer, D. Reidel, Dordrecht, **1980**, pp. 419–428.
- 739 R. C. Benson, R. C. Hoffman, R. S. Potember, E. Bourkoff, T. O. Poehler, *Appl. Phys. Lett.* **1983**, *42*, 855, and references therein.
- 740 R. Kumai, Y. Okimoto, Y. Tokura, *Science* **1999**, *284*, 1645.
- 741 S. Koshihara, Y. Tokura, Y. Iwasa, T. Koda, G. Saito, T. Mitani, *Synth. Met.* **1991**, *42*, 2351.
- 742 F. O. Karutz, J. U. von Schutz, H. Wachtel, H. C. Wolf, *Phys. Rev. Lett.* **1998**, *81*, 140.
- 743 T. Naito, T. Inabe, H. Niimi, K. Asakura, *Adv. Mater.* **2004**, *16*, 1786.
- 744 O. Drozdova, K. Yakushi, K. Yamamoto, A. Ota, H. Yamochi, G. Saito, H. Tashiro, D. B. Tanner, *Phys. Rev. B* **2004**, *70*, 075107.
- 745 S. Aoyagi, K. Kato, A. Ota, H. Yamochi, G. Saito, H. Suematsu, M. Sakata, M. Takata, *Angew. Chem., Int. Ed.* **2004**, *43*, 3670.
- 746 K. Saito, S. Ikeuchi, A. Ota, H. Yamochi, G. Saito, *Chem. Phys. Lett.* **2005**, *401*, 76.
- 747 N. Uchida, S. Koshihara, T. Ishikawa, A. Ota, S. Fukuya, C. M. Cholle, H. Yamochi, G. Saito, *J. Phys. IV* **2004**, *114*, 143.
- 748 T. Kobayashi, T. Saito, H. Ohtani, *Nature* **2001**, *414*, 531.
- 749 A. Ota, H. Yamochi, G. Saito, *Synth. Met.* **2003**, *133–134*, 463.
- 750 H. Yamochi, G. Saito, S. Koshihara, *Mol. Cryst. Liq. Cryst.* **2006**, *455*, 105.
- 751 M. J. Rice, E. J. Mele, *Phys. Rev. Lett.* **1982**, *49*, 1455.
- 752 T. Mitani, Y. Kaneko, S. Tanuma, Y. Tokura, T. Koda, G. Saito, *Phys. Rev. B* **1987**, *35*, 427.
- 753 M. H. Lemée-Cailleau, M. Le Cointe, H. Cailleau, T. Luty, F. Moussa, J. Roos, D. Brinkmann, B. Toudic, C. Ayache, N. Karl, *Phys. Rev. Lett.* **1997**, *79*, 1690.
- 754 E. Collet, M.-H. Lemée-Cailleau, M. Buron-Le Cointe, H. Cailleau, M. Wulff, T. Luty, S. Koshihara, M. Meyer, L. Toupet, P. Rabiller, S. Techert, *Science* **2003**, *300*, 612.
- 755 S. Horiuchi, R. Kumai, Y. Okimoto, Y. Tokura, *Phys. Rev. Lett.* **2000**, *85*, 5210, and references therein.
- 756 S. Horiuchi, R. Kumai, Y. Okimoto, Y. Tokura, *J. Am. Chem. Soc.* **1999**, *121*, 6757.
- 757 S. Horiuchi, F. Ishii, R. Kumai, Y. Okimoto, H. Tachibana, N. Nagaosa, Y. Tokura, *Nat. Mater.* **2005**, *4*, 163.
- 758 A. Girlando, A. Painelli, *Phys. Rev. B* **1986**, *34*, 2131.
- 759 Y. Matsunaga, *Nature* **1966**, *211*, 183.
- 760 T. Nakamura, *Electrically Conductive Langmuir-Blodgett Films*, in *Handbook of Organic Conductive Molecules and Polymers*, ed. by H. S. Nalwa, John Wiley & Sons, Chichester, **1997**, Vol. 1, pp. 727–780.
- 761 P. Delhaes, *NATO ASI Ser., Ser. C* **1991**, *343*, 247.
- 762 A. Ulman, *Chem. Rev.* **1996**, *96*, 1533.
- 763 R. M. Metzger, *Chem. Rev.* **2003**, *103*, 3803.
- 764 J. C. Love, L. A. Estroff, J. K. Kriebel, R. G. Nuzzo, G. M. Whitesides, *Chem. Rev.* **2005**, *105*, 1103.
- 765 J. K. Jeszka, *Pol. J. Chem.* **2002**, *76*, 201.
- 766 A. Ruau-del-Teixier, M. Vandevyver, A. Barraud, *Mol. Cryst. Liq. Cryst.* **1985**, *120*, 319.
- 767 A. Barraud, P. Lesieur, J. Richard, A. Ruau-del-Teixier, M. Vandevyver, M. Lequan, R. M. Lequan, *Thin Solid Films* **1988**, *160*, 81.
- 768 A. Barraud, M. Lequan, R. M. Lequan, P. Lesieur, J. Richard, A. Ruau-del-Teixier, M. Vandevyver, *J. Chem. Soc., Chem. Commun.* **1987**, 797.
- 769 M. Vandevyver, J. Richard, A. Barraud, A. Ruau-del-Teixier, M. Lequan, R. M. Lequan, *J. Chem. Phys.* **1987**, *87*, 6754.
- 770 T. Nakamura, H. Tanaka, K. Kojima, M. Matsumoto, H. Tachibana, M. Tanaka, E. Manda, Y. Kawabata, *Thin Solid Films* **1989**, *179*, 183.
- 771 Y. F. Miura, M. Takenaga, A. Kasai, T. Nakamura, Y. Nishio, M. Matsumoto, Y. Kawabata, *Thin Solid Films* **1992**, *210–211*, 306.
- 772 Y. F. Miura, Y. Okuma, H. Ohnishi, T. Kawasaki, M. Sugi, *Jpn. J. Appl. Phys.* **1998**, *37*, L1481.
- 773 Y. F. Miura, M. Takenaga, A. Kasai, T. Nakamura, M. Matsumoto, Y. Kawabata, *Jpn. J. Appl. Phys.* **1991**, *30*, 3503.
- 774 C. Dourthe, M. Izumi, C. Garrigou-Lagrange, T. Buffeteau, B. Desbat, P. Delhaes, *J. Phys. Chem.* **1992**, *96*, 2812.
- 775 A. S. Dhindsa, Y. P. Song, J. S. Badyal, M. R. Brice, Yu. M. Lvov, M. C. Petty, J. Yarwood, *Chem. Mater.* **1992**, *4*,

724.

776 L. M. Goldenberg, V. Yu. Khodorkovsky, J. Y. Becker, P. J. Lukes, M. R. Bryce, M. C. Petty, J. Yarwood, *Chem. Mater.* **1994**, *6*, 1426.

777 H. Ohnuki, T. Noda, M. Izumi, T. Imakubo, R. Kato, *Supramol. Sci.* **1997**, *4*, 413.

778 H. Ohnuki, T. Noda, M. Izumi, T. Imakubo, R. Kato, *Phys. Rev. B* **1997**, *55*, R10225.

779 Y. Ishizaki, M. Izumi, H. Ohnuki, K. Kalita-Lipinska, T. Imakubo, K. Kobayashi, *Phys. Rev. B* **2001**, *63*, 134201.

780 Y. Kawabata, T. Nakamura, M. Matsumoto, M. Tanaka, T. Sekiguchi, H. Komizu, E. Manda, G. Saito, *Synth. Met.* **1987**, *19*, 663.

781 M. Matsumoto, T. Nakamura, E. Manda, Y. Kawabata, K. Ikegami, S. Kuroda, M. Sugi, G. Saito, *Thin Solid Films* **1988**, *160*, 61.

782 K. Ikegami, S. Kuroda, K. Saito, M. Saito, M. Sugi, T. Nakamura, M. Matsumoto, Y. Kawabata, G. Saito, *Synth. Met.* **1988**, *27*, B587.

783 T. Nakamura, G. Yunome, R. Azumi, M. Tanaka, M. Yumura, M. Matsumoto, S. Horiuchi, H. Yamochi, G. Saito, *Synth. Met.* **1993**, *57*, 3853.

784 T. Nakamura, G. Yunome, R. Azumi, M. Tanaka, H. Tachibana, M. Matsumoto, S. Horiuchi, H. Yamochi, G. Saito, *J. Phys. Chem.* **1994**, *98*, 1882.

785 K. Ikegami, S. Kuroda, T. Nakamura, R. Azumi, G. Yunome, M. Matsumoto, S. Horiuchi, H. Yamochi, G. Saito, *Synth. Met.* **1995**, *71*, 1909.

786 S. V. Ayrapetiants, T. S. Berzina, S. A. Shikin, V. I. Troitsky, *Thin Solid Films* **1992**, *210–211*, 261.

787 T. S. Berzina, S. A. Shikin, P. S. Sotnikov, V. I. Troitsky, V. Yu. Khodorkovskii, O. Neilands, G. Pukitis, *Top. Mol. Organ. Eng.* **1991**, *7*, 99.

788 T. S. Berzina, S. L. Vorobyova, V. I. Troitsky, V. Yu. Khodorkovsky, O. Ya. Neilands, *Thin Solid Films* **1992**, *210–211*, 317.

789 T. S. Berzina, V. I. Troitsky, E. Stussi, M. Mule, D. de Rossi, *Synth. Met.* **1993**, *60*, 111.

790 S. L. Vorob'eva, T. S. Berzina, *J. Chem. Soc., Perkin Trans. 2* **1992**, 1133.

791 Y. Xiao, Z. Yao, D. Jin, *J. Phys. Chem.* **1993**, *97*, 8519.

792 Y. Xiao, Z. Yao, D. Jin, *Thin Solid Films* **1993**, *232*, 261.

793 Y. Liu, Y. Xu, D. Zhu, *Thin Solid Films* **1996**, *284–285*, 526.

794 M. Fujiki, H. Tabei, *Synth. Met.* **1987**, *18*, 815.

795 T. Yumoto, T. Akutagawa, T. Hasegawa, T. Nakamura, H. Ikegami, G. Saito, *Synth. Met.* **1999**, *102*, 1733.

796 K. Ogasawara, T. Ishiguro, S. Horiuchi, H. Yamochi, G. Saito, *Jpn. J. Appl. Phys., Part 2* **1996**, *35*, L571.

797 J. Richard, M. Vandevyver, P. Lesieur, A. Ruaudel-Teixier, A. Barraud, R. Bozio, C. Pecile, *J. Chem. Phys.* **1987**, *86*, 2428.

798 A. S. Dhindsa, M. R. Bryce, J. P. Lloyd, M. C. Petty, *Synth. Met.* **1987**, *22*, 185.

799 R. J. Ward, A. S. Dhindsa, M. R. Bryce, H. S. Munro, M. C. Petty, *Thin Solid Films* **1991**, *198*, 363.

800 K. Ogasawara, T. Ishiguro, S. Horiuchi, H. Yamochi, G. Saito, Y. Nogami, *J. Phys. Chem. Solids* **1997**, *58*, 39.

801 H. Tsukada, T. Goto, K. Ogasawara, S. Horiuchi, H. Yamochi, G. Saito, *J. Phys. Soc. Jpn.* **1998**, *67*, 1556.

802 H. Tsukada, *Phys. Rev. B* **1999**, *59*, 2301.

803 Y. F. Miura, M. Horikiri, S.-H. Saito, M. Sugi, *Solid State*

*Commun.* **2000**, *113*, 603.

804 P. Wang, R. M. Metzger, S. Bandow, Y. Maruyama, *J. Phys. Chem.* **1993**, *97*, 2926.

805 K. Ikegami, S. Kuroda, M. Matsumoto, T. Nakamura, *Jpn. J. Appl. Phys.* **1995**, *34*, L1227.

806 R. G. Nuzzo, D. L. Allara, *J. Am. Chem. Soc.* **1983**, *105*, 4481.

807 C. Ganzorig, K.-J. Kwak, K. Yagi, M. Fujihira, *Appl. Phys. Lett.* **2001**, *79*, 272.

808 C. M. Yip, M. D. Ward, *Langmuir* **1994**, *10*, 549.

809 H. Skulason, D. Frisbie, *Langmuir* **1998**, *14*, 5834.

810 R. Yuge, A. Miyazaki, T. Enoki, K. Tamada, F. Nakamura, M. Hara, *J. Phys. Chem. B* **2002**, *106*, 6894.

811 R. Yuge, A. Miyazaki, T. Enoki, K. Tamada, F. Nakamura, M. Hara, *Jpn. J. Appl. Phys.* **2002**, *41*, 7462.

812 J. K. Jeszka, J. Ulanski, M. Kryszewski, *Nature* **1981**, *289*, 390.

813 E. E. Laukhina, V. A. Merzhanov, S. I. Pesotskii, A. G. Khomenko, E. B. Yagubskii, J. Ulanski, M. Kryszewski, J. K. Jeszka, *Synth. Met.* **1995**, *70*, 797.

814 J. K. Jeszka, A. Tracz, A. Sroczynska, M. Kryszewski, H. Yamochi, S. Horiuchi, G. Saito, J. Ulanski, *Synth. Met.* **1999**, *106*, 75.

815 S. Horiuchi, H. Yamochi, G. Saito, J. K. Jeszka, A. Tracz, A. Sroczynska, J. Ulanski, *Mol. Cryst. Liq. Cryst.* **1997**, *296*, 365.

816 A. Tracz, *Pol. J. Chem.* **2002**, *76*, 457.

817 B. Hilti, C. W. Mayer, *Helv. Chim. Acta* **1978**, *61*, 501.

818 P. Delhaes, C. Coulon, S. Flandrois, B. Hilti, C. W. Mayer, G. Rihs, J. Rivory, *J. Chem. Phys.* **1980**, *73*, 1452, and references therein.

819 H. Okamoto, T. Mitani, Y. Tokura, S. Koshihara, T. Komatsu, Y. Iwasa, T. Koda, G. Saito, *Phys. Rev. B* **1991**, *43*, 8224.

820 P. Chaudhari, B. A. Scott, R. B. Laibowitz, Y. Tomkiewicz, J. B. Torrance, *Appl. Phys. Lett.* **1974**, *24*, 439.

821 K. Yase, O. Okumura, T. Kobayashi, N. Uyeda, *Bull. Inst. Chem. Res., Kyoto Univ.* **1984**, *62*, 242.

822 D. B. Tanner, C. S. Jacobsen, A. F. Garito, A. J. Heeger, *Phys. Rev. Lett.* **1974**, *32*, 1301.

823 S. Garelik, J. Vidal Gancedo, A. Figueras, J. Caro, J. Veciana, C. Rovira, E. Ribera, E. Canadell, A. Seffar, J. Fontcuberta, *Synth. Met.* **1996**, *76*, 309.

824 M. Yudasaka, K. Hironaga, H. Yamochi, K. Nakanishi, G. Saito, *Mater. Res. Soc. Symp. Proc.* **1990**, *173*, 137.

825 M. Yudasaka, K. Hironaga, H. Yamochi, G. Saito, *J. Appl. Phys.* **1991**, *70*, 3501.

826 R. B. Somoano, A. Gupta, V. Hadeck, *J. Chem. Phys.* **1975**, *63*, 4970.

827 K. Kawabata, K. Tanaka, M. Mizutani, *Solid State Commun.* **1990**, *74*, 83.

828 K. Kawabata, K. Tanaka, M. Mizutani, *Synth. Met.* **1990**, *39*, 191.

829 M. Yudasaka, K. Hironaga, K. Nakanishi, *J. Appl. Phys.* **1991**, *69*, 3402.

830 U. Niebling, J. Moldenhauer, T. Ludwig, D. Schweitzer, W. Strunz, *Solid State Commun.* **1996**, *97*, 837.

831 J. Aihara, *Bull. Chem. Soc. Jpn.* **1975**, *48*, 1031.

832 A. Otsuka, G. Saito, T. Nakamura, M. Matsumoto, Y. Kawabata, K. Honda, M. Goto, M. Kurahashi, *Synth. Met.* **1988**, *27*, B575.

833 A. Otsuka, G. Saito, O. Kina, Y. Yoshida, H. Yamochi, O. O. Drozdova, K. Yakushi, K. Honda, to be published.



- 834 I. Tabushi, K. Yamamura, K. Kominami, *J. Am. Chem. Soc.* **1986**, *108*, 6409.
- 835 R. Hagiwara, T. Hirashige, T. Tsuda, Y. Ito, *J. Electrochem. Soc.* **2002**, *149*, D1.
- 836 J. Kommandeur, G. J. Korinek, W. G. Schneider, *Can. J. Chem.* **1958**, *36*, 513.
- 837 V. A. Starodub, E. M. Gluzman, K. I. Pokhodnya, M. Ya. Valakh, *Theor. Exp. Chem.* **1994**, *29*, 240.
- 838 M. Šorm, S. Nešpůrek, M. Procházka, I. Koropecský, *Collect. Czech. Chem. Commun.* **1983**, *48*, 103.
- 839 M. C. Grossel, P. B. Hitchcock, K. R. Seddon, T. Welton, S. C. Weston, *Chem. Mater.* **1994**, *6*, 1106.
- 840 K. Nishimura, G. Saito, *Synth. Met.* **2005**, *153*, 385.
- 841 S. Niwa, *Synth. Met.* **1987**, *18*, 665.
- 842 S. Niwa, Y. Taketani, *J. Power Sources* **1996**, *60*, 165.
- 843 I. Isa, *Nikkei New Materials* **1989**, 48.
- 844 J. S. Wilkes, J. A. Levisky, R. A. Wilson, C. L. Hussey, *Inorg. Chem.* **1982**, *21*, 1263.
- 845 J. S. Wilkes, M. J. Zaworotko, *J. Chem. Soc., Chem. Commun.* **1992**, 965.
- 846 T. Welton, *Chem. Rev.* **1999**, *99*, 2071.
- 847 P. Wasserscheid, W. Keim, *Angew. Chem., Int. Ed.* **2000**, *39*, 3772.
- 848 R. Hagiwara, Y. Ito, *J. Fluorine Chem.* **2000**, *105*, 221.
- 849 R. Hagiwara, T. Hirashige, T. Tsuda, Y. Ito, *J. Fluorine Chem.* **1999**, *99*, 1.
- 850 R. Hagiwara, K. Matsumoto, Y. Nakamori, T. Tsuda, Y. Ito, H. Matsumoto, K. Momota, *J. Electrochem. Soc.* **2003**, *150*, D195.
- 851 D. R. MacFarlane, J. Golding, S. Forsyth, M. Forsyth, G. B. Deacon, *Chem. Commun.* **2001**, 1430.
- 852 Y. Yoshida, K. Muroi, A. Otsuka, G. Saito, M. Takahashi, T. Yoko, *Inorg. Chem.* **2004**, *43*, 1458.
- 853 A. A. Fannin, D. A. Floreani, L. A. King, J. S. Landers, B. J. Piersma, D. J. Stech, R. L. Vaughn, J. S. Wilkes, J. L. Williams, *J. Phys. Chem.* **1984**, *88*, 2614.
- 854 Y. Yoshida, A. Otsuka, G. Saito, S. Natsume, E. Nishibori, M. Takata, M. Sakata, M. Takahashi, T. Yoko, *Bull. Chem. Soc. Jpn.* **2005**, *78*, 1921.
- 855 G. Saito, in *Ionic Liquids: The Front and Future of Material Development*, ed. by H. Ohno, CMC, Tokyo, **2003**, pp. 137–143.
- 856 A. B. McEwen, H. L. Ngo, K. LeCompte, J. L. Goldman, *J. Electrochem. Soc.* **1999**, *146*, 1687.
- 857 A. Noda, K. Hayamizu, M. Watanabe, *J. Phys. Chem. B* **2001**, *105*, 4603.
- 858 T. Nishida, Y. Tashiro, M. Yamamoto, *J. Fluorine Chem.* **2003**, *120*, 135.
- 859 J. D. Holbrey, K. R. Seddon, *J. Chem. Soc., Dalton Trans.* **1999**, 2133.
- 860 M. Hirao, H. Sugimoto, H. Ohno, *J. Electrochem. Soc.* **2000**, *147*, 4168.
- 861 P. Walden, *Z. Phys. Chem.* **1912**, *78*, 257.
- 862 A. Einstein, *Ann. Phys.* **1905**, *17*, 549.
- 863 J. P. Hasan, I. R. McDonald, *Theory of Simple Liquids*, Academic Press, London, **1986**.
- 864 P. Bonhôte, A.-P. Dias, M. Armand, N. Papageorgiou, K. Kalyanasundaram, M. Grätzel, *Inorg. Chem.* **1996**, *35*, 1168.
- 865 S. A. Bolkan, J. T. Yoke, *J. Chem. Eng. Data* **1986**, *31*, 194.
- 866 K. Matsumoto, R. Hagiwara, Y. Ito, *J. Fluorine Chem.* **2002**, *115*, 133.
- 867 K. Matsumoto, R. Hagiwara, R. Yoshida, Y. Ito, Z. Mazej, P. Benkic, B. Zemva, O. Tamada, H. Yoshino, S. Matsubara, *Dalton Trans.* **2004**, 144.
- 868 E. I. Cooper, E. J. M. O'Sullivan, *Proc.-Electrochem. Soc.* **1992**, *92-16*, 386.
- 869 A. B. McEwen, J. L. Goldman, D. Wasel, L. Hargens, *Proc.-Electrochem. Soc.* **2000**, *99-41*, 222.
- 870 P. Wang, S. M. Zakeeruddin, J.-E. Moser, R. Humphry-Baker, M. Grätzel, *J. Am. Chem. Soc.* **2004**, *126*, 7164.
- 871 S. D. Williams, J. P. Schoebrechts, J. C. Selkirk, G. Mamantov, *J. Am. Chem. Soc.* **1987**, *109*, 2218.
- 872 Z.-B. Zhou, H. Matsumoto, K. Tatsumi, *Chem. Eur. J.* **2004**, *10*, 6581.
- 873 P. Wang, S. M. Zakeeruddin, R. Humphry-Baker, M. Grätzel, *Chem. Mater.* **2004**, *16*, 2694.
- 874 S. R. Marshall, C. D. Incarvito, W. W. Shum, A. L. Rheingold, J. S. Miller, *Chem. Commun.* **2002**, 3006.
- 875 Y. Yoshida, O. Baba, G. Saito, *J. Phys. Chem. B*, accepted.
- 876 F. Hensel, *Angew. Chem., Int. Ed. Engl.* **1980**, *19*, 593, and references therein.
- 877 S. Odenbach, *J. Phys.: Condens. Matter* **2004**, *16*, R1135.
- 878 N. Hirota, T. Homma, H. Sugawara, K. Kitazawa, M. Iwasaka, S. Ueno, H. Yokoi, Y. Kakudate, S. Fujiwara, M. Kawamura, *Jpn. J. Appl. Phys.* **1995**, *34*, L991.
- 879 E. G. Awere, N. Burford, C. Mailer, J. Passmore, M. J. Schriver, P. S. White, A. J. Banister, H. Oberhammer, L. H. Sutcliffe, *J. Chem. Soc., Chem. Commun.* **1987**, 66.
- 880 W. V. F. Brooks, N. Burford, J. Passmore, M. J. Schriver, L. H. Sutcliffe, *J. Chem. Soc., Chem. Commun.* **1987**, 69.
- 881 S. Brownridge, H. Du, S. A. Fairhurst, R. C. Haddon, H. Oberhammer, S. Parsons, J. Passmore, M. J. Schriver, L. H. Sutcliffe, N. P. C. Westwood, *J. Chem. Soc., Dalton Trans.* **2000**, 3365.
- 882 H. Du, R. C. Haddon, I. Krossing, J. Passmore, J. M. Rawson, M. J. Schriver, *Chem. Commun.* **2002**, 1836.
- 883 Y. Yoshida, J. Fujii, K. Muroi, A. Otsuka, G. Saito, M. Takahashi, T. Yoko, *Synth. Met.* **2005**, *153*, 421.
- 884 S. Hayashi, H. Hamaguchi, *Chem. Lett.* **2004**, *33*, 1590.
- 885 M. Faraday, *Experimental Researchs in Electricity*, **1939**, **1844**, **1855**.
- 886 V. Cannella, J. A. Mydosh, *Phys. Rev. B* **1972**, *6*, 4220.
- 887 S. F. Edwards, P. W. Anderson, *J. Phys. F: Met. Phys.* **1975**, *5*, 965.
- 888 W. Xu, E. I. Cooper, C. A. Angell, *J. Phys. Chem. B* **2003**, *107*, 6170.
- 889 Y. Yoshida, G. Saito, *J. Mater. Chem.* **2006**, *16*, 1254.
- 890 P. Kölle, R. Dronskowski, *Inorg. Chem.* **2004**, *43*, 2803.
- 891 H. J. Pedersen, J. C. Scott, K. Bechgaard, *Phys. Scr.* **1982**, *25*, 849.
- 892 Y. Yoshida, M. Sakata, G. Saito, K. Matsumoto, R. Hagiwara, to be published.
- 893 M. A. Kastner, R. J. Birgeneau, G. Shirane, Y. Endoh, *Rev. Mod. Phys.* **1998**, *70*, 897.
- 894 J. Kondo, *Prog. Theor. Phys.* **1964**, *32*, 37.
- 895 T. Enoki, A. Miyazaki, *Chem. Rev.* **2004**, *104*, 5449.
- 896 M. N. Baibich, J. M. Broto, A. Fert, V. D. F. Nguyen, F. Petroff, *Phys. Rev. Lett.* **1988**, *61*, 2472.
- 897 R. Chiarelli, M. A. Novak, A. Rassat, J. L. Tholence, *Nature* **1993**, *393*, 147.
- 898 J. S. Miller, J. C. Calabrese, A. J. Epstein, R. W. Bigelow, J. H. Zhang, W. M. Reiff, *J. Chem. Soc., Chem. Commun.* **1986**, 1026.

- 899 G. Du, J. Joo, A. Epstein, J. S. Miller, *J. Appl. Phys.* **1993**, 73, 6566.
- 900 M. Y. Ogawa, B. M. Hoffman, S. Lee, M. Yudkowsky, W. P. Halperin, *Phys. Rev. Lett.* **1986**, 57, 1177.
- 901 G. Quirion, M. Poirier, K. K. Liou, B. M. Hoffman, *Phys. Rev. B* **1991**, 43, 860.
- 902 L. Brossard, R. Clerac, C. Coulon, M. Tokumoto, T. Ziman, D. K. Petrov, V. N. Laukhin, M. J. Naughton, A. Audouard, F. Goze, A. Kobayashi, H. Kobayashi, P. Cassoux, *Eur. Phys. J. B* **1998**, 1, 439.
- 903 N. Hanasaki, H. Tajima, M. Matsuda, T. Naito, T. Inabe, *Phys. Rev. B* **2000**, 62, 5839.
- 904 K. Ishii, A. Fujiwara, H. Suematsu, Y. Kubozono, *Phys. Rev. B* **2002**, 65, 134431.
- 905 H. Tamaki, Z. J. Zhong, N. Matsumoto, S. Kida, M. Koikawa, N. Achiba, Y. Hashimoto, H. Okawa, *J. Am. Chem. Soc.* **1992**, 114, 6974.
- 906 H. Tamaki, M. Mitsumi, K. Nakamura, N. Matsumoto, S. Kida, H. Okawa, S. Iijima, *Chem. Lett.* **1992**, 1975.
- 907 E. Coronado, J. R. Galán-Mascarós, C. J. Gómez-García, *Synth. Met.* **1999**, 102, 1459.
- 908 L. O. Atovmyan, G. V. Shilov, R. N. Lyubovskaya, N. S. Ovanesyan, Yu. G. Morozov, S. I. Pirumova, I. G. Gusakovskaya, *Pis'ma Zh. Eksp. Teor. Fiz.* **1993**, 58, 818.
- 909 E. Coronado, J.-R. Galán-Mascarós, C.-J. Gómez-García, J. Ensling, P. Gütllich, *Chem. Eur. J.* **2000**, 6, 552.
- 910 E. Coronado, M. Clemente-León, J. R. Galán-Mascarós, C. Gliménez-Saiz, C. J. Gómez-García, E. Martínez-Ferrero, *J. Chem. Soc., Dalton Trans.* **2000**, 3955.
- 911 C. Mathoniere, C. J. Nuttall, S. G. Carling, P. Day, *Inorg. Chem.* **1996**, 35, 1201.
- 912 C. Mathoniere, S. G. Carling, D. Yusheng, P. Day, *J. Chem. Soc., Chem. Commun.* **1994**, 1551.
- 913 S. Bénard, P. Yu, T. Coradin, E. Riviére, K. Nakatani, R. Clément, *Adv. Mater.* **1997**, 9, 981.
- 914 E. Coronado, J. R. Galán-Mascarós, C. J. Gómez-García, V. Laukhin, *Nature* **2000**, 408, 447.
- 915 H. Yamochi, T. Kawasaki, Y. Nagata, M. Maesato, G. Saito, *Mol. Cryst. Liq. Cryst.* **2002**, 376, 113.
- 916 A. Alberola, E. Coronado, J. R. Galán-Mascarós, C. Giménez-Saiz, C. J. Gómez-García, *J. Am. Chem. Soc.* **2003**, 125, 10774.
- 917 H. Kobayashi, H. Tomita, T. Naito, A. Kobayashi, F. Sakai, T. Watanabe, P. Cassoux, *J. Am. Chem. Soc.* **1996**, 118, 368.
- 918 H. Matsui, H. Tsuchiya, T. Suzuki, E. Negishi, N. Toyota, *Phys. Rev. B* **2003**, 68, 155105.
- 919 N. Toyota, Y. Abe, H. Matsui, E. Negishi, Y. Ishizaki, H. Tsuchiya, H. Uozaki, S. Endo, *Phys. Rev. B* **2002**, 66, 033201.
- 920 H. Kobayashi, A. Sato, E. Arai, H. Akutsu, A. Kobayashi, P. Cassoux, *J. Am. Chem. Soc.* **1997**, 119, 12392.
- 921 E. Fujiwara, H. Fujiwara, H. Kobayashi, T. Otsuka, A. Kobayashi, *Adv. Mater.* **2002**, 14, 1376.
- 922 C. L. Lin, J. Teter, J. E. Crow, T. Mihalisin, J. Brooks, A. I. Abou-Aly, G. R. Stewart, *Phys. Rev. Lett.* **1985**, 54, 2541.
- 923 L. Ouahab, *Chem. Mater.* **1997**, 9, 1909.
- 924 L. Ouahab, *Coord. Chem. Rev.* **1998**, 178–180, 1501.
- 925 Y. Maruyama, S. Motohashi, N. Sakai, K. Watanabe, K. Suzuki, H. Ogata, Y. Kubozono, *Solid State Commun.* **2002**, 123, 229.
- 926 H. Posselt, H. Muller, K. Andres, G. Saito, *Phys. Rev. B* **1994**, 49, 15849.
- 927 H. Posselt, K. Andres, G. Saito, *Physica B* **1995**, 204, 159.
- 928 Yu. V. Sushko, K. Murata, H. Ito, T. Ishiguro, G. Saito, *Synth. Met.* **1995**, 70, 907.
- 929 S. Lefebvre, P. Wzietek, S. Brown, C. Bourbonnais, D. Jérôme, C. Mézière, M. Fourmigué, P. Batial, *Phys. Rev. Lett.* **2000**, 85, 5420.
- 930 P.-M. Allemand, K. C. Khemani, A. Koch, F. Wudl, K. Holczer, S. Donovan, G. Grüner, J. D. Thompson, *Science* **1991**, 253, 301.
- 931 A. Omerzu, D. Mihailovic, S. Tomic, O. Milat, N. Biskup, *Phys. Rev. Lett.* **1996**, 77, 2045.
- 932 T. L. Makarova, B. Sundqvist, R. Höhne, P. Esquinazi, Y. Kopelevich, P. Scharff, V. A. Davydov, L. S. Kashevarova, A. V. Rakhmanina, *Nature* **2001**, 413, 716.
- 933 T. L. Makarova, P. Scharff, B. Sundqvist, B. Narymbetov, H. Kobayashi, M. Tokumoto, V. A. Davydov, A. V. Rakhmanina, L. S. Kashevarova, *Synth. Met.* **2001**, 121, 1099.
- 934 V. D. Blank, S. G. Buga, N. R. Serebryanaya, G. A. Dubitsky, B. N. Mavrin, M. Yu. Popov, R. H. Bagramov, V. M. Prokhorov, S. N. Sulyanov, B. A. Kulnitskiy, Ye. V. Tatyatin, *Carbon* **1998**, 36, 665, and references therein.
- 935 T. Sugimoto, K. Ueda, S. Endo, N. Toyota, T. Tada, K. Nishimura, M. Kohama, K. Shiwaku, K. Yamamoto, T. Yamaguchi, Y. Suenaga, M. Munakata, *Chem. Phys. Lett.* **1998**, 288, 767.
- 936 F. Wudl, P. M. Allemand, P. Delhaes, Z. Soos, K. Hinkelmann, *Mol. Cryst. Liq. Cryst.* **1989**, 171, 179.
- 937 C. Reichardt, *Chem. Rev.* **1994**, 94, 2319.
- 938 N. A. Bell, D. J. Crouch, D. J. Simmonds, A. E. Goeta, T. Gelbrich, M. B. Hursthouse, *J. Mater. Chem.* **2002**, 12, 1274.
- 939 R. M. Metzger, N. R. Heimer, G. J. Ashwell, *Mol. Cryst. Liq. Cryst.* **1984**, 107, 133.
- 940 R. M. Metzger, B. Chen, U. Höpfner, M. V. Lakshmikantham, D. Vuillaume, T. Kawai, X. Wu, H. Tachibana, T. V. Hughes, H. Sakurai, J. W. Baldwin, C. Hosch, M. P. Cava, L. Brehmer, G. J. Ashwell, *J. Am. Chem. Soc.* **1997**, 119, 10455.
- 941 J. W. Baldwin, B. Chen, S. C. Street, V. V. Konovalov, H. Sakurai, T. V. Hughes, C. S. Simpson, M. V. Lakshmikantham, M. P. Cava, L. D. Kispert, R. M. Metzger, *J. Phys. Chem. B* **1999**, 103, 4269.
- 942 R. M. Metzger, *Acc. Chem. Res.* **1999**, 32, 950.
- 943 G. J. Ashwell, R. Hamilton, L. R. High, *J. Mater. Chem.* **2003**, 15, 1501.
- 944 D. J. Williams, *Angew. Chem., Int. Ed. Engl.* **1984**, 23, 690.
- 945 H. E. Katz, K. D. Singer, J. E. Sohn, C. W. Dirk, L. A. King, H. M. Gordon, *J. Am. Chem. Soc.* **1987**, 109, 6561.
- 946 S. R. Marder, J. W. Perry, G. Bourhill, C. B. Gorman, B. G. Tiemann, K. Mansour, *Science* **1993**, 261, 186.
- 947 S. R. Marder, C. B. Gorman, F. Meyers, J. W. Perry, G. Bourhill, J.-L. Bredas, B. M. Pierce, *Science* **1994**, 265, 632.
- 948 M. Barzoukas, C. Runser, A. Fort, M. Blanchard-Desce, *Chem. Phys. Lett.* **1996**, 257, 531.
- 949 M. Szablewski, P. R. Thomas, A. Thornton, D. Bloor, G. H. Cross, J. M. Cole, J. A. K. Howard, M. Malagoni, F. Meyers, J.-L. Bredas, W. Wenseleers, E. Goovaerts, *J. Am. Chem. Soc.* **1997**, 119, 3144.
- 950 J. Garin, J. Orduna, J. I. Ruperez, R. Alcala, B. Villacampa, C. Sanchez, N. Martin, J. L. Segura, M. Gonzalez, *Tetrahedron Lett.* **1998**, 39, 3577.
- 951 M. R. Bryce, A. Green, A. J. Moore, D. F. Perepichka, A. S. Batsanov, J. A. K. Howard, I. Ledoux-Rak, M. Gonzalez,

- N. Martin, J. L. Segura, J. Garin, J. Orduna, R. Alcala, B. Villacampa, *Eur. J. Org. Chem.* **2001**, 1927.
- 952 G. J. Ashwell, *Thin Solid Films* **1990**, *186*, 155.
- 953 T. Kogej, D. Beljonne, F. Mayers, J. W. Perry, S. R. Marder, J. L. Bredas, *Chem. Phys. Lett.* **1998**, *298*, 1.
- 954 D. Beljonne, T. Kogej, S. R. Marder, J. W. Perry, J. L. Bredas, *Nonlinear Opt.* **1999**, *21*, 461.
- 955 K. Higashino, T. Nakaya, E. Ishiguro, *J. Photochem. Photobiol., A* **1994**, *79*, 81.
- 956 R. M. Williams, J. M. Zwier, J. W. Verhoeven, *J. Am. Chem. Soc.* **1995**, *117*, 4093.
- 957 J.-F. Eckert, J.-F. Nicoud, J.-F. Nierengarten, S.-G. Liu, L. Echegoyen, F. Barigelletti, N. Armaroli, L. Ouali, V. Krasnikov, G. Hadzioannou, *J. Am. Chem. Soc.* **2000**, *122*, 7467.
- 958 G. J. Ashwell, E. J. C. Dawnay, A. P. Kucznski, M. Szablewski, I. M. Sandy, M. R. Bryce, A. M. Grainger, M. Hasan, *J. Chem. Soc., Faraday Trans.* **1990**, *86*, 1117.
- 959 Y. Oganer, M. Yin, D. R. Bessire, E. L. Quitevis, *J. Phys. Chem.* **1993**, *97*, 2344.
- 960 T. Suzuki, S. Miyinari, Y. Tsubata, T. Fukushima, T. Miyashi, Y. Yamashita, K. Imaeda, T. Ishida, T. Nogami, *J. Org. Chem.* **2001**, *66*, 216.
- 961 M. Szablewski, *J. Org. Chem.* **1994**, *59*, 954.
- 962 D. Buckley, S. Dunstan, B. Henbest, *J. Chem. Soc.* **1957**, 4880.
- 963 A. Broo, C. Zerner, *Chem. Phys.* **1995**, *196*, 407.
- 964 M. Pickholz, M. C. dos Santos, *J. Mol. Struct.* **1998**, *432*, 89.
- 965 J. S. Miller, J. C. Calabrese, *J. Chem. Soc., Chem. Commun.* **1988**, 63.
- 966 H. Seo, *J. Phys. Soc. Jpn.* **2000**, *69*, 805.
- 967 J. Catalan, E. Mena, W. Meutermans, J. Elguero, *J. Phys. Chem.* **1992**, *96*, 3615.
- 968 A. Broo, M. C. Zerner, *Chem. Phys.* **1995**, *196*, 423.
- 969 E. Alcalde, I. Dinarés, J. Elguero, J.-P. Fayet, M.-C. Vertut, C. Miravittles, E. Molins, *J. Org. Chem.* **1987**, *52*, 5009.
- 970 C.-H. Chong, M. Makihara, G. Saito, *Mol. Cryst. Liq. Cryst.* **2002**, *376*, 183.
- 971 G. Saito, C.-H. Chong, M. Makihara, A. Otsuka, H. Yamochi, *J. Am. Chem. Soc.* **2003**, *125*, 1134.
- 972 G. Saito, C.-H. Chong, K. Nishimura, Y. Enomoto, G. Honda, S. Khasanov, H. Yamochi, K. Kamada, K. Ohta, and J. Kawamata, to be published.
- 973 Y. Ogata, J. Kawamata, C.-H. Chong, A. Yamagishi, G. Saito, *Clays Clay Miner.* **2003**, *51*, 181.
- 974 C. Runser, A. Fort, M. Barzoukas, C. Combellas, C. Suba, A. Thiebault, R. Graff, J. P. Kintzinger, *Chem. Phys.* **1995**, *193*, 309.
- 975 Ref. 149, p. 382.
- 976 Th. Förster, *Z. Elektrochem.* **1939**, *45*, 549.
- 977 C. G. Swain, E. C. Lupton, Jr., *J. Am. Chem. Soc.* **1968**, *90*, 4328.
- 978 G. J. Ashwell, J. R. Sambles, A. S. Martin, W. G. Parker, M. Szablewski, *J. Chem. Soc., Chem. Commun.* **1990**, 1374.
- 979 A. S. Martin, J. R. Sambles, G. J. Ashwell, *Phys. Rev. Lett.* **1993**, *70*, 218.
- 980 J. C. Cole, J. A. K. Howard, *Acta Crystallogr., Sect. C* **1995**, *51*, 715.
- 981 S. Flandrois, D. Chasseau, *Acta Crystallogr., Sect. B* **1977**, *33*, 2744.
- 982 R. H. Baughman, B. E. Kohler, I. J. Levy, C. Spangler, *Synth. Met.* **1985**, *11*, 37.
- 983 For ionic C<sub>2</sub>-N<sub>1</sub> bonds, adopted the average value in seven crystal structures containing of open-form spiropyrans (CCDC reference: BAPNAH, BETGAI, GETGEM, FAFPOR, GUWFEJ, MOVYEB, WOGKIM). For neutral C<sub>2</sub>-N<sub>1</sub> bonds, adopted the average value in six crystals of indole-containing adducts (CCDC reference: EADIND, EBASEF, GIYKOO, HMAJIO, XATFAZ, ZIRFOV).
- 984 J. L. Brédas, C. Adant, P. Tackx, A. Persoons, B. M. Pierce, *Chem. Rev.* **1994**, *94*, 243.
- 985 R. S. Mulliken, *J. Am. Chem. Soc.* **1952**, *74*, 811.
- 986 J. Ducuing, C. Flytzanis, in *Optical Properties of Solids*, ed. by F. Abeles, North-Holland Pub., Amsterdam, **1972**, p. 863.
- 987 T. Gotoh, T. Kondoh, K. Egawa, K. Kubodera, *J. Opt. Soc. Am. B* **1989**, *6*, 703.
- 988 P. G. Huggard, W. Blau, D. Schweitzer, *Appl. Phys. Lett.* **1987**, *51*, 2183.
- 989 K. D. Truong, P. Grenier, D. Houde, A. D. Bandrauk, *Chem. Phys. Lett.* **1992**, *196*, 280.
- 990 W. Krätschmer, L. D. Lamb, K. Fostiropoulos, D. R. Huffman, *Nature* **1990**, *347*, 354.
- 991 R. C. Haddon, A. F. Hebard, M. J. Rosseinsky, D. W. Murphy, S. J. Duclos, K. B. Lyons, B. Miller, J. M. Rosamilia, R. M. Fleming, A. R. Kortan, S. H. Glarum, A. V. Makhija, A. J. Muller, R. H. Eick, S. M. Zahurak, R. Tycko, G. Dabbagh, F. A. Thiel, *Nature* **1991**, *350*, 320.
- 992 A. F. Hebard, M. J. Rosseinsky, R. C. Haddon, D. W. Murphy, S. H. Glarum, T. T. M. Palstra, A. P. Ramirez, A. R. Kortan, *Nature* **1991**, *350*, 600.
- 993 P. W. Stephens, L. Mihaly, P. L. Lee, R. L. Whetten, S.-M. Huang, R. Kaner, F. Diederich, K. Holczer, *Nature* **1991**, *351*, 632.
- 994 M. J. Rosseinsky, A. P. Ramirez, S. H. Glarum, D. W. Murphy, R. C. Haddon, A. F. Hebard, T. T. M. Palstra, A. R. Kortan, S. M. Zahurak, A. V. Makhija, *Phys. Rev. Lett.* **1991**, *66*, 2830.
- 995 K. Tanigaki, T. W. Ebbesen, S. Saito, J. Mizuki, J.-S. Tsai, Y. Kubo, S. Kuroshima, *Nature* **1991**, *352*, 222.
- 996 R. M. Fleming, A. P. Ramirez, M. J. Rosseinsky, D. W. Murphy, R. C. Haddon, S. M. Zahurak, A. V. Makhija, *Nature* **1991**, *352*, 787.
- 997 M. J. Rosseinsky, D. W. Murphy, R. M. Fleming, O. Zhou, *Nature* **1993**, *364*, 425.
- 998 T. T. M. Palstra, O. Zhou, Y. Iwasa, P. E. Sulewski, R. M. Fleming, B. R. Zegarski, *Solid State Commun.* **1995**, *93*, 323.
- 999 Y. Yoshida, Y. Kubozono, S. Kashino, Y. Murakami, *Chem. Phys. Lett.* **1998**, *291*, 31.
- 1000 O. Zhou, T. T. M. Palstra, Y. Iwasa, R. M. Fleming, A. F. Hebard, P. E. Sulewski, D. W. Murphy, B. R. Zegarski, *Phys. Rev. B* **1995**, *52*, 483.
- 1001 T. Yildirim, L. Barbedette, J. E. Fischer, C. L. Lin, J. Robert, P. Petit, T. T. M. Palstra, *Phys. Rev. Lett.* **1996**, *77*, 167.
- 1002 M. Kosaka, K. Tanigaki, K. Prassides, S. Margadonna, A. Lappas, C. M. Brown, A. N. Fitch, *Phys. Rev. B* **1999**, *59*, R6628.
- 1003 R. M. Fleming, M. J. Rosseinsky, A. P. Ramirez, D. W. Murphy, J. C. Tully, R. C. Haddon, T. Siegrist, R. Tycko, S. H. Glarum, P. Marsh, G. Dabbagh, S. M. Zahurak, A. V. Makhija, C. Hampton, *Nature* **1991**, *352*, 701.
- 1004 O. Zhou, J. E. Fischer, N. Coustel, S. Kycia, Q. Zhu, A. R. McGhie, W. J. Romanow, J. P. McCauley, Jr., A. B. Smith, III, D. E. Cox, *Nature* **1991**, *351*, 462.
- 1005 M. Knupfer, J. Fink, *Phys. Rev. Lett.* **1997**, *79*, 2714.
- 1006 E. Özdas, A. R. Kortan, N. Kopylov, A. P. Ramirez, T.

- Siegrist, K. M. Rabe, H. E. Bair, S. Schuppler, P. H. Citrin, *Nature* **1995**, 375, 126.
- 1007 X. H. Chen, G. Roth, *Phys. Rev. B* **1995**, 52, 15534.
- 1008 M. Baenitz, M. Heinze, K. Lüders, H. Werner, R. Schlögl, M. Weiden, G. Sparn, F. Steglich, *Solid State Commun.* **1995**, 96, 539.
- 1009 C. M. Brown, S. Taga, B. Gogia, K. Kordatos, S. Margadonna, K. Prassides, Y. Iwasa, K. Tanigaki, A. N. Fitch, P. Pattison, *Phys. Rev. Lett.* **1999**, 83, 2258.
- 1010 Y. Ksari-Habiles, D. Claves, G. Chouteau, Ph. Touzain, Cl. Jeandey, J. L. Oddou, A. Stepanov, *J. Phys. Chem. Solids* **1997**, 58, 1771.
- 1011 O. Gunnarsson, *Rev. Mod. Phys.* **1997**, 69, 575.
- 1012 D. V. Konarev, I. S. Neretin, Yu. L. Slovokhotov, A. L. Litvinov, A. Otsuka, R. N. Lyubovskaya, G. Saito, *Synth. Met.* **2002**, 131, 87.
- 1013 A. Izuoka, T. Tachikawa, T. Sugawara, M. Konno, Y. Saito, H. Shinohara, *J. Chem. Soc., Chem. Commun.* **1992**, 1472.
- 1014 G.-W. Wang, K. Komatsu, Y. Murata, M. Shiro, *Nature* **1997**, 387, 583.
- 1015 A. V. Soldatov, G. Roth, A. Dzyabchenko, D. Johnels, S. Lebedkin, C. Meingast, B. Sundqvist, M. Haluska, H. Kuzmany, *Science* **2001**, 293, 680.
- 1016 J. C. Hummelen, B. Knight, J. Pavlovich, R. Gonzales, F. Wudl, *Science* **1995**, 269, 1554.
- 1017 O. Chauvet, G. Oszlányi, L. Forró, P. W. Stephens, M. Tegze, G. Faigel, A. Jánossy, *Phys. Rev. Lett.* **1994**, 72, 2721.
- 1018 M. Kosaka, K. Tanigaki, T. Tanaka, T. Atake, A. Lappas, K. Prassides, *Phys. Rev. B* **1995**, 51, 12018.
- 1019 E. Bommeli, L. Degiorgi, P. Wachter, Ö. Legeza, A. Jánossy, G. Oszlányi, O. Chauvet, L. Forró, *Phys. Rev. B* **1995**, 51, 14794.
- 1020 P. W. Stephens, G. Bortel, G. Faigel, M. Tegze, A. Jánossy, S. Pekker, G. Oszlányi, L. Forró, *Nature* **1994**, 370, 636.
- 1021 Q. Zhu, D. E. Cox, J. E. Fischer, *Phys. Rev. B* **1995**, 51, 3966.
- 1022 G. Oszlányi, G. Bortel, G. Faigel, M. Tegze, L. Gránásy, S. Pekker, P. W. Stephens, G. Bendele, R. Dinnebier, G. Mihály, A. Jánossy, O. Chauvet, L. Forró, *Phys. Rev. B* **1995**, 51, 12228.
- 1023 G. Oszlányi, G. Bortel, G. Faigel, L. Gránásy, G. M. Bendele, P. W. Stephens, L. Forró, *Phys. Rev. B* **1996**, 54, 11849.
- 1024 V. Brouet, H. Alloul, F. Quere, G. Baumgartner, K. Follo, *Phys. Rev. Lett.* **1999**, 82, 2131.
- 1025 V. Brouet, H. Alloul, L. Forro, *Phys. Rev. B* **2002**, 66, 155123.
- 1026 D. V. Konarev, S. S. Khasanov, G. Saito, R. N. Lyubovskaya, *Recent Res. Dev. Chem.* **2004**, 2, 105.
- 1027 K. Mizoguchi, M. Machino, H. Sakamoto, T. Kawamoto, M. Tokumoto, A. Omerzu, D. Mihailovic, *Phys. Rev. B* **2001**, 63, 140417.
- 1028 S. Garaj, T. Kambe, L. Forró, A. Sienkiewicz, M. Fujiwara, K. Oshima, *Phys. Rev. B* **2003**, 68, 144430.
- 1029 K. Mizoguchi, M. Takei, M. Machino, H. Sakamoto, M. Tokumoto, T. Kawamoto, A. Omerzu, D. Mihailovic, *J. Magn. Magn. Mater.* **2004**, 272–276, e215.
- 1030 D. V. Konarev, S. S. Khasanov, G. Saito, A. Otsuka, Y. Yoshida, R. N. Lyubovskaya, *J. Am. Chem. Soc.* **2003**, 125, 10074.
- 1031 A. Hönnerscheid, L. van Wüllen, M. Jansen, J. Rahmer, M. Mehring, *J. Chem. Phys.* **2001**, 115, 7161.
- 1032 A. Hönnerscheid, R. Dinnebier, M. Jansen, *Acta Crystallogr., Sect. B* **2002**, 58, 482.
- 1033 D. V. Konarev, S. S. Khasanov, A. Otsuka, G. Saito, *J. Am. Chem. Soc.* **2002**, 124, 8520.
- 1034 K. Oshima, T. Kambe, M. Fujiwara, Y. Nogami, *Synth. Met.* **2003**, 133–134, 699.
- 1035 D. V. Konarev, S. S. Khasanov, I. I. Vorontsov, G. Saito, M. Yu. Antipin, A. Otsuka, R. N. Lyubovskaya, *Chem. Commun.* **2002**, 2548.
- 1036 Y. Yoshida, A. Otsuka, D. V. Konarev, G. Saito, *Synth. Met.* **2003**, 133–134, 703.
- 1037 Y. Yoshida, A. Otsuka, O. O. Drozdova, K. Yakushi, G. Saito, *J. Mater. Chem.* **2003**, 13, 252.
- 1038 H. Brumm, E. Peters, M. Jansen, *Angew. Chem., Int. Ed.* **2001**, 40, 2069.
- 1039 U. Wedig, H. Brumm, M. Jansen, *Chem. Eur. J.* **2002**, 8, 2769.
- 1040 G. M. Bendele, P. W. Stephens, K. Prassides, K. Vavekis, K. Kordatos, K. Tanigaki, *Phys. Rev. Lett.* **1998**, 80, 736.
- 1041 K. Prassides, K. Vavekis, K. Kordatos, K. Tanigaki, G. M. Bendele, P. W. Stephens, *J. Am. Chem. Soc.* **1997**, 119, 834.
- 1042 S. Margadonna, K. Prassides, K. Knudsen, M. Hanfland, M. Kosaka, K. Tanigaki, *Chem. Mater.* **1999**, 11, 2960.
- 1043 G. Oszlányi, G. Baumgarther, G. Faigel, L. Forró, *Phys. Rev. Lett.* **1997**, 78, 4438.
- 1044 D. V. Konarev, I. S. Neretin, G. Saito, Yu. L. Slovokhotov, A. Otsuka, R. N. Lyubovskaya, *Eur. J. Inorg. Chem.* **2004**, 1794.
- 1045 D. V. Konarev, I. S. Neretin, G. Saito, Yu. L. Slovokhotov, A. Otsuka, R. N. Lyubovskaya, *Dalton Trans.* **2003**, 3886.
- 1046 D. V. Konarev, S. S. Khasanov, G. Saito, R. N. Lyubovskaya, Y. Yoshida, A. Otsuka, *Chem. Eur. J.* **2003**, 9, 3837.
- 1047 D. V. Konarev, S. S. Khasanov, A. Otsuka, Y. Yoshida, G. Saito, *J. Am. Chem. Soc.* **2002**, 124, 7648.
- 1048 Q. Zhu, O. Zhou, J. E. Fischer, A. R. McGhie, W. J. Romanow, R. M. Strongin, M. A. Cichy, A. B. Smith, III, *Phys. Rev. B* **1993**, 47, 13948.
- 1049 M. C. Martin, D. Koller, X. Du, P. W. Stephens, L. Mihaly, *Phys. Rev. B* **1994**, 49, 10818.
- 1050 A. Lappas, M. Kosaka, K. Tanigaki, K. Prassides, *J. Am. Chem. Soc.* **1995**, 117, 7560.
- 1051 P. R. Birkett, A. G. Avent, A. D. Darwish, H. W. Kroto, R. Taylor, D. R. M. Walton, *J. Chem. Soc., Chem. Commun.* **1993**, 1230.
- 1052 P. R. Birkett, P. B. Hitchcock, H. W. Kroto, R. Taylor, D. R. M. Walton, *Nature* **1992**, 357, 479.
- 1053 Y. Yoshida, A. Otsuka, O. O. Drozdova, G. Saito, *J. Am. Chem. Soc.* **2000**, 122, 7244.
- 1054 M. Keshavarz-K, B. Knight, G. Srdanov, F. Wudl, *J. Am. Chem. Soc.* **1995**, 117, 11371.
- 1055 Y. Yoshida, A. Otsuka, G. Saito, *Mol. Cryst. Liq. Cryst.* **2002**, 376, 189.
- 1056 Z. Suo, X. Wei, K. Zhou, Y. Zhang, C. Li, Z. Xu, *J. Chem. Soc., Dalton Trans.* **1998**, 3875.
- 1057 M. Tokumoto, Y. Tsubaki, K. Pokhodnya, A. Omerzu, T. Uchida, D. Mihailovic, *Synth. Met.* **1999**, 103, 2316.
- 1058 T. Kambe, Y. Nogami, K. Oshima, *Phys. Rev. B* **2000**, 61, R862.
- 1059 Y. Deligiannakis, G. Papavassiliou, M. Fardis, G. Diamantopoulos, F. Milia, C. Christides, K. I. Pokhodnya, V. Barchuk, *Phys. Rev. Lett.* **1999**, 83, 1435.
- 1060 B. Narymbetov, H. Kobayashi, M. Tokumoto, A. Omerzu, D. Mihailovic, *Chem. Commun.* **1999**, 1511.
- 1061 A. Mrzel, P. Cevc, A. Omerzu, D. Mihailovic, *Phys. Rev. B*

- 1996, 53, R2922.
- 1062 B. Narymbetov, A. Omerzu, V. V. Kabanov, M. Tokumoto, H. Kobayashi, D. Mihailovic, *Nature* **2000**, 407, 883.
- 1063 D. V. Konarev, R. N. Lyubovskaya, *Russ. Chem. Rev.* **1999**, 68, 19.
- 1064 B. Gotschy, *Fullerene Sci. Technol.* **1996**, 4, 677.
- 1065 R. Saito, G. Dresselhaus, M. S. Dresselhaus, *Chem. Phys. Lett.* **1993**, 210, 159.
- 1066 F. Negri, G. Orlandi, F. Zerbetto, *J. Am. Chem. Soc.* **1992**, 114, 2909.
- 1067 P. C. Trulove, R. T. Carlin, G. R. Eaton, S. S. Eaton, *J. Am. Chem. Soc.* **1995**, 117, 6265.
- 1068 P. D. W. Boyd, P. Bhyrappa, P. Paul, J. Stinchcombe, R. D. Bolskar, Y. Sun, C. A. Reed, *J. Am. Chem. Soc.* **1995**, 117, 2907.
- 1069 T. F. Fässler, A. Spiekermann, M. E. Spahr, R. Nesper, *Angew. Chem., Int. Ed. Engl.* **1997**, 36, 486.
- 1070 P. Paul, K.-C. Kim, D. Sun, P. D. W. Boyd, C. A. Reed, *J. Am. Chem. Soc.* **2002**, 124, 4394.
- 1071 D. V. Konarev, S. S. Khasanov, G. Saito, I. I. Vorontsov, A. Otsuka, R. N. Lyubovskaya, Yu. M. Antipin, *Inorg. Chem.* **2003**, 42, 3706.
- 1072 A. Otsuka, G. Saito, T. Teramoto, Y. Sugita, T. Ban, A. A. Zakhidov, K. Yakushi, *Mol. Cryst. Liq. Cryst.* **1996**, 284, 345.
- 1073 A. Otsuka, G. Saito, Zakhidov, K. Yakushi, M. Kusunoki, K. Sakaguchi, *Mol. Cryst. Liq. Cryst.* **1996**, 285, 187.
- 1074 C. Bossard, S. Rigaut, D. Astruc, M.-H. Delville, G. Félix, A. Février-Bouvier, J. Amiell, S. Flandrois, P. Delhaès, *J. Chem. Soc., Chem. Commun.* **1993**, 333.
- 1075 P. Bhyrappa, P. Paul, J. Stinchcombe, P. D. W. Boyd, C. A. Reed, *J. Am. Chem. Soc.* **1993**, 115, 11004.
- 1076 R. E. Douthwaite, M. A. Green, M. L. H. Green, M. J. Rosseinsky, *J. Mater. Chem.* **1996**, 6, 1913.
- 1077 C. Janiak, S. Mühle, H. Hemling, K. Köhler, *Polyhedron* **1996**, 15, 1559.
- 1078 T. F. Fässler, R. Hoffmann, S. Hoffmann, M. Wörle, *Angew. Chem., Int. Ed.* **2000**, 39, 2091.
- 1079 D. V. Konarev, S. S. Khasanov, G. Saito, R. N. Lyubovskaya, *J. Porph. Phthal.* **2003**, 7, 801.
- 1080 C. A. Foss, Jr., D. L. Feldheim, D. R. Lawson, P. K. Dorhout, C. M. Elliott, C. R. Martin, B. A. Parkinson, *J. Electrochem. Soc.* **1993**, 140, L84.
- 1081 W. C. Wan, X. Liu, G. M. Sweeney, W. E. Broderick, *J. Am. Chem. Soc.* **1995**, 117, 9580.
- 1082 W. E. Broderick, K. W. Choi, W. C. Wan, *Proc.-Electrochem. Soc.* **1997**, 97-14, 1102.
- 1083 H. Moriyama, M. Abe, S. Hanazato, H. Motoki, T. Watanabe, H. Kobayashi, *Synth. Met.* **1999**, 103, 2374.
- 1084 H. Yamochi, G. Saito, T. Sugano, M. Kinoshita, C. Katayama, J. Tanaka, *Chem. Lett.* **1986**, 1303.
- 1085 T. Ida, K. Yakushi, H. Kuroda, H. Yamochi, G. Saito, *Chem. Phys.* **1991**, 156, 113.
- 1086 M. Sakata, M. Maesato, G. Saito, T. Yamamoto, K. Yakushi, S. S. Khasanov, N. G. Spitsina, A. D. Dubrovskii, E. B. Yagubskii, P. Deplano, M. L. Mercuri, in *Multifunctional Conducting Molecular Materials*, ed. by G. Saito, F. Wudl, R. C. Haddon, K. Tanigaki, T. Enoki, H. E. Katz, M. Maesato, RSC Publishing, Cambridge, **2007**, pp. 91–96. (ET)<sub>3</sub>(AuBr<sub>2</sub>)<sub>2</sub>-(AuBr<sub>4</sub>)<sub>2</sub> exhibits the charge disproportionation in spite of metallic conductivity.
- 1087 A. Ota, Ph.D. thesis, Kyoto University, **2005**.

#### Award recipient



Gunzi Saito received his Ph.D. degree from Hokkaido University in 1972. He was a postdoctoral fellow in U.S.A. and Canada (1973–1979), a research associate at the Institute for Molecular Science (1979–1984), an associate professor at the Institute for Solid State Physics of The University of Tokyo (1984–1989), and a professor at the Department of Chemistry, Faculty of Science, Kyoto University (1989–1994). Now he has been a professor at the Chemistry Division, Graduate School of Science, Kyoto University (1994–). He was also a visiting professor in Université de Rennes I (1998, 2002, 2003). From 2002, he is serving as a leader of the 21st Century COE Program entitled “Kyoto University Alliance for Chemistry.” His awards include the Inoue Prize for Science (1987), the Nishina Memorial Prize (1988), the SSSJ Paper Award (1991), the CSJ Award (2003), and the BCSJ Award (2005). He was a chairman of the ISSP international conference (1989) and the fourth ISCOM (2001). He has been devoted in the development of molecular compounds in the  $\pi$ -system with exotic functionality.



Yukihiro Yoshida received his B.Sci. degree from Okayama University in the study on C<sub>60</sub> superconductors (1996), and Ph.D. degree from Kyoto University in the study on charge-transfer complexes based on C<sub>60</sub> derivatives (2001). He currently is a postdoctoral research fellow at Kyoto University. In 2005, he received the BCSJ Award for his work on paramagnetic ionic liquids. His present research interests include charge-transfer complexes, organic–inorganic layered compounds, and ionic liquids.